OXIDATION BEHAVIOUR OF TiAlN BASED NANOLAYERED HARD COATINGS

Mirkka Ingrid Lembke

A thesis submitted in partial fulfilment of the requirements of Sheffield Hallam University for the degree of Doctor of Philosophy.

October 2001

ABSTRACT

The oxidation behaviour of TiAlN based hard coatings with the addition of Cr and/ or Y was investigated using scanning electron microscopy, scanning/ transmission electron microscopy, energy dispersive X-ray analysis, thermogravimetry and X-ray diffraction. The coatings were deposited using the combined cathodic arc/ unbalanced magnetron deposition technique. The main practical application of these films is dry high speed cutting in difficult to cut materials such as AISI A2 steel. Especially in the case of TiAlCrYN coating with an oxynitride and Cr-enriched overcoat, extensive research on the oxidation behaviour was performed and described here. Heat treatments in air between 600-1000°C for different duration were carried out.

The $Ti_{0.44}Al_{0.54}Cr_{0.02}N$ coating was used as the starting point for the investigations. The effect of heat on the composition of the interface region was investigated. This region is of utmost importance for the adhesion of the film. In the case of TiAlCrN the interface stability was not guaranteed because of diffusion of the substrate elements Cr and Fe to the coating surface after annealing for 1h at 900°C. In comparison, the diffusion of substrate elements Cr and Fe in a ~2.3μm thick coating of $Ti_{0.43}Al_{0.52}Cr_{0.03}Y_{0.02}N$ and of $Ti_{0.34}Al_{0.62}Cr_{0.03}Y_{0.01}N$ with overcoat, reached only a distance of ~600nm into the coating. This was achieved by the diffusion of Y to the grain boundaries. Y probably reacted at the same time with inward diffusing O. The diffusion of Y to the boundaries was observed after heat treatment for 1h at 900°C or 10h at 800°C.

$Ti_{0.26}Al_{0.26}N/Cr_{0.48}N$ was the coating with the least oxide layer growth after oxidation for 1h at 900°C. An oxide layer thickness of only ~100nm was measured. For the TiAlCrYN coating with overcoat an oxide layer of 230nm and for TiAlCrYN of 430nm formed after 1h at 900°C. TiAlCrN in comparison formed an oxide layer of ~800nm after 1h at 900°C.

The oxide layers formed after 1h at 900°C consisted mainly of an Al_2O_3 and TiO_2 bi-layer in the case of TiAlCrN and TiAlCrYN. The addition of a Cr-rich oxynitride overcoat led to the formation of a mixture out of Al_2O_3, Cr_2O_3 and TiO_2 in the oxide layer. In the case of TiAlN/CrN, a solid solution consisting of Cr_2O_3 and Al_2O_3 was observed. In general a stress relief after heat treatment was observed. At the same time the formation of voids along the column boundaries was identified. This was explained with the relaxation and diffusion of defects created during the deposition process.

The effect of different substrate materials on the oxidation behaviour was also investigated. It was found that the formation of substrate oxides on the coating surface is very much dependent on the onset point of oxidation of the substrate material itself. The oxidation of substrate material occurred mainly through growth defects and pinholes. In cases where cracks formed during heat treatment of the coating, the formation of oxides out of substrate elements were observed in cracks connecting the substrate with the coating surface. Changing the bias voltage altered the formation of cracks.

This research emphasises the importance of Y in the oxidation mechanism of TiAlN based hard coatings. Y blocks the diffusion path along the column boundaries and thus slowed down the diffusion and oxidation process. At the same time the addition of Cr can increase the oxidation resistance considerably, which was observed in the TiAlCrYN coating with and without overcoat.

ACKNOWLEDGEMENTS

I like to thank the following people:

- Thanks to my family.
- Thanks to Prof. Dieter Münz who offered me the PhD post in the first place.
- Special thanks to Prof. John Titchmarsh who helped me and this thesis a great deal with access to special equipment and a lot of his time although he is no longer with Sheffield Hallam University.
- Thanks to Dr. Brian Lewis for being a friend, spending time in fine tuning my English, doing Friday papers and helping me with my "science".
- Thanks to Gary Robinson and Russ Day.
- Thanks to Prof. Ivan Petrov to invite me over to America and Mr. Chan-Soo Chin who did the RBS measurements and analysis for me.
- Thanks to John Muirhead and Cornelia Schöhnjahn who shared an office with me and were good friends.
- Special thanks to my dear friends Nick Jackson and Maria Romero for their ever available support.

There are of course many more people that would deserve personalised acknowledgement: The people at various departments at the University that helped with explanations or with malfunctioning equipment. Friends that made my life fun outside work with coffee breaks, salsa dancing, badminton, cinema and video nights, chocolate fondue (chocolate had to be mentioned), unforgettable dinners and parties and of course English pool billiard!

PUBLICATIONS

Papers directly related to this work:

*M.I. Lembke, J.M. Titchmarsh, W.-D. Münz, *Transmission microscopy investigation of the oxidation of hard coatings for high speed machine tools*, Proceedings of Electron Microscopy and Analysis 2001, Dundee UK, September 2001

W.-D. Münz, M.I. Lembke, D.B. Lewis, I.J. Smith, *Microstructure, composition and performance of PVD coatings designed for successful dry high speed milling*, Proceedings 15th International Plansee Seminar, Reutte, Austria, April 2001

*M.I. Lembke, D.B. Lewis, W.-D. Münz, J.M. Titchmarsh, *Significance of Y and Cr in TiAlN hard coatings for dry high speed cutting*, **Surface Engineering**, 17, 2, 153-158

*M.I. Lembke, J.M. Titchmarsh, D.B. Lewis, W.-D. Münz, *Investigation of the oxidation behaviour of a TiAlCrYN PVD hard coating*, Proceedings MRS Fall Meeting 2000, Boston USA, 28 November, 2000

M.I. Lembke, D.B. Lewis, W.-D. Münz, *Improvement in the oxidation behaviour of superlattice structured TiAlN/CrN grown by cathodic arc/ unbalanced magnetron deposition technique*, Proceedings of Materials Week, Munic, Germany, 25-28. September 2000

*M.I. Lembke, D.B. Lewis, W.-D. Münz, *Localised oxidation defects in TiAlN/CrN superlattice structured hard coatings grown by cathodic arc/ unbalanced magnetron deposition on various substrate materials*, **Surface and Coatings Technology**,125 (2000), 263-268

M.I. Lembke, D.B. Lewis, J.M. Titchmarsh, W.-D. Münz, *Structural changes after heat treatment of physical vapour deposited TiAlCrYN coatings*, IOM Conference Proceedings, Quantitative microscopy of high temperature materials, Sheffield UK, 22-24 November 1999

*D.B. Lewis, L.A. Donohue, M. Lembke, W.-D. Münz, R. KuzelJr., V. Valvoda, C.J. Blomfield, *The influence of the yttrium content on the structure and properties of TiAlCrYN hard coatings*, **Surface and Coatings Technology**, 114 (1999), 187-199

Papers not directly related to this PhD

*H. Paritong, M. Lembke, D.B. Lewis, W.-D. Münz, *Characterisation of co-sputtered Nb:Cr coatings grown by the combined cathodic arc/ unbalanced magnetron sputtering technique*, **Surface and Coatings Technology**, 116-119 (1999), 1145-1151

*G. Nayal, D.B. Lewis, M. Lembke, W.-D. Münz, J.E. Cockrem, *Influence of sample geometry on the effect of pulse plasma nitriding of M2 steel*, **Surface and Coatings Technology**, 111 (1999), 148-157

The refereed and/ or published papers are included in APPENDIX I
Refereed papers are marked with a *

ADVANCED STUDIES

The following conferences, workshops were attended and talks given during my PhD studies:

(i) The Third – Sixth ABS Days at Sheffield Hallam University, 1997 – 2000

(ii) Workshop on high temperature wear by the Institute of Materials in London, June, 1998

(iii) The 14th International Vacuum Congress in Birmingham, August 1998

(iv) The European Materials Society Spring Meeting (E-MRS) in Strasbourg, France, June 1999

(v) The Quantitative Microscopy of High Temperature Materials, Conference from the Institute of Materials in Sheffield, November 1999

(vi) Postgraduate research student poster competition at The University of Leeds, May, 2000

(vii) New developments in FEG/EM organised by the Royal Microscopy Society and the Electron Microscopy Analysis Group in Oxford, July, 2000

(viii) The Euromat Conference in Munich, September 2000

(ix) Presentation on the occasion of the Bodycote Prize Paper Competition in Maccesfield, November 2000

(x) The Fall Meeting 2000 from the Materials Research Society in Boston, USA, November, 2000

It was a great experience to present my results at the University of Urbana Champaign, Urbana, USA to the research group of Prof. J. Greene and Prof. I. Petrov.

ABBREVIATIONS

A2	AISI A2 steel
ABS	Arc Bond Sputtering
BF	Bright Field Image
CA	Cathodic Arc
CC	Cemented Carbide (WC in 10% Co matrix, Sandvik H 10 F)
DF	Dark Field Image
DP	Diffraction Pattern
d_{ox}	Oxide Layer Thickness
E_a	Activation Energy
EDX-analysis	Energy Dispersive X-ray analysis
GDOES	Glow Discharge Optical Emission Spectroscopy
I_{coil}	Coil Current During Coating Process
M2	High speed steel AISI M2 grade
MD	Movchan and Demchishin Model
Me	Metal
PECVD	Plasma Activated Chemical Vapour Deposition
R_a	Roughness [in microns] on Polished Substrates
RT	Room Temperature, used to indicate as-deposited samples
RBS	Rutherford Backscattering
SEA	Selected Area Aperture
SEM	Scanning Electron Microscopy
SNMS	Secondary Neutral Mass Spectroscopy
SS	Stainless Steel AISI 304
STEM	Scanning Transmission Electron Microscopy
T	Temperature in °C
T_m	Melting Temperature
T_s	Substrate Temperature
t	Time
TEM	Transmission Electron Microscopy
TG	Thermogravimetry
TiAlCrYN+Ox	TiAlCrYN with oxynitride overcoat
TiAlN/CrN	The / indicates the presence of a nanolayered structure out of TiAlN and CrN identified using XRD
U_{bias}	Bias Voltage at the Substrate during Coating Process
UBM	Unbalanced Magnetron
XRD	X-ray Diffraction
XTEM	Cross Sectional TEM
Z	Mass of Atom

The composition of the coatings is given in the text in atomic percent (at%) with the metal content normalised to 100%.

Non SI Units used:

Zero at the Celsius Temperature Scale used (°C) ~ 273K

CONTENT

1 INTRODUCTION

One of the research interests of the Surface Engineering Group at Sheffield Hallam University is the development of physical vapour deposited hard coatings to protect dry high speed cutting tools [1, 2, 3]. In 80% of all performed cutting operations coated tools are used [4]. Industry demands faster cutting process, higher quality and longer life-time of the cutting tools, hence further development of hard coatings is necessary. By the term hard coating, films with hardness values in the range of $HK_{0.25}$ 2000-4000 are implied.

The physical vapour deposition technique uses ion bombardment to produce a thin film on a substrate. The main advantages of PVD over other techniques like CVD are the low deposition temperatures, typically below 500°C, the smooth surface finish and the good adhesion [5]. Higher reliability of PVD coated tools over CVD coated tools was also reported [6]. Thin films of around 2-3μm are generally sufficient to protect the cutting edge. A combination of cathodic arc and sputter deposition was shown to create good adhesion, smooth surfaces and the use of a wide variety of materials [7].

Through the low deposition temperatures (below 500°C) metastable structures are observed, which create a unique set of materials with new properties. These new materials can be used in hard material coating systems up to 1000°C [8]. These hard coatings can be improved in many ways, changing the structure and/ or composition, increasing the hardness and improving the wear behaviour [9, 10]. More and more sophisticated coatings are needed to be able to keep up with different specialised demands like low temperature deposition, high corrosion resistance, oxidation resistance and good wear resistance.

Binary coatings are also referred to as first generation and ternary coatings as second generation films. The second generation coatings TiAlN and TiCN used for tool protection were a break through, because of higher hardness and longer life-time than the first generation coating TiN. TiAlN has advantages over TiCN and TiN, because of its high oxidation resistance up to 850°C [11, 12] compared to TiN and TiCN, which oxidise at 550°C and 450°C, respectively.

The development of specialised hard coatings like TiAlCrYN [13] was a solution from Sheffield to satisfy this demand.

Composite or layered structures are ways of improving properties of hard coatings. Nanolayered coatings have typically two different alternating components and layered structure of less than 10nm [14, 15]. Various combinations of nanolayers have proven to increase the properties of coatings in terms of hardness [14], wear resistance [16, 17] and corrosion resistance [18], [19] and [20]. TiN and TiAlN are frequently used layer materials. Combinations like TiN/Ti [19], and TiAlN/CrN [21] were reported to have improved properties in terms of corrosion protection and oxidation behaviour, respectively. Improvement in dry high speed cutting and oxidation resistance of TiAlN was achieved by adding Cr and Y [13]. The oxidation resistance is a very important parameter for the development of coatings for dry high speed cutting, due to the temperatures developed at the cutting edge [21, 22, 23].

TiAlCrYN has been successfully applied mainly on cemented carbide tools in a commercial production machine [1]. Other coatings like TiAlN/CrN, due to its high oxidation resistance [21] and with the very low friction coefficient are also very interesting coatings for dry high-speed cutting. The oxidation behaviour is seen as one of the key factors to improve the life-time in dry high speed cutting operations. To be able to further improve these properties an in depth knowledge of the coatings oxidation behaviour is necessary.

The aim of this study was to understand the oxidation behaviour of the TiAlCrYN coating and nanolayered TiAlN/CrN coating in more detail and to compare it to TiAlCrN. Wear creates oxidised particles; it might therefore help to understand the coating properties, when the oxidation behaviour is analysed. Another important part of these investigations was the behaviour of growth defects during heat treatment. Growth defects are inevitably created, due to droplet deposition using a cathodic metal ion etch to create the good adhesion needed in cutting applications [24, 25].

Investigations in the oxidation behaviour of PVD hard coatings exist, but they are reported mainly for specific coatings and compounds. TiN, CrN and TiAlN are systems long enough on the market to have a more extended coverage in terms of oxidation behaviour [11, 12, 26, 27, 28, 29, 30, 31]. From these coating systems it was obvious, that the deposition process can vary

those properties. Research results from other systems like MeCrAlY alloys can offer hints and ideas only, because of the different nature of the system. For a specialised application, like dry high speed cutting, investigations on the real coating system are important to be able to improve it further.

The following aspects of oxidation of hard coatings were investigated:

The first investigations were made on $Ti_{0.44}Al_{0.54}Cr_{0.02}N$, because it is used as a basis for the other coatings under investigation, by adding Y or increasing the amount of Cr in the coating. The combination of thermogravimetry, scanning and transmission electron microscopy, X-ray diffraction and STEM with EDX analysis should allow investigation of the coating in detail. Thermogravimetry and XRD allow the overall oxidation behaviour to be investigated. With SEM and EDX it was possible to study some local differences in the oxidation behaviour on defects. TEM and STEM-EDX on cross sectional samples provided information about the structure and changes in composition of the surface and the interface region of the coating. The combination of research methods employed should contribute to existing knowledge of TiAlN based coatings. An understanding of the properties of $Ti_{0.44}Al_{0.54}Cr_{0.02}N$ will help to understand the other films under investigation. Additions of Y or Cr into the TiAlCrN process led to the formation of TiAlCrYN and TiAlN/CrN. The results on $Ti_{0.44}Al_{0.54}Cr_{0.02}N$ shall help to point out specific points of excellence of the other films.

In the case of $Ti_{0.43}Al_{0.52}Cr_{0.03}Y_{0.02}N$, the original film [32, 33] and coatings out of the production machine with ($Ti_{0.34}Al_{0.62}Cr_{0.03}Y_{0.012}N$) and without a special designed oxynitride topcoat ($Ti_{0.48}Al_{0.48}Cr_{0.03}Y_{0.14}N$) were compared to each other. TiAlCrYN with a topcoat (Supercote 11) is an improvement of the original TiAlCrYN coating and used in commercial applications. It is frequently produced by Bodycote SHU Ltd. Some of the research methods were not previously applied to the original coating, therefore it was re-characterised in this study to be able to make comparison to the TiAlCrYN with oxynitride topcoat. The effect of temperature (constant time of 10h) and time (constant temperature of 900°C) was investigated.

The effect on the oxidation behaviour of the nanolayered $Ti_{0.26}Al_{0.26}N/Cr_{0.28}N$ coating was investigated (i) by adding Cr to $Ti_{0.44}Al_{0.54}Cr_{0.02}N$ and (ii) by varying

the bias voltage in the TiAlN/CrN system. The TiAlN/CrN coating deposited with 8kW power on the Cr target has the best mechanical properties [21].

The TiAlCrYN coating and the TiAlN/CrN 8kW systems were additionally analysed concerning the oxidation behaviour of growth defects.

2 LITERATURE REVIEW

TiAlN based hard coatings are used in dry high speed cutting applications to increase the life-time of the cutting tools. The tool requires protection against the high temperatures and forces created at the cutting edge. An understanding of the oxidation mechanism of the hard coating and the coating process will allow an improvement in the coating behaviour.

2.1 Physical Vapour Deposition

There are many different PVD techniques. Steered CA and UBM, are two techniques of the PVD family and have been used in a combined process known as ABS to deposit the coatings used. In both methods target material is vaporised and transported through the chamber under vacuum conditions (10^{-3} – 10^{-2}mbar) to the substrate material. An arc is used to vaporise material from the target in arc evaporation. In sputter deposition the target material is vaporised by ion bombardment. The reaction between metal species and reactive species like N_2 or O_2 takes place on the substrate surface to generate, e.g. nitrides and oxides. The CA and UBM techniques are described in detail after the ABS technology. A more detailed understanding is necessary to interpret the appearance of growth defects or a fine grained microstructure, instead of a columnar growth structure, in the films produced.

2.1.1 ABS Technology

The Arc Bond Sputter technique, employed in the present study, combines the two PVD techniques of 'Steered Cathodic Arc Evaporation' and 'Closed Field- Unbalanced Magnetron Sputtering' [7]. The idea behind this arrangement is the combination of the advantages of each technology into one system [7], [34]. The main advantages used from both techniques are summarised in

Figure 2-1. The superior film adhesion needed for dry high speed cutting operations can be obtained by ion implantation with species stemming from a steered CA discharge. The substrate is bombarded with multiply charged metal ions from the arc source with energies of typically 2.4keV [35]. This provides in case of Cr^{+2} as etchant high etching rates and less influence of residual gases [36, 37]. The UBM sputtering allows droplet free material deposition and a high controllable degree of ion bombardment of the growing film, which is important to adjust the film properties. The degree of ionisation of the magnetron plasma is around 10%, whereas the arc plasma has a maximum of 90% ionisation measured close to the target [38]. The UBM technique offers also the bigger versatility in material selections.

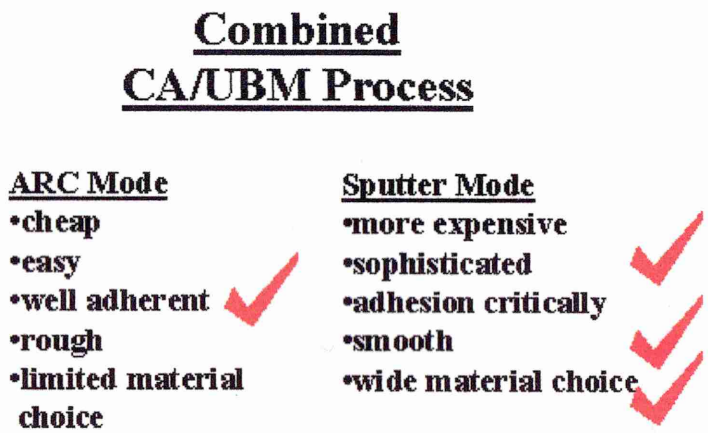

Figure 2-1: Advantages of the combined cathodic arc/ unbalanced magnetron deposition process.

As a result of these characteristics a "typical" ABS process employs the arc source for the substrate sputter cleaning and ion implantation step prior to coating deposition, while the film deposition is carried out using unbalanced magnetron sputtering. The key process steps have been described in [2, 7].

To enable CA and UBM deposition the cathodes were specially designed. This was an important step to be able to combine the properties of both techniques [7, 34]. High pumping speed and good process control are needed

for reactive sputter deposition of stoichiometric films. These important features are described in more detail below:

2.1.1.1 *Cathode design*

The special configuration of the magnets at the cathode (Figure 2-2) and the special layout of the power supply enabled the change between the different techniques. The magnetron arrangement of the permanent magnet array (CoSm magnets) is enhanced (Figure 2-2). The degree of unbalancing can be adjusted using concentric electron coils (B≈200-300 Gauss). This provides practically free control over the magnetic field confinement and the bias current density by adjusting the coil current. In the arc mode the distance between the pole areas of the magnetic array behind the cathode and the cathode body is increased, which lowers the magnetic field at the target surface (B≈50 Gauss), to allow steered arc operation via the coils. The difference between the horizontal magnetic component in magnetron sputter and cathodic arc mode is approximately 200-500G to 20-50G, respectively. A magnetic coil surrounds each target and enables, to some extent, a control over the racetrack of the arc [7]. Work in designing a multi-purpose cathode was also performed by [39].

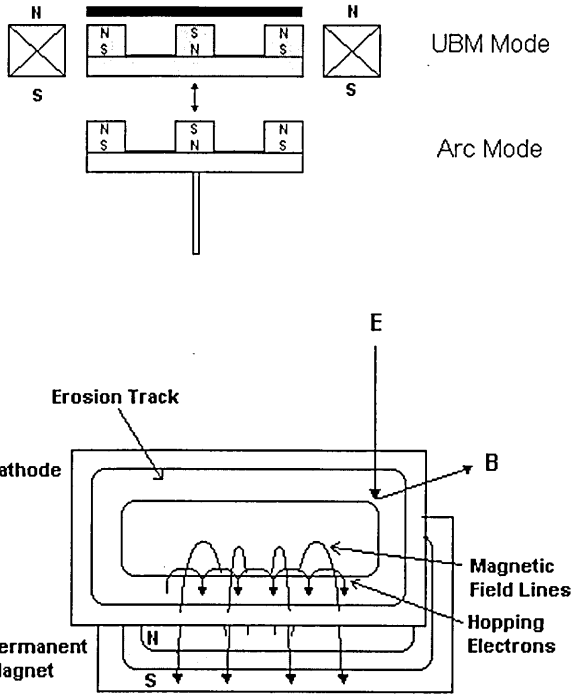

Figure 2-2: Special cathode designed for combined CA and UBM process and a target with field lines and erosion zone.

2.1.1.2 Process control

Process control is of major importance in reactive sputtering. A slight change in parameters can change the properties of the coating deposited. Some important features for process control on the machine used are the high pumping speed, the reactive gas control, the cathode design and the unbalancing via the outer coils. The high pumping speed allows to control the amount of reactive gas (nitrogen) over the pressure instead of a mass spectrometer. The reason for this is that a hysteresis found in a pressure flow diagram (Figure 2-3) disappears by increasing the pumping speed [40], [2].

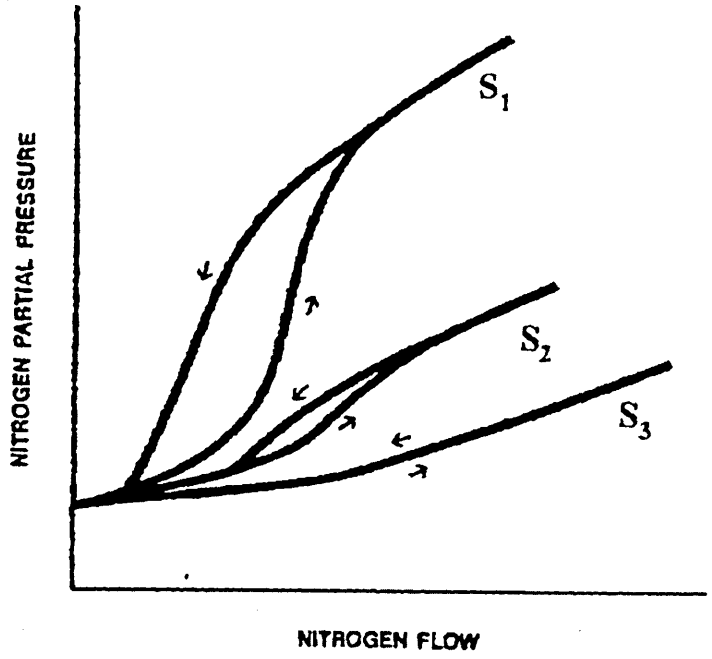

Figure 2-3: Schematic drawing of the effect of system pumping speed S on the hysteresis loop for S1 < S2 < S3 [41]

2.1.1.3 Pumping speed

The Hauzer HTC 1000-4 and HTC 1000/5 coating machines provide a very high nominal pumping speed (4400 ls^{-1} providing optimum suitability for reactive coating processes [34]. The vacuum system pumping speed is one way to

ensure stoichiometric films and avoid target poisoning, by avoiding the partial pressure/ gas flow hysteresis effect [41], [34]. Argon gas is used as working gas and to create a minimum pressure level. The total pressure is precisely controlled by a highly accurate manometer (Leybold Viscovac $\pm 0.2X10^{-3}$mbar). The gas consumption is controlled by this instrument using constant total pressure control in the range from $5x10^{-5}$ to $8x10^{-3}$ mbar. The resulting partial pressure, depending on the gas type used, is virtually proportional to the flow-regulated argon gas feed. [34]. This allows control over the stoichiometry of the coating via the total gas pressure.

2.1.2 Unbalanced Magnetron Deposition

Sputtering is a vaporisation process in which surface atoms are physically ejected from a surface by momentum transfer from an energetic bombarding species of atomic/ molecular size [42]. It is an attractive method, because of the wide choice of materials available for sputter deposition. The typical voltage/ current region to create a glow discharge is shown in Figure 2-4. The principle arrangement for DC sputtering uses the material to be bombarded by ions as a cathode (target) and the substrate holder as anode under specific vacuum conditions.

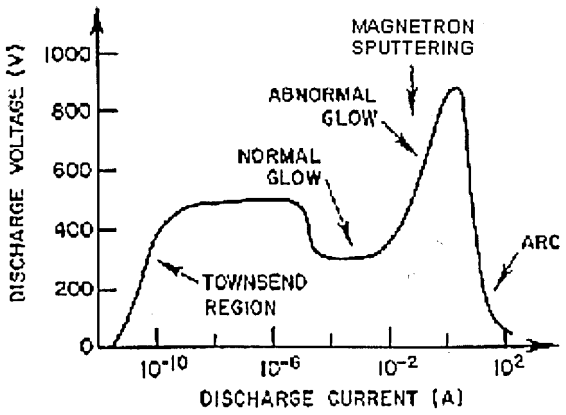

Figure 2-4: Current-voltage relation for the various types of plasma discharges between two powered electrodes

UBM deposition is a development of the simple DC arrangement. Argon is mostly used as a working gas to bombard the target, because it is non-reactive, relatively cheap and its ions have, due to their mass, enough kinetic energy to produce a good sputter yield [38]. Ions from the working gas are accelerated towards the target surface. An ion that strikes the cathode generates heat, neutral atoms, some ions and secondary electrons. The secondary electrons are primarily responsible to sustain the glow discharge [38], [42]. The energetic state and the energy of impinging ions on the substrate surface is in general lower than for arc evaporation, hence the rate of film growth is lower than for arc evaporation.

A higher efficiency of the sputter method is achieved by magnetron deposition. With a magnetic field behind the target surface the electrons are confined and the ionisation is increased. In case of the planar magnetron a looping magnetic field is used, which restricts the sputter erosion of the target to a "racetrack" [38] (p. 268). Magnetron sputtering allows high deposition rates. However, the resulting bias current densities and the influence on the current density at the substrate are low. This influence is of major importance, enabling changes in the coating structure without using the bias voltage, which would increase the amount of trapped working gas the incorporation of defects and stress in the coating [42]. With unbalancing the magnetron it is possible to alter the ion flux on the substrate Figure 2-5 [43]. It also provides the possibility to increase the target substrate distance. TiN deposited films on substrates 200mm away from the target with current densities as high as 6mA/cm^2 have been reported [44], which is similar to ion plating techniques [45]. This allows production of hard wear resistant coatings at low substrate temperatures [44]. The unbalanced magnetron has the additional benefit that the ion energy and the ion flux can be varied independently of one another.

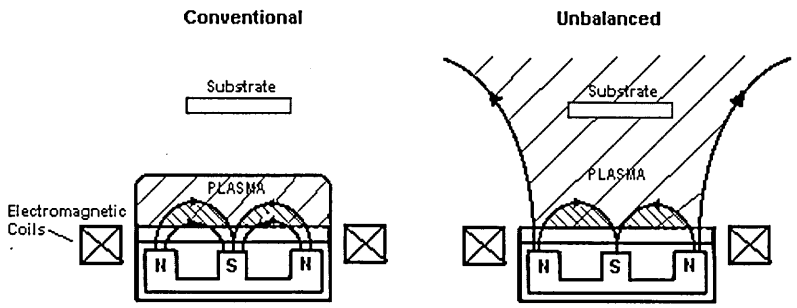

Figure 2-5: Magnetic field confinement in planar geometry and in UBM geometry.

2.1.2.1 *Closed field unbalanced magnetron sputtering*

The ABS system utilises a closed magnetic field system, which confines the plasma between the cathodes through magnetic fields. This system increases the efficiency of the UBM further and allowed coating of complex three dimensional substrates [7], [46].

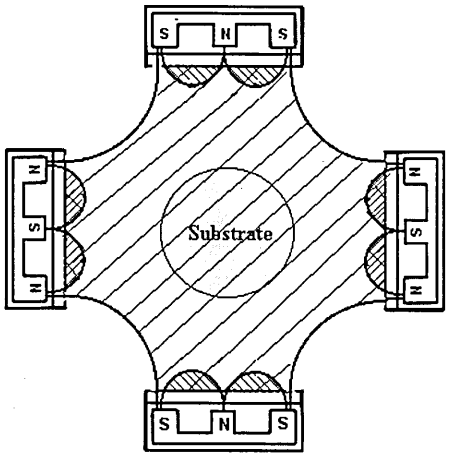

Figure 2-6: Cathode, substrate and magnetic field arrangement in the Hauzer machine used. The coils surrounding the cathode are not shown.

The Hauzer 1000-4 coating machine is an unbalanced magnetron four-cathode system of industrial size (cathode 600x198mm^2). The magnetic polarisation in this machine alternates from cathode to cathode (Figure 2-6). Opposing cathodes have the same polarisation. The closed magnetic field minimises the loss of charge carriers to the machine walls. The confined plasma creates a mean bias current density of 2 mAcm^{-2} in a distance of approximately 30cm. The ion-to-neutral arrival ratio achieved is similar to an ion plating system. The electromagnets around the cathode control the unbalancing effect and allow an adjustment of the degree of ionisation in the chamber. The substrate temperature and the ion to neutral ratio are adjustable independently of the coating rate [7]. This allows deposition of dense coatings at low temperatures.

2.1.3 Cathodic Arc Deposition

In the arc deposition technology a highly energetic cathode spot is created to vaporise the target material thermally. To create an arc the target material is used as cathode, where the arc is initiated, and the vacuum chamber wall as an anode. The voltage/ current energy region for creating an arc is illustrated in Figure 2-4. The ions have high energies (multiply charged), typically 50-100eV, and are predominantly emitted perpendicular to the target surface [47]; [48].

The substrate material is often negatively biased to attract more ions. The high energy of impinging ions on the substrate can lead to sputter etching or ion implantation. The applied substrate bias voltage and the resulting bias current density play a key role in changing the effects upon the substrate surface and in creating the adhesion needed [37, 47, 49]. A cathodic arc Cr-ion etch with -1200V bias was shown to remove at least 100nm material after 20min etching time thus providing a thoroughly cleaned surface and to generate an implantation zone of 7nm in the steel substrate [37].

In the steered arc method developed by [50] the arc is captured by the magnetic field of a permanent magnet. Rotation of the magnet during evaporation causes the arc to follow. The advantage of the steered arc technology over the random arc is, that the arc spot cannot stay for a prolonged period on a spot, which reduces the amount of droplets produced. A stationary magnetic field coil, positioned behind the target, can be used to guide the arc and increase the velocity of the arc spot over the surface [51]. The higher the speed of the arc the lower is the number of droplets produced. Without this magnetic array the arc moves randomly. Additional confinement of the arc spot cathode was achieved by using a magnetic permeable ring (boron nitride) [52]. This confinement guides the arc back on the target surface and prevents other parts of the machine from flash evaporation.

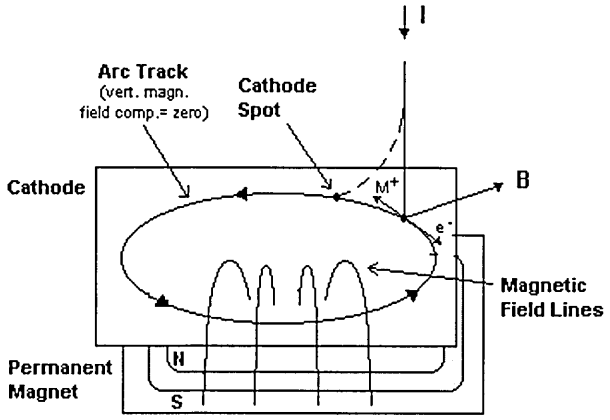

Figure 2-7: Arc spot motion in a steered cathodic arc

The arc spot creates electrons and ions. The charged state of this source is the reason why the arc can be steered by a magnetic field. The arc spot sits preferentially at the point where the vertical component of the magnetic field is zero [53], resulting in an arc track as shown in Figure 2-7. Due to the Hall effect, the arc will travel along this track at high velocity. The spot velocity increases with increasing magnetic field and saturates at a certain field (V = 10-100ms^{-1}) [47]. The direction of the arc motion is known as "retrograde", it moves against the Ampere rule. This arises from the fact that the current is mainly carried by the positive ions, hence reversing the direction of the Hall effect occurs.

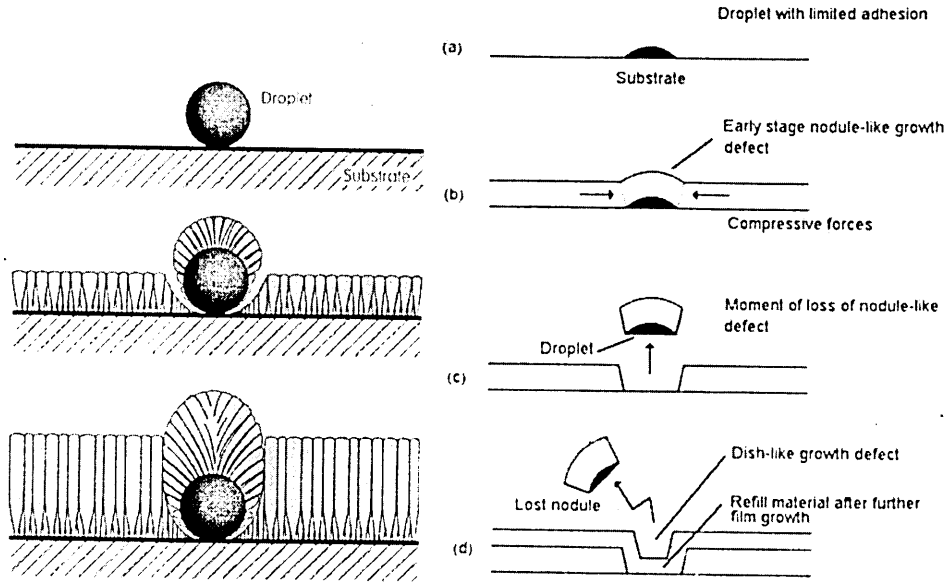

Figure 2-8: Schematic of the formation of a nodular defect overgrowing an arc-induced macro-particle [54] and of the creation of defects in TiN and TiAlN coatings [55].

One of the drawbacks of the cathodic arc deposition are macroparticles generated in the metal ion etching stage which result in the formation of growth defects [24, 25, 34, 55, 56]. It was shown, that the size and the number of droplets are substantially reduced by the steered cathodic arc Cr metal ion etch in comparison to Ti or Ar etches [24, 25]. The droplet size can be reduced with the different melting point of the cathode material. Other ways to reduce the amount of droplets would be to increase the speed of the arc, reduce the cathode current density and effective cleaning of the cathodes [47], [56].

Why are droplets problematic? Droplets are shadowing the surface to be coated. This results in an attenuated ion and deposition flux, creating a defect structure that surrounds the droplet. A low-density zone or even a gap between growth defect grain structure and the coating is produced (Figure 2-8) [54]. In other cases the droplets and the defects, grown on the droplets, may be expelled from the coating during film growth (Figure 2-8), due to compressive stresses generated by the growing film [55]. The low density zone is preferentially attacked by corrosive media [18], [57] and oxidation at elevated temperatures [58].

2.2 Microstructure and properties

In vapour deposition processes coatings are formed from a flux of atoms that approaches the substrate from a limited range of directions and as a result of this the microstructure of the coating is columnar in nature. It is obvious that the columnar structure is a disadvantage for oxidation or corrosion protection of substrates, because a quick diffusion path between substrate and coating surface exists along the column boundaries [59], [60]. It is desirable to control the structure of the coating and to know more about the influencing factors.

2.2.1 Structure Zone Models – Influence of Various Coating Parameters

It has been mentioned before that the process parameters, such as substrate temperature, gas pressure, ion-to-neutral ratio and the bias voltage, influence the coating structure. The coating structure influences coating properties such as hardness and stress, which was demonstrated for various coating systems (TiAlN) [62], (TiN) [63], (general) [64], (Ta) [65].

Movchan and Demchishin [66] developed the first model of a coating based on observations from vacuum evaporation. It correlated three structural zones to the ratio T/T_m , where T_m is the melting point of the coating material. The model described three zones. The first zone has a porous tapered columnar structure with domed tops; zone II consists of denser columnar grains with

smooth surfaces; and zone III consists of dense equiaxed grains. Computer simulations showed that low adatom mobility can account for the microstructure in zone I because it leads to atomic self-shadowing which results in incorporation of microvoids. At a certain substrate temperature the adatom mobility is sufficiently high to change the structure from porous columnar to a structure with no microvoids [67].

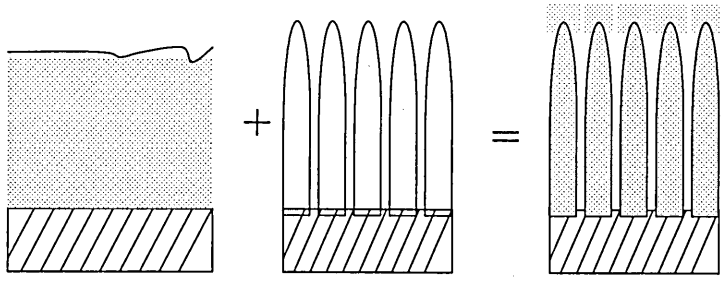

Figure 2-9: Schematic of a PVD coating structure. An intrinsic grain structure is superimposed upon a columnar structure that can be defined by voided boundaries [59].

Thornton introduced a schematic [59] of the superposition of growth and microstructures for films deposited under conditions of low adatom mobility (zone I) and pointed out that the boundaries are energetically preferred (Figure 2-9). The activation energies for surface, grain boundary, and bulk diffusion are typically in the ratio 1:2:4 so that at T/T_m < 0.5 surface and grain boundary diffusion rates can be orders of magnitude larger than bulk diffusion rates. Messier pointed out that it is important to consider voids and columns not as singular entities in modelling; practical considerations like diffusion through voids cannot be thought of in terms of Fick's law but rather like blood flowing through a system of veins and arteries as they permeate every part of a body [60]. Fortunately, it has been shown that by increasing the adatom mobility, the structure of PVD coatings can be positively influenced:

Thornton and Messier investigated the influence of gas pressure and bias voltage (ion bombardment) on the microstructure, respectively, and developed the Movchan-Demchishin model further. The Thornton model [61] includes an additional 'Zone T' which consists of densely packed fibrous grains between zone I and II (Figure 2-10). Messier [68] replaced the pressure axis with a bias

voltage axis. His model includes therefore an additional ion energy contribution to the film growth. He found that an increase in bias voltage suppressed the formation of zone 1 or widened zone T, due to the enhanced adatom mobility.

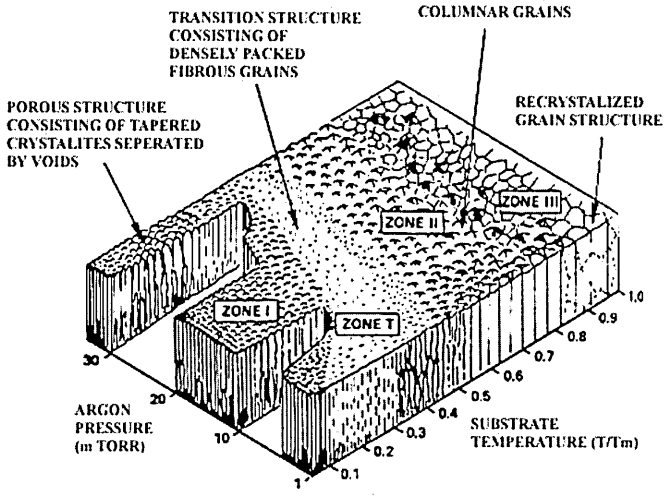

Figure 2-10: Thornton's structure zone model [61].

Freller et al. [69] postulated the growth of dense coatings at bias current densities > 2 mA cm^{-2} and a substrate temperature of 300°C. Transmission electron microscope investigations on coatings where the ion-to-neutral arrival ratio at the substrate was varied showed, that an ion-to-neutral ratio of/ or above 4 was sufficient to cause the growth of dense films with a more equiaxed grain structure, due to renucleation [70]. Grain refinement was achieved by increasing the ion-to-neutral ratio arrival ratio on the substrate [63]. An attempt was made to find a universal energy parameter to account for the ion energy and the ion to neutral ratio incident at the growing film [71]. Investigations performed on TiAlN films showed that the properties of the coating are different, depending on varying the ion energy or the ion-to-neutral ratio. From this it was concluded that no universal parameter exists combining these two parameters. Ion energy and ion flux are considered as fundamental parameters with separate effects [72].

The variations of the previously mentioned parameters have a direct influence when specimens with edges (such as end mills) are coated. It was found in arc deposition that the surface roughened towards the edge, due to a higher concentration of macro-particles, if a bias voltage was applied. The

reason was seen in the ion current density, which is higher at the edge than on the flat surface. When an interrupted bias (0V/ -100V) coating process was used, reduced macro-particle accumulation on the edge was observed. Additionally, variations of the deposition rate and the atomic composition were observed between the edge and the flat surface, due to different ion current densities [73].

These models showed the possibility of engineering the coating structure for a particular application and the importance of controlling the parameters separately. Grain refinement and a dense structure are important properties for corrosion or high temperature resistant films.

2.2.2 Multicomponent and Multilayer coatings

Coatings designed to fulfil a specialised task are frequently multicomponent or multilayer coatings. The binary coatings are often not able to fulfil all required properties at the interface and at the coating surface at the same time (Figure 2-11). Holleck was one of the first to discuss the possibilities of multicomponent coatings to improve certain properties [9], together with other researchers in this field (TiN) [74] (TiAlN) [12].

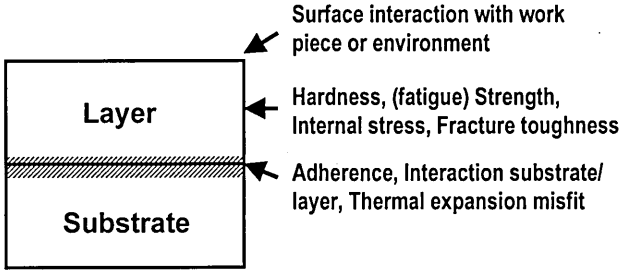

Figure 2-11: Schematic showing important regions of a coating, that need to be optimised for a specific task [9]. The properties required of a coating for dry high speed cutting are: (i) low friction coefficient, good wear resistance of the surface, (ii) heat resistant coating, (iii) interface that has to withstand the mechanical forces applied.

Another way of improving tool coatings was achieved by using multilayer coatings with a layer thickness in the nm range. These coatings have properties that cannot be achieved with a multicomponent coating of a similar composition. Helmersson and co-workers [14] combined TiN and VN and achieved an increase in hardness by about 2.5 times more than would be expected from the "rule of mixtures". The unique properties of multilayered hard coatings could lead to materials with hardness approaching that of diamond (Figure 2-12).

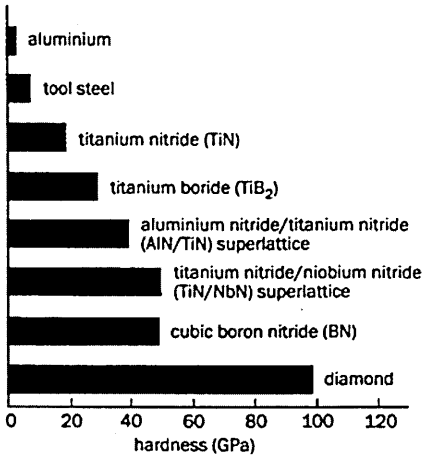

Figure 2-12: Comparison of hardness values of a range of common materials [75].

The high hardness materials achievable with multilayering have many applications wherever resistance to abrasion and wear are important. Other terms used for multilayer coatings are superlattice structure [14], [76] and nano-laminates [27]. The increase in hardness at a certain bi-layer period was termed the "superlattice-" or "supermodulus-effect". The superlattice effect was reported when the bi-layer was in the range of several nanometers. Table 2-1 shows various nanolayered compounds where a superlattice effect has been reported.

Coatings	Multilayer Version
TiVN $HV_{0.01}$ 2200 $_{01}$ [14]	TiN/VN $HV_{0.01}$ 5400 $_{01}$ [14]
TiNbN $HK_{0.025}$ 2200-2400 [77]	TiN/NbN HV 3400 [78]
TiAlN $HK_{0.025}$ 2300-2400 [77]	TiN/AlN $HK_{0.05}$ 4000 $_{05}$ [79]
TiZrN $HK_{0.025}$ 2400-3600 [77]	TiAlN/ZrN $HK_{0.025}$ 4000 [77]

Table 2-1: Various examples of coatings were a supermodulus effect was achieved by multilayering.

Various reasons for the superlattice effect are given, all relate to restricted dislocation movement: Dislocations are mainly responsible for plastic deformation in crystals. Restricting the dislocation movement should strengthen the material; an energy barrier is created by the lattice close to the interface. It takes a higher degree of energy for a dislocation to move over the interface barrier. For miscible materials such as TiN/NbN the interfaces between layers can be at least 1nm wide. Broader interfaces reduce the effect of the alternating layers as the interface occupies a much greater proportion of the layer thickness. This also happens when the bi-layer is very small (1-2nm). It has been suggested that multilayers that are not isostructural could have an advantage over isostructural materials because their interface would be more abrupt.

Multilayer coatings showed other positive properties arising from the layered structure. It was found that cracks are deflected at the interface zone [16], different failure mechanism were reported for a TiAlN/CrN and a TiAlN coating in the initial stages of the wear behaviour. The multilayer coating abraded by delamination of the first view layers [17].

Non-isostructural and immiscible superlattice structures are also under speculations that their superlattice structure would stay stable at elevated temperatures [75].

2.3 General Oxidation Theories

Basic oxidation principles can be explained by referring to the oxidation behaviour of metals. Most metals, with the exception of noble metals such as gold form an oxide film on the surface when in contact with oxygen, although the reaction is sometimes very slow. The thickness and appearance of the oxide film depends on variables such as temperature, purity of oxygen gas, the surface of the metal and the crystallographic orientation [80] (p.1).

Oxidation starts at the metal gas interface and a very thin oxide layer will form, between the metal and the reactive gas. The layer between the metal and the gas interface can have various shapes. Further reactions can take place through a compact layer or one that contains pores and/ or cracks. This further reaction may involve atomic diffusion or the diffusion of gas molecules through the cavities or along grain boundaries, leading to many possible diffusion behaviours, and rate controlling models. Oxide layer formation can be observed in a metal if various different oxides exist (e.g. Fe). In the case of an alloy either one or all the components react with the gas. The resulting layer may be a mixture of different particles or clearly subdivided into individual layers. [81] (p.88, 112).

2.3.1 Effects on Rate laws

Careful analysis of rate data can help to limit the possible oxidation mechanisms. The most common rate mechanisms are of logarithmic, parabolic, and linear nature (Figure 2-13), although they represent only limited and ideal cases. A combination of laws is also quite often encountered.

In the case of rate law investigations of oxidation on hard coatings the parabolic rate law is frequently observed [11, 28, 29, 82, 83]. The investigated time frame ranges from typically 30min to 2 hours. Unfortunately, often no detailed description of the oxidation method and the structure of the oxide layer formed is given. The data was often presented only as an Arrhenius type plot,

which makes cross comparison difficult. In the following section the parabolic rate law and its most common interpretation are presented in more detail, an explanation of the Arrhenius equation will be given.

Furthermore, diffusion mechanism, oxide layer properties and the effect of expansion of the oxide layer will be explained in more detail in chapter 2.3.1 and 2.3.2. These are properties that can be altered by changing the composition of the coating.

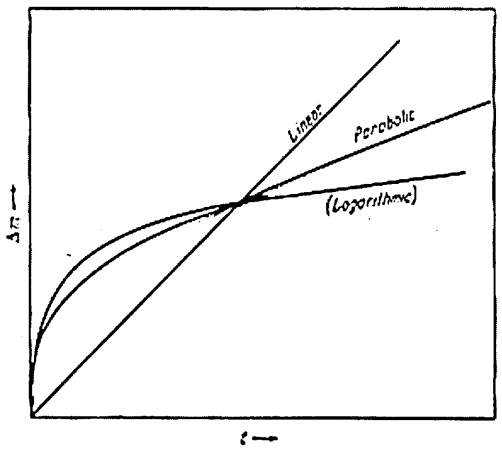

Figure 2-13: Different rate laws, weight gain plotted against time [80] (p.36)

2.3.1.1 *Parabolic rate equation*

At high temperatures many metals and coatings (chapter 2.3.1) were found to follow a parabolic time dependence. The parabolic rate equation is given by:

$$x^2 = k_p t \qquad \text{Equation 2-1}$$

where k_p is the parabolic rate constant and t the time the reaction was monitored. The variable x can be the weight gain or the oxide layer thickness.

High-temperature parabolic oxidation is characteristic of processes where thermal diffusion is rate determining. It can contain either a uniform diffusion of one or both of the reactants through a growing compact scale (Wagner mechanism) or a uniform diffusion of gas into metal.

However, without careful investigation the parabolic and logarithmic curves can appear quite similar.

2.3.1.2 *Wagner's Theory*

Wagner's theory explains the parabolic behaviour observed in oxidation investigations. It applies to solid scales resulting from oxidation. It explains the parabolic oxidation behaviour by considering the diffusion of anions, cations and electrons as a rate controlling mechanism. Pores or cracks modify this oxidation mechanism. The following assumptions are made when this model is applied: The oxide scale shows only small deviations from stoichiometry and the oxygen solubility in the metal can be neglected [84].

The diffusion occurs through the oxide layer. Thermodynamic equilibrium is established at these interfaces by the diffusion of charged particles (ions and electrons) through the oxide layer. The driving force of the reaction is the free energy change (by forming the metal-oxide) and, as a result, concentration gradients are established through the scale. P- and N-type semiconductor oxides diffuse in different ways, due to their defect structure [80]. The established equation for this type of diffusion is parabolic in nature. After 50 years of research Wagner's assumption is still valid for understanding the parabolic oxidation rate. Even so, there are numerous conditions for which his assumptions do not apply, including: a) non-stoichiometric precipitants, b) internal-oxide bands, c) dual oxidants and d) precipitate morphology [85].

2.3.1.3 *Defect structures*

For reactions involving the diffusion in oxides a knowledge of the defect structures of the oxides is essential [80] (p.15). However, in practical oxidation work, pores and cracks have to be considered as diffusion paths [80] (p.64), [59]. If a lower electrical conductivity is achieved by e.g. alloying (doping), fewer electrons and ions diffuse, hence the oxidation rate is lowered [80] (p.25). The knowledge of the oxidation rate allows the prediction of the oxidation mechanism to a certain degree.

2.3.1.4 *Tamman Temperature*

Grain boundary or short circuit diffusion is an important mechanism below the Tamman temperature. The Tamman temperature is ~⅔ that of the melting temperature of e.g. the oxide formed. For Al_2O_3 and TiO_2 the Tamman temperature are ~1367°C and ~1217°C, respectively, [86]. The importance of grain boundary diffusion increases with decreasing temperature, because the activation energy for grain boundary diffusion is lower than that for volume diffusion. Additionally, small crystals will favour grain boundary diffusion. This will enhance the reaction rate [81].

2.3.1.5 *Arrhenius Plot*

Having obtained evidence that the reaction is isokinetic at different temperatures the Arrhenius equation can be used to establish the activation energy E_a. In this plot the logarithm of the rate is plotted against the inverse of the absolute temperature. The use of the Arrhenius equation and the meaning of the activation energy must be seriously considered when it is applied to solid state reactions [87].

$k = Ae^{-Ea/RT}$ (Arrhenius equation) Equation 2-2

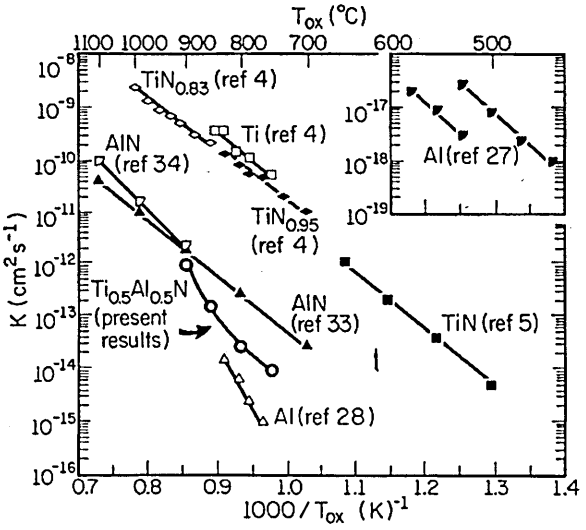

Figure 2-14: Arrhenius plot with the parabolic rate constant K plotted as a function of oxidation temperature T_{ox} for various coatings [11].

This should give a straight line for most reaction constants [88]. With variations in the scale (parabolic or logarithmic) it can be shown that with a reaction obeying the rate law chosen a straight line will be obtained in the plot. Such a plot shows the temperature dependence of an oxidation reaction and, furthermore, shows if the rate at which the reaction occurs changes (change in slope of graph). From the slope the activation energy can be extracted. The activation energy, E_a, is a measure of the complex transport mechanism during oxidation. A change in E_a indicates, therefore, a change in the oxidation mechanism. For interpretation of the oxidation kinetics and mechanism the rate measurements must be correlated to the composition and the microstructure of the oxide layer formed. Figure 2-14 shows an Arrhenius plot featuring various binary coatings, Al and Ti in comparison with $Ti_{0.5}Al_{0.5}N$.

In the case of a oxide bi-layer growth, where the activation energies differ, the rate constant for total oxidation cannot be expressed by an Arrhenius type equation, the E_a will change continuously as the relative importance of the two layers changes with temperature [81] (p.128). This behaviour is seen for TiAlN, which forms a bi-layer consisting of TiO_2 (rutile) and Al_2O_3 (corundum) [11].

2.3.2 Properties of the oxide scale

Heat treatment and oxidation causes problems like different thermal expansion coefficient between oxide and substrate material. Volume expansion frequently occurs in the growing oxide film. Stresses are created because of different expansion coefficients between the scale and the substrate. This can lead to the formation of pores and/ or cracks. Some oxide scales form through outward diffusion of cations. This leaves vacancies behind, which will eventually form voids in the oxide layer, thus altering the oxidation mechanism and rate with the exposure time [81] (p.228). Voids below and in the oxide layer reduce the adhesion to the substrate material.

2.3.2.1 Volatile oxides

A process that changes the rate of oxidation is the formation of volatile species, as in the case of Cr-oxide, W-oxide and V-oxide (1023°C for Cr_2O_3, 675°C for V_2O_5). At a specific temperature volatilisation of the oxide competes

with the growth of the layer, leading at some stage to catastrophically fast oxidation rates [81] (p. 247).

2.3.2.2 ***Cracks***

Stresses generated due to different expansion coefficient between the oxide scale and the substrate material are an important factor to determine the rate of oxidation, e.g. Cr_2O_3 scale tends to buckle due to compressive stress build-up. The diffusion of oxygen anions occurs along grain boundaries and generates compressive stresses on the metal-scale interface [84] (p.83). Scale cracking is another form of oxidation caused by stresses at the scale-metal interface. There cracks lead to accelerated linear oxidation [84] (p.89). Figure 2-15 shows schematically, how cracking occurs on edges.

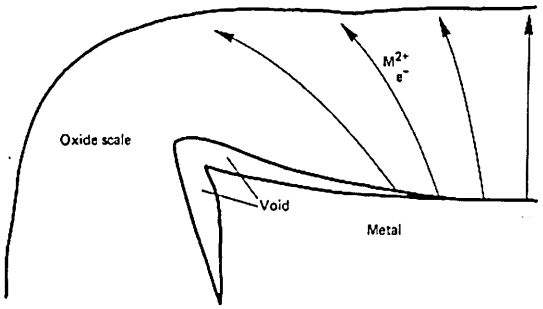

Figure 2-15: Schematic diagram showing longer diffusion distance for cations to supply scale-gas interface when scale-metal separation occurs at edges and corners [84].

Stresses in coatings and their oxide layer are also generated during cooling down, due to the different thermal expansion coefficients (Table 2-2) of metals, oxides and substrate materials. The magnitude of this stress at temperature T can be expressed by the following equation:

$$\sigma_{th} = \frac{E_L}{1-\mu_L}(\alpha_L - \alpha_S)(T_d - T) \qquad \text{Equation 2-3 [89], [90]}$$

where σ_{th} is the thermal induced stress, E_L and μ_L are, respectively, the elastic modulus and Poisson's ratio of the coating, α the thermal expansion

coefficient of either the coating or the substrate and T_d the deposition temperature.

It should be possible to calculate, from cracks in coatings (measuring their width) after oxidation, how much stress there was inherent in the deposited film, with the formula:

$$\sigma_x = \frac{E}{1-\mu^2}(\varepsilon_x + \mu\varepsilon_y) \qquad \text{Equation 2-4}$$

where, additionally to previous described symbols, ε is the measured width in *x* or *y* direction [84].

Generally the thermal expansion coefficient will be less for the oxide than the metal, which means, that during cooling, compressive stresses will form in the oxide layer. Differences in the coefficient lead to spallation or cracking of the oxide layer, if the adherence is weaker than the stress that has built up. The same is true for stresses built up between coating and substrate during heat treatment [89, 91-93]. Values in Table 2-2 can be used to estimate the stresses that are generated upon heat treatment.

Phase	Hardness/ HV	E modulus/ kN/mm^2	Thermal exp. coeff./ 10^{-6} K^{-1}	Density/ g/cm^3
AlN	1230	350	5.7	3.26
Al_2O_3	2100	400	8.4	3.98
CrN	1100	400	(2.3)	6.12
Cr_2O_3			7.3	5.23
TiN	2100	590	9.4	5.40
TiO_2	1100	205	9.0	4.25
VN	1560	460	9.2	6.11
WC	2350	720	3.8-3.9	15.72
TiAlN	2400	400	7.5	
Steel (like SS or M2) has an expansion coefficient of ~11x10^{-6}K^{-1}.				

Table 2-2: Data from ref. [9], Cr_2O_3 from ref. [84], (p.122), Cr_2O_3 Density from ref. [94], TiAlN ref. [11], E-modul TiAlN from ref. [13]

In coatings the situation is complicated, because (at least) three different layers are involved during heat treatment, the substrate, the coating and the oxide layer. The effect on the stress in the coating, due to cooling after deposition and heat treatment was illustrated schematically by [92]. Additionally, interactions between oxides and coating will occur. This means the adherence of the oxide layer does not solely depend on the difference between thermal expansion coefficient coating – oxide layer. The substrate – coating interactions interfere with this, i.e. it depends on the total system of substrate, coating and oxides.

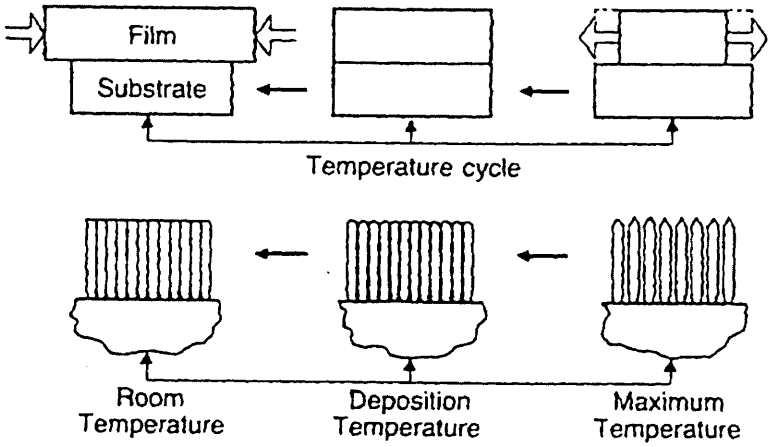

Figure 2-16: Effect of thermal mismatch stresses on microstructure of PVD coatings where $\alpha_{film} < \alpha_{substrate}$ [92].

2.4 Properties and Oxidation Investigation of Hard Coatings

2.4.1 Oxidation effects

Heat treatment of metals and hard coatings causes several mechanisms: Firstly, overall oxidation of the coating surface. Secondly, diffusion is occurring. Furthermore, defects or impurities in the material, coating can behave in a different way to the overall material. All three aspects of oxidation have been investigated in this thesis.

2.4.1.1 Coatings for dry high speed cutting

As the rotational speeds of cutting tools are increased, so are the demands for improvement in their mechanical properties and oxidation resistance. The coatings applied to protect the cutting tools operate at elevated temperatures because of the friction between the tool and the work-piece and the higher forces used. The performance of the cutting tool depends not only on the mechanical properties of the hard coating applied, but also on its oxidation resistance. Additionally, for interrupted cutting operations the coating requires good thermal shock resistance. Oxidation of hard coatings is one of the important mechanisms leading to a decrease of the mechanical properties such as hardness, fatigue strength and cutting performance [21], [22]. Coated cutting tools perform 80% of all machining tasks in modern industry [4]. Therefore an improvement of the oxidation resistance is important and effects due to oxidation have to be studied at both the surface and the interface. Investigations have shown that cutting performance can decrease considerably due to a loss in interfacial adhesion [22]. The cutting temperatures that can be expected at the cutting edge for cutting speeds of 50, 100, 150 and 200 m min^{-1} were calculated to be 680°C, 830°C, 950°C and 1050°C, respectively [95]. For TiN coated tools a chip temperature of ~720°C at a cutting speed of 300m min^{-1} was measured [96]. Materials that are difficult to cut, such as hardened steel (> 60-65 HRC), create temperatures as high as 700-900°C using cutting speeds of

300-400 m min^{-1} [97]. Temperatures of ~880°C were generated at the cutting edge of TiAlCrYN coated 8mm ball nosed end mill after 5min operation when machining AISI A2 steel (~60 HRC) at a cutting speed of 385 min^{-1} [23]. The high temperatures produced in dry high speed cutting demand good heat protection between the hot chip and the tool. Without protection cemented carbide tools oxidise rapidly at approximately 600°C [98]. It is important that the protective coating provides a good heat isolation [4], [99]. The low thermal conductivity of TiAlN, in comparison to TiN and TiCN, allows most of the heat of the turning operation to be transferred into the chip [100], [4], [99].

The mismatch in thermal expansion coefficients between coating and substrate should be low otherwise cracking of the coating can occur during heat treatment [89], [93]. It is therefore important that not only the oxidation resistance of the coating is high, but also that the difference in thermal expansion of the coating and the substrate is small.

Superior mechanical properties and oxidation resistance of PVD hard coatings can be achieved by engineering the structure as will be shown in this PhD Thesis, by using metastable alloy nitrides (multicomponent coatings) such as TiAlN and compositionally modulated films (e.g. nanolaminates, multilayers, superlattices) Another possible method to improve oxidation behaviour is the implantation of metal ions into hard coatings e.g. Al into TiC and TiN [83] or Y into TiN [101].

For binary nitrides information about the oxidation behaviour is readily available. Recently a review paper was published about the thermal stability of thin nitride films containing tabulated values about the diffusion behaviour of light elements in a wide range of binary nitrides [27]. The binary nitrides are the basis of the multilayer coatings under investigation. In the case of multicomponent or multilayered films, direct comparison is rarely possible, because of the uniqueness of the coating composition and structure. A comparison of the oxidation resistance of coatings with a similar elemental composition will be given.

The oxidation resistance of hard coatings in this Thesis has been investigated using TG [29], [102], [13], optical and electron microscopy, XRD [26], [102], [21], EDX-analysis in the SEM [21] and TEM [11], [21], [27]. Other

common methods used are GDOES [13], [103], XPS [102], [31], RBS [26], [104] and electrical resistivity measurements [82].

2.4.2 AlN

Thermogravimetric analysis showed that the oxidation of AlN powder starts above 700°C in air. Two stages of oxidation were observed. The first is characterised by a linear increase in weight with time and the formation of an oxynitride, the second corresponds to the formation of a thick oxide layer of Al_2O_3. The initial stage is controlled by surface reactions while the second stage is controlled by diffusion [105]. Oxidation of sintered AlN between 900°C and 1100°C up to 3h showed a parabolic weight gain behaviour [106].

The influence of growth induced stresses on high frequency magnetron sputtered AlN coatings deposited on different substrates and heat treated at various temperatures was investigated. In coatings with compressive stresses an increased resistance against microcracks and improved wear behaviour was found [90, 93].

2.4.3 TiN

TiN is a widely used, golden coloured, PVD coating with a face centred cubic structure (fcc) and known to oxidise rapidly above 550°C following a parabolic rate law. The diffusion of O through the oxide is the rate-limiting process (Figure 2-17) [107], [108], [26], [12].

TiN oxidises by the formation of a rutile TiO_2 layer when heat treated for 50min at 600°C, following a parabolic growth law [26], [28]. Above 700°C only the rutile form of TiO_2 was observed [26]. The parabolic rate showed that the diffusion of O through the oxide is the rate limiting process (Figure 2-17). A high diffusion coefficient of $D_0 = 4.3 \times 10^{-2}$ cm^2 s^{-1} is responsible for the low temperature oxidation of TiN.

Deviations from the parabolic rate were also observed: Measurements on the oxidation behaviour of TiN between 625°C and 1075°C showed that the activation energy has a parabolic plus a linear contribution above 900°C,

attributed to a simultaneous diffusion and phase-border reaction in the oxide layer [107]. The formation of an oxide scale with a layered structure above 850°C growing at a faster rate than predicted by a parabolic law was observed by [108].

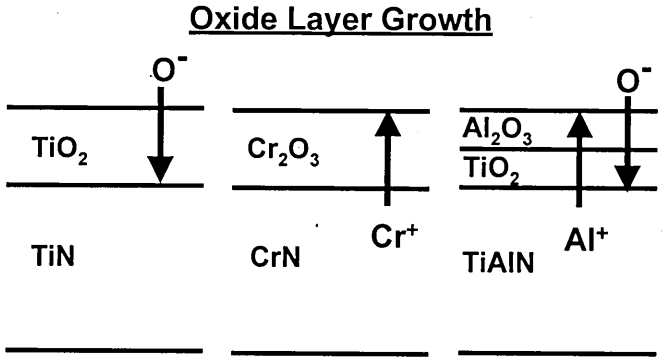

Figure 2-17: Schematic of the different mechanism of oxide layer growth.

2.4.4 TiAlN

2.4.4.1 TG analysis and drilling tests of TiAlN

The development of $Ti_{0.5}Al_{0.5}N$ increased the maximum working temperature to 700°C and the onset point of rapid oxidation to 850°C by the development of a protective Al_2O_3 layer [12]. In Figure 2-18 the TG behaviour of TiAlN together with TiAlCrN and TiAlCrYN is presented. These coatings will be discussed later. This method is useful to changes in the overall oxidation behaviour of hard coatings.

In drilling operations $Ti_{0.5}Al_{0.5}N$ coating outperformed TiN by a factor of two or more [12], [109]. In addition, improved wear behaviour was observed in dry drilling tests, due to the superior high temperature properties of this coating [12], [110]. This coating is the basis of the multilayer coatings under investigation, being similar to the $Ti_{0.44}Al_{0.53}Cr_{0.03}N$ coating used earlier [32].

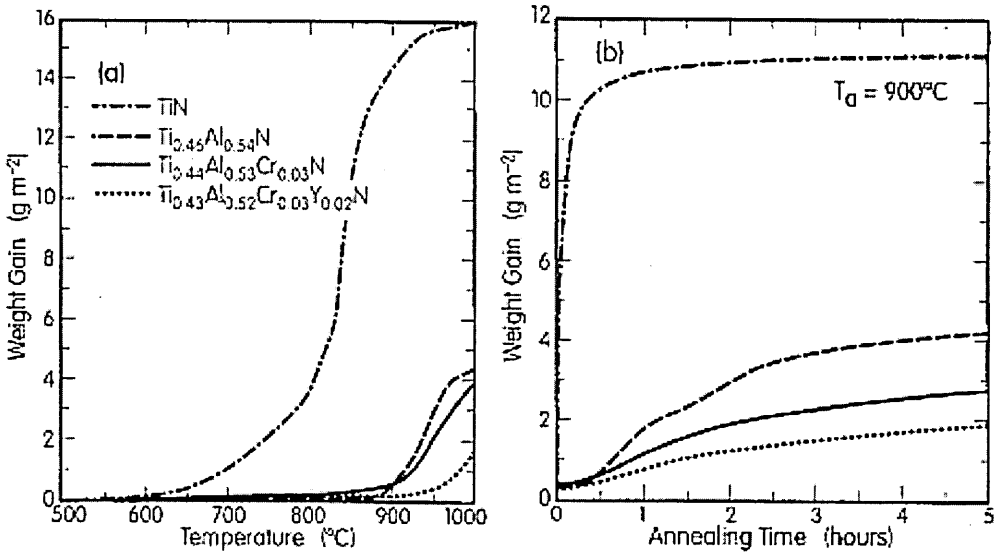

Figure 2-18: TG measurements on TiN, TiAlN, TiAlCrN and TiAlCrYN a) continuous and b) isothermal [33], [32].

2.4.4.2 ***Structure of TiAlN***

A metastable B1-NaCl structure Figure 2-19 was observed for $Ti_{1-x}Al_xN$ compositions of $x \leq 0.52$ using magnetron sputter deposition and a substrate temperature of 500°C [111]. A slightly higher value of $x \leq 0.6$ was reported by [112] using arc deposition and by [113] using a calculated TiAlN value valid for vapour deposition techniques in general. To achieve the formation of a metastable TiAlN, the films have to be grown under kinetically limited conditions, i.e. low substrate temperatures and/ or high deposition rates. The coating structure, cubic (fcc) or hexagonal (hcp), is dependant on the deposition parameters and the adatom mobility on the surface of the substrate material [111]. Of course, changes also occur by altering the composition of TiAlN.

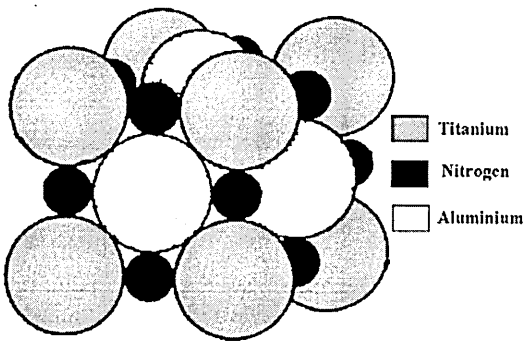

Figure 2-19: Schematic of the TiAlN lattice, where Ti has been partially replaced by Al.

A transition between the different phase fields of TiN and AlN for low-temperature vapour deposition techniques is shown in Figure 2-20. If normal conditions (non coating) are used, the solubility of TiN and AlN is extremely limited, with less than 2 at% Al in TiN at 1000°C [27].

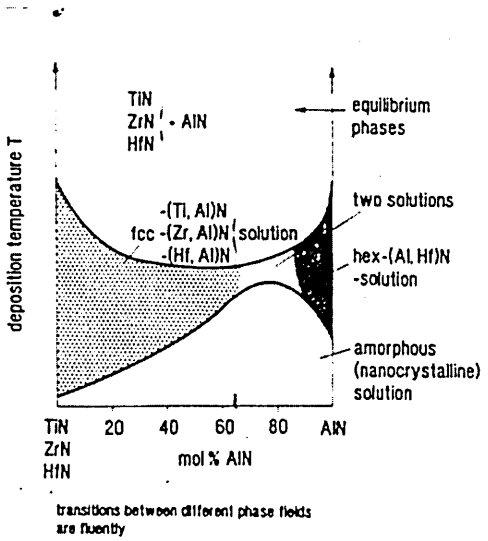

Figure 2-20: PVD phase fields (schematic) for the TiN-AlN, ZrN-AlN and HfN-AlN systems after [113].

2.4.4.3 *Effect of process parameters on TiAlN*

The effect of process parameters (e.g. pressure, bias voltage) on the mechanical performance and structure of magnetron sputtered $Ti_{0.5}Al_{0.5}N$ was investigated by [36, 63, 111, 114]. An increase in bias voltage from U_b=0V to -150V results in the formation of a finer grain size, a denser film, a flatter surface and an increase in the lattice parameter. Adibi and co-workers [115] showed that, with increasing the substrate temperature during sputter deposition, the coating structure of $Ti_{0.5}Al_{0.5}N$ was altered from a fcc structure to a two-phase structure consisting out of a fcc and a hcp phase. The separation was first noticed at $T_s \geq 560°C$.

2.4.4.4 *Effect of altering the TiAlN composition*

A study of the effect of alterations in the Al content on the performance of TiAlN coated tools in dry drilling operations showed that best wear resistance and highest hardness was achieved for $Ti_{0.5}Al_{0.5}N$ [116] and [117]. [95] found the best results in drilling operations for a cutting speed of 100 and 150m min^{-1} with an Al content between 25 and 50at%.

The lattice parameter varied between 0.418nm and 0.424nm depending on the Al content using sputter deposition [111] and [118]. Lattice parameter of 0.428nm for TiN and 0.423nm for $Ti_{0.5}Al_{0.5}N$ were found for arc deposited coatings [116].

By applying Vegard's law, the lattice parameter of TiAlN can be changed by varying the Al content. The $Ti_{0.46}Al_{0.54}N$ coatings grown at SHU using sputter deposition have a *fcc* structure with {111} preferred orientation with a lattice parameter of 0.418nm [13].

The Al content changes not only the mechanical but also the oxidation behaviour of $Ti_{1-x}Al_xN$. This has shown by many researchers using various deposition techniques.

Magnetron sputtered $Ti_{1-x}Al_xN$ onto high speed steel showed the same trend. The oxidation resistance increased with increasing the Al content in the coating [12]. The highest content examined was $Ti_{0.42}Al_{0.58}N$ [119].

The Al content was varied also in TiAlN arc evaporated coatings (T_s=400°C) deposited onto Mo and Pt. The best oxidation resistance (lowest weight gain) was found for the composition $Ti_{0.4}Al_{0.6}N$ [120]. A study on arc-deposited $Ti_{1-x}Al_xN$ onto stainless steel ($T_s \approx 330°C$) showed that, with increasing Al content, the oxidation resistance and the activation energy increased. It was also stated that after prolonged oxidation the activation energy of $Ti_{0.9}Al_{0.1}N$ and $Ti_{0.6}Al_{x0.4}N$ became similar, due to grain boundary diffusion along rutile crystals [102].

A systematic study on $Ti_{1-x}Al_xN$ deposited by PECVD (T_s = 530°C) onto high speed steel showed, that with $x \leq 0.25$, the formation of a protective Al_2O_3 (corundum) layer could not be identified by XRD, after heat treatment for 1h at 900°C [31]. It was observed using TG and a heating rate of 5°C/min that $Ti_{1-x}Al_xN$ coatings with lower Al content i.e. $x \leq 0.25$, the onset point of rapid oxidation occurred at ~830°C whereas for those with higher Al contents ($x > 0.25$) the onset of rapid oxidation occurred at ~900°C. This investigation showed also that the activation energy increased with increasing Al content. With Al content $x \leq 0.25$, the activation energy E_a is similar to that of TiN. This is connected to the formation of a protective Al_2O_3 scale, which was observed in coatings with an Al content of about $x \approx 0.25$ [31].

These examples show that the Al content influences the oxidation behaviour in terms of oxide layer growth and diffusion of substrate material to the coating surface. Furthermore, comparing these results to the results of the drilling tests (chapter 2.4.4.4) shows that good oxidation performance ($x \geq 0.25$) and good cutting performance ($0.25 < x < 0.5$) are related.

2.4.4.5 Oxide layer formation for TiAlN

$Ti_{0.5}Al_{0.5}N$ oxidises with the formation of a bi-layer (Figure 2-21) consisting of Al_2O_3 and TiO_2. The inner layer (adjacent to the nitride) is Ti-rich and the outer Al-rich. Segregation of the scale into two sub-layers was observed from the very beginning of the oxidation process (1h at 500°C) on cathodic arc deposited TiAlN [121].

The formation of an amorphous Al oxide layer at the beginning of the oxidation process was reported by [12], [120], [119], [122]. Huang [119] proposed that the formation of an amorphous Al oxide layer occurs when lower

annealing temperatures are used. His heat treatment was carried out for 6h at 600°C.

The formation of a crystalline bi-layer was observed for sputtered films after heat treatment at temperatures between 750 and 900°C [11], [27] using TEM and EDX analysis and for coatings deposited using PECVD after heat treratment between 500°C and 800°C [31] and after heat treatment between 750°C and 950°C [122] using SEM and auger electron spectroscopy. XPS studies by [121] have confirmed the results reported by McIntyre [11]. In [11] the oxide layer had a thickness of 200nm after heat treatment for 5h at 850°C for sputtered TiAlN coatings deposited onto stainless steel (T_s=400°C).

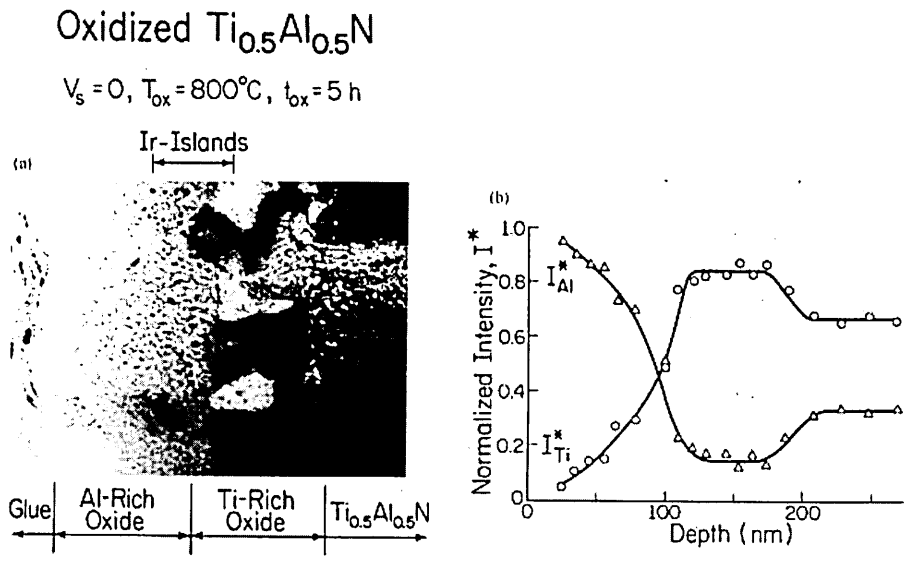

Figure 2-21: $Ti_{0.5}Al_{0.5}N$ oxidised for 5h at 800°C in O. The position of the Ir markers indicate that Al and O are the mobile species. Al diffused through the Ti-rich oxide layer to the atmosphere. O counter-diffused towards the TiAlN [11], [27].

The oxide layer growth followed a parabolic law [11] and [102]. However, the mechanism leading to a parabolic oxide layer growth was explained differently for an arc deposited TiAlN coating to a sputter deposited one. The investigated TiAlN coatings were sputter deposited at T_s = 400°C ($Ti_{0.5}Al_{0.5}N$) [11] and arc deposited at T_s = 330°C ($Ti_{0.6}Al_{0.4}N$) [102].

For the sputter deposited coating the formation of an equal thick Al-rich and Ti-rich oxide layers below 850°C was reported, indicating similar mobility of Al and O. With increasing temperature the oxidation rate increased, due to changes in the microstructure and a decrease in the active diffusion pathways, due to an increase in crystal perfection of the oxides. At $T \geq 850°C$ the activation energy changes from 2.2 eV/K to 4.2 eV/K; the rate-limiting step at this stage is O diffusion through the Al-rich oxide layer (Table2-3). The activation energy is temperature dependent and increases with increasing temperature. This is in accordance with an increased growth of the Ti-rich layer compared to the Al-rich layer [11]. Similar observations regarding the oxidation mechanism were reported by [122] who deposited $Ti_{0.88}Al_{0.12}N$ onto silica using PECDV and heat-treated the samples at lower temperatures between 500-800°C.

In contrast to this on cathodic arc deposited $Ti_{0.6}Al_{0.4}N$ ($T_s \approx 330°C$) it was found that the activation energy E_a decreases with increasing temperature (Table 2-3). Heat treatments were carried out between 700°C and 900°C. The change in E_a was explained by the following: The oxidation rate is first controlled by oxygen diffusion. The Ti-ions oxidise to rutile TiO_2 and Al-ions form an amorphous phase in the early stages therefore acting as a barrier for further oxidation. As oxidation proceeds Al ions diffuse through the TiO_2 layer to the oxide layer/ gas interface leading to the formation of Al_2O_3 at the surface. Oxygen diffusion occurs through pores in the Al_2O_3 layer [102]. However, the rate law was also stated as being parabolic in nature.

In addition to the formation of an oxide bi-layer, the phase separation of the metastable TiAlN into TiN and AlN was observed after heat treatment for 1.5h at 900°C [11]. Another effect of heat treatment was the segregation of Al to the boundaries in the Ti-rich oxide layer after annealing for 7min at 900°C [11].

E_a TiN	E_a $Ti_{0.5}Al_{0.5}N$	Reference
	2.2 eV/K initial	[11], sputter dep., 750-800°C
	4.2 eV/K later	[11], sputter dep., 850-900°C
1.95 eV	~3.5 eV	[31], PECVD, 750-950°C
1.2 eV[x]	4.7 eV initial	[102], arc dep., 700-900°C
	1.9 eV later	[102], arc dep., 830-900°C
2.05 eV		[26]

Table 2-3: Activation energies E_a for the oxidation of TiN and TiAlN coatings. Some values have been converted from kJ/mol to eV by using 1eV = 96.485 kJ/mol [88]. [x] This value is very low. It is normally stated between 1.9 – 2.1 eV.

2.4.4.6 Crack formation in TiAlN

Additionally, to overall oxidation effects different oxidation behaviour was observed in cracks and at pinholes.

Another effect of heat treatment was the appearance of cracks on sputter deposited $Ti_{0.5}Al_{0.5}N$ (T_s=400°C) on stainless steel using a bias voltage of V_s = 0, after heat treatment between 750-900°C. At higher bias voltage (U_b = 150V) no cracks were observed following annealing. In the cracks Fe and Ti diffused to form oxides [11]. This shows that the thermal expansion coefficient of the coating and the substrate material are important as well as the stresses induced during the deposition process [11], [89]. Deposition at higher bias voltages increases the stress in the coating. Examples for this behaviour are given by [62] for TiAlN, by [63] for TiN and a general overview by [64].

Independently of Fe oxides discovered in cracks connecting the coating surface with the substrate material, Fe oxides were detected in the oxide layer of magnetron sputtered, tensile stressed $Ti_{1-x}Al_xN$ deposited onto AISI A2 tool steel (T_s=400°C). The amount of Fe oxides decreased with increasing Al content [119].

[122] reported that cracking was observed at 700°C on $Ti_{1-x}Al_xN$ deposited onto a silicon wafer using PECVD (T_s=500°C). In a different study where TiAlN is deposited onto high-speed steel using PECVD (T_s=530°C) Fe oxides were observed in cracks and in the oxide layer due to the heat treatment at 900°C. This led to the assumption that Fe diffused not only rapidly through cracks, but also along the column boundaries at elevated temperatures [31].

2.4.5 CrN

The oxidation behaviour of CrN was investigated by [29], [30], [123]. CrN is widely used in wear protection [124]. Various CrN-based coatings have been investigated to improve the mechanical and the oxidation properties [29], [30].

Magnetron sputter deposited CrN onto high-speed steel formed a Cr_2O_3 (eskolite) layer after oxidation for 1h at 650°C, as identified by XRD measurements. The rate of oxide layer growth (Cr_2O_3) on CrN in comparison to TiN is considerably decreased. This was shown by heat treatments carried out for 4 hours in a furnace at 600°C. The oxide layer formed on CrN was 90nm thick whereas in comparison that on TiN was 560nm thick [58]. An oxide scale of ~9nm was reported after oxidation for 2.5h at 700°C [123]. After oxidation at 800°C for 1h a 450nm thick scale was observed [29]. XRD measurements showed, that in addition to the formation of a Cr_2O_3 the oxide phase, a Cr_2N formed after heat treatments between 500°C and 800°C [125].

Cr diffused from the nitride to the coating surface and through the oxide to form Cr_2O_3 (Figure 2-18) [29]. The coating oxidises following a parabolic rate law from 650 to 900°C [28]. The oxidation process of CrN is controlled by Cr diffusion [29], [28], whereas in the case of TiN the oxidation rate was controlled by O diffusion. The activation energy of CrN is 2.3eV [29] compared with ~2eV for TiN (see Table).

2.4.5.1 *Oxidation through pinholes*

Penetration of Fe, probably through pinholes in a CrN coating sputter deposited onto Ck 45 steel, was observed after heat treatment for 2.5h at 600°C [123]. At higher temperatures the number of Fe containing oxides islands was observed to increase in both number and size and diffusion through pinholes is probably no longer the dominating mechanism. The rate of diffusion increases at elevated temperatures, because of the mismatch of the thermal expansion coefficients and the interface becomes permeable at local defects, thus allowing the rapid ingress of Fe. The local islands are surrounded by a continuous protective layer of Cr_2O_3 [123].

2.4.6 CrAlN

$Cr_{1-x}Al_xN$ formed ~16nm, ~50nm and ~100nm thick oxide layers after heat treatment for 30min at 500°C, 1h at 800°C and 1h at 900°C, respectively [30], [29], [126]. The outermost oxide layer is Cr-rich followed by Cr/ Al oxides. Below this, a Cr/ Al oxynitride was identified with the N and O concentration slowly rising/ falling respectively to the bulk values [29], [30].

The oxidation mechanism for CrAlN is more complicated. The following was observed after heat treatment for 1h at 900°C: A Cr-rich oxide layer of Cr and Al is generated, with the Cr content of the oxide layer increasing at higher temperatures and for longer exposure times; a typical multilayer structure is eventually formed. The reason for this can be understood by considering the transport properties and the thermodynamic stability of the oxides. The diffusion rate of Cr towards the surface is higher than that of Al, but conversely Al_2O_3 is the more stable oxide. The diffusion rate of Al in Cr-rich oxide is lower, leading to a build up of Al beneath this layer. The Al-rich layer in turn hampers the out-diffusion of Cr leading to a build up of Cr in a second layer and so on [29], [126].

Al_2O_3 and Cr_2O_3 are isomorphous, with almost identical rhombohedral structure [94]. Hence, the possibility is high to form a mixed oxide rather than two separate phases. The oxidation process is, therefore, mainly controlled by Cr diffusion [29]. The $Cr_{1-x}Al_xN$ compositions were $Cr_{44}Al_{15}N_{40}$ for [29] and $Cr_{50}Al_{25}N_{25}$ for [30]. The composition in both cases were determined using Auger electron spectroscopy.

2.4.6.1 *Effect of altering the CrAlN composition*

The role of Al content in CrAlN was investigated on arc evaporated coatings. It was shown that, with increasing Al content, the oxidation resistance increased. The best results in mechanical and oxidation performance was achieved by a CrN/CrAlN multilayer structure (layer thicknes ~1000nm) [127].

2.4.7 TiCrN – TiN/CrN

Investigations on an arc deposited TiCrN showed a maximum hardness at the composition $Ti_{0.70}Cr_{0.30}N$ (two phases) [128]. A parabolic diffusion law was found for the composition of sputter deposited (T_s=130°C) $Ti_{0.70}Cr_{0.30}N$. The oxidation reaction rate was lower than for TiN or CrN coatings [82].

To improve the performance of TiN and CrN, further TiN/CrN multilayer structures (multilayer period between 35-55nm) were investigated. Electrical resistivity measurements on TiN/CrN coatings indicated that the multilayer coating exhibited better oxidation resistance than either TiN or CrN. These measurements also indicated that grain boundary diffusion is one of the operating mechanism [82].

2.4.8 $Ti_{0.44}Al_{0.53}Cr_{0.03}N$

The onset point of rapid oxidation of $Ti_{0.5}Al_{0.5}N$ was raised from 870°C to 920°C by the incorporation of 3at% Cr into the coating. The weight gain of was substantially reduced from ~4.2 g m^{-2} for $Ti_{0.5}Al_{0.5}N$ to ~2.7 g m^{-2} for $Ti_{0.44}Al_{0.43}Cr_{0.03}N$ as measured in isothermal TG experiments at 900°C [32]. The microhardness of both coatings was $HK_{0.025}$ 2400. The texture develops as {111}, which is the mechanism for films where the strain energy dominates during film growth [129]. The $Ti_{0.44}Al_{0.53}Cr_{0.03}N$ coating exhibited a similar oxide bi-layer formation as the previously described for $Ti_{0.50}Al_{0.50}N$. However, Cr enrichment was observed before and after the Ti-rich layer [33]. Heat treatment for 1h at 950°C showed, that the interface integrity no longer persisted and that the film (~3μm) was almost entirely oxidised [33].

2.4.9 TiAlN/CrN

It was shown that the oxidation resistance of both TiN and CrN increased with the addition of Al. In addition, the mechanical performance improved. Investigation into the nanolayer system TiAlN/CrN was a further step to improve the mechanical properties (see 2.2.2) as well as the oxidation resistance. Multilayer combinations of TiAlN and CrN with a nanolayer period between 2.4nm and 4.7nm were deposited using the ABS technology [13], [21]. The compositions of various TiAlN/CrN systems have been determined using GDOES and quantitative EDX analysis [130].

A gradual increase in Cr content altered the hardness, nanolayer periodicity and the oxidation resistance of the coating (Figure 2-23) [130]. Figure 2-22 shows that the oxidation resistance increased systematically with increasing Cr content [13], [21].

A multilayer structure was observed, when the applied power on the Cr target was 2kW resulting in an average composition of $Ti_{0.38}Al_{0.44}N/Cr_{0.18}N$ [130]. The highest hardness was achieved for $Ti_{0.22}Al_{0.26}N/Cr_{0.52}N$ with a layer periodicity of 3.6nm, which was achieved using a power of 8kW on the Cr target [13], [21], [130]. The hardness decreased after heat treatments in air from $HK_{0.01}$ 3400 to $HK_{0.01}$ 1500, for the 8kW coating, after annealing for 16h at 750°C [21].

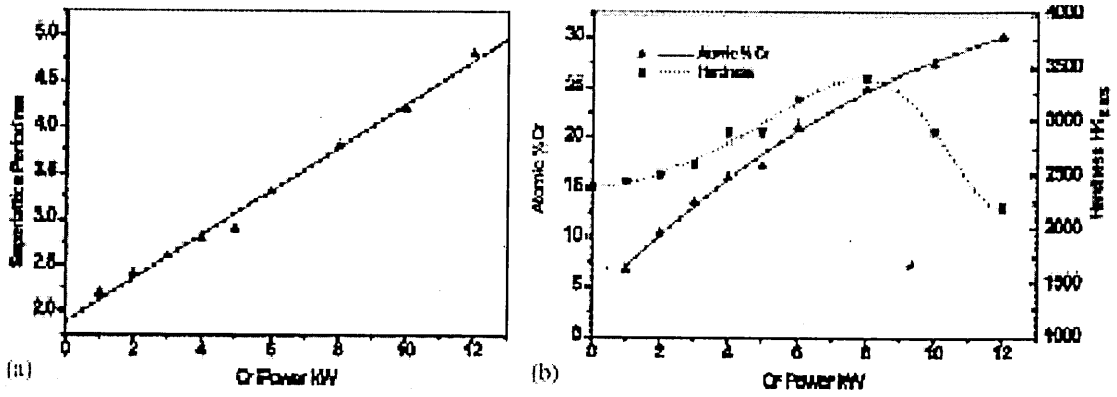

Figure 2-22: Cr power (Cr content) versus hardness and periodicity of the TiAlN/CrN nanolayers (superlattice period) [130].

Low angle XRD measurements were performed on heat treated TiAlN/CrN coatings deposited with a Cr target power of 8kW. Annealing in air for 4h at 650°C showed a similar peak height to that measured for the as-deposited film. After annealing for 4h at 750°C the intensity of the low angle XRD peak decreased, indicating some interdiffusion between the individual layers. However, the existence of a thin oxide film on the coating surface would lead to some attenuation of the X-ray beam [21].

Severe oxidation was observed after 5h at 1000°C using SEM. The underlying oxide had a complex structure (Figure 2-23). Adjacent to the remnant coating (C) a thin band of Al_2O_3 formed. Beyond this region the oxide consisted predominantly of Cr_2O_3 which was bordered by a zone of $Al_xCr_{2-x}O_3$ becoming progressively depleted in Cr (A) towards the Al_2O_3/ $Al_xCr_{2-x}O_3$ interface, thus the composition fluctuated from being Cr-rich to Al-rich. The outermost oxide layer consisted mainly of TiO_2, but also contained a dispersion of Fe-rich oxides (traces of Cr and Ni were also detected in these phases). A Cr-rich layer was formed in the remaining coating underneath the Al_2O_3-layer [21].

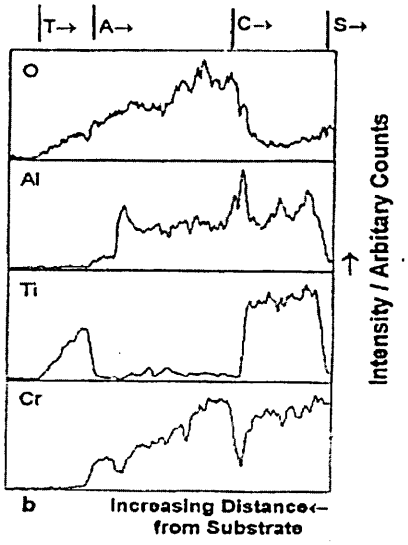

Figure 2-23: EDX line scan using a 6nm probe, on a TiAlN/CrN coating deposited using 4kW power on the Cr target, after heat treatment for 5h at 1000°C [21].

2.4.10 TiYN

To investigate the oxidation behaviour, the microstructure and the mechanical properties, Y was incorporated in concentrations from 1.1 at% to 7.6 at% in magnetron sputtered TiN [131].

2.4.10.1 Structure

The lattice parameter increased with increasing Y content from 0.4235 (TiN) to 0.4287 ($Ti_{0.8}Y_{0.16}N$), which can be attributed to the substitution of Ti by Y at the Ti lattice sites in the TiN lattice. The deposited coatings also had an open columnar structure. Grain refinement occurred with increasing Y content, which was associated with the reduced surface adatom mobility and the numerous nucleation sites caused by Y. The hardness increased with increasing Y content from 7 GPa (TiN) to 23 GPa ($Ti_{0.8}Y_{0.16}N$) deposited onto steel [131]. Reactive ion plating was used to deposit Y at the TiN/ stainless steel interface. This resulted in an increased corrosion and wear resistance of TiN [132]. A gettering effect for surface oxides by a Y interlayer was shown by [133], which improved the adhesion of the subsequently deposited TiN film.

2.4.10.2 Oxidation behaviour

The oxidation resistance of TiN was substantially improved by the addition of Y. TiN coatings were fully oxidised and spalled off the substrate, whereas a $Ti_{0.88}Y_{0.07}N$ coating and coatings with higher Y content remained attached to the substrate surface after heat treatment for 20min at 800°C [131]. Furthermore, the oxide layer formed on the $Ti_{0.88}Y_{0.07}N$ coating after the heat treatment showed grain refinement when compared with the TiN coating.

Oxidised TiYN consisted of rutile TiO_2, anatese TiO_2 or $Y_2Ti_2O_7$, depending on the Y content. XPS measurements were conducted on the surface Ar^+ etched for 0.5min and 10min, respectively. It was assumed from the difference in Y content that Y out-diffuses through intercolumnar open pores or grain boundaries [131]. It was also speculated that the out-diffusion of Y contributed to the decrease in the oxidation rate of the films. Vacancies, crucial for oxide nucleation, may be trapped by Y atoms [131].

Cracks were observed for TiYN coatings on Si substrate material, but not on those deposited onto steel. This was attributed to the difference in thermal expansion coefficient of the various substrates.

2.4.11 TiAlYN

The incorporation of Y into $Ti_{0.5}Al_{0.5}N$ films improved the oxidation behaviour [134]. Further comparisons between $Ti_{0.5}Al_{0.5}N$ and $Ti_{0.495}Al_{0.495}Y_{0.01}N$ were made: Fractured cross sections after annealing for 1h at 900°C in air showed a fine crystalline oxide scale of ~40nm on TiAlYN and a coarse scale of ~195nm on the TiAlN coating. TG measurements also indicated reduced oxidation of the TiAlYN coating. A maximum working temperature of 800°C was suggested [134].

2.4.12 TiAlCrYN

$Ti_{0.43}Al_{0.52}Cr_{0.03}Y_{0.02}N$ is the state of the art development for tool protection in dry high speed cutting operations of difficult to cut materials like AISI A2 steel (58 HRC). This coating was introduced into commercial production in 1998. TiAlCrYN has been compared with, and has outperformed TiCN and TiAlN by 1.6 and 3 times respectively [1]. This coating exhibits a fine-grained interrupted, columnar growth structure and has a hardness of $HK_{0.025}$ 2700. The lattice parameter increased with the addition of Y from 0.4183 for $Ti_{0.44}Al_{0.53}Cr_{0.03}N$ to 0.4223 for $Ti_{0.43}Al_{0.52}Cr_{0.03}Y_{0.02}N$. The immobile Y caused repeated nucleation and, therefore, the texture develops as for thin films, orientated in <100> direction, where the surface energy dominates the growth mechanism. [129].

With the addition of Y to $Ti_{0.44}Al_{0.53}Cr_{0.03}N$ it was possible to raise the onset point of rapid oxidation from 920°C to 950°C. Both coatings followed a parabolic rate law [13]. On the $Ti_{0.43}Al_{0.52}Cr_{0.03}Y_{0.02}N$ coating the formation of an oxide bi-layer of ~400nm was observed after heat treatment for 1h at 950°C. In comparison the $Ti_{0.44}Al_{0.53}Cr_{0.03}N$ coating formed an oxide layer of >3000nm after the same treatment.

The surface oxide layer of TiAlCrYN exhibited a dense, partially crystalline structure and a coarser (grain size = 100nm) polycrystalline underlayer. In addition to the formation of an Al-rich and Ti-rich bi-layer, a Cr-rich band before and after this zone was measured. The XTEM image, STEM-EDX and SNMS showed no change in the interface between substrate and coating in comparison to $Ti_{0.44}Al_{0.53}Cr_{0.03}N$ (see 2.4.8).

The reason for improved oxidation behaviour was seen in the refinement in the coating grain structure resulting in longer diffusion paths. More importantly, Y segregation was identified at the grain boundaries close to the oxide surface after heat treatment for 1h at 950°C. This is thought to have inhibited the diffusion of cation species towards the surface and oxygen penetration into the film [33], [13].

2.4.12.1 Role of Y

Compositional changes in TiN, TiAlN and TiAlCrN with Y were made to increase the oxidation resistance further. Y is known to belong to the oxygen-active elements and is incorporated into alloys to increase the oxidation resistance. Typically one or two at% are sufficient to change the oxidation properties in an alloy [135], [136]. This was shown for Y additions in MeCrAlY alloys, where Y is used e.g. to increase the adherence of the Al_2O_3 or Cr_2O_3 based oxides, reduce the rate of scale growth and to decrease the grain size of the oxides. Y is incorporated as an alloying element, by oxide dispersion or by ion implantation. The positive effect of a Y-rich interlayer between substrate and TiN films was shown by [133], [132]. Beneficial effects of Y have also been discussed in numerous papers e.g. [135-141]. However, the role of Y in improving the oxidation resistance, is still not clearly understood. Improvement in e.g. the scale adherence can also be achieved by oxygen-active metals like Hf, rare earth elements, the incorporation of an oxide dispersion like ThO_2, or an addition of noble metals to the alloys [84], (p.122).

2.4.12.2 Oxynitride Overcoat

Investigations in the wear behaviour of TiN coated stainless steel at elevated temperatures identified the development of oxide 'glaze' which ensured that low friction and wear were maintained for extended periods. Oxide formation during sliding-wear conditions was beneficial to protect the surface [142]. [143] showed that the deposition of amorphous oxides can increase the wear resistance of hard coatings, because no grain boundaries interrupt the homogeneity of the material. The problem with pure oxides is that they are very brittle. Additionally, at elevated temperature crystallisation occurs. Addition of N improved the thermal stability of Al_2O_3. The effect of a pre-deposited oxide layer on $Ti_{0.46}Al_{0.54}N$ was found to be beneficial in TG investigation as well as in cutting operations [144], [22].

On this basis an oxynitride topcoat was applied to the TiAlCrYN coating discussed in the previous section (2.4.12). The oxynitride coating was deposited at the end of the coating process, by changing the reactive atmosphere from nitrogen to dry air. Pin-on-Disc tests performed on this coating showed the improved performance in terms of wear behaviour of this topcoat (Figure 2-24) [145].

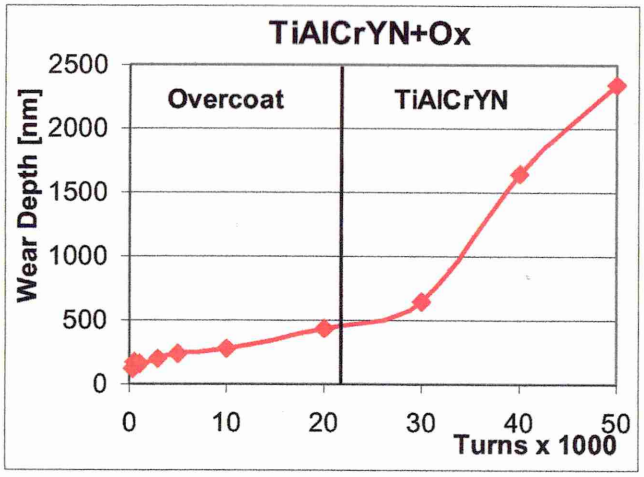

Figure 2-25: Pin-on-Disc test results from TiAlCrYN with topcoat (TiAlCrYN+Ox) [145].

2.5 Summary

It was shown that the addition of Cr, Al and Y to TiN improves the oxidation behaviour. The mechanism of the oxide layer formation of more complicated coatings like TiAlN is still not fully understood. It is for example uncertain under what conditions the amorphous oxide layer forms. The existence of an amorphous layer is thought to be beneficial for wear applications. The oxidation kinetics so far established for hard coatings obey a parabolic rate law, which is associated with a diffusion mechanism. Unfortunately, often a detailed description of the structure of the oxide layer formed is missing. However, knowledge of the structure is of major importance in understanding the kinetics involved in oxide layer formation. Some researchers reported that after prolonged heat treatment the formation of a porous oxide layer and a deviation of the parabolic law occurs. This behaviour is in agreement with oxidation behaviour investigated on metals. Metals tend to change the oxidation rate with increasing temperature. The influence of the coating composition and properties is of importance in order to protect the substrate material. In some cases local diffusion of substrate elements through the coating was observed. This thesis presents a more detailed analysis of TiAlN base hard coatings using TG in conjunction with XRD, SEM, TEM and STEM with EDX analysis. Using these techniques the structural and compositional changes occurring during heat treatment will be investigated. With this knowledge it should be possible to improve existing hard coatings further and to develop a new generation of coatings for the specialised application “dry high speed cutting”.

3 EXPERIMENTAL

The advantage of each technique used is given in form of a short overview. All of the methods used are already established in hard coating research. Additionally, the parameters of the coating deposition process are given together with the composition of the coatings produced.

3.1 Sample preparation prior coating deposition

Austenitic stainless steel AISI 304 (DIN No. 1.4307 or X 5 Cr Ni 18 10) was chosen as substrate material for most of the work. The non-magnetic behaviour made it ideal for TEM microscopy. Other substrate materials used were high-speed steel (AISI M2 or DIN 1.3343) and cemented carbide (Sandvik, WC and 10% Co binder, H 10 F, ISO K20-30).

For the TG measurements mirror polished stainless steel SS 304 was used with a sheet thickness of 0.8mm cut to a size of 60x15mm. A hole of 1.5 mm in diameter was drilled in the sample, so that it could be supported in the TG (3.4) by a hook. The samples were coated from both sides. During the coating process the TG samples were fixed to a rod, which prevented them from spinning. Additional rotation will alter the multilayer bi-layer thickness of the samples [77]. After the coating process the sample was shortened to 50x15mm (Figure 3-1). The area below the red line (arrow) was removed.

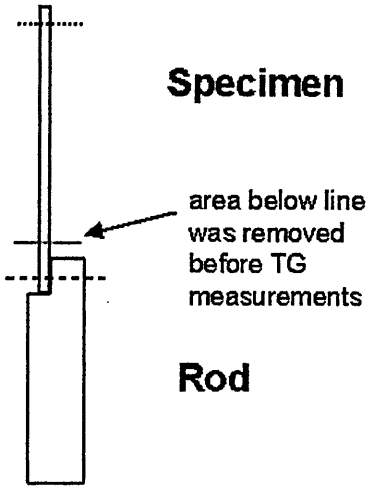

Figure 3-1: Fixing method used to coat the TG samples.

Apart from the TG substrates, all samples (high-speed steel-, cemented carbide-, stainless steel coupons and stainless steel sheet material) were ground and polished manually to a roughness of ~R_a = 0.01 μm. Prior to coating, all samples were cleaned and dried in an automated cleaning line that consisted of a series of heated ultrasonic baths including ionic and non-ionic surfactants for cleaning. De-ionised water and a vacuum dryer are used in the final stages. The substrates were then screwed onto stainless steel sample holders. All samples, especially the AISI M2 coupons, were introduced as quickly as possible into the coating machine, to minimise the risk of oxidation and dirt accumulation.

3.2 Deposition conditions used

The samples used in all analyses were coated in a Hauzer Techno Coating 1000-4 ABS unit (machine A) at Sheffield Hallam University. Except for TiAlCrYN-Ox, which was produced in a HTC 1000/5 MK II ABS coating unit (machine B). This machine belongs to the Bodycote-SHU company and is used for commercial deposition of coatings (fully loaded machine). The differences between the two machines are minor, e.g. the size of the targets and the shutter mechanism.

Both coating machines have a stainless steel vacuum chamber measuring 1m diagonally from cathode to cathode. The cathodes in machine A are 600 x 190mm and in machine B 800 x 160mm in size. In Table 3-1 the target material and the fabrication process are listed. Each cathode can be run either in unbalanced magnetron deposition mode or the steered cathodic arc technique. The latter was used for the Cr target. They were used in the cathodic metal ion etch, as well as in the subsequent sputter deposition process. The deposition processes were performed in the following sequences [7]:

- Pump down to base pressure and heating up of the coating chamber
- Target cleaning
- Cathodic arc metal ion etch
- Reactive sputter deposition of base layer and coating
- Cooling down of the chamber

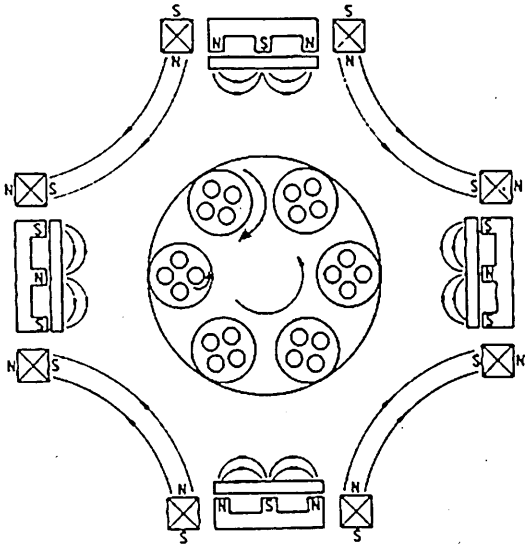

Figure 3-2: Target and Magnetic field arrangement in the ABS machine with location of the position of the substrates.

The substrates are mounted onto a turntable allowing to turn them in one, two or three fold rotation (Figure 3-2). All substrates were positioned at a medium height towards the cathodes and were rotated three fold. The chamber was, in the case of machine A, only approximately 10% filled with samples. Machine B is used for commercial production. Hence, the chamber was filled to full capacity. Both machines are heated using heater arrays positioned in the door and under the turntable. The cathodes are water cooled. The temperature during deposition was 450±10°C for all deposition processes.

Target Material	Fabrication
Cr	Hot isostatically pressed
Ti:Al/ 50:50	Vacuum cast
Ti:Al:Y/ 48:48:4	Powder metallurgically prepared and forged

Table 3-1: Overview on targets used

In the case of the Y-containing coatings, two TiAlY cathodes were opposing each other. Additionally, one Cr and one TiAl target was used. TiAlN/CrN or TiAlCrN were deposited using one Cr and three TiAl targets.

3.2.1 Detailed process steps

The process starts with the sputter cleaning of the targets, when a pressure of ~2 x 10^{-5} mbar and a temperature of 400°C are reached. This step is important to remove any impurities that were formed and deposited during a previous process or the opening of the chamber doors. The CA Cr metal ion etch follows immediately after the target cleaning step. This step is used to clean the substrate and to implant metal ions to provide a sufficiently high adhesion for the sputter deposited film [37]. After this step all four cathodes are used in UBM mode. A TiAlCrN base layer was deposited prior to the main coating to grade the stresses between substrate and coating. The process parameters used for TiAlCrN and TiAlN/CrN were previously described in [13, 21, 130]. Deposition parameters for the TiAlCrYN coating were previously reported in [13, 33]. The deposition parameters of TiAlCrYN+Ox (with oxynitride overcoat) and TiAlN/CrN are mentioned in Table 3-2. All Y containing coatings were produced in machine B.

Deposition Step	**TiAlNCrN** **TiAlN/CrN** Machine A	**TiAlCrYN** **TiAlCrYN+Ox** Machine B
Non changing values	Rotation Speed 8rpm 1and 2 =TiAl, 3 and 4 = Cr	Rotation speed 7.5rpm 1=TiAl, 2=TiAlCrY, 3=TiAl and 4=Cr
Pump Down,	Until $1x10^{-5}$mbar and 400°C was reached	Until 2.5×10^{-5}mbar and 400°C reached
Target Cleaning	For 2min 1kW and 5min 5kW on all targets, Ar:200sccm, $p=2.4x10^{-3}$mbar, T=400°C	5kW on all targets, t=15min, Ar:200sccm, $p=2.4x10^{-3}$mbar, T=450°C [x]
CA Me ion etch	Ubias=-1200V, Cr:100A, t=20min, Ar:41sccm, $p=6.7x10^{-4}$mbar, T=450°C	Ubias=-1200V, Cr:100A, t=12min, Ar:44sccm, $p=7x10^{-4}$mbar, T=450°C
UBM base layer dep.	Cr:0.5kW, 3xTiAl:8kW, Icoil=6A, Ubias=-75V, t=30min, Ar:200sccm, N_2:120sccm, $p=3.5x10^{-3}$mbar, T=450°C	Cr:0.7kW, 2xTiAl:10.7kW, TiAlY:0.5kW, Icoil=7.5A Ubias=-75V, t=45min, Ar:200sccm, N_2:175sccm, $3.4x10^{-3}$mbar, T=450°C
UBM coating dep.	Cr: **Y**kW, 3xTiAl:8kW, Icoil=6A, Ubias=-75V, t=3h30min, Ar:200sccm, N_2: **Z**sccm, $p=3.5x10^{-3}$mbar, T=450°C	Cr:0.7kW, 2xTiAl:10.7kW, TiAlY:10.7kW, Icoil=7.5A Ubias= -75V, t=4h, Ar:200sccm, N_2:215sccm, $p=3.5x10^{-3}$mbar, T=450°C
Overcoat	– – –	See detailed description

Table 3-2: Overview of the process parameters used

The gas flow values were averaged over the entire process-step time and are subjected to fluctuations.

[x]No target cleaning and shutters were used in the case of TiAlCrYN. This coating was part of a different trial series and was later used in the oxidation studies, because of the composition.

TiAlN/CrN: **Y** This parameter was changed for various processes to change the multi-layer thickness between 0.5 and 12kW. **Z** This parameter varied between 120 and 190sccm depend upon the power chosen. The power at the Cr target was stepwise increased. Arcing did occur at 10 and 12kW on the Cr target for a very short moment.

3.2.2 Overcoat

Special attention has been paid to the deposition of the overcoat. To achieve a sufficiently strong mechanical support for the glassy and extremely smooth oxynitride overcoat, a thin particularly hard nanolayered coating was grown. By increasing the power on the Cr target stepwise from 0.7 kW to 10.7kW an inter-layer, with TiAlYN and CrN nanolayers, was produced [145]. These conditions were held for 10min, then the Cr target power was gradually decreased to 1kW. In parallel the nitrogen gas flow was progressively reduced and gradually replaced by medical dry air. In this way a Cr and oxygen containing TiAl-oxide surface was obtained (Figure 3-4).

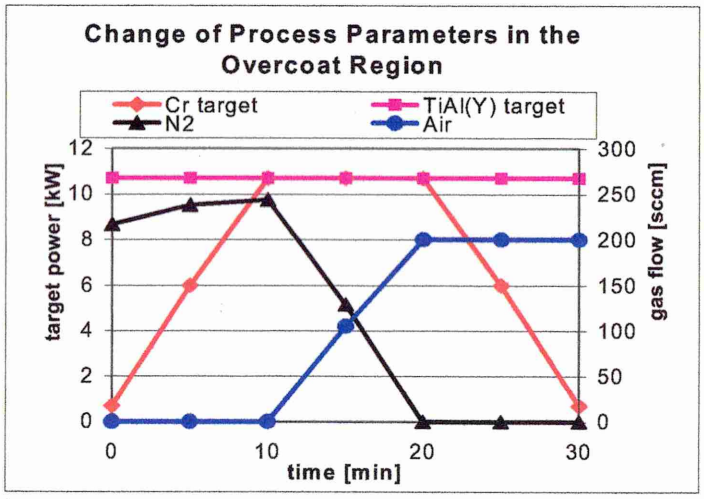

Figure 3-4: Detailed schematic of the process parameters used to deposit the multilayer structured oxynitride overcoat region. TiAl(Y) indicates the two TiAl and one TiAlY target used.

3.2.3 Principle structure of the coatings

Schematics (Figure 3-3) of the coatings were made to clarify the terms used to describe various regions of the coating. Between substrate and coating is the interface region (red) created by the cathodic arc metal ion etch [37]. The base layer is deposited between the main coating and the substrate to grade the stresses introduced during coating deposition. As can be seen from the deposition conditions, all coatings were deposited with a TiAlN type base layer. The base layer was deposited utilising mainly the TiAl targets. All other targets were protected from contamination by using a low power, high enough to prevent contamination by other targets. Therefore, the base layer contains, next to TiAlN, traces of other elements like Cr and Y. Figure 3-3 a) shows the $Ti_{0.44}Al_{0.54}Cr_{0.2}N$ coating. This coating was used as base layer in the case of all TiAlN/CrN type multilayer coatings (Figure 3-3 b). In case of TiAlCrYN a very small percentage (<<1at%) of Y is in the base layer. Figure 3-3 c) shows the overcoat or topcoat region of the TiAlCrYN+Ox coating. The deposition of the overcoat is explained in detail below.

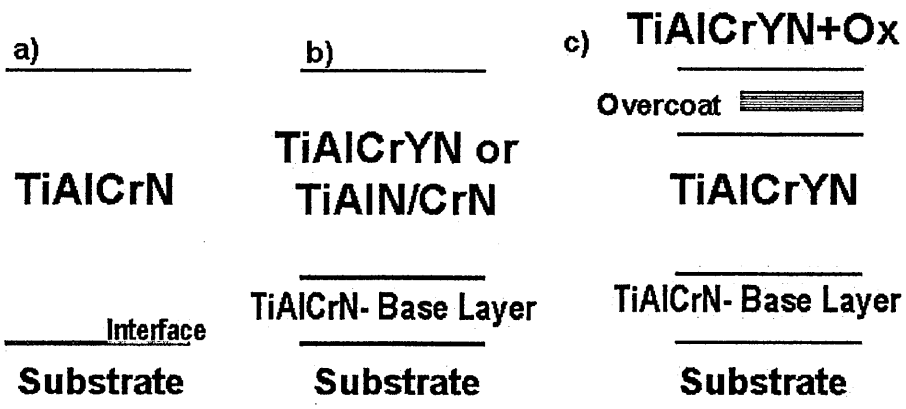

Figure 3-3: Schematic of the coatings under investigation: a) TiAlCrN b) original TiAlCrYN and TiAlN/CrN c) TiAlCrYN with overcoat as produced in the commercial production machine

3.2.4 Composition of the as-deposited coatings

The coating composition of the as-deposited samples was measured using the Rutherford backscattering method with 2MeV He^+ ions at an incident angle of 22.5° relative to the sample surface normal and detector set at a 150° scattering angle. The total accumulated ion dose was 100μC. The spectrum was analysed using the RUMP simulation program [146].

The RBS equipment used was located at the University of Urbana Champaign in Illinois, USA and both the measurements and analysis were performed by Mr. Chan-Soo Chin. An example of the data collected from the backscattering measurement is shown in Figure 3-5.

The amount of Cr and Ti were difficult to analyse, because they have similar backscattering values. The results gained from these measurements were compared to previously published ones (grey) and quantitative EDX analysis (Table 3-3). The values tabulated in the table are normalised to a 100at% including N. A detailed description of the technique can be found in [147]. A short summary of it is given below:

RBS is a non-destructive technique using a beam of high-energy low-mass ions to bombard the sample. The backscattered atoms are energy analysed using a detector. The energy E_1 of a projectile with mass m_1 that has been elastically scattered from a surface target atom of mass m_2 is given by

$$E_1 = k^2 E_o \qquad \text{Equation 3-1:}$$

$$k = \frac{m_1 \cos\theta}{m_1 + m_2} + \left[\left(\frac{m_1 \cos\theta}{m_1 + m_2} \right)^2 + \frac{m_2 - m_1}{m_1 + m_2} \right]^{1/2} \qquad \text{Equation 3-2:}$$

E_0 is the incident energy of the accelerated ion, and θ is the scattering angle between the incident beam and the detector. Thus a measurement of E_1 specifies the target atom. Incident ions not scattered by surface atoms will penetrate the target and lose energy by inelastic ionisation and excitation

process before finally experiencing an elastic nuclear backscattering event. The particle will then lose further energy during its transition back to the surface. The rate of energy loss by inelastic processes is given by the stopping power, $\sigma_{(x)}$, which is tabulated for most materials. Standards are generally not required.

Samples consisting of multiple elements or of low-Z-element coatings on high-Z-element substrates provide difficulties for RBS analysis due to overlapping profiles. Some prior knowledge of the sample composition is often necessary. In favourable cases RBS can provide a detection limit of approximately 0.1at% and a depth resolution of 20nm. The lateral resolution is poor, typically about 2mm [148].

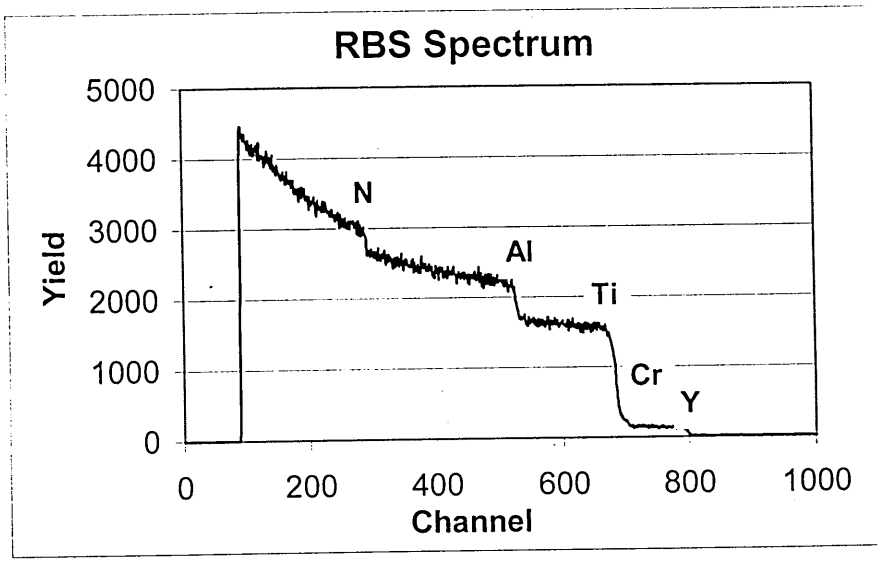

Figure 3-5: Example of backscattered data

	Elements (in at%)				
Coating:	Ti	Al	Cr	Y	N
TiAlCrN 0.5kW	22	27	1	- - -	50
TiAlCrN 0.5kW	22	26.5	1.5	- - -	50
TiAlN/CrN 1kW	22	26	3	- - -	49
TiAlN/CrN 2kW	19	22	9	- - -	50
TiAlN/CrN 4kW	17	18	15	- - -	50
TiAlN/CrN 4kW	16	18	16	- - -	50
TiAlN/CrN 8kW	13	13	24	- - -	50
TiAlN/CrN 8kW	11	13	26	- - -	49
TiAlN/CrN 10kW				- - -	
TiAlN/CrN 10kW	10	11	29	- - -	48
TiAlN/CrN 12kW	10	10	32	- - -	48
TiAlN/CrN 12kW	9	11	30	- - -	50
TiAlCrYN	24	24	1.5	0.7	50
TiAlCrYN	21.5	26	1.5	1	50
TiAlCrYN + Ox	17	31	1.3	0.6	50
EDX analysis	15	32	2	0.6	-.-.-
SNMS	20	30	1.4	-.-.-	50

Table 3-3: Composition of the coatings used in the investigations. Values from the literature are blue. For TiAlCrN and TiAlN/CrN reference [130] and for TiAlCrYN reference [33] was used.

3.3 Mechanical properties

The coatings were characterised after each coating process using Rockwell C indentation [149], scratch test with a Rockwell Diamond and a tip with 200µ [150], calo-test [151] and Knoop hardness measurement with 25g load [152]. This was necessary to ensure the coatings exhibited the expected mechanical properties in terms of adhesion, hardness and thickness [33, 21, 13]. All samples were found to exhibit parameters consistent with the earlier studies (Table 4).

Coating	Hardness HK	Rockwell C	Scratch Test	Thickness
TiAlCrN	2400	H 1-2	55 N	3 μm
TiAlCrYN	2700	H 1-2	40 N	2.3 μm
TiAlN/CrN	3400	H 1-2	55 N	4 μm

Table 3-4: Measured mechanical properties on the coatings used. The standard deviation for the hardness is HK ± 400, for the scratch test ±10N and for the coating thickness evaluated using the calo test ±0.2μm.

3.4 Thermogravimetry (TG)

A Cahn TG 131 microbalance was used for the thermogravimetry work. The specifications for this microbalance are a temperature drift stability of 10 μg/°C, temperature repeatability of ±3°C and a mass sensitivity of 1 μg. The TG allowed comparison of the onset point of oxidation and the different weight gain in air of the coatings under investigation. All coatings were deposited onto stainless steel 304. The SS 304 sheet was covered from all sides with coating material during the process, including the hole drilled for fixing the sample in the TG. A stainless steel edge was exposed to the heat treatment in the TG, due to the way the samples were fixed in the coating machine and treated afterwards (see Figure 3-1). The samples were heated using continuous and isothermal programs.

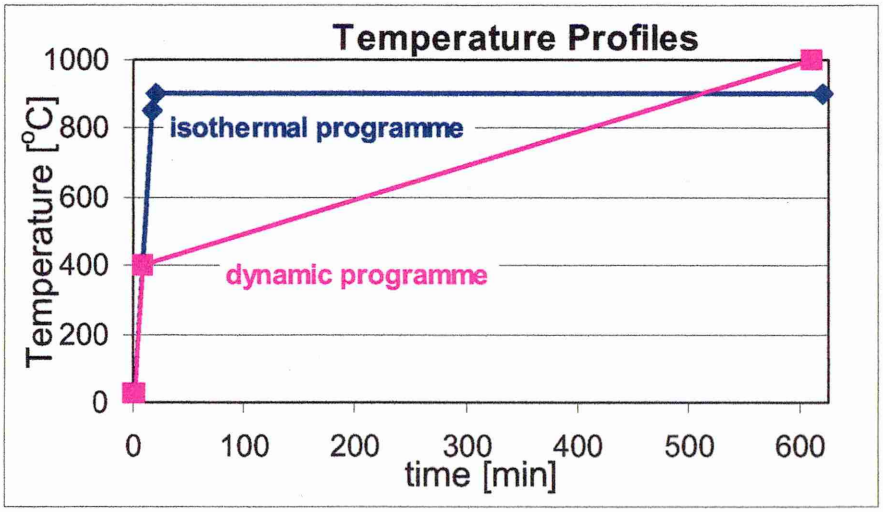

Figure 3-6: Temperature profiles of the TG programmes used

In the dynamic (continuous) measurements the samples were heated at a rate of 50°C min^{-1} to 400°C and then at 1°C min^{-1} until 1000°C was reached (see Figure 3-6). The total duration of the continuous measurement was 10.5h. The samples were more than 5h at temperatures above 600°C. In isothermal measurements, a heating rate of 50°C min^{-1} up to -50°C below the final temperature was chosen. Ramping typically required ~30min to reach the up to -50°C of the final temperature. This rapid heating ensures that the oxidation occurs mainly at the chosen temperature and not during ramping. Thereafter a rate of 15°C min^{-1} was chosen to reach the final temperature. The lower ramp rate was used to keep the temperature from rising more than +2°C above the final temperature. The final temperature was held for 10h. The gas flow rate in the furnace of the TG was 12.6 ml min^{-1}.

3.5 Scanning electron microscopy (SEM)

A Philips XL 40 SEM was used to investigate the effects of oxidation at the sample surface. The various responses created by impinging electrons on the sample are shown in Figure 3-7. Emitted secondary and backscattered electrons are used to create an image of the sample surface. The image gained from the secondary electron detector gives an impression about the topography of the sample. Backscattered electron images show differences in elemental composition.

In some oxidised specimens the surface charged heavily. In this case a carbon coat was applied.

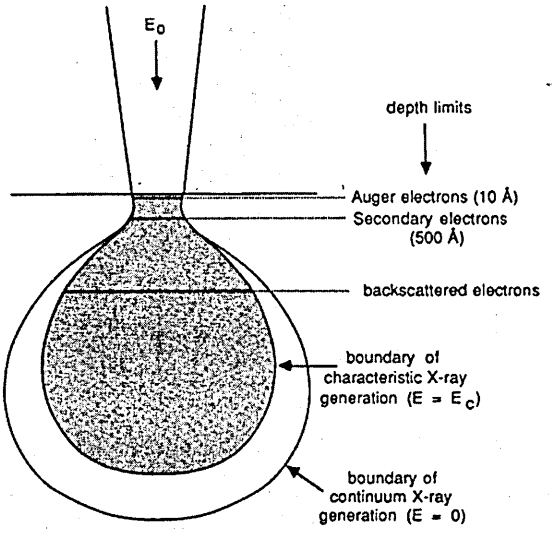

Figure 3-7: View of the X-ray excitation volume created [153].

For EDX analysis a detector with an ultra thin window was used at 10kV accelerating voltage. In this case continuum and characteristic X-rays contribute to the signal detected. The probability of exciting X-rays depends on the energy of the electron beam, the excitation volume or cross section and the composition of the target. The emission of X-rays for low Z elements (e.g. N, O, C) has a low probability in a SEM. Furthermore, the detection of low Z elements is often not possible; because of the type of detector chosen. The detector can adsorb the few incoming X-rays of the low Z elements. Hence, they are outside the detection limit. Additionally, X-rays stemming from L-lines (Ti, Cr) contribute to the low energy region. The energy separation is 133eV at FWHM measured on Mn. The excitation volume in bulk samples is the reason why the resolution in the SEM is ~1μm, even though the imaging resolution is ~5nm for a tungsten filament. There are many books covering the subject on electron microscopy and EDX analysis, see for example [154, 155, 156].

3.6 Transmission electron microscopy (TEM)

The TEM was used to view microstructural features of the coating and composition before and after heat treatment using cross sections. The microstructural features of interest are differences in e.g. grain size, micro-voids and cracks. Due to its high resolution (<0.5nm), TEM provides the ideal tool to view such extremely small features. In a TEM or STEM it is possible to obtain information concerning the grain size and morphology, the density of extended defects, the lattice constant, the degree of preferred orientation and the film composition – all of the same region of the film with a lateral dimension of the order of 5 nm.

The use of cross sectional TEM (XTEM) provides the opportunity to obtain depth dependant information in order to, e.g., investigate the evolution of film microstructure and composition between the film/ substrate interface and the coating surface.

The XTEM samples have been prepared by cutting 1x3x1mm pieces from a coated sheet or coupon. Several steps of grinding and polishing of both sides of the specimen were necessary until a thickness of 50-60μm was reached. The specimens were glued onto a glass slide using 'crystal bond'. During the grinding and polishing step two specimens face each other, and thus benefit from additional protection of the coating surface. The relatively thick samples (60μm), allowed the preparation of XTEM specimens by this simple method. It was shown that the support the larger coating area offers is sufficient to preserve oxides on the coating surface throughout the grinding and polishing step. For as-deposited samples the same method was used but the samples were reduced to a thickness of ~20-30μm during the grinding and polishing step. The polished metal foils were mounted with super glue onto a copper grid and ion beam thinned until electronically transparent (Figure 3-8). The coating was facing the middle of the copper grid. Incident angles of 10 degree and an accelerating voltage of 5keV were chosen on the ion beam miller (Gatan PIPS 691 system) until a sample thickness of ~10μm was reached. In the final step of the ion milling process, the chosen incident angles were 8 and -5 degree, using

5keV to accelerate the Ar-ions. The low angle and voltage should protect the specimen from ion beam damage. The foils had a thickness of ~70±20nm at the electron transparent region.

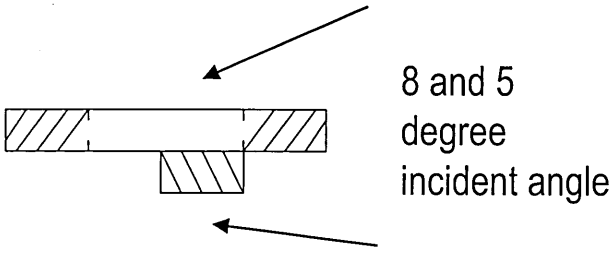

Figure 3-8: Position of the sample during the ion beam milling process.

A Philips CM 20 TEM was used for all recorded bright field, dark field and diffraction patterns. Bright and dark field imaging describes techniques to enhance contrast created by the electron beam. The contrast mechanism that arises in a TEM from both elastically and in-elastically scattered electrons and how they are used to provide information are summarised in many texts, e.g. [154, 156]. In the case of BF imaging the central transmitted beam is used to form the information. In contrast, in the DF image technique the diffracted beam can be utilised to study grain orientation.

Diffraction information can be obtained by inserting an aperture below the objective lens in the column. This method is termed selected area diffraction. Selected area diffraction, using an aperture of about 500nm in size, from the middle of XTEM samples was used to observe the structure before and after heat treatment. Annular dark field images with an angle of 30mrad were taken from the oxide layer to show if void formation – lack of mass contrast occurred. This is a region beyond the {420} ring formed on a diffraction pattern (DP). In this region the influence of diffraction contrast created should be minimal [157].

The majority of the X-ray analysis (EDX) work was performed on a VG HB 501 STEM with a FEG. A windowless EDX detector and a very low pressure of 10^{-9} mbar, was employed for such analysis. EDX analysis in the TEM has the advantage that the excitation volume is approximately the size of the incident electron beam in the lateral dimension (Figure 3-7). Spatial resolution achieved

in the VG HB501 was estimated to be ~3nm. Elemental mapping was used to demonstrated local changes in composition. The maps created were transferred into a tif file format using the AN 10000 conversion software and Adobe PhotoShop graphic program.

EDX point analysis profiles of XTEM samples were recorded perpendicular to the coating surface. Point of interests were the stability of the substrate/ coating interface, the composition of the coating surface and oxide layer. All measurements were taken inside a column; boundaries were avoided. A typical absolute error (sensitivity) was calculated using:

$$\frac{f}{a} \times c = typical\ absolut\ error\ in\ at\% \qquad \text{Equation 3-3:}$$

Where f is the fraction error, a the counts under the peak and c the concentration in at%.

	Al	Ti	Cr	Fe	Y
Steel	0.6	0.4	0.3	0.4	0.1
Coating	0.6	0.4	0.2	0.2	0.2

Table 3-5: Typical absolute errors for STEM EDX measurement

The calculated error is effected by the total number of counts and the sample thickness.

Differences occurring in the N or O counts were plotted by using the ratio of the N or O peak counts divided by the sum of all counts. This allowed the concentration to be plotted because changes in the number of counts caused by a different background were avoided.

Elemental maps taken from XTEM samples have to be carefully interpreted. The intensity of a map changes with the total number of counts collected for a corresponding selected energy range. The number of counts varies not only with concentration but also with the sample thickness. Sample thickness effects can be recognised if the same change in intensity appears in various elemental

maps taken at the same area of the TEM sample. A rise in sample thickness also leads to a rise in the background counts in all elemental windows. In the case of the Y maps the intensity of the map is quite low, due to the low concentration of Y in the sample. The intensity of the map, therefore, can be strongly effected by a change of background counts. Also important in the case of N and O maps is that, although a narrow keV range was used for collection this was still partially overlapped by the Ti_L line (in the case of N) and the Cr_L line (in the case of O). This means that N and O maps have to be compared carefully with the Ti and Cr map in order to confirm the integrity of intensity variations in the maps.

3.7 X-ray diffraction (XRD)

The X-ray analysis was performed with a Philips PW 1830 goniometer using CuKα radiation produced with a current of 40A and a voltage of 40keV in Bragg-Brentano and thin film (glancing angle) geometry.

X-ray diffraction is a widely used technique in coating analysis. Its non-destructive nature is suitable for microstructural and phase studies, lattice parameter and stress analysis. Information about the crystal orientation, texture, stress and to, some extent, composition of the film can be obtained. Detailed information about X-ray diffraction techniques is described in [158].

In coating analysis the diffraction peaks observed are often quite broad since the films typically have small grain sizes and high defect concentrations. The precision of lattice constant determination is generally not better than ~0.001nm. This accuracy is sufficient for general phase identification. Higher precision is, however, required for compositional determinations, distinguishing between phases with similar lattice constants, and performing stress/strain analyses based upon peak positions [148]. The lattice parameter for the same coating can vary over a wide range due to the superimposition of stress (see for example TiAlN Literature review) depending on the process parameters used. Intrinsic stresses are caused by defects in the films. Shifts in XRD peaks have been used for investigating macrostress (i.e., uniformly distributed stress, see Figure 3-9) [159, 160].

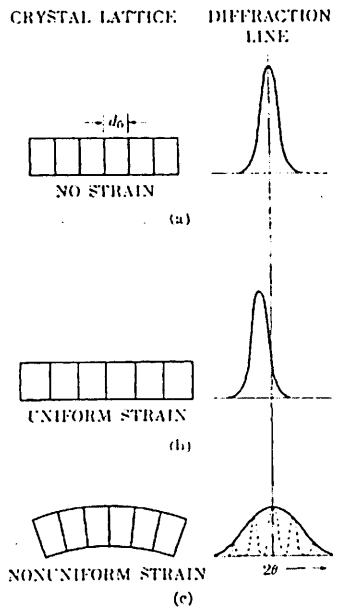

Figure 3-9: Schematic illustration of lattice strain on the width and position of diffraction peaks [158].

In the Bragg-Brentano arrangement the specimen is maintained at an angle θ and the counter at an angle 2θ respectively to the x-ray beam to satisfy the Bragg conditions (Equation 3-4).

$n\lambda = 2\,d\sin\theta$ Bragg equation Equation 3-4:

The wavelength is λ, d is the interplanar spacing and θ the measured angle (see Figure 3-10). Thus, the only planes to diffract are those parallel with the surface, hence it is known as symmetrical diffraction. In thin coatings the X-ray intensity from the deposit is low because the irradiated volume is small.

Low angle X-ray diffraction (2-8° 2θ) was used to determine the multilayer period. The position of the low angle peaks were measured and the multilayer period calculated using the Bragg equation, where *d* is redefined as the multilayer spacing.

In the glancing angle technique the angle of incidence to the sample remains fixed at a low angle e.g. 0.5-5 degree (i.e. the specimen does not move) and the counter is driven. In this technique the diffracting planes are at an angle $\theta - \alpha$ to the specimen surface. The advantage of glancing-angle parallel beam XRD is that because of the low incidence angles the path length in thin coatings is dramatically increased, resulting in an increased signal from the coating relative to the substrate. An incident angle of 0.5° provided a good peak separation in the oxidised sample, which is necessary to be able to identify the peaks. The phases present were identified by comparing the peak position with powder diffraction data [94].

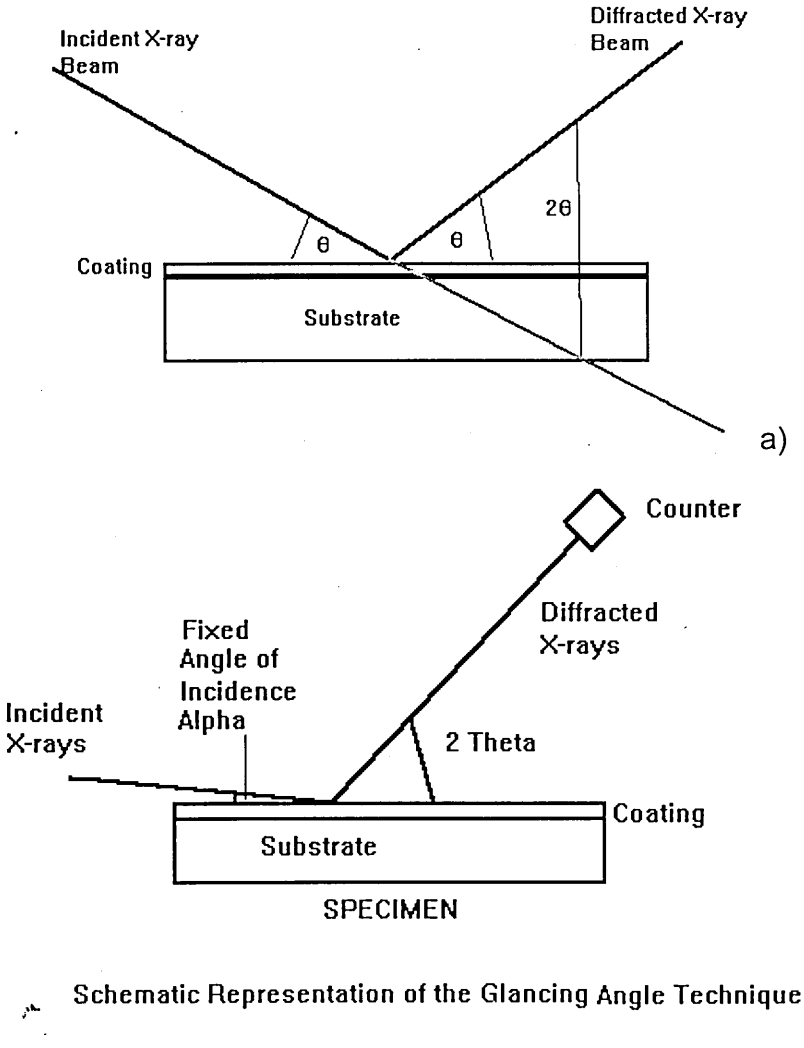

Figure 3-10: Geometry in a) Bragg-Brentano and b) glancing angle geometry.

The fixed angle of incidence allowed analysis of the sample with an almost constant penetration depth. The penetration depth is defined as the distance from the surface over which the diffracting planes in the specimen contribute to the whole diffracted intensity [159].

The depth of penetration X_e is often defined as the depth from which the diffracted intensity has a value of *1/e* of the incident intensity for a linear absorption coefficient μ, with γ being the angle of incidence.

For Bragg-Brentano geometry $$X_e = \frac{\sin\theta}{2\mu}$$ Equation 3-5:

For Parallel Beam geometry $$X_e = \frac{\sin\gamma \sin(2\theta-\gamma)}{\mu\left(\sin\gamma + \sin(2\theta-\gamma)\right)}$$ Equation 3-6:

A major advantage of glancing angle parallel beam geometry over the Bragg-Brentano geometry for analysis is that above $2\theta = 30°$ the penetration depth is almost constant over a wide range of diffraction angles. The linear absorption coefficient needed for the calculation was calculated to be 620cm^{-1} for TiAlN [129]. The penetration depth for glancing angle stress measurements at 5° incident angle is therefore 1200nm. The penetration depth at 0.5° would be ~200nm. The compositional and structural differences on the coating surface after heat treatment (e.g. increased roughness at the sample surface, porous oxide layer) allowed only a very rough assumption of the true penetration depth.

The residual stress present in the coating was determined using glancing angle parallel beam geometry [161], with a fixed incident angle of 5° and all reflections between 30 and 140°. Another method used was an asymmetric Bragg-Brentano scan (Ω-tilt) using the {422} reflection by varying the tilt angle between 0° and 50° [159, 162]. The glancing angle method was not available at the beginning of this PhD and for this reason two different methods to determine the stress in coatings were used. The following tilt angles were used 16°, 24°, 32°, 38° and 44°. In this work the stress considered is parallel to the surface. The stress is calculated with the following equation:

$$\sigma_{stress} = \frac{E \cdot slope}{a_o \cdot (1+\mu)}$$ Equation 3-7

where E is the elastic-modulus of the material, the slope is the gradient measured from a lattice parameter a_ψ versus $sin^2\psi$ plot, a_o is the unstressed lattice parameter and μ is Poisson's ratio [159, 162]. A value of 0.3 was reported for the Poisson's ratio of TiN films [163]. This value was used in all calculations.

The lattice parameter a_ψ is determined over the peak position measured. The lattice parameter a_ψ is plotted versus $sin^2\psi$. The slope from this plot is a measure of the strain distribution. Therefore the stress can be calculated using Equation 3-7.

4 OXIDATION BEHAVIOUR OF MACRO DEFECTS

The coatings in this investigation were produced using the combined cathodic arc/ unbalanced magnetron sputter technique (ABS™). The cathodic arc chromium metal ion-etching step is an important step in the combined technique. It allows high and reliable adhesion values for PVD hard coatings on steel substrates [34]. One of the drawbacks of the cathodic arc deposition are macroparticles generated in the metal ion etching stage which result in the formation of local growth defects [24, 25, 48, 54, 55]. In previous papers [24, 55] it was shown that the size and the amount of droplets are substantially reduced by the cathodic arc Cr metal ion etch. However, the few remaining droplets lead to a shadowing effect underneath the droplet, which results in an attenuated ion and deposition flux. The defect structure that surrounds a droplet leaves a low-density zone or even a gap between the growth defect grain structure and the coating [54]. In other cases the droplets and the defects, grown on the droplets, may be expelled from the coating during film growth due to compressive stresses generated by the growing film, causing craters [55]. The effect of heat treatment on the coatings deposited on different substrates was observed using mainly scanning electron microscopy. In case of high speed steel and cemented carbide only the TiAlN/CrN coating deposited at 8kW was investigated.

4.1 Growth Defects

4.1.1 SEM imaging

Examination at low magnification of the surface of the as-deposited coating using SEM showed the presence of growth defects and craters (Figure 4-1). Droplets produced by the cathodic arc metal ion etch led to growth defects in the coating, which can extend from the substrate to the coating surface [54]. Because of the inherent high residual compressive stresses in the coating, some defects become detached [55] resulting in the formation of craters as pointed out by the arrow in Figure 4-1.

4.1.2 TEM imaging

Figure 4-2 shows a TEM BF micrograph of a cross section of a growth defect. At the substrate/ coating interface the amount of material removed during the Cr metal ion etch is visible, because the droplet shadowed parts of the substrate surface. The droplet itself has been reshaped due to the ion bombardment. The coating grain structure on the droplet has a different growth direction in comparison to the general perpendicular columnar growth observed in the coating. The effect caused by shadowing of the droplet and the low-density zone surrounding the droplet is clearly visible.

4.2 Effect of different substrate materials

Stainless steel AISI 304 (SS) was mainly used for the oxidation investigations because it is non-magnetic, it has a high oxidation resistance and therefore low interference with the investigation of the oxidation behaviour of the coating. However, tools are manufactured from high-speed steel AISI M2 (M2) and cemented carbide WC-Co (CC). Eventual differences occurring after heat treatment have been observed using SEM. The oxidation behaviour and the oxidation products formed from CC and M2 was observed using TG and XRD.

4.2.1 TG measurements

The TG measurements in Figure 4-3 revealed that the CC starts to oxidise rapidly at temperatures above 700°C. In contrast to CC, rapid oxidation in M2 high-speed steel does not occur before 900°C. The weight gain of cemented carbide is higher than that of M2 and SS by a factor 5 and a factor 100, respectively when heated to 1000°C. Cemented carbide is well known for its rapid oxidation behaviour starting at temperatures as low as 600°C [98]. It needs therefore a protective coating to enable its use in high-speed cutting operations. The weight gain of SS 304 is plotted for comparison purposes in Figure 4-4.

4.2.2 XRD analysis

XRD diffraction patterns of the surface of CC and M2 heat treated at 900°C for 1h (CC) and 1000°C for 1h (M2) are shown in Figure 4-5 and Figure 4-6. The oxides identified on CC were two different forms of tungsten oxide, both of type WO_3 with a monoclinic crystal structure (JCPDS 24-747) and a triclinic crystal structure (JCPDS 20-1323), respectively together with a mixed tungsten cobalt oxide $CoWO_4$ with a cubic crystal structure (JCPDS 15-867) [94]. The mixed $CoWO_4$ oxide resulted from the oxidation of the cobalt binder used in

liquid phase sintering of the tungsten carbide matrix. On M2, hematite (JCPDS 24-0072) Fe_2O_3, magnetite (JCPDS 19-0629) Fe_3O_4 and a mixed $FeCr_2O_4$ (JCPDS 24-0512) oxide were identified. The M2 substrate material was not fully oxidised, as can be seen from the presence of the remaining iron (JCPDS 06-0696) peaks in the XRD pattern in Figure 4-6.

4.2.3 SEM investigations

After heat treatment of TiAlN type coatings with different Cr content deposited onto stainless steel the formation of oxide needles around growth defects was observed. TiAlCrN and TiAlN/CrN produced using a power 0.5kW to 12kW power on the Cr target were heat treated for 5h at 900°C [21]. The coating surface was examined using SEM. Oxide nodules covered the coating and the growth defects observed in the as-deposited condition after heat treatment.

On a number of growth defects larger oxides were observed surrounding the defect area (Figure 4-7). The oxidation had increased, because of the low-density region, surrounding a defect in the coating. With increasing Cr content and increasing oxidation resistance of the coating [21] the incidence of needles surrounding a growth defect decreased.

Spot analysis on oxides in defect free regions and on a needle surrounding a growth defect are shown in Figure 4-7 and were made using 10kV accelerating voltage. The needles surrounding the growth defect are richer in Ti than the oxides formed in defect free regions. Because of the large excitation volume the X-rays collected stem from a relatively large volume surrounding and under the needle. It is likely that the primary cation in the crystallites is Ti. Additionally, the needles grow with a morphology similar to a rutile structure (TiO_2) crystals [94]. The formation of Ti-rich oxides was observed forming in cracks after heat treatment for 3h at 850°C of TiAlN deposited onto SS on the coating surface after [11].

Elemental mapping of a growth defect found on a $Ti_{0.44}Al_{0.53}Cr_{0.3}N$ coating showed that oxide needles are rich in Ti (Figure 4-8). Even though the beam spread is in the range of 1μm, it can be concluded from both the elemental maps and the point analysis that the enlarged oxide needles surrounding a defect are rich in Ti.

Oxidation of $Ti_{0.26}Al_{0.26}N/Cr_{0.48}N$ coatings deposited onto CC at temperatures as low as 700°C showed that oxides were formed at the bottom of craters (Figure 4-9a). These craters were formed from growth defects, which were expelled during deposition due to the development of high compressive stresses [55]. Increasing the temperature to 800°C leads to a significant increase in oxide formation in the crater, which resulted in cracking of the adjacent coating (Figure 4-9b). EDX analysis of the oxidation product in the crater showed the presence of both tungsten and oxygen (Figure 4-10a). The presence of the element tungsten in the oxides formed in the crater clearly shows that these oxides are formed by the oxidation of the substrate. Previous XRD measurements on the oxidised substrate indicated that the oxides formed were $CoWO_4$ and WO_3 (Figure 4-5).

A possible mechanism for the formation of cracks in the coating adjacent to craters containing oxide is the high volume expansion of tungsten oxide relative to that of tungsten (38% increase in volume). In contrast to CC local oxidation of substrate material in holes occurred at higher temperatures on M2. The first oxides were observed at 700°C on CC and at 900°C on M2. This result is not surprising as the TG analysis clearly showed that CC oxidises at a significantly lower temperature than M2 (Figure 4-3).

Another type of oxidation product is shown in the micrograph in Figure 4-11a) at 700°C on coated CC. At low magnifications, accumulations of very small globular defects were observed as shown by the arrows in Figure 4-11a). At higher magnifications (Figure 4-11b) a continuous oxide layer is observed covered with both smaller and larger sized globular oxides. In these regions only a small concentration of substrate elements were observed for a coated CC oxidised at 800°C (see Figure 4-10b). This special defect may be related to

areas where the droplet and the growth defect were expelled during film growth and the crater created has been partially filled with coating material [55]. Pores formed in the under-dense region at the rim of the growth defect on the deposited film material exhibited localised oxidation. Further oxidation led to the formation of spherical oxides as shown in the micrograph in Figure 4-11c) and the appearance of substrate elements in the oxidation product as shown in the EDX spectrum in Figure 4-10c) at 800°C on coated CC. Similar shaped defects were observed on coated M2. An EDX spectrum in Figure 4-10d) taken at 900°C showed the presence of Fe and O on the surface of the coated M2 steel. However, on coated M2 this defect formation was in general less pronounced than that on coated CC and the first defects containing substrate elements occurred in the oxidation products at 900°C on M2. These results are reflected in the relative oxidation resistance of the M2 high speed steel, in comparison to CC as can be seen using thermogravimetry Figure 4-3.

4.3 Cutting edge and coupon

TiAlCrYN+Ox is a coating deposited onto mills for dry high speed cutting of difficult to cut materials (A2) [1]. SEM was used to compare TiAlCrYN+Ox coated CC coupon with a TiAlCrYN+Ox coated ball nosed end mill. Results previously observed (chapter 4.2) [168], on a TiAlN/CrN coated CC coupon were compared with the TiAlCrYN+Ox coated coupon and ball nosed end mill. Both specimens were coated in the same process and heat treated for 1h at 900°C in a furnace in air.

4.3.1 SEM investigations

A surface containing a few growth defects was observed in the case of the as-deposited coated coupon similar to Figure 4-1. In case of the as-deposited end mill a higher concentration of growth defects was observed around the cutting edge (Figure 4-12). The growth defects around the cutting edge region seemed to be larger than the average defect size. This indicates a preferred

accumulation of macro-particles around the cutting edge. The increased accumulation of macro-particles at the cutting edge was explained by [73], who deposited CrN onto various edge shapes using ion plating, by an increased ion current density at the edge region. An increased number of macro-particles was also observed with increasing sharpness of the edge.

After heat treatment the formation of defects containing substrate elements Co and W was observed in both specimens. On the coupon three different kind of defects were observed (Figure 4-13). The first type showed radial cracks in the coating emanating from an area where substrate oxides penetrated the coating surface. Point analysis taken in the centre of the defect shows the presence of the element W. The second type shows an accumulation of oxides of ~20μm in diameter also rich in W. The third type of defect is thought to have formed from a hole left from a growth defect that had been expelled during the coating process [55]. Again, EDX point analysis revealed the presence of W in this type of defect (Figure 4-13).

In the case of the oxidised end mill the increase in volume of the Co and W oxides is clearly visible when comparing the oxidised shaft of the non-coated part of the mill with the coated cutting edge region Figure 4-14. The coating showed a green interference colour, indicating the formation of a very thin oxide layer. Closer examination of the cutting edge region using SEM revealed similar features to those observed on the coupon (Figure 4-15). However, the appearance of defects on the cutting edge is higher than on the coupon. A typical defect is shown in a magnified region of the cutting edge (top of Figure 4-15).

EDX analysis showed the presence of W and Co. Previous XRD analysis indicated that the oxide products would be of type WO_3 and $CoWO_4$.

These results show a preferred deposition and oxidation of macro-particles at the cutting edge region. After heat treatment an increased number of oxides containing substrate oxides (probably WO_3 and $CoWO_4$) was observed in this region. This shows clearly that the amount of substrate material on the surface is dependent on the number of defects generated during deposition. The

defects formed in a similar manner as described in a previous section (see chapter 4.2).

4.4 The formation of Cracks

Previous investigations showed that the oxidation resistance of the TiAlCrN coating increases as the CrN component of the nanolayered coating increased [21]. It was reported that evidence of cracking was also found in some of these coatings.

Secondly, an increase in hardness and a smother interface of the layers was observed with increasing bias voltage on nanolayered coatings by [3]. A nanolayered $Ti_{0.26}Al_{0.26}N/Cr_{0.48}N$ coating was deposited using bias voltages of -75V, -85V and -95V at a constant Cr target power of 8kW. Special attention was paid to the $Ti_{0.26}Al_{0.26}N/Cr_{0.48}N$ system, because of its advantageous mechanical properties [21].

These investigations will show that a dependency exists between the deposition parameters, the Cr content and the occurrence of cracking. For this purpose TiAlN/CrN was deposited onto stainless steel substrates.

4.4.1 Effect of bias voltage variation on TiAlN/CrN using 8kW power on the Cr target

All the specimens had a similar appearance in the as-deposited condition as previously observed using SEM (Figure 4-1). The samples were heat treated for 1h and 5h in a furnace at 900°C in air.

Optical and SEM microscopy showed the presence of a crack network on the coating surface of TiAlN/CrN after heat treatment for 1h at 900°C (Figure 4-16). Cracks appear to pass through existing defects in the coating. At higher negative applied bias voltage the amount and incidence of observed cracking decreased. The width of the cracks and the amount of local pronounced oxidation inside the cracks also seemed to decrease with increasing bias voltage. McIntyre et al. [11] reported the appearance of crack networks upon

heating $Ti_{0.5}Al_{0.5}N$ coatings deposited at low bias voltages and their disappearance when the bias voltage was increased to -150V. This dependency on bias voltage was associated with an increase in residual stress with increasing bias voltage. Similar observations were made by [90] using AlN on various substrate materials by increasing the deposition temperature. This increases also the mobility of the adatom on the substrate surface. In the current investigation the residual stress increases from –5.1 GPa at –75 V bias to –9.2 GPa at –95 V bias. The cracks observed were generated upon heating, due to differences in the thermal expansion coefficients of substrate and film. The method of linear extrapolation of the coefficients of expansion of the binary components was used by [11] to determine the coefficient of linear expansion of TiAlN. Assuming that this method can be applied to a TiAlN/CrN nanolayer structure a value of $4.7x10^{-6}$ K^{-1} was obtained. The coefficient for the binary components were AlN ($5.7x10^{-6}$ K^{-1}), TiN ($9.4x10^{-6}$ K^{-1}) and CrN ($2.3x10^{-6}$ K^{-1}) [9]. The linear expansion coefficient for austenitic SS 304 is $19x10^{-6}$ K^{-1} [164]. During heating, the additional expansion of the substrate superimposes a tensile stress in the nitride film leading to crack formation [92; 90; 89]. The theoretical temperature at which cracking would first occur is induced when the tensile stresses produced during heating, $\sigma_{th,}$ exceed the residual compressive stresses developed during deposition. σ_{th} was calculated using:

$$\sigma_{th} = E_L/(1-\nu_L)\times(\alpha_L-\alpha_S)\times(T_{ox}-T_d) \qquad \text{Equation 1 [89]}$$

where the subscripts *L* stands for layer, *S* for substrate, *OX* for oxidation or heat treatment temperature and *d* for deposition temperature.

From purely theoretical considerations, i.e ignoring any stress relief within the coating, cracking could first occur in the –75V bias sample at 630°C, at the –85V bias sample at 900°C and at the –95V bias sample at 1120°C, thus cracking is more likely to occur when TiAlN/CrN superlattice coatings are deposited at –75V bias.

The oxide formation locally in the cracks was more pronounced than on the general coating surface. Some oxides had a bulge shape with facets at the surface of the oxide. After heat treatment for 5h at 900°C the presence of Fe

and Cr in these oxides was confirmed by EDX (Figure 4-17). Additional to the needle type oxide in the cracks, a more protruding type of oxide was observed. These protrusions were richer in Fe and Cr than those of the needle type oxides, which were associated with rutile (TiO_2) formation. The presence and the different shape of oxides in the cracks might be depending on the depth and width of the crack.

On the -75V bias sample, a crack connecting the coating surface with the substrate that was filled with oxides was imaged using TEM (Figure 4-18). The bright field image montage shows clearly how oxidation progressed through the crack and how substrate material was consumed. EDX analysis, recorded at the top-centre of the crack filling oxide, revealed an additional amount of Ti, suggesting the formation of a Ti_xO_y oxide. The cross sectional TEM bright field image showed that cracks formed in the coating can propagate through the entire coating layer. The cracks provide direct pathways for the penetration of oxygen allowing oxidation on the substrate and substrate elements to diffuse through to the coating surface.

The activation energy and the free energy of formation of oxides from nitrides is shown in Table 4-1. This showed that the formation of Cr_2O_3 is favoured over TiO_2 and Al_2O_3 (Table 4-1). The formation of a Cr rich oxide layer was expected, whereas the formation of a Ti-rich oxide in the crack showed that theoretical considerations are not true in all cases.

	Ionic radius [nm] of most common valence [X]	Activation Energy [E_a/eV]	$\Delta G_{900°C}$ [kJ/mol O_2] [Y]	$\Delta G_{nitrides900°C}$ [kJ/mol O_2]
TiO_2	Ti 0.068	2.0 [Z]	-170	-500 (TiN)
αAl_2O_3	Al 0.053	2.2-2.4 [Z]	-205	-620 (AlN)
Cr_2O_3	Cr 0.063	1.6 [*]	-130	-585 (CrN)

Table 4-1: ΔG nitrides have been calculated from the ΔG of metal nitrides and ΔG of metal oxides. ΔG produced by the formation of oxides directly from the nitrides was made at 900°C, the nitrides used are given in brackets. X=[165], Y=[166], Z=[11], *=[29]

4.4.2 Effect of Cr target power

After heat treatment for 1h at 900°C, formation of cracks in the coating surface was observed (Figure 4-19) for a Cr concentration exceeding 30at% (normalised to the total metal content). This was observed when the power applied to the Cr target was 4kW. The addition of Cr changes the thermal coefficient of expansion of this coating. The method of linear extrapolation introduced in the previous section (4.4.1) was applied to calculate the thermal expansion coefficient for various compositions of TiAlN/CrN. Table 4-2 shows the concentration measured using RBS, the calculated thermal expansion coefficient and the observations made in the SEM after heat treatment for 1h at 900°C.

Coatings (Cr target power used)	SEM after 1h at 900°C Cracking?	Thermal expansion coefficient α_{Th} [10^{-6} K^{-1}]
$Ti_{0.44}Al_{0.54}Cr_{0.02}N$ (0.5kW)	No	7.26
$Ti_{0.435}Al_{0.515}Cr_{0.05}N$ (1kW)	No	7.14
$Ti_{0.38}Al_{0.44}N/Cr_{0.18}N$ (2kW)	---	6.49
$Ti_{0.34}Al_{0.36}N/Cr_{0.30}N$ (4kW)	Yes	5.94
$Ti_{0.22}Al_{0.26}N/Cr_{0.52}N$ (8kW)	Yes	4.75
$Ti_{0.19}Al_{0.19}N/Cr_{0.62}N$ (12kW)	Yes	4.66
SS 304 [164]	---	4.30

Table 4-2: Concentration of coatings normalised to a 100at% metal content, observations made after heat treatment and the calculated thermal expansion coefficient. A difference between monolithic (TiAlCrN) and nanolayered (TiAlN/CrN) coatings is made in the writing, for the measurements of the bi-layer thickness see [130].

The table shows that cracking occurred on a stainless steel substrate coated with a Cr containing TiAlN type coating if the thermal expansion coefficient fell below 6.5×10^{-6} K^{-1}. Previous investigations [130] showed an increase in residual

stress from –3.8GPa for TiAlCrN coating, deposited using 0.5kW Cr target power, to –6.15GPa for a TiAlN/CrN coating deposited, using 12kW Cr target power. This shows that with increasing difference between thermal expansion coefficient of the stainless steel substrate and the coating the compressive stress increases, too. The compressive stress in the coating should counteract cracking to some extent.

4.5 Discussion

Localised a different oxidation behaviour to the overall coating was observed. Two major kinds of oxides emerged at defects. Oxides rich in Ti or oxides formed by substrate material were observed. The formation of either one or the other is probably dependent on the depth of the defect (connection with substrate material) and time of the heat treatment.

The influence of pinholes in the coating and the diffusion of substrate materials through the coating was also observed by [167], [123]. Penetration of Fe, probably through pinholes in a CrN coating sputter deposited onto Ck 45 steel, was observed after heat treatment for 2.5h at 600°C [123]. Fe oxides were found on the coating surface of TiN deposited onto M2 steel by ion plating after oxidation occurred in a sterilisation process at 130°C and 210 kPa steam pressure [167]. The deposition process in this case produced, through the formation of droplets, an additional number of defects at the coating surface. These defects and the diffusion of substrate elements through pinholes led to the formation of substrate element oxides at the coating surface. It was found that the influence of the substrate material forming oxides on the coating surface increases with decreasing oxidation properties (onset point of rapid oxidation) of the substrate material. The formation of substrate oxides becomes critical if they have a large volume expansion. This was visible in the case of WO_3, which led to crack formation in the coating.

It was shown that by altering the composition of the coating or the coating parameters it was possible to influence the oxidation behaviour and the formation of cracks, if they are occurring. An increase in bias voltage decreased

the presence of cracks in the coating. However, cracks only occurred if the thermal expansion coefficient decreases below ~$6x10^{-6}$ K^{-1}. The importance of adjusting the process parameters to achieve the best results, in order to improve the oxidation behaviour, was shown by [90] and [89]. Both investigated the influence of heat treatment of the stress in the coating deposited onto different substrate materials.

4.6 Summary

The importance of the oxidation resistance of the substrate materials used for deposition in connection with growth defects and cracks was shown. In the case of CC, which has an onset point of rapid oxidation at 600°C, oxides formed out of substrate elements W and Co were observed at the coating surface. In the case of M2 steel this was the case at 900°C.

On the coating TiAlN/CrN deposited onto SS 304 the importance of the thermal expansion coefficient was demonstrated. Cracks occurred in the film deposited using 4kW power on the Cr target. This is equivalent with a Cr content of 30at% (normalised metal content). Cracks only occurred if the thermal expansion coefficient fell below ~$6x10^{-6}$ K^{-1}.

In the case of TiAlN/CrN deposited using 8kW power on the Cr target the bias voltage was altered. This effects the formation of cracks. At higher bias voltages a decrease in the crack formation and oxide formation was observed. The higher stresses induced into the coating were responsible for this effect.

4.7 Figures

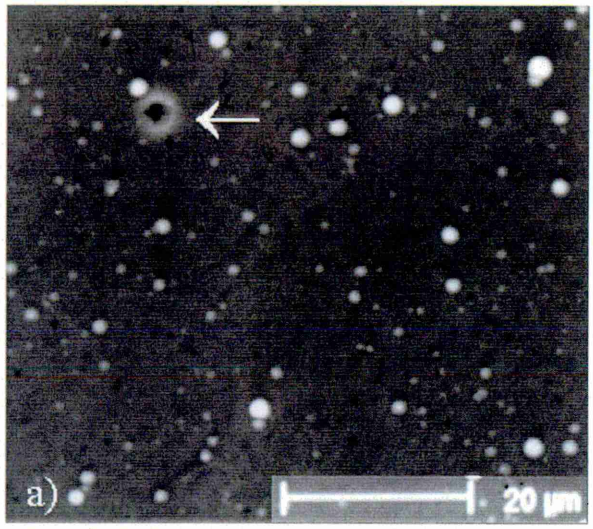

Figure 4-1: SEM micrograph of as-deposited sputter deposited coating after a Cr metal ion etch

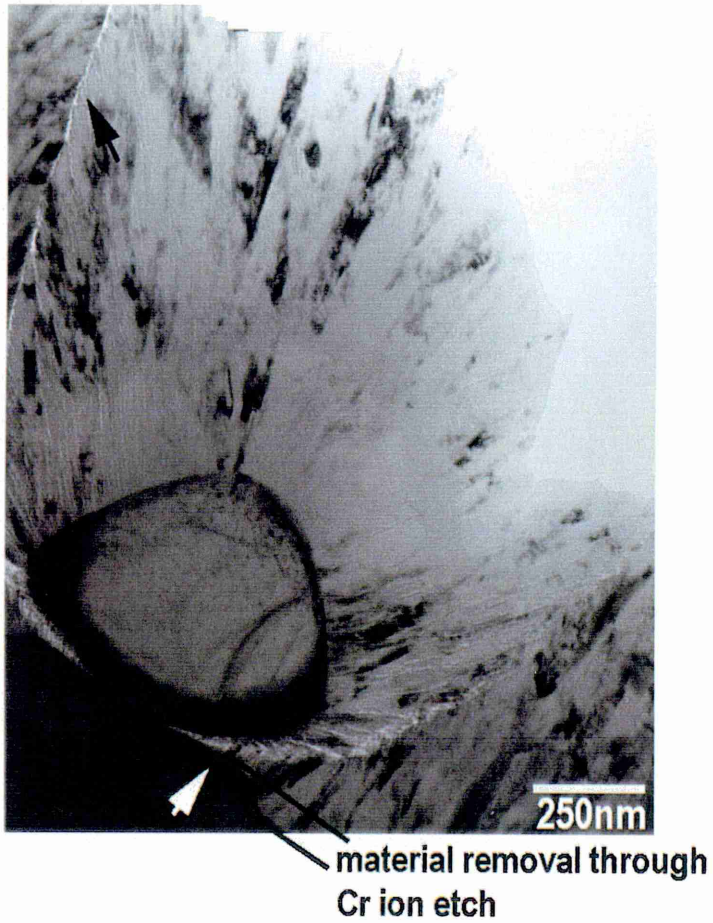

Figure 4-2: Cross sectional TEM BF micrograph of a growth defect

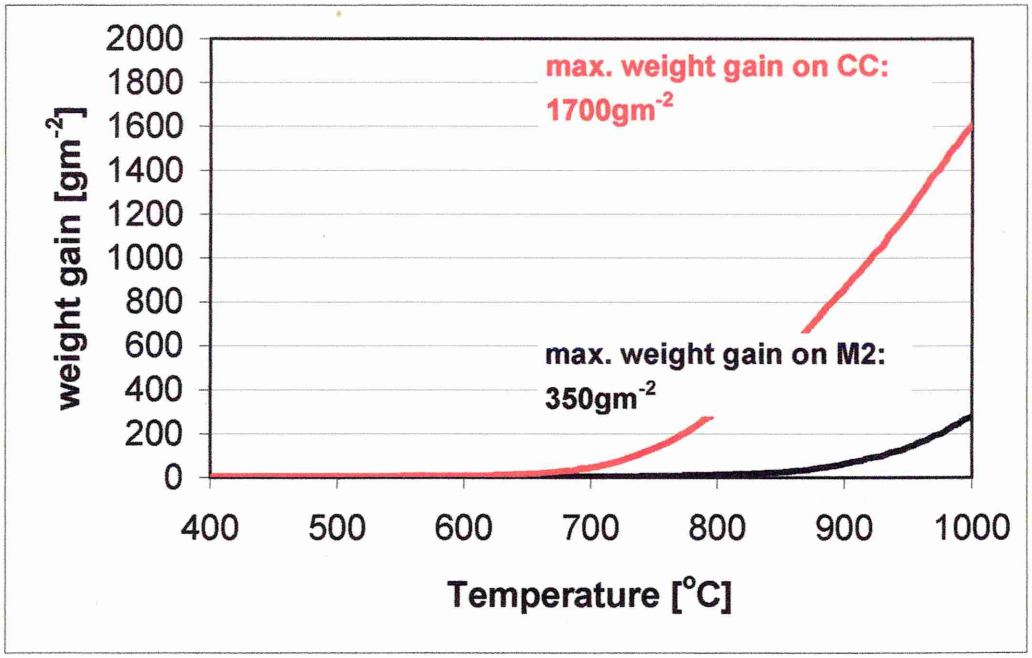

Figure 4-3: Continuous TG measurements on CC and M2

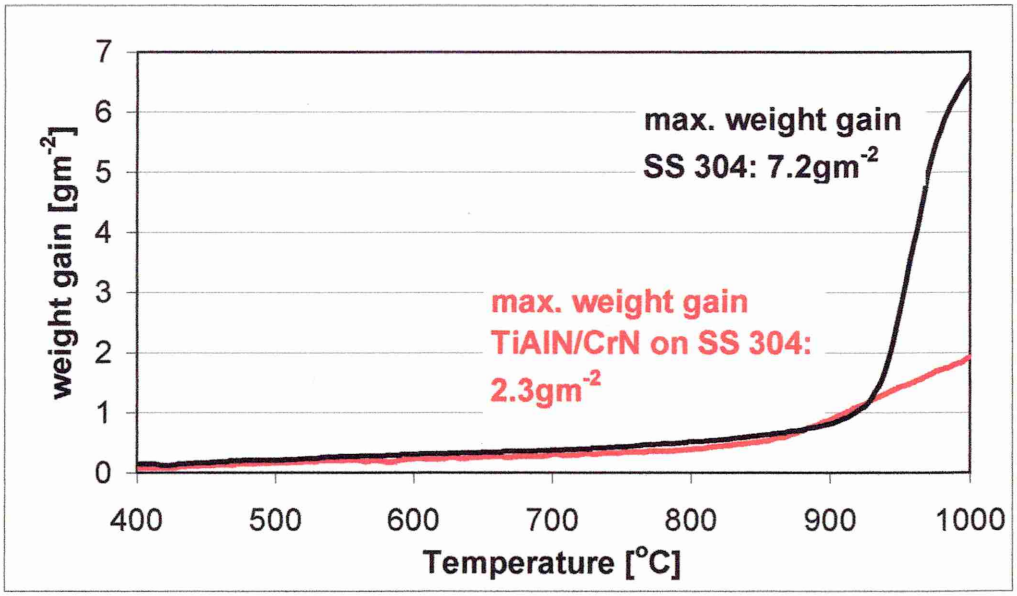

Figure 4-4: Continuous TG measurements on SS and $Ti_{0.26}Al_{0.26}N/Cr_{0.48}N$

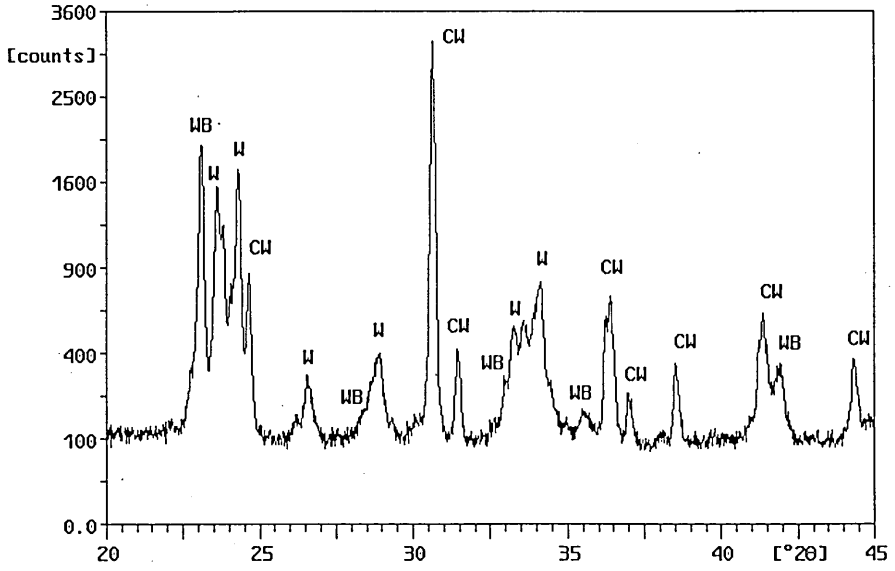

Figure 4-5: Oxidised CC substrate (900°C, 1h) with W indicating the monoclinic version of WO_3 and WB the triclinic form. CW stands for $CoWO_4$.

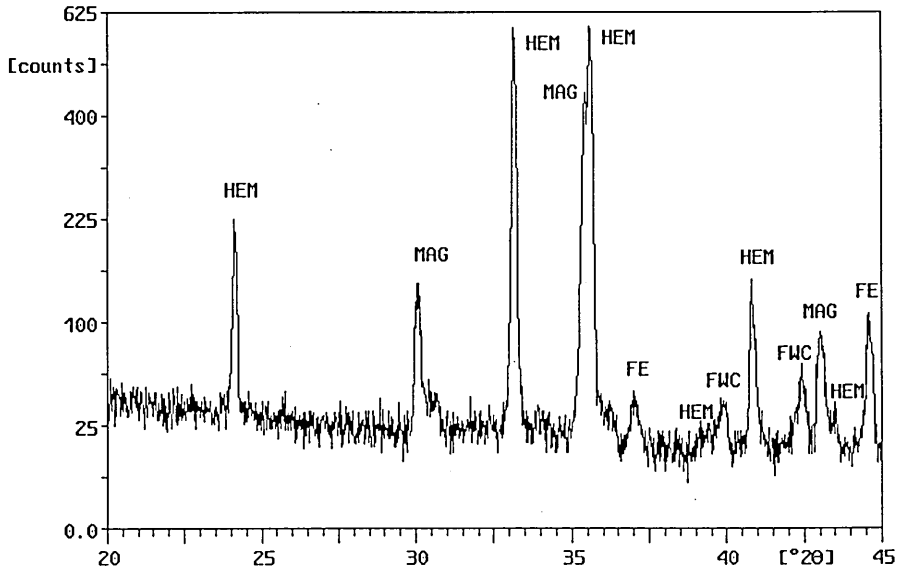

Figure 4-6: Oxidised M2 substrate (1000°C, 1h). MAG stands for Fe_3O_4, HEM for Fe_2O_3 and FWC for the mixed $FeCr_2O_4$ oxide. FE is iron.

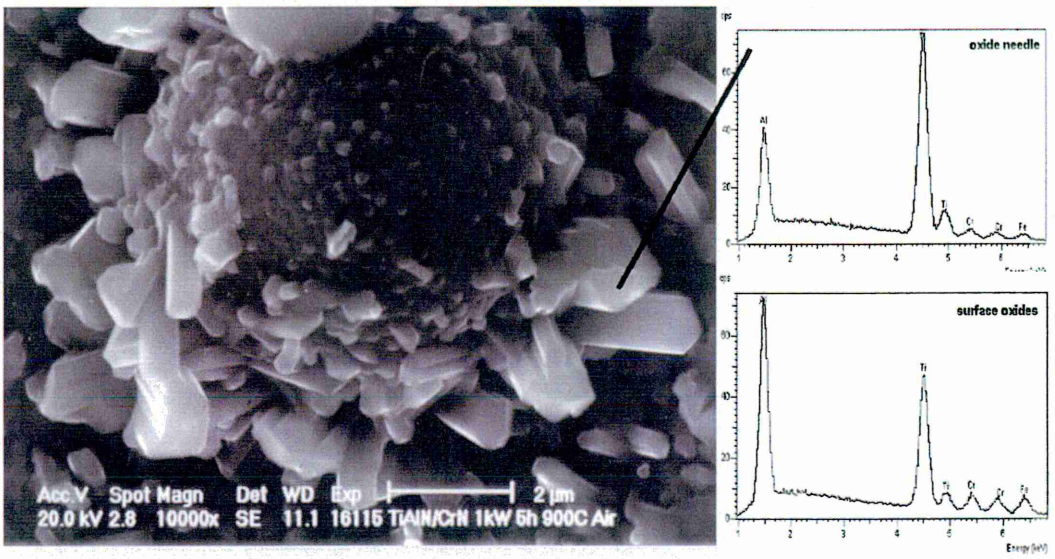

Figure 4-7: SEM micrographs after heat treatment for 5h at 900°C of growth defect

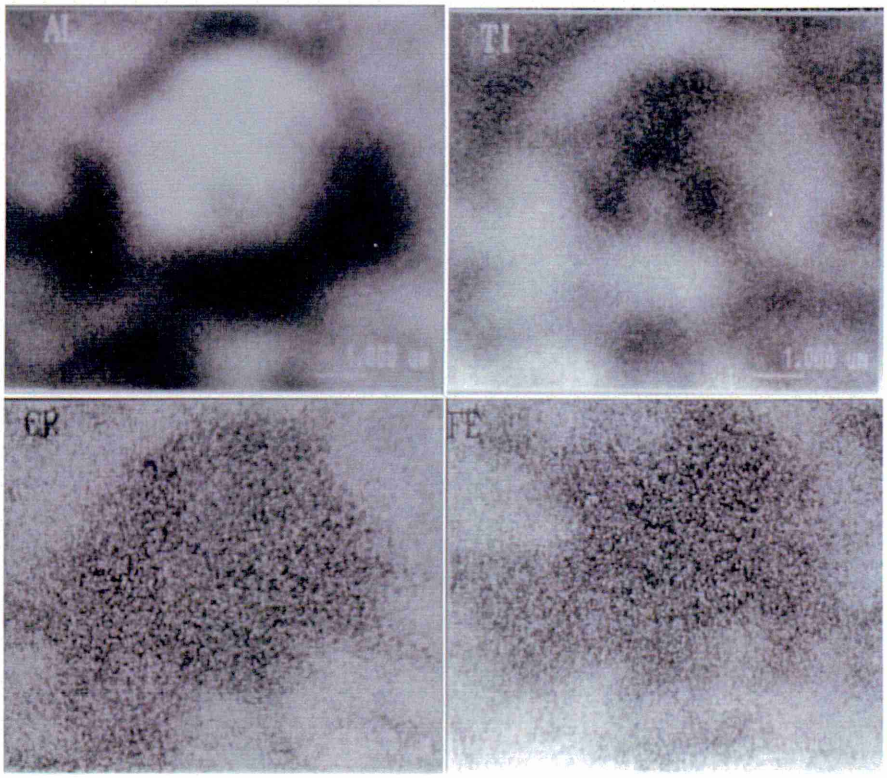

Figure 4-8: EDX map of a growth defect found on TiAlCrN after heat treatment for 5h at 900°C

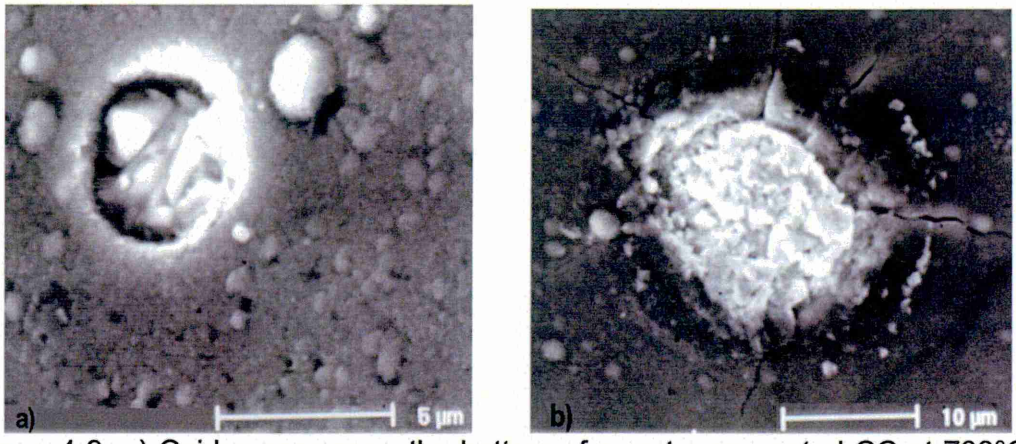

Figure 4-9: a) Oxides appear on the bottom of a crater on coated CC at 700°C b) Oxide formation on coated CC initiated local cracking of the coating at 800°C

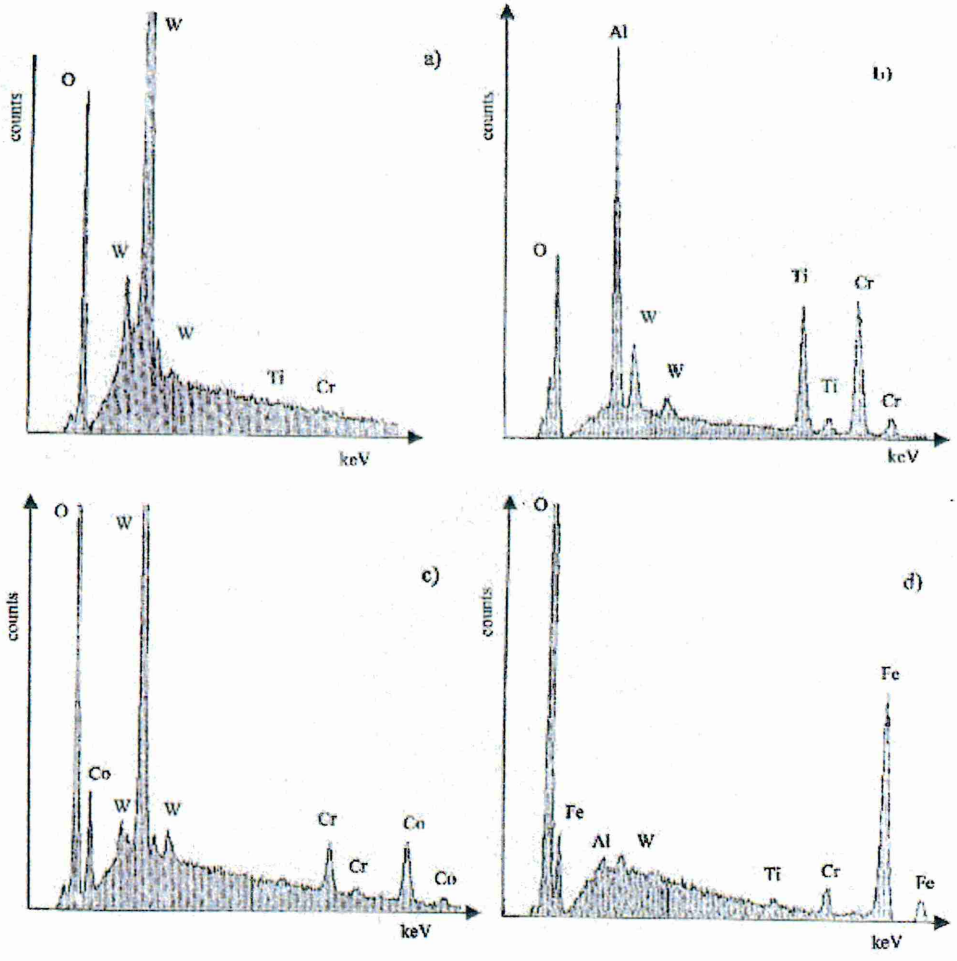

Figure 4-10: EDX spot analysis of (a) oxide breaking through the surface on coated CC. Ti and Cr indicate the areas where the K_a lines of these elements would be observed. (b) of accumulated globular oxides on coated CC after heat treatment at 800°C. (c) of big oxide formed in the globular oxide region on CC at 800°C. (d) of big oxide formed in the globular oxide region on M2 at 900°C.

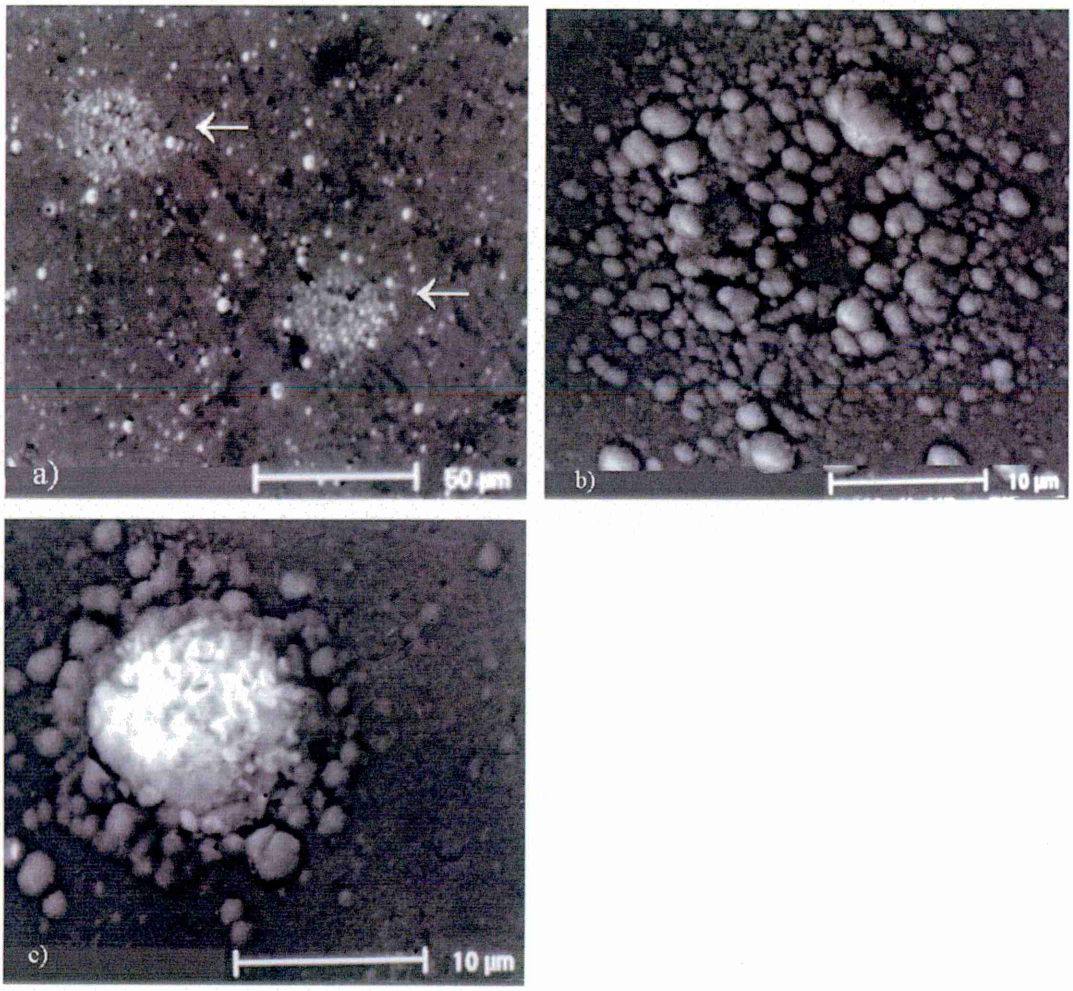

Figure 4-11: a) Low magnification survey on an oxidised coated CC at 700°C b) Accumulated globular oxides in detail on CC at 800°C c) Big oxide formed in globular oxides on CC at 800°C

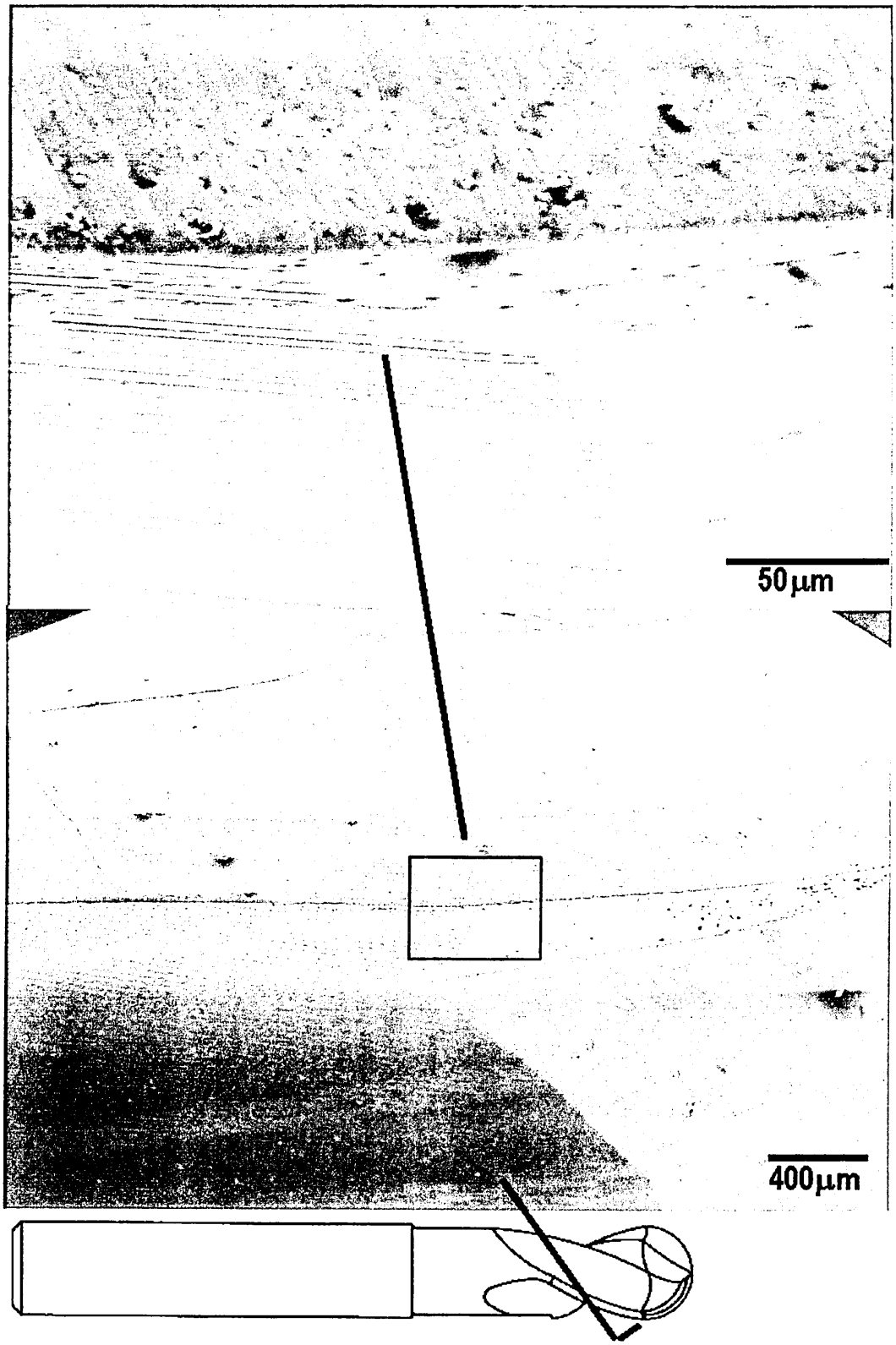

Figure 4-12: Surface of the cutting edge of an end mill coated with TiAlCrYN+Ox coating after heat treatment for 1h at 900°C.

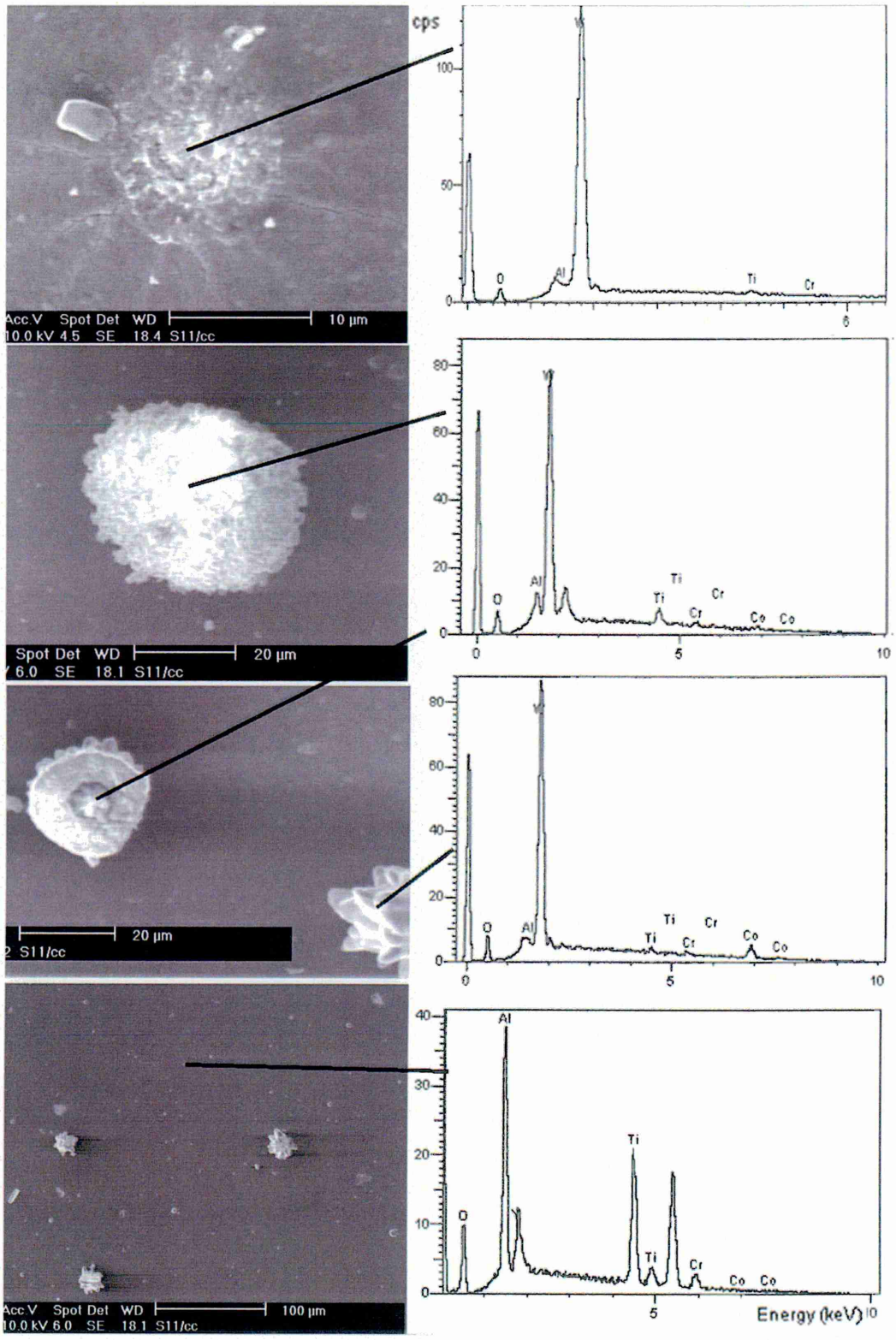

Figure 4-13: Three different defects on TiAlCrYN+Ox coated coupon after heat treatment for 1h at 900°C

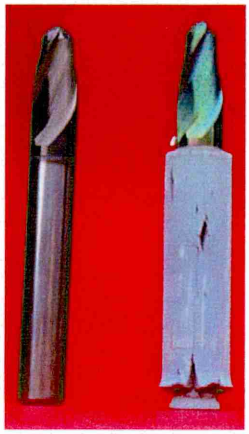

Figure 4-14: As-deposited and coated end mill after heat treatment

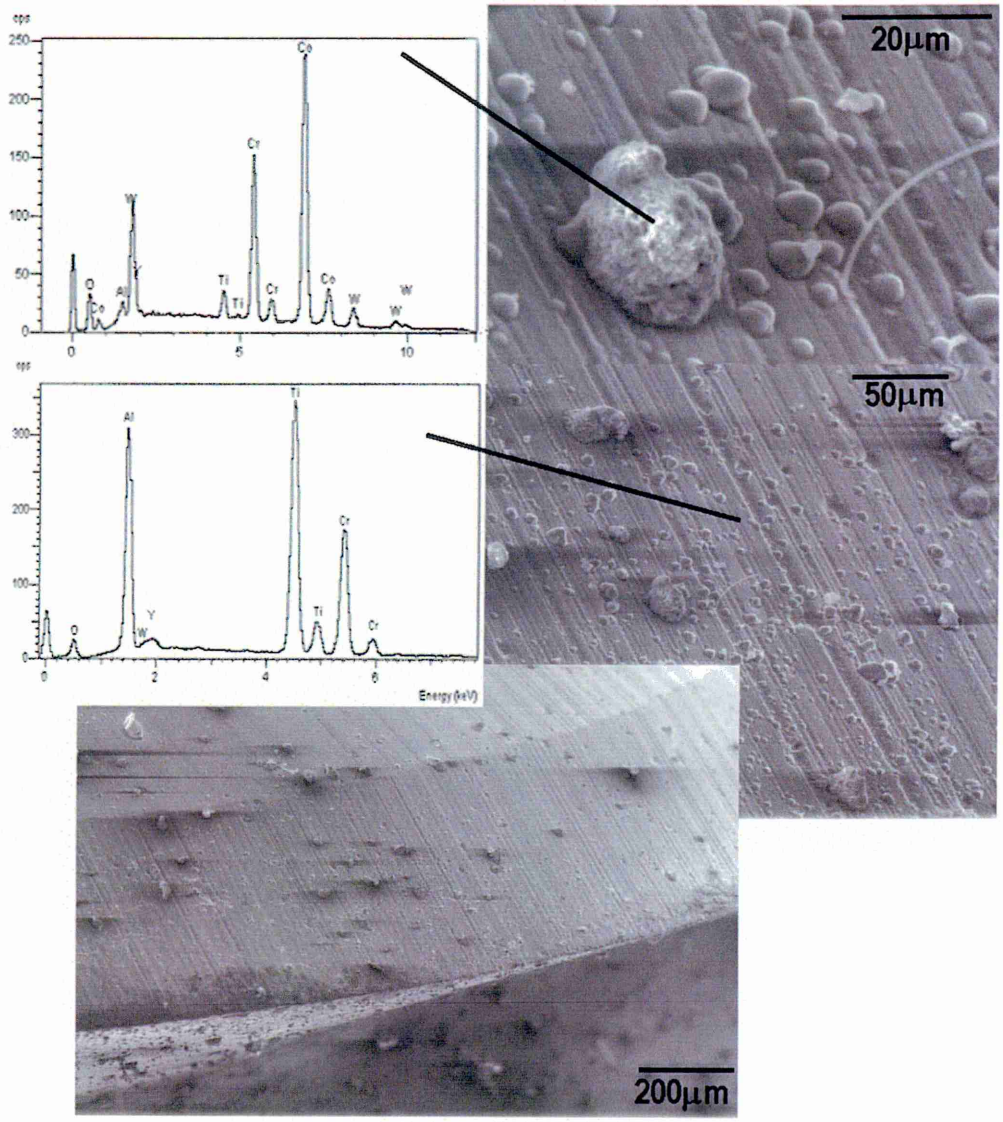

Figure 4-15: TiAlCrYN+Ox coated end mill after heat treatment for 1h at 900°C

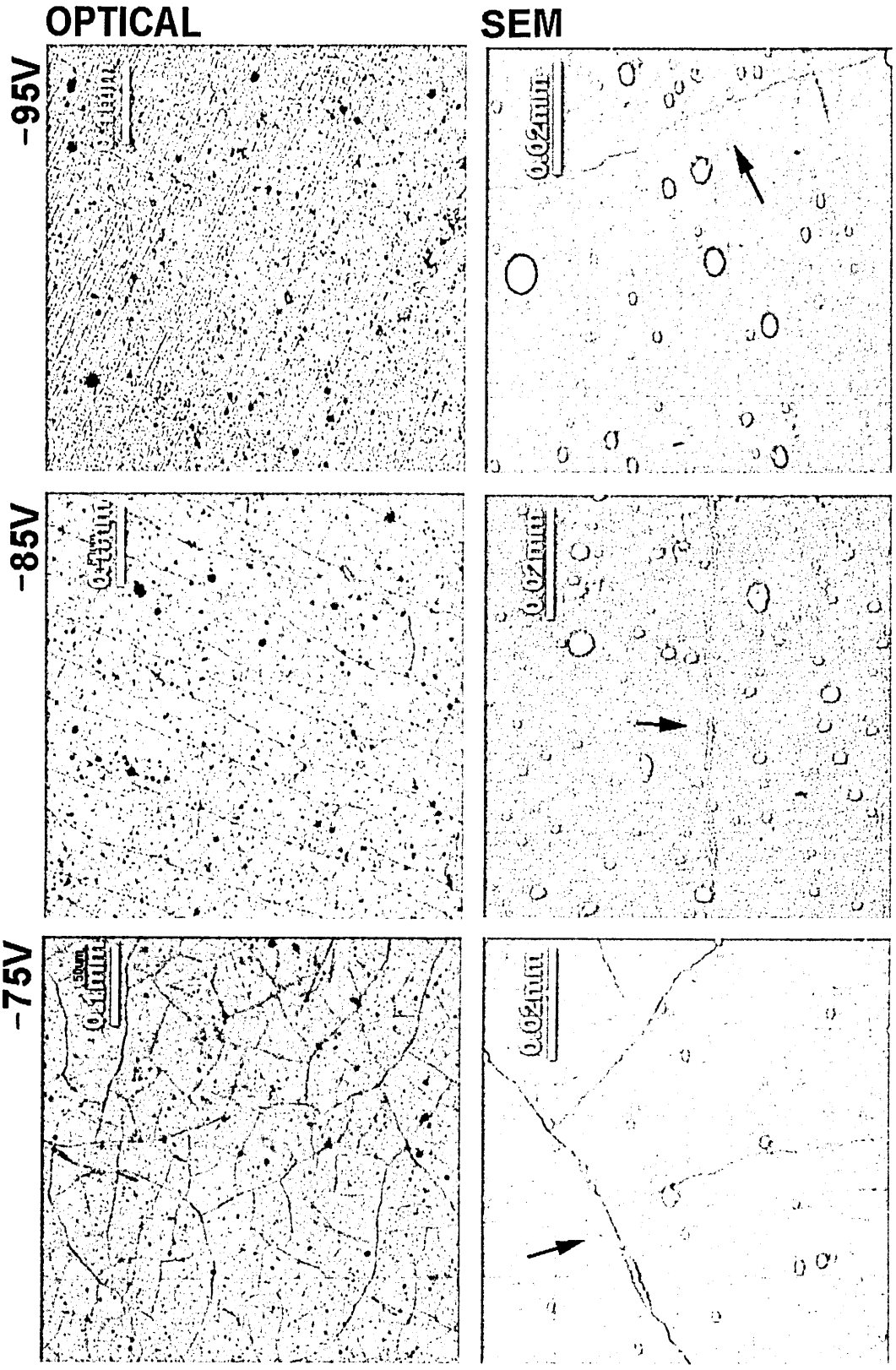

Figure 4-16: Cracks observed optically and using SEM on TiAlN/CrN deposited using different bias voltages after heat treatment for 1h at 900°C

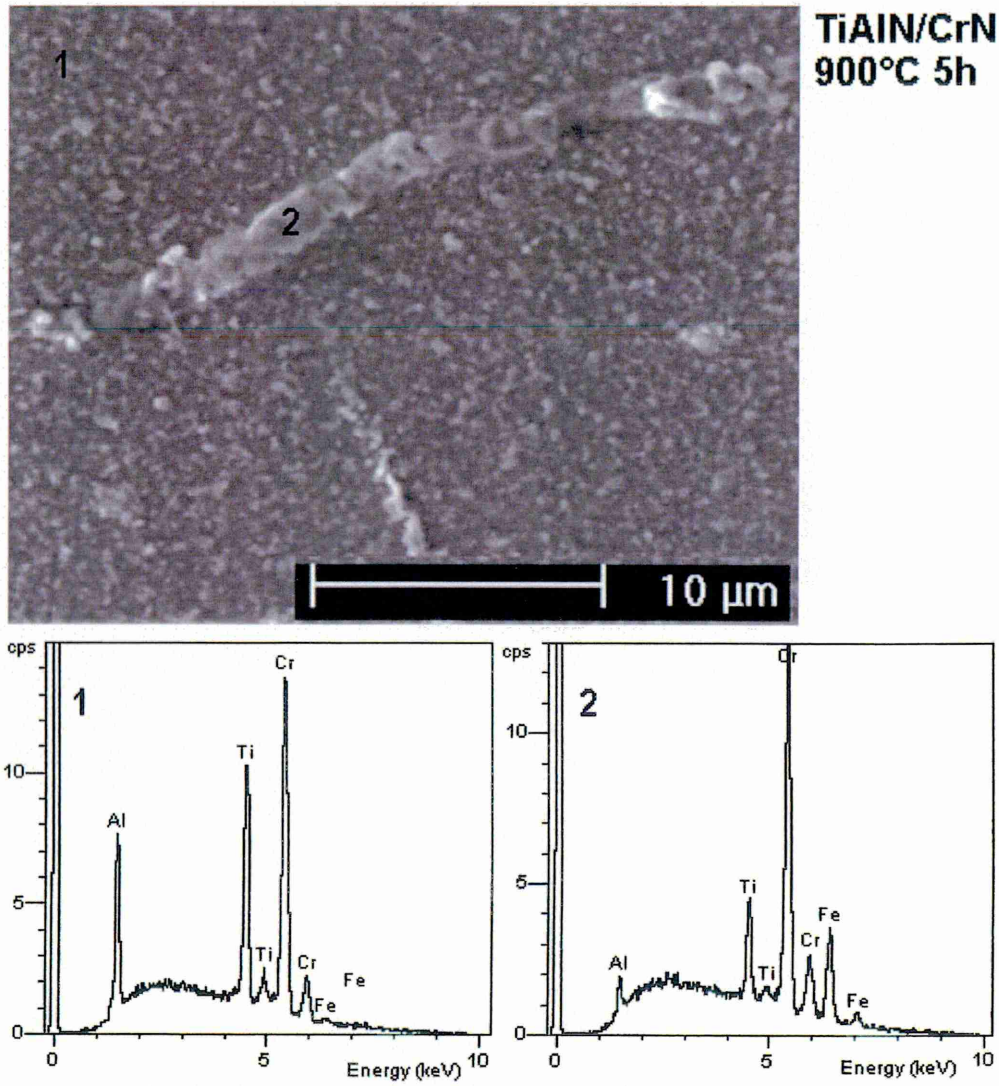

Figure 4-17: Formation of oxides in a crack after heat treatment for 5h at 900°C

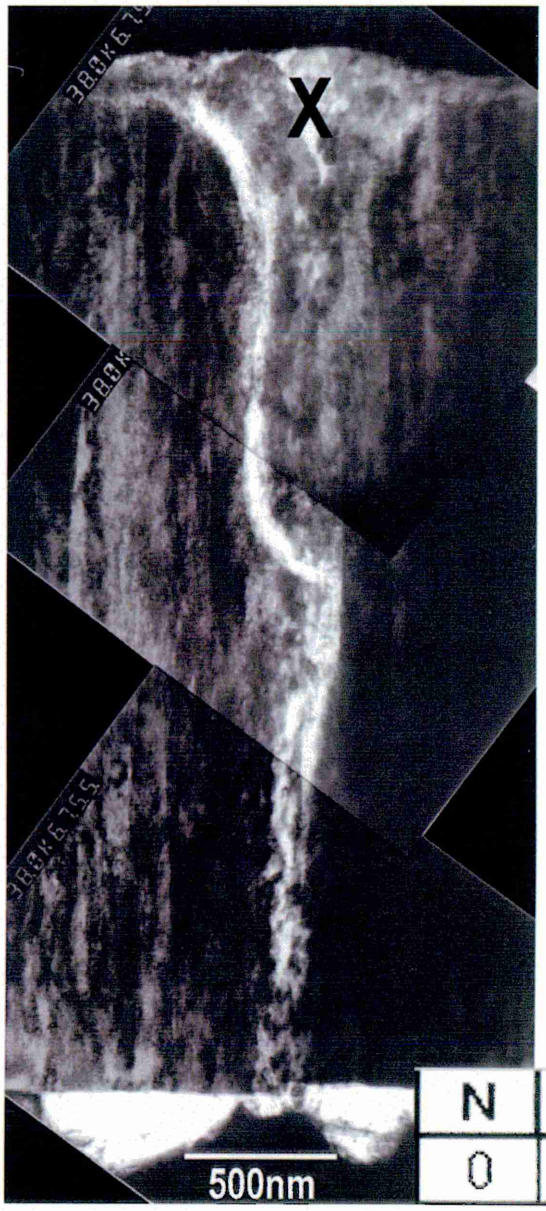

N	O	Al	Ti	Cr
0	2.3	9.88	39.8	40.8

Figure 4-18: TEM BF micrograph with EDX spot analysis on TiAlN/CrN after heat treatment for 1h at 900°C

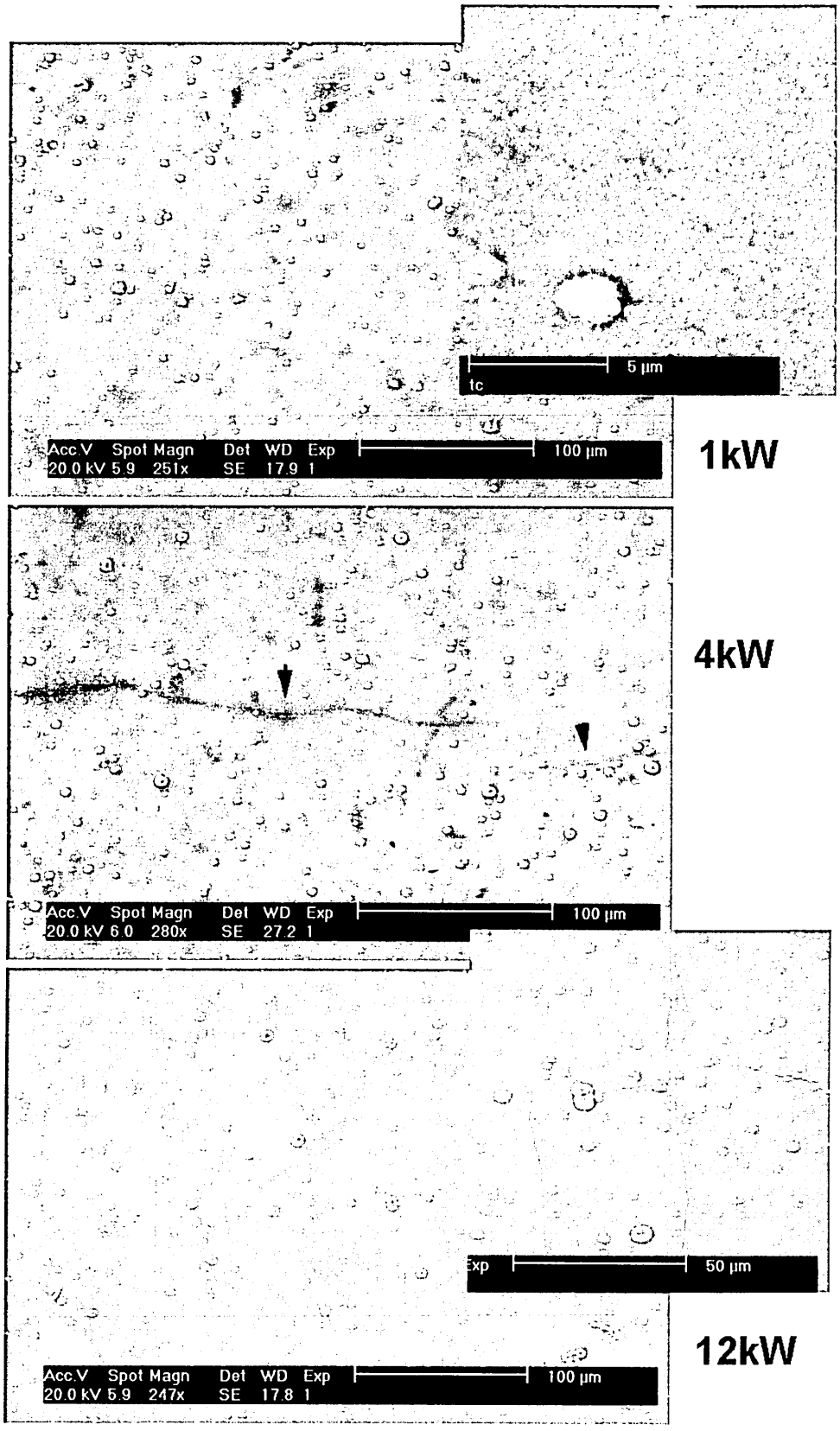

Figure 4-19: SEM micrographs from various TiAlN/CrN after heat treatment for 1h at 900°C

5 $Ti_{0.44}Al_{0.54}Cr_{0.02}N$

This coating is the basis for observations on TiAlCrYN and TiAlN/CrN. Investigations of this film were made with the same methods used on the main coatings of interest: TiAlCrYN and TiAlN/CrN. This should make it possible to discuss differences/ advantages of the other films. The samples had in the as-deposited condition a shiny dark grey appearance. After heat treatment for 1h at 900°C the sample had a grey interference colour.

5.1 TG measurements

$Ti_{0.44}Al_{0.54}Cr_{0.02}N$ is the basic coating material under investigation. The $Ti_{0.44}Al_{0.54}Cr_{0.02}N$ coating was deposited onto type 304 stainless steel and compared with TiN, a widely used coating material, with an onset point of rapid oxidation in the region of 600°C and a maximum weight gain of ~10 g m^{-2} [32]. The basic substrate material for dry high-speed cutting is cemented carbide. In this case, WC embedded in a Co matrix was used. Another substrate material interesting for cutting tools in general is M2 high-speed steel. These materials have been analysed using thermogravimetry to find out basic data about their oxidation behaviour. The various materials were heated up to 1000°C using a linear heating rate of 1°C min^{-1} from 400°C to 1000°C (see Chapter 3.4). As can be seen from Figure 5-1, where the temperature is plotted against the weight gain, the oxidation reaction of cemented carbide and M2 steel is very rapid in comparison to the hard coatings (TiN and $Ti_{0.44}Al_{0.54}Cr_{0.02}N$). From these data an onset point for rapid oxidation of 600°C and 800°C for the cemented carbide and M2 steel was determined. The maximum weight gain for cemented carbide (outside scale of Figure 5-1) in this measurement was ~1700 g m^{-2} and for M2 ~350 g m^{-2} [168]. The TiN oxidation behaviour was plotted as a reference. This coating starts to oxidise rapidly at temperatures above 600°C. For the $Ti_{0.44}Al_{0.54}Cr_{0.02}N$ coating an onset point of ~900°C and a maximum weight gain of ~4 g m^{-2} was found.

Isothermal thermogravimetric measurements presented in Figure 5-2 show the oxidation behaviour of $Ti_{0.44}Al_{0.54}Cr_{0.02}N$ in more detail. It is important to note that the regime of constant temperature started about 45 min (for 900°C) after the measurement started. The isothermal results are in good agreement with the continuous ones. From the increase in weight gain from 820°C to 920°, it is obvious that the rate of reaction speeds up considerably. The profile of the 920°C curve shows a very steep increase in weight gain in the first hour. After this the reaction changes into a moderate increase of weight, the rate of weight gain between 2h – 10h is approximately half of that between 0.5 to 2h. This means the reaction process was altered. Saturation of the reaction process, converting all TiAlCrN into oxides is not achieved after 10h.

The measurements on substrate materials using TG were compared to results reported in the literature. Cemented carbide is well known for its rapid oxidation behaviour starting at temperatures as low as 600°C [98]. The onset point of rapid oxidation derived from the TG measurement of 600°C for the cemented carbide used in this investigation fits well into this observation. The onset point for M2 steel is considerably higher (800°C). Unfortunately this steel starts to soften at temperatures above 600°C and hence, it cannot be used at such high temperatures.

The isothermal curves suggested that no saturation of the sample with oxygen is achieved after 10h. To determine when the whole coating is oxidised on stainless steel is difficult because of interactions of the substrate material. It was shown that after oxidation for 1h at 950°C almost all the TiAlCrN coating was oxidised using SEM [33].

5.2 TEM observations

Transmission electron bright field images from the whole cross section of the as-deposited film Figure 5-3a), a magnified image of the middle Figure 5-3b) and a selected area diffraction pattern Figure 5-3c), with an aperture of 500nm diameter, is shown to characterise the film. The film thickness of the as-deposited film was 2.8±0.1μm. Along the column boundaries voids alternate with dense regions. The length of a void along the column boundaries is about 500±200nm. Some of the void bands are marked in Figure 5-3b). The selected area DP, taken with an aperture of 500nm in size, has a speckled appearance and shows no specific orientation. A selected area diffraction pattern recorded from the near substrate region indicated a (111) orientated film growth.

Bright field images taken after heat treatment for 1h at 900°C in air revealed an oxide layer growth of 600 – 900nm (Figure 5-4a). The total thickness of the sample was measured as 3.15±0.1μm. This means that about 2.4μm of the film are not yet oxidised. The oxide layer appeared to have various structured zones. It is split into an outer darker band and an inner brighter band. The outer layer has a measured thickness of 150±50nm and the layer beneath it of 400-750nm. Interestingly, observation of the columns from the middle of the coating revealed no voids, even at considerably higher magnification than chosen for the as-deposited sample (Figure 5-4b). Also the substrate interface seemed to be unaffected. The coating appeared perfectly dense. The diffraction pattern showed a fcc crystal structure in ⟨110⟩ direction (Figure 5-4c). It was taken in the same way as for the as-deposited sample. The DP indicates an increase in preferred orientation of the coating structure after heat treatment.

A micrograph of the oxide layer at higher magnification revealed an outer dense oxide layer (Figure 5-5). Beneath this layer a brighter porous crystalline region was found. Between the oxide layer and the nitride a mottled zone of about 50nm was visible (arrow). Oxygen should, after diffusing through the outer layer, be able to rapidly reach the remaining nitride through the porous layer. The mottled zone might be the first visible change caused by oxidation in the nitride layer.

5.3 XRD measurements

Glancing angle parallel beam measurements with 0.5° incident angle were taken from the as-deposited sample and after heat treatment for 1h at 900°C. The as-deposited sample shows reflections at 37.30 °2θ for {111}, at 43.30 °2θ for {200} and at 62.99 °2θ for {220} position (Figure 5-6). The mean peak width for these reflections was 0.348 °2θ at full width half maximum. The peak heights can not be used to identify the preferred orientation in a glancing angle measurement.

After heat treatment a diffraction pattern using similar conditions was taken (Figure 5-7). Reflections arising from the coating were not observed. The diffraction pattern revealed a series of mainly overlapping peaks. The reflections arise mainly from TiO_2 (JCPDS 21-1276) in its rutile form and corundum Al_2O_3 (JCPDS 42-1468). The anatase form of TiO_2 (JCPDS 21-1272) was also observed along with Fe_3O_4 (JCPDS 19-629) or $FeCr_2O_4$ (JCPDS 34-0140) [94]. The two Fe oxide phases have the same crystal structure (cubic) and are isomorphous, hence either or both of them can be present. Additionally, two peaks were observed that could not clearly be identified to belong to a specific oxide. These peaks probably arise of a complex oxide of Fe and/ or Cr.

In [130] {111} was the preferred orientation of $Ti_{0.44}Al_{0.53}Cr_{0.03}N$ coating. The coating peaks in Figure 5-6 show a strong reflection caused by {111} and {110} planes. However, glancing angle measurements cannot be used to gain texture information because there is no common diffraction vector.

5.4 EDX point analysis

A series of EDX point analyses through the oxide layer revealed that the outer layer is Al-rich and the lower one is Ti-rich (Figure 5-8). The Ti-rich zone is ~600nm wide and the Al-rich zone is ~250nm wide. The Ti-rich area contains also some points rich in Al. At the beginning of the Ti-rich area, an increase in Cr content from ~2.5 at% to ~7.5 at% was observed. The Fe concentration stayed constant. The Fe profile was not plotted in order to improve the clarity of

the other elemental profiles. For the N and O line the change in intensity in a narrow keV of the EDX spectra range was examined. To avoid influences of the sample thickness, the N or O gross integral counts were divided through by the total counts of all EDX-peaks under investigation. To make the N and O signal visible in this graph they had to be multiplied by a scaling factor. The N line stays almost constant throughout the nitride and oxide region. The O line, instead, shows a clear change in intensity. Below the oxide layer the concentration of O is considerably lower.

Comparisons between the concentration of various elements before and after heat treatment were made for the substrate/ coating region (Figure 5-9). The integrity of this region after heat treatment is important for the adhesion of the coating. The Ti and Al content measured by the EDX analysis for the as-deposited sample were 35at% and 60at%, respectively. These values differ from the ones measured using RBS ($Ti_{0.44}Al_{0.54}Cr_{0.02}N$).

The comparison of the Al and Ti concentrations showed a shallower rise in Al and Ti content at the interface after heat treatment than in the as-deposited specimen. In the case of Fe and Cr clear evidence of diffusion into the coating (~150nm) was observed. The concentration of Fe and Cr in the SS 304 substrate decreased in comparison to the as-deposited sample. This suggests an out-diffusion of these elements.

5.5 EDX mapping

Elemental distribution maps for the substrate region of the as-deposited sample are shown in Figure 5-10. The intensity in the maps varies from the left to the right side with the sample thickness. The interface between substrate and coating is sharp. The change in contrast occurs in less than 8nm. The O map mainly shows in this case the increase of background counts, depending on the position of the beam on the sample, which gives a good impression of change in sample thickness.

A montage was made out of maps taken from the substrate/ coating interface to the coating surface after heat treatment for 1h at 900°C (Figure 5-11). For the maps the K line of the elements was used. The bi-layer formation, an Al-rich and a Ti-rich zone, is very obvious in the maps. Furthermore, Al and

Cr enrichment in the Ti zone was observed. The Cr map has a region of high intensity above the Al-rich zone and below the Ti-rich zone. Comparisons with the TEM image suggest that the Cr on top of the Al-rich layer was re-deposited during the ion beam milling process (sample preparation). Cr diffusing from the substrate to the coating surface probably causes the increased intensity between the oxide and the nitride in the Cr map. This region of increased intensity is approximately 90±15nm wide (see arrow in Cr map Figure 5-11). In the TiAlCrN coating higher intensity of Al, Ti and even N and O along the column boundaries is visible. More striking is the high intensity of the Cr and Fe maps mainly along the column boundaries from the stainless steel substrate to the coating surface. Diffusion of Cr and Fe was also observed in the columns themselves. The lack in intensity of these elements at the near substrate region is probably sample thickness dependent.

Comparison between the EDX-point analysis and the EDX-mapping in the base layer region demonstrated that it is important to have both results. One reveals information about the local concentration and the other gives qualitative information about the distribution of an element. In the case of the substrate/ coating region the results between the point analysis and the mapping differ. The point analysis suggested a diffusion of substrate elements of 150nm into the coating, whereas the elemental maps clearly show that the substrate elements Cr and Fe diffused mainly along the boundaries from the substrate to the coating surface. The point analyses were made inside the columns, which might explain this difference. Earlier measurements by [33] suggested a depletion of Cr and Fe in the stainless steel substrate material after heat treatment for 1h at 950°C (Figure 5-12). They also noted an increase in Cr and Fe throughout the nitride film, this is probably directly related to the temperature, which is above the onset point of rapid oxidation.

The point analysis and the elemental maps from the oxide layer compare well. It was shown by [33] that after 1h at 950°C in the oxide layer formed Cr was found below and after the Ti-rich zone. The maps from this investigation showed that the Cr content in the oxide layer is dependent on the place of the measurement. The results gained from the compositional investigation with the structural information from the bright field micrographs and the XRD suggests that the Al_2O_3 oxide layer is dense and the layer beneath it, mainly TiO_2, forms

a porous oxide layer. The formation of a dense Al_2O_3 layer within 1h at 900°C (see Figure 5-2) is seen as a reason for the decrease in the rate of weight gain.

5.6 Summary

The oxidation behaviour of $Ti_{0.44}Al_{0.54}Cr_{0.02}N$ during thermogravimetric measurements was compared with substrate materials used for tools and the well understood coating TiN. After annealing for 1h at 900°C in air TiAlCrN formed an oxide bi-layer of ~800nm thickness mainly out of Al_2O_3 and TiO_2. At the same specimen elemental EDX maps revealed the diffusion of substrate elements Cr and Fe along the column boundaries to the coating surface. Fe_3O_4 and Fe_2CrO_4 were indeed observed using XRD at the surface. This showed that the substrate/ coating interface integrity is not guaranteed by TiAlCrN after heat treatment for 1h at 900°C. The coating structure changed due to the heat treatment, as was observed by transmission electron microscopy. The orientation in the columns seemed to be more uniform after annealing.

5.7 Figures

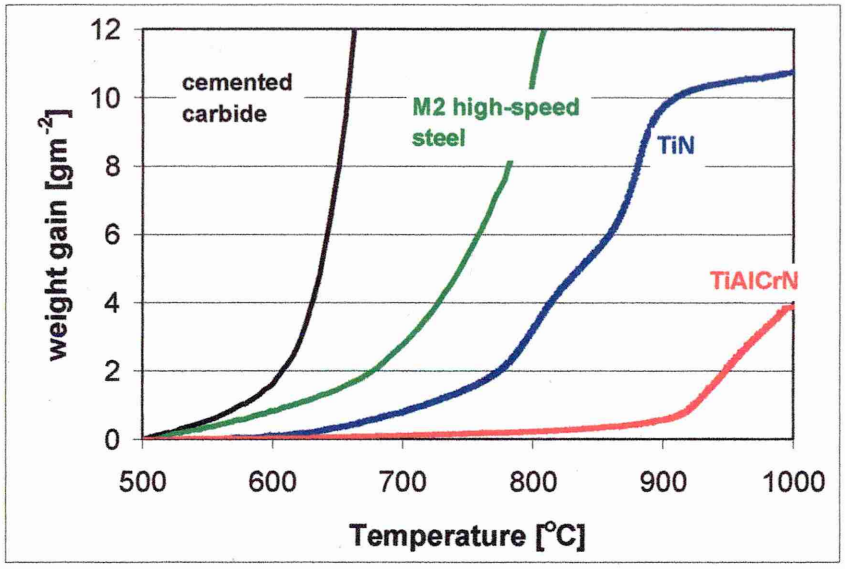

Figure 5-1: Continuous thermogravimetric measurement from $Ti_{0.44}Al_{0.54}Cr_{0.02}N$ in comparison to tool materials.

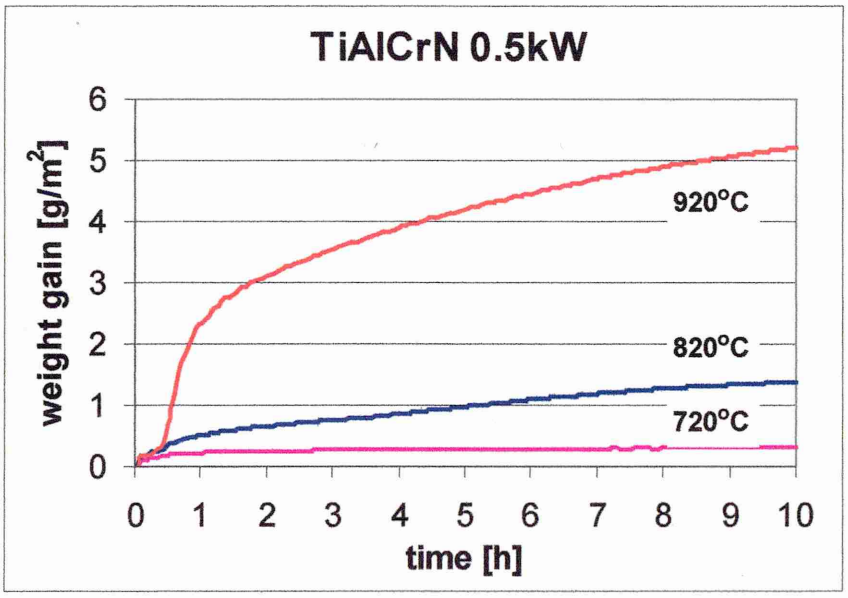

Figure 5-2: Isothermal thermogravimetric measurements of $Ti_{0.44}Al_{0.54}Cr_{0.02}N$.

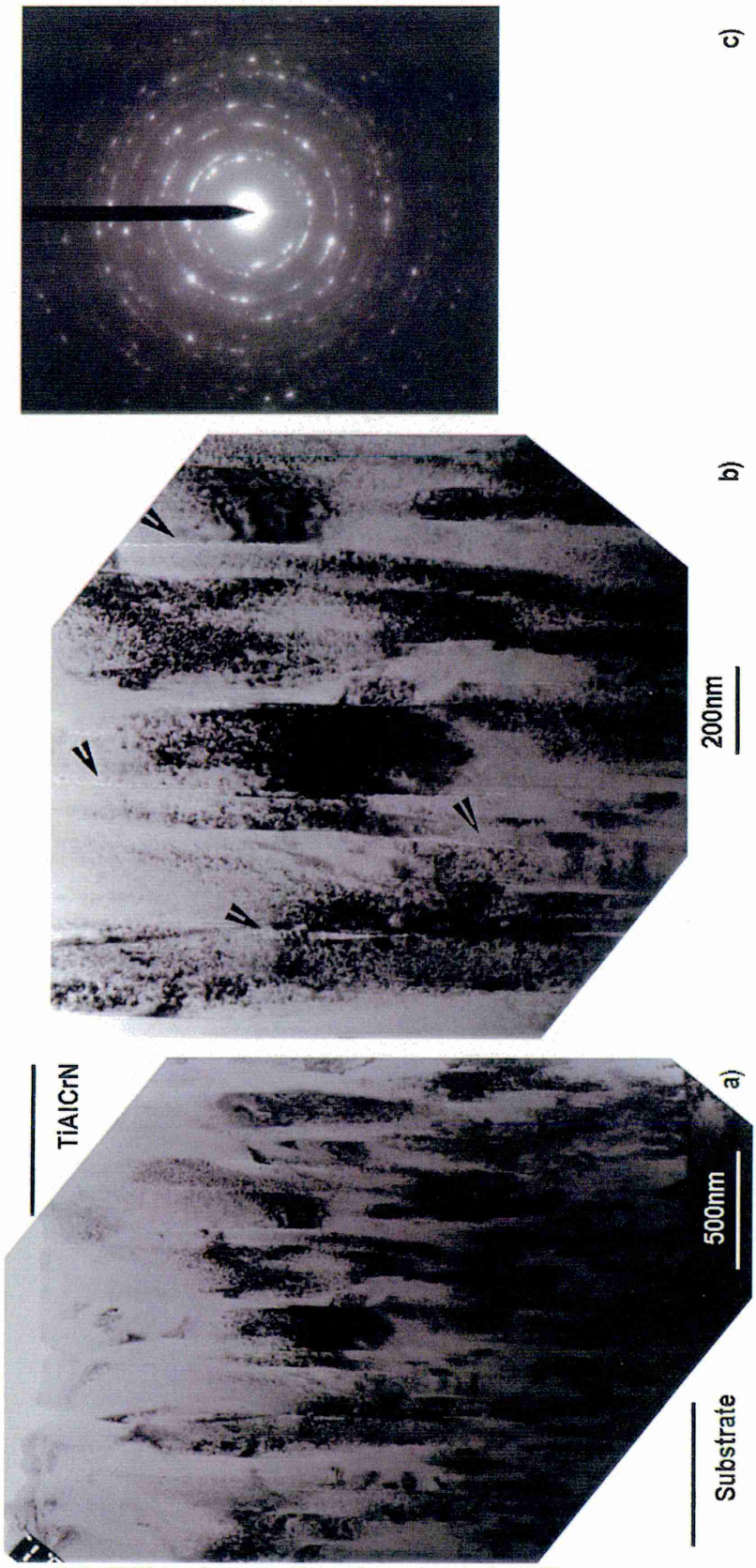

Figure 5-3: TEM micrographs of as-deposited TiAlCrN.

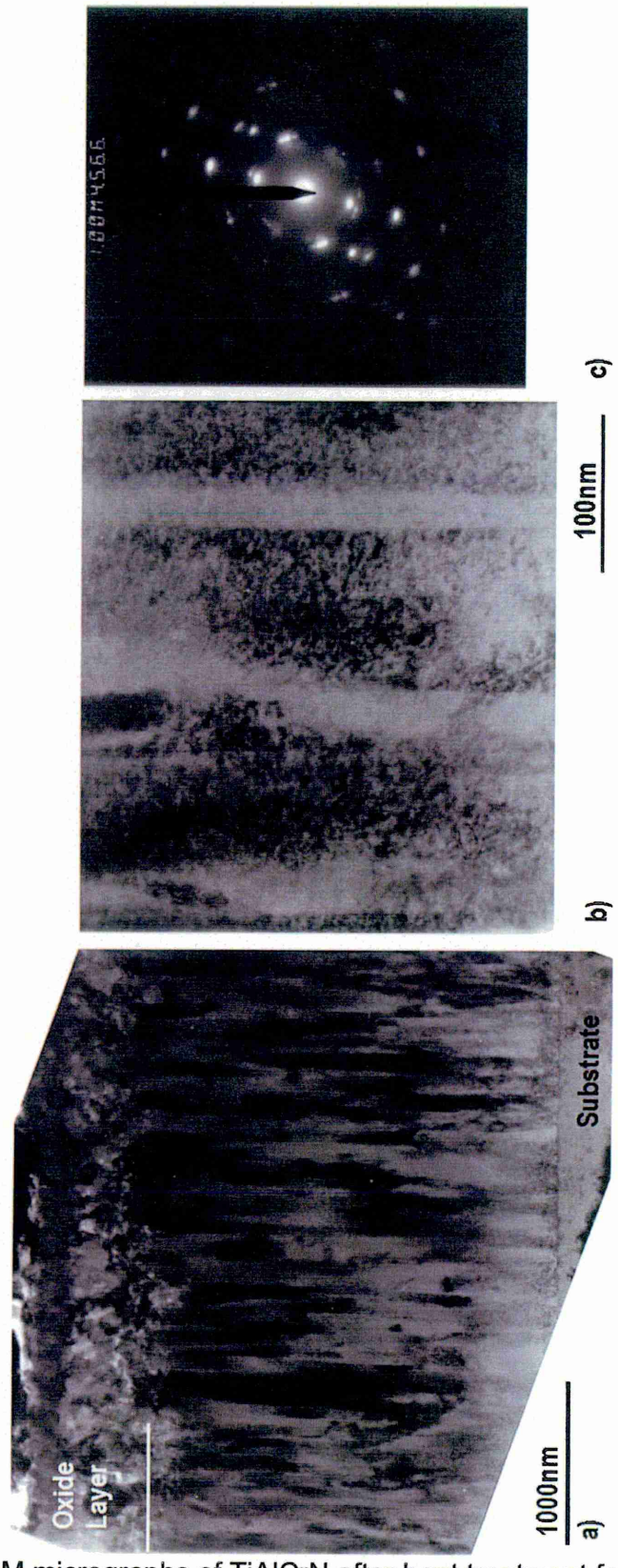

Figure 5-4: TEM micrographs of TiAlCrN after heat treatment for 1h at 900°C

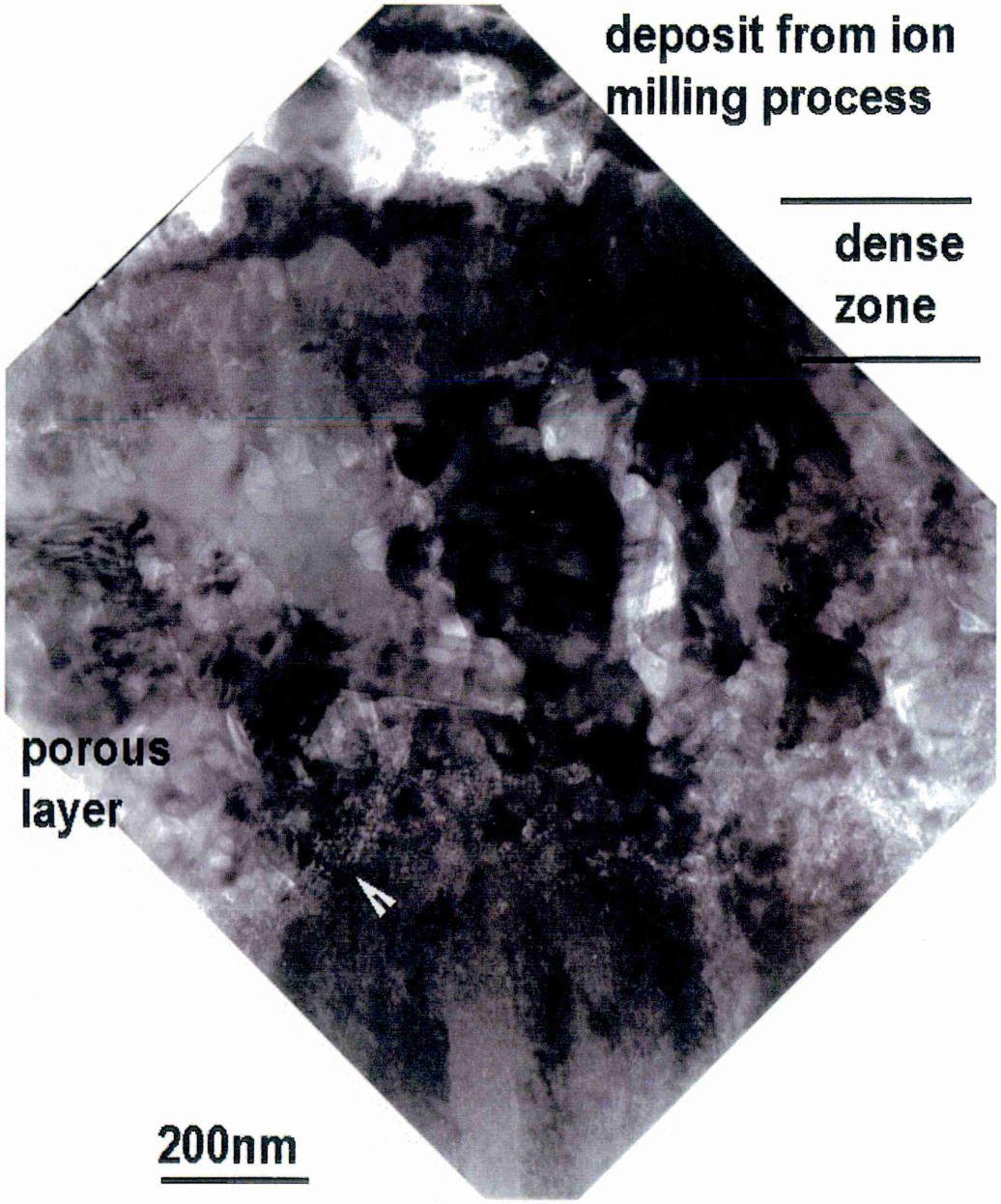

Figure 5-5: TEM micrograph of the oxide layer formed on TiAlCrN after 1h at 900°C

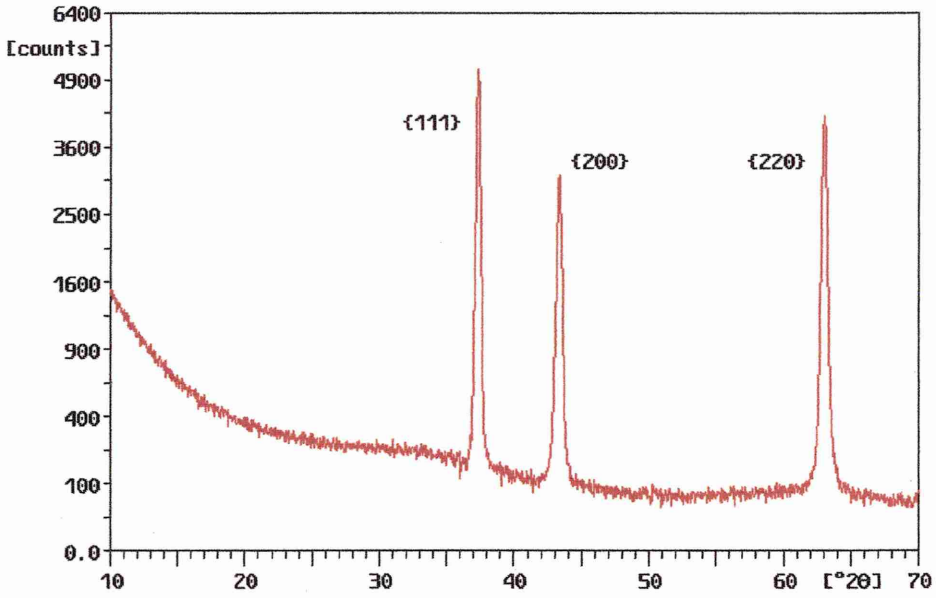

Figure 5-6: Glancing angle XRD pattern form TiAlCrN in as-deposited condition

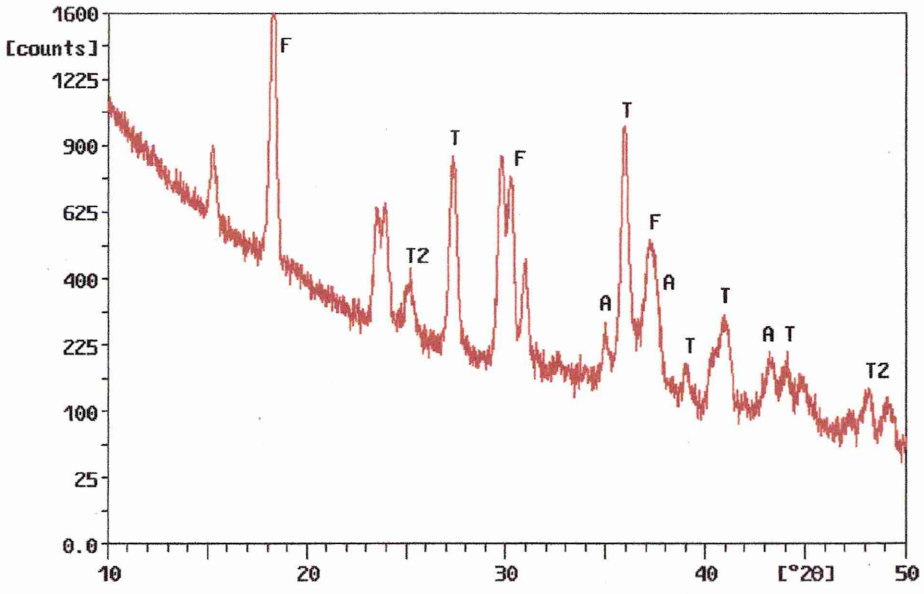

Figure 5-7: Glancing angle XRD with 0.5° incident angle after 1h at 900°C. F = Fe_2O_3 or $FeCr_2O_4$, T = TiO_2 (rutile), T2 = TiO_2 (anatese), A = Al_2O_3

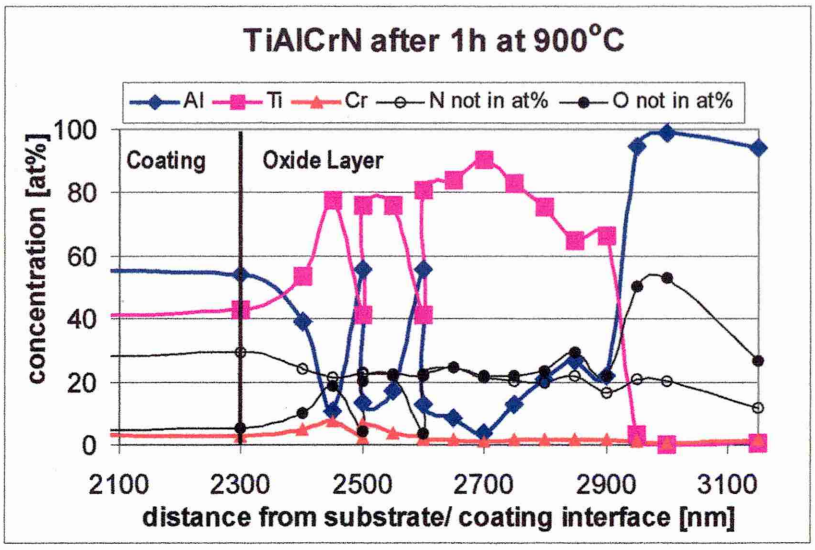

Figure 5-8: Point analysis through the oxide layer of TiAlCrN after heat treatment for 1h at 900°C

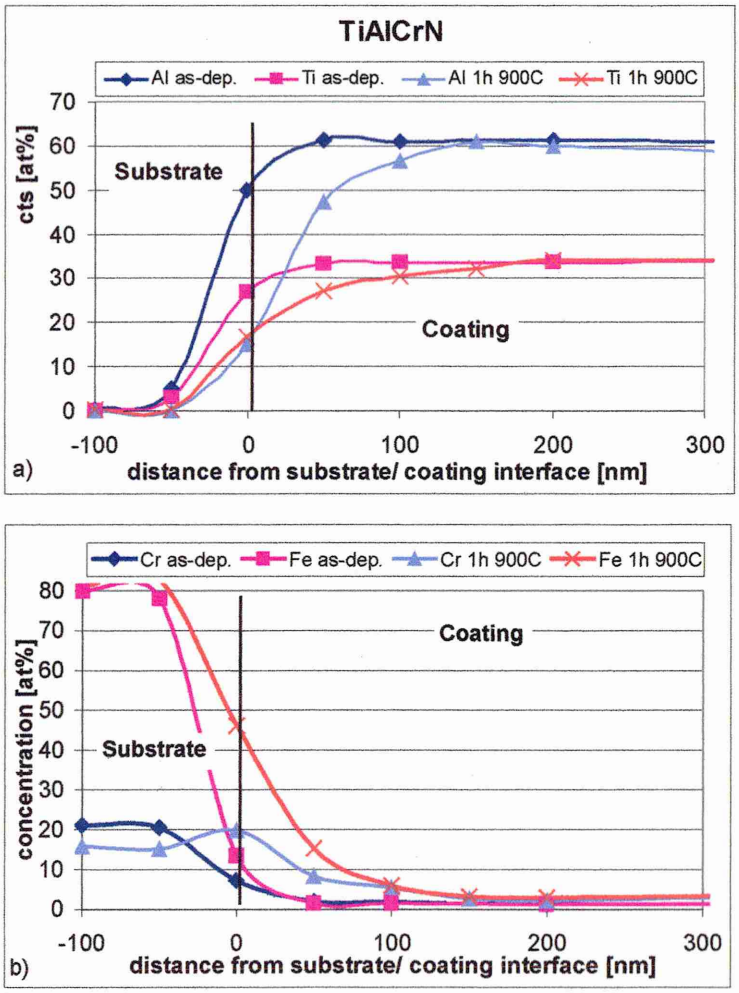

Figure 5-9: A comparison between the concentration measured at the substrate region before and after heat treatment a) Al and Ti, b) Cr and Fe

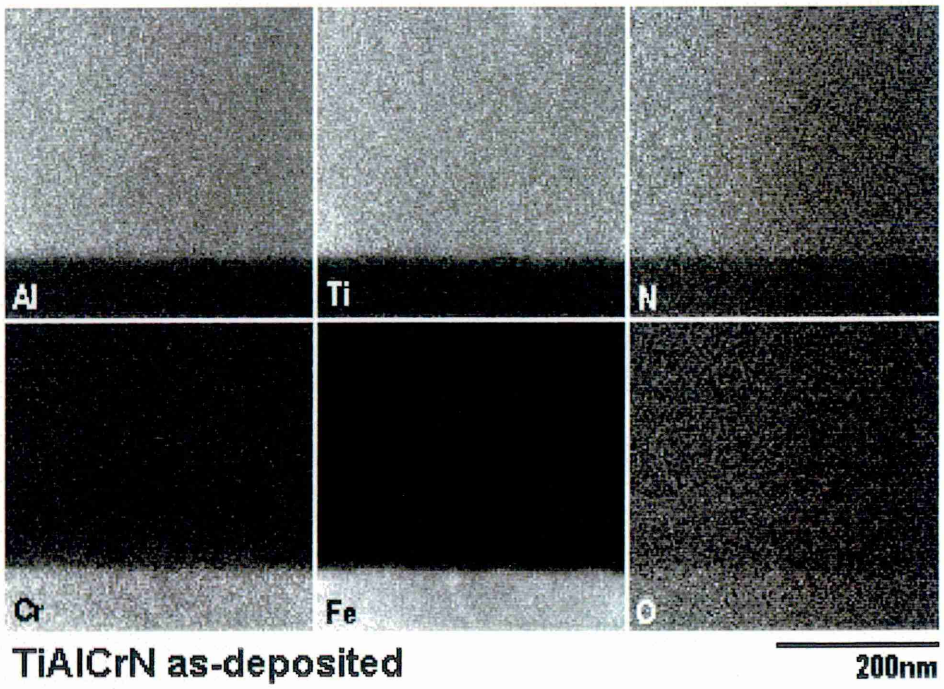

Figure 5-10: Elemental maps from the substrate/ coating region of the as-deposited TiAlCrN coating. The substrate material was SS 304.

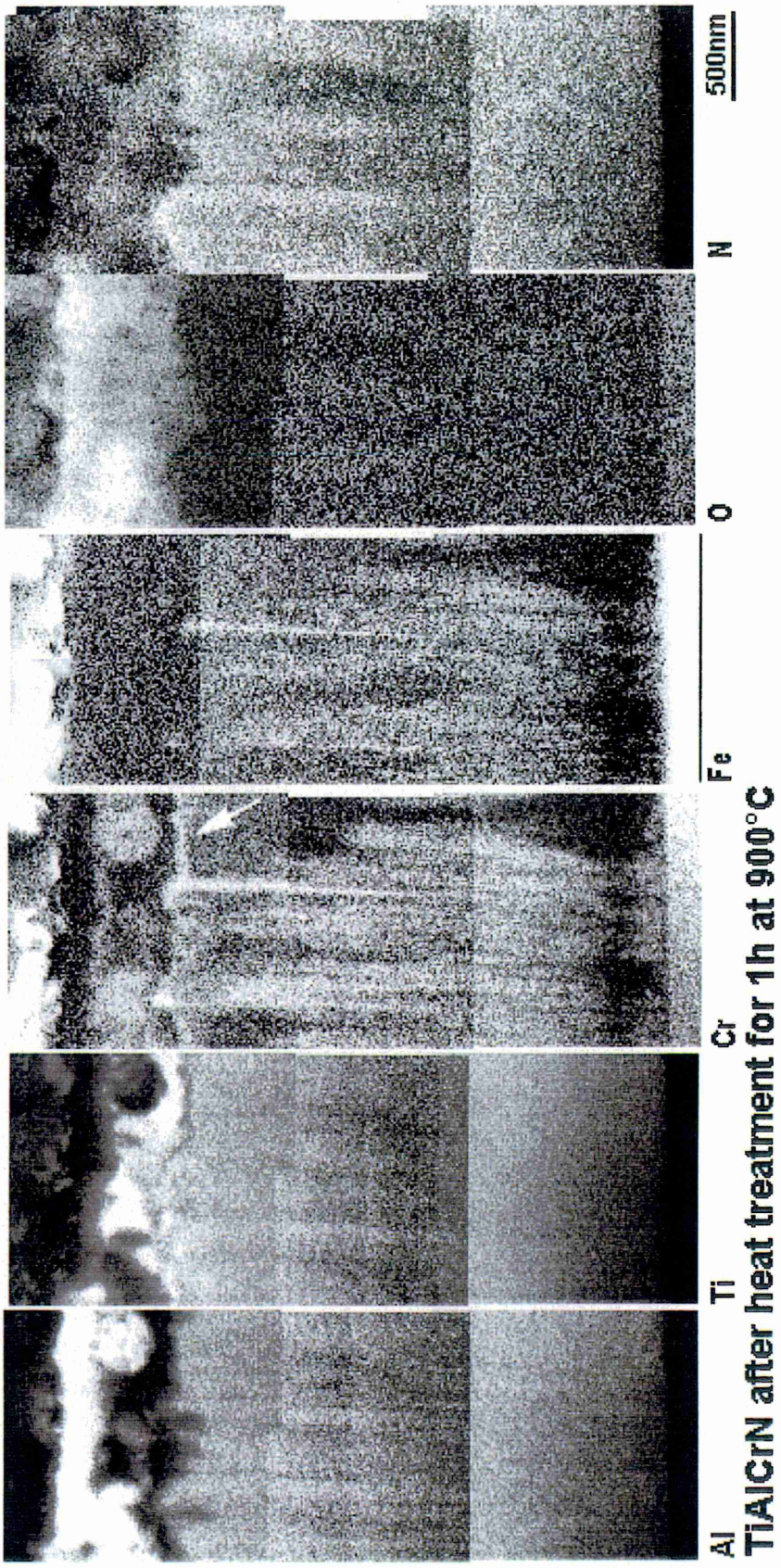

Figure 5-11: Elemental maps from TiAlCrN heat treated for 1h at 900°C

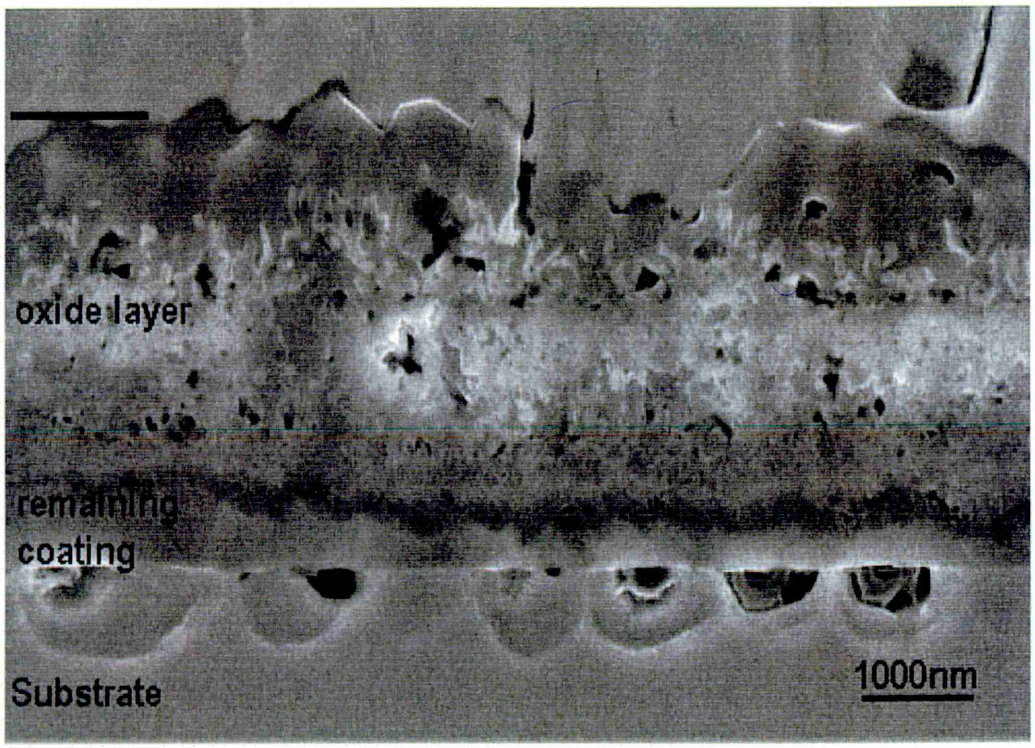

Figure 5-12: SEM micrograph of TiAlCrN deposited onto stainless steel heat treated for 1h at 950°C [33].

6 $Ti_{0.43}Al_{0.52}Cr_{0.03}Y_{0.02}N$ without OVERCOAT

$Ti_{0.43}Al_{0.52}Cr_{0.03}Y_{0.02}N$ was developed especially for dry high speed cutting of difficult to cut materials like AISI A2 steel [13, 32]. $Ti_{0.43}Al_{0.52}Cr_{0.03}Y_{0.02}N$ deposited on stainless steel was investigated to show eventual differences between the "original" coating and the main investigations on TiAlCrYN with overcoat (Chapter 7) produced in machine B (commercial production) after heat treatment.

The sample has in the as-deposited condition a bluish dark grey colour. After heat treatment for 1h at 900°C the interference colour of the sample was of shiny reddish dark black.

6.1 TEM observations

XTEM investigation of the original as-deposited TiAlCrYN coating (Figure 6-1) showed an interrupted columnar growth structure, when compared with the columnar growth morphology of the $Ti_{0.44}Al_{0.54}Cr_{0.02}N$ coating (Figure 5-3). A selected area DP taken from the middle of the coating (Figure 6-1b) showed a ring pattern associated with a micro-crystalline structure. Small separate void bands of ~50 nm at the boundaries were found at high magnification (Figure 6-1c).

After heat treatment for 1h at 900°C an oxide layer growth of 430±50nm was observed using XTEM. The microstructure presented in Figure 6-2a) exhibits a dense crystalline surface overlayer with a thickness ranging from 140 to 200nm and a less dense crystalline underlayer with a thickness ranging form 220 to 280nm. The contrast of the crystals in this layer varied, whereas the toplayer had a more uniform contrast. The crystal size in the less dense layer was between 50 and 90nm. Beneath that a mottled zone of ~60nm was observed. This zone seemed to mark the beginning of the oxide layer. It is the border between the nitride structure and the more equiaxed nature of the oxide layer. A

ring pattern is shown using a selected area diffraction pattern from the middle of the annealed sample (Figure 6-2b). In comparison with the ring pattern observed in the as-deposited coating, the DP of the annealed sample appeared to have some points of increased intensity, which would indicate a coarsening of the structure. The stainless steel substrate seemed unaffected by the heat treatment.

The different growth structure of TiAlCrYN in comparison with $Ti_{0.44}Al_{0.54}Cr_{0.02}N$ was explained by [33] with a continuous re-nucleation mechanism initiated by the addition of Y. Similar microstructures were generated and observed through ion-irradiation damage in TiN [169] and in TiAlN [115] through the formation of wurtzite-AlN phase during the film growth ($T_{filmgrowth} \geq 560°C$). Diffraction patterns were taken before and after heat treatment for 1h at 950°C from TiAlCrYN and compared by [33]. Essentially identical selected area diffraction patterns were observed. The DP recorded in this investigation indeed show minimal differences.

6.2 XRD measurements

The as-deposited coating was analysed using glancing angle parallel beam with 0.5° incident angle. The as-deposited sample shows reflections at 37.15 °2θ for {111}, at 42.98 °2θ for {200} and at 62.75 °2θ for {220} position (Figure 6-3). The mean peak width from these reflections was 1.067 °2θ at full width half maximum. The peak of the TiAlCrYN is considerably broader than from TiAlCrN (0.348 °2θ). This is supported by the evidence of a finer grain size observed by TEM in the Y containing coating. The integrated intensities can not be used to identify the preferred orientation in a glancing angle measurement, because there are no common diffraction vectors.

After heat treatment (Figure 6-4) the presence of mainly Al_2O_3 (JCPDS 42-1468) and TiO_2 (JCPDS 21-1276) was identified plus small amounts of Cr_2O_3 (JCPDS 38-1479) in solid solution with Al_2O_3 [94]. No reflections from the coating could be identified because of the shallow angle of incidence used. The oxide layer thickness (~430nm) was greater than the penetration depth of the X-ray beam.

6.3 EDX point analysis

Point analysis showed that a bi-layer was formed after heat treatment. The Ti-rich and Al-rich region were ~250 nm and ~100 nm in size. The oxide layer consisted out of a Al-rich outer region and a Ti-rich underlayer. Below the Ti-rich region (~50 nm) an increase in Cr content from 3 at% to 13 at% was observed. The N and O line cross over at a point which is marked by a line in the diagram (Figure 6-5a). The Cr-rich region seemed to be below this crossover point. The Y concentration increased from 1 at% in the coating up to 3 at%, on some points in the Ti-rich region, of the oxide layer. The high concentration of Y decreases with the start of the Al-rich oxide layer region.

Further profiles through the XTEM in the base layer region were compared to profiles taken before heat treatment (Figure 6-5b and c). The border between base layer (~160 nm) and TiAlCrYN coating is marked by the increase in Y concentration from 0 at% to ~1 at%. After annealing, the amount of Cr and Fe in the base layer, increased from 3.5 at% to 8.5 at% and from 0 at% to 2.9 at%, respectively (Figure 6-5b). The high concentration of Cr and Fe decreased after 70nm and 50nm in the base layer, respectively. The Al-profile did not change through the annealing. The alteration in the Ti-profile might indicate a migration of Ti towards the substrate/ coating interface, to perhaps form a Ti-precipitate (Figure 6-5c).

6.4 EDX mapping

Elemental XTEM maps of the coating surface after annealing are shown in Figure 6-6. An oxide bi-layer containing mainly Ti-oxide and Al-oxide was observed at the coating surface. This is consistence with the results gained from the point analysis. The regions of high intensity in the Ti map show decreased intensity in the O map. The Cr map shows an increased intensity in the Al-rich region. They might be an indication of void formation. Al_2O_3 and Cr_2O_3 are isostructural and can form a solid solution [80]. A thin Cr-rich band of ~30±7 nm was formed below the Ti-rich region. The Y map (L-line) showed a series of Y-particles in the Ti-rich layer of 10 – 25 nm in size. To unambiguously

identify, that the increase in intensity stemmed from Y, further maps were recorded at higher magnification both from the L- and K-line (Figure 6-7).

Elemental maps of the base layer from the as-deposited sample are shown in Figure 6-8. The maps show an alteration in intensity as expected from the point analysis profiles. No difference between base layer and coating was observed in the Al, Ti, Cr and N maps. In the Y_L map the base layer appeared less intense. The interface between substrate and coating does not appear as a straight line, because of drift of the sample during recording.

Cr, Fe and Y_L maps are shown from the base layer region after heat treatment (Figure 6-9). Cr and Fe started to diffuse into and beyond the base layer region along boundaries. The diffusion path has a length of approximately 570 nm measured from the substrate/ coating interface. The decrease in intensity in the Y_L map marks the base layer region. The Al, Ti and N map appeared in the same intensity, as in the as-deposited condition, therefore they are not shown in the Figure.

6.5 Discussion

The formation of an oxide bi-layer of TiO_2 and Al_2O_3 after heat treatment was previously reported by [11] for $Ti_{0.5}Al_{0.5}N$ and by [32, 33] for TiAlCrN and TiAlCrYN. The elemental maps from the oxide layer in connection with the XRD results fit well to these previously reported results. Furthermore the SNMS results and EDX depth profiles reported by [33] and co-workers showed the reported increase in Cr content before the oxide bi-layer. An oxide layer thickness of 600nm after 1h at 900°C measured by SNMS and an oxide layer thickness of ~400nm after annealing for 1h at 950°C was reported by [33]. Therefore, the oxide layer thickness of 430±50nm found in this investigation is of the same order of magnitude as those previously reported. Considering only the value derived by [33] after 1h at 950°C and the reported onset point of rapid oxidation of 950°C, the oxide layer measured in this investigation is relatively thick, at 430±20 nm. However, a delamination during XTEM sample preparation was also reported by [33], which might explain the difference in oxide layer thickness.

Through elemental mapping it was possible to contribute to the knowledge of the composition of the oxide layer and the interface integrity. EDX mapping and point analysis in combination are techniques very well suited to define variations in composition in coatings to get an overall idea and on small scales (probe size ~3nm). A good example of this is the investigation of the oxide layer. Point analysis revealed the increased amount of Y in the Ti-rich area, but with mapping it was possible to show that Y-particles had formed. The particles were relative small in comparison to the sample thickness. Depending on where the probe was placed the relatively small amount of 3at% of Y measured can be explained. It was previously reported [33], that YO_x accumulates at the interface between the Ti-rich and Al-rich sublayers, but not at the lower Ti-rich oxide-nitride interface. This is in contrast to the observation in this investigation. It might be that the temperature of 950°C led to a further out-diffusion of Y and its position between the Ti-rich and Al-rich sublayers. Differences in results between the EDX maps and point profiles were noted in the case of Cr and Fe diffusion into the coating. The Cr profile recorded after 1h at 900°C from the base layer region indicated that the diffusion of Cr stopped in the base layer after 70nm measured from the interface. The Cr map revealed a diffusion path of 570nm from the interface. It also showed that the diffusion was limited to the boundaries. A similar observation was made for Fe.

6.6 Summary

Further improvement of the oxidation behaviour in comparison to $Ti_{0.44}Al_{0.45}Cr_{0.02}N$ was achieved by the addition of 1 at% of Y (including all elements) into the TiAlCrYN coating. An oxide bi-layer with a thickness of ~430nm consisting mainly of Al_2O_3 and TiO_2 was observed after heat treatment for 1h at 900°C. Y-rich particles were observed in the Ti-rich part of the oxide layer. A Cr-rich band of ~50nm thickness at the border nitride-oxide was observed. Elemental mapping of the cross section revealed diffusion of the substrate elements Cr and Fe for ~570nm into the TiAlCrYN coating after annealing for 1h at 900°C. The addition of Y and the fine interrupted columnar growth structure of the as-deposited sample are responsible for this

improvement in interface protection and oxidation resistance, when compared to TiAlCrN.

6.7 Figures

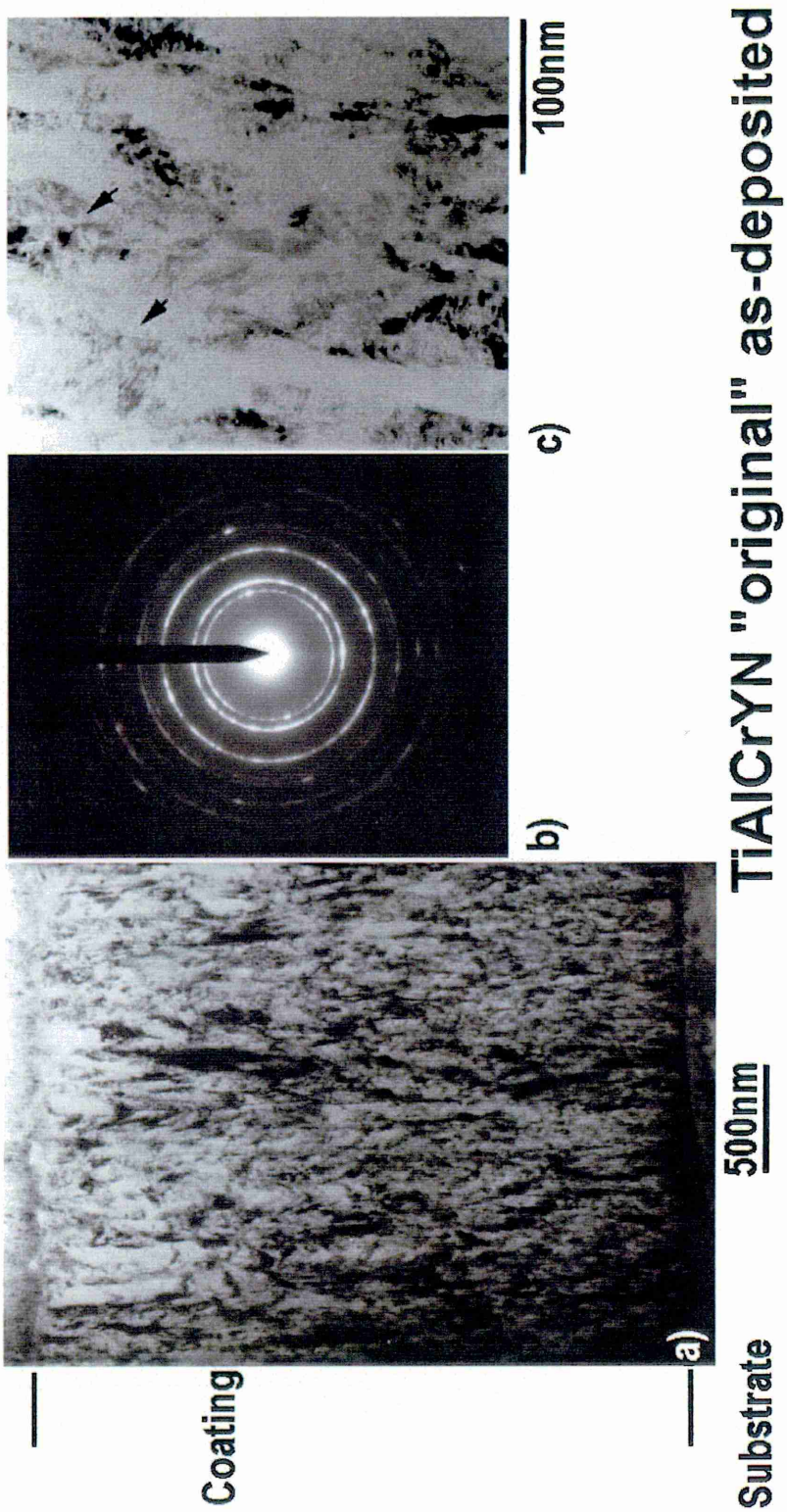

Figure 6-1: XTEM micrographs of as-deposited TiAlCrYN "original" a) shows the whole film, b) the DP taken from the middle, c) a magnified BF image from the middle of the coating.

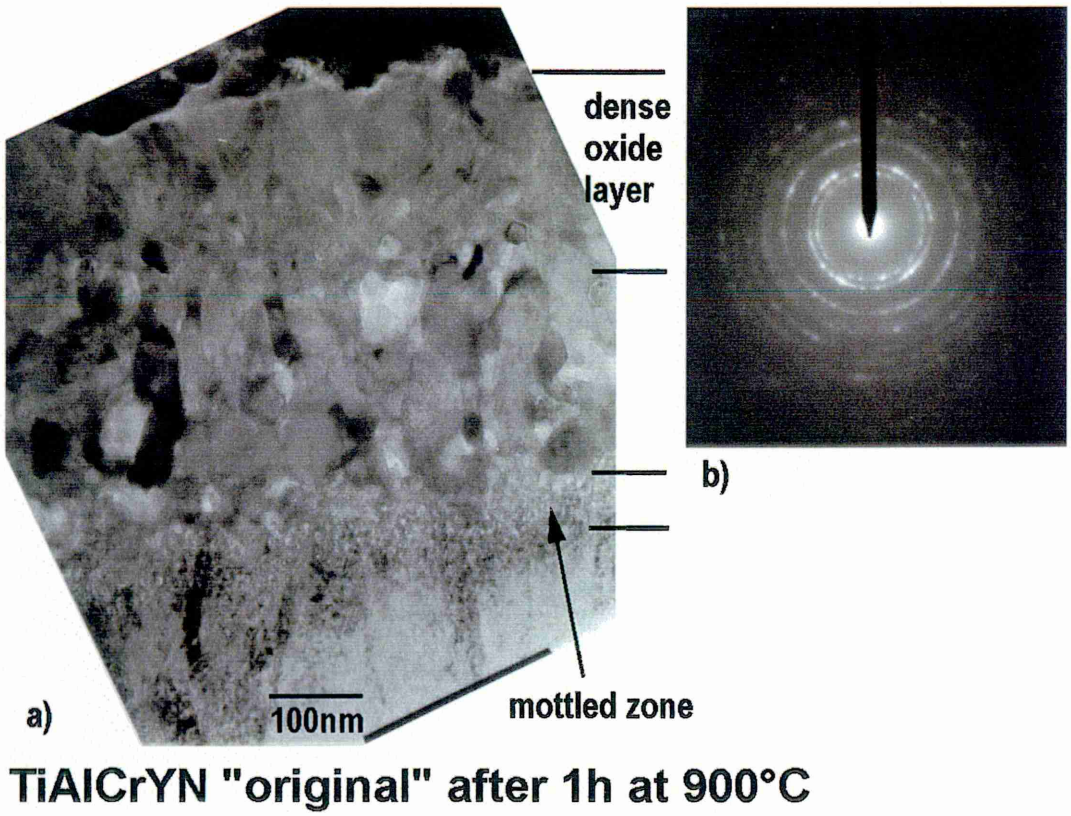

Figure 6-2: XTEM micrograph of TiAlCrYN "original" after heat treatment for 1h at 900°C: a) the oxide layer, b) the DP taken from the middle

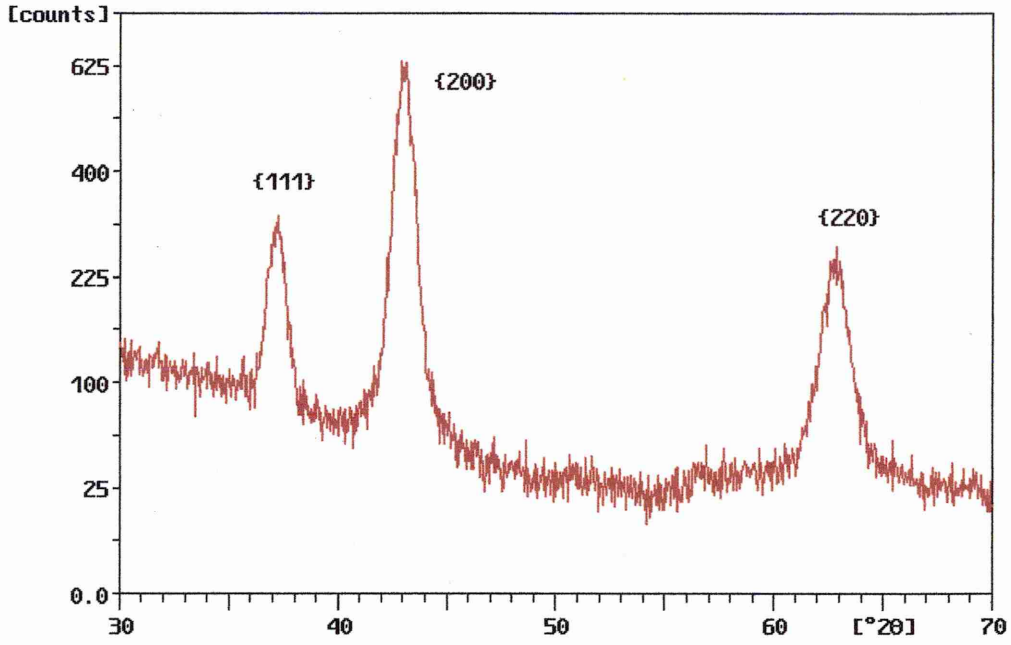

Figure 6-3: Glancing angle measurement of the as-deposited TiAlCrYN "original" sample.

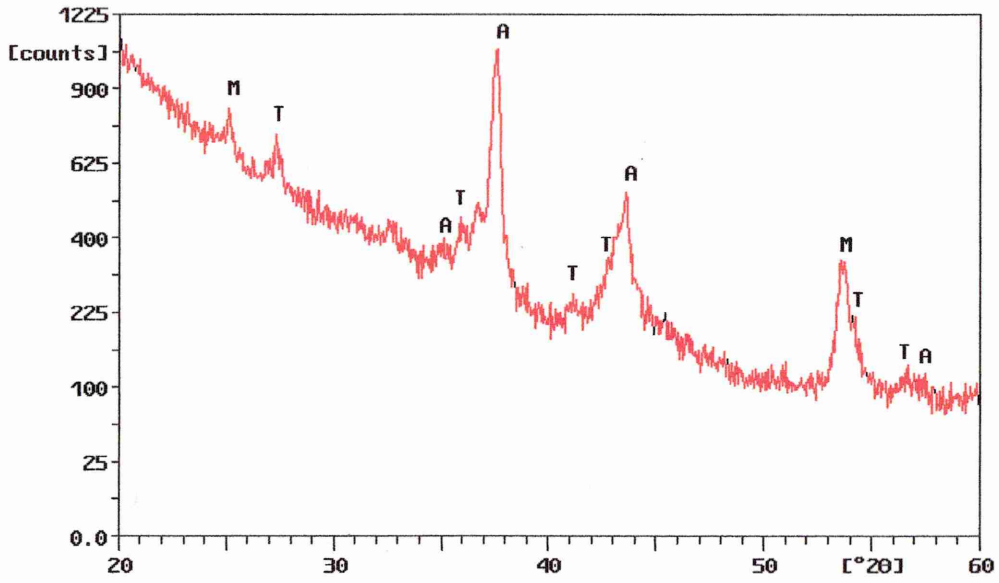

Figure 6-4: Glancing angle XRD with 0.5° fixed incident angle from TiAlCrYN after 1h at 900°C. A = Al_2O_3, T = TiO_2, M = solid solution of Al_2O_3 and Cr_2O_3.

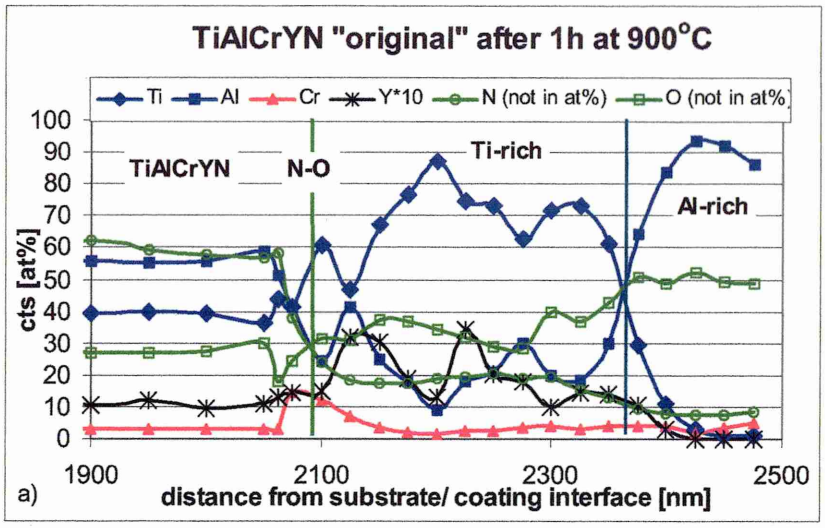

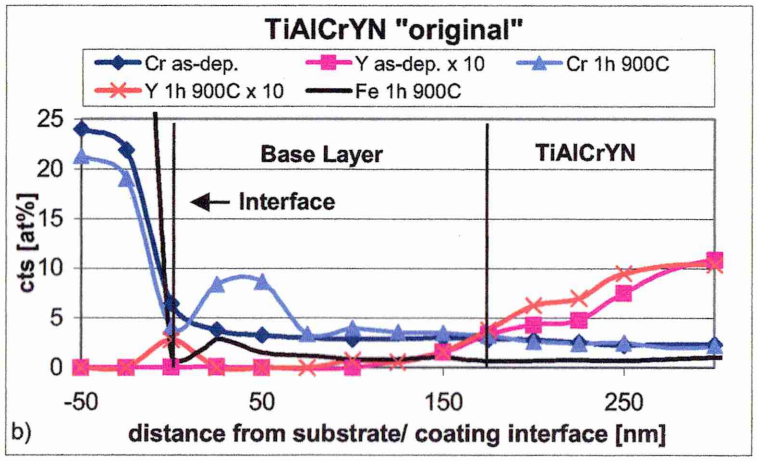

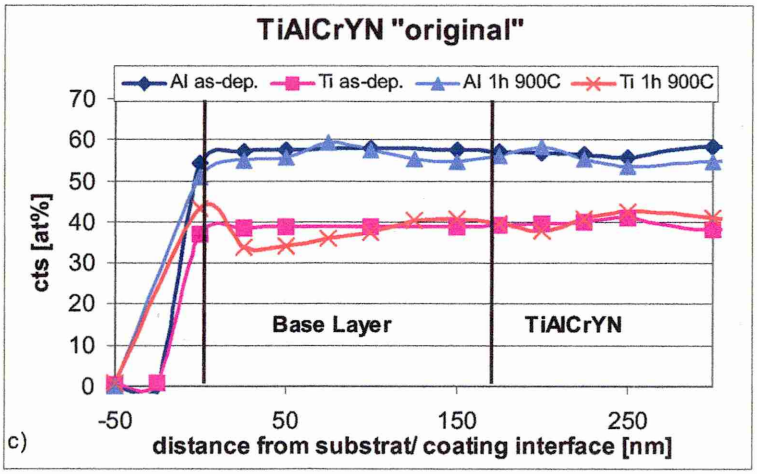

Figure 6-5: EDX profiles from the "original" TiAlCrYN before and after annealing for 1h at 900°C: a) point analysis through oxide layer Y, b) Cr and Fe profile of base layer, c) Al and Ti profile of base layer.

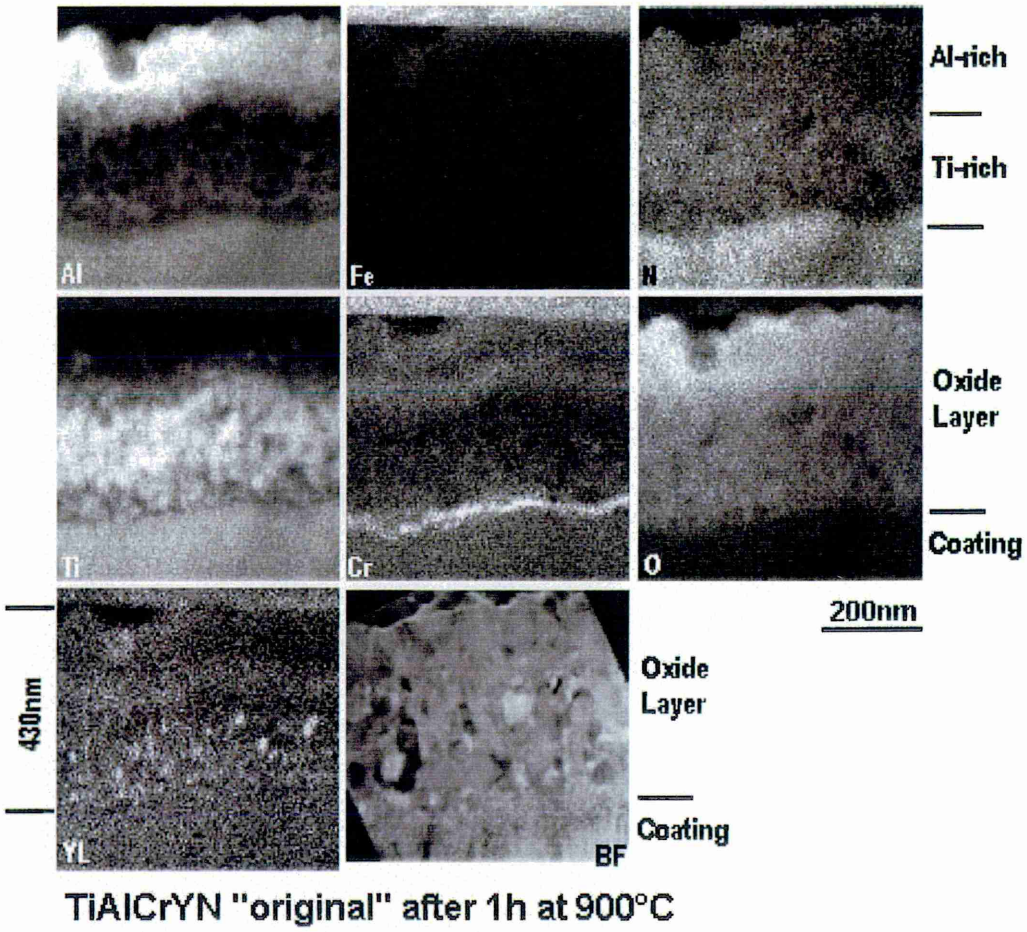

Figure 6-6: Elemental maps of TiAlCrYN heat treated for 1h at 900°C.

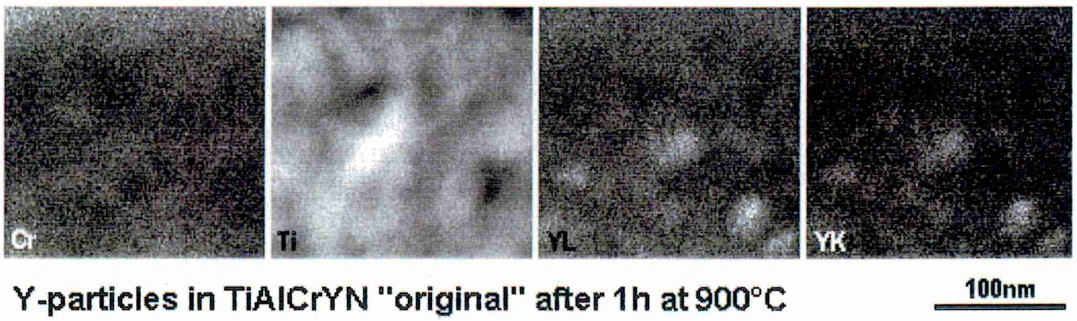

Figure 6-7: Elemental map from the Ti-rich region of the oxide layer formed on TiAlCrYN after heat treatment for 1h at 900°C.

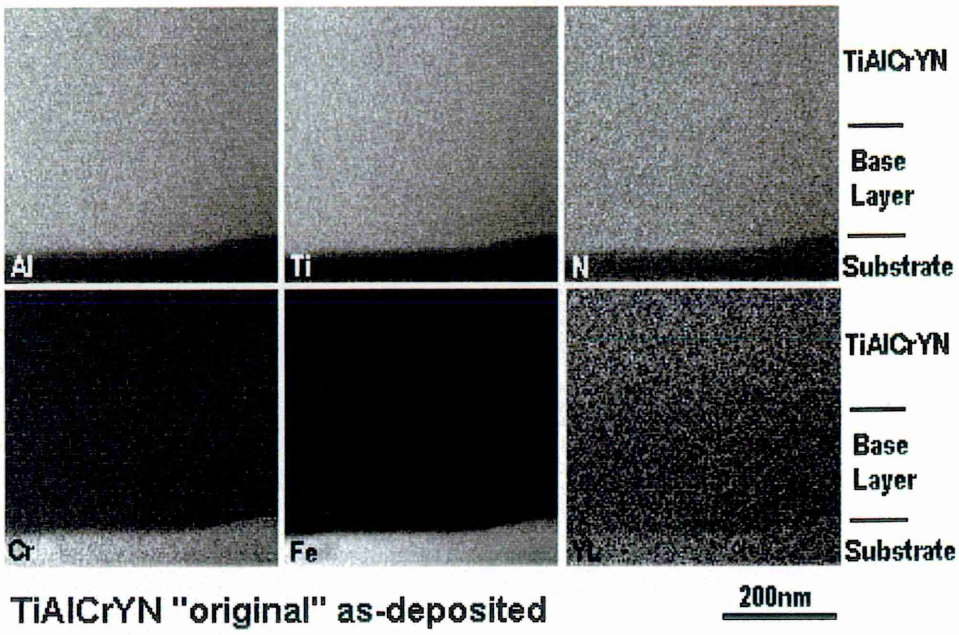

Figure 6-8: Elemental maps of the as-deposited TiAlCrYN "original" base layer.

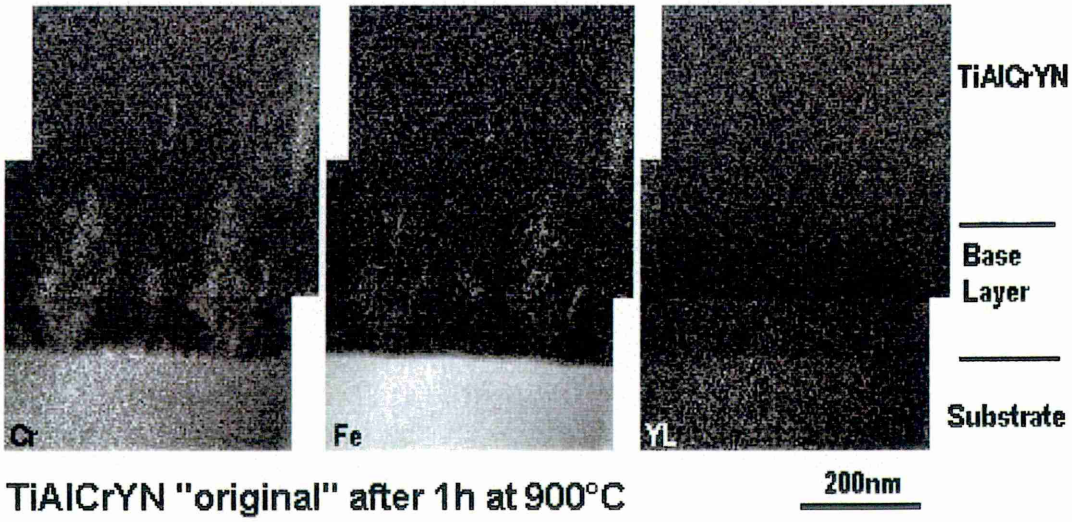

Figure 6-9: Cr, Fe and YL map from the base layer region of TiAlCrYN after heat treatment for 1h at 900°C.

7 TiAlCrYN with OVERCOAT

Dry high speed cutting of difficult to cut materials like AISI A2 demands a hard coating, which exhibits high toughness, high oxidation resistance, a limited amount of stress and excellent adhesion. The original TiAlCrYN coating already met the last three requirements. With the addition of a nanolayered oxynitride overcoat the first requirement the toughness of the surface was improved. This was shown in Pin-on-Disc tests as well as in high speed milling tests [145, 1]. Further investigations regarding the high temperature behaviour of the TiAlCrYN coating with overcoat (TiAlCrYN+Ox) were performed.

TiAlCrYN+Ox samples were examined in as-deposited condition and after heat treatment using TG, SEM, XRD, TEM and EDX analysis. The oxidation behaviour was investigated after heat treatment at 900°C with a variation in time and after 10h annealing at different temperatures. In some cases, the TiAlCrYN+Ox sample was compared to a TiAlCrYN coating without the overcoat deposited in the same coating machine.

7.1 TiAlCrYN+Ox in as-deposited condition

7.1.1 TEM

Figure 7-1 shows the structure visible in a TEM bright field image of the as-deposited film. The total film thickness was 2.3μm. In this micrograph three distinct regions were clearly visible, namely the base layer, the middle TiAlCrYN layer and the oxynitride layer. The structure changes from the base layer to the TiAlCrYN coating. In the TiAlCrYN layer (~1500nm) the coarse columnar structure of the base layer (~400nm) changes to one of fine interrupted columnar growth. The oxynitride layer (~380nm) appears as a coarser and darker band on top of the coating. The intensity of this layer is different, due to an enhanced content in Cr in the oxynitride layer, which increases the mass scattering contrast. The relative amount of Y decreases in the overcoat region,

which might explain the coarsening of the structure. Closer examination (higher magnification) of the boundaries showed void bands of 450±100nm (Figure 7-1) along some column boundaries.

The fine grained interrupted columnar growth observed in the as-deposited sample is caused by constant renucleation, due to the addition of Y. The microstructure is, except for the deposited oxynitride Cr-rich overcoat, similar to the one found by [13, 33]. Similar microstructures have been observed to form when renucleation was generated in TiN films by excessive ion-irradiation damage [63] and in TiAlN by AlN wurtzite phase precipitation during growth [115]. The number of voids found seemed slightly higher than in the original sample. The problem with this observation is that a TEM sample represents only a very small part of the coating structure.

7.1.2 XRD

Glancing angle X-ray diffraction indicated that the upper layer of the oxynitride overcoat was amorphous, because there was no evidence of reflections from the oxynitride overcoat only those from the coating (Figure 7-2a). Additionally, the slightly curved background under the {111} peak might be caused by diffused scattering from the amorphous layer.

The as-deposited sample showed reflections at 37.31 °2θ for {111}, at 43.42 °2θ for {200} and at 63.24 °2θ for {220} positions (Figure 7-2a). The mean peak width from these reflections was 1.082 °2θ at full width half maximum. The peak width of the TiAlCrYN+Ox coating is considerably broader than that of the TiAlCrN coating (0.348 °2θ) and of the same order (1.067 °2θ) as for the 'original' TiAlCrYN coating and showed a similar XRD pattern.

Low angle XRD (Figure 7-2b) from TiAlCrYN+Ox showed the formation of a diffraction peak from the nanolayer structure of the TiAlYN/CrN overcoat. TiAlCrYN in comparison to TiAlCrYN+Ox showed no such response. The d-spacing of the nanolayers in the overcoat region was 1.6nm.

7.1.3 EDX point analysis

For the as-deposited sample an EDX point analysis profile was shown above a BF XTEM micrograph (Figure 7-3) to relate variations in structure and composition simultaneously. Important to note was the rise of Y after the TiAlMeN base layer in the coating and the slight drop in Cr content from 3.6±0.4at% to 2.4±0.1at%. In this case the metal concentration was normalised to 100%. Hence, the agreement between the concentration of Cr in the $Ti_{0.17}Al_{0.31}Cr_{0.014}Y_{0.007}N_{0.50}$ sample measured by RBS and EDX was good. The concentration of Cr measured by EDX is 1.2at%, where N is assumed to be present with 50at% concentration. With RBS a Cr concentration of 1at% was measured.

The peaks are exaggerated in the N and O curve, due to the way this curve was created (see experimental). The cross over point (see arrow) between N and O line is important. It will be used as a measure of progress of oxidation in the heat treated specimens. At the coating surface the profiles of the coating elements also matched the changes in deposition parameters. The changes are more complex than in the base layer region. Therefore the point analysis profiles of the overcoat region were closely examined. A rise in Cr concentration to 40at % was achieved by increasing the power to the Cr target, as well as an analogous decrease in Ti, Al and Y contents in this region, as would be expected from the change in process parameters. The Cr-rich region (above 25at %) is approximately 250±20nm thick (total overcoat thickness 400nm). The graded transition from the nitride to the oxynitride started approximately 180±20nm from the coating surface. There is a slight inconsistency between measurements of the apparent overcoat thickness from XTEM and EDX analysis. The mass contrast contribution to the XTEM image is not discernible at the lower Cr concentrations, hence the measured overcoat thickness varies with the method used. The multilayer structure is contained within the Cr rich region.

7.1.4 EDX mapping

Al, Ti, Cr, and Y maps collected from the base layer region showed changes in intensity, according to the difference in composition between substrate and base layer (Figure 7-4). N and O maps showed variations between the substrate and coating material. Even the small difference in Cr content between base layer (~3.5at%) and TiAlCrYN coating (~2.5at%) is noticeable in the Cr-map. The Y content of the base layer was low (no peak was identified at the Y_L position), because the TiAlY target was run only at 0.5 kW during deposition of the base layer, compared with 10.7 kW during the deposition of the 'bulk' TiAlCrYN coating (1.1+0.3 at%). The slightly increased intensity of the Y map in the substrate region stems from the increased amount of continuum counts from the heavier elements (Fe, Cr, Ni) in the substrate contributing to the total counts collected. The variation in intensity in the O map is caused by the same effect.

Elemental maps were also obtained from the overcoat region (Figure 7-5). The Cr map confirmed the increase in Cr content initiated during the deposition process. In corresponding areas the Ti and Al maps appeared less intense than in the Cr-rich area, which was in accordance with their reduced composition in this area. At the end of the deposition process the power to the Cr target was reduced to 0.7kW. This was seen in the Ti and Al maps where the outermost layer was rich in Ti and Al. The change from nitrogen to dry air was also observed in the middle of the Cr-rich region, again consistent growth process parameters. The Ti_L peak and the N peak, the Cr_L peak and the O peak overlap in an EDX spectrum. The intensity in the N and O map was high enough to arise from the low atomic number elements. The actual crossover between N and O was probably closer to the surface than indicated by the map. Even though a narrow window for O (0.48-0.56keV) was chosen, the amount of Cr in this region probably produced a substantial number of Cr_L counts, enhancing the O intensity. The change in Y concentration, 1.1+0.3 at% to 0.6 at% (lowest concentration in the overcoat region), was not high enough to change the intensity of the map noticeably. Below the elemental maps a BF TEM image is shown. The overcoat region has been indicated at the same scale as in the maps.

7.1.5 Thermogravimetry

Continuous TG measurements (Figure 7-6) revealed a difference in weight gain at 1000°C between the stainless steel substrate (6.6 gm^{-2}), the TiN coating (10.8 gm^{-2}) [32], TiAlCrN (3.9 gm^{-2}) [32], TiAlCrYN (2.8 gm^{-2}) and TiAlCrYN with overcoat (1.1 gm^{-2}). The onset point of rapid oxidation is at ~950°C for the Y containing coatings, as previously reported by [32]. The weight gain versus temperature graph for the TiAlCrYN+Ox coating has a distinctly different shape to that of a similar TiAlCrYN coating without the overcoat, in the region from 900°C to 1000°C. It appears that the oxidation first begins slowly and then proceeds more rapidly. This could be explained by reference to difference in composition of the overcoat region (first ~400nm), mainly Cr, and the main coating. This is shown clearly by isothermal thermogravimetric measurements at 920°C where a significant difference in weight gain (Figure 7-7) was observed between the TiAlCrYN+Ox (2.6±0.2 gm^{-2}) and the one without overcoat (3.8±0.2 gm^{-2}). For comparison purposes, the weight gain of a $Ti_{0.44}Al_{0.54}Cr_{0.02}N$ coating (5.2±0.2 gm^{-2}) and the substrate material SS 304 (6.7±0.2 gm^{-2}) were also plotted. The lower values of the TiAlCrYN+Ox coating results from the improved oxidation resistance of the Cr-rich interlayer [21] in the oxynitride overcoat. Table 7-1 shows the difference in weight gain between various isothermal measurements taken from TiAlCrYN with and without the overcoat.

	Weight gain of TiAlCrYN and TiAlCrYN+Ox [gm^{-2}]							
T [°C]	**1h**		**2h**		**5h**		**10h**	
720	0.28	0.28	0.30	0.29	0.36	0.30	0.41	0.31
820	0.35	0.33	0.43	0.35	0.52	0.40	0.59	0.48
870		0.37		0.47		1.00		1.64
920	0.76	0.61	1.38	0.94	3.43	1.52	3.80	2.58
945		1.01		1.79		4.47		5.69
970		1.33		3.56		7.43		9.03

Table 7-1: Difference in weight gain between TiAlCrYN and TiAlCrYN+Ox out of the same machine. The right column contains the data for the Y coating with overcoat.

Further isothermal measurements of the TiAlCrYN+Ox alone were performed to show the oxidation behaviour at various temperatures (Figure 7-8). It is important to note that the regime of constant temperature started about 45 min (for 900°C) after the measurement started (see Chapter 3 - Experimental). The isothermal results are in good agreement with the continuous ones. The increase in weight gain is very moderate below 920°C. The temperature difference of 50°C between 870°C and 920°C doubles the weight gain. Between 945°C and 970°C the weight gain increases by a factor of two. The shape of the curves, especially the ones at higher temperatures, indicate that various reaction processes are taking place. Some explanations for possible reactions are given in Chapter 9 – Discussion. Saturation of the reaction process, converting all coating material into oxides is not achieved, even after 10h.

7.2 Observation after annealing at a constant time

Coated stainless steel specimens were heat treated for 10h in air at temperatures between 600°C and 900°C. Samples heat treated from 600°C - 800°C showed an interference colour, whereas, after heat treatment for 10h at 900°C, a porous flakey yellow oxide formed, showing that the oxidation was in the breakaway region. The results of all heat treated samples are discussed at the end of this chapter (7.5).

7.2.1 TEM

7.2.1.1 Coating structure

Cross sectional BF TEM micrographs revealed a change in structure from the as-deposited sample to the annealed samples in the 'bulk' coating (Figure 7-9). After heat treatment at 600°C a fine grained interrupted columnar microstructure, like in the as-deposited sample, was observed. Figure 7-9 shows also that, after heat treatment at 700 °C, the structure had begun to

change from one of interrupted columnar growth towards a fully columnar structure, from base layer to outer layer. After heat treatment for 10h at 800°C the structure was of columnar appearance, with the columns showing partial disruption through different orientations in the column. After 10h at 900°C the structure had a fully columnar appearance, with each column having one orientation. In Figure 7-10 a selected area diffraction pattern (aperture size <200nm) was taken showing the uniform (011) orientation of a single column. The line of brightest spots in the pattern is in the (200) direction.

Further diffraction patterns were taken for each heat treatment condition from the middle of the coating with an aperture of approximately 500 nm in diameter. An evolution from a typical ring pattern, where the rings were sharp and well defined, implying that the structure was micro-crystalline, to a spot pattern occurred. With increasing temperature the DP had a smaller number of discrete spots indicating fewer crystallites in the aperture area (Figure 7-11). These findings confirm the observations from the bright field images and are suitable as a qualitative measure of structural differences in the various specimens.

With the change in structure an elongation of the void bands along the column boundaries was noticed. In the as-deposited coating void bands of 450±100nm in length were detected (Figure 7-1). At 700 °C the void bands connect the coating surface with the stainless steel/ base layer interface, thus providing a quick diffusion path. These bands increase in length with increasing temperature. At 700°C the voids extend through the entire film thickness of 2.3μm. This creates a fast diffusion path [60] between substrate/ coating interface and top of the coating surface. No voids were detected at 900°C (Figure 7-9). The disappearance of the voids at the 900°C 10h sample might be caused by grain boundary movement.

7.2.1.2 Coating surface – oxide layer region

From further observation of the BF micrographs in Figure 7-9 uniform oxide layer formation over the whole surface started at 700°C. The oxide layer thickness for the 700°C specimen was measured to be 150±10nm, with 230±10nm remaining of the deposited overcoat. After 800°C an oxide layer between 320 and 380 nm in thickness was observed. The oxide layer grew with

at least three different structured regions and only a 50-70nm thin indication of a remaining overcoat was seen. Breakaway oxidation started after heat treatment at 900°C. The oxidation process consumed about 1200nm of the TiAlCrYN+Ox film (Figure 7-9 and Figure 7-10).

Annular dark field images with an inner angle of 30mrad were taken from the oxide layer to show if void formation occurred. This is a region beyond the {420} ring formed on a DP. In this region the influence of diffraction contrast created should be minimal [157]. A series of darker regions were observed. The darker regions are caused by a lack of mass. This could be caused by voids formed in the oxide layer, due to differences in volume expansion. The formation of voids within the oxide layer region was observed after heat treatment at 700°C (Figure 7-12). Of interest is the layered growth of the oxide film, which might be caused by the deposited nanolayers. Voids were also found in the oxide layer at 800°C between single oxide crystals and the oxide film/ coating region. This indicates a porous oxide film growth, it is therefore unlikely that the oxide layer would be stable during cutting operation in this form.

7.2.1.3 Substrate/ base layer region

An interesting side issue was a change in contrast observed in the base layer region from the as-deposited samples and the heat treated samples. Dark field images using the {111}, {200} and {220} ring position (very close together) showed after heat treatment a darker appearance of the base layer region (Figure 7-13). The dark field image contained in this case a high amount of diffraction information because of the position chosen for the aperture. At 600°C the contrast difference is only very subtle between the base layer and the Y-rich coating, but at 700°C, 800°C and 900°C the variation in contrast between those two areas is clear.

The darker appearance of the base layer in the heat treated sample can be caused by a series of effects: A change in diffraction contrast caused by defects or strain could alter the appearance of the base layer after heat treatment. Similarly mass contrast could effect the contrast mechanism in the base layer. In the case of mass contrast microvoids or micro accumulations of trapped gas

could cause a change. The contrast change through differences in mass contrast is supported by the following references:

The deposition parameters chosen, T_s = 450°C and U_b = -75V allow the formation of point defects in the TiAlCrN base layer. Point defect formation for similar parameters was observed by [62] on $Ti_{0.5}Al_{0.5}N$.

A change in stress of the base layer after heat treatment could cause a change in the contrast of the base layer. A difference in stress after heat treatment was reported by [89, 90, 92, 129].

It is also possible that under these conditions a small amount of Ar is trapped in the fcc lattice. It was shown by [169] that Ar incorporation occurs even at small bias voltages (1at% at –100V bias) in TiN sputter deposited at T_s = 300°C. The formation of inter granular pores after heat treatment of TiN coatings, deposited using arc ion plating and a substrate temperature of 450°C, was observed by [171].

7.2.2 EDX point analysis

7.2.2.1 Substrate/ base layer region

Point analysis profiles from the different heat treated specimens were compared to the as-deposited sample for the base layer region and the coating surface. Point analysis of Cr (Figure 7-14) and Fe (Figure 7-15) at the base layer region showed that diffusion from substrate elements into the coating started to occur at 700°C. Remarkable about this finding is that the diffusion profiles looked very unusual with the peak formed at the base layer/ coating interface. The peak shape at the base layer/ coating interface of the Cr and Fe line indicated a hampering of the diffusion. In the case of Cr the ~4at% found in the as-deposited sample increased to over 20at% after 900°C, which is the same amount found in the SS substrate. The amount of Fe after heat treatment at 900°C increased to 20at% at the base layer/ coating interface. Beyond the base layer 10at% of Cr (2.5at% in the as deposited sample) and 5at% of Fe were found. The additional amount of Y in the coating seems to be responsible for hampering the diffusion at the base layer/ coating interface. With increasing temperature the amount of Y in the coating started to decrease after the base

layer/ coating interface (Figure 7-16). An increase in Y concentration was noted for 700°C and 800°C before the base layer/ coating interface. This might be accumulated Y from the base layer region. The comparison of Al concentration showed that with increasing temperature the amount of Al dropped from ~52at% in the as-deposited sample to ~31at% at 900°C (Figure 7-17). Beyond the base layer the curves of the graph are getting "noisier" with rising temperature. For Ti an increase in fluctuation in the curves was noted, but no difference in the concentration. A comparison of the counts collected in the X-ray spectrum energy window from 0.48 to 0.56 (O position) was performed in Figure 7-18. A problem with these data arises because the Cr_L peak will overlap the O energy window. The data were the result of the gross integrals in the above mentioned energy range divided by the sum of counts from all windows. The O counts increase above 600°C, which would correlate with the observed void formation at 700°C in the coating. Unfortunately, the N profile shows the same response (Figure 7-19). The difference in counts is probably an effect of a variation in excitation volume of the thin film, which can change the background shape of the single spectrum.

7.2.2.2 Coating surface – oxide layer region

The variations at the substrate surface were investigated by comparing the concentrations before and after heat treatment. The cross over point between the N and O line (gross integrals divided by total counts) was taken as a reference point for the progress of oxidation (Figure 7-20). After annealing at 600°C no variation to the as-deposited profile was observed. A ~50nm shift towards the substrate was observed at the 700°C sample. After 800°C the cross over point was ~120nm further in the coating. At 900°C the oxidation progressed so far, that the cross over point was found at 1025nm from the substrate/ coating interface. The cross-over point of interest was marked in the following diagrams. It is interesting to note that in the Al and Ti, the Y, the Cr and the Fe diagram the cross over point is at the place were a change in concentrations starts (Al, Ti) or an accumulation occurs (Y, Cr, Fe). In the case of the latter Y is in the O rich region, whereas Fe and Cr are at the border. Measurements on the bright field TEM micrographs showed the oxide layer

starts to grow at ~1100nm from the substrate/ coating interface after heat treatment for 10h at 900°C (Figure 7-10).

The Al and Ti point analysis showed the same profile for the as-deposited condition and after annealing for 600°C. After heat treatment at 700°C the Al curve became slightly erratic in the knee of the curve. Changes in the compositional profiles of both Al and Ti started to occur at 800°C (Figure 7-21). Both profiles became erratic, indicating local differences in the Al and Ti composition existed. An Al enrichment of the surface with a Ti-rich zone below was observed. At 900°C the profile has no similarity with the as grown sample. From the TEM images it is known that large oxide crystals have formed. The changes in the profile occur, therefore, from single particles rather than layers.

The Y profile (Figure 7-22) behaved in a similar way to the Ti and Al profile. The profile became more erratic at 800°C, and probably revealed the presence of Y rich particles at 900°C. This would explain the relatively large increase in the amount of Y (2at%). A comparison with the measurements performed at the interface/ base layer region suggests an out-diffusion of Y.

The out-diffusion of Cr (Figure 7-23) was indicated by a change in shape of the Cr peak at 800°C, a sharp spike was formed increasing the Cr content from 45at% to 60at% for a 80nm broad area (total peak width 250nm). In the 900°C sample the O-rich region exceeded the deposited Cr-rich layer in the overcoat. Possibly during TEM sample preparation some of the oxide particles were abraded. Nevertheless one can state that the remaining unoxidised part of the coating was 1025nm thick. A very small band of Cr, ~60nm to 70nm broad, was found at the border between coating and oxide layer. The Cr in this layer is likely to have diffused from the substrate.

Comparison of the various Fe profiles (Figure 7-24) showed an increase in Fe at 800°C and 900°C towards the coating surface. Further comparison with Cu gained from the same region showed that the Cu line had a similar shape to the Fe profiles. This indicates that the detected Fe might arise as an artefact from the ion milling process. From the XRD results it is known that $FeCr_2O_4$ oxides were detected only at 900°C. This confirms that some of the detected Fe at 900°C must arise from ion-milled substrate material.

7.2.3 EDX mapping

7.2.3.1 Substrate/ base layer region

Heat treatment at 600°C for 10h did not change the appearance of the elemental maps from the as-deposited sample for the base layer region. After annealing at 700°C for 10h the intensity in the base layer region in the Cr and Fe map increased (Figure 7-25). The substrate species Cr and Fe started to diffuse into the base layer. Especially in the Fe map it was evident, that diffusion was occurring primarily along the column boundaries. Diffusion of these elements stopped at the base layer/ Y containing coating border. The other maps showed no variation in comparison to the as-deposited ones. However, all the maps show in general on the left side a decrease in intensity caused by a difference is specimen thickness.

For the sample heat treated at 800°C a series of maps was used to illustrate the compositional variations that occurred (Figure 7-27). Maps taken after heat treatment at 800°C at the substrate/ coating interface showed an increased intensity in Fe and Cr maps mainly along the column boundaries for a distance of 1000nm up to 1170nm. The total coating thickness of the as-deposited sample was 2300nm. In the base layer region the substrate elements Cr and Fe seemed to be in the bulk material as well. It appeared that the substrate element diffusion in the base layer was tailed back at the coating/ base layer interface, leading to diffusion into the bulk at the base layer/ coating interface.

Furthermore, at 800°C, Y was detected at the column boundaries along a distance of 1500nm from the substrate/ coating interface. Presumably, Y would be found in the whole Y containing part of the coating at the boundaries. A map from the Y_L and Y_K position at higher magnification (1 million) confirmed unambiguously, that the rise in intensity stemmed from Y_L (Figure 7-26).

Al, Ti and N maps showed a decrease in intensity at the column boundaries (Figure 7-27). The intensity inside the columns was not uniform. In the case of Al diffusion into the substrate was observed, which might indicate the formation of an AlN precipitate (Figure 7-30). The only elemental map not affected by the heat treatment was O. This map showed uniform intensity throughout.

7.2.3.2 *Whole coating after 10h at 900°C*

Map montages from the 900°C sample showed that substrate elements diffused to the substrate surface (Figure 7-28). Adjacent to the maps a BF TEM micrograph from the same area is shown. The Cr map had, for the entire base layer region an almost uniform intensity, which might mean that all possible lattice sites are "filled" with substrate elements. The diffusion of Cr spread in comparison to Fe over larger area of the columns. A Cr-rich band of ~70nm was formed on top of the nitride layer inside the O-rich region. Cr was also found to be present in some of the discrete oxide crystals. The diffusion of Fe is less severe. The larger size of the Fe in comparison to Cr slowed the diffusion down. In the substrate maps (Cr, Fe) a gap was visible at the same position where Al enrichment is seen in the Al map (Figure 7-29).

An Al and N map together with an EDX-spectra revealed the formation of an AlN precipitate in the substrate of 150x75nm (Figure 7-30). This suggested that, at the same time, Fe depletion of the substrate material occurs as AlN precipitates form.

Severe Al depletion in comparison with the Ti map was observed along the column boundaries (Figure 7-29). The Ti map had an almost equal intensity in the nitride coating. Again the difference might be attributed to the difference in size between Al and Ti. The smaller size of Al eases diffusion. In the oxide layer region both elements show the formation of discrete particles of ~150nm in size (Figure 7-30). Remarkably, in the Al map in the oxide layer region, is a decrease in intensity in the area of the Cr-rich band. The N and O map sectioned the TEM cross section clearly into an oxide layer region and a nitride region (Figure 7-29).

The Y map showed no increase in intensity along the boundaries. Instead concealed particles of ~40±10nm in size were detected in the oxide layer in the nearby region of Ti. This suggested that Y started to out-diffuse. The formation of Y_2O_3 or $Y_2Ti_2O_7$ particles in TiYN coatings after heat treatment was observed by [131].

Various EDX spectra were recorded from the Y particles, the Al-rich oxide and the Ti-rich oxide. The positions where the spectra were recorded were marked on the elemental maps (Figure 7-31). It shows the formation of TiO_x and Al_xO_y. At the Y particles Y was found together with Ti and Al. If the

formation of an $Y_2Ti_2O_7$ particle formation is assumed, then the additional Al might stem from beam spreading or from Al in the third dimension.

7.2.3.3 *Coating surface– oxide layer region*

For the lower temperatures a series of maps from the overcoat region were recorded. The 600°C sample showed no change in the elemental maps recorded from the overcoat region of the as-deposited sample (Figure 7-5, as-deposited sample). First changes were noticed after heat treatment at 700°C (Figure 7-32). The O-rich area in the overcoat was interrupted by voids, although the elemental distribution was similar to the as-deposited sample. The areas lacking intensity correlate with the observations from the annular DF images shown in Figure 7-12. Defects and diffusion in the 700°C sample might lead to void formation. At the column boundary the Al map showed an increased intensity; in contrast the intensity of the Ti and Cr map is decreased.

At 800°C three distinct regions determined by differences in structure were visible in the oxide layer in the TEM image and in elemental maps (Figure 7-33). The outermost layer showed a mixture of equal sized Ti, Al and Cr-rich areas. The Ti rich particles appeared in slightly higher concentration and closer to the surface, on average, then other oxides. The second layer was Cr-rich and has a crystal size of ~40nm. In the middle of this layer was a Cr-depleted band that was noticeable in the Ti and N map, too. The Al map showed no such behaviour. The drop in Cr intensity was also seen to some extent in the point analysis profile. The depleted zone was in the region where the N and O maps suggest the location of the interface between coating and oxidised overcoat.

7.2.4 XRD

Results from glancing angle XRD, at an incident angle of 0.5°, are shown (Figure 7-34) after heat treatment for 10h at a temperature from 600°C to 900°C. The as-deposited sample is shown as a comparison. After 10h at 600°C no obvious change had occurred in the diffraction pattern from the overcoat region.

After 10h at 700°C peaks from the rutile form of TiO_2 (JCPDS 21-1276) and a solid solution of the isostructural oxides (rhombohedral) Al_2O_3 (JCPDS 42-1468) and Cr_2O_3 (JCPDS 38-1479) were observed [94]. The peaks for the solid solution were between the position corresponding to those of Cr_2O_3 and Al_2O_3. Pronounced oxidation started to occur in the sample heat treated at 800°C for 10h. The intensity of the {110} rutile peak increased with increasing temperature and the peak shape sharpened with increasing temperature, consistent with the increase in grain size observed in TEM images.

The composition of the Al_2O_3/Cr_2O_3 solid solution was determined using Vegard's law (Equation 7-1) and tabulated (Table 7-1). The oxide layer changed from Al_2O_3 rich (93mol% after 10h at 700°C) to a oxide layer rich in Cr_2O_3 (84mol%) after 10h at 800°C. After prolonged oxidation (10h 900°C) The composition of the oxide layer was again Al_2O_3 rich (73%). The {012} peak contained 73mol% Al_2O_3 and the {214} peak 81mol%. The precision increases with increasing angle, hence the composition measured from the {214} peak is closer to the true composition. The composition was calculated as follows:

$$Cr_2O_3\,[mol\ fract.] = (d_{\{hkl\}sol.\ solut\ (measured)} - d_{\{hkl\}Al2O3}) / (d_{\{hkl\}\ Cr2O3} - d_{\{hkl\}Al2O3})$$

Equation 7-1

The change in composition of the solid solution was attributed to the progress of oxidation through the overcoat region (rich in Cr) to the TiAlCrYN coating containing only a view percent of Cr. At 700°C oxidation occurred only at the outermost region of the overcoat (low Cr content), which would be an explanation for the high content of Al_2O_3 in the solid solution. The observations made at the constant temperature of 900°C and different times reflect this observation as well.

Heat treatment	{012} at ~25°2θ	{024} at ~50°2θ
600°C 10h	- - -	- - -
700°C 10h	7%	- - -
800°C 10h	84%	77%
900°C 10h	27%	{214} 19%
900°C 1h	70%	{104} 70%
900°C 5h	77%	72%

Table 7-2: Cr_2O_3 content in mol% of the solid solution Al_2O_3/Cr_2O_3. The values were calculated using Vegard's law using the peak positions indicated on top of the table. Differences in the Cr_2O_3 content between the positions result from the resolution of the peak (low count rate) and the large number of overlapping peaks. The XRD patterns were taken at 0.5° incidence angle using a glancing angle geometry.

In addition to the solid solution and the rutile phase, peaks can be attributed solely to the single oxides Al_2O_3 and Cr_2O_3. Cr_2O_3 produced a sharp peak between 30° 2θ and 40° 2θ. This was also observed for Al_2O_3 when oxidised at 800°C, but the peaks were small. Between 45° and 70°2θ Al_2O_3 and Cr_2O_3 did not produce a separate peak.

Fe_3O_4 (JCPDS 19-629) or $FeCr_2O_4$ (JCPDS 34-0140) was observed at 900°C indicating that elements from the SS substrate diffused to the coating surface [94]. The two Fe oxide phases have the same crystal structure (cubic) and are isomorphous, hence either or both of them can be present. The coarsening of the structure observed in the TEM was also noticeable in the coating peaks in the glancing angle XRD patterns: i.e. with increasing temperature the coating peaks became sharper.

7.2.4.1 Stress analysis

Stress measurements in glancing angle geometry at an incidence angle of 5°C were performed on heat treated samples up to 800°C. Beyond this temperature a reliable peak fit was not possible because of the large number of overlapping reflections from oxides. Against expectations (void formation along the boundaries at 700°C) an increase in stress was observed from –2.5 GPa for

the as-deposited sample to –3.6 GPa for the specimen heat treated at 700°C, before relaxation to –0.85 GPa after heat treatment at 800°C occurred.

Similar behaviour was observed for coatings deposited onto cemented carbide during annealing in vacuum. It was concluded that the increase in stress was imposed by the substrate, because the falling lattice parameter and the diffraction peak width of the coating indicated stress relief [91]. Stress relaxation at elevated temperatures is associated with either thermally activated plastic deformation [92] or with recovery due to annihilation of the stress active defects produced during coating deposition [89, 90, 92].

7.3 Heat treatment at 900°C as a function of annealing time

Coated stainless steel samples were annealed at 900°C in air for 1h, 5h and 10h. The 10h specimen was already described in the previous chapter, but will be still used for comparisons in this section. The heat treatments modified the shiny bluish dark-grey surface colour of the sample. The interference colour was an indication of a thin oxide film growth. After annealing for 1h at 900°C the surface appeared green. Heat treatment for 5h changed the colour into a bluish tone. Various techniques have been used to study changes in composition and structure in detail. The results are discussed together with the previous chapter at the end in section 7.5.

7.3.1 TEM

Examination by TEM of the surface of the heat treated TiAlCrYN+Ox coating showed various stages of oxide layer growth. After heat treatment for 1h and 5h at 900°C (Figure 7-35) an oxide layer growth of ~230nm and ~950nm was observed. In contrast to the as-deposited specimen, the sample heat treated for 1h at 900°C shows a different structure. In the bright field image the microstructure of the coating in the base layer/ coating region shows a distinctly coarser columnar morphology (Figure 7-35) compared to the as-deposited specimen (Figure 7-1). After 5h heat treatment (Figure 7-35) the change in structure is more obvious when compared to the as-received sample. Measurements on the BF 1h and 5h specimen showed an increase in column size, using the mean linear intercept method on the BF TEM image, from 60 nm for the 1h specimen to 120 nm for the 5h specimen, with an error of 20%. These changes in the microstructure are clearer in the DF images where the highlighted bright regions of the heat treated specimens are broader and longer than of the as-deposited sample (Figure 7-36). The main contrast mechanism stems from crystals diffracting the electron beam. Diffraction patterns of the middle of the coating were taken using an aperture of ~500nm in size from the

as-deposited sample and specimens heat treated for 1h, 5h and 10h at 900°C Figure 7-37. An evolution from a typical ring pattern, where the rings were sharp and well defined, implying that the structure was micro-crystalline, to a spot pattern occurred. With increasing time the DP had a smaller number of discrete spots indicating fewer crystallites in the aperture area. Hence, the coarsening of the structure occurs with time and temperature.

After annealing for 1h at 900°C, there was clear evidence of additional void formation at the column boundaries (Figure 7-38). The substrate/ coating interface region showed the formation of precipitates in the substrate (Figure 7-39) after annealing for 5h at 900°C.

7.3.2 EDX point analysis

EDX point analysis from the base layer, oxide layer and over boundaries was performed to record the variations in elemental composition after the heat treatment. Profiles of the concentration of an element for different heat treatments have been compared.

7.3.2.1 Substrate/ base layer region

Point analysis at the base layer region of the coating revealed an inward diffusion of mainly Cr (Figure 7-40) and Fe (Figure 7-41). Similar to the previous results a decrease in Cr and Fe at the base layer/ coating interface is observed. After 1h enhanced concentration of Cr was detected as far as 375nm away from the substrate/ coating interface. After 5h the diffusion of Cr into the coating was detected for ~800nm. The concentration of Cr, for both the 1h and 5h, specimen was ~12at% in the base layer region. The concentration of Fe increased to 5at% for the 1h sample. For the 5h specimen no increase was measured. The concentration of Y stayed at ~1at% after heat treatment for 1h and 5h (Figure 7-42). The 10h specimen, in comparison, showed a decrease to ~0.2at%. No significant alteration was observed for the Al and Ti concentration after heat treatment for 1h and 5h.

7.3.2.2 *Observations over boundaries*

Additional examination of the grain boundaries of the as-deposited and heat treated specimen showed an increase of Y at the column boundary region (Figure 7-43-Figure 7-45). In the as-deposited sample no difference within the error margin was noticed. For the 1h sample the nominal concentration of Y increased from 0.9 at % (bulk) to 2.1at% (boundary) and for the 5h sample from 0.8 at% (bulk) to 2.8 at% (boundary). The size of the electron probe is large compared with the grain boundary and therefore the actual concentration of Y at the grain boundary is considerably higher than the nominal 2.1 at % value measured [172]. This preferential diffusion of Y to the grain boundary is understandable. The Y atom is large in comparison to Al, Ti and Cr. It distorts the lattice in as-deposited condition. In the heat-treated sample, the Y diffuses to the lower energy grain boundary sites, which decreases the distortion in the bulk TiAlCrN lattice. This diffusion is made even more attractive for a reactive element such as Y with a high affinity for oxygen, due to the easy ingress of oxygen at the column and grain boundaries.

7.3.2.3 *Coating surface – oxide layer region*

Point analysis profiles were made from the N and O keV position to compare the cross over between those lines (Figure 7-46). This should give an indication for the progress of oxidation. After heat treatment for 1h no change to the as-deposited sample was observed; in fact the position of the cross over point was 25nm further outside. After 5h the cross over point moved 200nm further into the coating. This is small considering that, after 10h at 900°C, the cross over point was located 1250nm away from the coating surface. This is a further demonstration of the increased oxidation resistance of the oxynitride TiAlYN/CrN nanolayer structured overcoat.

Measurements from Al and Ti (Figure 7-47), similar to the $Ti_{0.44}Al_{0.54}Cr_{0.02}N$ coating, showed no bi-layer formation. Instead, an out-diffusion of both Al and Ti was observed after 1h. After 5h the curve showed a high fluctuation, which was explained by the presence of discrete oxide particles [177].

Figure 7-48 shows a clear step for Cr in the compositional profile after 1h at 900°C. After longer heat treatment at 900°C (5h) the Cr had clearly started to out-diffuse to the surface.

The Y profile (Figure 7-49) showed a similar behaviour to Al and Ti. Large fluctuations in the Y content were observed after annealing for 5h at 900°C, which indicated the presence of discrete YO_x particles.

7.3.3 EDX mapping

7.3.3.1 Substrate/ base layer region

Elemental maps were recorded from the base layer and the surface region of the coatings after annealing for 1h and 5h at 900°C. After annealing for 1h at 900°C diffusion of Cr and Fe into the base layer region was observed (Figure 7-50), similar to the "original" TiAlCrYN coating (Figure 6-9). The difference in the Fe map is very weak, indicating only a slight increase of Fe in the base layer, which is in agreement with the point analyses. The base layer region is visible in the Y map were the intensity decreases in the base layer region. Other elemental maps, Al, Ti, and O, showed no variation in intensity compared with the maps recorded from the as-deposited specimen (Figure 7-4).

7.3.3.2 Coating surface – oxide layer region

The surface of the coating was analysed after 1h and 5h at 900°C. Elemental maps recorded after the heat treatment show that the structure is rather complicated and disruption of the layered growth starts to occur after 1h (Figure 7-51). The region adjacent to the nitride coating consists of a mixture of Ti-rich, Al-rich and Cr-rich crystals of 10 ± 5nm in diameter. The structure of the outermost layer is coarser and voided with a crystal size of 50 ± 15nm.

In the 5h specimen, layers rich in each element, Al, Ti, Cr, are visible (Figure 7-52). A BF TEM image is shown next to the maps taken from the same area. Closest to the coating is a Ti-rich layer, then a Al + Cr-rich layer and, finally, a Cr-rich layer. The outermost oxides are large crystals containing Ti, Al and Cr with typical diameters of 200 nm ± 50 nm. Elemental maps indicate that the large crystals consist of a mixed Cr/Al oxide and Ti oxide. This is in consistent with XRD analysis presented in (7.3.4). Y particles of approximately 10nm in size are detectable behind the 70nm Cr-band in the Ti-rich region (Figure 7-53). Pores are also observed in the Ti-rich layer. The pores increase in size towards

the scale/air interface. Disruption in the outermost oxide layer is clearly visible in elemental maps in Figure 7-54. It shows also the presence of Al, Cr and O at the same locations, suggesting a crystal formed from these elements. Furthermore, it can be clearly seen that Ti-rich and Al,Cr-rich particles are discrete.

7.3.4 XRD

A glancing angle X-ray diffraction pattern from TiAlCrYN with and without overcoat after heat treatment for 1h at 900°C is shown in Figure 7-56. The comparison shows, that peaks stemming from the coating (labelled with a C) are visible for the coating with overcoat, but not for the one without. This indicates that a thicker oxide layer has grown on the coating without the oxynitride overcoat.

The amount of TiO_2 is higher for the coating without overcoat. The reflections from the solid solution were compared between the two coatings. The {012} and the {104} reflections were used for the calculation in the case of TiAlCrYN. The results for the Y coating with overcoat are presented in Table 7-2. In the case of the 'original' TiAlCrYN the Cr_2O_3 content is 28 mol%, whereas 70 mol% Cr_2O_3 were found in TiAlCrYN+Ox. The higher Cr content of the results clearly from the additional amount deposited in the overcoat region. The Cr content found for the 'original' TiAlCrYN coating is reflected in the elemental maps presented in Figure 6-6.

Measurements in glancing angle geometry at 0.5° incident angle from specimens heat treated for 1h and 5h at 900°C in comparison to the as-deposited coating are plotted in Figure 7-57. Glancing angle X-ray diffraction has been used to support the EDX results and to identify the phases formed after annealing. After heat treatment for 1h some reflections stemmed from the coating, indicating that the oxide layer has a thickness of about 200nm. After annealing for 5h only peaks from oxides could be identified. After heat treatment the formation of an isostructural solid solution of Al_2O_3/Cr_2O_3 (rhombohedral) was observed together with TiO_2 (rutile). This is consistent with

the observations in the elemental maps. The composition of the solid solution, assuming Vegard's law is obeyed, was calculated and presented in Table 7-2. The miscibility of Al_2O_3 and Cr_2O_3 was mentioned in 1962 by [80] and reported in [29] for oxidation of a CrAlN PVD coating. Furthermore, it is noticeable that the {110} TiO_2 rutile peak is sharper in its appearance in the 5h sample than in the 1h sample, which is consistent with the increase in crystallite size of the rutile phase observed in the TEM.

7.3.4.1 Stress analysis

To determine the stress inherent in the coating before and after heat treatment an asymmetric Bragg-Brentano scan using the {422} reflection was used. The glancing angle diffraction method used in the other investigations was not available at that time. The stress changed from -4GPa, for the as-deposited sample, to -2GPa after 1h annealing at 900°C (Figure 7-55). The relative low temperature of the deposition process (450°C) and the bias voltage (-75V bias) induces a range of defects into the coating [62]. Stress relaxation at elevated temperatures is associated with either thermally activated plastic deformation or with recovery due to annihilation of the stress active defects produced during coating [89, 90, 92].

7.4 TiAlCrYN+Ox deposited on cemented carbide

The TiAlCrYN+Ox coating is mostly deposited onto cemented carbide ball nosed end mills. In Chapter 4 it was shown that the CC substrate material oxidises at lower temperatures than M2 high-speed steel or SS 304 stainless steel. This caused the local formation of substrate oxides ($CoWO_4$) at the coating surface at a temperature of 700°C. It is therefore interesting to see the effects of heat treatment in a TEM cross section of TiAlCrYN+Ox deposited onto CC.

7.4.1 TEM

Figure 7-58 shows a bright field micrograph of the whole coating. Interesting are two pinholes formed by a pore in the cemented carbide substrate and a crack visible in the coating. The crack was most likely produced during the sample preparation. Also, parts of the coating detached during the final polishing stages. This indicates that the adhesion of TiAlCrYN+Ox on cemented carbide is less than on stainless steel. The coating shows along some columns the transformation of fine interrupted columnar growth to columnar growth. Voids were found along the column boundaries (Figure 7-58b) similar to the coating deposited onto SS 304 and heat treated for 1h at 900°C. The oxide layer thickness is 200-350nm in thickness, which is similar to the oxide layer thickness measured for TiAlCrYN+Ox on SS 304. Furthermore, the base layer has a brighter appearance than the Y-rich coating, which was not observed before. A micrograph at higher magnification showed a mottled appearance of the base layer region (Figure 7-58c). This might indicate the presence of voids in the base layer region, or the accumulation of low atomic number elements due to the heat treatment.

7.4.2 EDX point analysis

Point analysis perpendicular through the substrate/ base layer region showed a concentration up to 8at% for Co and for W up to 2.5at% in the base layer (Figure 7-59). An increase of W was only measured in the first 50nm of the base layer region, whereas an increase Co concentration was found in the whole base layer region.

7.4.3 EDX mapping

Elemental maps gained from the base layer region of the specimen after heat treatment show diffusion of Co into the base layer region in a similar manner to the observed Cr and Fe diffusion on stainless steel (Figure 7-60). The fluctuation in the Co concentration (point analysis) can be explained by the variation in intensity observed in the Co map. W diffusion was not detected. The W ion is a far larger ion than Cr, Fe and Y. The diffusion is therefore slowed down considerably, considering that in the case of Cr and Fe (larger than Cr) a significant difference in diffusion speed was observed. The maps obtained from the coating elements (Al, Ti, Cr and YK) show the same response as on the stainless steel specimen.

7.4.4 XRD

X-ray diffraction in glancing angle geometry from the as-deposited and heat treated coating were performed using an incidence angle of 0.5°. The spectra of the as-deposited TiAlCrYN+Ox is shown in (Figure 7-2a). Figure 7-61 shows the reflections after heat treatment for 1h at 900°C. The presence of TiO_2 (JCPDS 21-1276) and oxides from the substrate material $CoWO_3$ (JCPDS 15-0867), WO_3 (JCPDS 20-1323), and CoO_3 (JCPDS 42-1467) were identified [94]. Many of the reflections of the cobalt and tungsten oxides overlap both with each other, and reflections from the Al_2O_3 and Cr_2O_3 solid solution and the coating (Figure 7-61).

In comparison with previous results (stainless steel) it is obvious that almost no reflections of the coating are found in the heat treated specimen. TEM micrographs have shown that the oxide layer thickness is comparable to that formed on the coating deposited onto stainless steel and out-diffusion of Co was detected only to the base layer/ coating interface. SEM investigations showed the formation of large (1μm) tungsten and cobalt rich particles on the coating surface (see Chapter 4) indicating that the tungsten and cobalt oxide peaks are generated from oxides formed through defects. Either W might oxidise at the substrate through O diffusing through pinholes or defects, or alternatively W might diffuse through pinholes or defects. The volume expansion of the W oxides formed (38% increase in volume) leads to the formation of relative large oxides at the coating surface.

7.5 Discussion

The addition of a nanolayered oxynitride overcoat to the 'original' TiAlCrYN has a beneficial effect on the mechanical [145] and on the oxidation behaviour. This was shown by the following investigations:

A reduction in weight gain for the TiAlCrYN coating with overcoat compared to the 'original' TiAlCrYN coating was observed using TG. This improvement resulted from the Cr-rich interlayer in the oxynitride overcoat. Previous investigations on TiAlN/CrN nanolayers showed the positive effect of Cr [21]. Saturation of the reaction process occurring in the TG was not observed. This fits to the observations made using TEM. The micrographs show that even after 10h at 900°C the coating was not fully oxidised. Additionally, the substrate material reacts during the heat treatment.

TEM, EDX point analysis and mapping showed the growth of the oxide layer was hampered by the overcoat. EDX point analysis indicated through a small shift, ~50nm after 1h at 900°C and ~100nm after 10h at 800°C, in the cross over point of N and O, that the oxynitride TiAlYN/CrN overcoat provides an enhanced oxidation resistance.

EDX mapping revealed the disruption of the oxide bi-layer observed for the 'original' TiAlCrYN coating. The disruption of the oxide bi-layer formation observed for the 'original' TiAlCrYN and the enhanced oxidation resistance can

be explained with reference to the following observations on CrAlN by [29]. It was stated, that in CrAlN coatings Al oxidises initially, because it has a more negative free energy of formation. However, because the diffusion rate of Cr is higher than that of Al an increase in Cr content in the oxide layer was achieved in a second stage. This in turn hampered the outward diffusion of Al. Al was found to reduce the growth rate of the outer Cr-rich layer.

The formation of oxides was seen as beneficial from [142] to reduce the friction coefficient. This supports the beneficial effects that an oxynitride layer topcoat would have when brought into tribological contact

An explanation for the increased oxidation resistance in the Y-containing coating was the increase in diffusion paths, due to disrupted columnar growth during deposition [33]. However, this disruption clearly disappears with heat treatment of the hard coating as was shown by various temperatures and times. Thus, this coating structure can have, such a positive effect only for temperatures below 700°C and 10h or below 900°C for 1h.

After heat treatment a coarsening of the fine grained coating structure was observed. This means the fine grained coating structure created during deposition using an additional TiAlY target is superimposed over the columnar growth structure of the coatings (e.g. TiAlCrN). Due to grain growth and void formation it is possible to see the columnar nature of the coating again. Recrystallisation behaviour in sputter deposited TiB_xN_y and TiB_xC_y coatings after heat treatment was reported by [173]. It was also shown that it is possible to increase the onset point of rapid oxidation by refining the grain structure of the coating.

A loss of the Al_2O_3 / TiO_2 bi-layer structure observed for TiAlCrN and TiAlCrYN [33] was seen for the TiAlCrYN+Ox coating. An important factor causing disruption in the oxide layer and void formation is the difference in unit cell volumes of the different oxides formed (Table 7-3). The ratio between the molecular volume of the oxide and the nitride is a measure of the disruption resulting from stress creation caused by the oxide layer formation. This is especially the case when the values differ significantly from that of unity. In the case of high volume ratios, porosity created by stresses is to be expected. This

rule might be less significant in the case of outward migrating species [80] (p.14, 96).

	$Ti_{0.5}Al_{0.5}N$	TiO_2	Al_2O_3	Cr_2O_3
Volume [cm^3]	11	18.8	25.6	29
φ	1	1.71	1.16	1.32

Table 7-3: Unit cell volumes and unit cell volume ratios (φ) of various oxides in comparison to TiAlN. The ratio φ is calculated with regard of the amount of metal atoms, e.g. Al_2O_3 has 2 Al atoms hence the TiAlN value has been doubled. All unit cell volumes are from [11] and [80].

Stress relaxation in the hard coatings was observed after heat treatment for 1h at 900°C and after 10 at 800°C. Residual stresses in PVD coatings are generated by defects formed during the deposition process. Thus, stress relaxation at elevated temperatures is associated with either thermally activated plastic deformation [92] or with recovery, due to annihilation of the stress active defects produced during coating [89, 90, 92]. A reduction in stress leads to a reduction in hardness as was shown in [21; 130].

The disappearance of voids in the 10h 900°C specimen along the column boundaries is also interesting. The investigations have shown that a heat treatment at this temperature led to a significant stress relaxation, which might explain why no voids were detected after 10h heat treatment at 900°C in the BF TEM image. Another hypothesis is that the voids do not exist because all available space is blocked through diffusing species.

In earlier investigations by [32] and [33] the positive effect of Y onto the oxidation behaviour of TiAlCrN was shown. It was proposed that Y segregated at the grain boundaries is responsible for the improved oxidation behaviour.

EDX point analysis and elemental mapping helped to refine the knowledge of migration of Y in the coating at various times and temperatures. Y was clearly identified at the column boundaries after heat treatment at 1h at 900°C and after 10h at 800°C. The elemental maps and the point analysis showed at the

same time that substrate species are diffusing into the coating and in turn precipitates are formed in the substrate. It can be assumed that Y reduces the rate of inward diffusion of O by the formation of an Y oxide. The importance of Y incorporation could clearly be observed at the base layer/ Y-rich coating interface, where the diffusion was blocked by the presence of Y. This effect of Y was suggested by [33]. A gettering effect of Y (e.g. of O) was found by [133] for TiN PVD coatings where Y was used as an interlayer between the coating and the substrate. He reported an improved adhesion through the Y interlayer. Improved adhesion of TiN on mild steel through an Y interlayer was also reported by [174].

The accumulation of Y between the Al-rich and Ti-rich sublayers after heat treatment for 1h at 950°C was found by [33]. Elemental mapping showed that Y or $Y_xMe_yO_z$ particles had formed in the oxide layer after heat treatment for 1h at 900°C. To confirm the presence of any specific oxide as e.g. $Y_2Ti_2O_7$ found by [131] was not achieved. However, the particles seemed to be in close proximity to TiO_2 crystals. This observation is in agreement with XPS analysis which found that in the Ti and Al-rich regions of the oxide layer Y segregated to the Ti sites. Analysis of the Y 3d core level identified one chemical species in the oxidised film at Y 3d 158 eV [129]. Identification by XRD was probably not possible due to the low volume fraction of the Y oxides present.

Some comparison to the observed beneficial effects of Y in MeCrAlY alloys is made, because it is a well researched field. The main observed protection mechanism of Y in these alloys is segregation along grain boundaries, a reduction in oxide layer thickness, grain refinement of the oxide layer and "pegging" of the oxide layer, which leads to better oxide adhesion. The formation of oxide pegs, is one way of improving the adherence of the coating [141]. Depending on the scale formed, Al_2O_3 or Cr_2O_3, the effects vary. However, the actual operating mechanism of Y is still under discussion [136, 137, 139]. From all those results the segregation of Y to the boundaries was observed. In comparison with TiAlCrN the oxide layer thickness decreased considerably after the incorporation of Y; oxide pegs,. however were not observed.

The temperature at the cutting edge of coated end mills cutting A2 die steel at a speed of 380m min^{-1} was ~880°C [23]. This temperature is high enough to initiate the above described mechanism to occur.

7.6 Summary

The development of the oxide layer at different temperatures and at 900°C for different periods was investigated. At the same time the coating structure and the interface integrity was examined. The addition of an oxynitride overcoat rich in Cr increased the oxidation resistance and the tribological properties in comparison to the 'original' TiAlCrYN coating [145]. However, in comparison to TiAlCrN and TiAlCrYN the observed oxide layer (~230nm) does not form a bi-layer after annealing for 1h at 900°C. Instead, the oxide layer consisted out of a crystal mix out of Al_2O_3, Cr_2O_3 and TiO_2 on top of the remaining Cr-rich overcoat region.

The coating structure changed gradually form one of fine grained interrupted columnar growth to a columnar growth structure after heat treatment for 10h at 900°C in air and after heat treatment at 900°C at various times. Voids connecting the substrate and the coating surface formed along the column boundaries after heat treatment for 10h at 700°C and after heat treatment for 1h at 900°C. However, the interface integrity was preserved by the additional amount of Y in the coating, in the same way as observed for the original TiAlCrYN coating after 1h at 900°C. A diffusion zone of ~650nm was measured from the substrate/ coating interface.

Heat treatment of TiAlCrYN+Ox deposited onto cemented carbide revealed the diffusion of Co into the base layer region (250nm) mainly along the column boundaries. The diffusion of W was not observed after annealing for 1h at 900°C along the column boundaries using EDX mapping. The diffusion of W must mainly occur through the pinholes and defects to the coating surface.

STEM - elemental mapping was seen as a powerful tool to show different concentration occurring on a small scale. Additionally information about the speed of diffusion was gained, e.g. it was clearly seen that Cr diffuses faster than Fe.

7.7 Figures

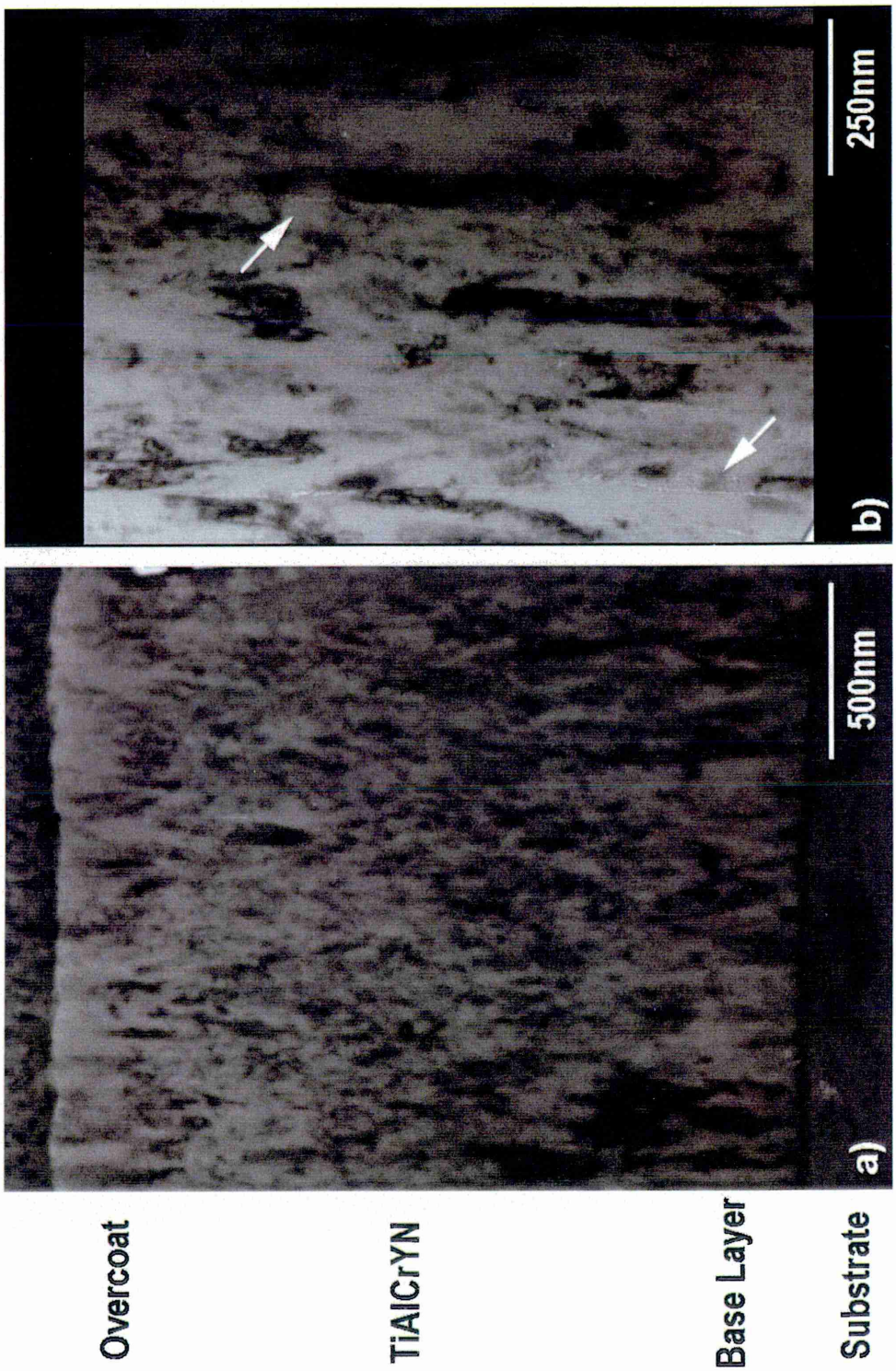

Figure 7-1: a) XTEM bright field image of TiAlCrYN+Ox in as-deposited condition. b) Magnified section of a) showing voids

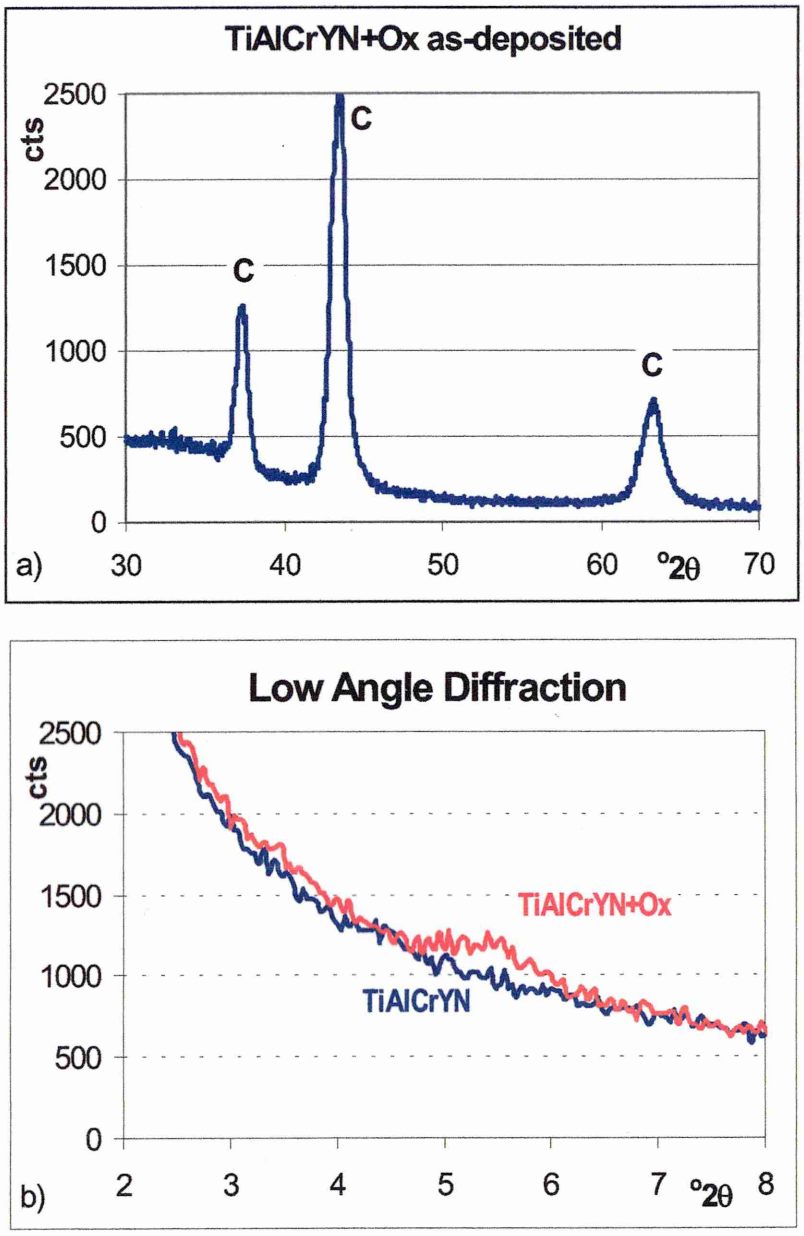

Figure 7-2: a) Glancing angle XRD with fixed incidence angle of 0.5° of TiAlCrYN in as-deposited condition. b) Low angle XRD from TiAlCrYN+Ox and TiAlCrYN.

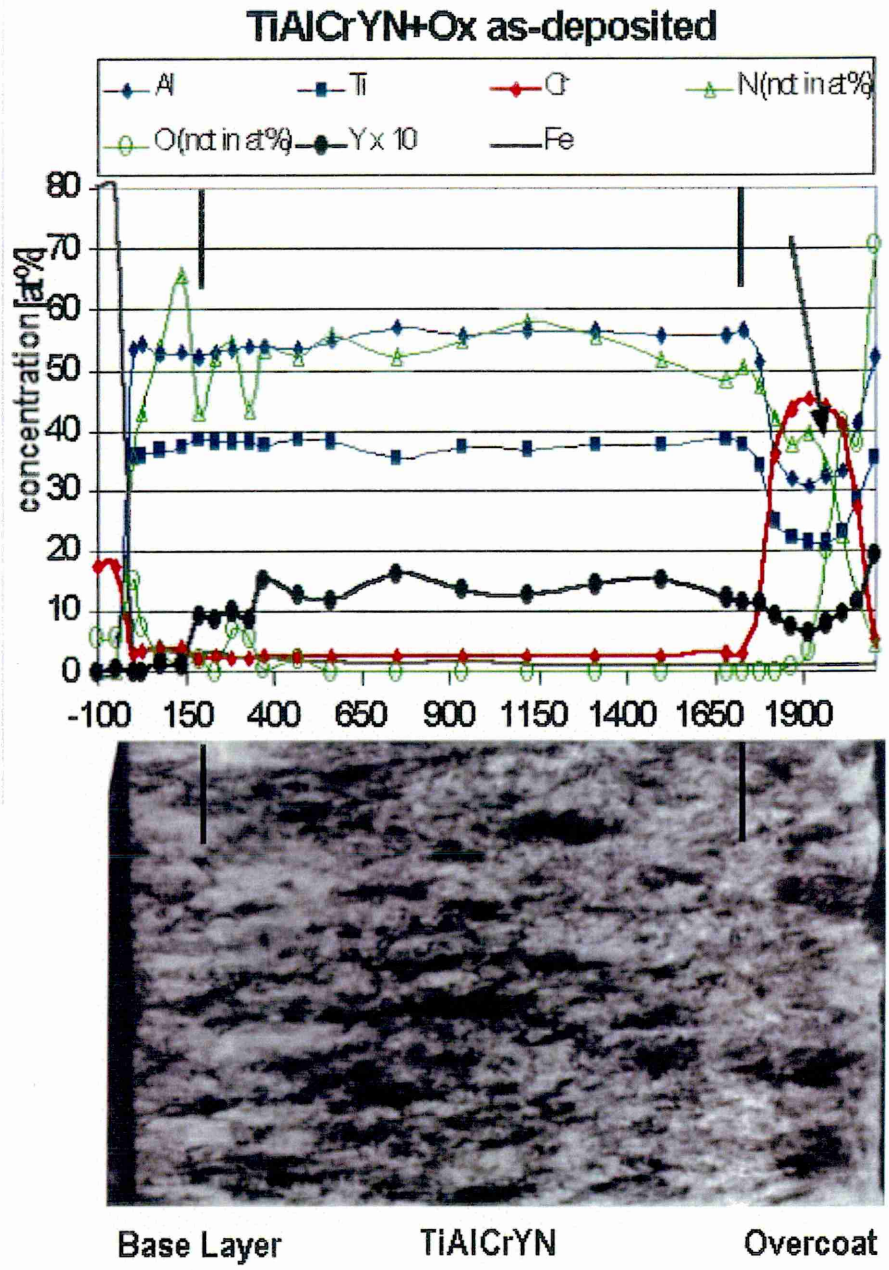

Figure 7-3: EDX point analysis perpendicular through the as-deposited XTEM sample.

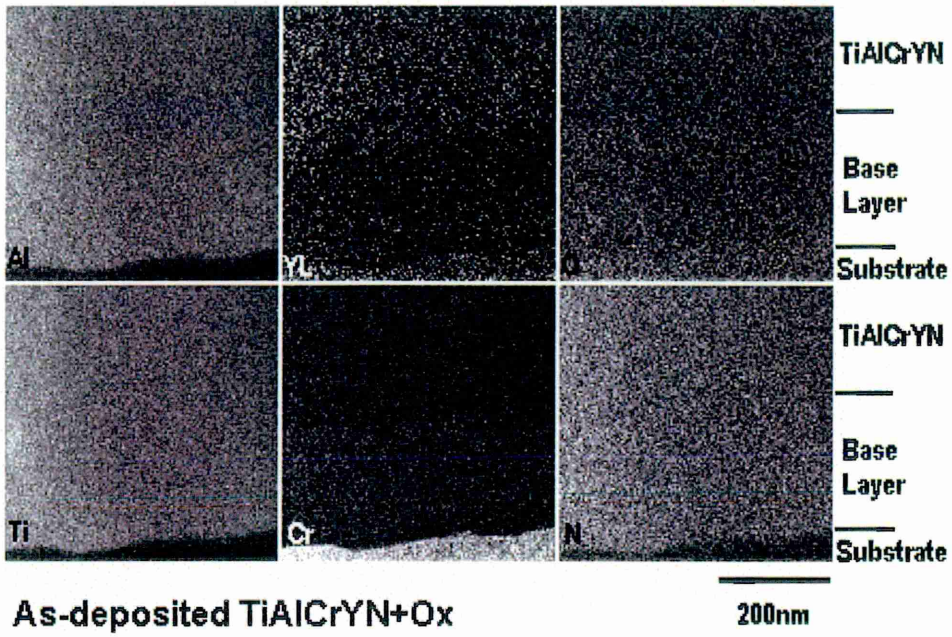

Figure 7-4: Elemental maps from the base layer region of as-deposited TiAlCrYN+Ox.

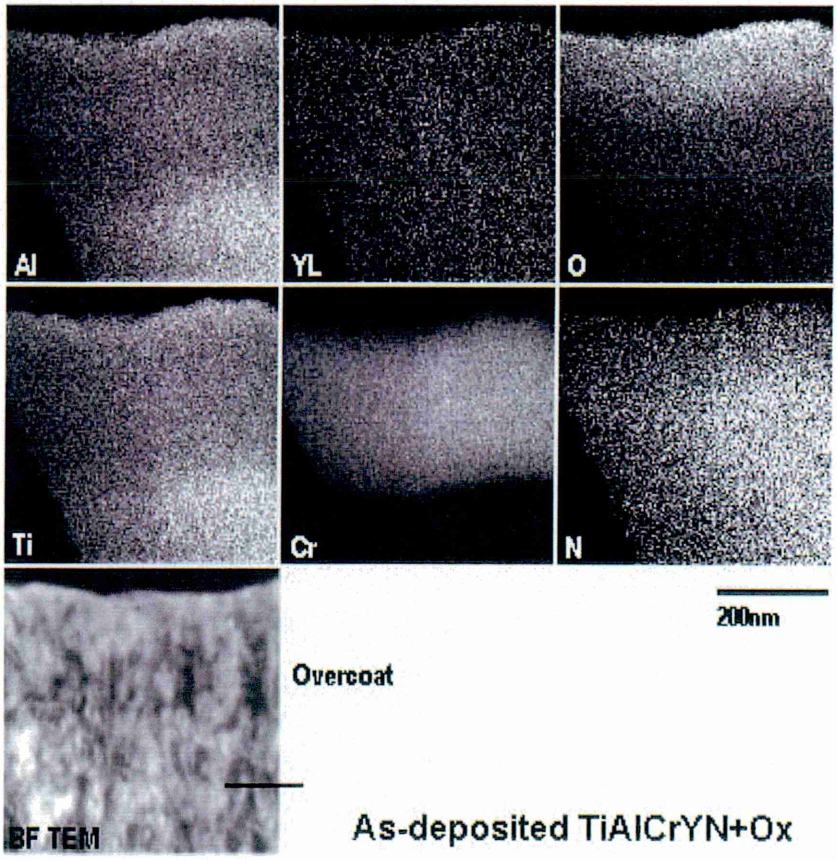

Figure 7-5: Elemental maps from the overcoat region of an as-deposited TiAlCrYN+Ox coating.

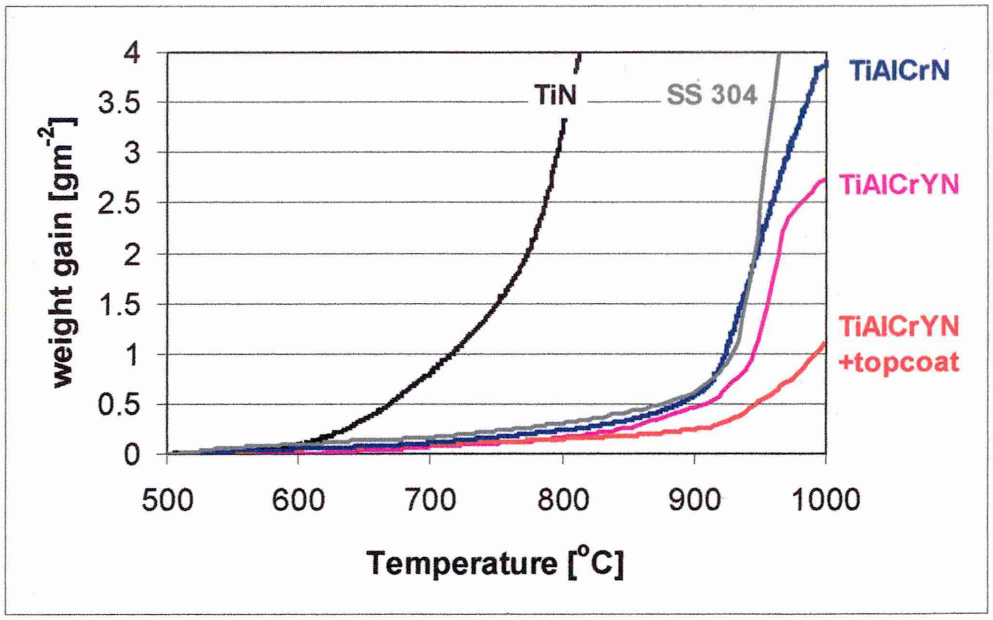

Figure 7-6: Continuous TG measurement on TiAlCrYN with and without overcoat and the substrate material.

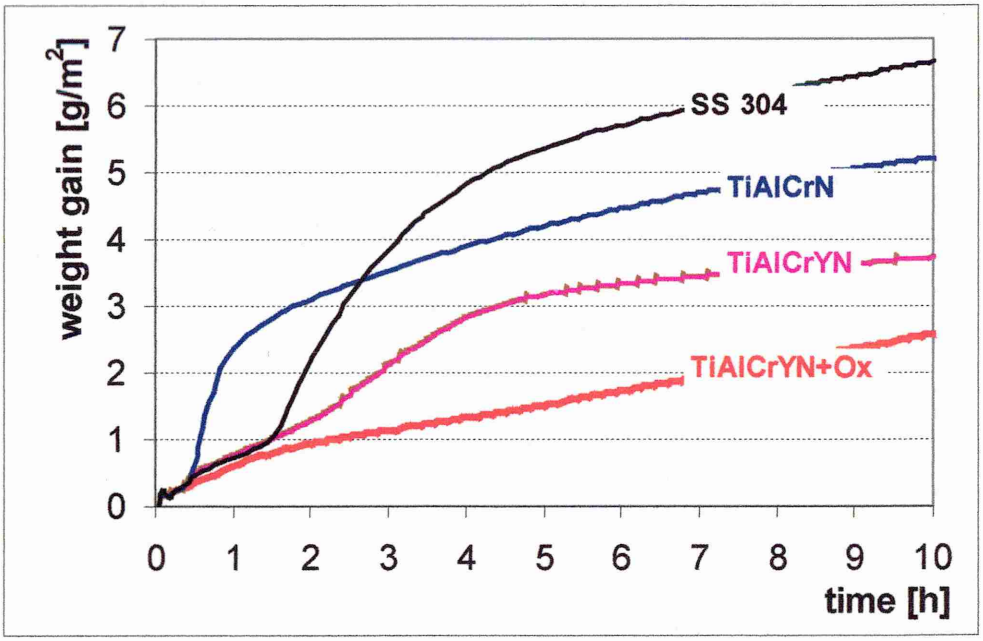

Figure 7-7: Isothermal TG measurements at 900°C.

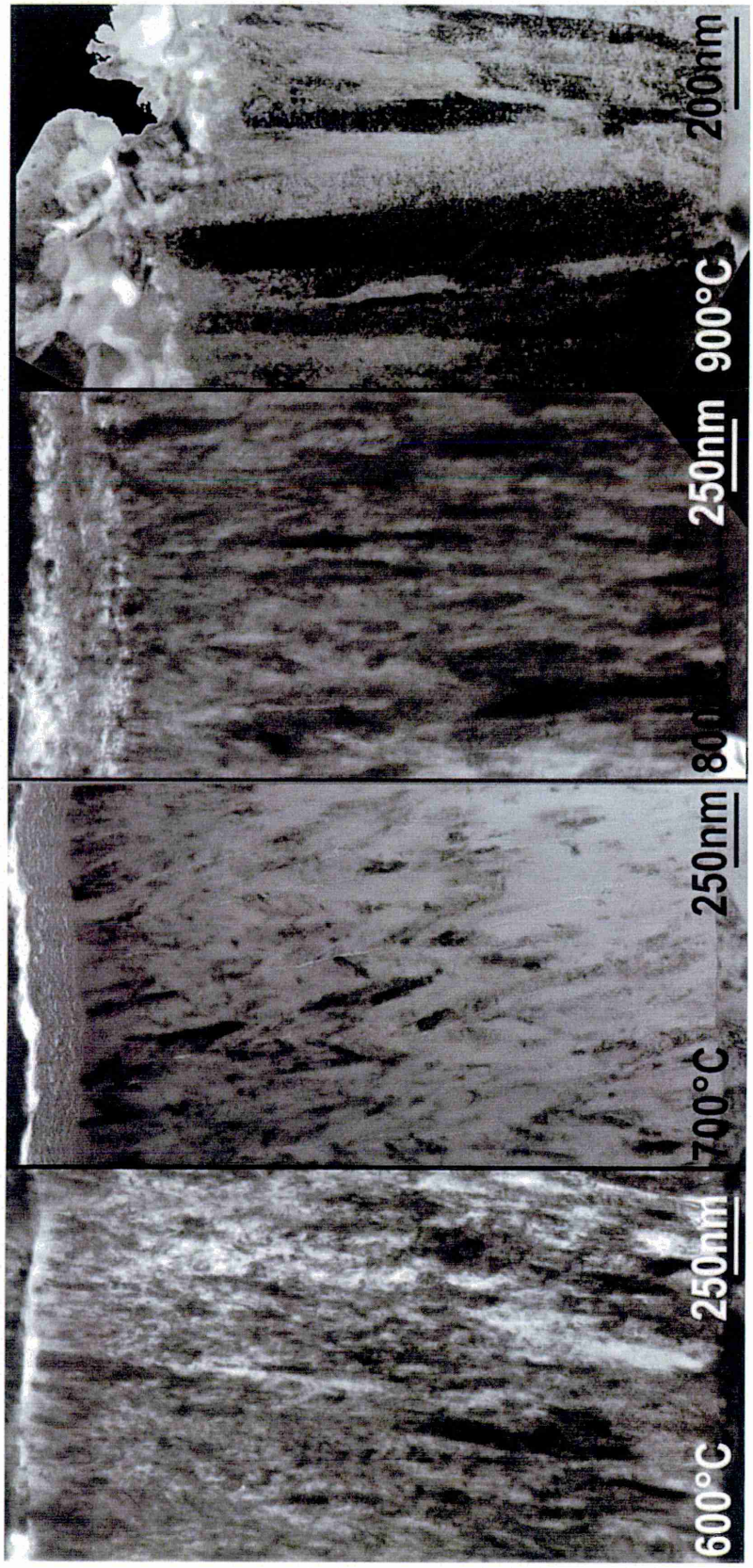

Figure 7-9: TEM BF images from TiAlCrYN+Ox specimens heat treated for 10h at various temperatures

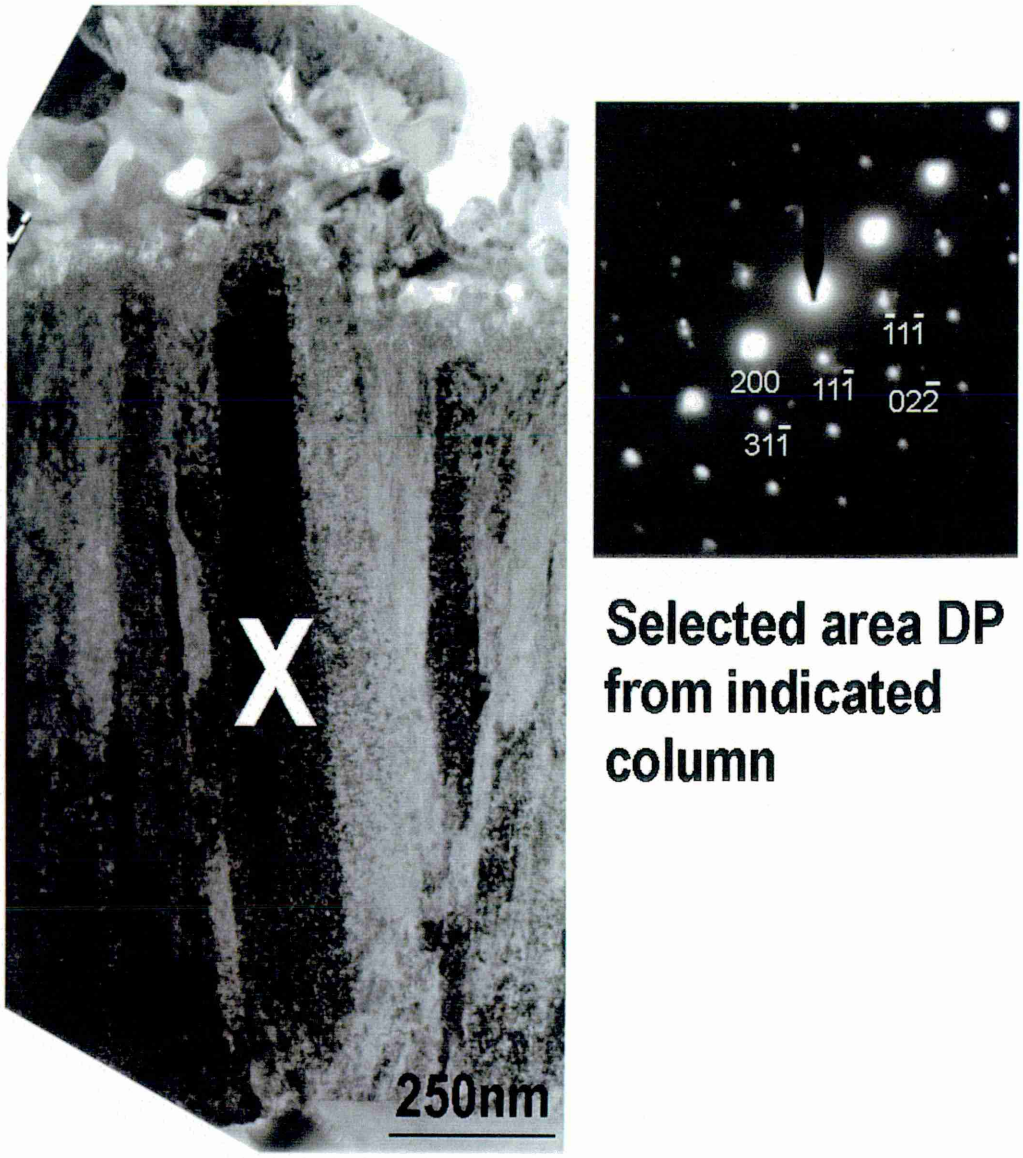

Figure 7-10: Selected area DP from TiAlCrYN+Ox heat treated for 10h at 900°C.

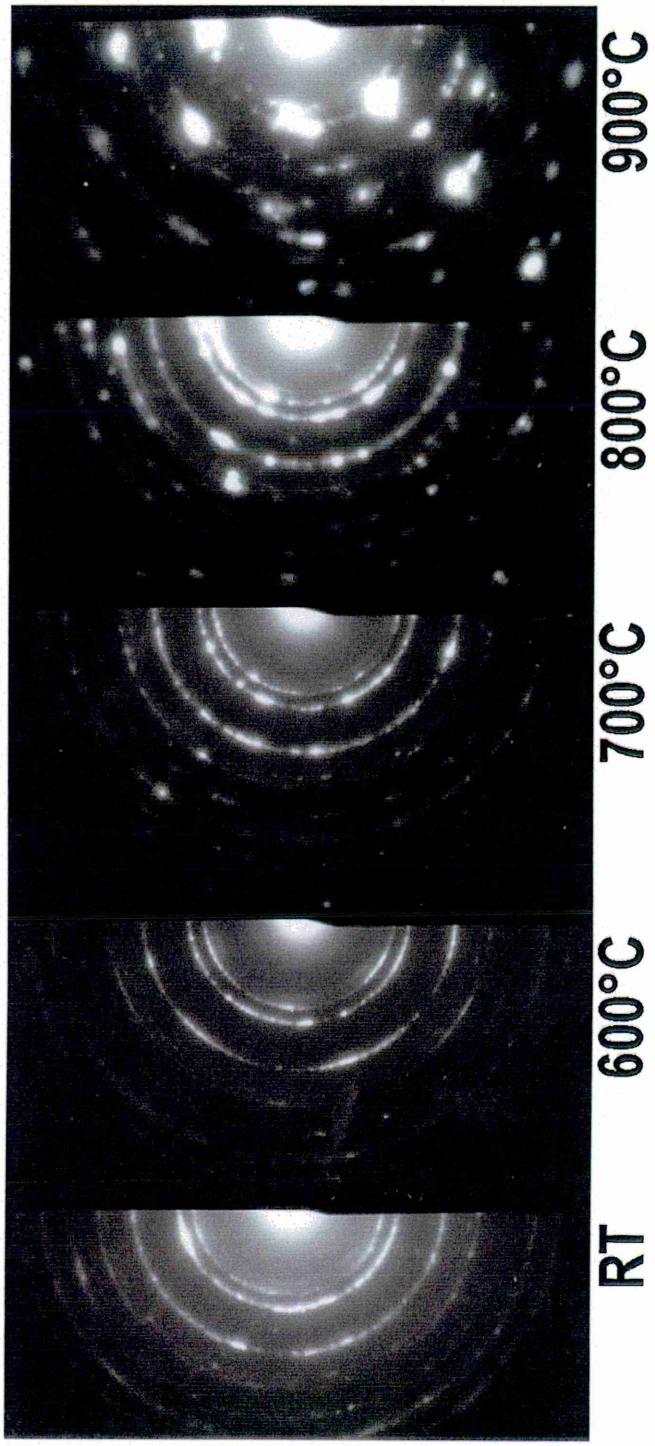

Figure 7-11: DP taken from the middle of heat treated samples after 10h at the indicated temperature.

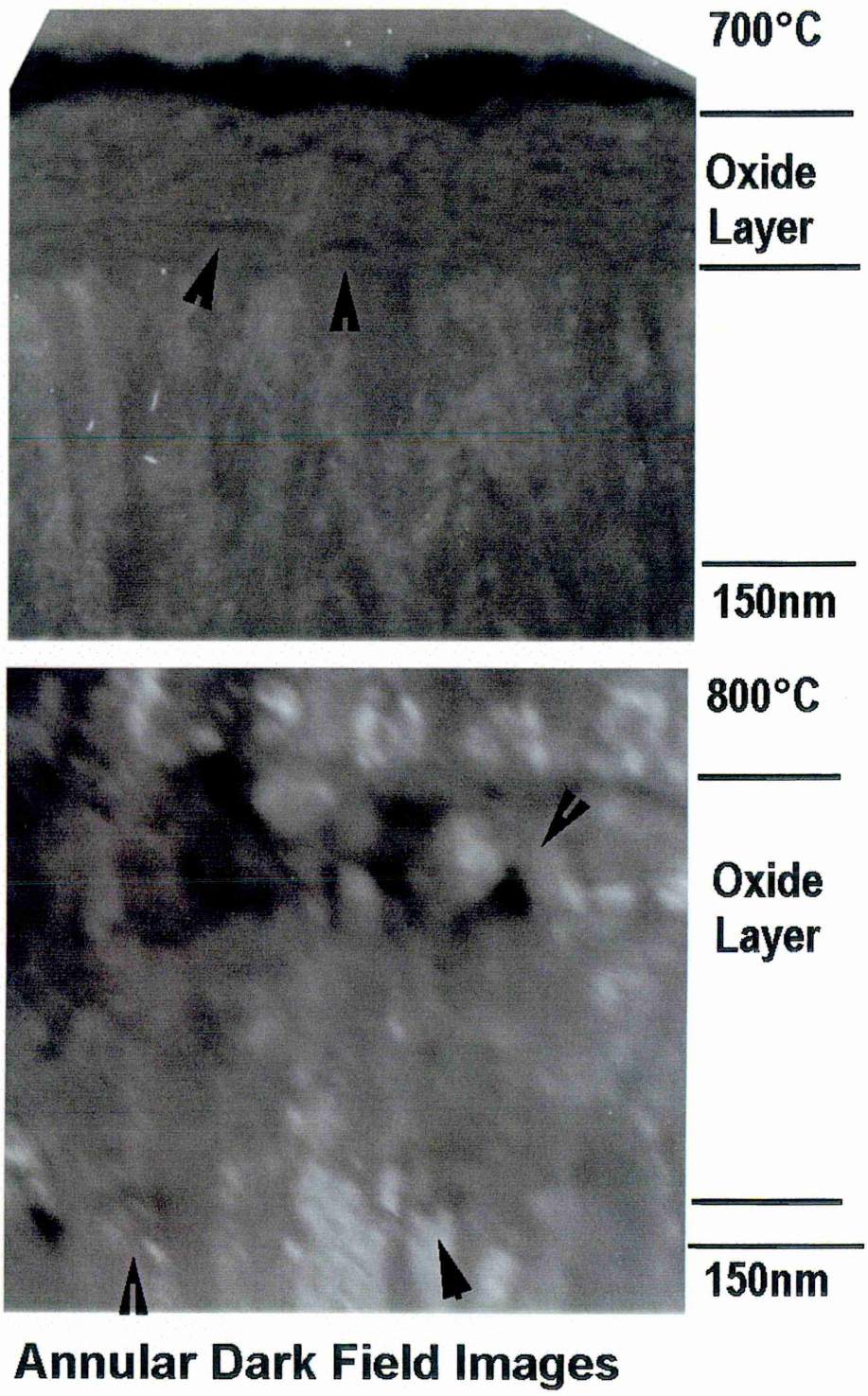

Figure 7-12: Annular dark field images of the oxide layer grown on TiAlCrYN+Ox after 10h at the indicated temperatures.

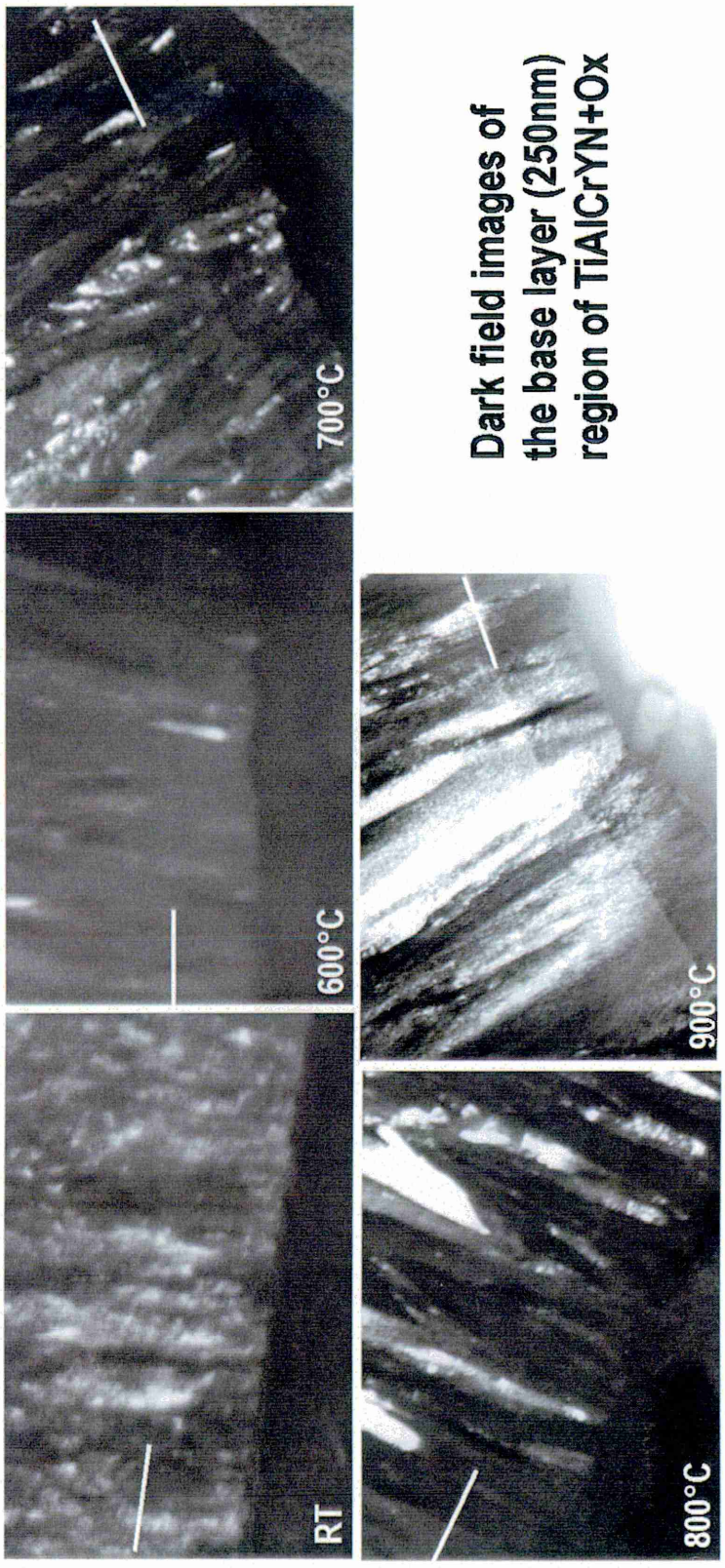

Figure 7-13: DF TEM of TiAlCrYN+Ox base layer after heat treatment for 10h

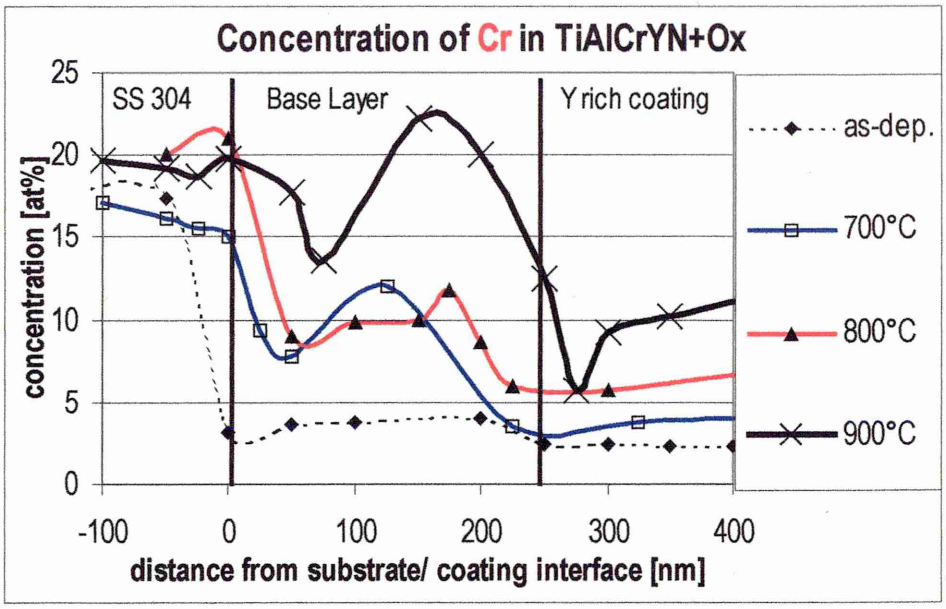

Figure 7-14: Cr content in the base layer of TiAlCrYN+Ox at various temperatures

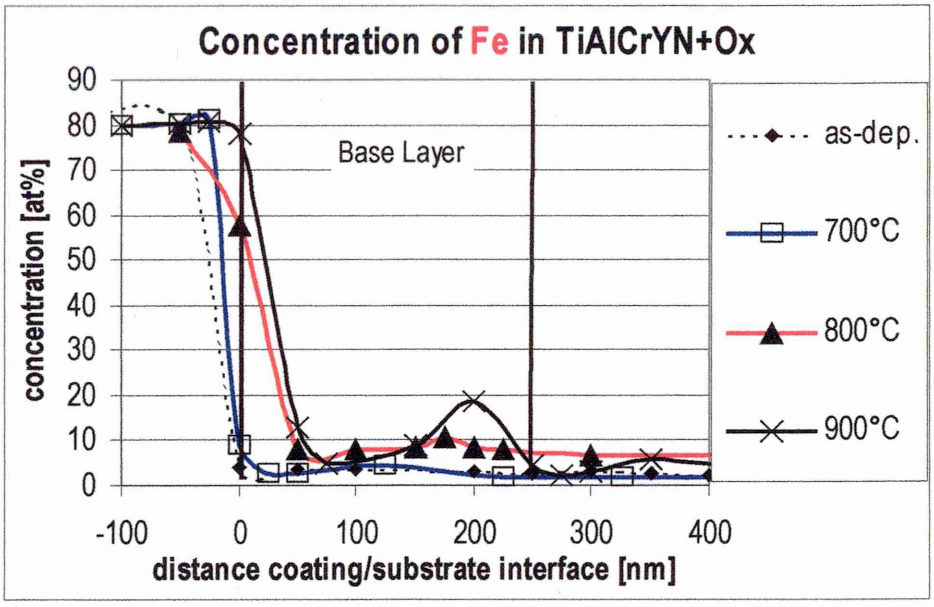

Figure 7-15: Fe content in the base layer of TiAlCrYN+Ox at various temperatures

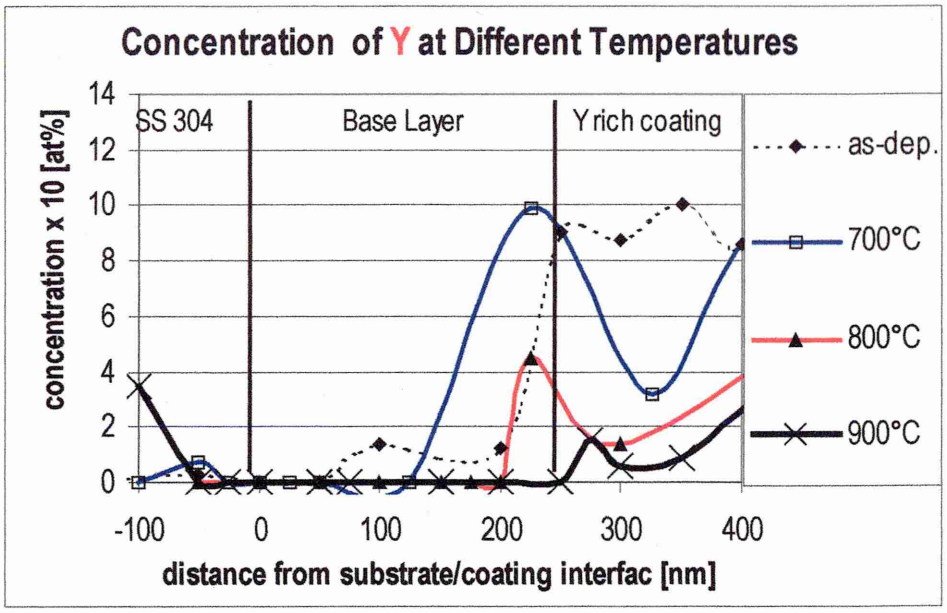

Figure 7-16: Y content in the base layer of TiAlCrYN+Ox at various temperatures

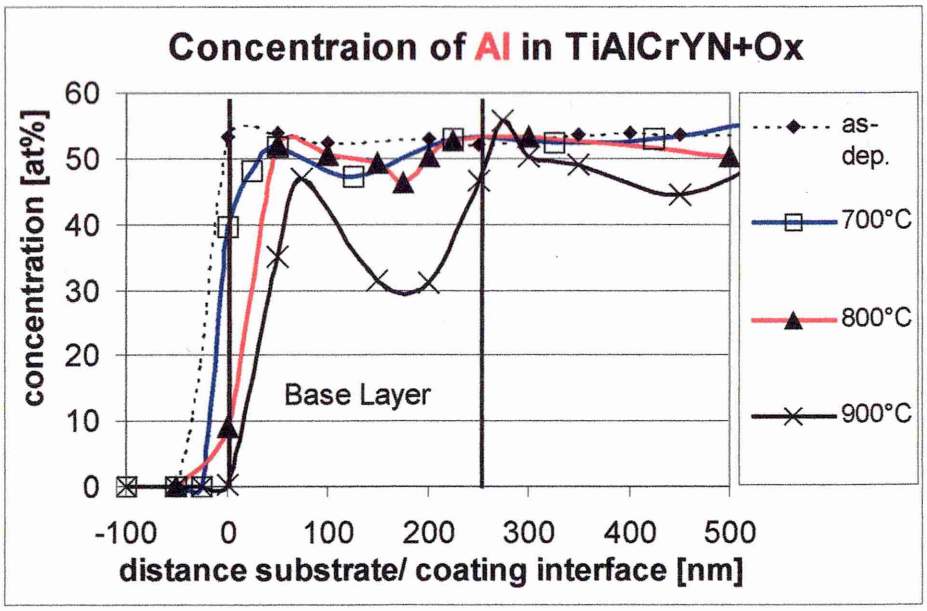

Figure 7-17: Al content in the base layer of TiAlCrYN+Ox at various temperatures

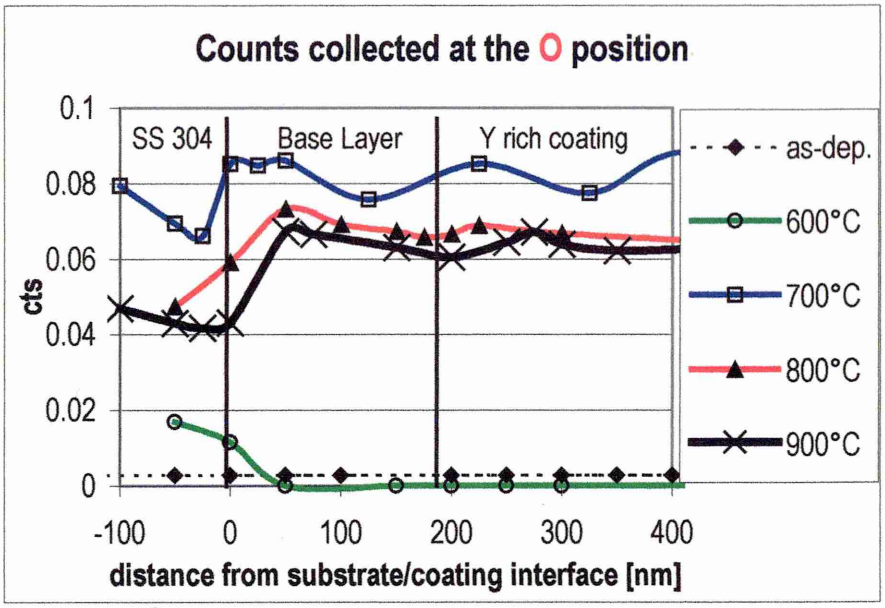

Figure 7-18: O content in the base layer of TiAlCrYN+Ox at various temperatures

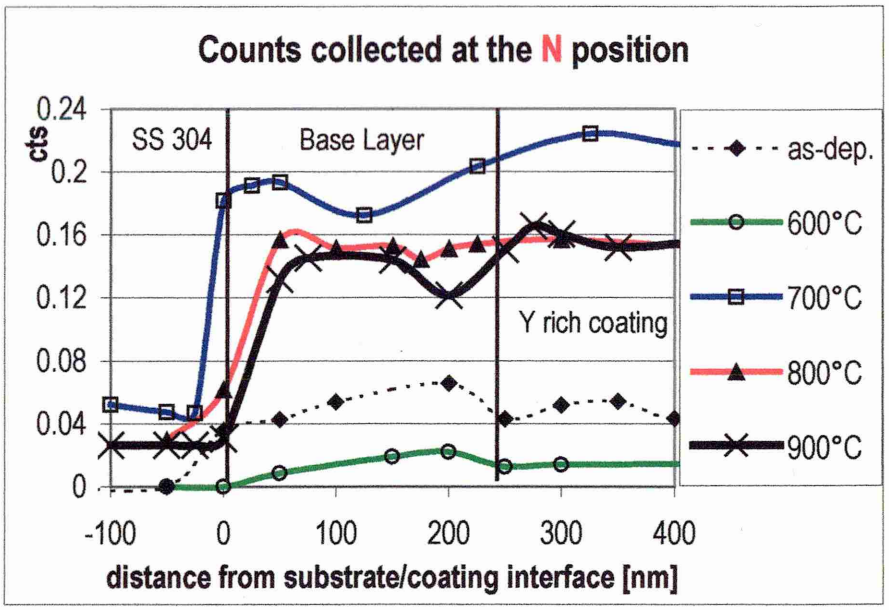

Figure 7-19: N content in the base layer of TiAlCrYN+Ox at various temperatures

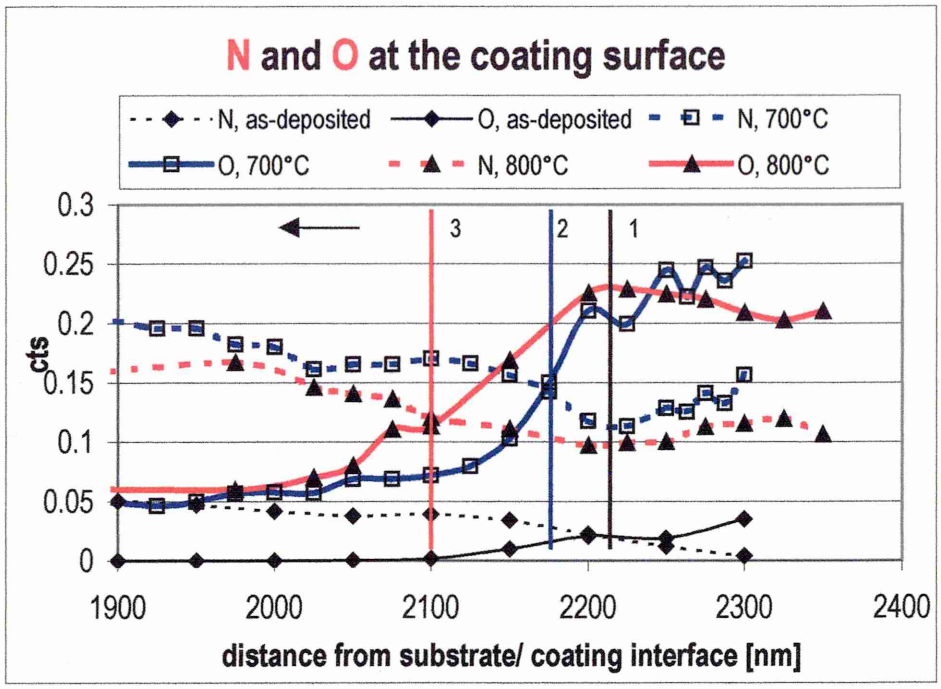

Figure 7-20: N and O cross over at the surface of TiAlCrYN+Ox at various temperatures

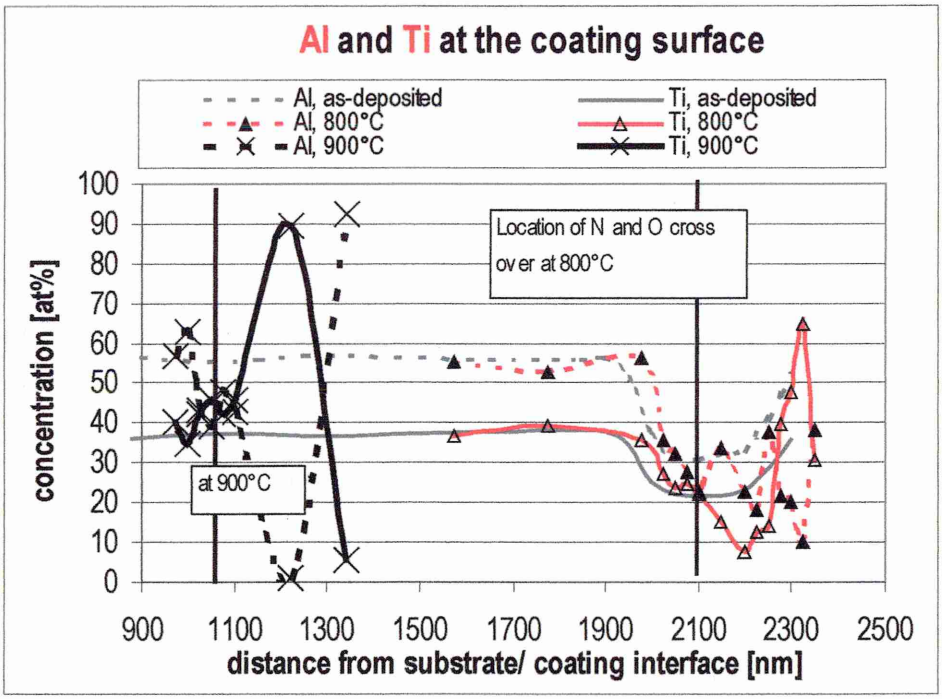

Figure 7-21: Al and Ti content at the surface of TiAlCrYN+Ox at various temperatures

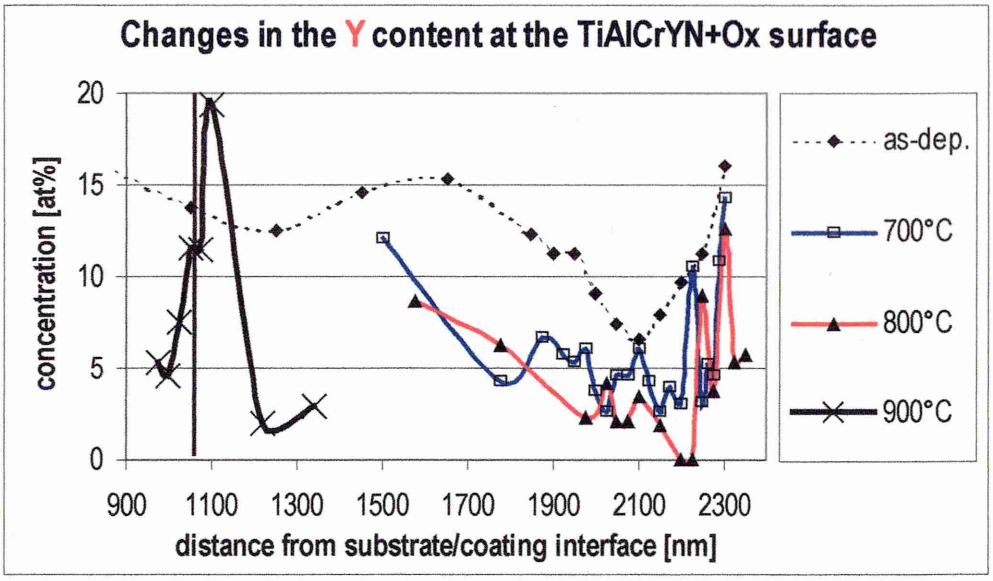

Figure 7-22: Y content at the surface of TiAlCrYN+Ox at various temperatures

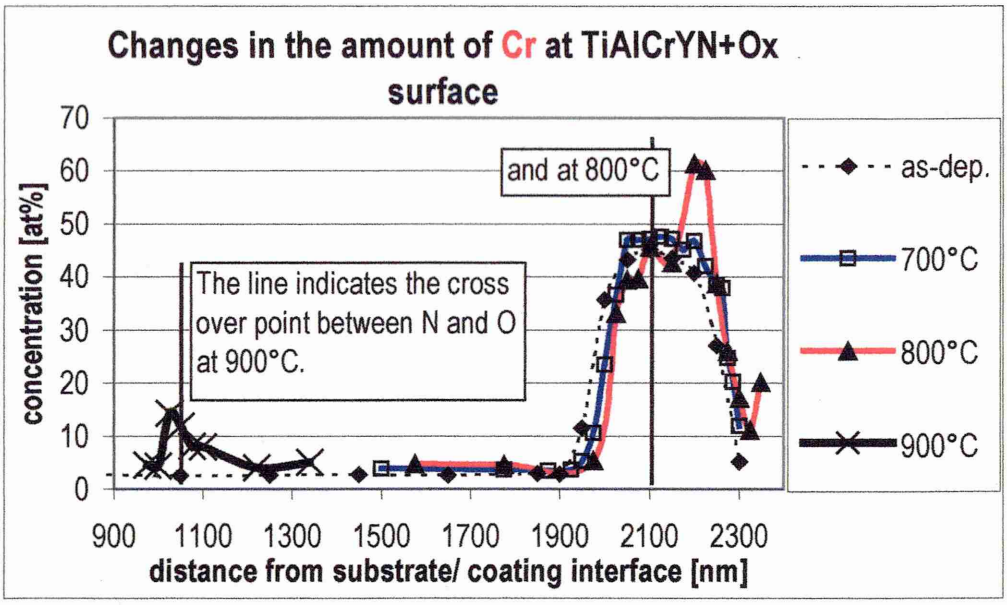

Figure 7-23: Cr content at the surface of TiAlCrYN+Ox at various temperatures

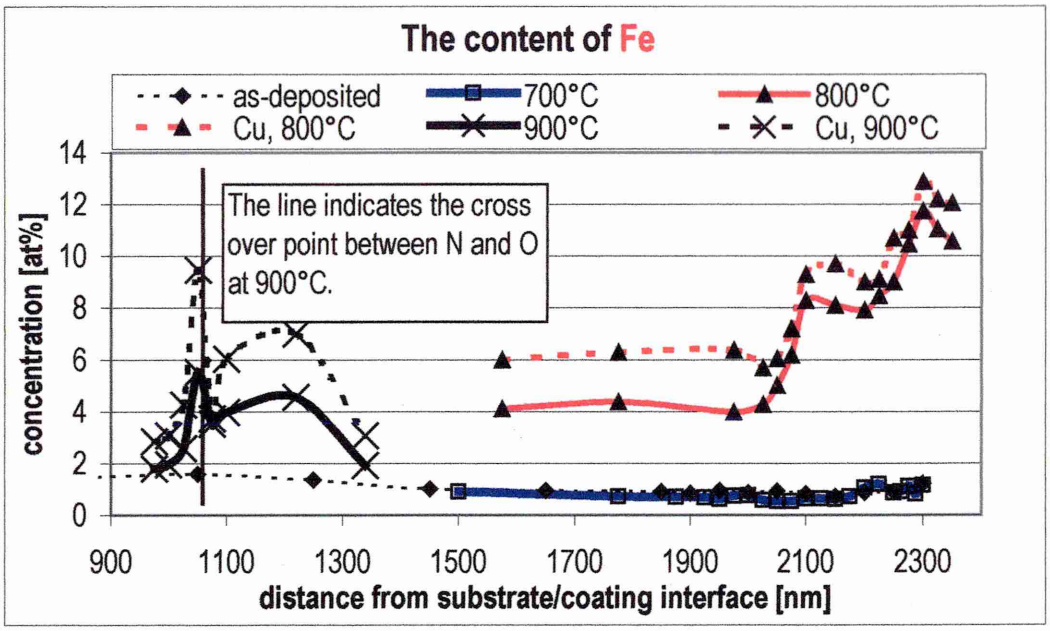

Figure 7-24: Fe content at the surface of TiAlCrYN+Ox at various temperatures

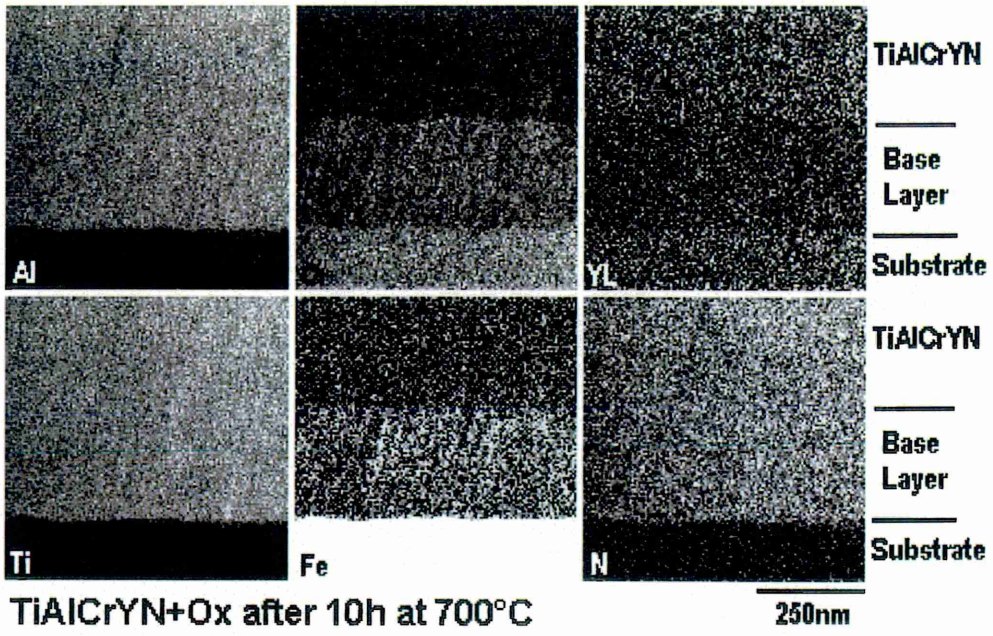

Figure 7-25: Elemental maps from TiAlCrYN+Ox heat treated for 10h at 700°C with a DF image from a similar area.

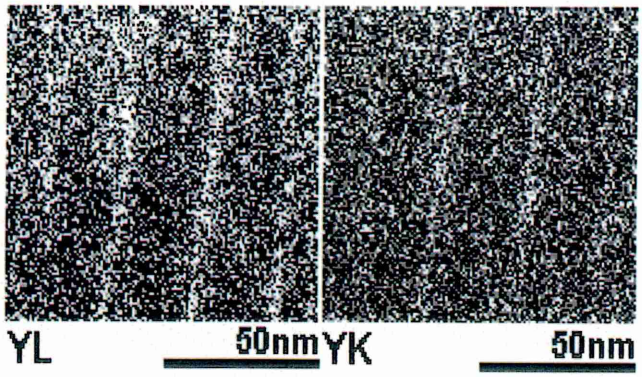

Figure 7-26: Elemental maps taken from TiAlCrYN+Ox.

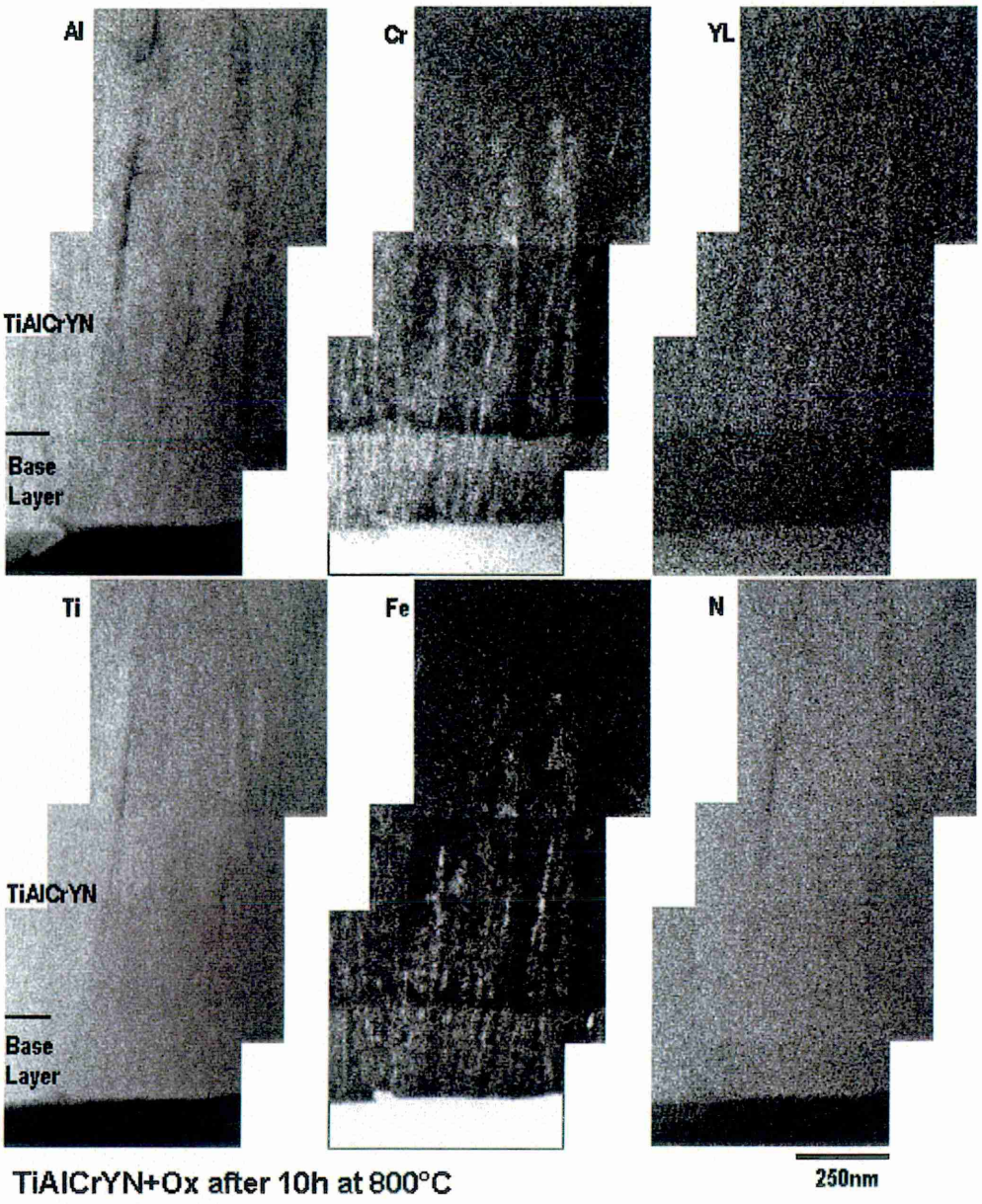

Figure 7-27: Elemental maps from the base layer region of TiAlCrYN+Ox after 10h at 800°C

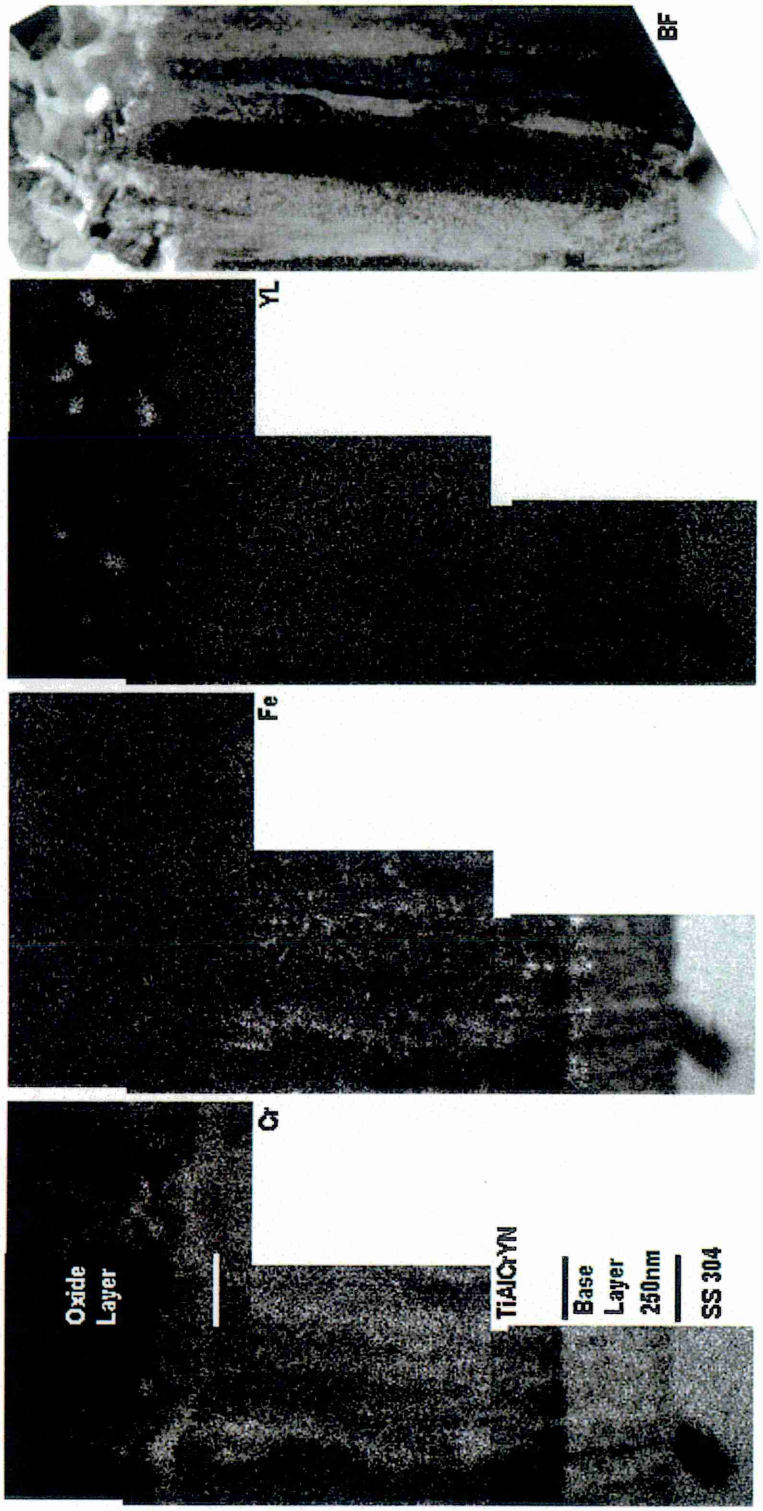

Figure 7-28: Elemental maps (Cr, Fe, Y) from TiAlCrYN+Ox after heat treatment for 10h at 900°C

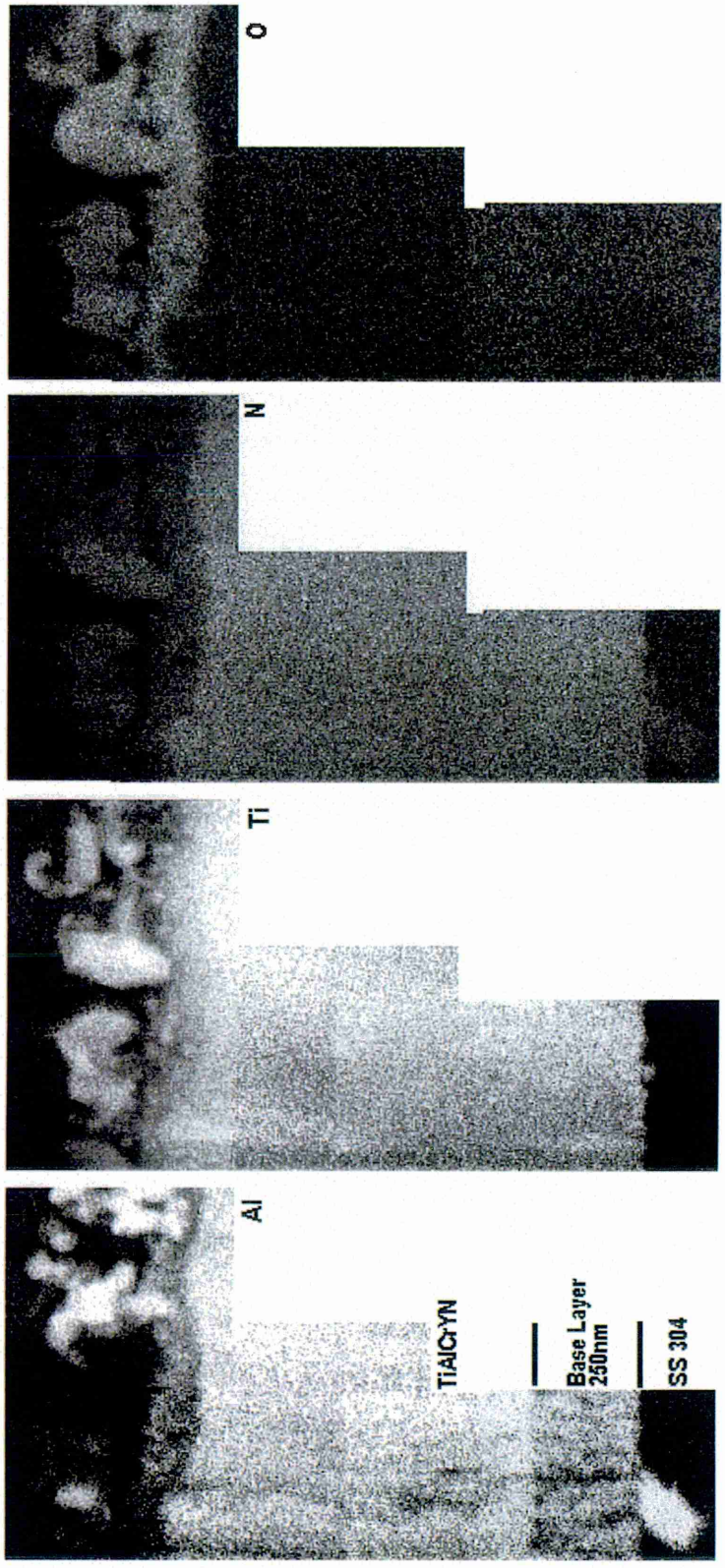

Figure 7-29: Elemental maps (Al, Ti, N, O) from TiAlCrYN+Ox after heat treatment for 10h at 900°C

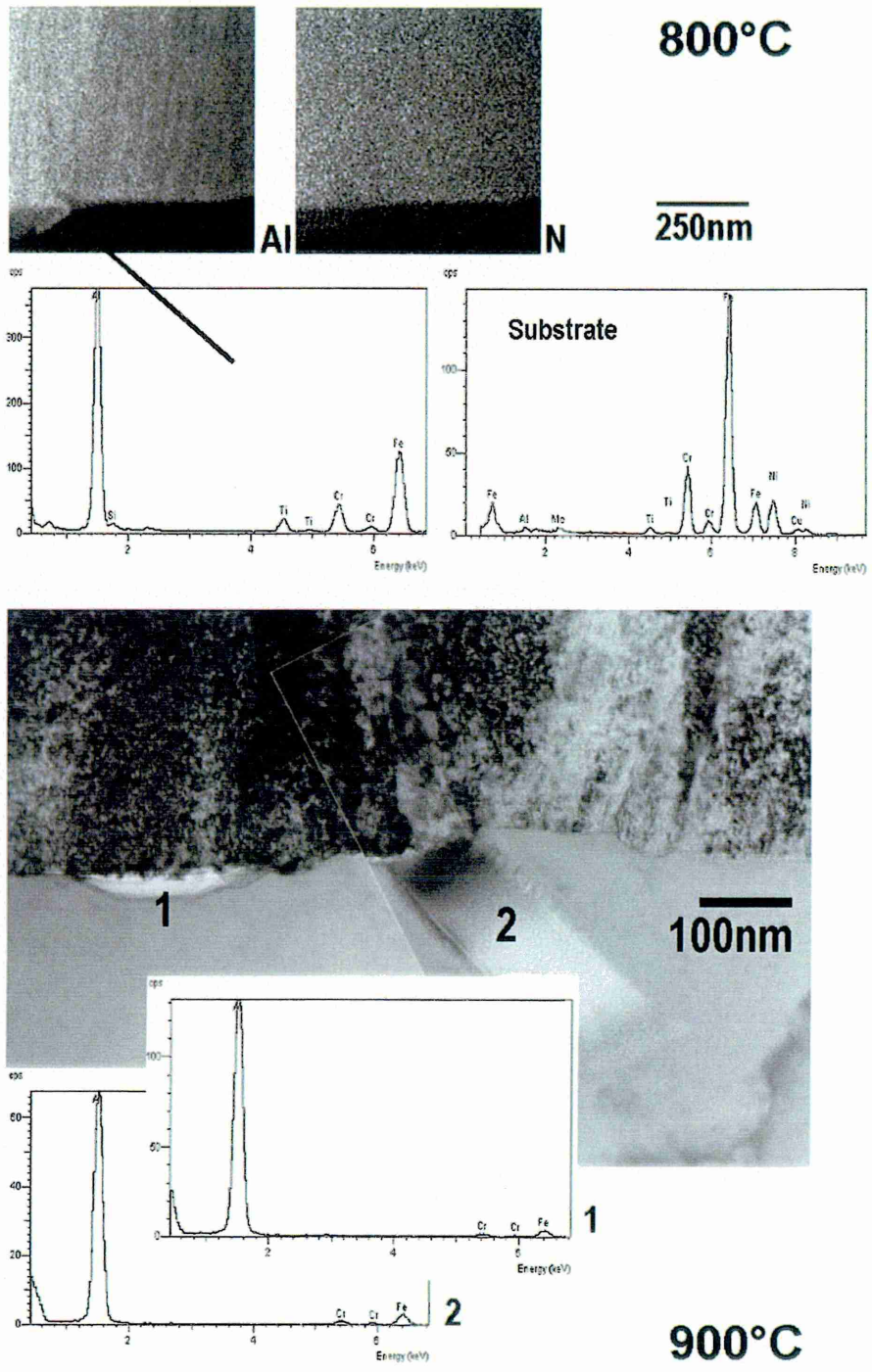

Figure 7-30: EDX spectra taken from TiAlCrYN+Ox base layer region after heat treatment for 10h showing the precipitates rich in Al and N

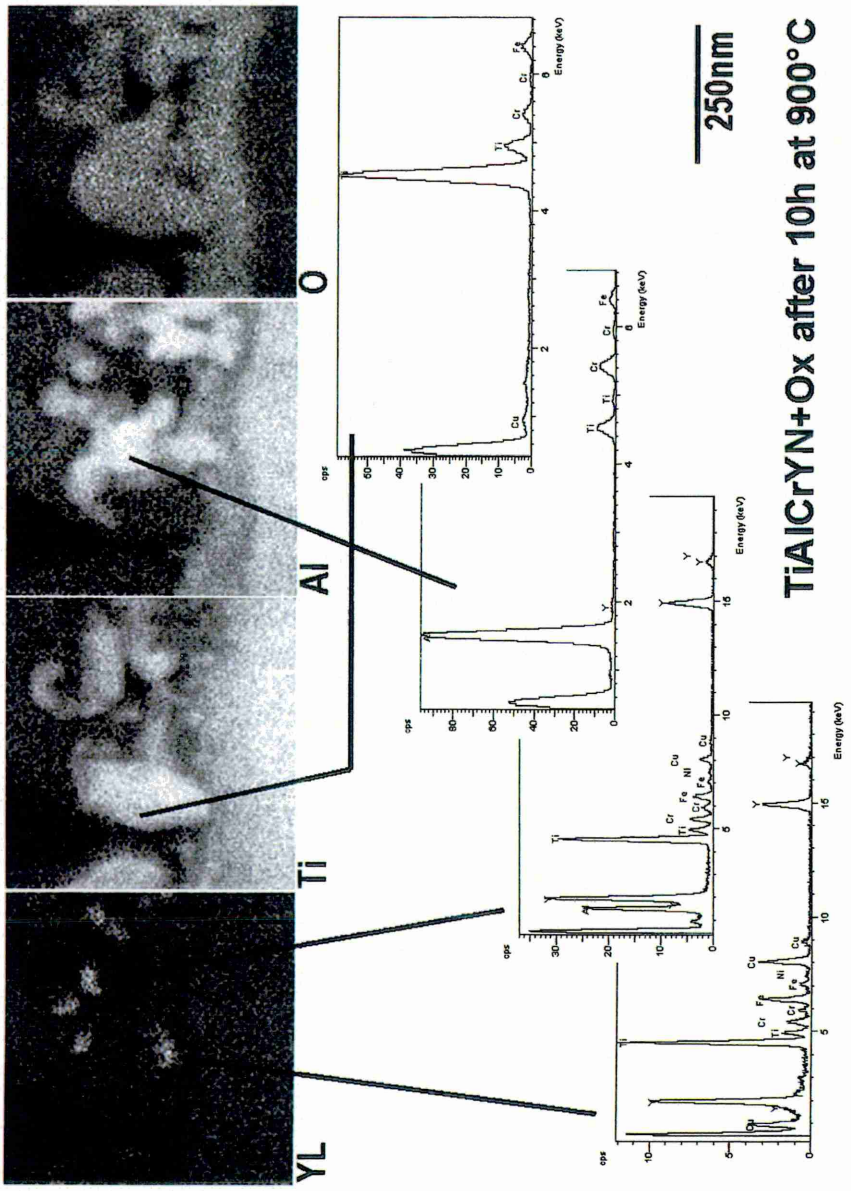

Figure 7-31: EDX maps and spectra from the oxide layer region of TiAlCrYN+Ox heat treated for 10h at 900°C

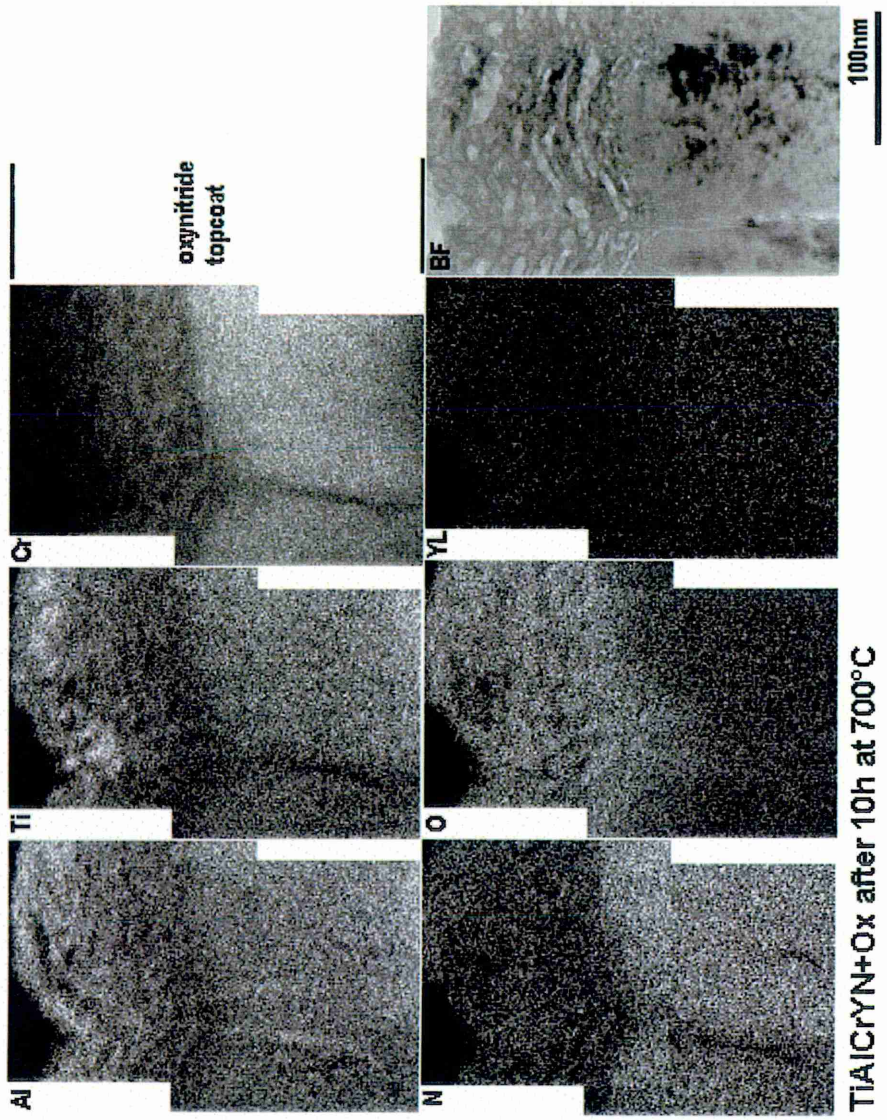

Figure 7-32: Elemental maps from the topcoat region of TiAlCrYN+Ox heat treated for 10h at 700°C.

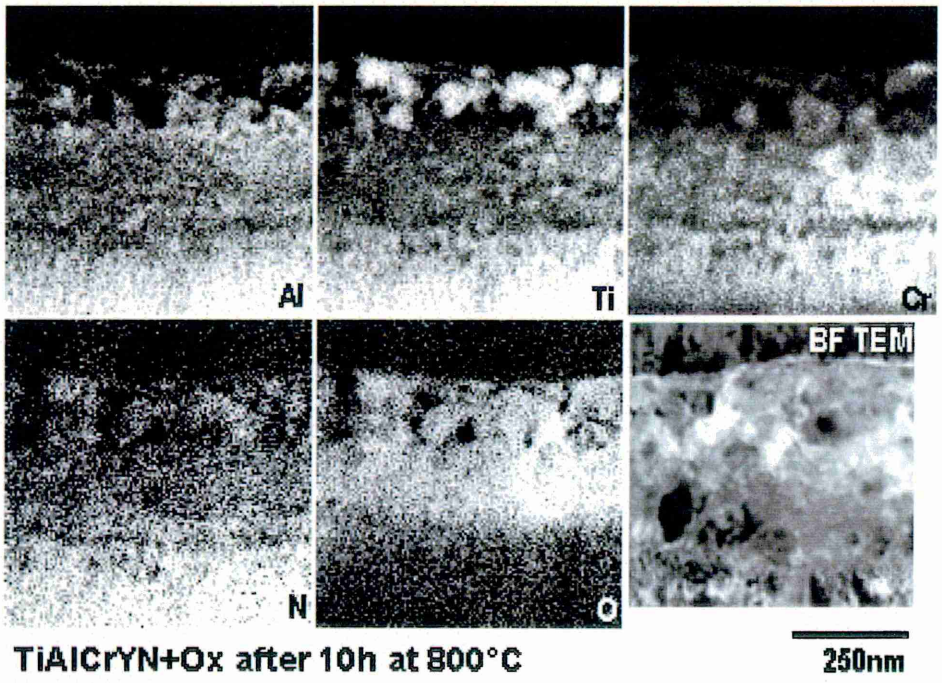

Figure 7-33: Elemental maps of the oxide layer region of TiAlCrYN+Ox heat treated for 10h at 800°C.

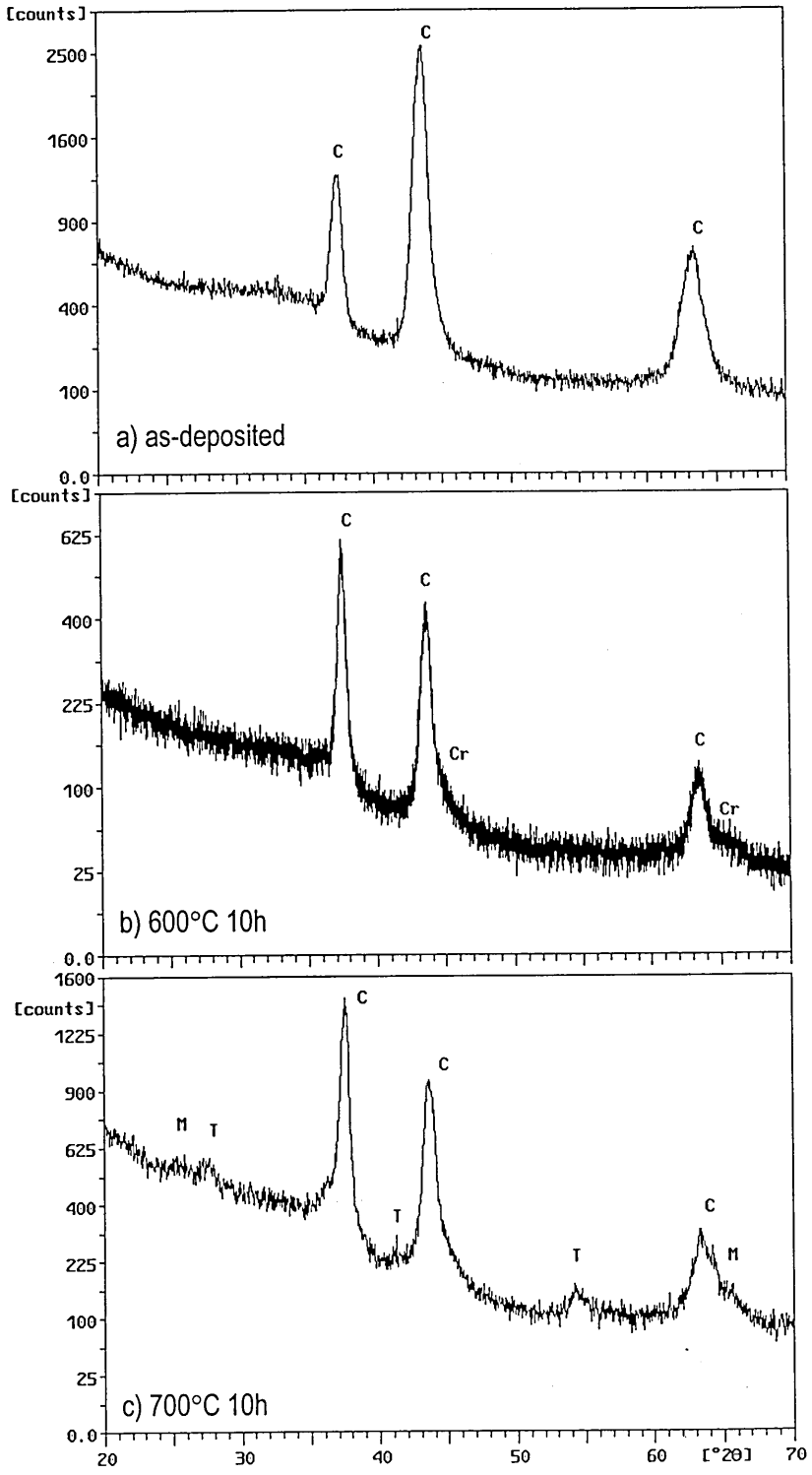
[counts]
2500
1600
900
400
100
0.0
C
C
C
a) as-deposited
[counts]
625
400
225
100
25
0.0
C
C
Cr
C
Cr
b) 600°C 10h
1600
[counts]
1225
900
625
400
225
100
25
0.0
C
C
M
T
T
T
C
M
c) 700°C 10h
20
30
40
50
60
[°2θ]
70

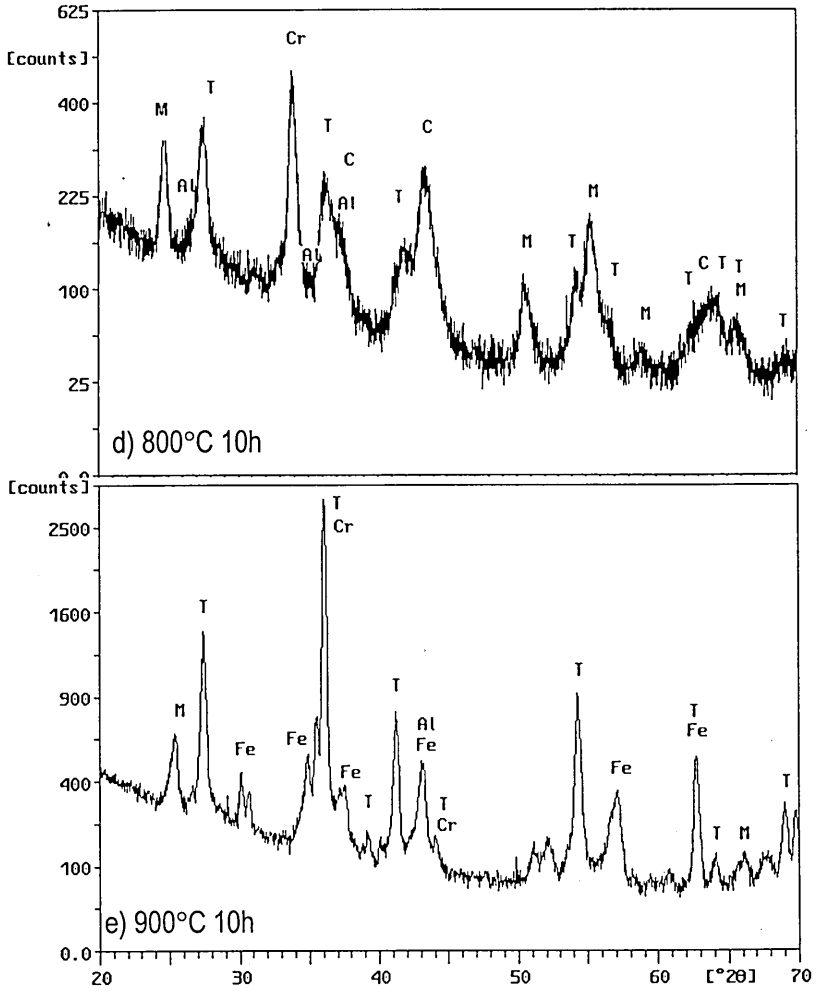

Figure 7-34: Glancing angle XRD at 0.5° incidence angle. TiAlCrYN+Ox at a) room temperature, b) after 600°C for 10h, c) after 700°C for 10h, d) after 800°C for 10h and e) after 900°C for 10h. The peak labels mean C=coating, T=TiO_2 (rutile), Al=Al_2O_3, Cr=Cr_2O_3, Fe=$FeCr_2O_4$ and M=solid solution out of Al_2O_3 and Cr_2O_3.

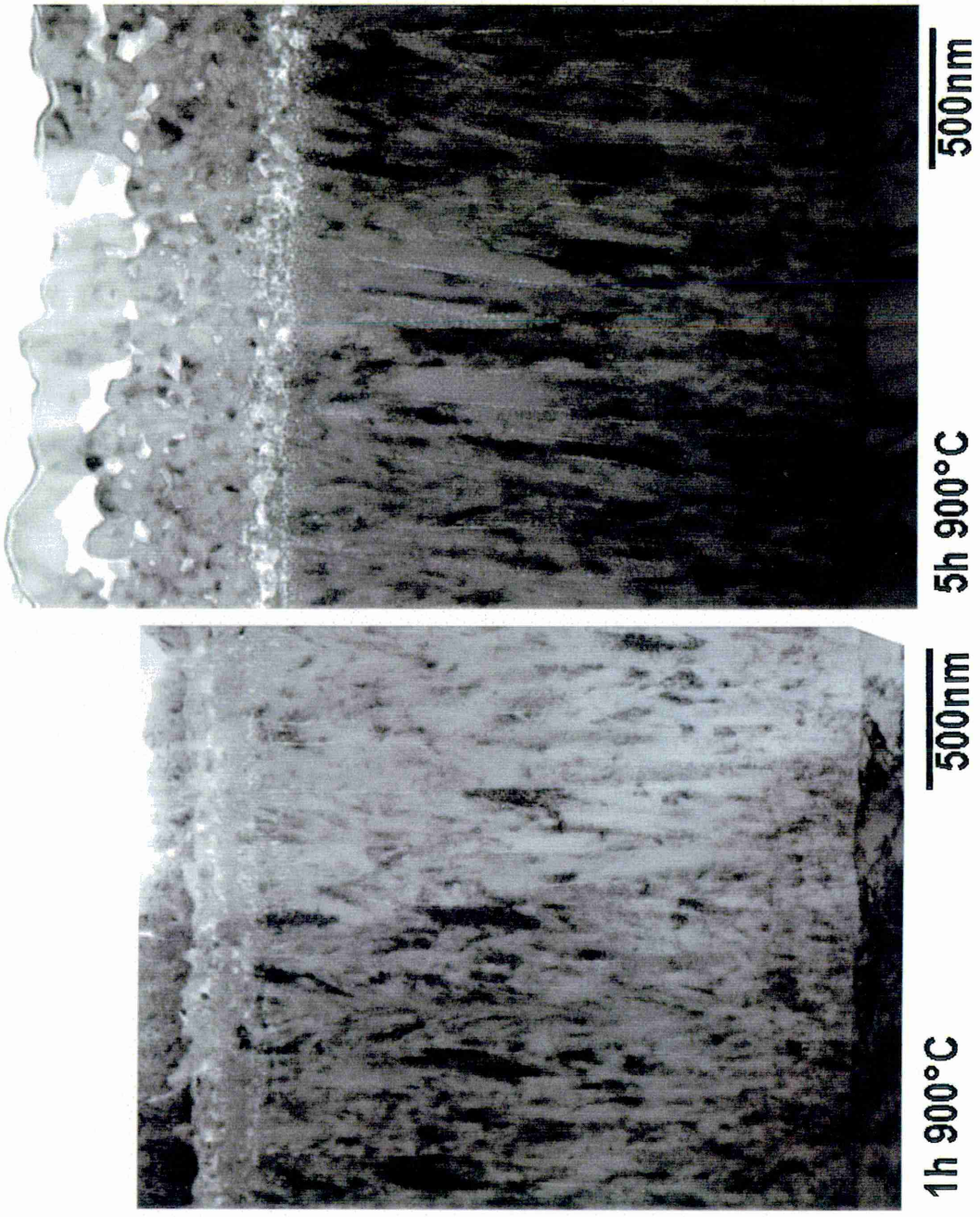

Figure 7-35: BF TEM micrographs of heat treated TiAlCrYN+Ox after heat treatment at 900°C

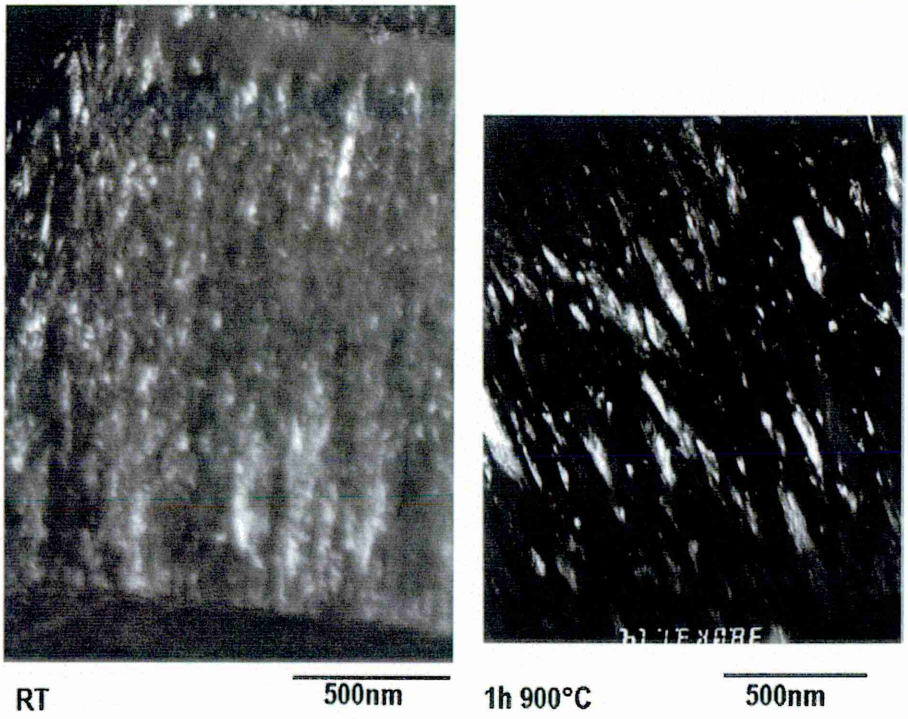

Figure 7-36: DF TEM micrographs of TiAlCrYN+Ox before and after heat treatment for 1h at 900°C

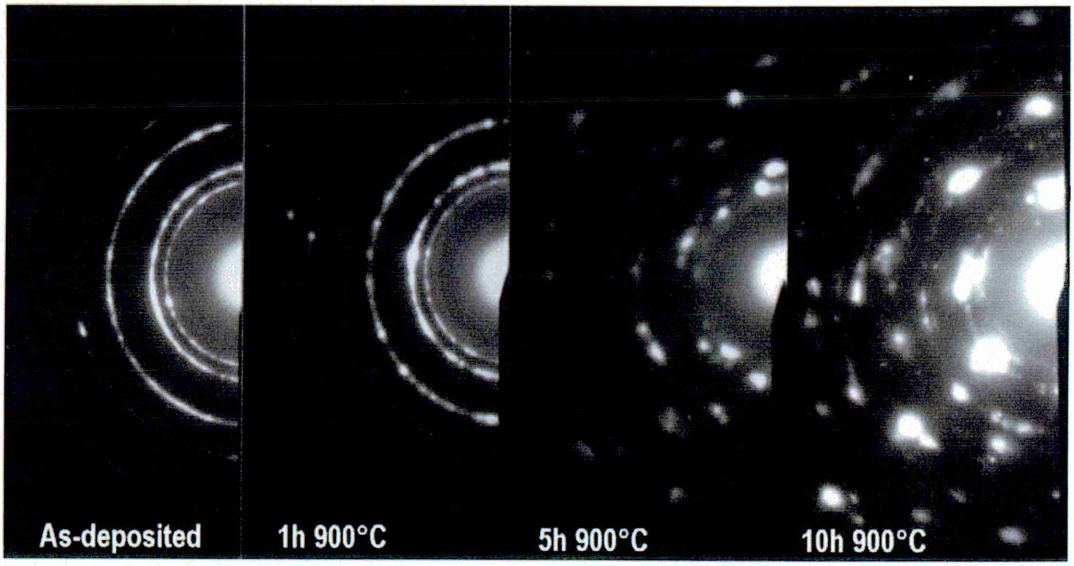

Figure 7-37: DP of an as-deposited sample and specimens heat treated at 900°C for different duration.

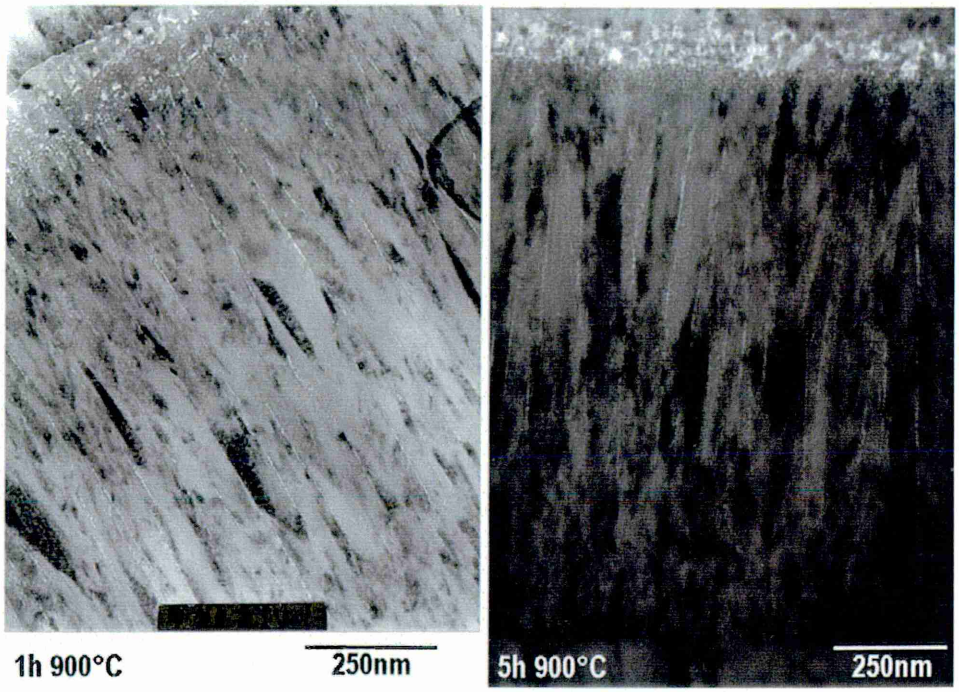

Figure 7-38: BF TEM images of TiAlCrYN+Ox showing void formation along the column boundaries after heat treatment for 1h and 5h at 900°C

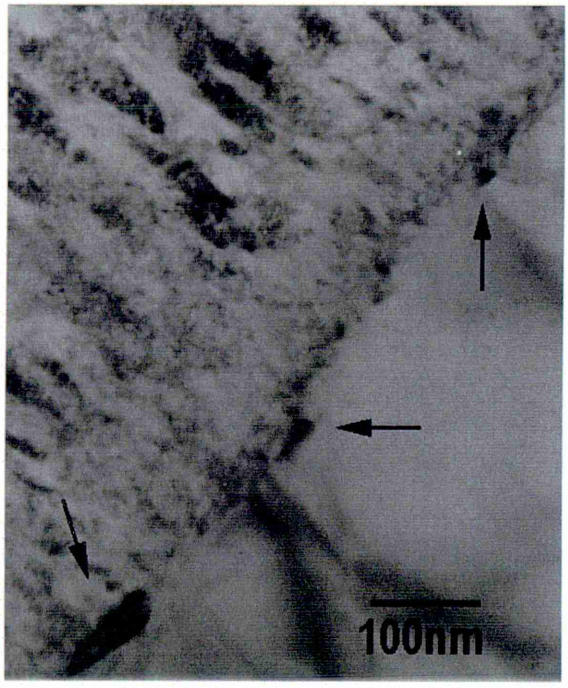

Figure 7-39: BF TEM micrograph of TiAlCrYN+Ox after heat treatment for 5h at 900°C

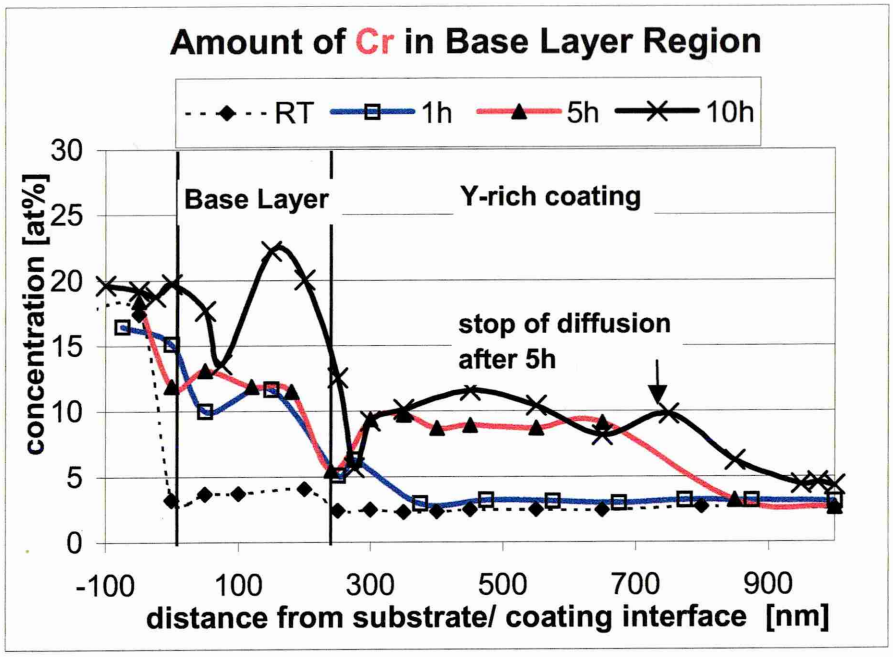

Figure 7-40: Cr concentration profile of TiAlCrYN+Ox heat treated at 900°C

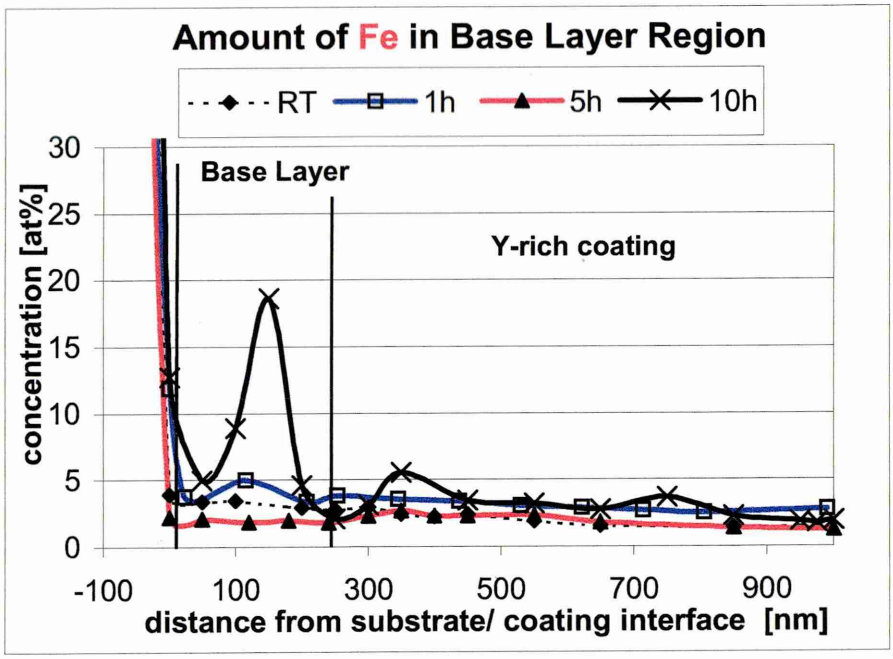

Figure 7-41: Fe concentration profile of TiAlCrYN+Ox heat treated at 900°C

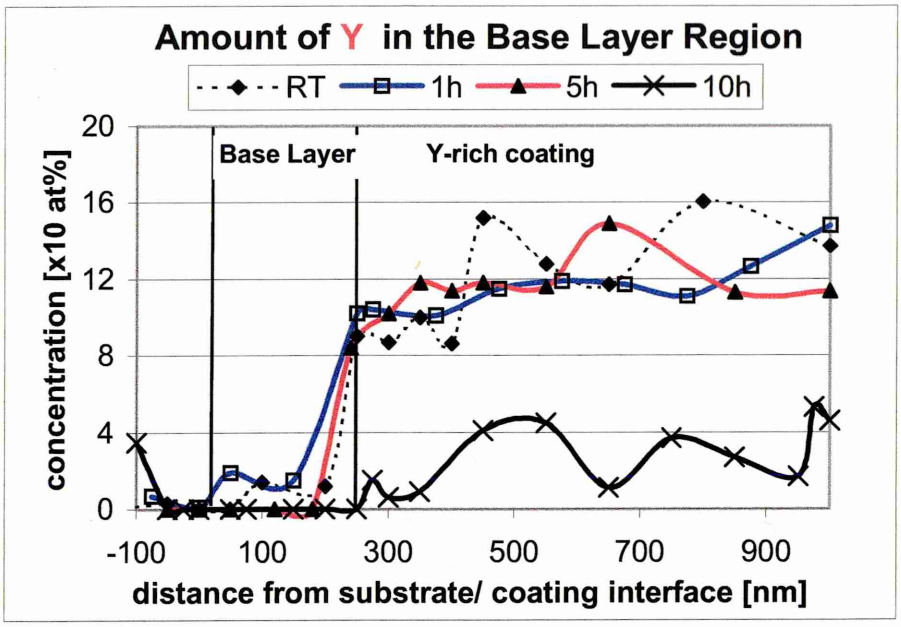

Figure 7-42: Y concentration profile of TiAlCrYN+Ox heat treated at 900°C

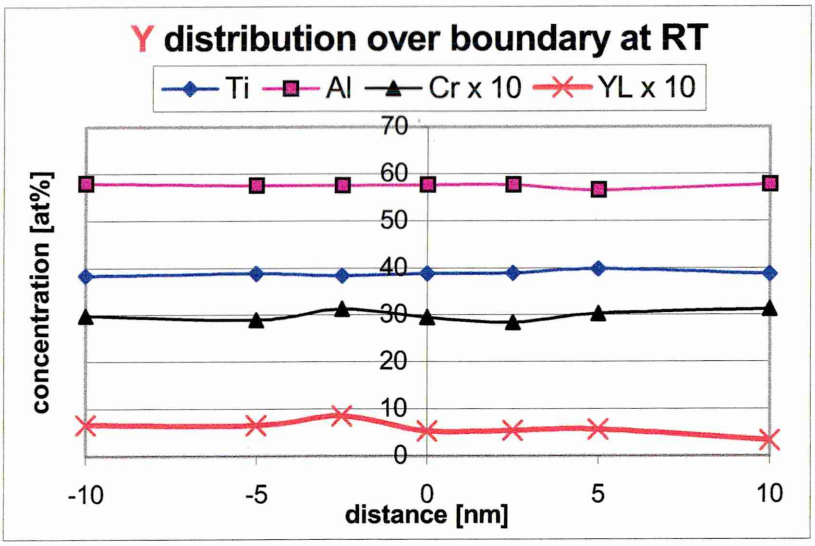

Figure 7-43: Y distribution over boundary of TiAlCrYN+Ox at room temperature

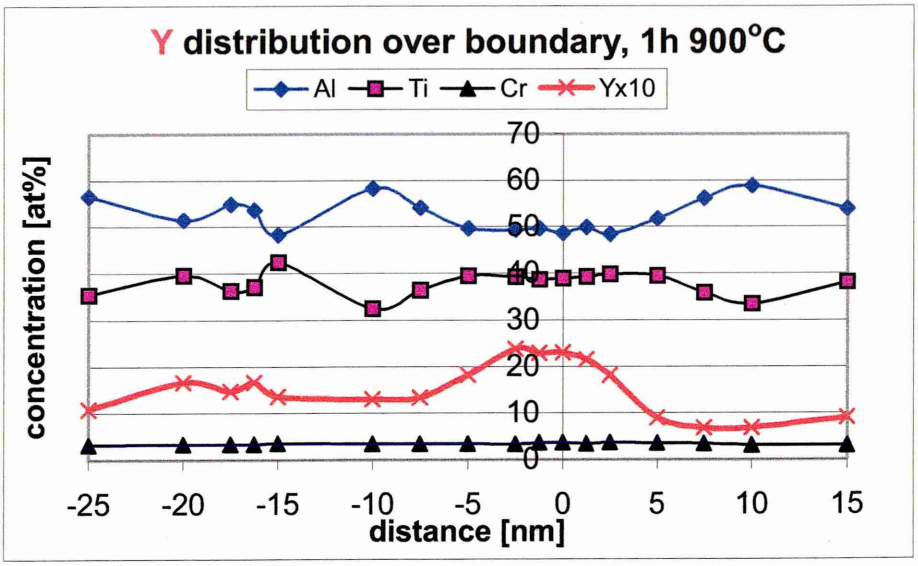

Figure 7-44: Y distribution over boundary of TiAlCrYN+Ox after 1h at 900°C

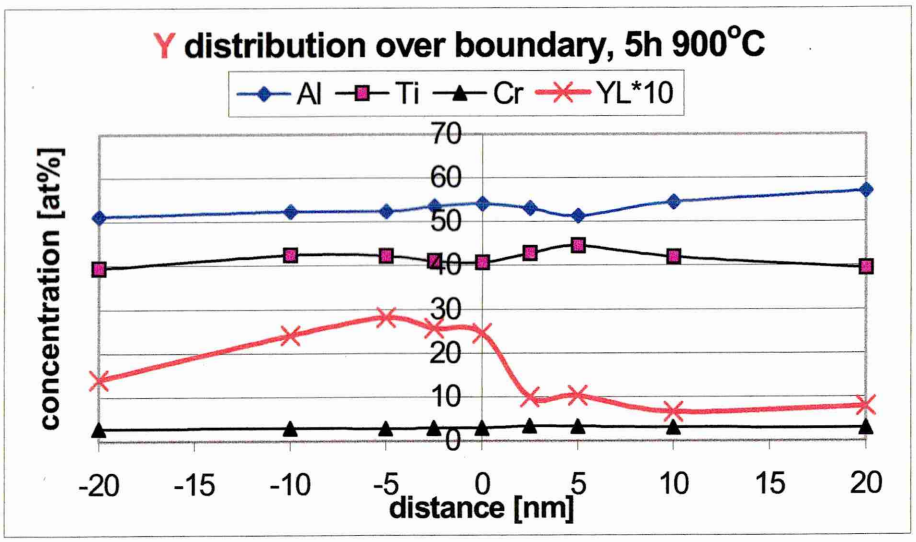

Figure 7-45: Y distribution over boundary of TiAlCrYN+Ox after 5h at 900°C

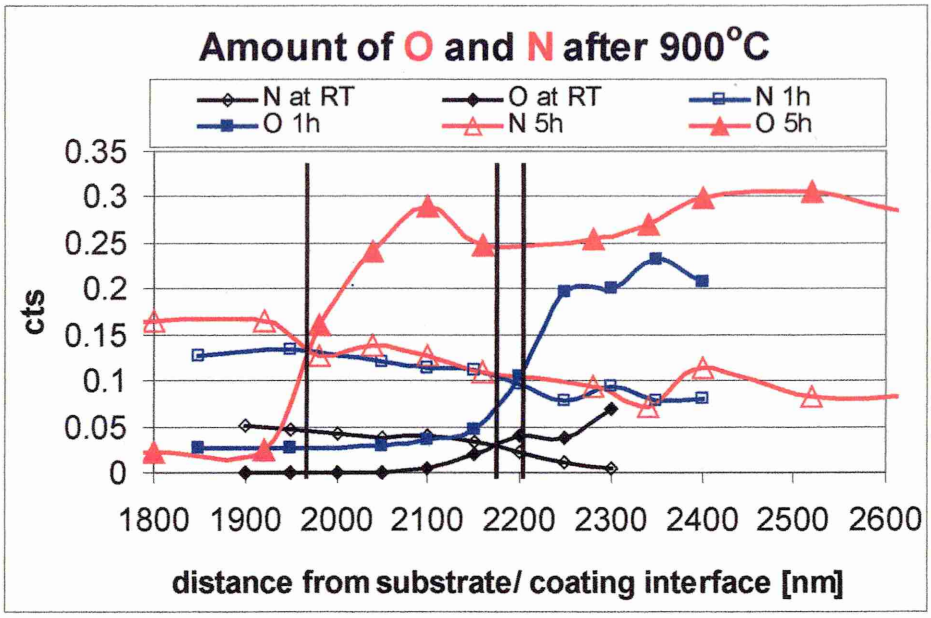

Figure 7-46: Point analysis on TiAlCrYN+Ox after heat treatment at 900°C

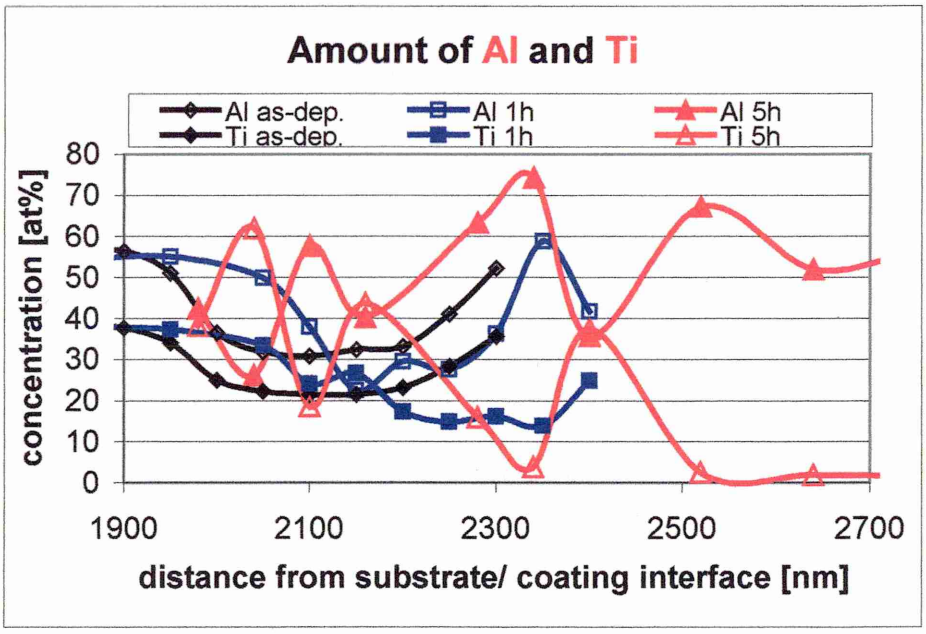

Figure 7-47: Al and Ti content at the TiAlCrYN+Ox surface after heat treatment at 900°C

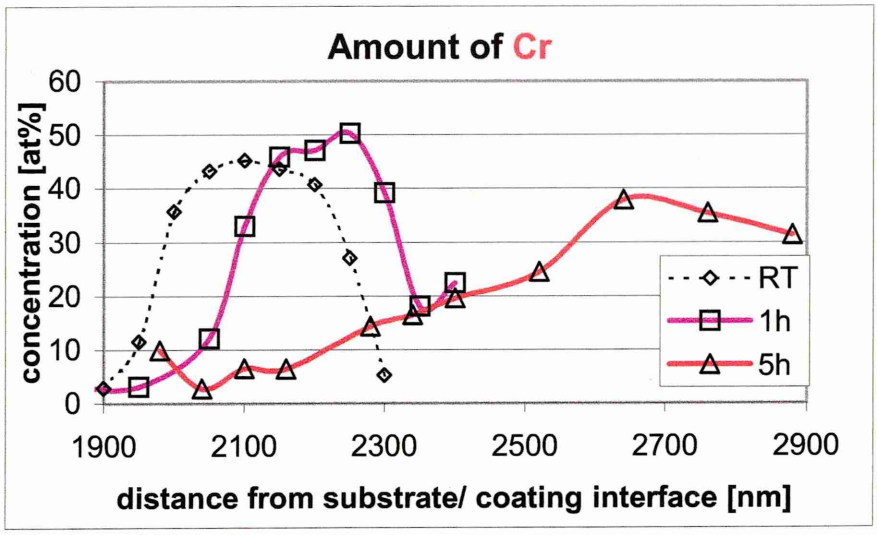

Figure 7-48: Cr content at the TiAlCrYN+Ox surface after heat treatment at 900°C. All point analysis was performed to the very surface.

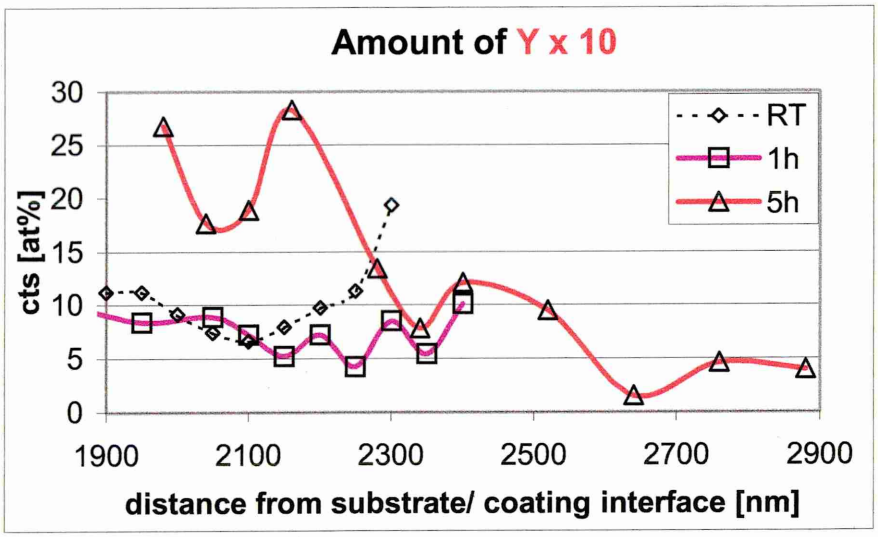

Figure 7-49: Y content at the TiAlCrYN+Ox surface after heat treatment at 900°C

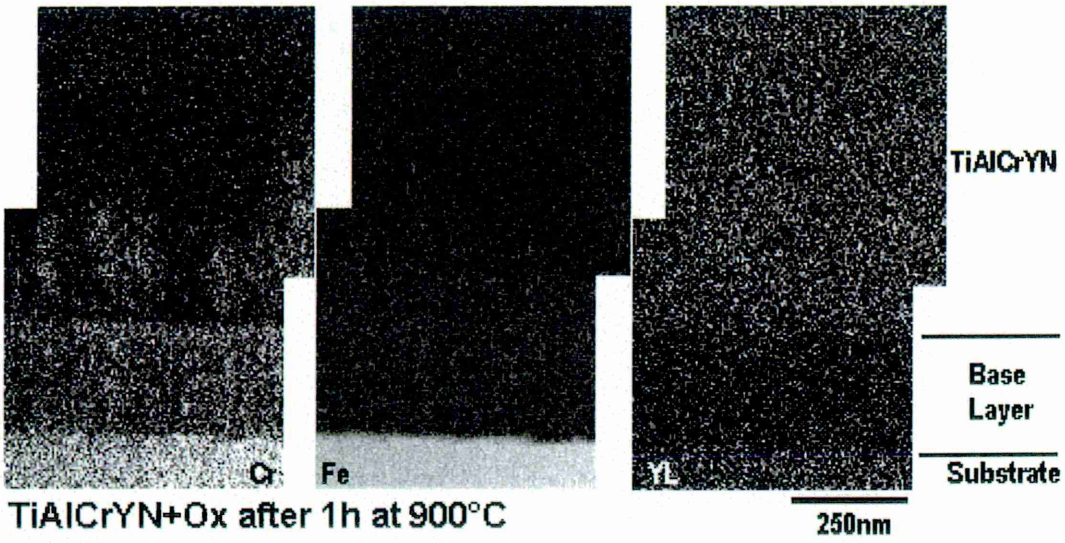

Figure 7-50: Elemental maps of TiAlCrYN+Ox after heat treatment for 1h at 900°C

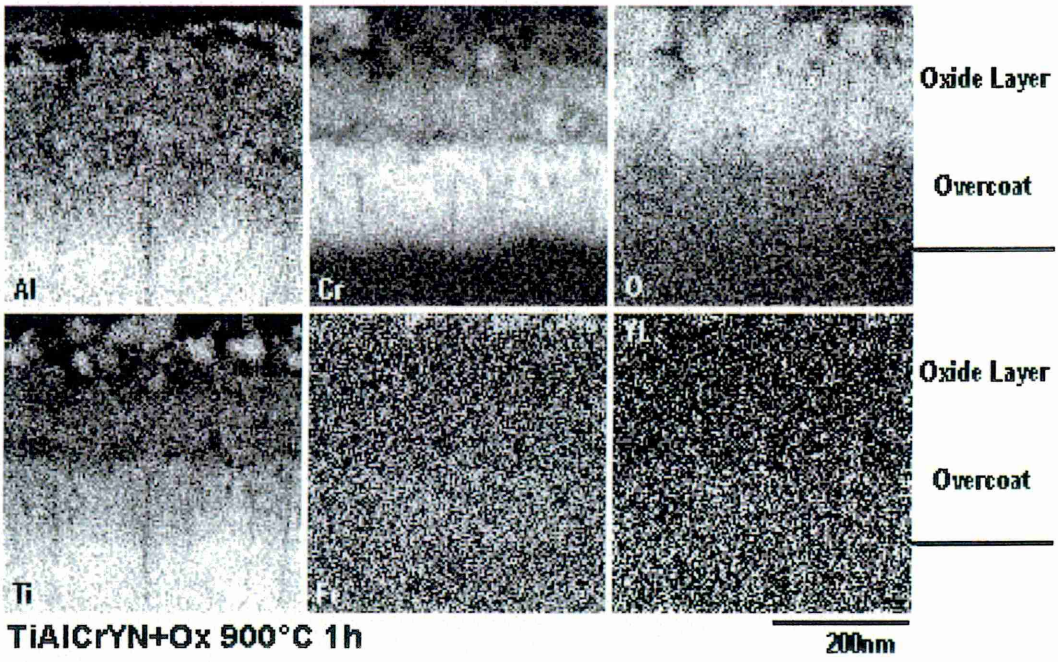

Figure 7-51: Elemental maps from the oxide layer of TiAlCrYN+Ox after heat treatment for 1h at 900°C

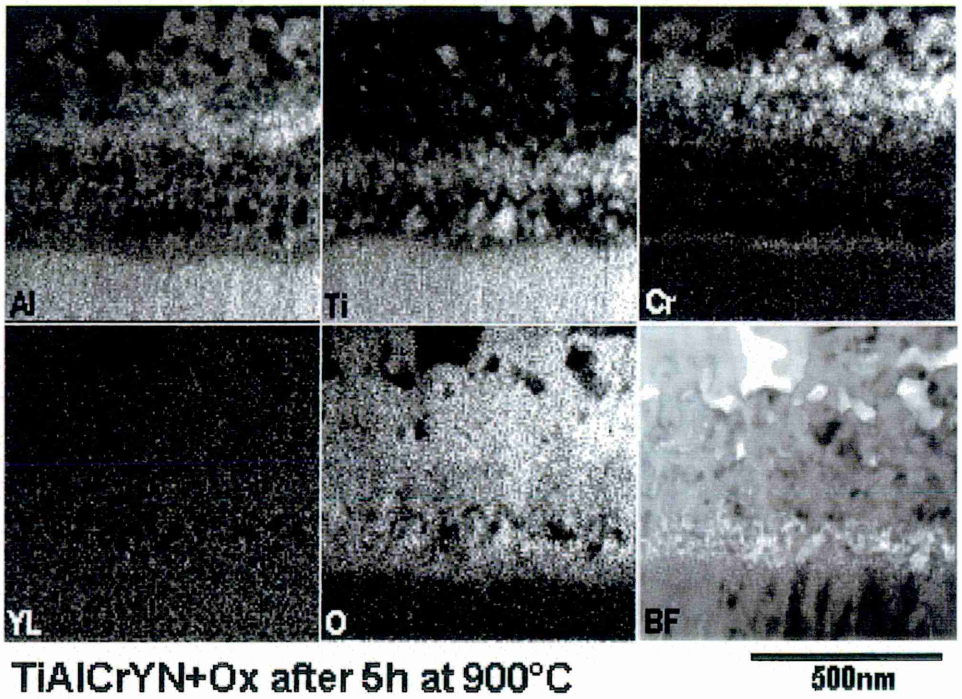

Figure 7-52: Elemental maps from the oxide layer of TiAlCrYN+Ox after heat treatment for 5h at 900°C

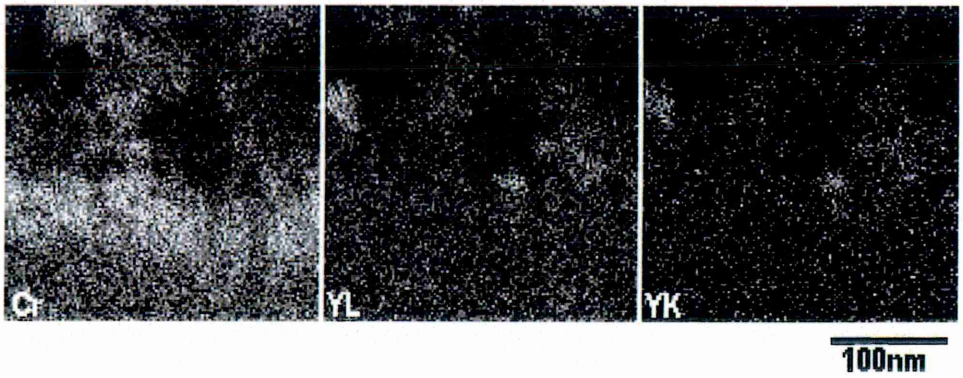

Figure 7-53: Elemental maps after the Cr-rich band in the oxide layer of TiAlCrYN+Ox

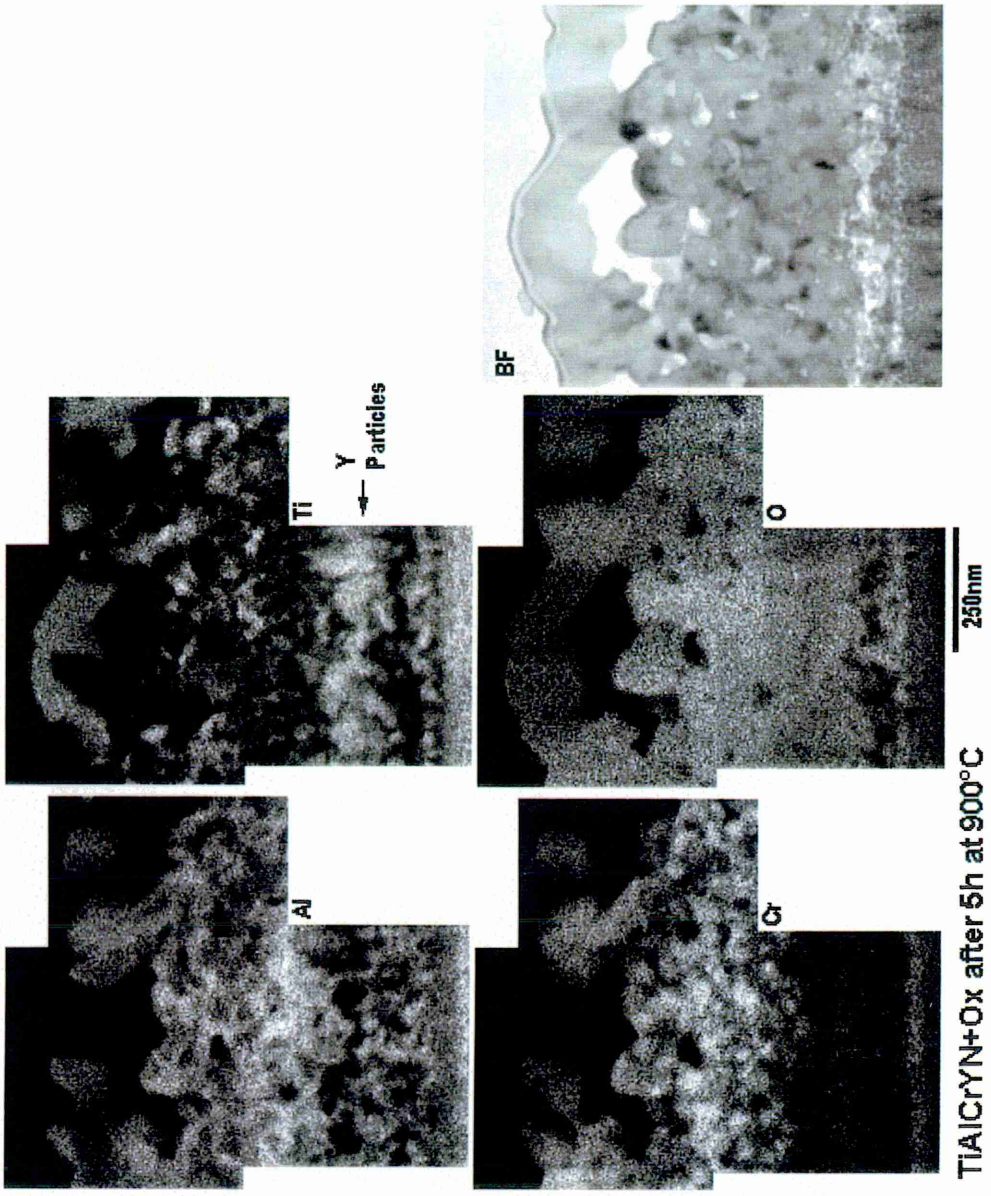

Figure 7-54: Elemental maps from the oxide layer of TiAlCrYN+Ox after heat treatment for 5h at 900°C

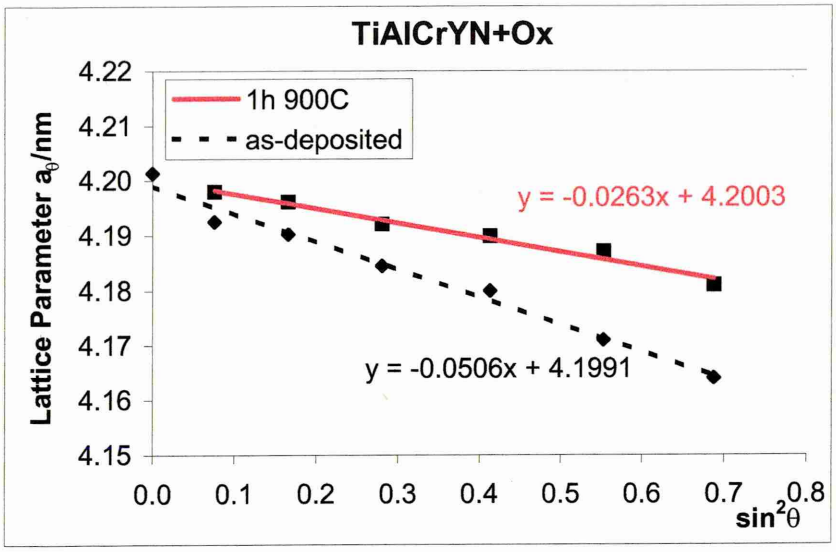

Figure 7-55: Stress measurement of TiAlCrYN+Ox before and after heat treatment

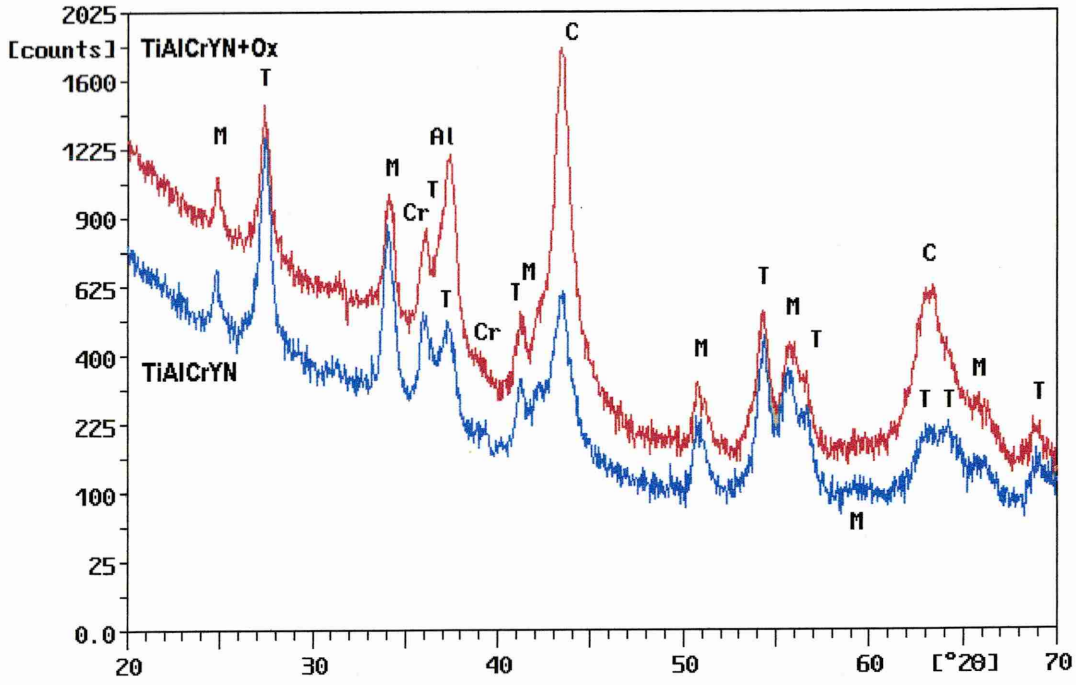

Figure 7-56: Glancing angle XRD after 1h at 900°C for TiAlCrYN with and without overcoat. M = solid solution out of Al_2O_3 and Cr_2O_3, T = TiO_2, Cr = Cr_2O_3, Al = Al_2O_3, C = Coating

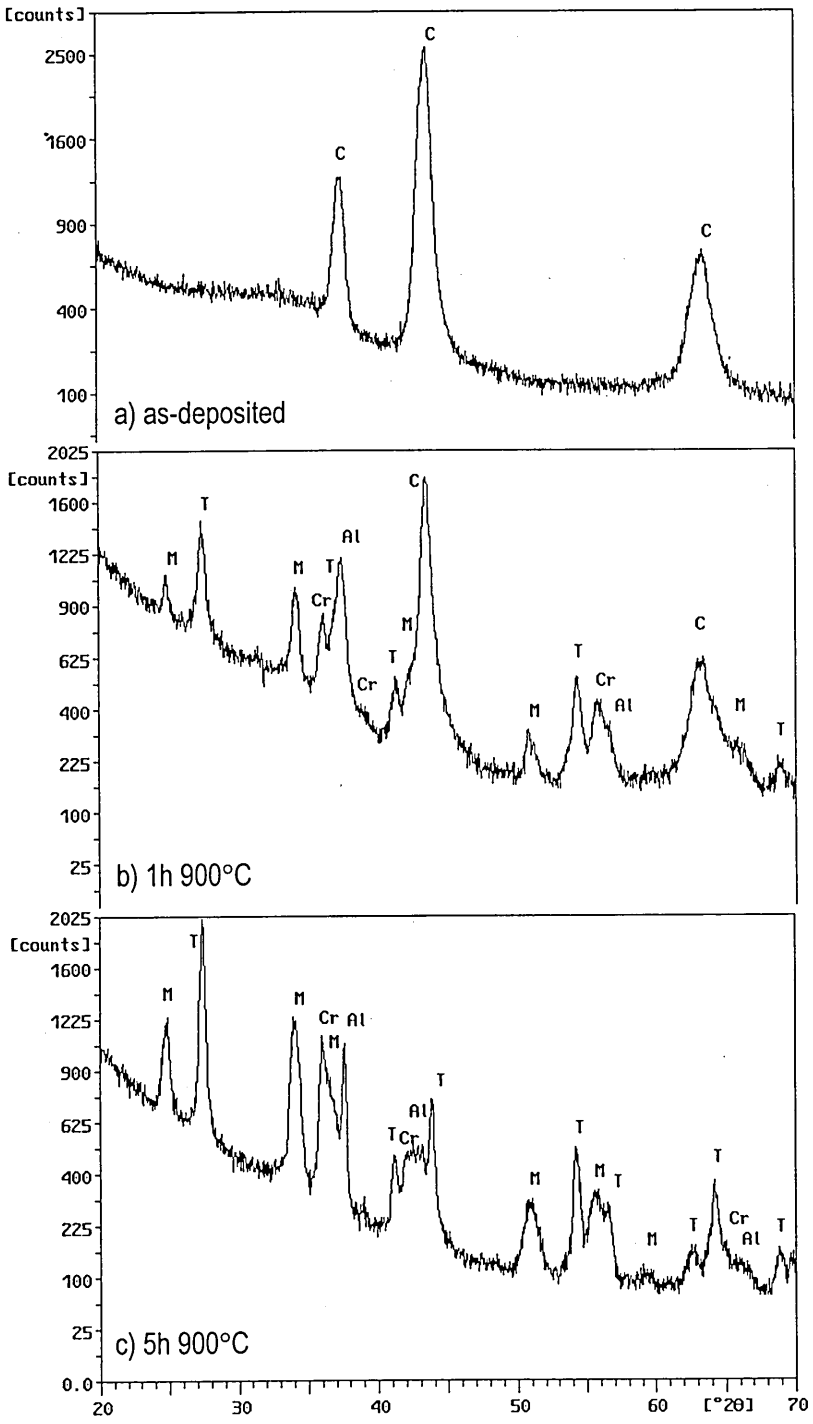

Figure 7-57: Glancing angle XRD from TiAlCrYN+Ox in a) as-deposited condition, b) heat treated for 1h at 900°C and c) heat treated for 5h at 900°C. The following letters indicate C = coating, M = solid solution out of Al_2O_3 (corundum) and Cr_2O_3 (eskolite), T = TiO_2 (rutile), Cr = Cr_2O_3, Al = Al_2O_3

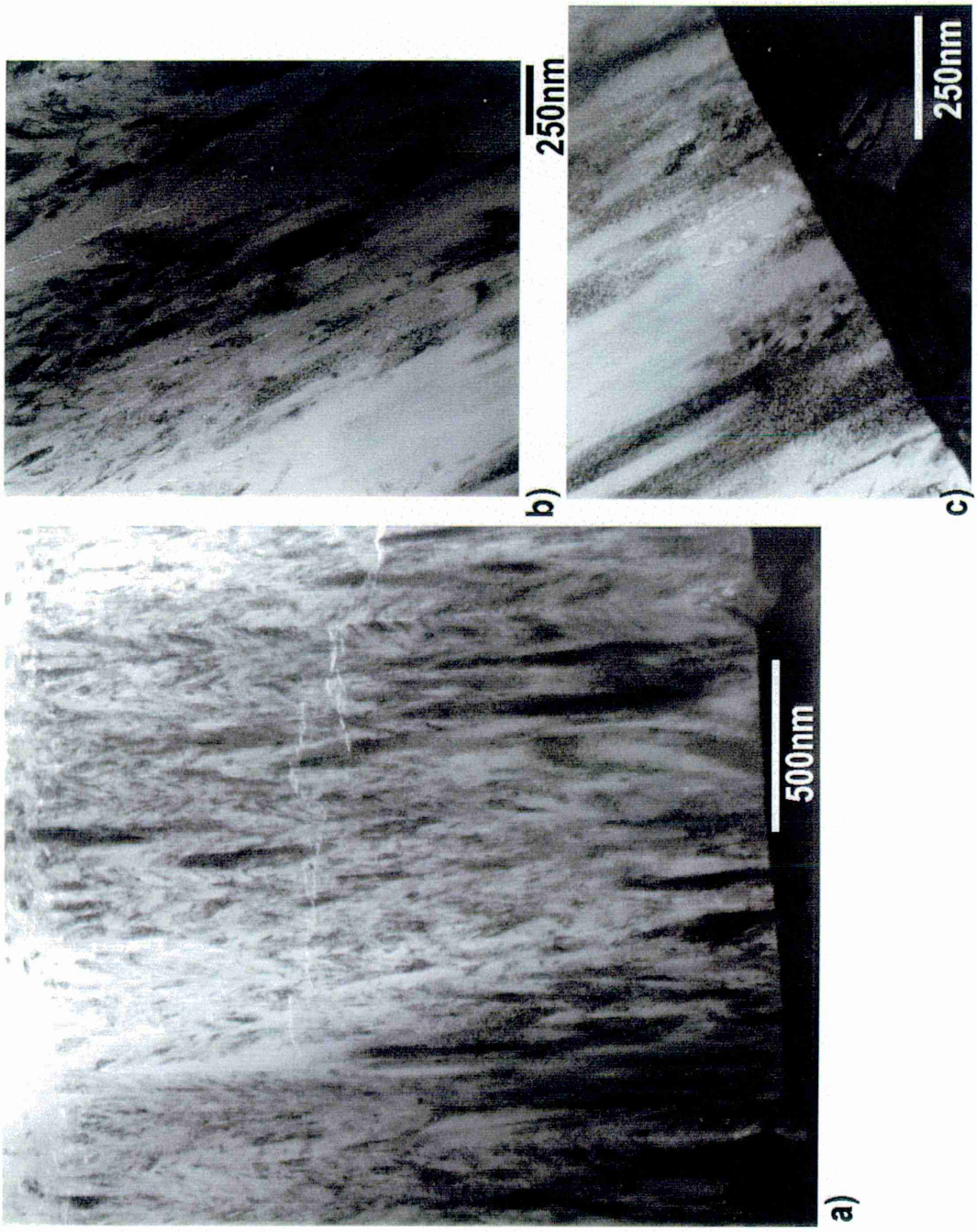

Figure 7-58: TEM BF micrographs of TiAlCrYN+Ox after heat treatment for 1h at 900°C b) from the middle of the coating c) from the base layer region

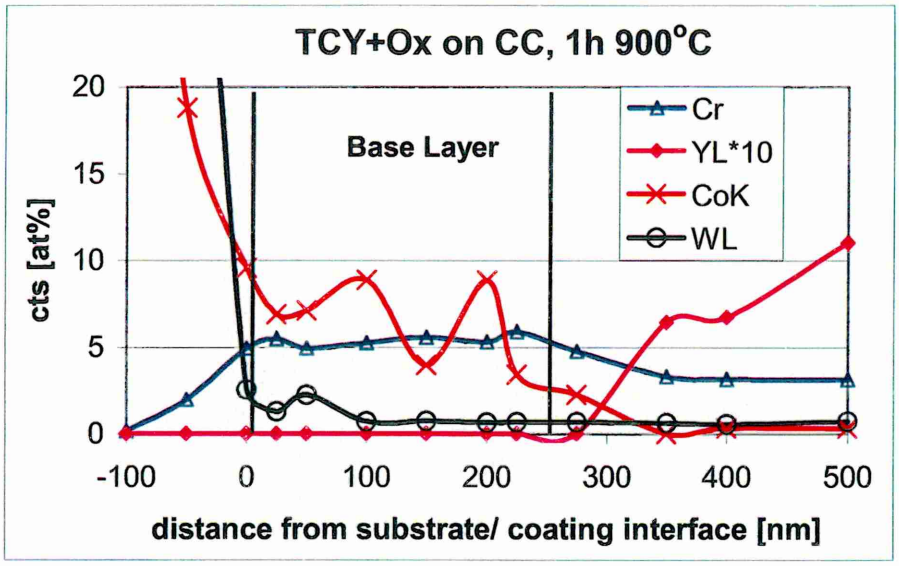

Figure 7-59: Point analysis profile in the base layer region of TiAlCrYN+Ox deposited onto stainless steel

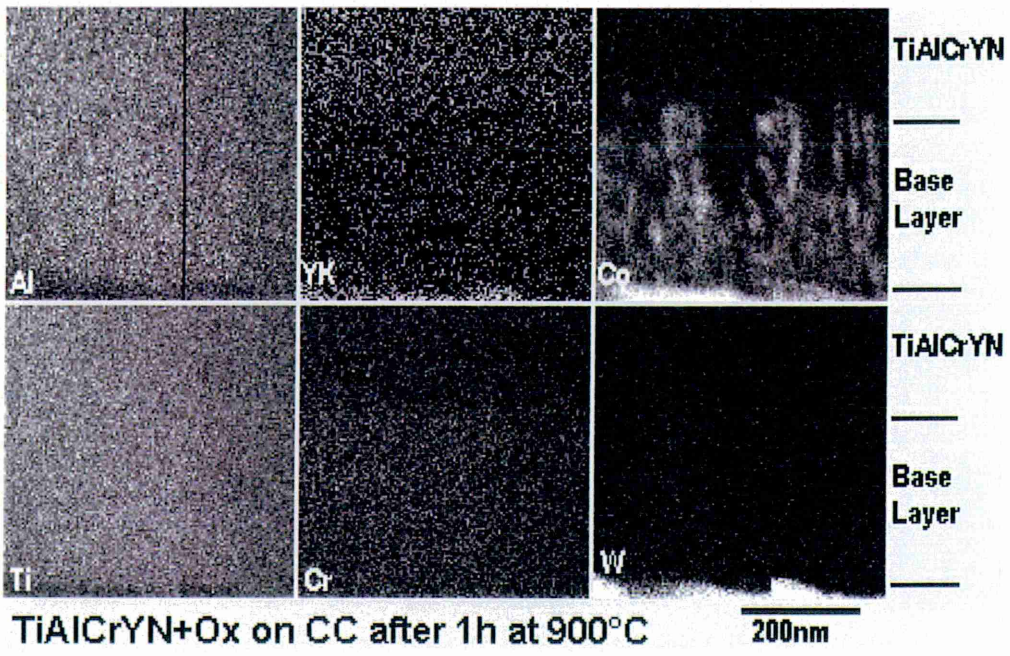

Figure 7-60: Elemental maps from the base layer region of TiAlCrYN+Ox deposited onto a cemented carbide substrate material.

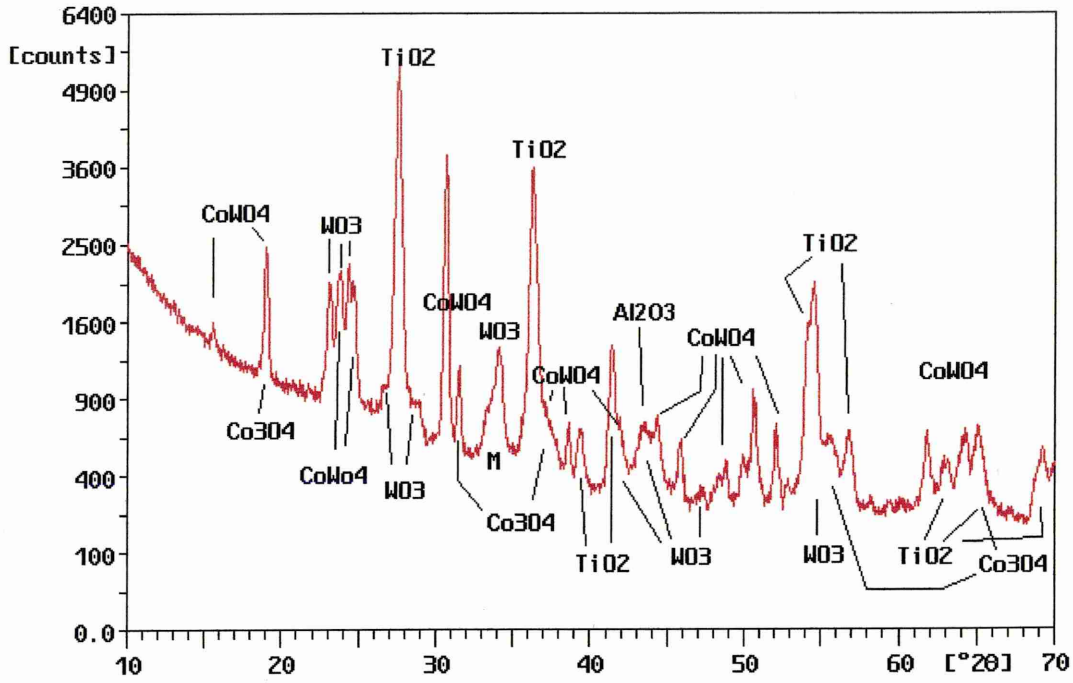

Figure 7-61: Glancing angle XRD from TiAlCrYN+Ox on cemented carbide after heat treatment

8 TiAlN/CrN

Additional research on the oxidation behaviour has been performed on the $Ti_{0.26}Al_{0.26}N/Cr_{0.48}N$ 8kW system. It has the best mechanical properties in a series of TiAlN and CrN layered structures with varied Cr content [13, 21].

8.1 As-deposited sample

8.1.1 TEM imaging

TEM analysis showed the beginning of a nanolayer formation on top of a $Ti_{0.44}Al_{0.54}Cr_{0.02}N$ base layer of 300nm (Figure 8-1). The nanolayers are visible after the base layer region, due to a difference in mass contrast. The nanolayer had a bi-layer thickness of 3.5nm. Additionally, a DP showing superlattice reflections close to the zero order spot was taken (Figure 8-2). The superlattice reflections had the shape of an arc caused by misorientation. The middle of the coating shows the nanolayered structure, as well as some voids along the column boundaries Figure 8-2.

In

Figure 8-3 it is obvious that the nanolayers follow the column in structure and orientation. Some voids along the column boundaries of 100 – 400nm in length were detected in over and under focused conditions at the column boundaries. The total coating thickness was ~3μm.

8.1.2 EDX mapping

Elemental maps from the as-deposited specimen show an increased intensity in the interface region, between substrate and coating (Figure 8-4). This was not seen before. Proper alignment of the sample interface region and/ or the higher resolution of this map (change of equipment) was the reason why

the interface could be viewed in this way for the first time. The intensity of the substrate region is weaker than for the nanolayered region, which is in accordance with the different amount of Cr in the SS 304 substrate (~20 at%) and the nanolayered region of the coating (~44 at%). The other maps show changes in accordance with the process parameters.

8.2 Oxidation behaviour

After heat treatment for 1h at 900°C the coating changed colour from dark grey to a blue interference colour, indicating the formation of a "pretty" thin oxide layer.

8.2.1 TG measurements

The dynamic (continuous) thermogravimetric measurements (weight gain in g m^{-2} over temperature in °C) were compared to the results gained from $Ti_{0.44}Al_{0.54}Cr_{0.02}N$ and TiAlCrYN with and without a Cr-rich topcoat. As can be seen from Figure 8-5 the weight gain for TiAlN/CrN is closer to the weight gain of TiAlCrYN+Ox than to TiAlCrYN.

Isothermal measurements of the same coatings, show the effect of the difference in slope between the TiAlCrYN+Ox and the TiAlN/CrN coating observed in the continuous measurement (Figure 8-6). The different slope is related to a decreased oxidation rate for the TiAlN/CrN coating. After 5h at 920°C, the weight gain of TiAlN/CrN increases at a slower rate compared to TiAlCrYN+Ox. The TiAlN/CrN curve shows a change in oxidation rate. After the first 2h the rate decreases noticeably. The weight gain measured at 2h is 1.1 gm^{-2} and after 10h 1.8 gm^{-2}.

This indicates, that the increased oxidation resistance of TiAlCrYN+Ox results from the increased amount of Cr in the overcoat region. The assumption earlier made comparing the weight gain of TiAlCrYN to TiAlCrYN+Ox is proven right.

Isothermal TG measurements for 10h showed a change in reaction kinetics after approximately 2h (Figure 8-7). The oxidation rate increases considerably above 920°C to 970° C, which is in accordance with the observations, made using continuous measurements.

It has been shown by [13] that oxidation of TiAlN/CrN follows a parabolic law for the first hour of the heat treatment between 850°C and 950°C. The parabolic rate indicates that the reaction might be governed by a solid state diffusion of the reactant through a compact and pore free scale [81]. The isothermal curves show a deviation occurred in this assumed ideal case. It has been shown that Cr ions belong to the outward migrating species [29, 102]. The outward diffusing Cr ions thus leaving vacancies behind, which might merge to form cavities and pores and produce appreciable porosity in the oxide scale after an extended reaction period. Additionally, the volume expansion and the stresses created might form pores. In such cases the cavities might act as barriers to the solid state diffusion process. In this case a phase boundary process becomes rate determining [81] (p. 228) and indeed, small cavities were observed by TEM in the oxide scale after heat treatment for 1h at 900°C. After annealing for 5h extended porosity was found. Hence, the reaction rate might be a combination of the reaction mechanism described here.

8.2.2 TEM imaging

TEM microscopy after heat treatment for 1h at 900°C showed the formation of an oxide layer, 80±20nm thick, on the coating surface (Figure 8-8). Along the columns and between oxide layer and coating rectangular speckles were observed, which stem from differences in mass contrast. The speckles had a size of ~6x6nm. In this case they might stem from void formation or a collection of gas atoms. The bright field images were taken using an objective aperture of 4mrad in size. The small aperture increases the contrast created by differences in mass contrast. Under and over focused imaging of the same area further confirmed the difference in mass. Interestingly, these areas had a square shape, caused probably by the underlying crystal structure of the material.

Additionally, to the formation of an oxide layer voids along the column boundaries connecting the coating surface with the interface were observed

(Figure 8-9). The amount of voids decreased in the base layer region, indicating the relation of void formation to defect and stress formation in the coating. A bright area in the substrate was observed. This region is probably caused by out-diffusion of substrate elements, as was found in TiAlCrN [33] and shown in Chapter 5 - TiAlCrN Figure 5-12. The contrast in the BF image between the layers decreased after the heat treatment. This is more apparent at the coating surface. In the middle of the coating the same speckles were observed in the columns indicating a lack of mass in this area (Figure 8-10). Some arrows have been placed to indicate regions were a faint nanolayer structure is visible. No superlattice reflections were observed from the nanolayered area. The base layer region shows no speckles in the columns (Figure 8-11). An arrow marked the start of the nanolayer region. Another arrow points out a bubbled zone at the substrate/ coating interface. These are areas lacking in mass contrast, too, probably created by out-diffusion of substrate species. From this observations it can be stated that the interfaces between the nanolayers start to dissolve from top to the bottom of the coating.

After heat treatment for 5h at 900°C an oxide layer on average of ~340nm in size, with oxide crystals locally as large as 170nm growing out of this layer, was observed (Figure 8-12). Beneath the oxide layer a region of about 100nm in size, including small speckles of ~4x4nm in size, reduced in mass contrast, were seen. Similar regions were observed in TiAlCrN and TiAlCrYN, where they were related to void formation. The contrast between the nanolayers is very week throughout the specimen. A BF image of the middle of the coating was taken as a comparison to previous ones (Figure 8-13). In addition, voids along the column boundaries and in the columns are visible.

8.2.3 EDX point analysis

An average content of 30±3at% Al, 20±2at% Ti and 44±2at% Cr was measured in the main coating body, in the case of the as-deposited and the heat treated specimen, for the normalised metal content using EDX analysis in the HB 501 STEM. The errors given for the EDX measurements represent fluctuations and do not represent the accuracy of the total result. In comparison

with the composition gained from RBS ($Ti_{0.26}Al_{0.26}N/Cr_{0.48}N$), especially the Ti and Cr value are not very close. The true value might lay in between the EDX and the RBS values, because of the difficulties analysing Cr and Ti with RBS.

8.2.3.1 Coating surface – oxide layer region

Spot analysis (Philips CM20), in connection with the TEM imaging, showed the increased amount of Cr in the oxide layer region after annealing for 1h at 900°C, this indicates the formation of Cr_2O_3 or a solid solution rich in Cr.

Point analysis was used to show detailed alterations in concentration through heat treatment at 1h at 900°C in the as-deposited sample, in the oxide layer as well as in the base layer region using a STEM microscope (HB 501 STEM). The profile shows in the last 150nm of the specimen a clear increase in the concentration of Cr and a drop in Al content (Figure 8-14). The highest amount of Cr is measured 75nm below the top of the specimen. The Cr content decreases from this peak until it drops to 33 at% on top of the sample. At the same time the Al content increases to 28 at %, which is equal to the average content in the main body of the nanolayered coating. The Ti content seems hardly effected by the heat treatment. The fluctuation increased to 20 ±5 at% for Ti in the oxide layer region. The cross over point between N and O is marked in the graph, indicating that the O-rich region starts behind the Cr-rich region. At the column boundaries, the maps show a decrease in intensity, indicating a lack of mass at the same region as observed in the TEM BF images.

8.2.3.2 Substrate/ base layer region

Comparisons of the Cr content in the base layer region before and after heat treatment showed similar results as found for $Ti_{0.44}Al_{0.54}Cr_{0.02}N$ (Figure 8-15). The Cr content in the base layer changes from ~4 at% to ~13 at% after heat treatment. Cr has diffused 300nm into the coating. A peak measured at the interface region, between substrate and base layer, stems probably from the Cr metal ion etch at the beginning of the deposition process. The electron probe of ~3nm would be sufficient to pick up significant changes in the interface region. The Cr-rich interface region is ~7nm thick [37]. Furthermore, in the stainless steel substrate a depletion of Cr of ~3at% was noticed after the heat treatment. In the case of Fe no significant difference in composition before and after heat

treatment was observed. This might be related to higher contamination, due to the ion milling process, of the as-deposited specimen. No difference in Al and Ti content in the base layer region was observed after heat treatment.

8.2.4 EDX mapping

Elemental maps of the coating surface were taken after heat treatment for 1h at 900°C (Figure 8-16). The difference in composition is not as clear as in the point analysis profile. The top of the coating surface shows a zone depleted in Ti and Cr. In the same region the O map shows the highest intensity. Below this region is an increased concentration of Cr visible in the map. The BF image, taken at the same time, indicates the presence of Al and Cr in the oxide layer. The presence of both elements would suggest the formation of a solid solution out of Cr and Al oxides.

After heat treatment for 1h at 900°C, differences in the intensity in the base layer region were visible, in elemental maps, stemming from the diffusion of Cr into this region (Figure 8-17). For Fe no such alteration of intensity was observed, which is in accordance with the point analysis. The Cr ion implanted zone visible at room temperature was not seen in the annealed specimen. Additionally, the base layer/ coating interface is not as well defined as in the as-deposited specimen. This indicates diffusion of Al, Ti and Cr in this region. For the Al map a variation of intensity is observed in the base layer region. The reaction of Al in this way was shown in similar $Ti_{0.44}Al_{0.54}Cr_{0.02}N$ and TiAlCrYN+Ox maps.

8.2.5 XRD analysis

Glancing angle XRD with an incident angle of 0.5° was used before and after heat treatment to determine the oxide phases formed (Figure 8-18). Although no significant oxide peaks were found after heat treatment for 1h at 900°C broad diffuse peaks were observed, which could not be identified as belonging to any particular oxide phase. The position of these peaks however, could indicate the formation of a solid solution (isomorphic compound) out of Al_2O_3/ Cr_2O_3. Using Equation 7-1 a content of 18 mol% Al_2O_3 was determined

from the {024} peak position. However, due to the weak response the result can not be very accurate. The weak response of the XRD scan results clearly from the thickness of the oxide layer and the very fine grain size of the oxide produced.

After annealing for 5h at 900°C XRD analysis showed the formation of TiO_2 (labelled T) together with $FeCr_2O_4$ or Fe_3O_4 (the two Fe oxides can form a solid solution) and the previously observed solid solution out of Al_2O_3/ Cr_2O_3 (labelled sol). The XRD pattern is shown in Figure 8-18. The content of Al_2O_3 in the solid solution was determined assuming Vegard's law and using Equation 7-1. The peak positions used were the {012} and {024} reflections. The content of Al_2O_3 in the solid solution is 8 mol% for the {012} and 11 mol% for the {024} peak position. That the peak shift is caused by stress can probably be neglected after annealing for 5h at 900°C.

8.2.5.1 Stress analysis

XRD with a fixed incidence angle of 5° was used to measure the stress before and after heat treatment (Figure 8-19). A reduction in stress from –5.1 GPa for the as-deposited sample to –2.8 GPa for the specimen annealed for 1h at 900°C was determined using an E modulus of 500 Nmm^{-2}.

8.3 Effects variation in bias voltage on the oxidation behaviour

Variations in the bias voltage during deposition of TiAlN/CrN were used to increase both the density and hardness of the coating; resulting in an increase in compressive stress in the coating [46, 130]. For the TiAlN/CrN system the hardness increased from $HK_{0.25}$ 3400 to $HK_{0.25}$ 4100 by increasing the bias voltage from –75V to –95V. In parallel the compressive stress increased from –5.1 GPa (-75V) to –9.2 GPa (–95V). In addition to this, the effect on the oxidation resistance was also studied.

8.3.1 TEM imaging

BF transmission electron microscopy of the as-deposited base layer region of the TiAlN/CrN specimen deposited using –95V bias (in the nanolayer region), showed a densification between the base layer and the nanolayer region (Figure 8-20). This densification effect of the increased bias voltage is more obvious when this image is compared to one shown previously from the same region deposited using –75V bias (Figure 8-1).

8.3.2 TG measurements

Figure 8-21 and Figure 8-22 show continuous and isothermal thermogravimetric results for coatings deposited at bias voltages of –75V, -85V and –95V. In both graphs the oxidation resistance of the coating increased with increasing bias voltage.

A graph of weight gain versus temperature Figure 8-21, shows that whilst the onset of rapid oxidation was not bias voltage dependent, i.e. was 870°C for all coatings, the increase in weight gain with temperature (slope) decreases with increasing bias voltage. For the isothermal TG measurements, the weight gain decreased from 1.8±0.2 g/m^2 to 1.3±0.2 g/m^2 as the bias voltage was increased from -75V to – 95 V after 10h (Figure 8-22). However, after 1h

exposure at 900°C there was no significant effect of bias voltage on the measured weight gain, see Table 8-1. In contrast after 5h exposure a significant decrease in weight gain was observed with increasing bias voltage, see Table 8-1. At the same time the isothermal diagram showed a change in rate of weight gain after 2h. The reaction showed no saturation after 10h heat treatment.

TiAlN/CrN	TG, isothermal [g/m^2]		
	1h	5h	10h
-75V	0.65	1.50	1.79
-85V	0.63	1.31	1.50
-95V	0.52	1.07	1.33

Table 8-1: Weight gain values measured at various positions of isothermal TG curves.

8.3.3 XRD analysis

In comparison to the -75V bias specimen no significant oxide peaks could be detected at the -85V and –95V bias after heat treatment for 1h at 900°C using XRD in glancing angle geometry (Figure 8-23). The thickness of the oxide layer formed after heat treatment for 1h at 900°C did not change markedly between the different bias voltages. The lack of significant oxide peaks found in the XRD pattern for coatings annealed for 1h at 900°C clearly results from both, the thickness of the oxide layer and the very fine grain size of the oxide produced, i.e. peak broadening. The differences in relative peak intensities of {111} and {200} reflections between coatings deposited at –75V bias and coatings deposited at –85 and –95 V bias was due to a textural effect. After heat treatment at 900°C for 5h (Figure 8-24) the following oxide phases could clearly be identified: TiO_2 (JCPDS 21-1276), Cr_2O_3 (JCPDS 38-1479), Fe_3O_4 (JCPDS 19-629) and $FeCr_2O_4$ (JCPDS 34-0140) [94]. The Cr_2O_3 phase contains after the previous observations some Al_2O_3 but this was not part of the investigations in this case. The two Fe oxide phases have the same crystal structure (cubic) and are isomorphous. Under the same conditions of

temperature and time the overall peak intensities for the oxide phases also decreased as the bias voltage was increased from -75V bias to -95V bias indicating a decrease in thickness of the oxide layer with increasing bias voltage.

8.3.3.1 Stress analysis

Glancing angle parallel beam geometry was also used to measure the residual stress of the TiAlN/CrN superlattice coatings before and after heat treatment. The results from the stress measurements on the -85V and the -95V specimen are given in Figure 8-25 and Figure 8-26. In all cases the stress state was compressive and increased with increasing bias voltage from -5.1GPa at -75V bias to -9.2GPa at -95V bias in the as-deposited coating. However, the amount of stress relaxation increased with increasing bias voltage. In case of the -75V bias, -85V and -95V bias samples a decrease in stress of 1.4GP, 3GPa and 6.2GPa was measured. Interestingly, the stress level after heat treatment was similar to a $Ti_{0.44}Al_{0.54}Cr_{0.02}N$ coating (-3.8GPa). It is known that an increase in bias voltage increases the amount of defects in the coating [63]. The difference in the ratio of reduction of residual stress indicates that mainly defects are responsible for the reduction in stress. The residual stress values for a monolithic $Ti_{0.44}Al_{0.54}Cr_{0.02}N$ coating were included for comparison purposes. The stress levels in the superlattice coatings were systematically higher than that of the monolithic coating.

8.4 Discussion

The positive effect of alloying Cr into a binary type coating was investigated by [29, 30]. In the case of CrAlN after heat treatment an outermost layer of a Cr-enriched oxide was found. The next layer (towards the nitride) contained a mixture of Cr and Al oxides. Beneath these layers is an oxynitride layer created by inward diffusion of O. In this study of TiAlN/CrN the oxide consists out of an outermost layer of Cr and Al oxides on top of a layer enriched in Cr after heat treatment for 1h at 900°C. After 5h annealing a speckled zone caused by oxidation was observed. The speckled area could be caused by a lack of mass. The CrAlN and the TiAlN/CrN coating have common features, like the solid

solution formation. Further investigations are necessary to show if the TiAlN/CrN zone influenced by oxidation in the nitride coating indicates the formation of an oxynitride. The monolithic TiAlCrN coating with a low content of Cr (3at%) still oxidised by the formation of a bi-layer out of Al_2O_3 and TiO_2. However, when the CrN component of the TiAlN/CrN nanolayer was increased the oxidation behaviour tended towards that of the CrAlN coating.

The observed length of voids along the column boundaries was less than for the $Ti_{0.44}Al_{0.54}Cr_{0.02}N$ coating in the as-deposited condition. However, after heat treatment for 1h at 900°C bands of voids could be observed along column boundaries connecting the coating surface with the substrate material. At the same time speckled areas in the BF image showed a lack of mass contrast in close proximity to the boundaries and in the column boundaries. This particular behaviour was not observed before and might be attributed to a high defect density in the nanolayered structure. The higher stress value and the increased rate of recovery (after thermal treatment decrease in residual stress) with increasing bias voltage are certainly an indication for this theory.

8.5 Summary

From all coatings observed the oxide layer grown after 1h at 900°C is minimal for the TiAlN/CrN coating. This layer showed no obvious discrete crystals in the oxide layer like the other coatings investigated. With XRD the formation of a solid solution of isomorphous rhombohedral Al_2O_3 and Cr_2O_3 after 1h at 900°C was noticed. The X-ray pattern showed broad peaks of 1.2 °2θ. Hence, the formation of a fine crystalline oxide layer can be concluded at –75V bias.

A densification of the coating was observed with increase of the bias voltage from –75V to –95V. However, after heat treatment all coatings showed bands of voids extending from the coating surface to the coating/ substrate interface.

The diffusion of substrate elements to the coating surface is somewhat slowed down in comparison to TiAlCrN, even so a Cr EDX map showed

diffusion into the base layer after 1h at 900°C, no Fe oxide was identified using XRD analysis on the coating surface. This indicates a positive effect of the nanolayered structure.

8.6 Figures:

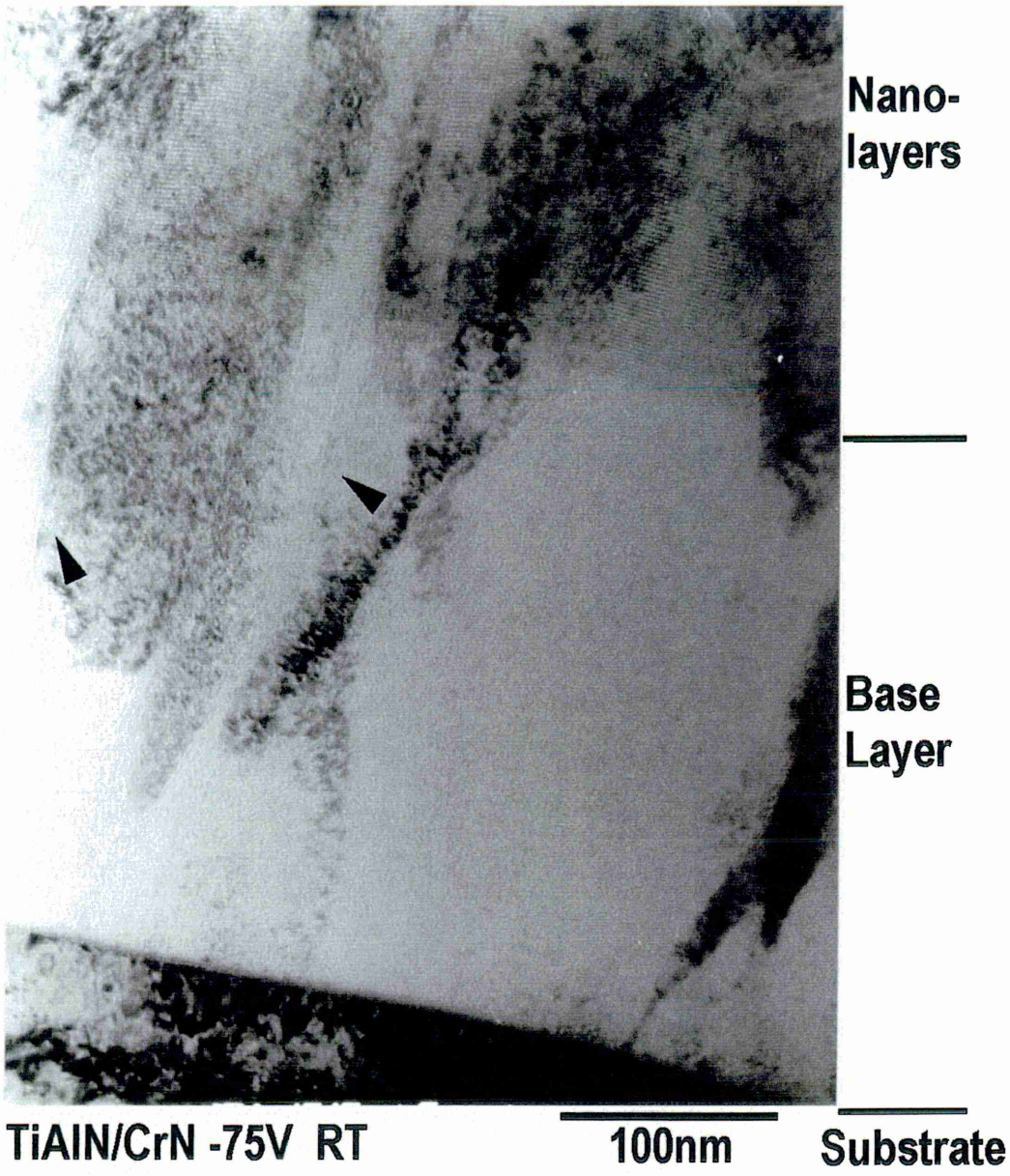

Figure 8-1: TEM BF image of the base layer region of the as-deposited TiAlN/CrN coating

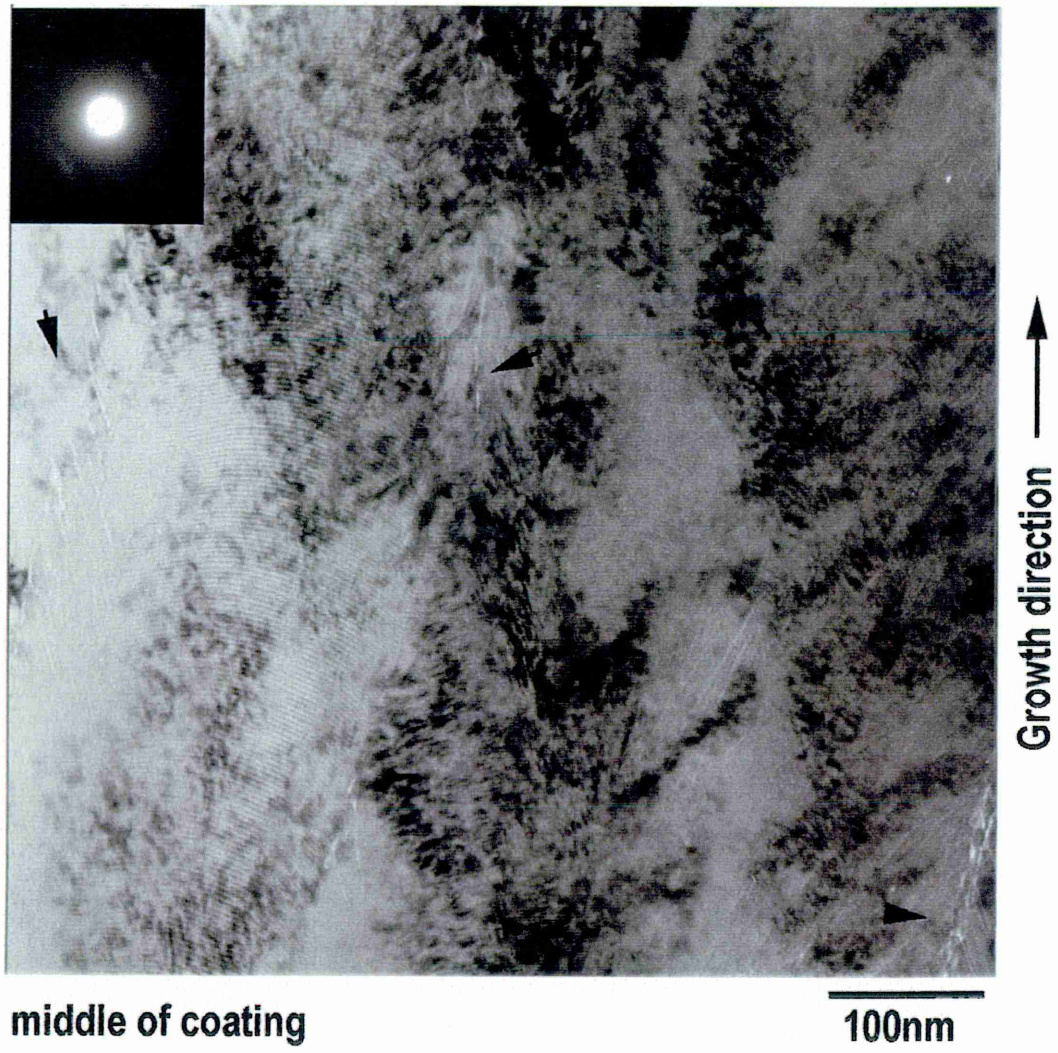

Figure 8-2: TEM BF image of the middle of the as-deposited TiAlN/CrN coating, together with a DP of the superlattice spots created by the nanolayer structure

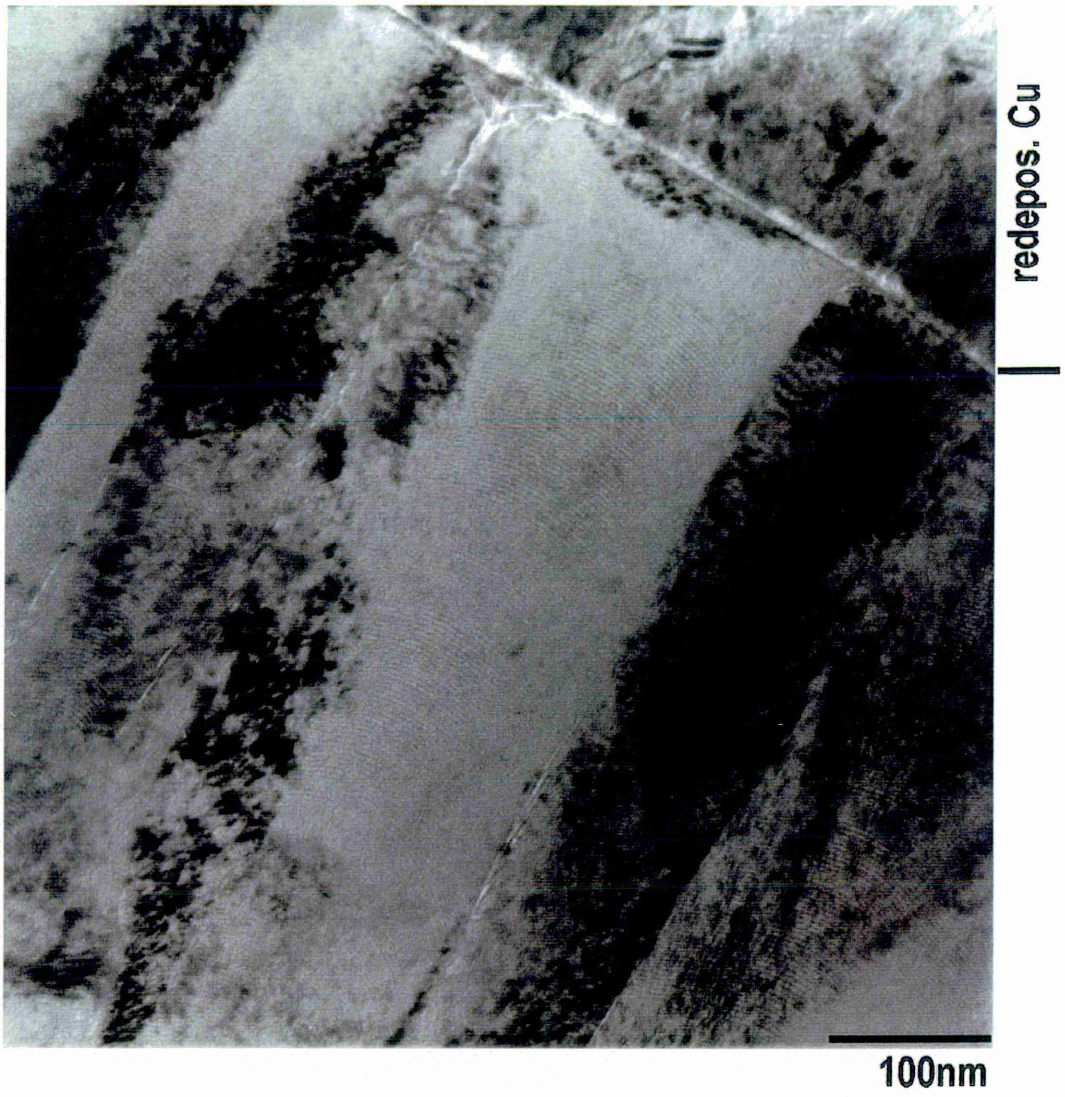

Figure 8-3: TEM BF image of the coating surface of the as-deposited TiAlN/CrN coating

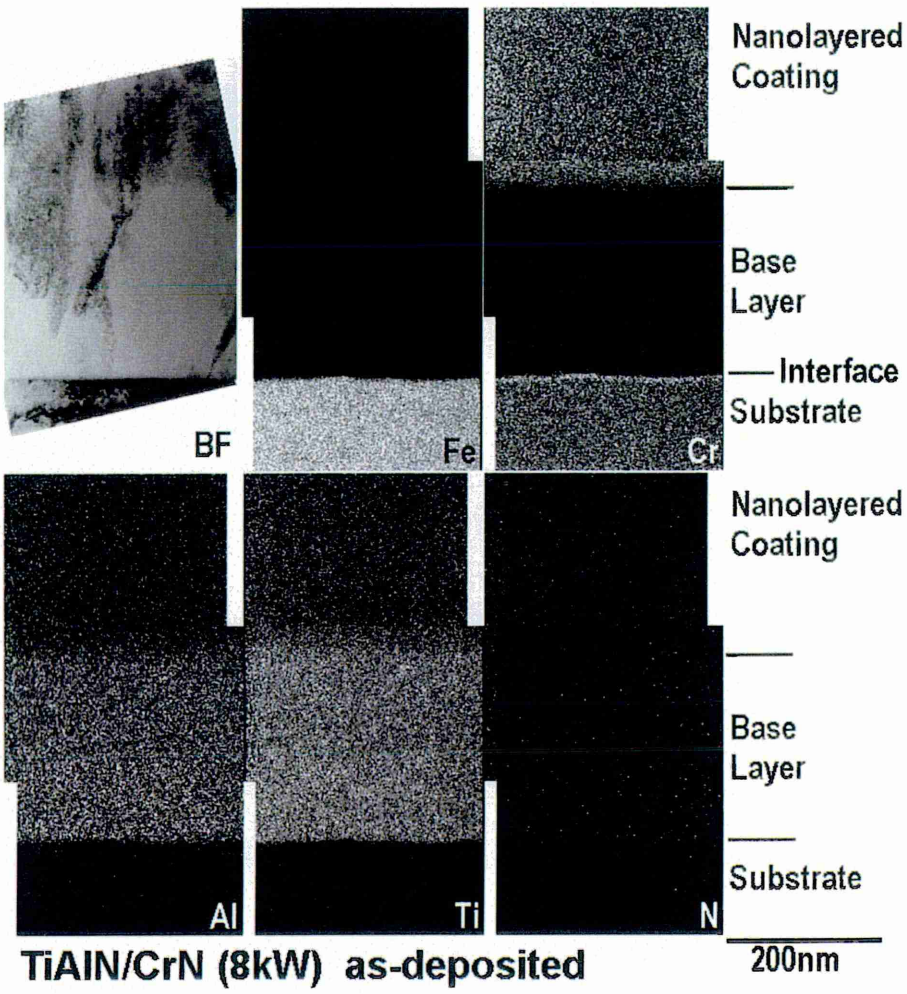

Figure 8-4: Elemental EDX map of the base layer region of the as-deposited TiAlN/CrN coating

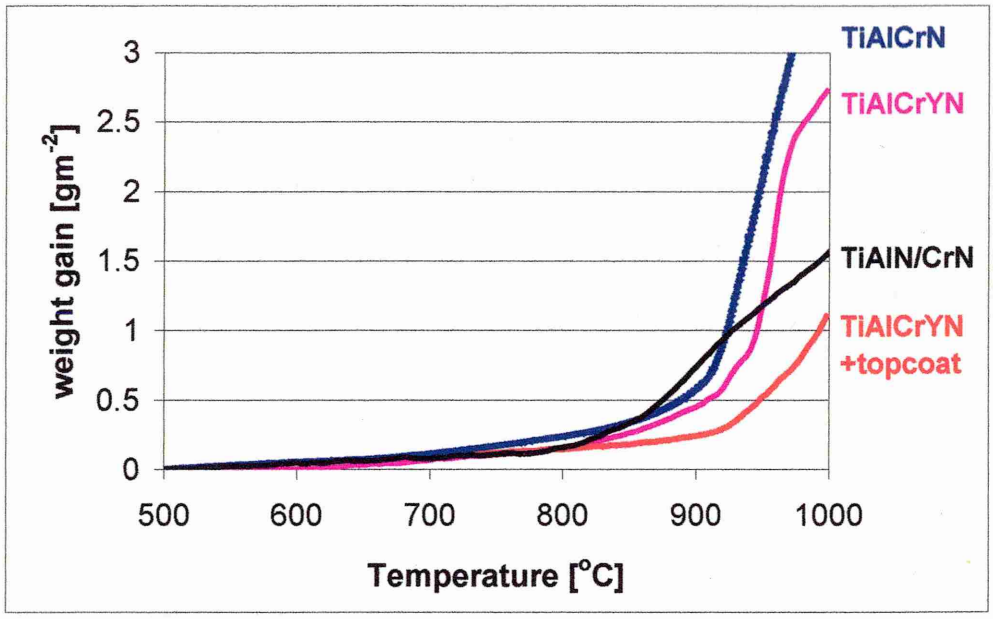

Figure 8-5: Continuous TG measurement of TiAlN/CrN in comparison to other coatings

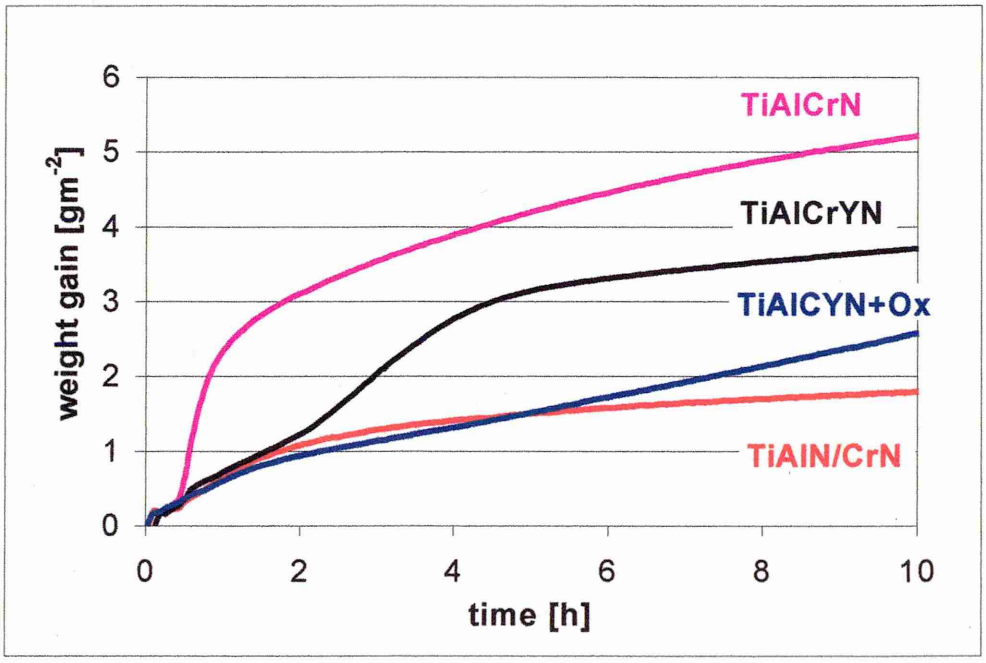

Figure 8-6: Isothermal TG measurement of TiAlN/CrN in comparison to other coatings

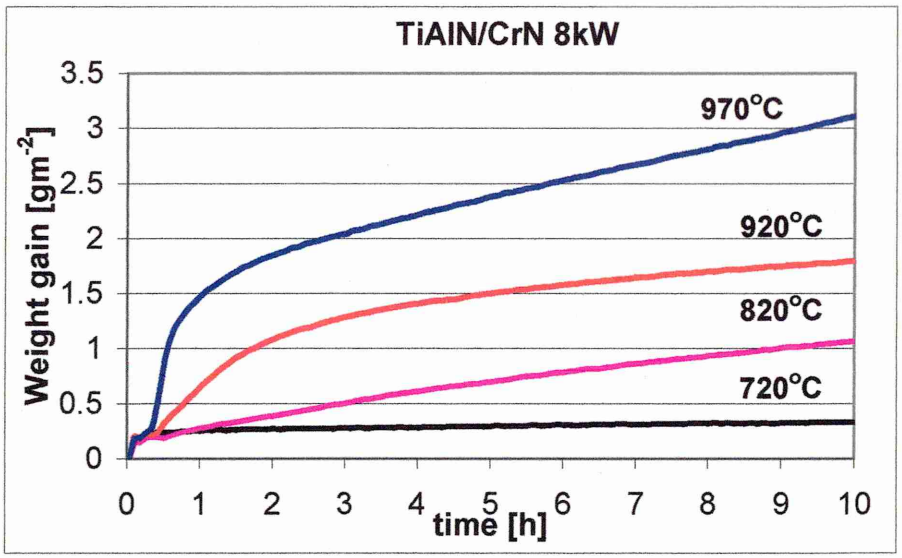

Figure 8-7: Isothermal TG measurements for TiAlN/CrN

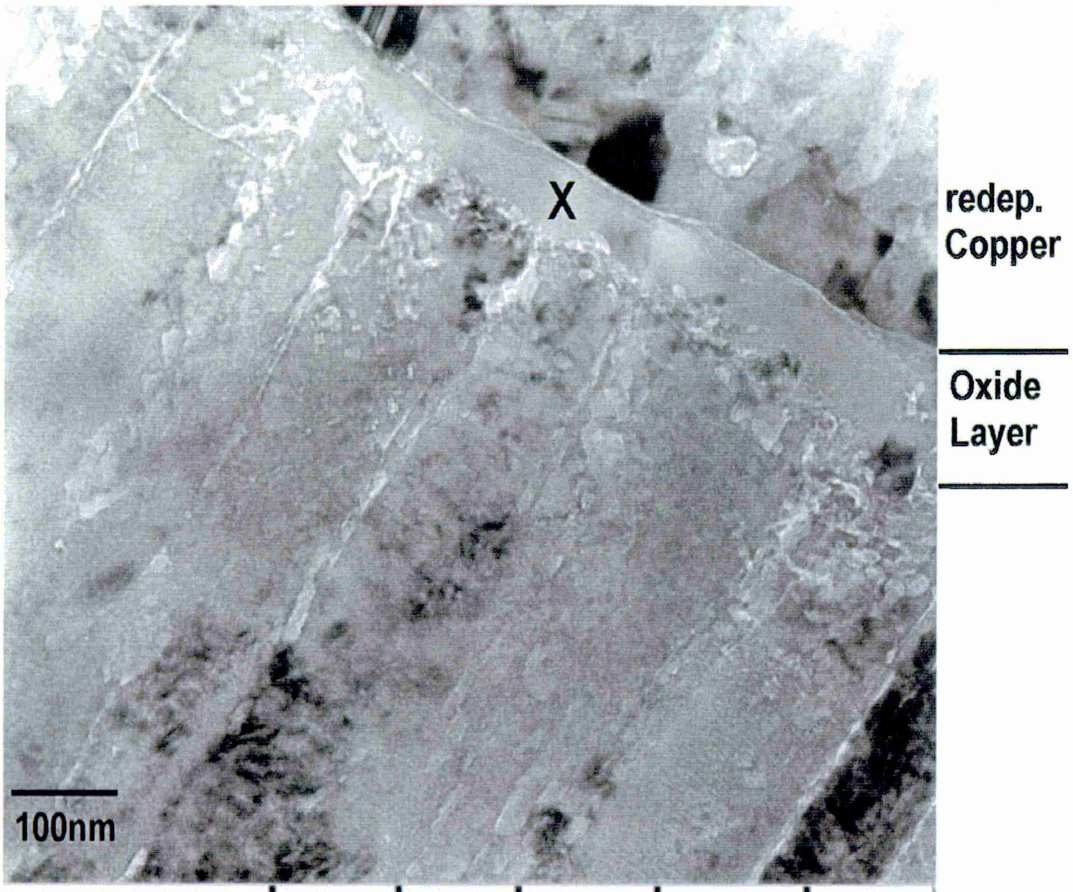

	N	O	Al	Ti	Cr
TiAlN/CrN RT	1	0.2	13.3	18.4	54
Oxide Layer	0	2.5	11.7	13	68.2

Figure 8-8: BF TEM image of the surface of TiAlN/CrN after heat treatment for 1h at 900°C, including results from EDX spot analysis performed using a probe of 40nm size in the TEM

Figure 8-9: Montage of BF TEM images of TiAlN/CrN after heat treatment for 1h at 900°C

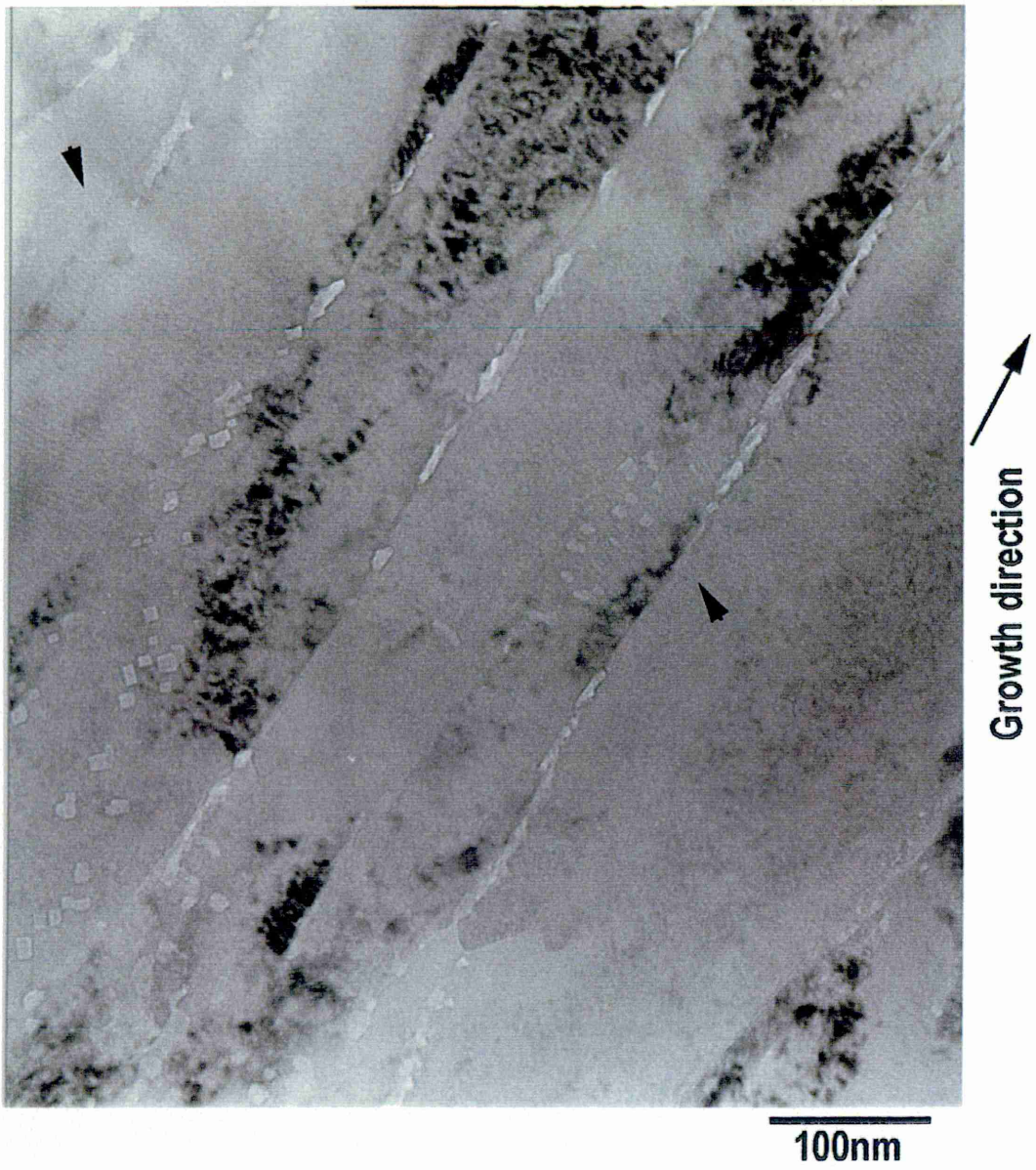

Figure 8-10: BF TEM image of the middle of TiAlN/CrN after heat treatment for 1h at 900°C

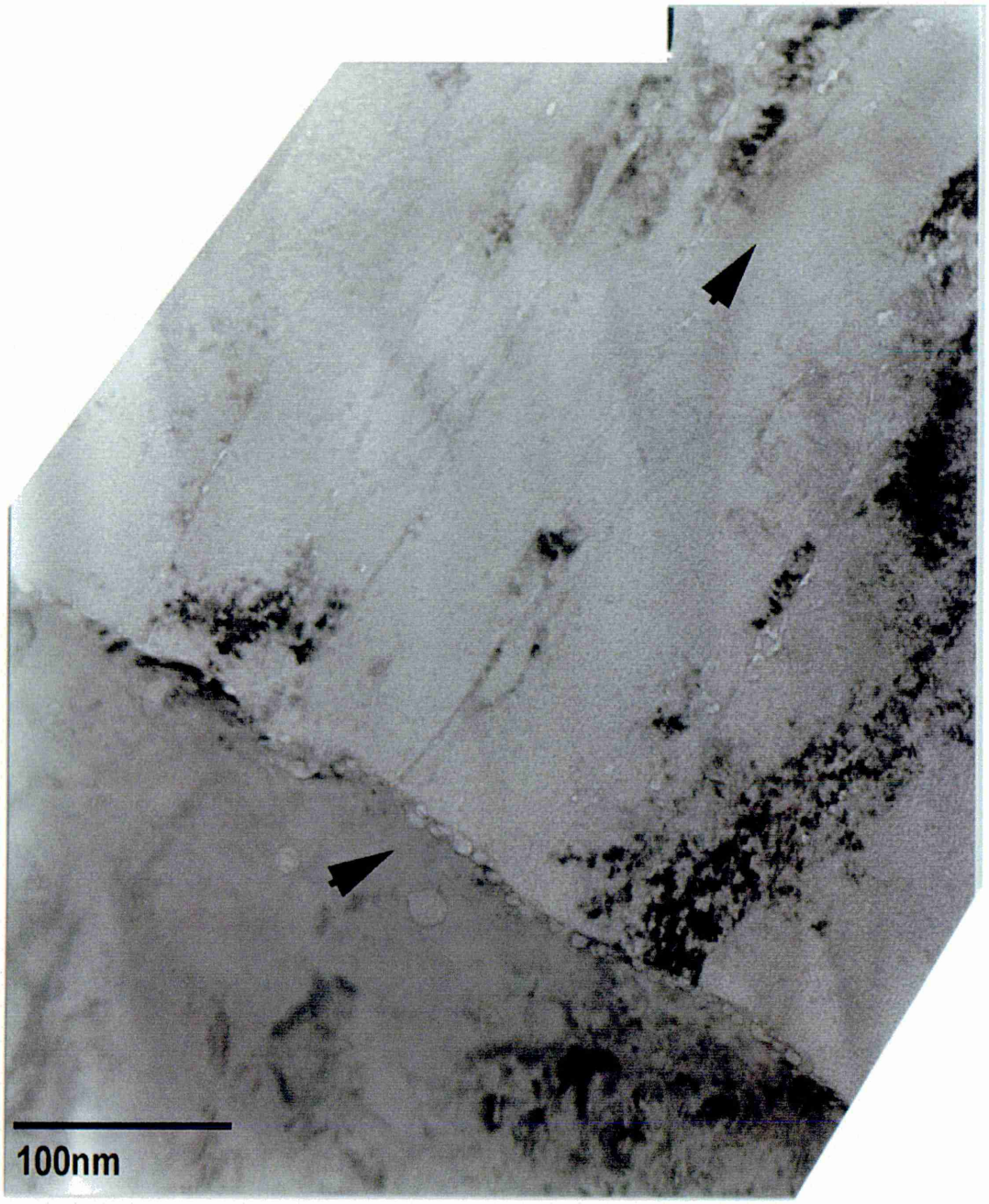

Figure 8-11: BF TEM image of the base layer region of TiAlN/CrN after heat treatment for 1h at 900°C

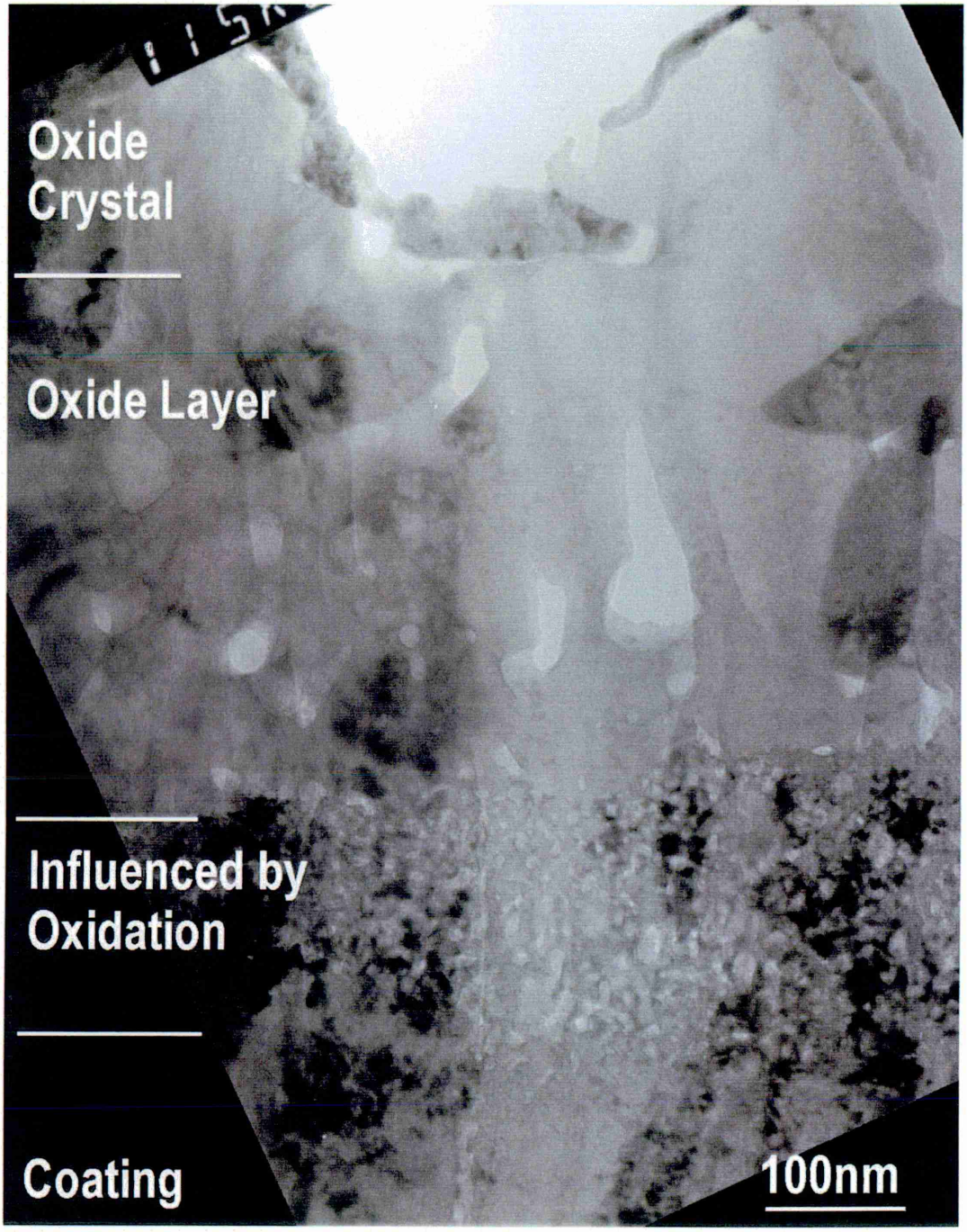

Figure 8-12: BF TEM image of the surface of TiAlN/CrN after heat treatment for 5h at 900°C, including results from EDX spot analysis performed using a probe of 40nm size in the TEM

Figure 8-13: BF TEM image of the middle of TiAlN/CrN after heat treatment for 5h at 900°C

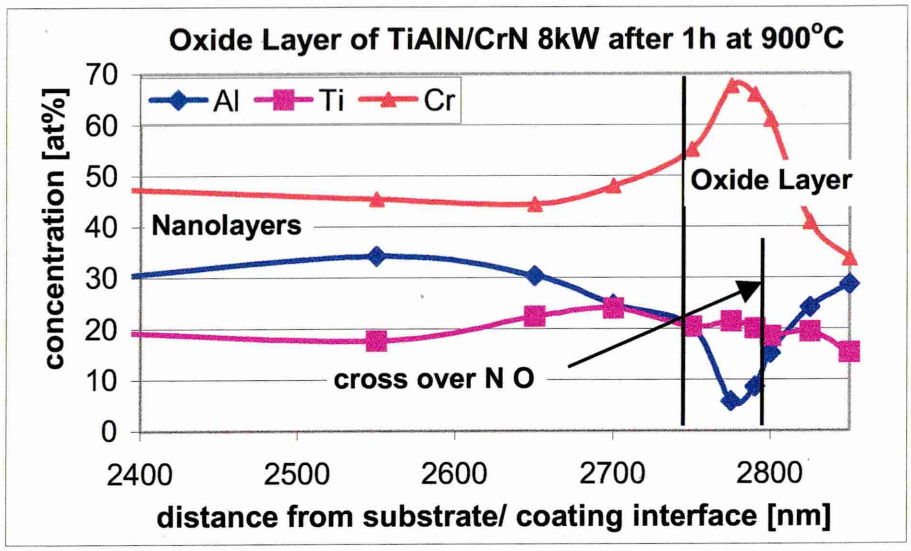

Figure 8-14: Point analysis through the oxide layer region of TiAlN/CrN after 1h at 900°C

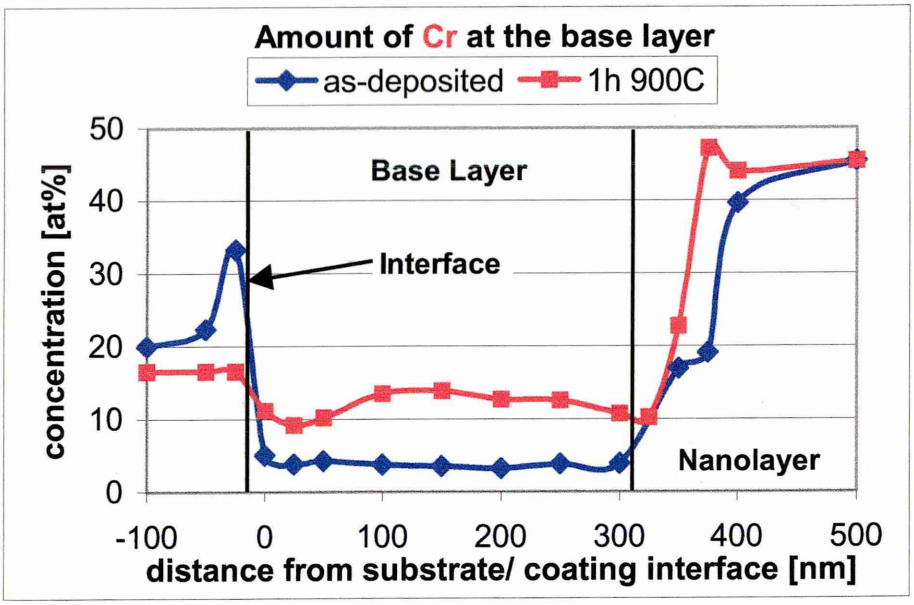

Figure 8-15: Point analysis in the base layer region of TiAlN/CrN comparing the Cr content before and after heat treatment

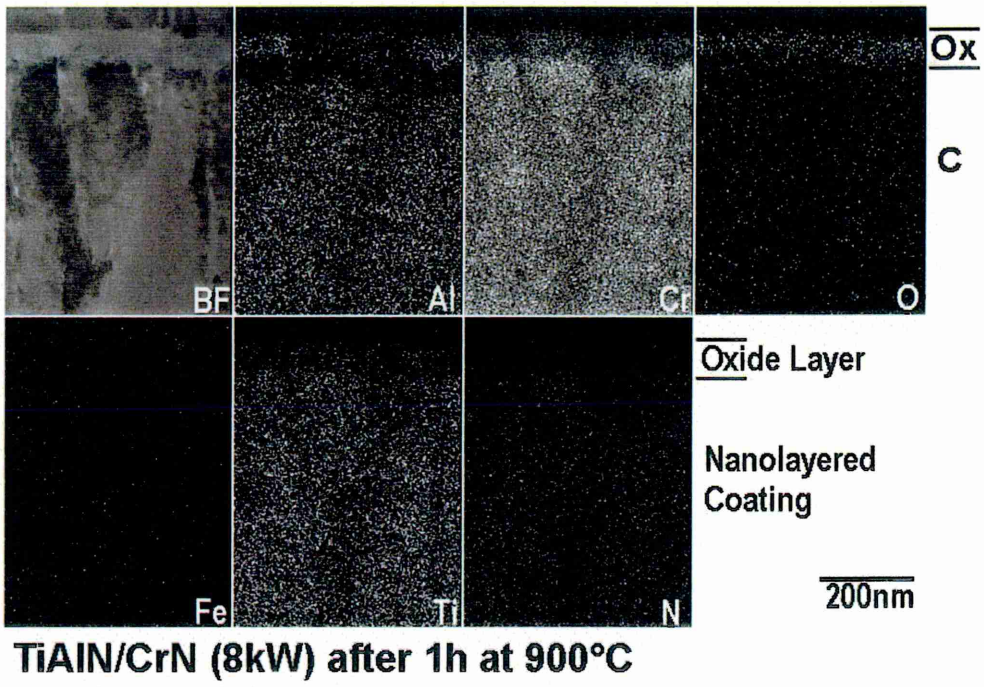

Figure 8-16: Elemental maps after heat treatment for 1h at 900°C of the surface of TiAlN/CrN

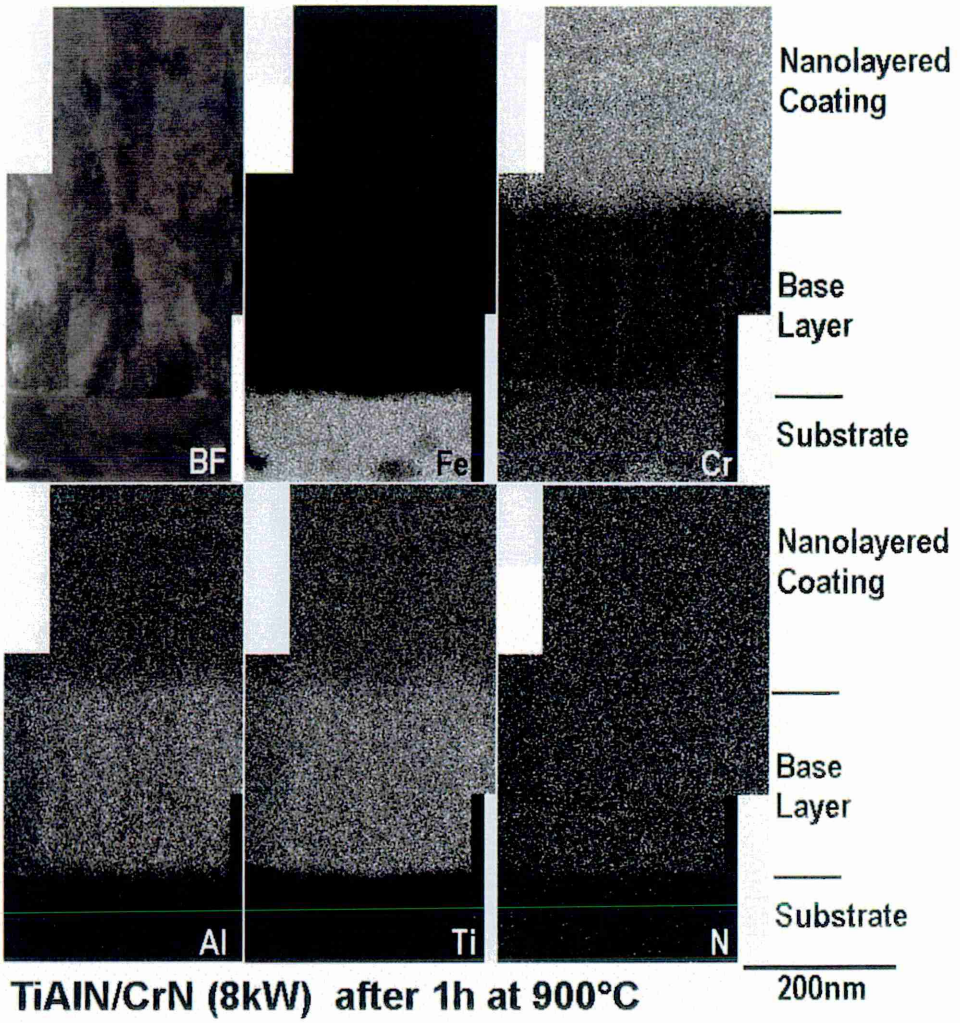

Figure 8-17: Elemental maps after heat treatment for 1h at 900°C of the base layer region of TiAlN/CrN

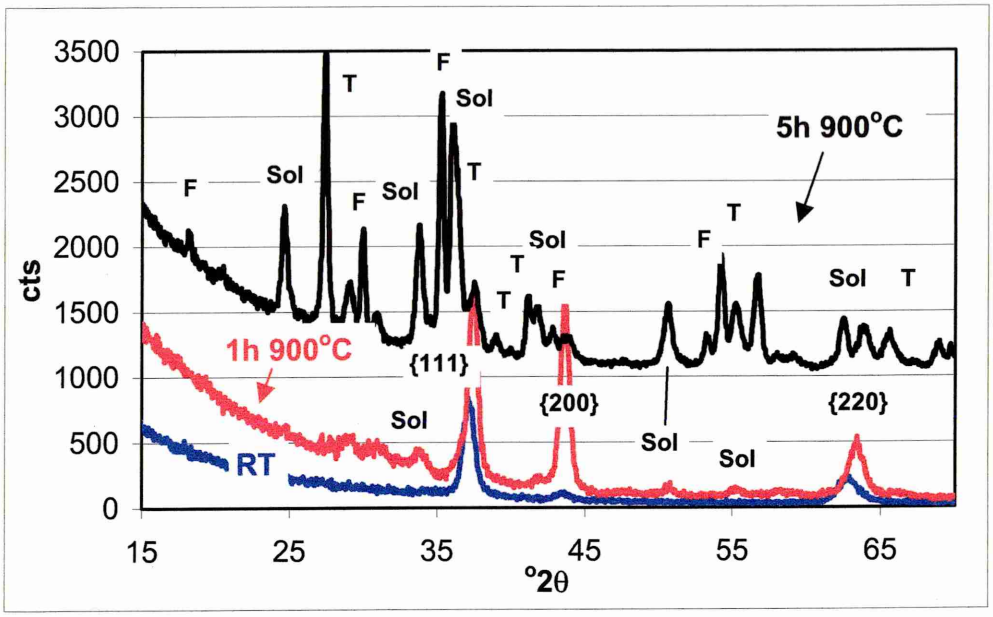

Figure 8-18: Glancing angle XRD using 0.5° incident angle of TiAlN/CrN after heat treatment at 900°C. F = $FeCr_2O_4$ or Fe_3O_4, Sol = solid solution of Al_2O_3/ Cr_2O_3, T = TiO_2

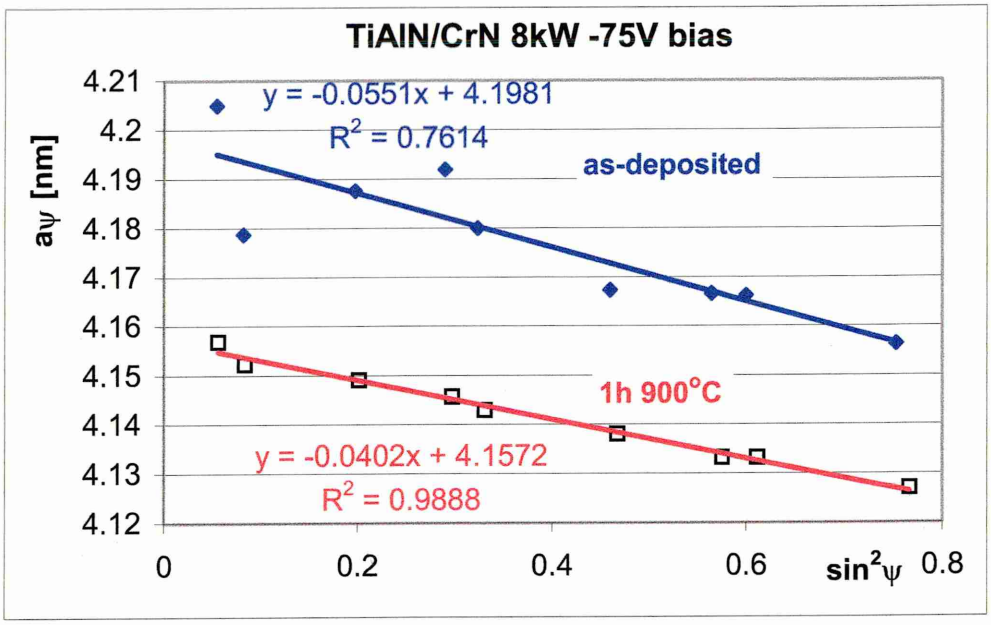

Figure 8-19: Stress measurement of TiAlN/CrN deposited with –75V bias, before and after annealing for 1h at 900°C using glancing angle XRD at 5° incident angle

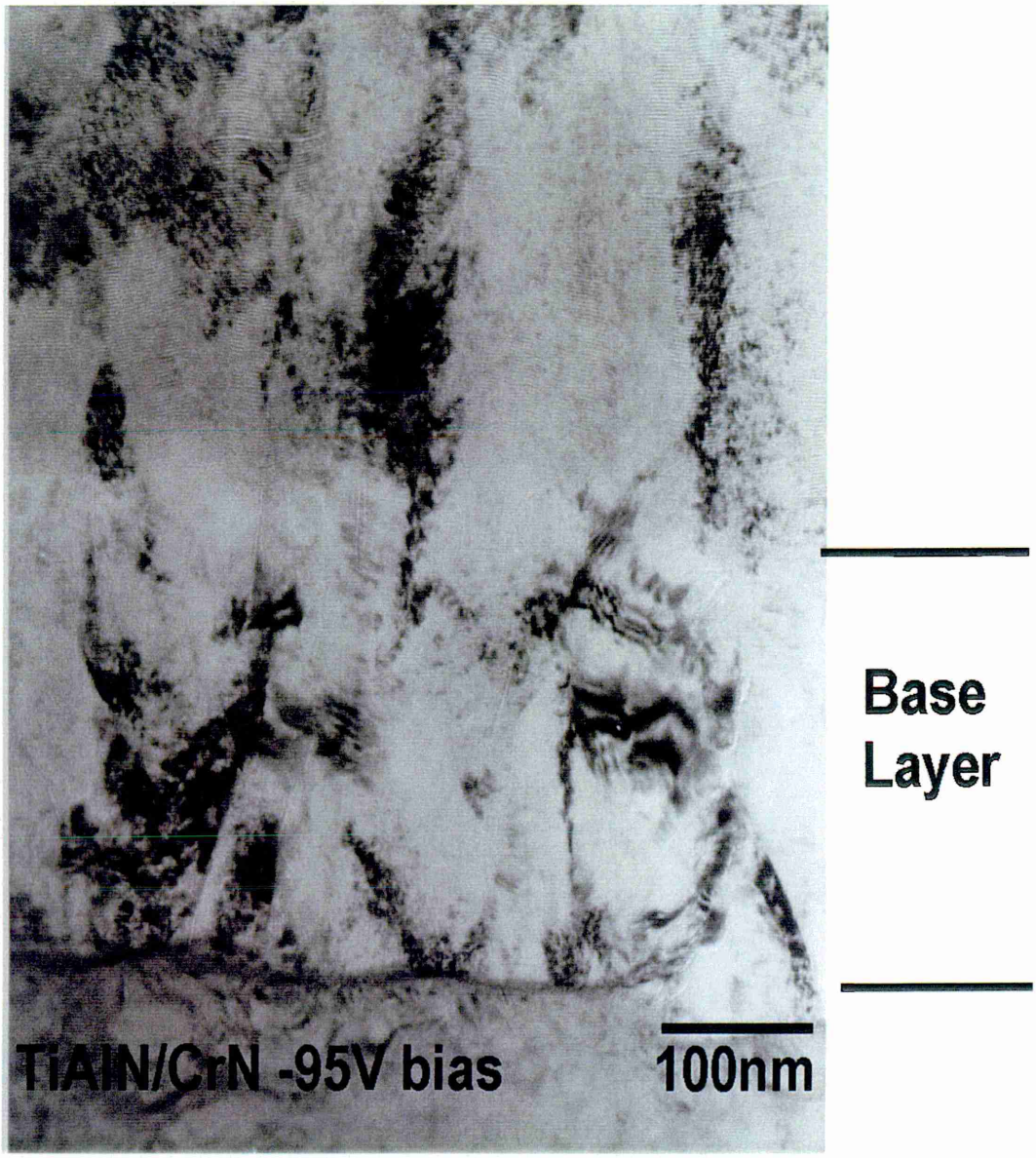

Figure 8-20: BF TEM image of the base layer region of TiAlN/CrN deposited using –95V bias

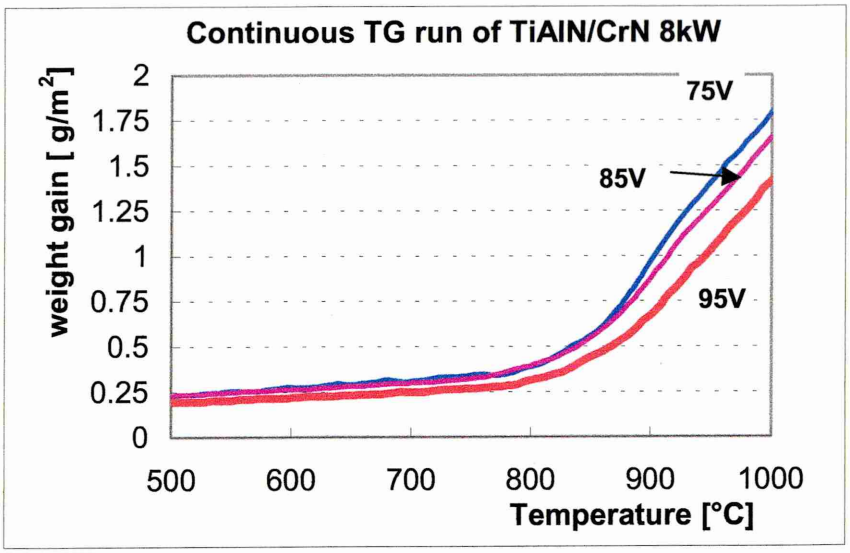

Figure 8-21: Continuous TG measurement of TiAlN/CrN deposited using various bias voltages

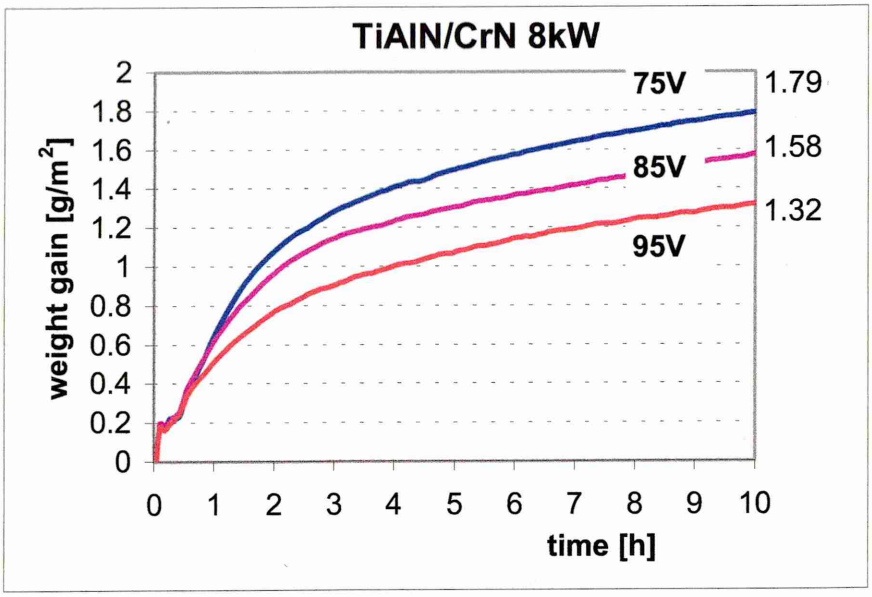

Figure 8-22: Isothermal TG measurement of TiAlN/CrN deposited using various bias voltages

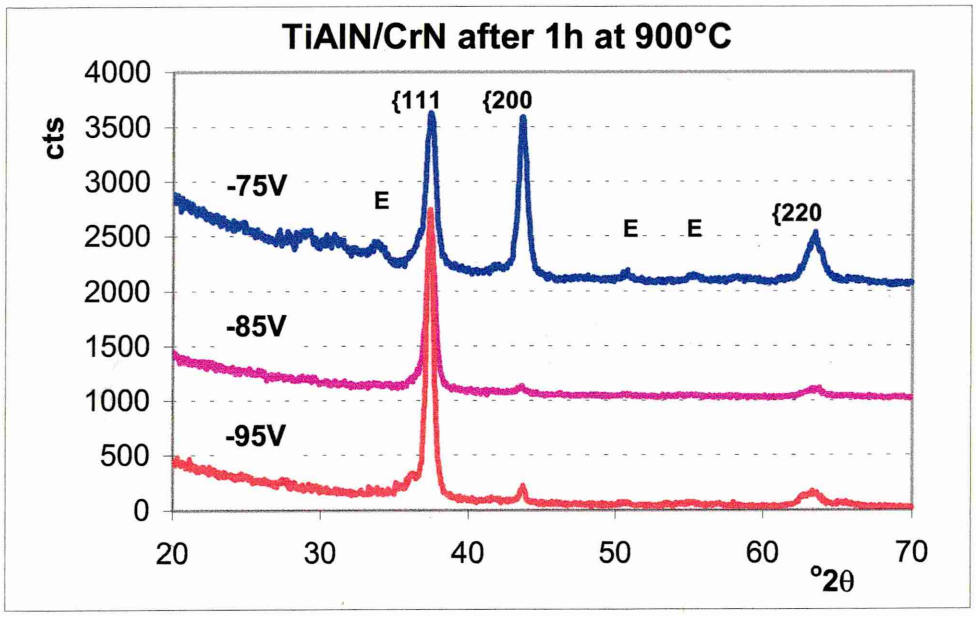

Figure 8-23: Glancing angle XRD of TiAlN/CrN after heat treatment for 1h at 900°C. E = peak position of Cr_2O_3 (eskolite).

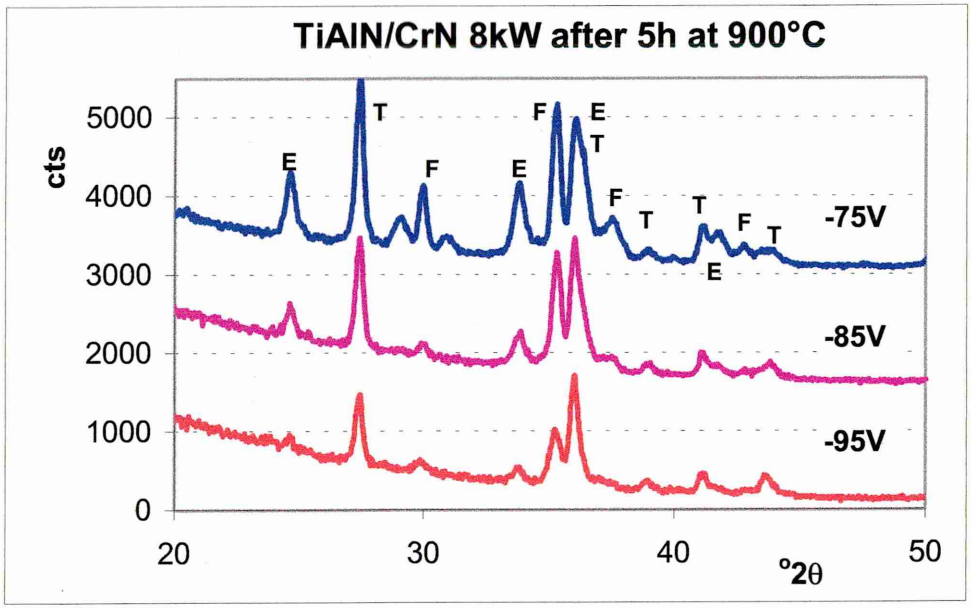

Figure 8-24: Glancing angle XRD of TiAlN/CrN after heat treatment for 5h at 900°C. E = peak position of Cr_2O_3 (eskolite), T = TiO_2, F = $FeCr_2O_4$ or Fe_3O_4.

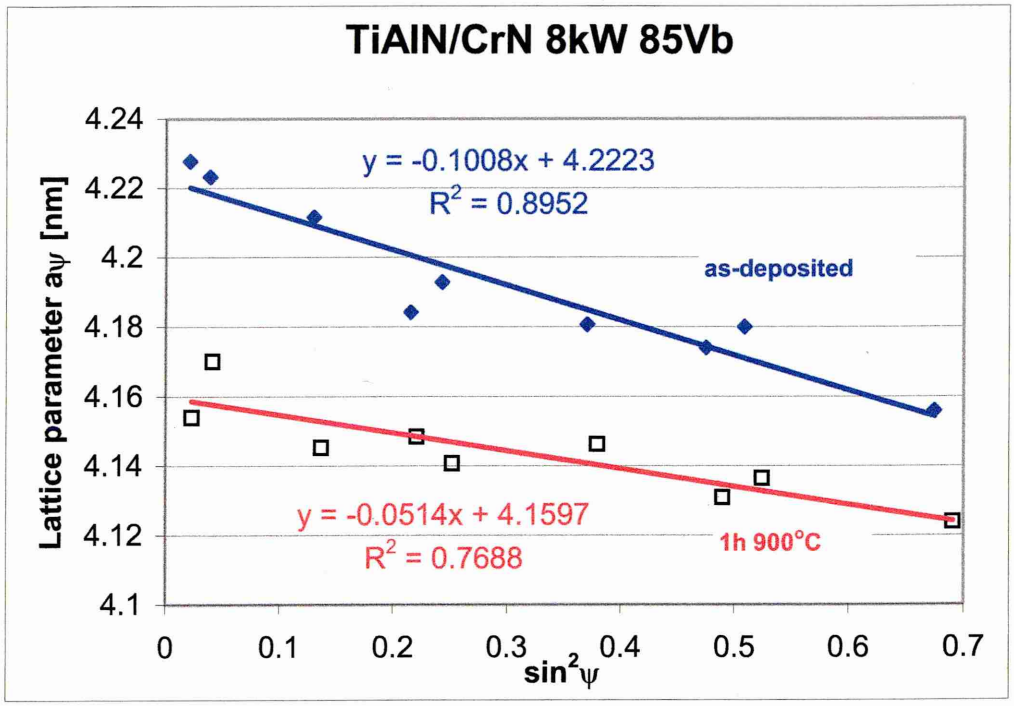

Figure 8-25: Stress measurement of TiAlN/CrN (–85V bias) before and after annealing for 1h at 900°C using glancing angle XRD at 5° incident angle

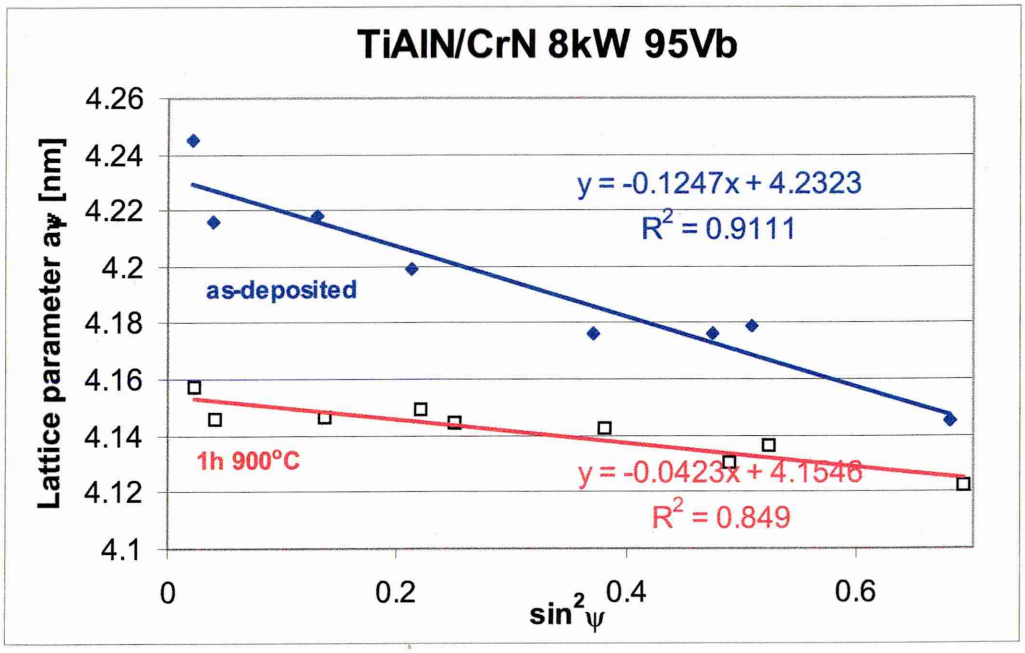

Figure 8-26: Stress measurement of TiAlN/CrN (–95V bias) before and after annealing for 1h at 900°C using glancing angle XRD at 5° incident angle

9 OVERALL DISCUSSION – COMPARISON BETWEEN COATINGS

Various TiAlN based nanolayered hard coatings have been investigated after heat treatment in air. The amount of oxidation and diffusion, differences in composition of the oxide layer and the annealed coating was examined. Additionally, the influence of the process parameters on the oxidation behaviour of nanolayered TiAlN/CrN was studied. TG and XRD measurements were used to show the overall effect of heat treatment. Using TEM and STEM combined with EDX analysis it was possible to show the changes in composition in the oxide layer and the nitride coating. This also allowed observations in the stability of the substrate/coating interface. Furthermore, local differences in the oxidation behaviour were observed at defects in the coating and at cracks formed, due to differences in the thermal expansion coefficient of the coating and substrate material during heat treatment using SEM and EDX analysis.

9.1 Effect of Defects

It was shown that the formation of oxides from substrate elements in and through defects (through growth defects or cracks) depends on the oxidation resistance of the substrate material. In the case of SS 304, M2 and cemented carbide (CC) the formation of substrate oxides increased from SS to CC. At higher temperatures the number of oxides formed from substrate elements increased at the coating surface in number and size. However, a continuous protective oxide layer formed by the nitride coating always surrounded these defects.

The localised formation of oxides from substrate elements after heat treatment was also mentioned by the following references:

Pinholes in the coating produce direct paths between the coating surface and the substrate material during heat treatment thus allowing transport of substrate elements to the surface and oxygen to the substrate [123, 167]. Fe oxides were observed on a CrN coating sputter deposited onto Ck45 steel after

heat treatment for 2.5h at 600°C [123]. Fe oxides were also found on the coating surface of TiN deposited onto M2 steel by ion plating where the oxidation occurred in a steam sterilisation process at 130°C and 210 kPa pressure [167].

These observations show that the coatings are permeable at localised defects and oxidation of substrate material is possible in localised regions. The question remains how important these effects are in dry high speed cutting, considering the greater number of defects deposited on the cutting edge [73]. A source of defects, namely droplets, has been investigated by [24, 25, 54, 56]. The surface area covered by droplets after a Cr etch (arc deposition) on a flat surface using similar parameters, as for the coatings investigated in this thesis, was 15 x 10^3 mm^{-2}. The number of pinholes found on coatings deposited onto a cemented carbide surface is greater when compared with similarly coated flat steel surface. One possible reason is that the porosity observed in cemented carbides [175] could produce shadowing effects during sputter deposition thus increasing the number of pinholes in the coating. However, the performance of $Ti_{0.34}Al_{0.62}Cr_{0.028}Y_{0.012}N$ with overcoat during dry high speed cutting outperforms coatings (~twice the life time of TiAlN) from other manufacturers in a material that is difficult to cut (A2) [23, 145].

Another form of defect resulted from the mismatch in thermal expansion coefficients between coating and substrate and the resulting residual stress developed in the coating due to the heat treatment. The investigations were performed on nanolayered TiAlN/CrN coatings. It was shown that an increase in Cr content in TiAlN increased the oxidation resistance [21]. However, at the same time the mismatch in thermal expansion coefficient between the stainless steel substrate and the coating increased due to the increasing amount of Cr. In coatings with an expansion coefficient less than $6x10^{-6}$ K^{-1} (Cr content ≥ 30at%) cracks were observed after heat treatment for 1h at 900°C.

The formation of substrate oxides adjacent to coating oxides in cracks was observed and the quantity of substrate oxide formed was dependent on the time and temperature of the heat treatment. The formation of oxides from substrate elements showed that cracks provide a direct diffusion path between coating surface and substrate material.

The formation of cracks in coatings was previously observed by [11] and [90]. These investigations demonstrate the importance of optimisation of coating properties, in this case the oxidation resistance, with respect to the substrate material by changing the deposition parameters. The influence of heat treatment of the stress in the coating deposited onto different substrate materials was investigated by [89, 90, 92].

Depending on the application, e.g. protection against high temperature corrosion or biomedical application, the PVD process has to be adjusted to suppress the formation of substrate oxides via direct diffusion paths.

9.2 TG measurements

In this section the overall oxidation observed using TG on the various coating systems is discussed and compared.

Table 9-1 gives an overview of the results for the various coatings after heat treatment for 1h at ~900°C. Additionally, the oxide layer thickness measured on cross sectional TEM micrographs is given in the table.

Coating	Oxide layer thickness [nm]	Weight gain [gm^{-2}]	Onset point of rapid oxidation [°C]
TiAlCrN	800	1	900
TiAlCrYN	430	0.8	950
TiAlCrYN with overcoat	230	0.65	950
TiAlN/CrN	100	0.5	850

Table 9-1: Overview of TG measurements and oxide layer thickness

It is apparent that the oxide layer thickness decreases from TiAlCrN to the nanolayered TiAlN/CrN from 800nm to 100nm, whereas at the same time the weight gain is reduced from 1 gm^{-2} to 0.5 gm^{-2}. This difference is partially due to the different mass of the oxides formed (see Table 9-2) caused by the difference in composition. In addition the formation of voids in the oxide layer (caused e.g. by differences in thermal expansion coefficient) contributes to the measured oxide layer thickness, but not to the measured weight gain.

In the case of $Ti_{0.44}Al_{0.54}Cr_{0.02}N$ and $Ti_{0.22}Al_{0.26}N/Cr_{0.52}N$ the major oxides formed after 1h at 900°C are Al_2O_3 (Corundum) - TiO_2 (Rutile) and a solid solution of Cr_2O_3/ Al_2O_3, respectively. The difference in volume expansion in the case of the oxide layer on $Ti_{0.44}Al_{0.54}Cr_{0.02}N$ and the 'original' $Ti_{0.43}Al_{0.52}Cr_{0.03}Y_{0.02}N$ coating promotes void formation in between the oxide crystals (Table 9-2). In the case of the TiAlN/CrN coating a solid solution out of Cr_2O_3 and Al_2O_3 is formed, which probably prevents the formation of voids in the oxide layer due to stresses caused by a difference in volume expansion of the oxides.

The difference between the oxide layer thickness for the 'original' $Ti_{0.48}Al_{0.48}Cr_{0.03}Y_{0.014}N$ and the TiAlCrN coatings cannot be totally accounted for purely from weight gain considerations. Both coatings oxidise by the formation of an oxide bi-layer out of Al_2O_3 and TiO_2. The oxide layer thickness measured for TiAlCrYN could be thicker and oxide material might have been lost by abrasion and fracture during the sample preparation. However, it has been proposed by [170] that the oxide layer thickness difference results from the addition of Y into the coating. This effect of Y on the growth of oxide scales is reported also by [136, 137, 139].

A similar comparison of TiAlCrYN with and without overcoat was made. The difference in weight gain and oxide layer thickness stems from the oxynitride formation in the overcoat during deposition. The overcoat also contains an average of 25at% Cr, which is contributing to the difference between oxide layer thickness and weight gain (see Table 9-2).

Oxide	Volume [cm^3]	Mass [g]
Al_2O_3	25.6	101.96
Cr_2O_3	29.0	151.99
$(AlCr)O_3$ (solid solution)	27.3	126.97
TiO_2	18.8	79.90

Table 9-2: Volume expansion coefficients and mass for oxides formed. The values for the solid solution were calculated from Al_2O_3 and Cr_2O_3. The values for the Volume are from [80] and for the mass of the oxides [94] was used.

Isothermal curves of TG measurements on coatings heat treated in air (oxide reaction) are often fitted to a parabolic rate law in the literature (see Literature review – Chapter 2.3.1). However, the most reported data was collected for a short period of time (1-2h) and temperature range. Apart from the transformation of nitride into oxide other reactions such as adsorption, disintegration, crystal growth etc will influence the oxidation kinetics [176].

Some known interpretation of rate laws will be mentioned if they fit with the observations made using TEM:

Adsorption of oxygen is the first reaction step. In case voids are present at the column boundaries in the as-deposited coating oxygen adsorption can occur not only at the coating surface but also in pores. The isothermal curves of the coatings under investigation are steep in the first 45min indicating a rapid reaction. The enhanced rate at the beginning of the isothermal curves might be explained by oxidation proceeding not only at the surface but also through discrete pores. This can be along grain boundaries, defects or lines of disordered atoms [81], (p.141).

A parabolic rate law was established for all coatings under investigation [13] for exposure times of less than two hours duration at temperatures between 800°C and 950°C. The parabolic rate law is often associated with the Wagner diffusion model (see Chapter 2.3.1.2) [11, 28, 103]. However, the Wagner diffusion model applies only to compact scales and lattice diffusion. An approximate parabolic behaviour can also be followed by grain boundary diffusion. All heat treatment was below the Tamman temperature (Tamman temperature ~1200°C) where the activation energy for grain boundary diffusion is favoured over the activation energy of lattice diffusion [81], (p.140).

After an extended period of time (> 2h) the oxide layers observed using TEM showed some porosity. It is commonly observed that the reaction rate is linear with time during porous oxide scale formation. A phase boundary reaction mechanism is proposed as diffusion mechanism [81], (p. 233). An attempt was made to combine the effects of parabolic and linear diffusion. However, it was not possible to fit isothermal curves for the whole 10h period. A plausible explanation is that after longer exposure times the oxidation product formed contains substrate element species in addition to those from the coating. This means the rate is not only dependent on the oxidation of coating material but

also on the substrate material. The observed formation of oxides from substrate elements at defects will also contribute to the overall weight gain, even though the number of growth defects observed (15 x 10^3 mm^{-2}) is small [24].

9.3 Oxide layer formation

Overall oxidation, oxide layer thickness and oxides formed were further investigated using TEM and XRD. Coatings heat treated for 1h at 900°C are compared and discussed in this section:

$Ti_{0.26}Al_{0.26}N/Cr_{0.48}N$ was the coating with a minimum of oxide layer growth after oxidation for 1h at 900°C. An oxide layer thickness of ~100nm was measured. For the TiAlCrYN coating with overcoat an oxide layer of ~230nm and for TiAlCrYN without overcoat of ~430nm formed after heat treatment for 1h at 900°C. TiAlCrN in comparison formed an oxide layer of ~800nm after 1h at 900°C (Table 9-1).

The oxide layer in the case of TiAlCrN and TiAlCrYN consisted mainly of an Al_2O_3 and TiO_2 bi-layer. An Al_2O_3 oxide layer protects the coating from rapid oxidation at temperatures above 550°C (onset point of rapid oxidation of TiN) [11, 12]. The increased oxidation resistance of TiAlCrYN (Table 9-1) was investigated by [32, 33]. They postulated that Y segregates to the grain boundary, which hampers the diffusion of cations and anions and therefore increased the oxidation resistance of TiAlCrYN in comparison to TiAlCrN.

The positive influence of Cr in enhancing the oxidation resistance of TiAlN hard coatings was shown by [21]. After heat treatment of the TiAlN/CrN coating for 1h at 900°C the formation of Cr_2O_3 oxide layer could be identified using XRD. Elemental mapping and point analysis showed that in addition to Cr, Al was also found in the oxide layer. Because Cr_2O_3 and Al_2O_3 are isomorphous compounds they readily form a solid solution of the type (Cr_2O_3/Al_2O_3). The capability of Cr_2O_3 and Al_2O_3 to form a solid solution was originally reported in 1962 by [80], (p. 14) and was observed by [29] in connection with oxidation of sputter deposited CrAlN coatings.

The incorporation of a Cr-rich oxynitride overcoat to the TiAlCrYN coating led to the formation of a crystal mixture of Al_2O_3, Cr_2O_3 and TiO_2 in the oxide layer. The further reduction of the oxide layer thickness can be correlated to the

high concentration of Cr in the oxide layer, as well as the presence of the oxynitride layer.

After an extended period of time or at high temperatures oxides stemming from the substrate material were also identified using glancing angle XRD. Without extended XRD experiments (measurements on known standards) it is not possible to say to what proportion of the oxide layer consists of oxides grown on elements of substrate material or from the coating. However, the SEM investigations on oxidised samples showed that the contribution of substrate oxides increases if cemented carbides were used as substrate materials in comparison to M2 high-speed steel or stainless steel.

In addition, to the described oxide layer formation a thin band enriched in Cr was observed between the oxide layer and the nitride coatings after heat treatment for 1h at 900°C using STEM-EDX mapping. In the case of the TiAlCrN coating the Cr band (90±15nm) clearly formed from Cr from the stainless steel substrate (see Chapter 9.5). This band was also observed in the TiAlCrYN coating. In the latter the thickness of the Cr band was 30±7nm thick. Previous observations on the TiAlCrN and the TiAlCrYN coating system proposed increased interface stability due to the addition of Y into the coating [33]. This would be in agreement with the above reductions in the thickness of the Cr band assuming the Cr is stemming from the stainless steel substrate.

The TiAlCrYN with overcoat contains high concentrations of Cr in the near surface region. After prolonged oxidation (5h at 900°C) a thin Cr band between the nitride and the oxide was present. In view of the observations on the other coatings the Cr in the band might stem from the stainless steel. However, the oxide layer did not proceed beyond the deposited overcoat region. Therefore it is not possible to state if the Cr band between the oxide layer and coating stems from sputter deposited Cr or from the substrate.

Interestingly, an increase in Cr concentration was also observed for the TiAlN/CrN coating between the oxide and the nitride. Due to the high Cr content of this coating (26at%) it is assumed that this band contains Cr from the coating as well as from the substrate material. The stainless steel material is seen as

source because of the columnar nature of the coating (see TiAlCrN) and therefore the substrate elements can diffuse along column boundaries. Furthermore, TEM observations at the substrate/coating interface revealed the formation of voids associated with the out-diffusion of cations from the substrate.

9.4 Protection of the substrate/ coating interface

It was discussed in a previous section (Chapter 9.1) that oxidation of substrate material can occur locally through defects in the coating at temperatures typical for the oxidation temperature of the substrate material.

Using STEM-EDX analysis the effect of the heat treatment at the substrate/ coating interface was investigated to show what happens if no defects (growth defects and cracks) are present. The combination of point analysis and mapping revealed (i) quantitative information about the local concentration and (ii) qualitative information about the distribution of an element along and across a column.

It was observed that after heat treatment for 1h at 900°C substrate elements diffused mainly along the column boundaries towards the coating surface. In case of $Ti_{0.44}Al_{0.54}Cr_{0.02}N$ the diffusion of Cr and Fe proceeded through the entire nitride coating of ~2.8μm thickness.

The length of the diffusion path in the case of the nanolayered TiAlN/CrN coating appeared to extend no further than the base layer/ nanolayer interface (300nm). The high Cr content of the nanolayered coating did not allow the observation of any changes in concentration of the Cr content resulting from diffusion along column boundaries. However, the observation of diffusion along boundaries using STEM-EDX is not only dependent on the concentration but also on the thickness of the TEM sample. In a slightly thicker sample (~100nm) the observation of small changes in concentrations at the boundaries would not be possible because of signal loss. However, since the Fe map did not show any clear diffusion along boundaries for TiAlN/CrN one may conclude that

extensive diffusion of substrate elements along column boundaries did not occur.

For the two TiAlCrYN coatings a diffusion path of ~600nm into the TiAlCrYN coating was determined after heat treatment for 1h at 900°C. The contrast observed in the Cr and Fe map taken from the XTEM sample of the TiAlCrYN coating with overcoat is better than for the 'original' TiAlCrYN coating. Again, the reason for this is seen in differences in the thickness of the XTEM samples.

Using the above values for a diffusion path x and time t a diffusion constant D can be determined and compared between the TiAlCrN coating and the TiAlCrYN coating using Fick's law (Equation 9-1).

$$D = \frac{x^2}{t}$$ Equation 9-1:

For Cr diffusion in TiAlCrN a constant $D = 2.5x10^{-4}\ cm^2s^{-1}$ was determined; in case of TiAlCrYN $D = 1x10^{-6}\ cm^2s^{-1}$. Comparing these two values clearly reflects the benefit of adding 1at% Y to the TiAlCrN coating. The diffusion coefficient changes by two orders of magnitude from 2.5×10^{-4} for the columnar structured TiAlCrN to 1×10^{-6} for the fine grained TiAlCrYN. The columnar structure of PVD hard coatings increases the rate of diffusion. Thornton [61] observed that grain boundary diffusion rates can be orders of magnitude faster than bulk diffusion rates. Messier [60] compared diffusion in columnar structured coatings with blood flowing through veins. The interruption of the columnar structure will contribute to an increase in the diffusion path even so this structure is not stable for an extended period at high temperatures (see Chapter 9.5). In the case of diffusion of Fe and W lower values for D are expected because of the increased size of the diffusing species.

The main reduction in diffusion of substrate elements is caused by the addition of ~1at% Y into the TiAlCrYN coating. It was postulated by [32, 33] that the enhanced high temperature and oxidation resistance stems from Y and YO_x inhibiting grain boundary diffusion of both cation species towards the surface and O penetration into the film.

With STEM-EDX it was possible to study the diffusion of Y to the column boundaries after heat treatment for 10h at 800°C and 1h at 900°C. The nominal measured concentration of Y increased from 0.9at% (bulk) to 2.1 at% (boundary) in TiAlCrYN after heat treatment for 1h at 900°C. The diameter of the electron probe is large compared with the column boundary and therefore the actual concentration of Y at the grain boundary is considerably higher than the nominal 2.1at% value measured [172]. This preferential diffusion of Y to the grain boundary is understandable. The Y atom is large in comparison to Al, Ti and Cr. In as-deposited condition the fcc TiACrlN lattice is distorted by the incorporation of Y at the metal atom sites in the lattice. In the heat-treated sample, the Y diffuses to the lower energy grain boundary sites, which decreases the distortion in the bulk TiAlCrN lattice. This diffusion is made even more attractive for a reactive element such as Y with a high affinity for oxygen, due to the easy ingress of oxygen at the column and grain boundaries.

The EDX analysis of the XTEM samples showed that Y hampers indeed the diffusion of cations (e.g. Fe and Cr) as proposed by [32, 33]. This effect of Y was made clearly visible by comparing the amount of diffusing substrate species in the base layer (without Y) to the TiAlCrYN coating and by the elemental maps taken after 10h at 700°C, 10h at 800°C and 1h at 900°C.

9.5 Coating structure

An increase in the number of voids along the column boundaries was also observed after heat treatment for the TiAlCrYN coatings and TiAlN/CrN. In parallel stress relaxation occurred [129, 130]. The reduction in compressive stress and the formation of voids along the columns was related to the decrease on density of point defects which had been produced during the deposition process [63], [89]. The nanolayer structured TiAlN/CrN in comparison to the other films exhibited a relatively high degree of void formation. The compressive stresses measured in the TiAlN/CrN coating is high (-5.8GPa) in comparison to $Ti_{0.44}Al_{0.54}Cr_{0.02}N$ (-3.6GPa) and TiAlCrYN+Ox (-4GPa). This indicates that the void formation is related to an increase in defects resulting from layering of TiAlN and CrN (different lattice parameter).

However, no voids along the column boundaries were observed in the TiAlCrN coating after heat treatment for 1h at 900°C and in TiAlCrYN+Ox after heat treatment for 10h at 900°C. In both cases substrate elements diffused from the substrate/ coating interface to the coating surface along the column boundaries. One possible explanation is that substrate elements that diffused over the column boundaries to the coating surface could have filled the voids between the columns and thus no voids were observed using cross sectional TEM [145].

Another effect on the coating structure was observed after heat treatment of the fine grained interrupted columnar structured TiAlCrYN coating. A coarsening in the coating structure occurred with increasing time and temperature [178, 179]. After prolonged heat treatment (10h at 900°C) the coating had a typically columnar PVD coating microstructure. This would indicate that the fine grained coating structure created during deposition using an additional TiAlY target is contained within a network of coarser columnar grains (e.g. TiAlCrN). During grain growth and void formation it is possible to see the columnar nature of the coating again. Recrystallisation behaviour in sputter deposited TiB_xN_y and TiB_xC_y coatings after heat treatment was reported by [176]. It was also shown that it is possible to increase the onset point of rapid oxidation by refining the grain structure of the coating.

The nanolayered structure of TiAlN/CrN is stable to a higher temperature (5h 900°C). However, it was observed that the contrast between the layers decreased at higher temperatures. Additionally, the contrast between the nanolayers decreased from top of the coating to the bottom of the coating/ base layer interface. The interdiffusion between the nanolayers was more pronounced for layers closer to the surface than those closer to the substrate material. The progressive interdiffusion for TiAlN/CrN nanolayers was investigated after heat treatment at 500°C, 750°C and 1000°C by [21]. After 16h heat treatment at 750°C the nanolayers were just resolvable using TEM and XRD.

9.6 Future work

The investigation of the thin films using a combination of analytical techniques has led to a significant contribution to knowledge related to the oxidation behaviour of TiAlN based coatings. In particular the combination of EDX with STEM/ TEM revealed interesting information e.g. diffusion of elements and confirmed proposed theories concerning differences in the high temperature behaviour of TiAlCrN and TiAlCrYN. However, it will be interesting to map the TEM cross sections using a technique with better sensitivity to detect low atomic number elements such as N and O to investigate their diffusion behaviour. Energy electron-loss spectroscopy (EELS) would be the ideal technique to reveal this information.

An area yet to be investigated is: What impact has the local oxidation of substrate material on the performance of coated cutting tools? In other applications the formation of substrate oxides might be detrimental. It should be possible to adjust the coating process to minimise the formation of pinholes and defects further.

The incorporation of ~1at% Y into the coating improved the high temperature behaviour of TiAlCrN. It would be interesting to investigate other elements (e.g. Ce, La, Sc, Hf, Ta) that are frequently used in high temperature protection of materials to see if they are able to further improve the TiAlN type coatings [136, 137].

The deposition of TiAlCrYN directly onto the substrate would be advantageous for the thermal stability of the hard coating. However, the compressive stress would increase with a concurrent decrease in the adhesion between coating and substrate. Investigations of a multilayer structure starting with a TiAlCrYN coating at the substrate and some intermediate stress reducing layers might lead to further improvements.

The addition of an oxynitride nanolayered TiAlYN/CrN overcoat to TiAlCrYN improved the mechanical and the oxidation behaviour of the coating. Adjusting

the deposition process might reduce the formation of underdense regions after heat treatment in the oxide layer.

Marker experiments or deposition of coatings on a material not containing Cr would be very interesting to determine to what extent the Cr band observed on the coatings stems from Cr diffused from the substrate or from sputter deposited Cr.

An important step would be to correlate the oxides generated during tribological contact with the ones observed on the samples heat treated in a furnace. This would give some information of the temperatures generated during tribological contact and whether a protective oxide layer is forming.

10 CONCLUSIONS

It was found that elemental mapping in the STEM is an ideal tool to investigate the migration of elements in thin films when used in combination with TEM imaging.

The interrupted columnar structure found in the as-deposited TiAlCrYN+Ox coating changed gradually towards a typical columnar structure with increasing annealing temperature. First changes were observed at 700°C after 10h and at 900°C after 1h. The formation of void bands that connected the coating surface with the interface region was seen in the same sample. At the same time a reduction in stress was observed after heat treatment for 1h at 900°C.

The oxidation resistance and interface stability was markedly improved by the incorporation of ~1at% Y into a TiAlCrN coating. The addition of Y reduced the diffusion of cations (substrate elements) to the coating surface and improved the interface stability. Y was found in the TiAlCrYN coating at the column boundaries after heat treatment for 10h at 800°C and after 1h at 900°C. Y started to out-diffuse after 10h at 900 °C.

The presence of Y in the coating also reduced the oxide layer growth when compared with $Ti_{0.44}Al_{0.54}Cr_{0.02}N$. The oxide layer thickness was reduced by the presence of Y in TiAlCrN from 800nm to 430nm after heat treatment for 1h at 900°C. A further improvement in the oxidation resistance, reduction of oxide layer growth and tribological properties was achieved by depositing a Cr-rich oxynitride overcoat [145]. The TiAlN/CrN coating deposited using 8kW Cr target power showed the lowest weight gain and an oxide layer thickness of ~100nm after 1h at 900°C. This demonstrated the importance of Cr in the overcoat region of TiAlCrYN+Ox.

The investigation of the nanolayer structured TiAlN/CrN coating showed the beneficial effects of Cr in increasing the oxidation resistance. However, the addition of Cr altered the thermal expansion coefficient such that the mismatch between the stainless steel substrate and the coating was compensated by the formation of cracks in the coating. Cracks were observed on coatings deposited onto stainless steel after heat treatment for 1h at 900°C when the thermal expansion coefficient drops below ~$6x10^{-6}$ K^{-1}. In the case of TiAlN/CrN multilayers deposited using 8kW power on the Cr target the influence of the process parameters was investigated by changing the bias voltage from –75V to –95V. The number of cracks found after heat treatment on stainless steel substrates decreased with increasing bias voltage because of higher residual compressive stress.

The influence of the substrate material on the oxidation behaviour of the coating was observed by depositing TiAlN/CrN on stainless steel, high-speed steel and cemented carbide. It was shown that the appearance of oxides containing substrate elements on the surface depends on the presence of defects in the coating. More importantly, the oxidation resistance of the substrate material is directly correlated to the amount of oxides present on the coating surface after heat treatment.

11 REFERENCES

1. W.-D. Münz and I.J. Smith "*Wear resistant PVD coatings for high temperature (950°C) applications*" in *Society of Vacuum Coaters Technical Conference*. 1999. Chicago.
2. W.-D. Münz, C. Schönjahn, H. Paritong and I.J. Smith "*Hard Coatings Deposited by Combined Cathodic Arc Evaporation and Magnetron Sputtering (Arc Bond Sputtering: ABS)*", Le Vide, 2000. **3/4**(297): p. 205.
3. W.-D. Münz, D.B. Lewis, P.E. Hovsepian, C. Schönjahn, E. Ehiasarian and I.J. Smith "*Industrial scale manufactured superlattice hard PVD coatings*", Surface Engineering, 2001. **17**(1): p. 15-27.
4. T. Cselle and A. Barimani "*Today's applications and future development of coatings for drills and rotating cutting tools*", Surface and Coatings Technology, 1995. **76-77**: p. 712-718.
5. "*Metallic Sputtering: The key to better hard coating for cutting tools .*", Metals and Materials, 1976. **October**: p. 38-39.
6. G.J. Wolfe, C.J. Petrosky and D.T. Quinto "*The role of hard coatings in carbide milling tools*", Journal of Vacuum Science and Technology A, 1986. **4**(6): p. 2747-2755.
7. W.-D. Münz, F.J.M. Hauzer, D. Schulze and B. Buil "*A new concept for physical vapor depsotion coating combining the methods of arc evaporation and unbalanced-magnetron sputtering*", Surface and Coatings Technology, 1991. **49**: p. 161-167.
8. H. Holleck and H. Schulz "*Advanced layer material constitution*", Thin Solid Films, 1987. **153**: p. 11-17.
9. H. Holleck "*Material selection for hard coatings*", Journal of Vacuum Science and Technology A, 1986. **4**(6): p. 2661-2669.
10. J.-E. Sundgren and T.G. Hentzell "*A review of the present state of art in hard coatings grown from the vapor phase*", Journal of Vacuum Science and Technology A, 1986. **4**(5): p. 2259-2279.

11. McIntyre, J.E. Greene, G. Hakansson, J.E. Sundgren and W.-D. Münz *"Oxidation of metastable single-phase polycrystalline TiAlN films: Kinetics and mechanism"*, Journal of Applied Physics, 1990. **67**(1990): p. 225.

12. W.-D. Münz *"Titan aluminium nitride films: A new alternative to TiN coatings"*, Journal of Vacuum Science and Technology A, 1986. **4**: p. 2717.

13. I.J. Smith "*The improvment of TiAlN coatings by the incorporation of Y and Cr*", PhD Thesis, Sheffield Hallam University: Sheffield, UK, 1998.

14. U. Helmersson, S. Todorova, S.A. Barnett and J.-E. Sundgren *"Growth of single-crystal TiN/VN strained-layer superlattices with extremely high mechanical hardness"*, Journal of Applied Physics, 1987. **62**(2): p. 481-484.

15. S.A. Barnett *"Deposition and mechanical properties of superlattice thin films"*, in *Physics of Thin Films*, J.L.V. M.H. Francombe, Editor. 1993, Academic Press: London. p. 2-73.

16. H. Holleck and V. Schier *"Multilayer PVD coatings for wear protection"*, Surface and Coatings Technology, 1995. **76-77**: p. 328-336.

17. Q. Luo, W.M. Rainforth and W.-D. Münz *"TEM observations of wear mechansims of TiAlCrN and TiAlN/CrN coatings grown by combined steered-arc/ unbalanced magnetron deposition"*, Wear, 1999. **225-229**: p. 74-82.

18. H.W. Wang, M.M. Stack, S.B. Lyon, P. Hovsepian and W.-D. Münz *"The corrosion behaviour of macroparticle defects in arc bond-sputtered Crn/NbN superlattice coatings"*, Surface and Coatings Technology, 2000. **126**: p. 279-287.

19. M. Herranen, U. Wiklund, J.-O. Carlsson and S. Hogmark *"Corrosion behaviour of Ti/TiN multilayer coated tool steel"*, Surface and Coatings Technology, 1998. **99**: p. 191-196.

20. M. Nordin, M. Herranen and S. Hogmark *"Influence of lamellae thickness on the corrosion behaviour of multilayered PVD TiN/CrN coatings"*, Thin Solid Films, 1999. **348**: p. 202-209.

21. I. Wadsworth, I.J. Smith, L.A. Donohue and W.-D. Münz *"Thermal stability and oxidation resistance of TiAlN/CrN multilayer coatings"*, Surface and Coatings Technology, 1997. **94-95**: p. 315.

22. K.-D. Bouzakis, N. Vidakis, N. Michailidis, T. Leyendecker, G. Erkens and G. Fuss *"Quantification of properties modification and cutting performance*

of (TiAl)N coatings at elevated temperatures" Surface and Coatings Technology, 1999. **120-121**: p. 34-43.

23. W.-D. Münz, M.I. Lembke, D.B. Lewis and I.J. Smith "*Microstructure, composition and performance of PVD coatings designed for successful dry high speed milling*". in *15. International Plansee Seminar.* 2001. Reutte, Austria: Plansee AG Reutte.

24. S. Creasey, D.B. Lewis, I.J. Smith and W.-D. Münz "*SEM image analysis of droplet formation during metal ion etching by a steered arc discharge*", Surface and Coatings Technology, 1997. **97**: p. 163-175.

25. W.-D. Münz, I.J. Smith, D.B. Lewis and S. Creasey "*Droplet formation on steel substrates during cathodic steered arc metal ion etching*", *Vacuum*, 1997. **48**(5): p. 473-481.

26. M. Wittmer, J. Noser and H. Melchior "*Oxidation kinetics of TiN thin films*", Journal of Applied Physics, 1981. **52**(11): p. 6659-6664.

27. L. Hultman "*Thermal stability of nitride thin films*", Vacuum, 2000. **57**: p. 1-30.

28. H. Ichimura and A. Kawana "*High temperature oxidation of ion plated TiN and CrN films*", in *1st International Conference on Processing Materials for Properties.* 1993. Honolulu, Hawaii: The Minerals, Metals & Materials Society.

29. S. Hofmann and H.A. Jehn "*Oxidation of CrN and CrAlN hard coatings*", Werkstoffe und Korrosion, 1990. **41**: p. 756-760.

30. E. Huber and S. Hofmann "*Oxidation behaviour of chromium based nitride coatings*", Surface and Coatings Technology, 1994. **68/69**: p. 64-69.

31. B.-J. Kim, Y.-C. Kim, J.-W. Nah and J.-J. Lee "*High temperature oxidation of TiAlN coatings made by plasma enhanced chemical vapor deposition*", Journal of Vacuum Science and Technology A, 1999. **17**(1): p. 133-137.

32. I.J. Smith and W.-D. Münz "*Improved TiAlN PVD coatings for dry high speed cutting operations*", Surface Engineering, 1998. **14**(1): p. 37.

33. L.A. Donohue, I.J. Smith, W.-D. Münz, I. Petrov and J.E. Greene "*Microstructure and oxidation resistance of TiAlCrYN layers grown by combined steered-arc/ unbalanced magnetron sputter deposition*", Surface and Coatings Technology, 1997. **94-95**: p. 226-231.

34. W.-D. Münz, D. Schulze and F.J.M. Hauzer "*A new method of hard coatings: ABS (arc bond sputtering)*", Surface and Coatings Technology, 1992. **50**: p. 169-178.

35. I.G. Brown, B. Feinberg and J.E. Galvin "*Multiply stripped ion generation in the metal vapor vacuum arc*", Journal of Applied Physics, 1988. **63**(10): p. 4889-4897.

36. G. Håkansson, L.Hultman, J.-E. Sundgren, J.E. Greene and W.-D.Münz "*Microstructures of TiN films grown by various physical vapour deposition techniques*", Surface and Coatings Technology, 1991. **48**: p. 51-67.

37. C. Schönjahn, L.A. Donohue, D.B. Lewis, W.-D. Münz, R.D. Twesten and I. Petrov "*Enhanced adhesion through local epitaxy of transition-metal nitride coatings on ferritic steel promoted by metal ion etching in a combined cathodic arc/ unbalanced magnetron deposition system*", Journal of Vacuum Science and Technology A, 2000. **18**(4): p. 1718.

38. B. Chapman "*Glow Discharge Processes*" 1980, New York: John Wiley & Sons.

39. P. Robinson and A. Matthews "*Characteristics of a dual purpose cathodic arc/ magnetron sputtering system*", Surface and Coatings Technology, 1990. **43/44**: p. 288-298.

40. S. Kadlec, J. Musil and J. Vyskocil "*Influence of the pumping speed on the hysteresis effect in the reactive sputtering of thin films*", Vacuum, 1987. **37**(10): p. 729-738.

41. W.P. Sproul "*High rate reactive sputtering process control*", Surface and Coatings Technology, 1987. **33**: p. 73-81.

42. S.L. Rohde "*Sputter Deposition*", in *ASM Handbook No.5*. 1994. p. 574-580.

43. B. Window and N. Savvides "*Charged particle fluxes from planar magnetron sputtering sources*", Journal of Vacuum Science and Technology A, 1986. **4**(2): p. 196-202.

44. S.L. Rohde, A.J. Nelson and W.D. Sproul "*Characterization of TiN films deposited using multicathode unbalanced magnetrons*", Journal of Vacuum Science and Technology A, 1992. **10**(4): p. 1797-1803.

45. W.-D. Münz "*The unbalanced magnetron: current status of development*", Surface and Coatings Technology, 1991. **48**: p. 81-94.

46. J. Musil, J. Vyskocil and S. Kadlec "*Hard coatings prepared by sputtering and arc evaporation*", in *Physics of Thin Films*, J.L.V. M.H. Francombe, Editor. 1993, Academic Press: London. p. 80-139.

47. P.C. Johnson "*Physics of Thin Films*", The cathodic arc plasma deposition of thin films, Vol. 14. 1989: Academic Press.

48. R.L. Boxman and S. Goldsmith "*Cathode-spot arc coatings: physics, deposition and heating rates and some examples*", Surface and Coatings Technology, 1987. **33**: p. 153-167.

49. P.A. Lindfors, W.M. Mularie and G.K. Wehner "*Cathodic arc deposition technology*", Surface and Coatings Technology, 1986. **29**: p. 275-290.

50. S. Ramalingam "*Controlled vacuum arc material deposition*" - *Methods and apparatus*, US Pat. N. 04673477 C23 C14/C22, 1987.

51. C.F. Morrison "*Method and apparatus for evaporation arc stabilisation including initial target cleaning*", US Pat. N. 4448659 C23 C15/00, 1984.

52. W.M. Mularie "*Evaporation arc stabilization*", US Pat. N. 4430189 C23 C15/00, 1989.

53. R.L. Boxman "*Handbook of Vacuum Science and Technology*", ed. P.J.M. R.L. Boxman, D.M. Sanders. 1995, New Jersey, USA: Noyes Publications.

54. I. Petrov, P. Losbichler, D. Bergstrom, J.E. Greene, W.-D. Munz, T. Hurkmans and T. Trinh "*Ion-assisted growth TiAlN/ TiNbN multilayers by combined cathodic-arc/ magnetron-sputter deposition*", Thin Solid Films, 1997. **302**: p. 179-192.

55. W.-D. Münz, D.B. Lewis, S. Creasey, T. Hurkmans, T. Trinh and W.v. Ijezendorn "*Defects in TiN and TiAlN coatings grown by combined cathodic arc. unbalanced magnetron technology*", Vacuum, 1995. **46**(4): p. 323-330.

56. R.L. Boxman and S. Goldsmith "*Macroparticle contamination in cathodic arc coatings: generation, transport and control*", Surface and Coatings Technology, 1992. **52**: p. 39-50.

57. H. Paritong "*Development of corrosion resistant niobium-based PVD coatings*", PhD Thesis, Sheffield Hallam University: Sheffield, UK, 2000.

58. I. Milosev, H.-H. Strehblow and B. Navinsek "*Comparison of TiN, ZrN, CrN hard nitride coatings: Electrochemical and thermal oxidation*", Thin Solid Films, 1997. **303**: p. 246-254.

59. J.A. Thornton "*The microstructure of sputter-deposited coatings*", Journal of Vacuum Science and Technology A, 1986. **4**(6): p. 3059-3065.

60. R. Messier "*Toward quantification of thin film morphology*", Journal of Vacuum Science Technology A, 1986. **4**(3): p. 490-495.

61. A. Thornton, "*Influence of apparatus geometry and deposition conditions on the structure and topography of thick sputtered coatings*" Journal of Vacuum Science and Techonology A, 1974. **11**(4): p. 666.

62. G. Håkansson, J.-E. Sundgren, D. McIntyre, J.E. Greene and W.-D. Münz "*Microstructure and physical properties of polycrystalline metastable Ti0.5Al0.5N alloys grown by D.C. magnetron sputter deposition*", Thin Solid Films, 1987. **153**: p. 55-65.

63. I. Petrov, L. Hultman, U. Helmersson, J.-E. Sundgren and J.E. Greene "*Microstructure modification of TiN by ion bombardment during reactive sputter deposition*", Thin Solid Films, 1989. **169**: p. 299-314.

64. S.J. Bull "*Correlation of microstructure and properties of hard coatings*", Vacuum, 1992. **43**(5-7): p. 387-391.

65. D.M. Mattox "*Surface effects on the growth, adhesion and properties of reactively deposited hard coatings*", Surface and Coatings Technology, 1996. **81**: p. 8-16.

66. B.A. Movchan and A.V. Demchishin, Phys. Met. Metallogr., 1969. **28**: p. 83.

67. K.-H. Müller "*Dependence of thin-film microstructure on deposition rate by means of a computer simulation*", Journal of Applied Physics, 1985. **58**(7): p. 2573-2576.

68. R. Messier, A.P. Giri and R.A. Roy "*Revised structure zone model for thin film physical structure*", Journal of Vacuum Science and Technology A, 1984. **2**(2): p. 500-503.

69. H. Freller and H.P. Lorenz "*Electrochemically measured porosity aof magnetron sputtered TiN films deposited at various substrate orientations*", Journal of Vacuum Science and Technology A, 1986. **4**(6): p. 2691-2694.

70. L. Hultman, W.-D. Münz, J. Musil, S. Kadlec, I. Petrov and J.E. Greene "*Low-energy (~100eV) ion irradiation during growth of TiN deposited by reactive magnetron sputtering: Effects of ion flux on film microstructure*", Journal of Vacuum Science and Technology A, 1991. **9**(3): p. 434-438.

71. J. Musil and S. Kadlec "*Reactive sputtering of TiN films at large substrate to target distances*", Vacuum, 1990. **40**(5): p. 435-444.

72. I. Petrov, F. Adibi, J.E. Greene, L. Hultman and J.-E. Sundgren "*Average energy deposited per atom: A universal parameter for describing ion-assisted film growth?*", Appl. Phys. Lett., 1993. **63**(1): p. 36-40.

73. S.S. Kim, J.G. Han and S.Y. Lee "*Deposition behaviours of CrN films on the edge area by cathodic arc plasma deposition process*", Thin solid films, 1998. **334**: p. 133-139.

74. H. Freller and H. Haessler, Surface and Coatings Technology, 1988. **36**: p. 219.

75. S. Barnett and A. Madan "*Superhard superlattices*", Physics World, 1998: p. 45-48.

76. W.P. Sproul "*Multilayer, multicomponent, and multiphase physical vapor deposition coatings for enhanced performance*", Journal of Vacuum Science and Technology A, 1994. **12**(4): p. 1595-1601.

77. L.A. Donohue, J. Cawley, D.B. Lewis, J.S. Brooks, W.-D. Münz "*Investigation of superlattice coatings deposited by combined steered arc evaporation and unbalanced magnetron sputtering technique*", Surface and Coatings Technology, 1995. **76-77**: p. 149-158.

78. M. Larsson, P. Hollman, P. Hedenqvist, S. Hogmark, U. Wahlstrom and L. Hultman "*Deposition and microstructure of PVD TiN-NbN multilayered coatings by combind reactive electron beam evaporation and DC sputtering*", Surface and Coatings Technology, 1996. **86-87**: p. 351-356.

79. M. Setoyama, A. Nakayama and M. Tanaka "*Formation of cubic AlN in TiN/AlN superlattice*", Surface and Coatings Technology, 1996. **86-87**: p. 225-230.

80. O. Kubaschewski and B.E. Hopkins "*Oxidation of metals and alloys*". 2 ed. 1962, London: Butterworths.

81. P. Kofstad "*High-temperature oxidation of metals*", Corrosion Monograph Series, ed. R.T. Foley, *et al.* 1966, New York: John Wiley & Sons, Inc.

82. P. Panjan, B. Navinsek, A. Cvelbar, A. Zalar and I. Milosev "*Oxidation of TiN, ZrN, TiZrN, CrN, TiCrN and TiN/CrN multilayer hard coatings reactively sputtered at low temperatures*", Thin Solid Films, 1996. **281-282**: p. 298-301.

83. A. Mitsuo, S. Uchida, N. Nihira and M. Iwaki "*Improvement of high-temperature oxidation resistance of titanium nitride and titanium carbide films by aluminum ion implantation*", Surface and Coatings Technology, 1998. **103-104**: p. 98-103.

84. N. Birks and G.H. Meier "*Introduction to high temperature oxidation of metals*", 1983, London: Edward Arnold.

85. D.L. Douglass "*A critique of internal oxidation in alloys during the post-Wagner era*", Oxidation of Metals, 1995. **44**(1/2): p. 81-107.

86. G.S. Brady and H.R. Clauser "*Materials Handbook*", 13 ed. 1991.

87. G.J. Keattch and D. Dollimore "*An introduction to thermogravimetry*", 2 ed. 1975, London: Heyden & Son.

88. P.W. Attkins "*Physikalische Chemie*", 1990.

89. H. Oettel and R. Wiedemann "*Residual stresses in PVD hard coatings*", Surface and Coating Technology, 1995. **76-77**: p. 265-273.

90. G. Kleer, R. Kassner, E.-M. Meyer, M.G. Schinker and W. Doell "*Effect of process parameters on the residual stresses and wear behaviour of aluminium nitride PVD coatings*", Surface and Coatings Technology, 1992. **54-55**: p. 172-176.

91. A.J. Perry and L. Chollet "*Physical vapor-deposited TiN on cemented carbide: tempering effects*", Surface and Coatings Technology, 1988. **34**(2): p. 124-131.

92. S.J. Bull, D.S. Rickerby, J.C. Knight and T.F. Page "*High temperature mechanical properties of physical vapour deposited titanium nitride*", Surface Engineering, 1992. **8**: p. 193.

93. G. Kleer and W. Döll "*Untersuchungen zum Einfluß von Schichtherstellparametern auf Hochtemperatur- und Verschleißverhalten von PVD-Schichten*", Mat. -wiss. u. Werkstofftech., 1993. **24**: p. 80-85.

94. I.C.f.D. Data, *JCPDS X-ray diffraction data*, 1993.

95. D.-F. Lii "*The effects of aluminium composition on the mechanical properties of reactivity sputtered TiAlN films*", Journal of Materials Science, 1998. **33**: p. 2137-2145.

96. S.H. Yeo and S.H. Ong "*Assessment of the thermal effects on chip surfaces*", Journal of Materials Processing Technology, 2000. **98**: p. 317-321.

97. T.I. El-Wardany, E. Mohammed and M.A. Elbestawi "*Cutting temperatures of ceramic tools in high speed machining of difficult to cut materials*", Int. J. Mach. Tools Manufact., 1996. **36**(5): p. 611-634.

98. E.M. Trent "*Metal Cutting*", 1977, London.

99. W. Grzesik "*The role of coatings in controlling the cutting process when turning with coated indexable inserts*", Journal of Materials Processing Technology, 1998. **79**: p. 133-143.

100. W. König and D. Kammermaier "*Performance of TiN-, TiCN-, TiAlN-coated cutting tools*", Material Science Forum, 1992. **102-104**: p. 623.

101. A.J. Perry and D.E. Geist "*High compressive stresses in titanium nitride made by CVD and post-implanted with yttrium ions*", Surface and Coatings Technology, 1997. **94-95**: p. 309-314.

102. H. Ichimura and A. Kawana "*High -temperature oxidation of ion-plated TiN and TiAlN films*", Journal of Materials Research, 1993. **8**(5): p. 1093-1100.

103. P. Panjan, B. Navinsek, A. Cvelbar, A. Zalar and J. Vlcek "*High-temperature oxidation of TiN/CrN multilayers reactively sputtered at low temperatures*", Surface and Coatings Technology, 1998. **98**: p. 1497-1502.

104. I. Suni, D. Sigurd, K.T. Ho and M.-A. Nicolet "*Thermal oxidation of reactively sputtered titanium nitride and hafnium nitride films*", J. Electrochem. Soc., 1983. **130**(5): p. 1210-1214.

105. A.D. Katnani and K.I. Papathomas "*Kinetics and initial stages of oxidation of aluminium nitride: Thermogravimetric analysis and x-ray photoelectron spectroscopy study*", Journal of Vacuum Science and Technology A, 1987. **5**(4): p. 1335-1339.

106. V.A. Lavrenko and A.F. Alexeev "*Oxidation of sintered aluminium nitride*", Ceramics International, 1983. **9**(3): p. 80-82.

107. A. Münster and G. Schlamp "*Über die Oxydation des Titannitrids I. Kinetik der Oxydation*", Zeitschrift für Physikalische Chemie Neue Folge, 1957. **13**: p. 59-75.

108. J. Desmaison, P. Lefort and M. Billy "*Oxidation mechanism of titanium nitride in oxygen*", Oxidation of Metals, 1979. **13**(6): p. 505-517.

109. H. Randhawa, P.C. Johnson and R. Cunningham "*Deposition and characterization of ternary nitrides*", Journal of Vacuum Science and Technology A, 1988. **6**(3): p. 2136-2139.

110. H.K. Tönshoff and A. Mohlfeld *"PVD-coatings for wear protection in dry cutting operations"*, Surface and Coatings Technology, 1997. **93**: p. 88-92.

111. U. Wahlström, L. Hultman, J.-E. Sundgren, F. Adibi, I. Petrov and J.E. Greene *"Crystal growth and microstructure of polycrystalline TiAlN alloy films deposited by ultra-high-vacuum dual-target magnetron sputtering"*, Thin Solid Films, 1993. **235**: p. 62-70.

112. Y. Tanaka, T.M. Gür, M. Kelly, S.B. Hagstrom, T. Ikeda, K. Wakihira and H. Satoh *"Properties of TiAlN coatings for cutting tools prepared by the cathodic arc ion plating method"*, Journal of Vacuum Science and Technolgy A, 1992. **10**: p. 1749-1757.

113. H. Holleck *"Metastable coatings - prediction of composition and structure"*, Surface and Coating Technology, 1988. **36**: p. 151-159.

114. H. Jehn, S. Hofmann, V.-E. Rückborn and W.-D. Münz *"Morphology and properties of sputtered (Ti,Al)N layers on high speed steel substrates as a function of deposition temperature and sputterin atmosphere"*, Journal of Vacuum Science and Technology A, 1986. **4**(6): p. 2701-2705.

115. F. Adibi, I. Petrov, L. Hultman, U. Wahlström, T. Shimizu, D. McIntyre, J.E. Greene and J.-E. Sundgren *"Defect structure and phase transitions in epitaxial metastable cubic TiAlN alloys grown on MgO (001) by ultra high vacuum magnetron sputter deposition"*, Journal of Applied Physics, 1991. **69**: p. 6437.

116. J.R. Ross, J.P. Celis, E. Vancoille, H. Veltrop, S. Boelens, F. Jungblut, J. Ebberink and H. Homberg *"Interrelationship between processing, coating properties and functional properties of steered arc physical vapour deposited TiAlN and TiNbN coatings"*, Thin Solid Films, 1990. **193/194**: p. 547-556.

117. K. Tönshoff, A. Mohlfeld, T. Leyendecker, H.G. Fuß, G. Erkens, R. Wenke, T. Cselle and M. Schwenk *"Wear mechanism of (Ti1-xAlx)N coatings in dry drilling"*, Surface and Coatings Technology, 1997. **94-95**: p. 603-609.

118. O. Knotek, F. Löffler and L. Wolkers *"Phase stability and formation of Ti-Al-C-N PVD coatings"*, Surface and Coatings Technology, 1994. **68/69**: p. 176-180.

119. C.-T. Huang and J.-G. Duh *"Stress and oxidation behaviour of r.f.-sputtered TiAlN films"*, Surface and Coatings Technology, 1996. **81**: p. 164-171.

120. T. Ikeda and H. Satoh *"Phase formation and characterization of hard coatings in the TiAlN system prepared by the cathodic arc ion plating method"*, Thin Solid Films, 1991. **195**: p. 99-110.

121. F. Esaka, K. Furuya, H. Shimada, M. Imamura, N. Matsubayashi, T. Sato, A. Nishijima, T. Kikuchi, A. Kawana and H. Ichimura *"Depth profiling of surface oxidized TiAlN film by synchrotron radiation excited X-ray photoelectron spectroscopy"*, Surface Science, 1997. **377-379**: p. 197-200.

122. C.W. Kim and K.H. Kim *"Anti-oxidation properties of TiAlN film prepared by plasma-assisted chemical vapor deposition and roles of Al"*, Thin Solid Films, 1997. **307**: p. 113-119.

123. I. Milosev, J.M. Abels, H.-H. Strehblow, B. Navinsek and M. Metikos-Hukovic *"High temperature oxidation of thin CrN coatings deposited on steel"*, Journal of Vacuum Science and Technology A, 1996. **14**(4): p. 2527-2534.

124. T. v.d. Kolk, Presentation at the ABS Days 2001 at Sheffield Hallam University, Sheffield UK.

125. O. Knotek, W. Bosch, M. Atzor, W.-D. Münz, D. Hoffmann and J. Goebel *"Properties of chromium nitrides deposited by reactive sputtering"*, High Temperature - High Pressures, 1986. **18**: p. 435-442.

126. S. Hofmann *"Formation and diffusion properties of oxide films on metals and on nitride coatings studied with auger electron spectroscopy and x-ray photoelectron spectroscopy"*, Thin Solid Films, 1990. **193/194**: p. 648-664.

127. J. Vetter, E. Lugscheider and S.S. Guerreiro *"CrAlN coatings deposited by the cathodic vacuum arc evaporation"*, Surface and Coatings Technology, 1998. **98**: p. 1233-1239.

128. J. Vetter, H.J. Scholl and O. Knotek *"TiCrN coatings deposited by cathodic vacum arc evaporation"*, Surface and Coatings Technology, 1995. **74-75**: p. 286-291.

129. D.B. Lewis, L.A. Donohue, M. Lembke, W.-D. Münz, R. KuzelJr., V. Valvoda and C.J. Blomfield *"The influence of the yttrium content on the structure and properties of TiAlCrYN PVD hard coatings"*, Surface and Coatings Technology, 1999. **114**: p. 187-199.

130. D.B. Lewis, I. Wadsworth, W.-D. Münz, R. KuzelJr. and V. Valvoda *"Structure and stress of TiAlN/CrN superlattice coatings as a function of CrN layer thickness"*, Surface and Coatings Technology, 1999. **116-119**: p. 284-291.

131. W.S. Choi, S.K. Hwang and C.M. Lee "*Microstructure and chemical state of TiYN film deposited by reactive magnetron sputtering*", Journal of Vacuum Science and Technology A, 2000. **18**(6): p. 2914-2921.

132. Z. Yu, Z. Jin, C. Liu, L. Yu and S. Dai "*Preparation and properties of TiYN coatings*", Journal of Vacuum Science and Technology A, 1995. **13**(5): p. 2303-2309.

133. A.M. Jones, A.R. McCabe, S.J. Bull and G. Dearnaley "*The effects of deposition temperature and interlayer thickness on the adhesion of ion-assisted titanium nitride films produced with yttrium metal interlayers*", Nuclear Instruments and Methods in Physics Research, 1993. **B80/81**: p. 1397-1401.

134. W.-D. Münz "*Oxidation resistance of hard wear resistant TiAlN coatings grown by magnetron sputter deposition*", Werkstoffe und Korrosion, 1990. **41**: p. 753-754.

135. E. Lang (editor) "*The role of active elements in the oxidation behaviour of high temperature metals and alloys*", 1989, Elsevier Science Publ.: New York.

136. D.P. Moon "*Role of reactive elements in alloy protection*", Materials Science and Technology, 1989. **5**: p. 759.

137. A.M. Huntz "*Influence of active elements on the oxidation mechansim of M-Cr_Al alloys*", Materials Science and Engineering, 1987. **87**: p. 251-260.

138. G.E. Murch "*Materials Science Forum*", The reactive element effect of high temperature oxidation after fifty years, E. Wayne (editor), Vol. 43. 1989, Trans Tech Publications.

139. T.A. Ramanarayanan, R. Ayer, Petkovic-Luton and D.P. Leta "*The influence of Yttrium on oxide scale growth and adherence*", Oxidation of Metals, 1988. **29**(5-6): p. 445-472.

140. K.Y. Kim, S.H. Kim, K.W. Kwon and I.H. Kim "*Effect of Y on the stability of aluminide-yttrium composite coatings in a cyclic high-temperature hot-corrosion environment*", Oxidation of Metals, 1994. **41**(3/4): p. 179-201.

141. H.M. Tawancy, N.M. Abbas and A. Bennett "*Role of Y during high temperature oxidation of an M-Cr-Al-Y coating on an Ni-base superalloy*", Surface and Coatings Technology, 1994. **68/69**: p. 10-16.

142. F.H. Stott and D.R.G. Mitchell "*The effects of high-temperature oxidation on the friction and wear of titanium-nitride-coated steel*", Materials at High Temperatures, 1991. **9**(4): p. 185-192.

143. O. Knotek, W. Bosch and T. Leyendecker "*Wear resistant Ti-Al-C-N-O films produced by sputtering*". in *International Conference on Vacuum Metallurgy*. 1985. Linz, Austria.

144. K. Tönshoff, B. Karpuschewski, A. Mohlfeld, T. Leyendecker, G. Erkens, H.G. Fuß and R. Wenke "*Performance of oxygen-rich TiAlON coatings in dry cutting applications*", Surface and Coatings Technology, 1998. **108-109**: p. 535-542.

145. M.I. Lembke, D.B. Lewis, W.-D. Münz and J.M. Titchmarsh "*Significance of Y and Cr in TiAlN hard coatings for dry high speed cutting*", Surface Engineering, 2001. **17**(2): p. 153-158.

146. R.L. Doolittle "*Algorithms for the rapid simulation of rutherford backscattering spectra*", Nucl. Instrum. Methods Phys. Res. B, 1985. **15**: p. 344.

147. W.K. Chu, J.W. Mayer and M.-A. Ni "*Backscattering Spectroscopy*". 1978, New York: Academic Press.

148. J.-E. Sundgren, A. Rockett and J.E. Greene "*Microstructural and microchemical characterisation of hard coatings*", Journal of Vacuum Science and Technology A, 1986. **4**(6): p. 2770-2783.

149. VDI Richtlinie 3198, Rockwell C Test, 1992, Verein Deutscher Ingenieure: Düsseldorf, Germany.

150. German Industry Standard DIN V 1071 T3, "*Scratch Test*", 1993.

151. German Industry Standard DIN V 1071 T2, "*Calowear Test*", 1993.

152. S.J. Bull and D.S. Rickerby "*Evaluation of coatings*", in *Advanced Surface Coatings*, D.S. Rickerby and A. Matthews, Editors. 1991, Blackey & Sons Ltd: London.

153. K.L. Williams "*Introduction to X-ray Spectrometry*", 1987, Winchester (MA): Allen & Unwin.

154. P.J. Goodhew and F.J. Humphreys "*Electron microscopy and analysis*", 2 ed. 1988: Taylor and Francis.

155. S.J.B. Reed "*Electron Microprobe Analysis*", 2 ed. 1993, Cambridge: Cambridge University Press.

156. D.B. Williams and C.B. Carter "*Transmission Electron Microscopy*", 1996, New York: Plenum Press.

157. P.D. Nellist and S.J. Pennycook "*The principles and interpretation of annular dark-field Z-contrast imaging*", Advances in imaging and electron physics, 2000. **113**: p. 147-203.

158. B.D. Cullity "*Elements of X-ray Diffraction*", 2 ed. 1978, Reading (MA): Addison-Wesley Publ.

159. A.J. Perry, J.A. Sue and P.J. Martin "*Practical measurement of the residual stress in coatings*", Surface and Coatings Technology, 1996. **81**: p. 17-28.

160. J.A. Thornton and D.W. Hoffman "*Stress-related effects in thin films*", Thin Solid Films, 1989. **171**: p. 5-31.

161. D.E. Geist, A.J. Perry, J.R. Treglio, V. Valvoda and D. Rafaja "*Residual stress in ion implanted titanium nitride studied by parallel beam glancing incidence X-ray diffraction*", Advanced X-ray analysis, 1995. **38**: p. 471.

162. D.S. Rickerby, A.M. Jones and B.A. Bellamy "*X-ray diffraction studies of PVD coatings*", Surface and Coatings Technology, 1989. **27**: p. 111-131.

163. A.J. Perry "*A contribution to the study of Poisson's ratios and elastic constants of TiN, ZrN and HfN*", Thin Solid Films, 1990. **193/194**.

164. Avesta "*Corrosion Handbook*", 1994.

165. W.D. Callister "*Materials Science and Engineering an Introduction*", 4th ed. 1997: Wiley.

166. Darken and Gurry "*Physical Chemistry of Materials*", Metallurgy and Metallurgical Engineering Series. 1953, London: McGrawHill.

167. C.W. Louw, I.L. Strydow, K.v.d. Heever and M.J.v. Staden "*Selective steam oxidation of titanium and aluminium in TiN and TiAlN physically vapour-deposited coatings on dental surgical tools*", Surface and Coatings Technology, 1991. **49**: p. 348-352.

168. M.I. Lembke, D.B. Lewis and W.-D. Münz "*Localised oxidation defects in TiAlN/CrN superlattice structured hard coatings grown by cathodic arc/ unbalanced magnetron deposition on various substrate materials*", Surface and Coatings Technology, 2000. **125**: p. 263-268.

169. I. Petrov, L. Hultman, J.-E. Sundgren and J.E. Greene "*Polycrystalline TiN films deposited by reactive bias magnetron sputtering: Effects of ion bombardment on resputtering rates, film composition and microstructure*", Journal of Vacuum Science and Technology A, 1992. **10**(2): p. 265-273.

170. L.A. Donohue, D.B. Lewis, W.-D. Münz, M.M. Stack, S.B. Lyon, H.-W. Wang and D. Rafaja "*The influence of low concentrations of chromium and yttrium on the oxidation behaviour, residual stress and corrosion performance of TiAlN hard coatings on steel substrates*", Vacuum, 1999. **55**: p. 109-114.

171. W. Mader, H.F. Fischmeister and E. Bergmann "*Defect structure of ion-plated titanium nitride coatings*", Thin Solid Films, 1989. **182**: p. 141-152.

172. I.A. Vatter and J.M. Titchmarsh, Surface and Interface Analysis, 25, 760-776, "*Comparison of FEG-STEM measurements of equilibrium segregation of phosphorus in 9% Cr ferritic steel*", Surface and Interface Analysis, 1997. **25**: p. 760-776.

173. P.H. Mayrhofer and C. Mitterer "*High-temperature properties of nanocomposite TiBxNy and TiBxCy coatings*", Surface and Coatings Technology, 2000. **133-134**: p. 131-137.

174. C. Liu, W. Wu, Z. Yu and Z. Jin "*Correlation of interfacial structure and microstress of yttrium-modified ion-plated titanium nitride film with its adhesion property*", Thin Solid Films, 1992. **207**: p. 98-101.

175. E. Kny, T. Bader, C. Hohenrainer and L. Schmid "*Corrosion and high resistant hard metals*", Werkstoffe und Korrosion, 1986. **37**: p. 230-235.

176. P.H. Mayrhofer, H. Willmann and C. Mitterer "*Microstructure and mechanical/ thermal properties of CrN coatings deposited by reactive unbalanced magnetron sputtering*", Surface and Coatings Technology, 2001 to be published.

177. M.I. Lembke, D.B. Lewis, J.M. Titchmarsh and W.-D. Münz "Structural changes after heat treatment of physical vapour deposited TiAlCrYN coatings", in Quantitative Microscopy of High Temperature Materials: Institute of Materials, Sheffield, 1999.

178. M.I. Lembke, J.M. Titchmarsh, D.B. Lewis and W.-D. Münz "*Investigation of the oxidation behaviour of a TiAlCrYN PVD hard coating*",Fall Meeting 2000 of the Materials Research Society in Boston, USA: MRS publishing, P6.57

179. M.I. Lembke, J. Titchmarsh and W.-D. Münz "*Transmission microscopy investigation of the oxidation of hard coatings for high speed machine tools*", in Electron Microscopy and Analysis 2001: Institute of Physics Publishing.

12 Appendix

Scientific papers written during the PhD by M.I. Lembke

Transmission microscopy investigation of the oxidation of hard coatings for high speed machine tools

M I Lembke, J M Titchmarsh* and W-D Münz

MRI, Sheffield Hallam University, Howard Street, Sheffield S1 1WB, UK
* Dept of Materials, Oxford University, Parks Road, Oxford OX1 3PH,UK

ABSTRACT: The oxidation of TiAlN based nitride hard coatings on steel substrates has been investigated as a function of time and temperature. The addition of Y during deposition changed the normal columnar growth into a fine interrupted columnar growth. XTEM examination revealed changes in the chemical composition of samples heat treated in air at 900°C. Moreover, in the Y-containing coating, grain growth due to the heat treatment was observed. FEG-STEM EDX analysis and elemental mapping showed that the nitride grain boundaries provided paths for substrate elements to diffuse rapidly to the surface. Y greatly inhibited such diffusion, probably by segregating to boundaries. At high temperatures Y diffused towards the surface to form discrete Y-rich particles within a layered polycrystalline structure of Al_2O_3, TiO_2 and Cr_2O_3.

1. INTRODUCTION

High speed machining without the use of environmentally harmful lubricants requires milling tools to withstand continuous stress and temperature variations without degradation. In materials such as A2 steel that are difficult to cut, temperatures above 800°C are frequently reached, which prevents the use of conventional tool steel and cemented carbides because such materials are rapidly oxidised (Münz, 2001). Recently, more complex nanolayered hard tool coatings have been developed, incorporating Y with an oxynitride surface coating, that have demonstrated significantly superior machining performance (Donohue, 1997, Lembke 2001). With this tool coating, A2 steel can be machined without lubrication using a cutting speed of 365m/s and a rotation speed of 15000rpm for 1h, compared with 20min for TiAlN coated tools (Lembke et al, 2001). The oxidation of such nanolayered coatings has been investigated using TEM and STEM as a function of ageing time and temperature to determine the role of Y and to characterise the changes in the microstructure compared with more conventional TiAlN coatings.

2. EXPERIMENTAL

Coatings were grown on stainless steel substrates by the PVD ABS method (Munz et al, 1992, Munz et al, 2000) that combines a steered arc of Cr ions, to clean the substrate surface, improve adhesion and minimise growth defects, with unbalanced magnetron sputtering in a commercial coating apparatus. Four magnetrons were employed with one Cr,

two TiAl targets and one TiAlY target. The deposition parameters were adjusted throughout the reactive process to control the chemical composition and microstructure (Donohue et al, 1997, Lembke et al, 2001). Two types of coating were grown on to stainless steel substrates: (i) TiAlCrN (3μm thick) and (ii) TiAlCrYN (2.3μm thick) plus an oxynitride topcoat. Y is distributed throughout the coating. Samples of both were heated in air between 1 and 10 hours at 900°C. XTEM specimens were prepared by mechanical grinding and ion beam thinning and examined in a Philips CM20 TEM and a VG HB501 FEG-STEM equipped with a windowless EDX system. The distributions of substrate (Fe, Cr), coating (Ti, Al, Cr, Y) and surface oxide elements were revealed by EDX elemental mapping. Maps of O and N were also attempted by selecting only a narrow energy window on the lower energy side of the O and N peaks to minimise the influence of overlap with the Cr and Ti L peaks, respectively. Composition profiles and point analyses were recorded across grain boundaries and at selected features.

3. RESULTS AND DISCUSSION

Fig.1 compares bright field TEM cross-sections through the as-grown TiAlCrN (Fig.1a) and TiAlCrYN plus oxynitride topcoat (Fig.1b) multilayer structures. The incorporation of Y, following growth of the TiAlCrN base layer, caused a significant refinement of the grain size of TiAlCrN (Fig.1b) suggesting that the presence of the large Y atoms caused grain nucleation. The process parameters were not responsible for this change. Some grain boundary porosity was also observed. During oxidation for up to 10 hours there was a noticeable grain coarsening, revealed by changes in SADPs, using a 0.5μm diameter aperture, from a spotted ring to a textured spot pattern (Fig. 2). The intergranular voids disappeared as the grains grew.

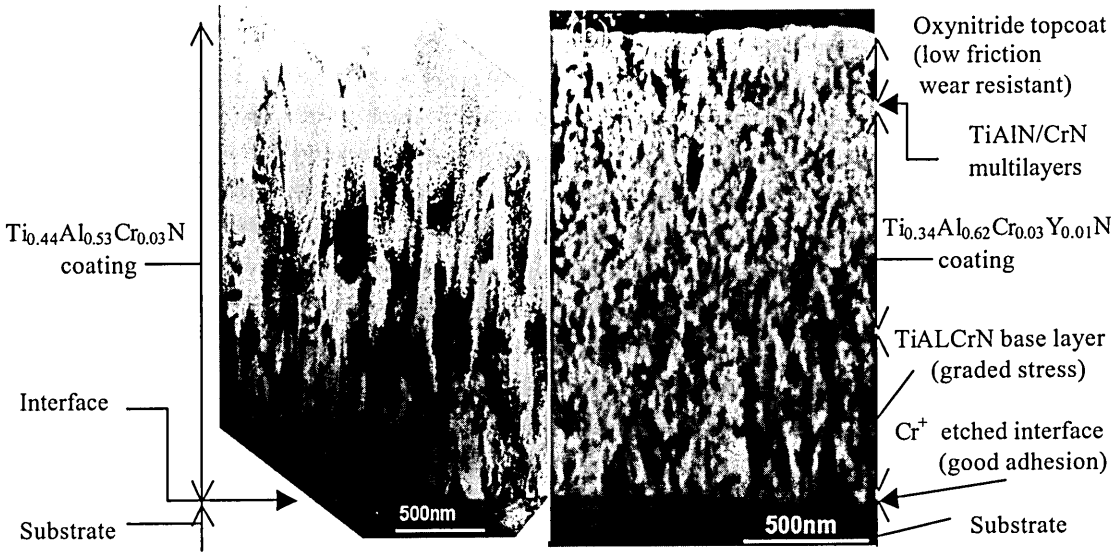

Fig. 1 Comparison of the structures of the $Ti_{0.44}Al_{0.53}Cr_{0.03}N$ (a) and $Ti_{0.34}Al_{0.62}Cr_{0.03}Y_{0.01}N$ plus oxynitride topcoat coating (b).

Elemental maps were obtained from cross sections of both coatings after heat treatment for 1h at 900°C. Diffusion of substrate elements through the coatings was observed to occur along nitride grain boundaries (not illustrated) but was significantly inhibited by the Y-containing region. X-ray mapping revealed an abrupt fall in Cr concentration and also Fe, to

a lesser extent, at the boundary where Y was introduced. The influence of Y on substrate element diffusion can be clearly seen by comparing map intensities in the TiAlN base layer and the Y-containing coating (Fig. 3). A clear border between those two layers is visible. After heating for 10 hours the inhibiting effect of Y was overcome and diffusion of Cr was observed to occur right through the coating up to the surface oxide layer. The presence of Y is well known to improve the high temperature oxidation resistance of metal alloys (Moon, 1989) and a similar benefit apparently occurs here in alloy nitrides.

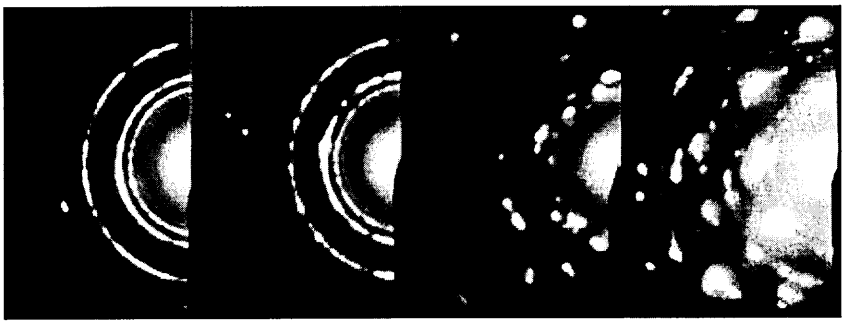

Fig.2 SADP from TiAlCrYN coating: as-deposited (a) and heated at 900°C for (b) 1, (c) 5 and (d) 10 hours

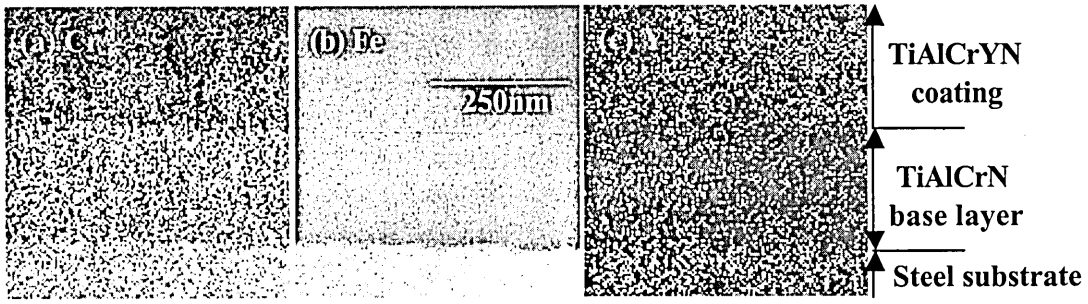

Fig.3 Elemental maps of substrate/base/TiAlCrYN coating region, heated 900°C for 1 hour, showing diffusion of Cr from substrate into base layer inhibited by Y-containing coating.

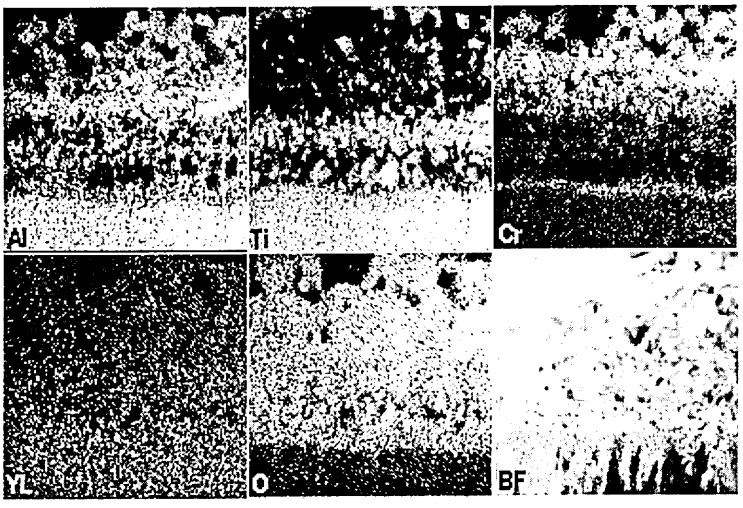

Fig.4 Elemental maps showing formation of Al, Ti and Cr-rich layers within oxide at the surface of the TiAlCrYN-oxynitride coating after heating for 5 hours at 900°C.

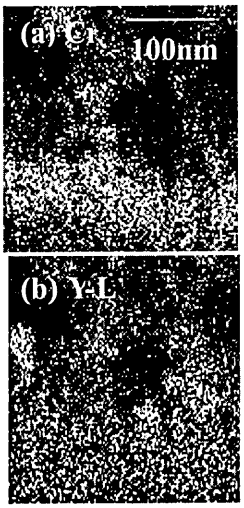

Fig.5 Detail from same area as Fig.4, showing Y-rich particle in oxide layer.

TiAlN has previously been intensively examined and is known to oxidise by the formation of a bi-layer composed of TiO_2 and Al_2O_3 (McIntyre et al, 1990). After annealing for 1h at 900°C the TiAlCrN coating formed an oxide layer of ~750nm thickness. In the TiAlCrYN coating the oxide layer growth was only ~230nm thick after the same heat treatment. Fig. 4 shows surface oxide elemental maps from TiAlCrYN with the oxynitride overcoat after oxidation for 5 hours at 900°C. As with TiAlN, the surface oxide structure was again complex, with an outermost layer rich in Al_2O_3, adjacent to a TiO_2 layer. Cr, present in the superlattice region of the oxynitride top coating (Fig.1), became concentrated just below the oxide layer and also formed Cr_2O_3 and $(AlCr)_2O_3$ within the oxide layer (XRD confirmed the presence of the various oxide phases). Only after prolonged heating at very high temperatures (900°C) is Y itself able to diffuse towards the growing surface oxide layer to form discrete particles, almost certainly oxides. Y-rich particles were observed within the Ti-rich oxide layer (Fig.5). EDX analysis of the N and O counts profiles revealed the progress of oxidation with time at 900°C. After 5h the oxidation accelerated considerably. The remaining nitride thickness was 1950nm and 1070nm for 5h and 10, respectively.

Equivalent examination of specimens oxidised between 600°C and 900°C for 10h confirmed the gradual development of the layered oxide and increasing diffusion of substrate elements.

5. CONCLUSIONS

EDX mapping was a valuable tool to evaluate the effects of oxidation heat treatment on TiAlN and TiAlCrYN hard coatings. Y was found to reduce the outward diffusion of substrate elements and the inward diffusion of oxygen along the grain boundaries of the coatings. The EDX evidence suggests that Y effectively blocks the grain boundary diffusion channels both for oxygen diffusing in and substrate elements diffusing out. This retardation permits longer machining before the coating degrades and spalls. The oxide layer thickness is markedly reduced by the incorporation of Y into the coating. Y eventually diffused to the oxide, forming particles, after 5h heating at 900°C.

6. REFERENCES

Donohue, L A, Smith I. J, Münz W-D, Petrov I and Greene J E 1997 Surface and Coatings Technology **94-95**, 226

Lembke M I, Lewis D B, Münz W-D and Titchmarsh J M 2001 Surface Engineering, **17(2)**, 153

McIntyre D, Greene J E, Hakansson G, Sundgren J E and Münz W-D 1990 J Appl. Phys. **67**, 225

Moon D P 1989 Mat. Sci. and Tech. **5**, 759

Münz W-D, Schulze D and Hauzer F J M 1992 Surface and Coatings Technology **50**, 169

Münz W-D, Schönjahn C, Paritong H and Smith I J 2000 Le Vide **3/4**(297), 205

7. ACKNOWLEDGEMENTS

JMT is grateful to the Royal Academy of Engineering, AEA Technology and the Institute of Nuclear Safety System for financial support.

Microstructure, Composition and Performance of PVD Coatings Designed for Successful Dry High Speed Milling

Münz Wolf-Dieter [a,b], Lembke Mirkka I. [a], Lewis D. Brian [a], Smith Iain J [b]

a) Sheffield Hallam University, Materials Research Institute, Sheffield; S1 1WB, UK

b) Bodycote SHU Coatings Ltd, Sheffield, S1 4QF, UK

Summary:

Dry high speed machining (HSM), particularly dry high speed milling, demands hard coatings, which exhibit high toughness, high oxidation resistance, a limited amount of residual stress and excellent adhesion to the cemented carbide (CC) substrate. These requirements are met by TiAlCrYN coatings grown by the combined cathodic arc/ unbalanced magnetron deposition method. Fully sufficient adhesion is achieved by ion implantation of Cr into the CC prior deposition. Residual stress is controlled by an Y – free base layer; high oxidation resistance is provided by an Y – containing 3μm thick hard coating with 29 GPa hardness and a residual stress well below -7 GPa. Under the influence of temperatures above 800°C, Y segregates along the columns of TiAlN and plugs the in/ outdiffusion of elements. A top layer of Y – containing oxynitride reduces the friction against the work piece material (0.9 to 0.65). Cutting tools coated as such may be used for dry milling up to 25k rpm in steels HRC > 60.

1. Keywords

High speed cutting, PVD, TiAlN hard coating, Yttrium, Oxidation resistance

2. Introduction

Dry high speed machining is gaining increasing importance in modern production technology. Dry high speed milling of dies and moulds represents the current state of the art. Cutting speeds between 15k-25k rpm have been reported to machine steels in the hardness range of 55-62HRC. In this application cemented carbide cutting tools must be protected with hard oxidation resistant coatings as localised temperatures are typically up to a 1000°C. In this temperature range tungsten carbide but also PVD – TiN, PVD - TiCN coating material, suffer severe oxidation. Since the introduction of

PVD – TiAlN, temperatures up to 800°C can be tolerated [1]. To increase the peak temperature still further, the addition of 1-2at% Y to TiAlN based coatings allows peak temperatures up to 950°C [2].

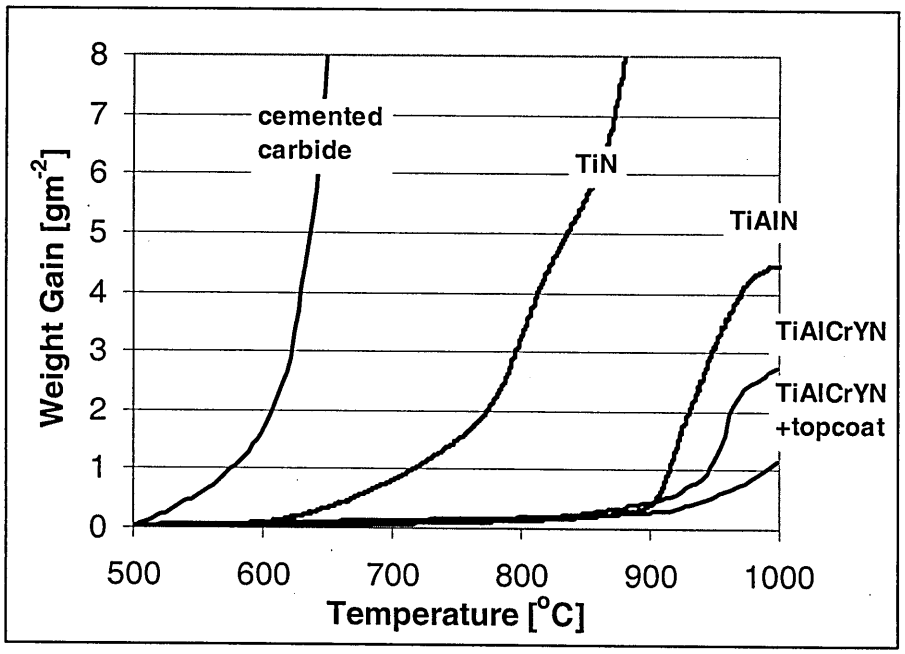

Figure 1: Continuous thermogravimetric measurement. Heating rate was with 50°C/min to 400°C and with 1°C/min to 1000°C.

Thermogravimetric data shown in Figure 1 confirm the dramatic difference in the oxidation behaviour of tungsten carbide when compared with TiAlCrYN. [2], [3]. Temperature measurements on the cutting tool indicate indeed the occurrence of cutting temperatures greater than 900°C (Table 1). These experiments have been evaluated by milling various steels with two flute 8mm diameter solid carbide end mills.

The coatings described in this paper have been deposited by the combined cathodic steered arc/ unbalanced magnetron deposition method (Arc Bond Sputtering: ABS - Technology) [4], [5].

Workpiece Material	DIN	Hardness (HRC)	Cutting Conditions	Temperature (after 5 minutes)
EN24 **C0.40Mn0.60Ni 1.5Cr1.1Mo0.3**	**1.6582**	**38**	Vc =385 m/min, Ax =3.8 mm, Radial Feed=1 mm, Feed =0.1 mm/rev, Spindle 16 000 rpm.	**< 700 ^{0}C**
P20 **C0.32Mn0.80Cr 1.60Mo0.40**	**1.2311**	**48**	Vc =385 m/min, Ax= 3.8 mm, Radial Feed= 0.4 mm, Feed= 0.1 mm/rev, Spindle 16 000 rpm.	**<700 ^{0}C**
			Vc= 510 m/min, Ax= 3.8, Radial Feed= 0.4 mm, Feed= 0.1 mm/rev, Spindle 20 000 rpm.	**~ 810 ^{0}C**
H13 **C0.35Si1.0Cr5.2 5Mo1.5W1.25V 0.30**	**1.2344**	**53**	Vc =385 m/min, Ax= 3.8 mm, Radial Feed= 0.4 mm, Feed= 0.1 mm/rev, Spindle 16 000 rpm.	**~ 810 ^{0}C**
A2 **C1.0Mn0.65Cr5 .0Mo1.0V0.3**	**1.2363**	**58**	Vc =385 m/min, Ax= 3.8 mm, Radial Feed= 0.4 mm, Feed= 0.1 mm/rev, Spindle 16 000 rpm.	**~ 880 ^{0}C**
			Vc= 510 m/min, Ax= 3.8, Radial Feed= 0.4 mm, Feed= 0.1 mm/rev, Spindle 20 000 rpm.	**~ 910 ^{0}C**

Table 1: Overview of temperatures at the cutting edge of coated cemented carbide ball nosed end mills.

3. The substrate/ coating interface

In dry high speed milling the tools are subjected to enormous interrupted reciprocating mechanical impacts and under these conditions adhesion is of paramount importance. Previous work has shown that the adhesion measured by scratch testing (critical load : L_c) can be directly related to the microchemistry of the interface resulting in localised epitaxial growth of the deposited TiAlN hard coating [6], [7]. The absolute value of the critical load L_c can be controlled by a dedicated low energy ion implantation process, carried out in a steered arc discharge, as process step of the ABS technology, during the metal ion etching procedure of the substrate surface (20min duration) prior to coating [4], [5]. The implantation of 1.2keV Cr^{++} ions prior to deposition of a TiAlN coating led to the highest scratch test values (L_c = 135N), when compared with a pre-treatment of 1.2keV Ar (L_c = 35N), Nb (L_c = 90N) and V (L_c = 115N) ions. Additionally a decrease of adhesion was observed, when the accelerating voltage during ion implantation was only 0.6keV (Cr; L_c = 60N). Figure 2 reflects the life-time of TiAlCrYN coated cemented carbide end mills machining HRC 58 A2 die steel (cutting speed 15k rpm). In these experiments two-flute end mills fabricated from identical cemented carbide material were pre-treated with various ion species and then coated with 3µm TiAlCrYN using identical deposition parameters.

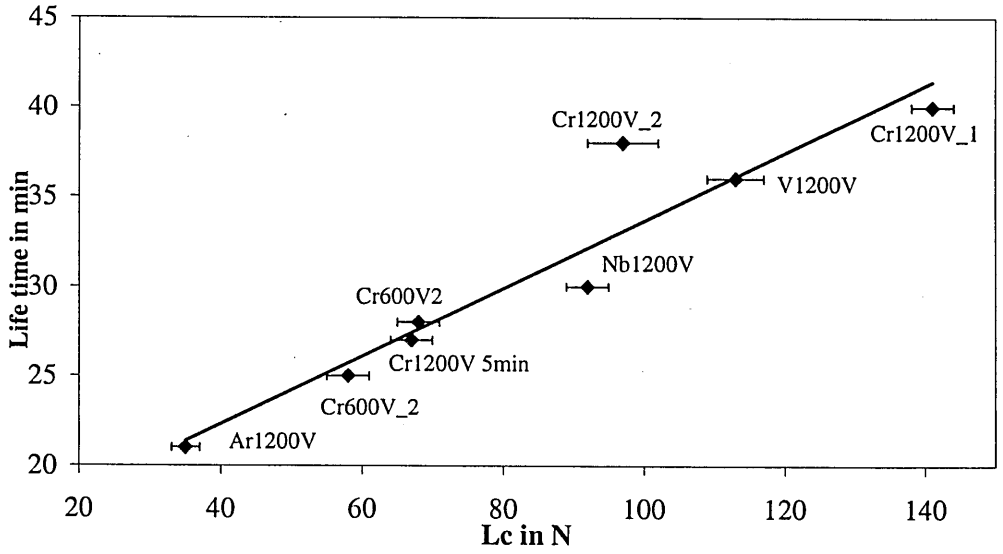

Figure 2: Life time in dry high speed machining versus critical load values in scratch adhesion testing

Figure 3: Local epitaxial growth of TiAlN on tungsten carbide after Cr ion bombardment at U_b=-1200V (a) Selected area diffraction pattern (SADP) of TiAlN grain (b) superimposition of the TiAlN pattern and tungsten carbide pattern (c) SADP of tungsten carbide grain.

Selected area electron diffraction patterns (Figure 3) explain the excellent adhesion of TiAlN based coatings deposited on cemented carbide after a 1.2keV Cr^{++} pre-treatment. Figure 3a) shows the electron diffraction pattern of fcc TiAlN, whereas Figure 3c) represents the diffraction pattern of hexagonal tungsten carbide. The superimposed patterns of fcc TiAlN and hexagonal tungsten carbide show perfect matching of the lattices at the interface between coating and substrate, which is a direct indication of localised epitaxial growth.

4. Successful Layer Architecture

TiAlCrYN based coatings with nanolayered Y incorporation have been proven particularly successful in dry high speed milling operations. However, these coatings exhibit relatively high compressive residual stresses up to -7GPa. To retain sufficient adhesion a stress reduced 250nm thick TiAlCrN base layer is employed to grade the stress between substrate interface and TiAlCrYN coating [8]. In addition, a 400nm thick special toplayer of has been developed to achieve a reduced friction coefficient (0.9 to 0.65) of the wear resistant ceramic hard coating against steel as work piece material. This toplayer consists of a TiAlYN/CrN nanoscaled multilayer, which is embedded in a TiAlCrY – oxynitride. The oxygen content is continuously increased during the deposition of the outermost 200nm of the coating by continuous replacing in the reactive sputter deposition process nitrogen with medical dry air [9]. Figure 4 shows a schematic diagram (a) and a TEM cross section (b) of the coating. Detailed description of the PVD deposition process is given in [4], [6], [5], [9].

This coating has been made commercially available as Supercote 11 by Bodycote SHU Coatings Ltd., Sheffield.

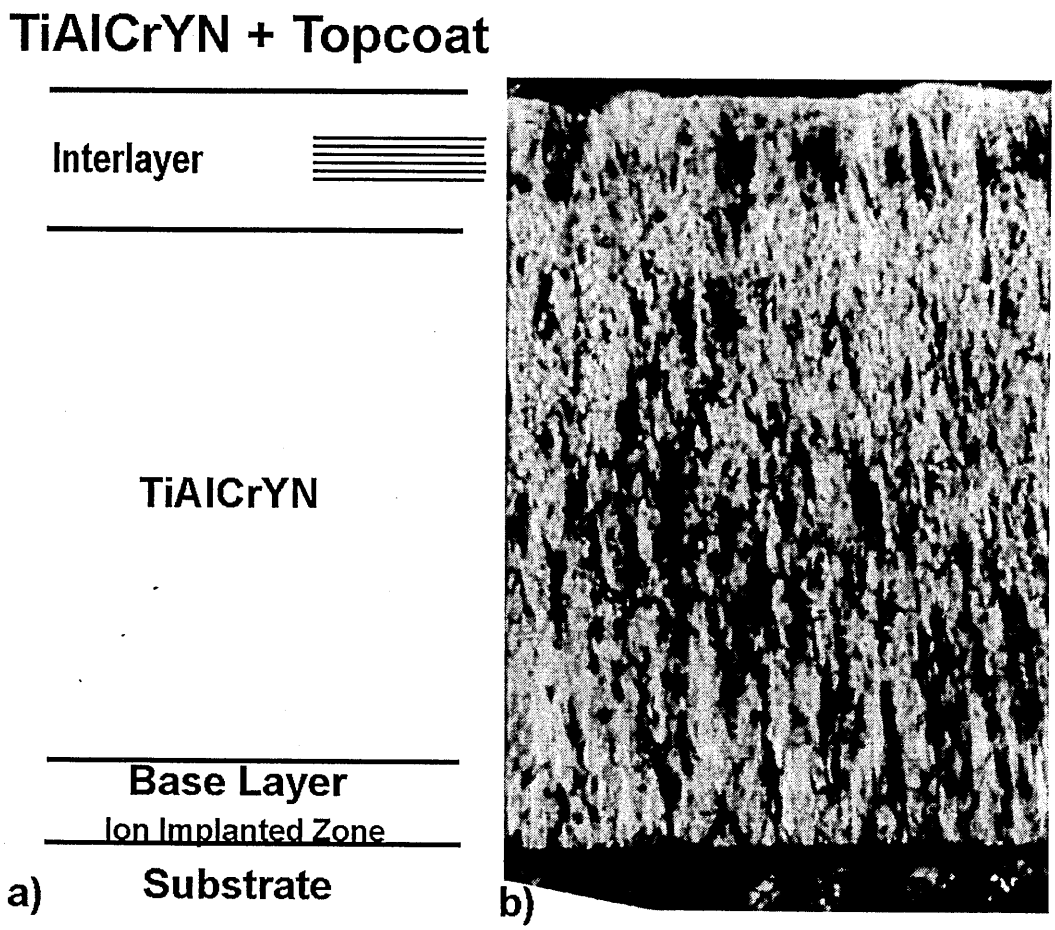

Figure 4: TiAlCrYN with topcoat as a) schematic and b) cross-sectional bright field image

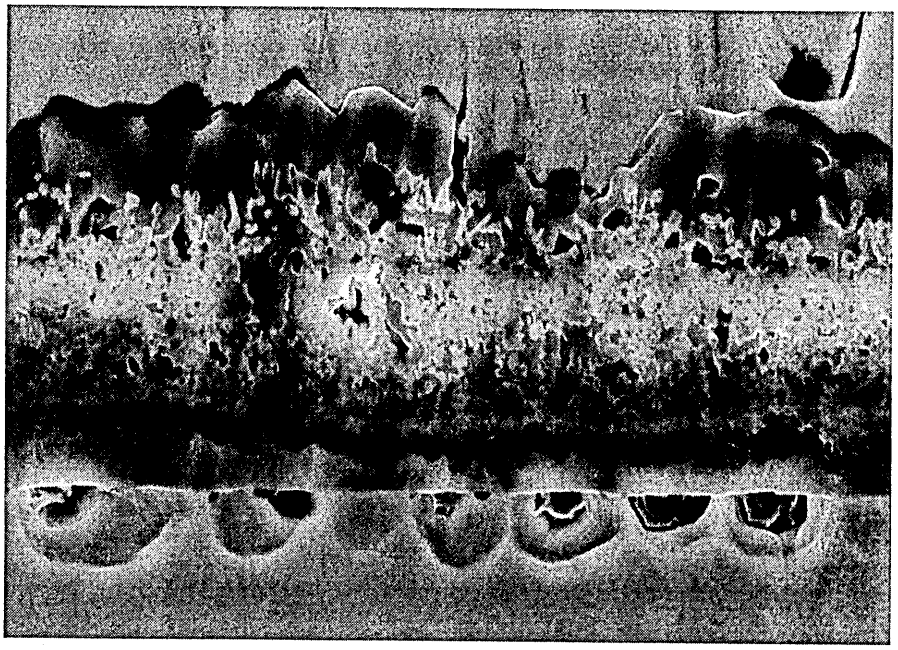

Figure 5: High resolution SEM micrograph of TiAlCrN on stainless steel after heat treatment for 1h at 950°C.

5. Diffusion of Substrate Elements at High Operating Temperature

Previous work on stainless steel substrates revealed a rapid diffusion of substrate material elements through the Y free coating above 800°C [2]. In extreme cases (1h at 950°C) cavities started to form at the interface between the stainless steel substrate and the hard coating, which leads automatically to a loss of adhesion (Figure 5). The outdiffusing substrate elements form complex mixed oxides at the coating surface containing both substrate and coating elements. These disintegrating effects can be completely avoided by incorporation of 1at% Y [2]. The incorporation of Y during deposition led to a fine grained interrupted columnar growth structure, which increases the diffusion path for in- and outward diffusion of substrate elements. Furthermore, it has already been reported that Y diffuses preferentially to the column boundaries after heat treatment for 1h at 950°C, thus further blocking this diffusion path [2]. In case of cemented carbide as substrate material, we have carried out extensive investigations using STEM and EDX mapping on cross sectional samples to localise the influence of Y. Distribution maps of the coating and substrate elements taken after heat treatment 1h at 900°C are shown in Figure 6. Whereas all elements such as Al, Ti and Cr are uniformly distributed in the coating, there is clear evidence of out-diffusion of Co from the cemented carbide substrate into the base layer. In parallel, we found a very uniform distribution of Y in the TiAlCrYN coating. Figure 6 is a clear indication that Co diffuses mainly along column boundaries in the base layer and is blocked in the Y containing layer section. At the higher magnification (Figure 7) the above mentioned Y segregation taking place in the Y containing part of the coating becomes evident, too.

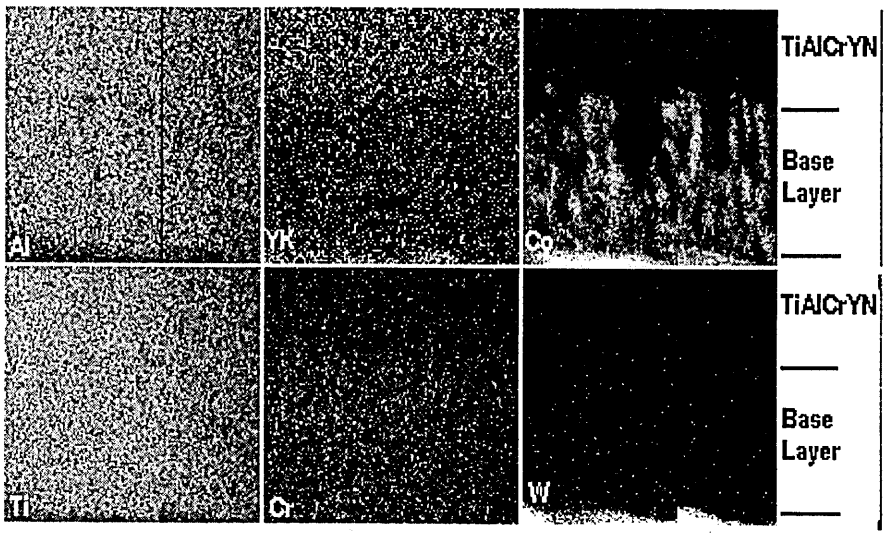

TiAlCrYN+Ox on CC after 1h at 900°C

Figure 6: Elemental distribution maps of TiAlCrYN with topcoat deposited onto cemented carbide after 1h at 900°C.

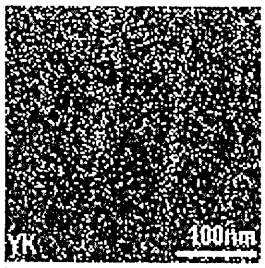

Figure 7: YK map of TiAlCrYN with topcoat.

6. Oxidation Behaviour of TiAlCrYN with Topcoat

The progress in improvement of oxidation resistance is shown in Figure 1. The oxidation resistance of TiN is substantially improved by the addition of Al and incorporation Y. The TG analyses indicate, that the oxidation behaviour of the layer described in Figure 4 shows an even improved performance when compared with the toplayer free TiAlCrYN. STEM - EDX point analysis (Figure 8) explains the important role of Cr in this context. The interlayer consisting of the nanoscale multilayer TiAlYN/CrN seems to be fully intact after the heat treatment in air. We observed in this region a decrease in N and the expected increase in O content stemming from the exchange of the reactive gases during the deposition process and indicating the formation of TiAlCrY - oxynitride. In the outermost region we found discrete particles of TiO_2 (rutile), Al_2O_3 (corundum) and Cr_2O_3 (eskolite). In the diagram shown here Al_2O_3 is predominant. XPS mapping of the surface confirmed the existence of the above mentioned discrete particles [8].

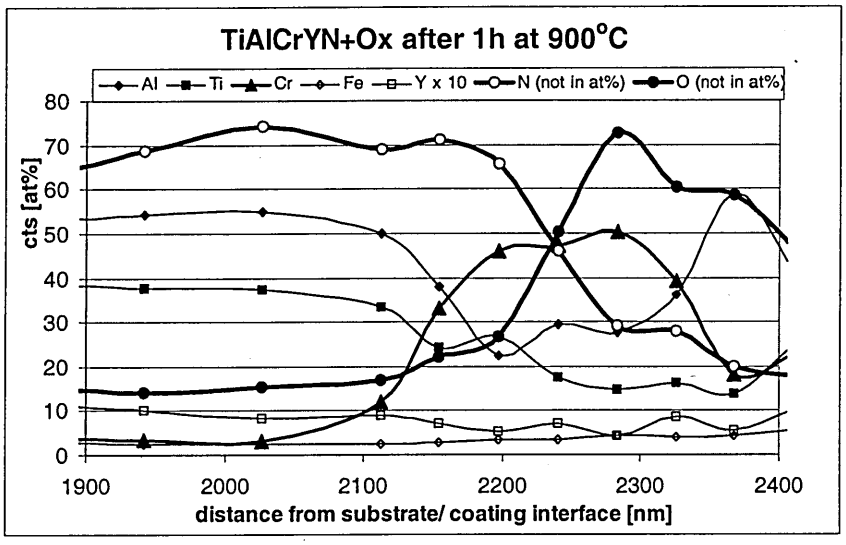

Figure 8: EDX point analysis through the topcoat region of TiAlCrYN after heat treatment for 1h at 900°C.

7. Results in Dry High Speed Milling

Finally, the performance of the here described TiAlCrYN with the Cr containing topcoat (Supercote 11) is compared with commercially available Y free TiAlN coatings deposited by cathodic arc evaporation (supplier I and II) and an increasingly popular sandwich coating TiN/TiAlN (~30 layers), also deposited cathodic arc [10]. All tools were manufactured by the same tool supplier using cemented carbide material stemming from an identical production lot. In the tests 8mm two flute ball nosed end mills were used to mill A2 (HRC 58) die steel. Figure 9 summarises the results of end of life tests for two different cutting speeds, namely v_c = 385 m min^{-1} (16krpm) and v_c = 500 m min^{-1} (20krpm). The tests at 16krpm illustrate the superiority of Supercote 11 against arc deposited TiAlN and the multilayer system TiN/TiAlN. In the 20krpm test Supercote 11 is compared with Supercote 02 a coating with a similar composition to Supercote 11 however, without the incorporation of Y. At these high cutting temperatures (see table 1, ~800°C) the influence of Y becomes again clearly evident. One at% Y doubles the life-time of TiAlN

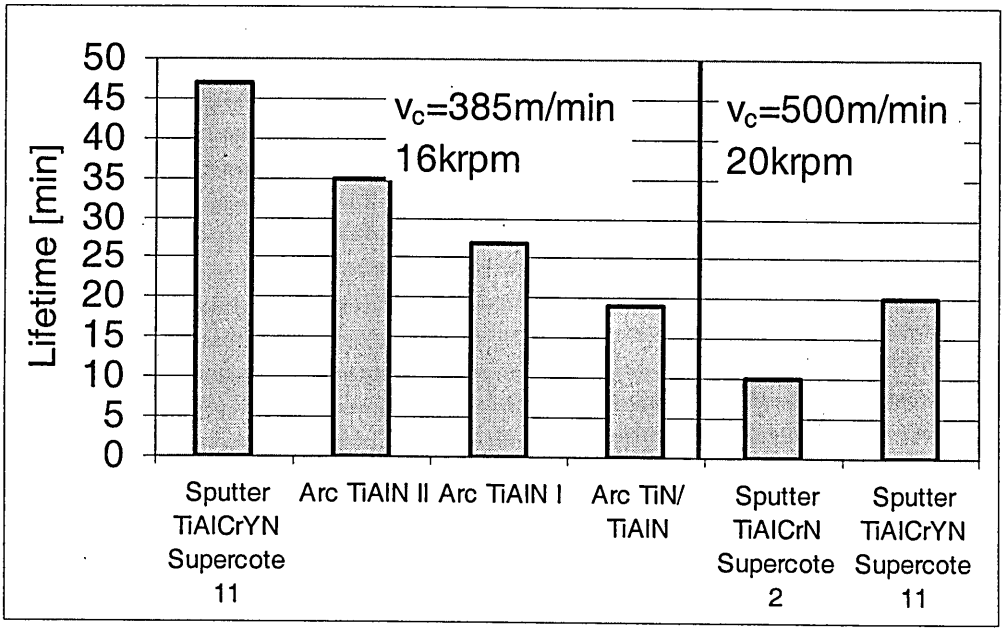

Figure 9: Milling test results from various coating grown on cemented carbide ball nosed end mills.

Acknowledgements

The investigations have been partially financed by the DTI - Link Surface Engineering Project GK/ K 76351 and by the Brite Euram Project Hidam (No: BRPR CT 98-0753). Particular gratitude is expressed to Hydra Tool International Plc Sheffield, and their managing director Mr A.P. Deeming, who have supported the project by supplying the cemented carbide test tools. We also like to acknowledge the Department of Materials at the University of Oxford for the use of the STEM HB501 microscope. The encouraging support of Prof. J.M. Titchmarsh was extremely helpful and is highly appreciated.

References

1. W.-D. Münz, *Titan aluminium nitride films: A new alternative to TiN coatings.* Journal of Vacuum Science and Technology A, 1986. **4**: p. 2717.
2. L.A. Donohue, I.J. Smith, W.-D. Münz, I. Petrov and J.E. Greene, *Microstructure and oxidation resistance of TiAlCrYN layers grown by combined steered-arc/ unbalanced magnetron sputter deposition.* Surface and Coatings Technology, 1997. **94-95**: p. 226-231.
3. M.I. Lembke, D.B. Lewis and W.-D. Münz, *Localised oxidation defects in TiAlN/CrN superlattice structured hard coatings grown by cathodic*

arc/ unbalanced magnetron deposition on various substrate materials. Surface and Coatings Technology, 2000. **125**: p. 263-268.
4. W.-D. Münz, D. Schulze and F.J.M. Hauzer, *A new method of hard coatings: ABS (arc bond sputtering).* Surface and Coatings Technology, 1992. **50**: p. 169-178.
5. W.-D. Münz, C. Schönjahn, H. Paritong and I.J. Smith, *Hard Coatings Deposited by Combined Cathodic Arc Evaporation and Magnetron Sputtering (Arc Bond Sputtering: ABS).* Le Vide, 2000. **3/4**(297): p. 205.
6. C. Schönjahn, L.A. Donohue, D.B. Lewis, W.-D. Münz, R.D. Twesten and I. Petrov, *Enhanced adhesion through local epitaxy of transition-metal nitride coatings on ferritic steel promoted by metal ion etching in a combined cathodic arc/ unbalanced magnetron deposition system.* Jornal of Vacuum Science and Technology A, 2000. **18**(4): p. 1718.
7. C. Schönjahn, *Surface treatment in a cathodic arc plasma - key step for interface engineering*, in *Materials Research Institute*. 2001, Sheffield Hallam University: Sheffield.
8. D.B. Lewis, L.A. Donohue, M. Lembke, W.-D. Münz, R.K. Jr., V. Valvoda and C.J. Blomfield, *The influence of the yttrium content on the structure and properties of TiAlCrYN PVD hard coatings.* Surface and Coatings Technology, 1999. **114**: p. 187-199.
9. M.I. Lembke, D.B. Lewis, W.-D. Münz and J.M. Titchmarsh, *Significance of Y and Cr in TiAlN hard coatings for dry high speed cutting.* Surface Engineering, 2001. **17**.
10. E. Zoestbergen, N.J.M. Carvalho and J.T.M. DeHosson, *Stress state of TiN/TiAlN PVD Multilayers.* Surface Engineering, 2001. **17**(1): p. 29-34.

Joint Second Prize

SIGNIFICANCE OF Y AND Cr IN TiAlN HARD COATINGS FOR DRY HIGH SPEED CUTTING

M. I. Lembke, D. B. Lewis, W.-D. Münz, and J. M. Titchmarsh

High speed cutting of die steels (A2, HRC58, 15 000 rev min^{-1}, 385 m min^{-1}) demands high wear and oxidation resistant and extremely well adherent coatings. PVD is the preferred deposition technique to tailor a coating for this application. With the development of TiAlN based hard coatings, an important step in the direction of improved cutting performance has been achieved. TiAlCrYN is a state of the art coating, which has proven to be very successful in demanding dry high speed cutting operations. A special feature of this coating is a double layered overcoat consisting of a lower fine multilayered TiAlYN/CrN with a periodicity of 1·6 nm graded into an upper glassy amorphous TiAlY oxynitride. The incorporation of Y leads to an enhanced oxidation resistance, whereas the most important effect of the double layered overcoat is the reduction of the friction coefficient. To confirm the beneficial effects of Y and Cr, sophisticated TEM has been employed with an X-ray resolution of approximately 3 nm. Segregation of Y and other elements in this system (tool/coating) were detected along the column boundaries in the TiAlCrYN coating at 900°C. Y is acting like a 'plug' against both inward and outward diffusion of foreign elements. The oxidation behaviour has been further quantified using highly sensitive thermogravimetric analysis and glancing angle X-ray diffraction. The successful impact of the incorporation of Y into TiAlCrN and the use of a Cr containing nanostructured oxynitride sputter deposited overcoat is shown by coated two flute ball nosed solid carbide cutters at a cutting speed of 385 m min^{-1}.

SE/393

Miss Lembke, Dr Lewis, and Professor Münz are at the Materials Research Institute, Sheffield Hallam University, Howard Street, Sheffield S1 1WB, UK. Professor Titchmarsh is in the Department of Materials, University of Oxford, Parks Road, Oxford OX1 3PH, UK. Contribution to the 2000 Bodycote International Paper Competition.

INTRODUCTION

Dry high speed cutting operations have made it necessary to develop new high temperature resistant PVD coatings to protect cemented carbide cutting tools against wear and oxidation. In this field TiAlN coatings are widely used because they exhibit oxidation resistance up to 750°C.[1] The improved oxidation resistance and thermal stability of $Ti_{0·5}Al_{0·5}N$ stems from its ability to form a stable passive double oxide layer, where the upper layer is Al rich and the lower layer is Ti rich.[2] Sputtered neutral mass spectrometry (SNMS) in a TiAlCrN coating with low concentration of Cr (0·03 at.-%) showed that after 1 h exposure at 900°C, elements Fe and Cr diffused from the stainless steel substrate material towards the coating surface.[3,4] It was shown that the interface stability was increased by the addition of Y to the TiAlCrN coating. Significantly reduced outward diffusion of substrate elements was observed for the $Ti_{0·43}Al_{0·52}Cr_{0·03}Y_{0·02}N$ coating.[4] The incorporation of Y reduced the oxide layer growth from ~3000 nm ($Ti_{0·44}Al_{0·53}Cr_{0·03}N$) to ~300 nm ($Ti_{0·43}Al_{0·52}Cr_{0·03}Y_{0·02}N$) after 1 h at 950°C. Apart from the different composition, the major difference between the Y containing coating and $Ti_{0·44}Al_{0·53}Cr_{0·03}N$ is the microstructure. The microstructure of the Y containing coating evolved by a process of interrupted columnar growth, whereas the $Ti_{0·44}Al_{0·53}Cr_{0·03}N$ coating showed a typical columnar structure.[4] The fine grain size in the Y coating increases the path for both outward diffusion of cations to the free surface and oxygen diffusion into the film. The segregation of Y to the grain boundaries was observed after heat treatment for 1 h at 950°C. Y is thought to act as a barrier to grain boundary diffusion.[4] The present paper deals with the fundamental understanding of the influence of Y and the addition of Cr in a TiAlN based hard coating. $Ti_{0·44}Al_{0·53}Cr_{0·03}N$ (type A),[3] $Ti_{0·43}Al_{0·52}Cr_{0·03}Y_{0·02}N$ (type B),[3] and an improved TiAlCrYN with an overcoat (type C, Fig. 1) were investigated after heat treatment at 900°C at the nanometre scale, using state of the art electron microscopy techniques.

EXPERIMENTAL

All coatings were deposited by the arc bond sputtering (ABS) technology using an industrially sized (Hauzer HTC 1000 ABS) physical vapour deposition machine.[5,6] Two opposing cathodes were equipped with TiAl targets. The other two positions were occupied by a Cr target and a TiAlY target containing 4 at.-%Y. The TiAl and TiAlY targets were operated in unbalanced magnetron deposition (UBM) mode,

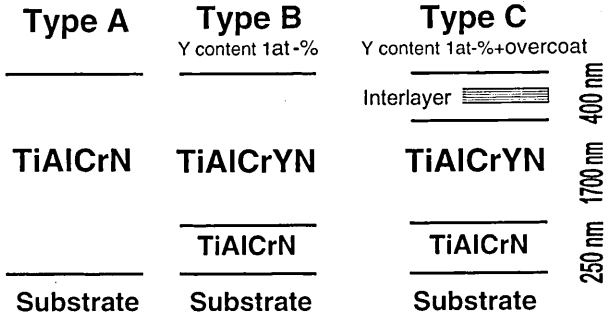

1 *Schematic illustration showing main differences between Y free and two TiAlCrYN coatings used*

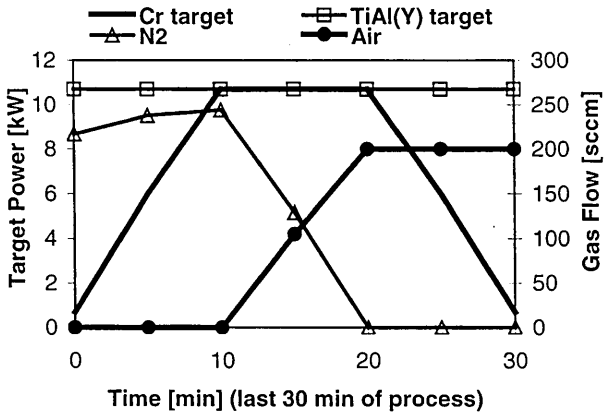

2 *Details of process parameters used to deposit multilayer structured oxynitride overcoat region: TiAl(Y) indicates two TiAl and one TiAlY target used*

whereas the Cr target was either operated in steered cathodic arc mode or in UBM mode. All substrates were subjected to a threefold rotation and the substrate table was rotated at a frequency of 7·5 rev min^{-1}. Before deposition all targets were sputter cleaned using a power of 5 kW on each target for 10 min at a pressure of $2{\cdot}4 \times 10^{-3}$ mbar. The deposition starts with cathodic arc Cr metal ion etch (1200 V bias, 12 min) to form a well defined interface which allows localised epitaxial growth[7] of the growing film to achieve a sufficiently high adhesion. In the case of coatings of type B and C, a TiAlCrN base layer (identical to that of type A) was deposited by UBM (45 min) using the two TiAl targets at 10·7 kW and the Cr and TiAlY targets at 0·7 kW, respectively. During deposition a substrate temperature of 450°C and a bias voltage of −75 V was applied. Condensation took place in a mixed $Ar+N_2$ atmosphere at a pressure of $3{\cdot}4 \times 10^{-3}$ mbar. The TiAlCrYN (type B) coating was subsequently deposited onto the base layer at the same temperature and bias voltage at a pressure of $3{\cdot}5 \times 10^{-3}$ mbar. For the deposition of the TiAlCrYN (4 h), the TiAlY and TiAl targets were each operated at a power of 10·7 kW, while the Cr target was operated at only 0·7 kW. The coating architecture of the type B coating was further improved by depositing an especially designed overcoat. The new version with the overcoat (type C) and the original version (type B) are outlined schematically in Fig. 1. Special attention has been paid to the deposition of the overcoat. To achieve a sufficiently strong mechanical support for the glassy and extremely smooth oxynitride overcoat, a thin particularly hard superlattice type coating was grown. By increasing the power on the Cr target stepwise from 0·7 to 10·7 kW, an interlayer with TiAlYN and CrN layers was produced.[8] These conditions were held for 10 min, then the Cr target power was gradually decreased to 1 kW. In parallel, the nitrogen gas flow was progressively reduced and gradually replaced by medical dry air. In this way, a Cr and oxygen containing TiAl oxide surface was obtained (Fig. 2).

The substrate material used was cold rolled stainless steel 304 polished to a surface roughness R_a of ~0·01 μm. The coated specimens were heat treated in air in a furnace at 900°C for 1 h.

The coating composition of type C was measured using Rutherford backscattering with 2 MeV He^+ ions at an incident angle of 22·5° relative to the specimen surface normal with the detector set at a 150° scattering angle. The total accumulated ion dose was 100 μC. The spectrum was analysed using the RUMP simulation program[9] and found to be $Ti_{0{\cdot}34}Al_{0{\cdot}62}Cr_{0{\cdot}03}Y_{0{\cdot}01}N$.

A Cahn TG 131 microbalance was used for the thermogravimetry (TG) work. The specimens were heated to 900°C (at 50 K min^{-1} to 850°C and then with 15 K min^{-1} to 900°C) and then held for 10 h in air. The gas flow rate in the furnace of the TG was 12·6 mL min^{-1}.

Pin on disk tests were performed on coated M2 high speed steel substrates using an alumina ball with a defined force of 5 N and a speed of 0·1 m s^{-1}.

Low angle X-ray diffraction using Bragg–Brentano geometry for 2θ values of 2–8° was used to measure the bilayer thickness of the multilayers.[10] Glancing angle XRD with a fixed shallow incident angle of 0·5° was used to determine the oxides formed on the coating surface after heat treatment.

A conventional Philips CM20 TEM operated with a LaB_6 filament at an accelerating voltage of 200 kV was used for the TEM imaging and a Vacuum Generators HB501 dedicated FEG scanning TEM operated at 100 kV was used for the high resolution energy dispersive X-ray (EDX) analysis and elemental mapping. A windowless detector was employed for such analyses. All TEM images and analyses were obtained on cross-sections. Cross-sectional specimens for the TEM were prepared by a mechanical grinding process to about 50 μm in thickness from thin slices (1 mm) and then ion milled with a shallow incidence angle of 8° from the top surface (specimen below copper grid) and 5° from the bottom surface until electron transparency was reached.

RESULTS AND DISCUSSION

A bright field cross-sectional TEM micrograph of a type C coating is shown in Fig. 3. The 250 nm thick base layer (type A coating) exhibits a columnar growth morphology. Type B and C coatings showed an interrupted columnar growth structure when compared with the columnar growth morphology of a TiAlCrN (type A) coating (Fig. 3). The addition of Y initiated a continuous renucleation mechanism, which was interpreted to be responsible for the interrupted columnar growth morphology.[4] Similar microstructures were generated and observed through ion irradiation damage in TiN[11] and in TiAlN[12] through the formation of a wurtzite–AlN phase during the film growth (temperature of film growth $\geqslant$560°C).

The region of the overcoat appears darker owing to the additional amount of the higher atomic number element Cr. Low angle XRD from a type C coating showed the formation of a diffraction peak stemming from the TiAlYN/CrN multilayer structure in the overcoat. The bilayer thickness of the multilayer was 1·6 nm. This peak is missing for the type B coating. Glancing angle X-ray diffraction indicated that the upper layer of the oxynitride overcoat was amorphous.

The as deposited XTEM specimen was further analysed in the overcoat region using EDX point

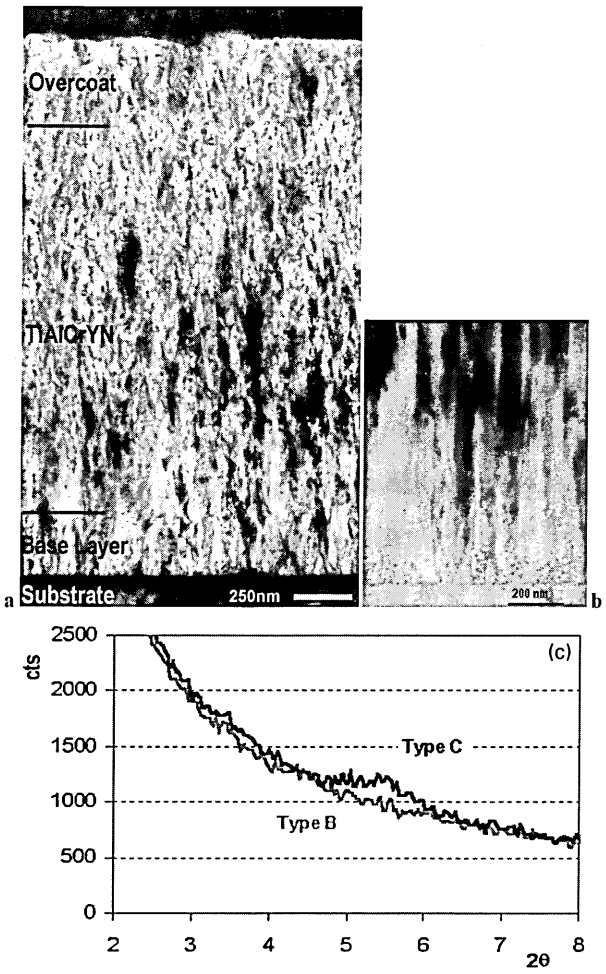

3 *a, b XTEM bright field images of type C and type A coatings, respectively and c XRD pattern of multilayer d spacing in overcoat where peak is generated by multilayer structure in overcoat: d spacing = 1·6 nm*

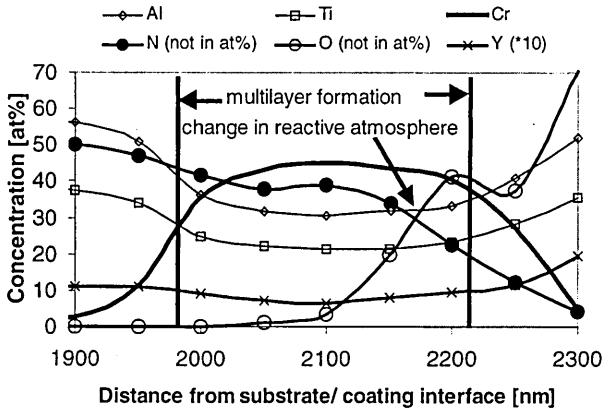

4 *EDX point analysis in overcoat region of as deposited TiAlCrYN with overcoat: marked multilayer region has d spacing of 1·6 nm*

analysis (Fig. 4), which showed a change in composition consistent with the process parameters. An increase in Cr concentration up to 40 at.-% was achieved by increasing the power to the Cr target, as well as an analogous decrease in Ti, Al, and Y contents in this region as would be expected from the change in process parameters. The Cr rich region (above 25 at.-%) is approximately 250 nm thick (total overcoat thickness 400 nm). The graded transition from the nitride to the oxynitride started approximately 180 nm from the coating surface. The slight

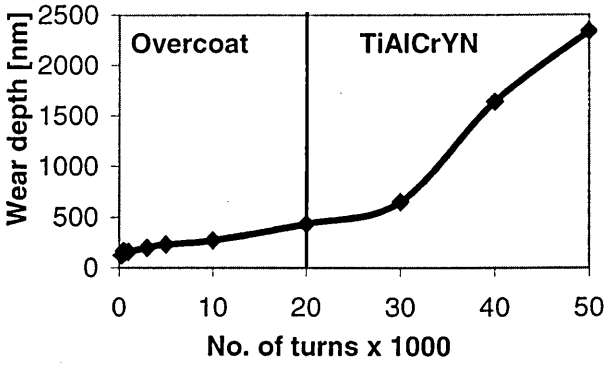

5 *Pin on disc test results on TiAlCrYN coating with overcoat: load 5 N; speed 0·1 m s^{-1}; alumina ball*

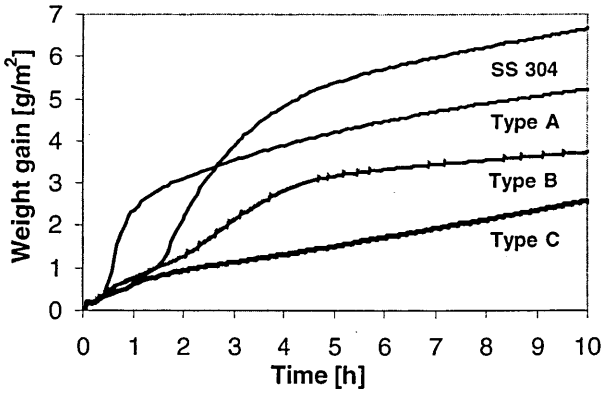

6 *Isothermal thermogravimetry (TG) measurements at 900°C of investigated coatings and substrate material: error approx. 0·2 g m^{-2}*

inconsistency between measurements in the apparent overcoat thickness from XTEM and EDX analysis is because the mass contrast contribution to the XTEM image is not discernible at the lower Cr concentrations (Fig. 3). The multilayer structure is contained within the Cr rich region.

Pin on disc tests on type C coatings showed a remarkable increase in wear rate with increasing wear depth (Fig. 5). In parallel, the friction coefficient increased from 0·65 to 0·92.[13] Thereby 0·65 stands for the friction coefficient of the coating of type C whereas 0·92 represents deeper regions in type C or type B alone. The positive behaviour of the overcoat in type C coatings can be explained by the excellent wear behaviour of superlattice architectured coatings,[14–16] which reduce crack propagation.

Isothermal thermogravimetric measurements at 900°C showed a clear difference in weight gain (Fig. 6) between type C ($2{\cdot}58 \pm 0{\cdot}2$ g m^{-2}) and type B ($3{\cdot}71 \pm 0{\cdot}2$ g m^{-2}) coatings. As a comparison the weight gain of a type A coating ($5{\cdot}21 \pm 0{\cdot}2$ g m^{-2}) and the substrate material stainless steel 304 ($6{\cdot}67 \pm 0{\cdot}2$ g m^{-2}) are also plotted in Fig. 6. The lower values of the type C coating resulted from the improved oxidation resistance of the Cr rich interlayer[8] and the oxynitride overcoat.

A montage of elemental distribution maps for the elements Cr and Fe in the coating and substrate in type A and C coatings are shown in Fig. 7*a* and *b*, respectively. In the type A coating, diffusion of the substrate elements Cr and Fe was observed mainly along the column boundaries, but also in the columns themselves, from the stainless steel substrate to the coating surface. In the type C coating, diffusion of

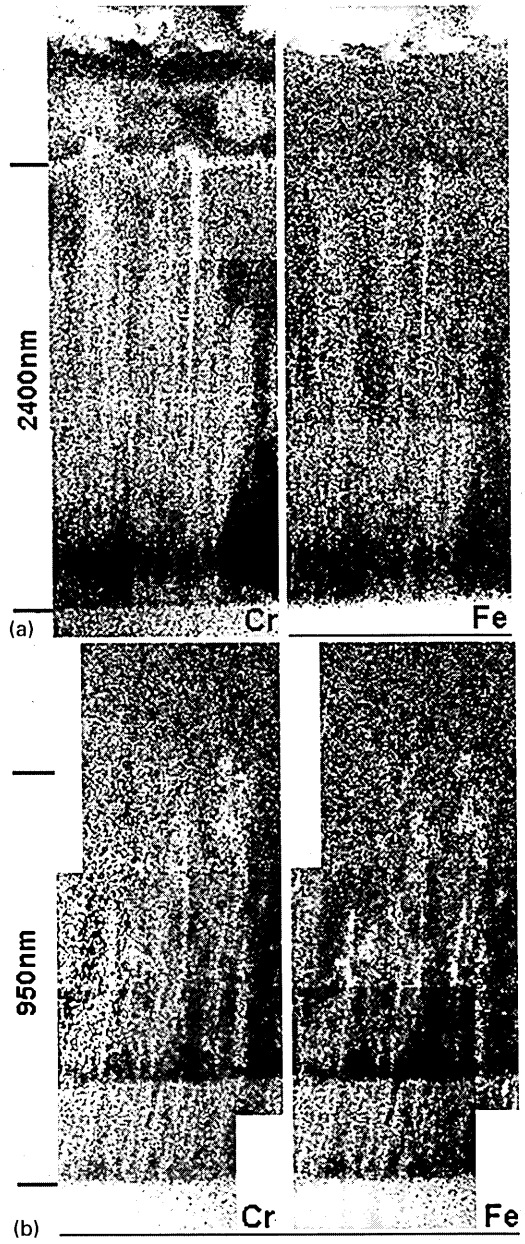

7 *Iron and chromium elemental mapping for heat treated (1 h, 900°C) **a** type A and **b** type C coatings: note difference in scale of maps*

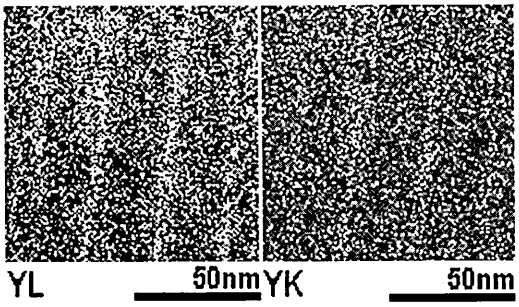

8 *Yttrium segregation at column boundaries of type C coating after heat treatment for 1 h at 900°C*

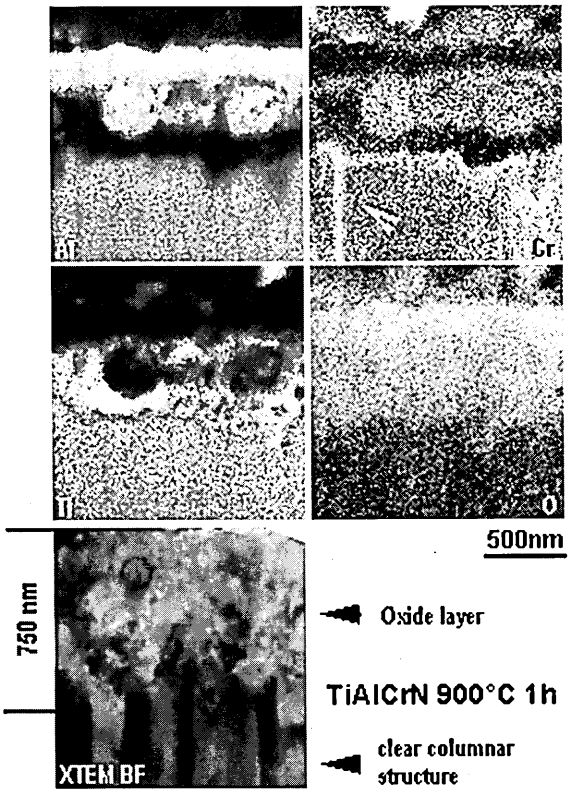

9 *Elemental maps and bright field (BF) image of type A coating heat treated for 1 h at 900°C*

Cr and Fe was observed mainly in the Y free base layer (type A) and its local vicinity above this layer, typically along column boundaries, as shown previously for the type A coating. A sharp decrease in the concentration of Cr and Fe was observed in the Y containing coating. Elemental maps for the element Y taken at higher magnification after heat treatment for 1 h at 900°C revealed Y segregation along the column boundaries (Fig. 8). To unambiguously identify Y, elemental maps using both the K and L lines were produced. This confirmation experiment again indicated that preferential segregation of Y is responsible for 'blocking' the path along the column boundaries for inward and outward diffusion.

Examination by TEM of the coatings under investigation after heat treatment for 1 h at 900°C (Figs. 9–11) showed a difference in oxide layer thickness, consistent with the previous findings of the TG results. The type A coating formed an oxide layer of 750 nm. In contrast, type B and C coatings had oxide layer thicknesses of 430 and 230 nm, respectively, thus showing a clear improvement in oxidation resistance resulting from the incorporation of Y and the additional amount of Cr in the overcoat region.

Further elemental XTEM maps of the coating surface of type A and B coatings after heat treatment in air for 1 h at 900°C are shown in Figs. 9 and 10. In the case of type A and B coatings an oxide bilayer containing mainly TiO_2 and Al_2O_3 was observed at coating surface as reported previously.[2–4] However, in the type A coating there was also evidence of Cr within of the Al_2O_3 regions. A thin Cr rich oxide band was also present in both type A and B films at the coating/TiO_2 interface. In the type B film, this Cr band formed by oxidation of Cr incorporated into the coating during sputtering (0·7 kW). Owing to the absence of Y, in type A films, additional Cr had diffused from the stainless steel substrate to the surface (Fig. 7*a*). Elemental maps of the surface of a type C coating after heat treatment in air for 1 h at 900°C are shown in Fig. 11. At the surface the heat treatment led to the formation of Al rich, Cr rich,

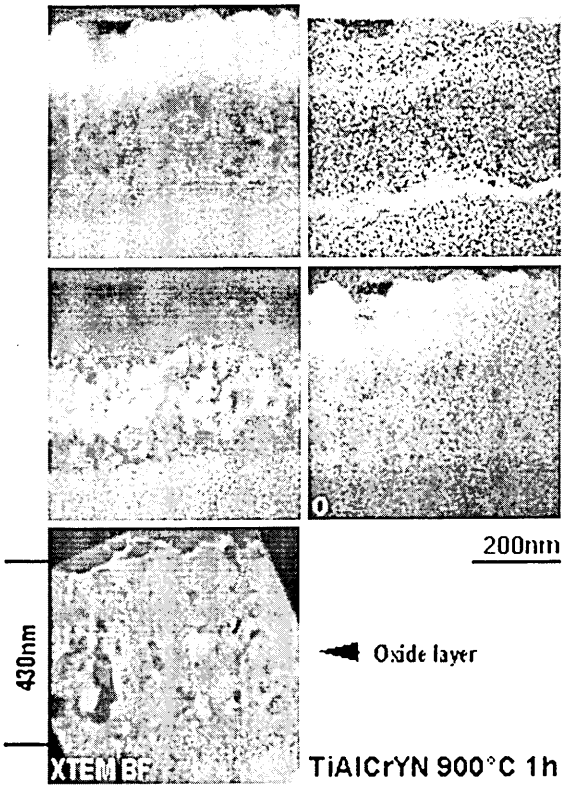

10 *Elemental map and BF image of type B coating heat treated for 1 h at 900°C*

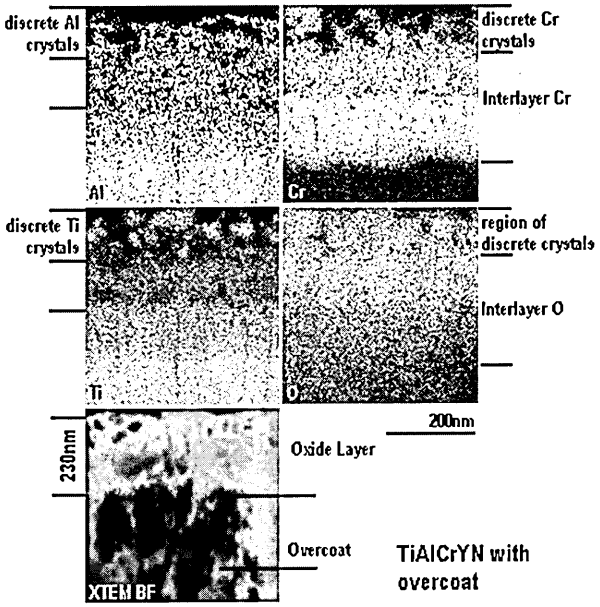

11 *Elemental map and BF image of type C coating heat treated for 1 h at 900°C*

and Ti rich discrete oxide crystals. A Cr rich oxide layer was formed between the remaining TiAlYN/CrN multilayer and the discrete surface oxide particles. A comparison of the Cr rich layer and the O map showed that the oxide layer stopped in the Cr rich layer.

Glancing angle XRD scans on heat treated type A and C coatings showed that after 1 h at 900°C the following phases were present: TiO_2 (21–1276) Al_2O_3 (42–1468) and Cr_2O_3 (38–1479)[17] (Fig. 12). In the case of the type A coating, $FeCr_2O_4$ (34–0140) was additionally observed, forming after diffusion of

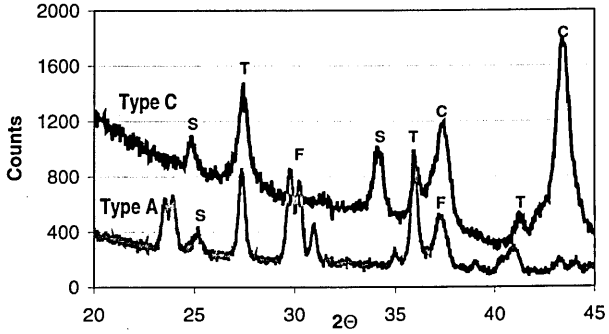

S: solid solution of Al_2O_3 (alumina) and Cr_2O_3 (eskolite); T: TiO_2 (rutile); F: $FeCr_2O_4$; C: coating

12 *Glancing angle XRD scan at 0·5° incident angle on type A and C coatings after heat treatment for 1 h at 900°C*

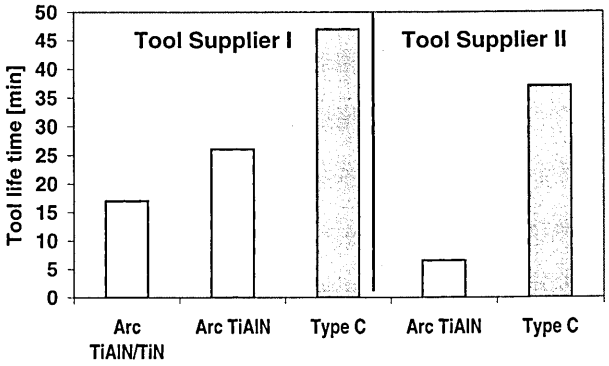

13 *Life time of coated end mills in dry high speed cutting operations: arc TiAlN/TiN has ~30 layers; workpiece material A2 (HRC 58); 8 mm B/N WC tool; cutting speed 385 m min^{-1}; feed rate 0·1 mm rev^{-1}; axial distance 3·8 mm, radial distance 0·4 mm*

substrate elements to the surface. In the type C coating peaks stemming from the coating were clearly visible in comparison to the type A coating, thus confirming the reduced oxide layer thickness in type C (type A, 750 nm; type C, 230 nm).

The improved oxidation and wear resistance of the oxynitride overcoat in the type C coating was directly transferred into coated cutting tools. Figure 13 shows a comparison between ball nosed end mills coated with sputter deposited type C and arc deposited TiAlN and TiAlN/TiN (approx. 30 layers) coatings from UK market leaders. Two different tool suppliers were used. In both cases the sputter deposited type C coating outperformed the arc deposited coatings.

CONCLUSIONS

1. The combined introduction of the Cr rich interlayer and the oxynitride overcoat resulted in a substantial improvement in oxidation resistance and mechanical performance.

2. Elemental mapping confirmed unambiguously that at elevated temperatures Y diffuses preferentially to the column boundaries. There it blocks the diffusion of substrate elements (Cr and Fe) to the surface.

3. The improvement in coating properties could be directly transferred into the performance of coated solid carbide tools in dry high speed cutting applications.

REFERENCES

1. W.-D. MÜNZ: *J. Vac. Sci. Technol. A*, 1986, **4**, (6), 2701.
2. D. McINTYRE, J. E. GREENE, G. HÅKANSSON, J. E. SUNDGREN, and W.-D. MÜNZ: *J. Appl. Phys.*, 1990, **67**, 225.
3. I. J. SMITH and W.-D. MÜNZ: *Surf. Eng.*, 1998, **14**, (1), 37.
4. L. A. DONOHUE, I. J. SMITH, W-.D. MÜNZ, I. PETROV, and J. E. GREENE: *Surf. Coat. Technol.*, 1997, **94–95**, 226.
5. W.-D. MÜNZ, D. SCHULZE, and F. J. HAUZER: *Surf. Coat. Technol.*, 1992, **50**, 169.
6. W.-D. MÜNZ, C. SCHÖNJAHN, H. PARITONG, and I. J. SMITH: *Le Vide*, 2000, **3–4**, 297, 205 (in French).
7. C. SCHÖNJAHN, L. A. DONOHUE, D. B. LEWIS, W.-D. MÜNZ, R. D. TWESTEN, and I. PETROV: *J. Vac. Sci. Technol. A*, 2000, **18**, (4), 1718.
8. I. WADSWORTH, I. J. SMITH, L. A. DONOHUE, and W.-D. MÜNZ: *Surf. Coat. Technol.*, 1997, **94–95**, 315.
9. R. L. DOOLITTLE: *Nucl. Instrum. Methods Phys. Res.*, 1985, **B15**, 344.
10. D. B. LEWIS, L. A. DONOHUE, M. LEMBKE, W.-D. MÜNZ, R. KUZEL, Jr, V. VALVODA, and C. J. BLOMFIELD: *Surf. Coat. Technol.*, 1999, **114**, 187.
11. I. PETROV, L. HULTMAN, J.-E. SUNDGREN, and J. E. GREENE: *J. Vac. Sci. Technol. A*, 1992, **10**, (2), 265.
12. F. ADIBI, I. PETROV, L. HULTMAN, U. WAHLSTROM, T. SHIMIZU, D. McINTYRE, J. E. GREENE, and J.-E. SUNDGREN: *J. Appl. Phys.*, 1991, **69**, (9), 6437.
13. U. SCHARF: 'Vergleich tribologischer Eigenschaften von monolytisch und mehrfach abgeschiedenen PVD Hartsoffschichten', Diploma thesis, Westsächsische Hochschule Zwickau, 1998 (in German).
14. Q. LUO, W. M. RAINFORTH, and W.-D. MÜNZ: *Wear*, 1999, **225–229**, 74.
15. H. HOLLECK and V. SCHIER: *Surf. Coat. Technol.*, 1995, **76–77**, 328.
16. W.-D. MÜNZ, L. A. DONOHUE, and P. Eh. HOVSEPIAN: *Surf. Coat. Technol.*, 2000, **125**, 269.
17. JCPDS-ICDD Diffraction Data Database, International Centre for Diffraction Data, Newton Square, PA, 1993.

Mat. Res. Soc. Symp. Proc. Vol. 648 © 2001 Materials Research Society

INVESTIGATION OF THE OXIDATION BEHAVIOUR OF A TiAlCrYN PVD HARD COATING

Mirkka I. Lembke, John M. Titchmarsh[x], D. Brian Lewis, W.-Dieter Münz
Materials Research Institute, Sheffield Hallam University, Sheffield, UK
[x]Department of Materials, University of Oxford, Oxford, UK

ABSTRACT

For dry high speed cutting the oxidation resistance of the protective hard coating of the cutting tool surface is very important. Therefore the effects of heat treatment on a TiAlN based hard coating deposited by the combined cathodic arc unbalanced magnetron sputtering technique have been studied using cross sectional transmission electron microscopy (XTEM) and energy dispersive X-ray analysis (EDX). The combination of these analytical techniques revealed the diffusion paths and preferences in diffusion of various coating and substrate elements in a physical vapour deposited (PVD) type coating after heat treatment. The structure comprises a ~2 μm thick TiAlCrYN coating on top of a 0.25 μm thick TiAlCrN base layer deposited on a stainless steel substrate. In the as-deposited sample Y was distributed in a fine layered structure (1.7 nm) throughout the coating. The coating was heat treated at temperatures between 600 °C and 900 °C in air for 10 hrs duration. With increasing temperature the microstructure changed gradually from interrupted columnar growth to a fully columnar structure at 900 °C as observed with XTEM. EDX analysis after heat treatment at 700 °C showed the presence of substrate elements Fe and Cr mainly at column boundaries in the base layer. In contrast no evidence of substrate elements could be observed in the TiAlCrYN coating, thus showing a sharp change in elemental composition concerning Cr and Fe between base layer and coating. This indicates that Y segregation in the TiAlCrYN coating along column boundaries inhibited column boundary diffusion of the substrate elements Cr and Fe. Energy dispersive X-ray distribution maps recorded after 800 °C annealing showed distinct segregation of Y along the column boundaries. The substrate elements, Fe and Cr, were observed through the coating along column boundaries up to 0.95 μm from the base layer/coating interface. After heat treatment at 900 °C the substrate elements had diffused from the substrate/coating interface to the coating surface. Y out-diffused, too and was concentrated adjacent to TiO_2 crystals in the oxide layer.

INTRODUCTION

Dry high speed cutting has made it necessary to develop new high temperature resistant PVD coatings to protect the cutting tools. The coatings are designed to protect cemented carbide cutting tools against wear and oxidation. In this field TiAlN coatings are widely used because they exhibit oxidation resistance up to 750 °C [1]. The improved oxidation resistance and thermal stability of TiAlN stems from its ability to form a thermally stable double oxide layer, where the upper layer is Al-rich and the lower layer is Ti-rich [2]. Previous investigations into the oxidation resistance showed that substrate elements were detected at the coating surface after 1 hr oxidation at 900 °C for a $Ti_{0.44}Al_{0.53}Cr_{0.03}N$ [3] type coating and after 1.5 hrs at 900 °C for $Ti_{0.5}Al_{0.5}N$ [2]. Both films were deposited onto a stainless steel substrate. The oxidation resistance was increased (up to 950°C) with the addition of Y into the coating. Incorporation of

3at % Cr and 2 % Y led to a massive suppression in cation/ anion in and out-diffusion. Even after 1 hr at 950 °C a completely stable interface was observed [3].

Most research on the oxidation behaviour of thin coatings is performed using scanning electron microscopy in connection with EDX, energy loss spectroscopy (EELS) and X-ray photo electron spectroscopy (XPS) for bulk samples. EELS is in general a better choice for light element analysis, but it requires even thinner TEM samples than those for EDX analysis. EELS is also more difficult to interpret in comparison with EDX. STEM/ EDX mapping is rarely used in oxidation investigations, even though it is a common tool in SEM oxidation investigations. The resolution of the elemental maps in a dedicated STEM (scanning TEM) is in the order of 3 nm thanks to the small probe size and the thin samples used (around 80 nm for TiAlN based films). Another advantage is, that the mapping technique displays the results for a relative large area, enabling understanding of complex, multiphase specimens much easier than by using point analysis.

First analytical experiments (EDX point analysis) have shown that Y segregated preferentially at the column boundaries in a TiAlCrYN coating as well as near the oxide layer after heat treatment for 1 hr at 950 °C [3]. In this paper EDX mapping shall be introduced as an ideal method to investigate the diffusion behaviour of substrate and coating elements in hard coatings and the role of Y to provide stability of the coating interface. Structure changes were investigated and recorded with XTEM (cross-sectional TEM) imaging techniques.

EXPERIMENTAL

The TiAlCrYN coatings with oxynitride top-layer were deposited by the ABS™ technology using an industrially sized (Hauzer HTC 1000/5 MK II ABS) physical vapour deposition machine [4]. The TiAlCrYN was deposited onto a TiAlCrN base layer of 250 nm thickness. The deposition parameters for the TiAlCrYN coating have been described elsewhere [5,6]. Additionally, the coating under investigation had an oxynitride top layer.

The substrate material was mirror-polished stainless steel (SS 304). The samples were heat treated in dry air between 600 °C at 900 °C for 10 hrs.

The composition of the bulk coating was measured from a polished cross-section sample in the JEOL 840 A SEM using EDX analysis. Care was taken to minimise contributions from the oxynitride top-layer and the base layer because these layers had significantly different proportions of the Ti, Al and Cr compared with the coating. The measured coating composition was $Ti_{0.30}Al_{0.65}Cr_{0.04}Y_{0.01}N$.

A conventional Philips CM 20 TEM operated with a LaB_6 filament at 200 kV was used for the TEM imaging and a Vacuum Generators HB501 dedicated FEG scanning transmission electron microscope operated at 100 kV was used for the high resolution EDX analyses and elemental mapping. The electron probe had a size of about 3 nm full width, half maximum. A windowless detector was employed for such analyses. Cross sectional samples for the TEM were prepared by a mechanical grinding process to about 50 µm in thickness. Ion milling with a shallow incidence angle of 8° from the top surface and 5° from the bottom surface was used to produce an electron transparent sample.

RESULTS AND DISCUSSION

The as-deposited sample comprises three different layers. Layer one in Figure 1a is the TiAlCrN base layer of 250 nm thickness upon which the TiAlCrYN coating (region 2) of 1700 nm is deposited. Y is distributed in a fine layered structure (periodicity 1.7 nm) in the as-deposited film through the coating process [7]. This layer structure was not resolved in the TEM images. The obvious change in the bright field image contrast in region 3 indicates the oxynitride topcoat. The as-deposited sample contains separated void bands of 400±200 nm in length at the columnar boundaries.

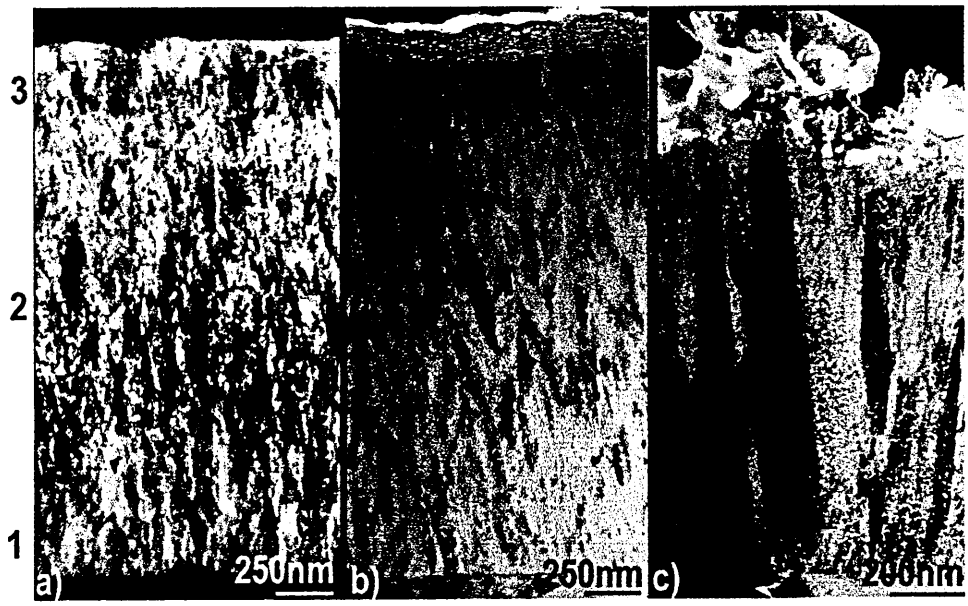

Figure 1. XTEM bright field images from TiAlCrYN with topcoat.

Figure 1b shows that, after heat treatment at 700 °C for 10 hrs, the structure had begun to change from one of interrupted columnar growth towards a fully columnar structure, from base layer to outer layer, which was observed following heat treatment at 900 °C (Figure 1c). Diffraction patterns (DP) were taken for each heat treatment condition from the middle of the coating with an aperture of approximately 500 nm. An evolution from a typical ring pattern, where the rings were sharp and well defined, implying that the structure was micro-crystalline was observed. However, as the temperature increased the DP had a smaller number of discrete spots indicating fewer crystallites in the aperture area (Figure 2). One explanation for the increased oxidation resistance in the Y-containing coating was the elongation of the diffusion path, due to its disrupted columnar growth [3]. However, this disruption clearly disappears with increasing temperature. The coating structure can have, therefore, such a positive effect only for temperatures below 800 °C. With the change in structure an elongation of the void bands along the column boundaries was also noticed. At 700 °C the void bands connect the coating surface with the stainless steel/ base layer interface, thus providing a quick reaction path. The eventual influence of the cooling rate has not been investigated here.

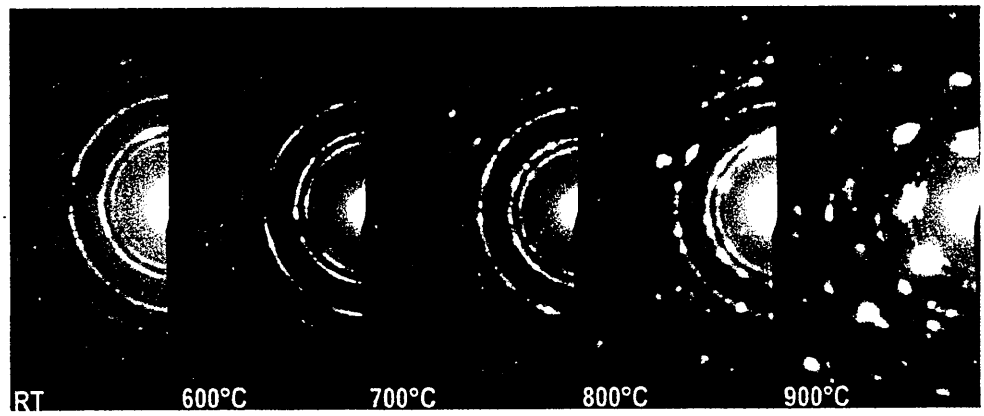

Figure 2. DP taken from the middle of TiAlCrYN with topcoat after annealing for 10 hrs.

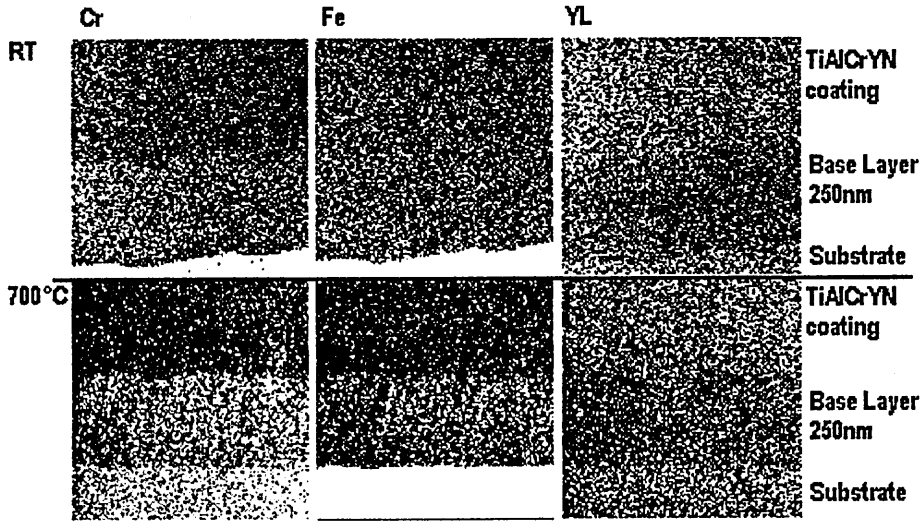

Figure 3. Elemental maps taken from the base layer region from the as-deposited sample (RT) and a coating heat treated for 10 hrs at 700 °C.

Elemental maps were used to investigate the integrity of the base layer region. They are, as will be shown, an ideal tool to investigate the migration of elements. Care has to be taken in the interpretation of these maps. The intensity of a map changes, due to the number of counts collected within the energy window set at the characteristic X-ray energy. However, the number of characteristic counts also varies e.g. with the sample thickness. Sample thickness effects can be recognised if the same change in intensity appears in corresponding elemental maps taken at the same area from the TEM sample. A rise in sample thickness leads also to a rise in background counts from all elements. In the case of the Y maps, where the intensity is quite low because of the concentration of Y in the sample, the consideration of change in intensity through change in the number of background counts is very important. A change in concentration of a major element can cause an apparent change in background intensity under a minor element peak. Also an increase in atomic number increases the amount of Bremsstrahlung contributing to the elemental maps.

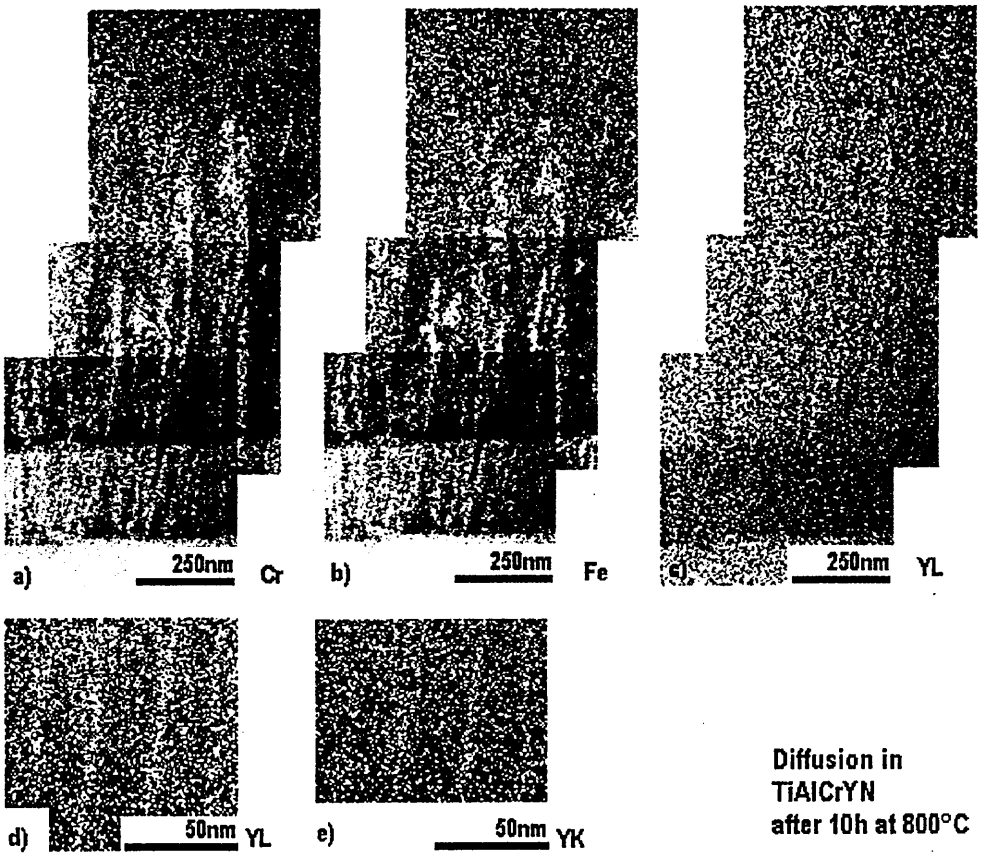

Figure 4. Elemental maps taken after heat treatment for 10 hrs at 800 °C in air.

Elemental maps from the as-deposited sample were produced and are shown in Figure 3. Cr, Fe and Y maps collected from the as-deposited sample showed the decreased or increased intensity in the base layer, as would be expected from the change in coating composition or from the change from substrate to coating. The substrate showed an increase in intensity in the Y map stemming from the increased amount of background counts and total counts collected. The background counts from the base layer to the TiAlCrYN coating should not change much. Additionally, the thickness stayed constant and hence, the higher intensity observed in the Y maps in the coating region stems from the incorporated Y. The difference in intensity observed by comparing the base layer to the TiAlCrYN coating stems from the different composition between base layer and coating.

The interface stability and the diffusion of coating elements was investigated after oxidation at 600 °C and 700 °C. No change in comparison to the as-deposited sample was observed at 600 °C. At 700 °C diffusion of substrate elements into the base layer was observed. A remarkable feature of this observation was the abrupt fall in diffusion at the base layer/ coating interface. The only difference between these two regions is the additional amount of Y in the main coating body. Hence, the reduced diffusion of substrate elements must be caused by this additional element. Closer inspection, especially of the Fe map, showed that diffusion occurred

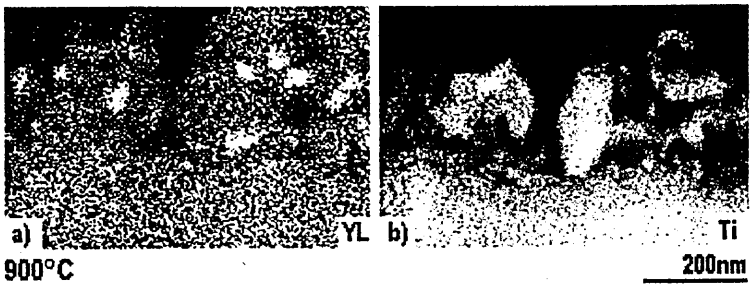

Figure 5. Elemental map from the surface of the coating after annealing for 10 hrs at 900 °C in air.

mainly along the grain boundaries. The operation of this fast diffusion path is predicted in e.g. [8] and is shown in X-ray distribution maps presented (Figure 3).

X-ray distribution maps taken after heat treatment at 800 °C showed an increased grain boundary intensity of Fe and Cr (Figure 4) in comparison to the maps from the coating annealed at 700 °C. As expected, the diffusion at higher temperature was more pronounced. The substrate elements are not only found at the boundary regions in the base layer but also in the bulk coating. Additionally, intensity distribution from Cr and Fe maps in the base layer region gave the impression that these elements were tailed back at the coating/ base layer interface, leading probably to diffusion into the columns at the base layer/ coating interface. The diffusion of substrate elements stopped entirely after 940±10 nm (measured from the base layer/ coating interface) in the TiAlCrYN coating. Furthermore, at 800 °C, Y was detected at the column boundaries. A map from the Y_K (Figure 4e), at higher magnification confirmed the rise in intensity from Y_L (Figure 4d). Y is large atom in comparison to the other coating species. Its presence disturbs the fcc coating lattice and increases the lattice parameter from 0.4183 nm to 0.4221 nm ($Ti_{0.43}Al_{0.52}Cr_{0.03}Y_{0.02}N$) in comparison to a $Ti_{0.44}Al_{0.53}Cr_{0.03}N$ coating (base layer) [7]. The segregation of Y along the column boundaries is explained through the higher degree of freedom at 800 °C to move by vacancy diffusion in the lattice and the desire to form an undisturbed TiAlN structure. The segregation of Y seen at 800 °C might provide an explanation for the abrupt stop in diffusion observed at 700 °C. The amount of Y at the boundaries at 700 °C was perhaps not high enough to be seen at the magnification chosen for mapping. However, Y atoms that were already present at the column boundaries probably blocked the diffusion.

After 10 hrs at 900 °C substrate elements diffused to the coating surface. Previous investigations have shown that a heat treatment at this temperature led to a significant stress relaxation [7] which might explain why no voids were detected at the 900 °C sample in the BF TEM image. Cr and Fe maps had nearly the same intensity for the entire base layer region, which means that all possible lattice sites might be "filled" with substrate elements. Diffusion in the TiAlCrYN coating was mostly limited to the column boundary regions. A higher concentration of Y was not observed in the TiAlCrYN layer following heating at 900 °C. A map of the Y_L intensity in the oxide layer showed regions of high intensity approx. 40±10 nm in size adjacent to Ti_xO_y particles (Figure 5). This would suggest that Y out-diffused, probably, to form Y_xO_y. However, the presence of a high oxygen concentration everywhere in this region prevented explicit confirmation that Y was in the form of an oxide.

CONCLUSIONS

The interrupted columnar structure found in the as-deposited sample changed gradually towards a typical columnar structure with increasing annealing temperature. First changes were observed at 700 °C after 10 hrs. The formation of void bands that connected the coating surface with the interface region was seen in the same sample.

Elemental mapping in the STEM is an ideal tool to investigate the migration of elements in thin films when used in combination with TEM imaging.

The diffusion of the substrate elements Cr and Fe was reduced by the presence of Y in the main coating body. Y was found in the TiAlCrYN coating at the column boundaries after heat treatment for 10 hrs at 800 °C. It started to out-diffuse after 10 hrs at 900 °C.

REFERENCES

1. W.-D. Münz, *Journal of Vacuum Science Technology A* **4** (6), 2701 (1986).
2. McIntyre, J.E. Greene, G. Håkansson, J.E. Sundgren,W.-D. Münz, *Journal of Applied Physics* **67** (1542), 225-261 (1990).
3. L. A. Donohue, I. J. Smith, W-.D Münz , I. Petrov and J. E. Greene, *Surface and Coating Technology* **94/95**, 226-231 (1997).
4. W.-D. Münz, D. Schulze, F.J. Hauzer, *Surface and Coating Technology* **50**, 169 (1992).
5. W.-D.Münz, I.J.Smith, Conference Proceedings of the Society of Vacuum Coaters in Chicago 17-22.4.1999, 350-356.
6. M.I. Lembke, D.B. Lewis, W.-D. Münz, *Surface Engineering* **17** (2), in press.
7. D.B.Lewis, L.A. Donohue, M.Lembke, W.-D. Münz, R.Kuzel Jr., V.Valvoda, C.J.Blomfield, *Surface and Coatings Technology* **114**, 187-199 (1999).
8. R. Messier, *Journal of Vacuum Science Technology A* **4** (3), 490-495 (1986).

Improvement in the Oxidation Behaviour of Superlattice Structured TiAlN/CrN Grown by Cathodic Arc/ Unbalanced Magnetron Deposition Technique

M.I. Lembke[1], D.B. Lewis, W.-D. Münz, Materials Research Institute, Sheffield Hallam University, Sheffield, UK

Abstract

TiAlN/CrN superlattice coatings with a bi-layer thickness of 3.8nm are known to resist oxidation up to a temperature of 900°C. In this investigation the bias voltage was varied between -75V and -95V, which led to an increase in coating hardness when measured on M2 high speed steel from HK 3400 (H_{plast} 55 GPa) at -75V bias to HK 4100 (H_{plast} 60GPa) at -95V bias measured on M2 steel. In parallel the internal stress increased from 5.1 GPa (75V) to 9.2 GPa (-95V) due to an increase in defect density. This investigation also shows that the applied bias voltage influences the oxidation behaviour. The measured weight gain from thermogravimetric investigations showed an increased oxidation resistance when the coating was deposited at -95V bias (1.57 g/m^2) when compared with that deposited at -75V bias (1.98g/m^2). Heat treatment for 1h at 900°C produced a shallow oxide scale of 80 ±20 nm thick. After 5h at 900°C the oxide layer contained mainly Cr_2O_3 and TiO_2 (rutile) oxides. Examination by optical and scanning electron microscopy of specimens heat treatment up to 900°C revealed a reduction in crack formation on the coating surface with increasing bias voltage, which was associated with the higher residual compressive stresses developed at the higher bias voltage. The formation of oxides in these cracks, of which some contain substrate material, was also reduced.

Introduction

A feature of PVD coating micro structure is the columnar morphology created by the ion flux that approaches the sample from a limited set of directions. Coatings are deposited at relatively low temperatures relative to the melting point of the material. This can lead to void formation in the deposited film. Anisotropic void and grain boundary morphologies can be directly related to the film properties (1). The TiAlN/CrN coating is produced using the cathodic arc/ unbalanced magnetron sputter technique. A cathodic arc metal ion etching step is used to provide the high adhesion required (2). One of the drawbacks of the cathodic arc deposition are the macroparticles generated during the metal ion etching stage, which result in the formation of growth defects during unbalanced magnetron deposition. Local growth defects and voided boundaries are known to the act as initiation sites for oxidation (3-5) and corrosion (6-7). Various techniques have been used to eliminate these problems. The direct diffusion path between coating surface and substrate via voided column boundaries can be reduced by increasing the bias voltage. Generally an increase in bias voltage increases the stress in the coating (8). Oxidation resistance at the higher Cr content superlattice coatings has been shown to be superior to those of monolithic TiAlCrN coatings (4). The paper reports results on the effect of bias voltage on the oxidation behaviour of TiAlN/CrN superlattice coatings.

Experimental

The TiAlN/CrN coatings were deposited by the ABS™ technology using a Hauzer HTC 1000-4 physical vapour deposition machine. This machine comprised 4 targets operated simultaneously in

[1] Corresponding author

a reactive atmosphere (2). Prior to the coating step the substrates were exposed to high negative bias voltage (-1.2kV) steered arc chromium metal ion etching treatment. The chromium metal ion etch minimises the amount of droplets produced (9). Before the actual coating step a $Ti_{0.44}Al_{0.53}Cr_{0.03}N$ stress reducing base layer of 300±30nm was deposited with at a bias voltage of -75V. Apart from one Cr target the remaining three targets were made from TiAl alloy. All targets were operated at 8kW in the coating step as this has been shown to give the maximum hardness (4). The bias voltage was varied between -75V and -95V. The coatings were approximately 4μm thick. The substrate material used was stainless steel 304 (SS), polished to a roughness of $R_a \cong 0.01\mu m$ finish.
The hardness of the coating was measured using a Knoop indenter with 25g load. Plastic hardness values and elastic moduli were obtained by using a Fisherscope nanoindenter with 50mN load.
Heat treatments were performed in a furnace in air at 900°C and the temperature during heat treatment was controlled to within an accuracy of ±3°C.
A Cahn TG 131 was used for the thermogravimetry work. The samples were continuously heated to 1000°C (at 50 °C/min to 400°C and from 400°C to 1000°C at 1°C/min) using a flow rate of 12.6 ml/min in dry air. For the isothermal investigations at 900 °C the samples were heated at 50 °C/min to 850°C, then with 15 °C/min to 900°C and then held for 10 hours.
The specimens were examined by SEM (Philips XL 40) at accelerating voltage 20kV for the imaging mode and at 10 kV for EDX analysis. The cross sectional TEM (XTEM) specimens were examined using a Philips CM 20 operated at 200kV with a LaB_6 filament.. For the optical micrographs a Vanox microscope was used.
The X-ray diffraction (XRD) was performed with monochromatic Cu-K_α radiation using glancing angle parallel beam geometry at 0.5° incidence angle to identify the oxides present. The phases present were identified using powder diffraction files data (10). Stress values were determined using glancing angle parallel beam geometry at an incidence angle of 5° (11).

Results and Discussion
The hardness of the TiAlN/CrN deposited onto M2 high-speed steel increased with increasing bias voltage, see table 1.

Bias Voltage	Stress [GPa]	Coating Thickness	HK	Hplast.
TiAlCrN 75V *	-3.8 (12)	3.23μm	3000	- - -
-75V	-5.1	4.46μm	3400	54
-85V	-7.4	4.12μm		52
-95V	-9.2	4.09μm	4100	65

*for comparison purposes only
Table 1: Results obtained from XRD and hardness measurements

Fig.1 (a and b) show continuous and isothermal thermogravimetric (TG) results for coatings deposited at bias voltages of –75 V, -85 V and –95 V. In all cases the oxidation resistance of the coating was found to increase with increasing bias voltage. For the continuous TG measurements the weight gain decreased from 1.97±0.17 g/m^2 to 1.56±0.17 g/m^2 as the bias voltage was increased from -75V to – 95 V (Fig. 1a). However, after 1h exposure at 900°C there was no significant effect of bias voltage on the measured weight gain, see table 2. In contrast after 5h exposure a significant decrease in weight gain was observed with increasing bias voltage, see table 2.

TiAlN/CrN	TG, continuous [g/m^2] At 1000°C	TG, isothermal [g/m^2]			Oxide	Density [10]
		1h	5h	10h		
-75V	1.98	0.65	1.50	1.79	Cr_2O_3	5.23
-85V	1.82	0.63	1.31	1.50	TiO_2	4.25
-95V	1.57	0.52	1.07	1.33	$FeCr_2O_3$	5.05

Table 2: Weight gain values measured at various positions of the investigations shown in Fig.1. The density of various oxides was provided for theoretical considerations.

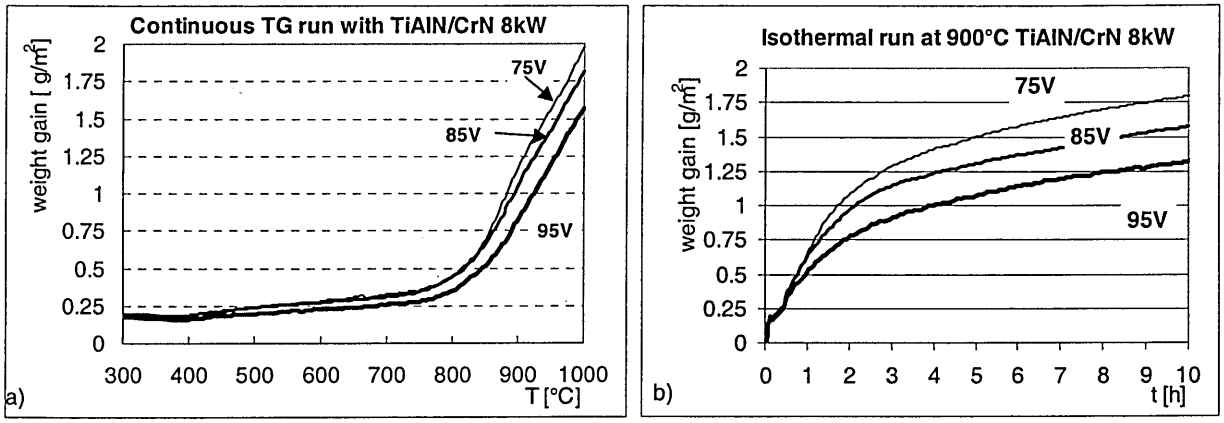

Fig.1: Thermogravimetric measurements on TiAlN/CrN deposited with various bias voltages.

Glancing angle parallel beam measurements after heat treatment for 1h at 900°C for the coating deposited at –75 V bias (Fig.2a) indicated peaks corresponding to Cr_2O_3 (38-1479). In the range 2θ = 25° to 35° a few peaks can be seen which could not be identified as belonging to any particular oxide phase. At the -85V and –95V bias no significant oxide peaks could be detected. The differences in relative peak intensities of {111} and {200} reflections between coatings deposited at –75V bias and coatings deposited at –85 and –95 V bias was due to a textural effect. After heat treatment at 900°C for 5h (Fig. 2b) the following oxide phases could clearly be identified: TiO_2 (21-1276), Cr_2O_3, Fe_3O_4 (19-629) and $FeCr_2O_4$ (34-0140). The two Fe oxide phases have the same crystal structure (cubic) and are isomorphous. The overall peak intensities for the oxide phases also decreased as the bias voltage was increased from -75V bias to -95V bias indicating a decrease in thickness of the oxide layer with increasing bias voltage.

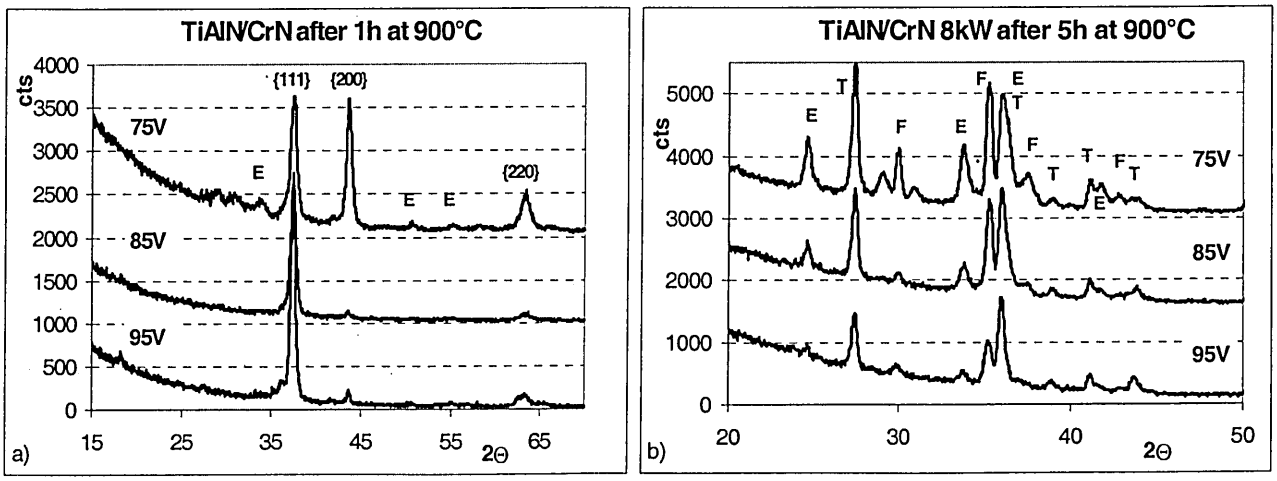

Fig.2: Glancing angle diffraction pattern taken after heat treatment for a) 1h and b) 5h at 900°C. E stands for eskolite Cr_2O_3, F for cubic Fe_3O_4 and $FeCr_2O_3$, T for rutile TiO_2

Glancing angle parallel beam geometry was also used to measure the residual stress of the TiAlN/CrN superlattice coatings and the results are given in table 1. In all cases the stress state was compressive and increased with increasing bias voltage from –5.1GPa at –-75V bias to –9.2GPa at –95V bias. Residual stress values for a monolithic TiAlCrN coating have also been included for comparison purposes. The stress levels in the superlattice coatings were systematically higher than that of the monolithic coating.

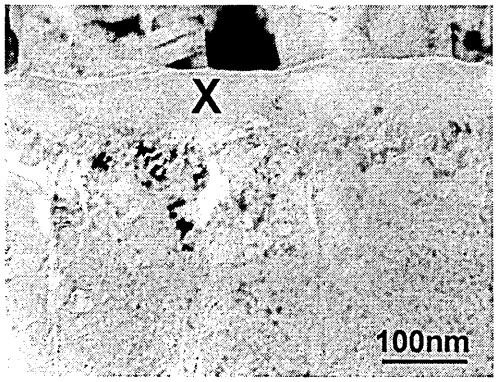

	N	O	Al	Ti	Cr
TiAlN/CrN RT	1	0.2	13.3	18.4	54
Oxide Layer	0	2.5	11.7	13	68.2
Oxide Crack	0	2.3	9.88	39.8	40.8

TiAlN/CrN after 1h at 900°C

Fig.3: TEM bright field micrographs of TiAlN/CrN deposited at –75 V bias heat-treated for 1h at 900°C. The X indicate points were the EDX analysis was taken from. The analysis of the TiAlN/CrN coating was taken of the middle of the sample.

After heat treatment for 1h at 900°C the formation of an 80±20nm dense very fine-grained oxide layer was observed (Fig.3). The oxide layer was richer in Cr than the superlattice coating, which indicated the formation of a Cr_xO_y layer, as measured by EDX. The thickness of the oxide layer formed did not change markedly between the different bias voltages. Theoretical calculations from the TG work and assuming an average oxide density (table 2) of $5g/m^3$ indicated an oxide layer thickness of approximately 100nm for all bias voltages, which fitted reasonably well with the measured thickness. The lack of significant oxide peaks found in the XRD pattern for coatings annealed for 1h at 900°C clearly results from both the thickness of the oxide layer the very fine grain size of the oxide produced.

After annealing the coating deposited at –75V bias for 5h at 900°C an oxide layer with an average layer thickness of ~340nm with oxide crystals locally as large as 170nm growing out of this layer (Fig.4) was observed. EDX analysis showed these large crystals to be rich in Ti and indeed the XRD pattern showed the presence of TiO_2 (rutile) in the oxide layer. Between the oxide layer and the coating an oxygen-enriched layer ~100nm thick was observed. The indicated decrease in

thickness of the oxide layer with increasing bias voltage after annealing for 5h at 900°C from glancing angle XRD results was supported both by the TG results, which show a decrease in weight gain with increasing bias voltage and cross sectional TEM. Calculations from the TG work and assuming an average oxide density (table 2) of $5g/cm^3$ indicated an oxide layer thickness of ~340nm for the coating deposited at –75V bias, which fits with the average measured thickness from TEM. Similar calculations for the coatings deposited at –85V and –95V bias gave oxide thicknesses of ~270nm and ~210nm respectively, thus supporting the XRD results which indicated a decrease in thickness of the oxide layer with increasing bias voltage.

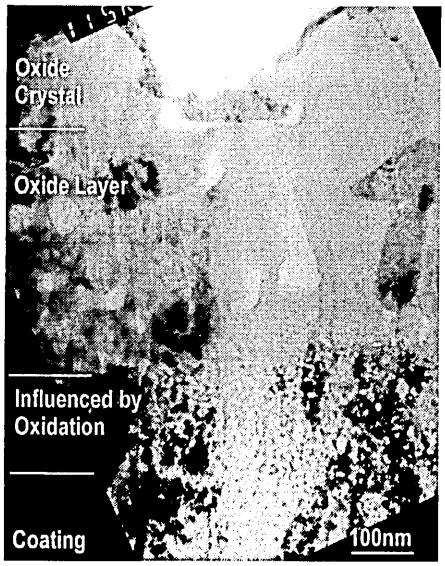

Fig.4: XTEM bright field image of TiAlN/CrN –75V bias after heat treatment for 5h at 900°C.

On the -75V bias sample a crack connecting the coating surface with the substrate that was filled with oxides was imaged (Fig.3). The bright field image montage shows clearly how oxidation progressed through the crack and how substrate material was consumed. EDX analysis, taken at the middle on top of the crack filling oxide, revealed an additional amount of Ti suggesting the formation of a Ti_xO_y oxide. The cross sectional TEM bright field image showed that cracks formed in the coating can propagate through the entire coating layer. The cracks provide direct pathways for the penetration of oxygen allowing oxidation on the substrate and substrate elements to diffuse through to the coating surface.
Regarding the activation energy and the free energy of formation of oxides from nitrides is shown in table 3. This showed that the formation of Cr_2O_3 is favoured over TiO_2 and Al_2O_3 (Table 2). The formation of a Cr rich oxide layer was expected, whereas the formation of a Ti-rich oxide in the crack showed that theoretical considerations are not true in all cases.

	Ionic radius [nm] of most common valence [19]	**Activation Energy [Ea/eV]**	**$\Delta G_{900°C}$ [kJ/mol O_2] [20]**	**$\Delta G_{nitrides900°C}$ [kJ/mol O_2]**
TiO_2	Ti 0.068	2.0 (3)	-170	-500 (TiN)
αAl_2O_3	Al 0.053	2.2-2.4 (3)	-205	-620 (AlN)
Cr_2O_3	Cr 0.063	1.6 (16)	-130	-585 (CrN)

Tabel 3: ΔG nitrides have been calculated out of the ΔG of metal nitrides and ΔG of metal oxides. A ΔG produced by the formation of oxides directly from the nitrides was gained at 900°C, the nitride used are given in brackets

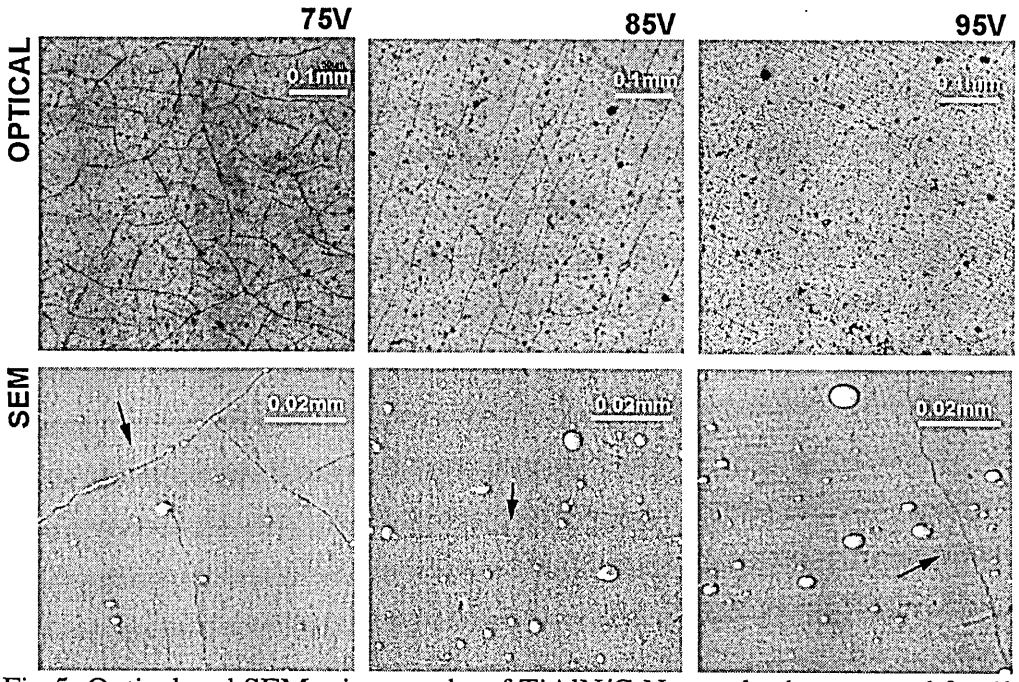

Fig.5: Optical and SEM micrographs of TiAlN/CrN samples heat treated for 1h at 900°C. The SEM images are typical examples of cracks on the coating.

Optical and SEM microscopy showed the presence of a crack network on the coating surface of TiAlN/CrN after heat treatment for 1h at 900°C (Fig.5). Cracks appear to pass through existing defects in the coating. At higher applied bias voltage the amount and incidence of observed cracking decreased. The width of the cracks and the amount of local pronounced oxidation inside the cracks also seemed to decrease with increasing bias voltage. McIntyre (3) et al. reported the appearance of crack networks upon heating $Ti_{0.5}Al_{0.5}N$ coatings deposited at low bias voltages and their disappearance when the bias voltage was increased to -150V. This dependency on bias voltage was associated with an increase in residual stress with increasing bias voltage. In the current investigation the residual stress increase from –5.1 GPa at –75 V bias to –9.2 GPa at –95 V bias. The cracks observed were generated upon heating due to differences in the thermal expansion coefficients of substrate and film. The method of linear extrapolation of the coefficients of expansion of the binary components was used by (3) to determine the coefficient of linear expansion of TiAlN. Assuming that this method can be applied also to a TiAlN/CrN superlattice a value of 4.7^{-6} K^{-1} was obtained. The coefficient for the binary components were AlN (5.7^{-6} K^{-1}), TiN (9.4^{-6} K^{-1}) and CrN (2.3^{-6} K^{-1}) (13). The composition of the TiAlN/CrN –75V bias voltage was taken from (12) to be $Ti_{0.11}Al_{0.13}N/Cr_{0.26}N$. The linear expansion coefficient for austenitic SS 304 is 19^{-6} K^{-1} (14). During heating, the additional expansion of the substrate superimposes a tensile stress in the nitride film leading to crack formation. The theoretical temperature at, which cracking would first occur, is when the induced tensile stresses produced during heating, σ_{th} exceeds the residual compressive stresses developed during deposition. The induced residual stress thermal stress σ_{th} was calculated using $\sigma_{th} = E_L/(1-\nu_L)\times(\alpha_L-\alpha_S)\times(T_{ox}-T_d)$ (15). Where the suffix L stands for layer, S for substrate, OX for oxidation or temperature used for heat treatment and d for deposition. From purely theoretical considerations i.e ignoring any stress relief within the coating, cracking could first occur in the –75V bias sample at 630°C, at the –85V bias sample at 900°C and at the –95V bias sample at 1120°C, thus cracking is more likely to occur when TiAlN/CrN superlattice coatings are deposited at –75V bias.

The oxide formation locally in the cracks was more pronounced than on the general coating surface. After heat treatment for 5h at 900°C the presence of Fe and Cr in these oxides was confirmed by EDX (Fig.6). Additional to the needle type oxide in the cracks a more protruded type of oxide was observed. These protrusions were richer in Fe and Cr than those of the needle type oxides, which were associated with rutile (TiO_2) formation. The presence and the different shape of oxides in the cracks might be depending on the depth and width of the crack.

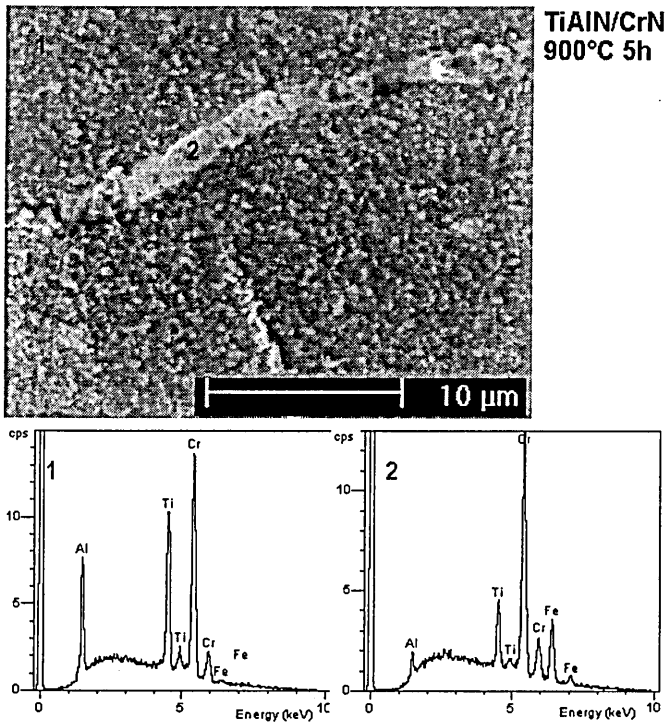

Fig.6: SEM micrograph of a TiAlN/CrN sample heat treated at 900°C for 5h.

Conclusions

- The rate of oxide formation decreased with increasing the bias voltage.
- TiAlN/CrN multilayers deposited onto SS 304 revealed a crack network after heat treatment for 1h at 900°C. The amount of cracks found after heat treatment on stainless steel substrates decreased with increasing bias voltage because of higher residual compressive stresses, which opposes the tensile stress induced during heat treatment.
- Two different types of oxides emerged in the cracks. The needle type was associated with TiO_2 and the protruded type with a Fe and Cr rich oxide. Growth defects or cracks allow access of oxygen to a larger area. This is seen as the reason for enhanced oxidation in these regions.

References

(1) J.A. Thornton, J. Vac. Sci. Technol., A4 (3) (1986), 490-495
(2) W.-D. Münz, D. Schulze, F.J.M. Hauzer, Surface and Coating Technology, 50 (1992) 169-178
(3) McIntyre, Journal of Applied Physics 67, 1542 (1990), 225-261
(4) I. Wadsworth, I.J. Smith, L.A. Donohue, W.-D. Münz, "Surface and Coating Technology", 94-95 (1997), 315-321

(5) M.I. Lembke, D.B. Lewis, W.-D. Münz, Surface and Coating Technology, 125 (2000), 263-268
(6) M.Herranen, U. Wiklund, J.-O. Carlsson, S. Hogmark, Surface and Coating Technology, 99 (1998), 191-196
(7) H.W.Wang, M.M. Stack, S. B. Lyon, P. Hovsepian, W.-D. Münz, Surface and Coatings Technology, 126 (2000), 279-287
(8) J. Musil, J. Vyskocil, S. Kadlec, Physics of thin films, 17 (1993), 130
(9) W.-D. Münz, I.J. Smith, D.B. Lewis, S. Creasey, Vacuum 48, 5 (1997), 473-481
(10) JCPDS-ICDD Diffraction Data Database, International Centre for Diffraction Data, 1993
(11) A.J. Perry, Thin Solid Films, 193/194 (1990)
(12) D.B. Lewis, I. Wadsworth, W.-D. Münz, R. KuzelJr, V.Valvoda, Surface and Coating Technology, 116-119 (1999), 187-199
(13) H. Holleck, Material selection for hard coatings, J. Vac. Sci. Technol. A4 (6), (1986), 2661-2669
(14) Avesta, Corrosion Handbook, 1994
(15) H. Oettel, R. Wiedemann, Surface and Coating Technology, 76-77 (1995), 265-273
(16) S. Hofmann, H.A. Jehn, Werkstoffe und Korrosion, 41 (1990), 756-760

Reprinted from

SURFACE & COATINGS TECHNOLOGY

Surface and Coatings Technology 125 (2000) 263–268

Localised oxidation defects in TiAlN/CrN superlattice structured hard coatings grown by cathodic arc/ unbalanced magnetron deposition on various substrate materials

M.I. Lembke, D.B. Lewis, W.-D. Münz *

Materials Research Institute, Sheffield Hallam University, Howard Street, Sheffield S1 1WB, UK

ELSEVIER

SURFACE AND COATINGS TECHNOLOGY

Scope
The increasing requirement for high technology materials with specific performance characteristics in various types of environments has dictated that these materials possess near-surface properties different from their bulk properties. This journal is a principal forum for the interchange of information on the science, technology and applications of thin and thick coatings and modified surfaces which alter the properties of materials. The scope includes all types of coatings and surface modification techniques (including physical vapour deposition, chemical vapour deposition, electroplating and surface modification by directed energy techniques). Of particular emphasis are the emerging advanced processes such as thermal spraying, sputter deposition, activated reactive evaporation, ion plating, molecular beam epitaxy, ion implantation and pulsed laser surface deposition. Contributions range from original scientific articles concerned with applied research or direct applications of coatings to reviews of current technology in specific areas. Papers are solicited on topics which include one or more of the following areas: (1) characterization of coatings and modified surfaces, which includes the determination of composition, structure, adhesion, and internal stresses; (2) the application of coatings and modified surfaces to alter the mechanical, chemical or optical properties of materials. Mechanical properties include friction, wear, erosion, hardness and load bearing capacity. Chemical properties include corrosion and oxidation. Optical and electro-optical properties include reflectivity, selective absorption and electroluminescence. Particular emphasis is also placed on the emerging surface engineering technologies and coatings with a diversity of applications such as diamond, diamond-like carbon, and cubic boron nitride. Other interdisciplinary areas include thermal barrier coatings and coatings for biomedical applications and materials conservation.

Abstracting/Indexing Services
This journal is cited by the following services:
Engineering Index, FIZ Karlsruhe, Metal Finishing Abstracts, Current Contents — Engineering, Technology and Applied Sciences, Physikalische Berichte, Cambridge Scientific Abstracts, Chemical Abstracts, Fluid Abstracts, Metals Abstracts, Physics Abstracts, PASCAL/Centre National de Recherche Scientifique, Solid State Abstracts.

Pre-publication abstracts of articles in *Surface and Coatings Technology* and other related journals are now available weekly in electronic form via CoDAS, a new direct alerting service in condensed matter and materials science run jointly by Elsevier Science and Institute of Physics Publishing. For details on a free one-month subscription contact Paul Bancroft on fax +44 1179 294318 or e-mail bancroft@ioppublishing.co.uk.

Publication Information: *Surface and Coatings Technology* (ISSN 0257-8972). For 2000 volumes 122–134 are scheduled for publication. Subscription prices are available upon request from the Publisher or from the Regional Sales Office nearest you or from this journal's website (http://www.elsevier.nl/locate/surfcoat). Further information is available on this journal and other Elsevier Science products through Elsevier's website: (http://www.elsevier.nl). Subscriptions are accepted on a prepaid basis only and are entered on a calendar year basis. Issues are sent by surface standard mail (surface within Europe, air delivery outside Europe). Priority rates are available upon request. Claims for missing issues should be made within six months of the date of dispatch.

Orders, claims and product enquiries: please contact the Customer Support Department at the Regional Sales Office nearest you:

New York: Elsevier Science, PO Box 945, New York, NY 10159-0945, USA;
phone: (+1) (212) 633 3730 [toll free number for North American customers: 1-888-4ES-INFO (437-4636)];
fax: (+1) (212) 633 3680;
e-mail: usinfo-f@elsevier.com

Amsterdam: Elsevier Science, PO Box 211, 1000 AE Amsterdam, The Netherlands;
phone: (+31) 20 4853757; fax: (+31) 20 4853432;
e-mail: nlinfo-f@elsevier.nl

Tokyo: Elsevier Science, 9-15 Higashi-Azabu 1-chome, Minato-ku, Tokyo 106-0044, Japan;
phone: (+81) (3) 5561 5033; fax: (+81) (3) 5561 5047;
e-mail: info@elsevier.co.jp

Singapore: Elsevier Science, No. 1 Temasek Avenue, #17-01 Millenia Tower, Singapore 039192;
phone: (+65) 434 3727; fax: (+65) 337 2230;
e-mail: asiainfo@elsevier.com.sg

Rio de Janeiro: Elsevier Science, Rua Sete de Setembro 111/16 Andar, 20050-002 Centro, Rio de Janeiro - RJ, Brazil;
phone: (+55) (21) 509 5340; fax: (+55) (21) 507 1991;
e-mail: elsevier@campus.com.br [Note (Latin America): for orders, claims and help desk information, please contact the Regional Sales Office in New York as listed above]

US mailing notice: *Surface and Coatings Technology* (ISSN 0257-8972) is published semimonthly by Elsevier Science S.A. (PO Box 211, 1000 AE Amsterdam, The Netherlands). Annual subscription price in the USA US$ 4969.00 (valid in North, Central and South America), including air speed delivery. Periodical postage rate paid at Jamaica, NY 11431.
USA POSTMASTER: Send address changes to *Surface and Coatings Technology*, Publications Expediting, Inc., 200 Meacham Avenue, Elmont, NY 11003.
AIRFREIGHT AND MAILING in the USA by Publications Expediting Inc., 200 Meacham Avenue, Elmont, NY 11003.

ELSEVIER

Surface and Coatings Technology 125 (2000) 263–268

SURFACE & COATINGS TECHNOLOGY

www.elsevier.nl/locate/surfcoat

Localised oxidation defects in TiAlN/CrN superlattice structured hard coatings grown by cathodic arc/ unbalanced magnetron deposition on various substrate materials

M.I. Lembke, D.B. Lewis, W.-D. Münz *

Materials Research Institute, Sheffield Hallam University, Howard Street, Sheffield S1 1WB, UK

Abstract

TiAlN/CrN superlattice coatings show excellent surface oxidation resistance up to 900°C, with an as deposited hardness maximum of HK 3400 (bi-layer 3.8 nm). Coated M2 high speed steel and cemented carbide samples have been examined by scanning electron microscopy (SEM) and energy dispersive X-ray analysis (EDX) after heat treatment in air between 600°C and 1000°C to study the influence of the oxidation behaviour. X-ray diffraction (XRD) and thermogravimetric (TG) measurements were performed on the uncoated substrates to gain an overall picture of the oxidation stability of the plain substrate materials at high temperatures. Globular oxides were observed on coated cemented carbide at 700°C, while on M2 high speed steel similar oxides did not form below 800°C. The small globular oxides were gradually replaced by spherical oxides mainly formed out of substrate material. Initially oxidation starts at the bottom of pores or craters produced by small droplets or by growth defects grown on the droplets. The droplets were deposited during the cathodic arc metal ion step whereas the growth defects developed during film growth. Some detached growth defects formed craters through which oxidation products formed from the substrate material. Elements from the substrate penetrated to the coating surface at temperatures far below the actual oxidation temperature of TiAlN/CrN (900°C), namely at temperatures as low as 700°C (on cemented carbide). On M2 and stainless steel SS304, this type of localised oxidation was observed at temperatures equal to and above 900°C.

Keywords: Cathodic arc deposition; Oxidation behaviour; PVD coatings; Superlattice structure; Unbalanced magnetron deposition

1. Introduction

Physical vapour deposited TiAlN coatings are used in dry cutting operations, because of their high oxidation temperature (850°C) and their wear resistance [1,2]. To further improve the hardness and the oxidation resistance, TiAlN/CrN multilayer coatings were produced leading to an increase in hardness up to $HK_{0.25}$ 3400 and an increase in oxidation temperature of up to 900°C. Previous investigations showed that the oxidation resistance of this coating increases as the CrN component of the multilayer increases. The superlattice coating has an equal layer thickness of CrN and TiAlN of 3.8 nm [3]. The coating is produced by using the combined cathodic arc/unbalanced magnetron sputter technique (ABS®). The cathodic arc chromium metal ion-etching step is an important step in the combined technique. It allows high and reliable adhesion values for PVD hard coatings on steel substrates [4]. One of the drawbacks of the cathodic arc deposition are macroparticles generated in the metal ion etching stage which result in the formation of growth defects [4–8]. In a previous paper [7], it was shown that the size and the number of droplets are substantially reduced by the cathodic arc Cr metal ion etch. However, the few remaining droplets are causing a shadowing effect underneath the droplet, which results in an attenuated ion and deposition flux. The defect structure that surrounds a droplet leaves a low-density zone or even a gap between the growth defect grain structure and the coating [8]. In other cases the droplets and the defects, grown on the droplets, may be expelled from the coating during film growth due to compressive stresses generated by the growing film, causing craters [5]. The influence growth defects on the localised oxidation behaviour of TiAlN/CrN superlattice coatings deposited on cemented carbide (CC) and M2

* Corresponding author. Tel.: +44-114-225-3500; fax: +44-114-225-3501.
E-mail address: m.lembke@shu.ac.uk (W.-D. Münz)

0257-8972/00/$ - see front matter
PII: S0257-8972(99)00571-X

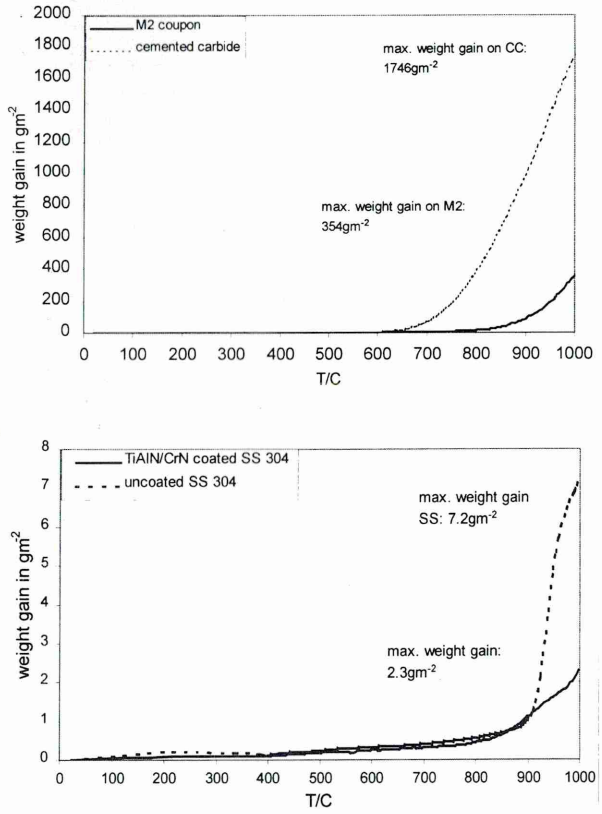

Fig. 1. (a) Continuous TG measurement on CC and M2 Fig. (b) Continuous TG measurement on coated SS and the uncoated substrate.

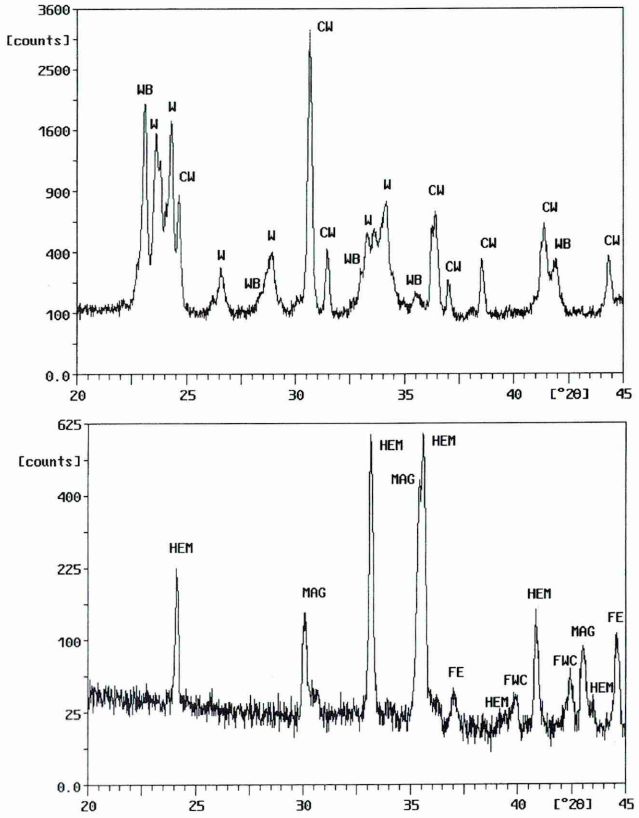

Fig. 2. (a) Oxidised CC substrate with W indicating the monoclinic version of WO_3 and WB the triclinic form. CW denotes $CoWO_4$. (b) Oxidised M2 substrate. MAG denotes Fe_3O_4, HEM denotes Fe_2O_3 and FWC denotes the mixed $FeCr_2O_4$ oxide. FE is iron.

high speed steel substrates of the substrate materials was investigated using Scanning Electron Microscopy (SEM) and Energy Dispersive X-ray Analysis (EDX).

2. Experimental details

The TiAlN/CrN coatings were deposited by the ABS® technology using a Hauzer HTC 1000-4 physical vapour deposition machine. This machine comprises four targets operated simultaneously in a reactive atmosphere [1]. Prior to the coating step the substrates were exposed to high negative bias voltage (−1.2 kV) steered arc chromium metal ion etching treatment. The chromium metal ion etch minimises the number of droplets produced [6]. The remaining three targets were TiAl targets. All targets were operated at 8 kW in the coating step; details are given in Ref. [3]. Under these conditions, the coating was grown with approximately equally thick TiAlN and CrN layers with a bi-layer thickness of 3.8 nm [3]. The substrate materials used were M2 high speed steel (M2), cemented carbide (CC) and stainless steel 304 (SS), polished to a roughness of $R_a \cong 0.01$ mm finish.

The samples were heat treated in a furnace in air at 600, 700, 800, 900 and 1000°C for 1 h. The temperature during the heat treatment was controlled with an accuracy of ±3°C. After each heat treatment the samples were examined.

A Cahn TG 131 was used for the thermogravimetry work. The samples were continuously heated to 1000°C (at 50°C/min to 400°C and from 400°C to 1000°C at 1°C/min) using a flow rate of 12.6 ml/min in dry air.

The specimens were examined by a SEM (Philips XL 40) at 20 kV accelerating potential for the imaging mode. The EDX analysis was performed using an ultra-thin window in front of the detector at a lower accelerating voltage of 10 kV.

The X-ray diffraction (XRD) was performed using monochromatic Cu–K_a radiation with Bragg–Brentano geometry. The phases present were identified using powder diffraction files data [9].

3. Results and discussion

The TG measurements in Fig. 1a revealed that the CC used starts to oxidise rapidly at temperatures above 700°C. In contrast to CC, rapid oxidation in M2 high speed steel does not occur before 900°C. The weight gain of cemented carbide is higher than that of M2 and

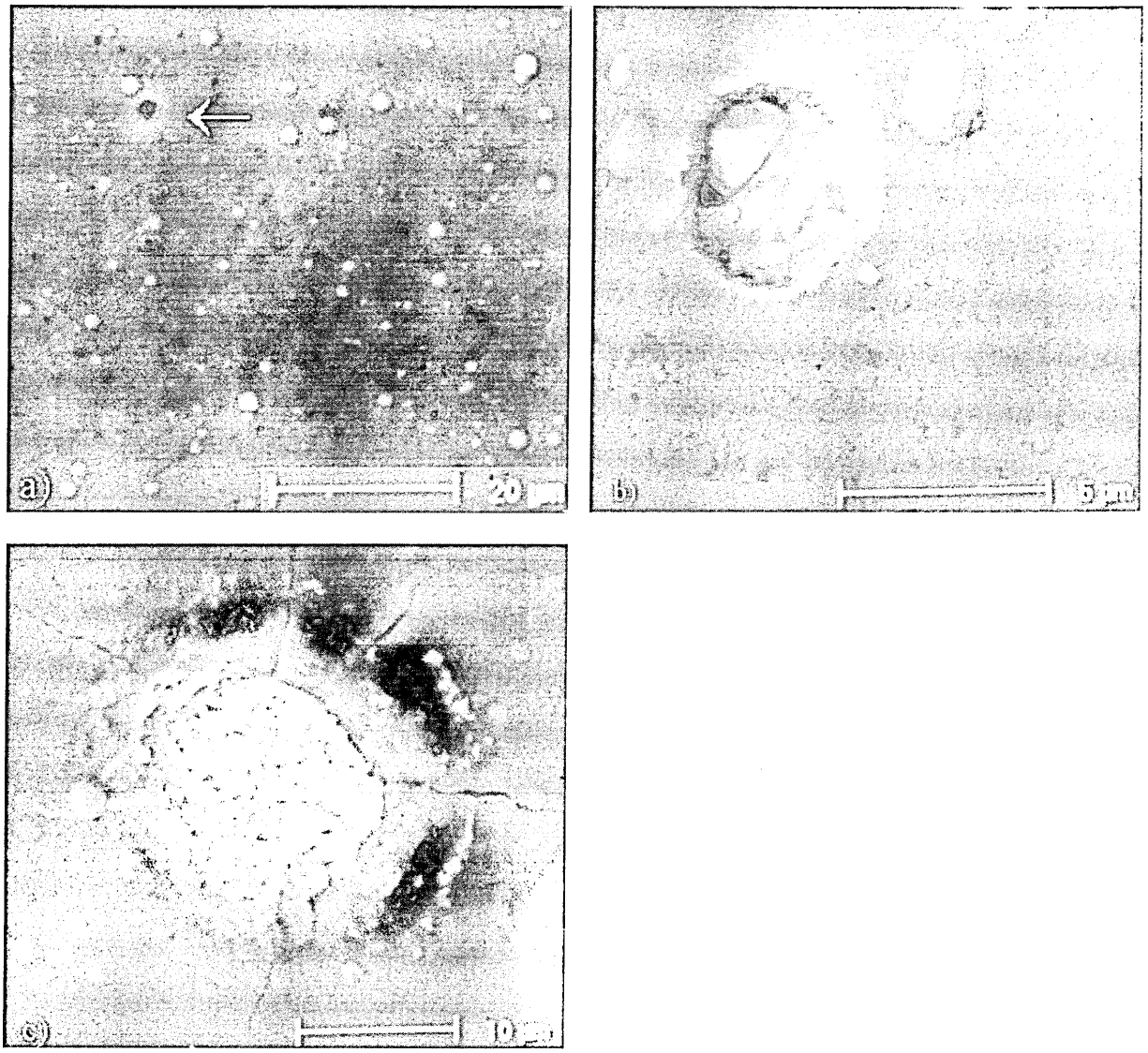

Fig. 3. (a) Low magnification survey from the as received coating surface. A crater is indicated through an arrow. (b) Oxides appear on the bottom of a crater on coated CC at 700°C. (c) Oxide formation on coated CC initiated local cracking of the coating at 800°C.

SS by factors of 5 and 100, respectively, when heated to 1000°C. Cemented carbide is well known for its rapid oxidation behaviour starting at temperatures as low as 600°C [10]. Therefore, it needs a protective coating to enable it to be used in high-speed cutting operations.

XRD diffraction patterns of the surface of CC and M2 heat treated at 900°C (CC) and 1000°C (M2) respectively are shown in Fig. 2. The oxides identified on CC were two different phases of tungsten oxide, WO_3, one with a monoclinic crystal structure (JCPDS 24-747) and the other with a triclinic crystal structure (JCPDS 20-1323), together with a mixed tungsten cobalt oxide, $CoWO_4$, with a cubic crystal structure (JCPDS 15-867) [9]. The mixed $CoWO_4$ oxide resulted from the oxidation of the cobalt binder used in liquid phase sintering of the tungsten carbide matrix. On M2, hematite (JCPDS 24-0072) Fe_2O_3, magnetite (JCPDS 19-0629) Fe_3O_4 and a mixed $FeCr_2O_4$ (JCPDS 24-0512) oxide were identified. The M2 substrate material was not fully oxidised, as can be seen from the presence of the remaining iron (JCPDS 06-0696) peaks in the XRD pattern in Fig. 2b.

Examination at low magnification of the surface of the as deposited coating using SEM showed the presence of growth defects and craters (Fig. 3a). Droplets produced by the cathodic arc metal ion etch led to growth defects in the coating, which can extend from the substrate to the coating surface [8]. Because of the inherent high residual compressive stresses in the coating, some defects become detached [5] resulting in the formation of craters as pointed out by the arrow in Fig. 3a. After heat treatment of coated CC samples, oxides were formed at the bottom of craters at temperatures as low as 700°C (Fig. 3b). On CC, increasing the

temperature to 900°C leads to a significant increase in oxide formation in the crater, which results in cracking of the adjacent coating (Fig. 3c). EDX analysis of the oxidation product in the crater showed the presence of both tungsten and oxygen (Fig. 4a). The presence of the element tungsten in the oxides formed in the crater clearly shows that these oxides are formed by the oxidation of the substrate. Previous XRD measurements on the oxidised substrate would indicate that these were of WO_3. A possible mechanism for the formation of cracks in the coating adjacent to craters containing oxide is the high volume expansion of tungsten oxide relative to that of tungsten (38% increase in volume). In contrast to CC local oxidation of substrate material in holes occurred at higher temperatures on M2. The first oxides were observed at 700°C on CC and at 900°C on M2. This result is not surprising as the TG analysis clearly showed that CC oxidises at a significantly lower temperature than M2.

Another form of oxidation is shown in the micrograph in Fig. 5a at 700°C on coated CC. At low magnifications, accumulations of very small globular defects were observed on CC as pointed out by the arrows in Fig. 5a. At higher magnifications (Fig. 5b) a more or less continuous coating is observed covered with smaller and larger sized globular oxides. Only a small concentration of substrate elements are observed for coated CC oxidised at 800°C as shown in Fig. 4b. This special defect may be correlated to areas where the droplet and the growth defect were expelled during film growth and the crater created has been partially filled with coating material [5]. Pores formed in the under-dense region at the rim of the growth defect on the deposited film material allowed localised oxidation. Further oxidation led to the formation of spherical oxides as shown in the micrograph in Fig. 5c and the appearance of substrate materials as shown in the EDX spectrum in Fig. 4c at 800°C on coated CC. Similar shaped defects were observed on coated M2. An EDX spectrum in Fig. 4d taken at 900°C showed the occurrence of Fe and O on surface of the coated M2 steel. However, on coated M2 this defect formation was in general less pronounced than that on coated CC and the first defects containing substrate elements occurred at 900°C on M2. These

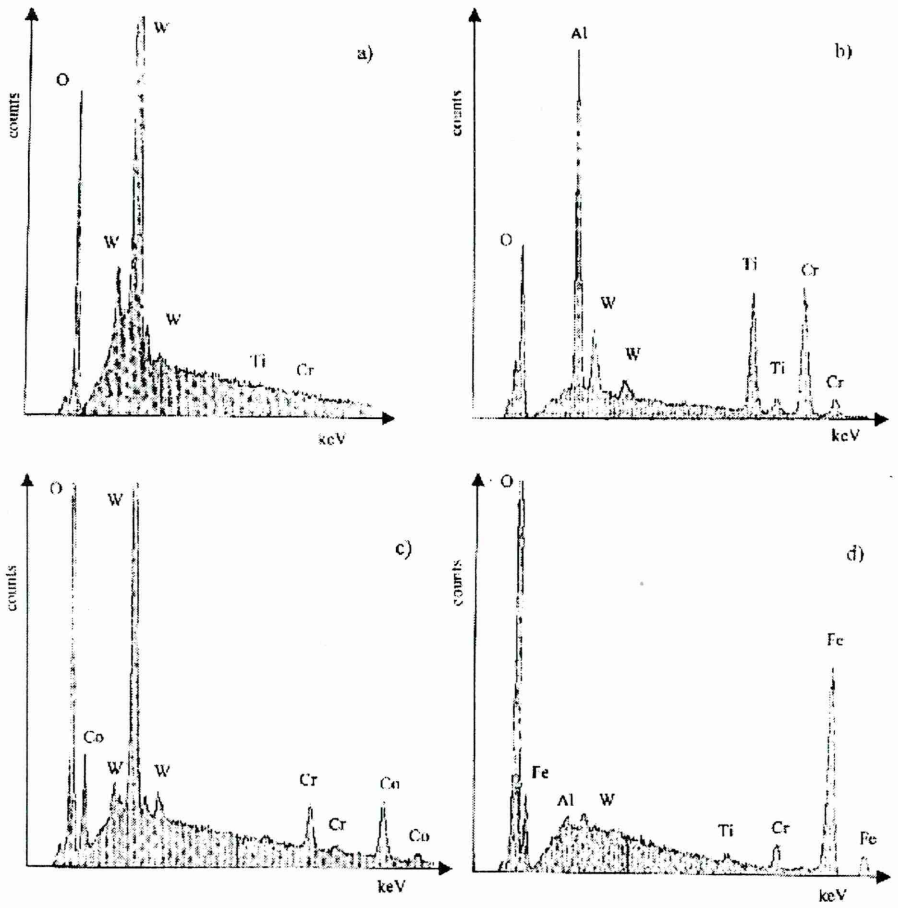

Fig. 4. (a) EDX analysis on oxide breaking through the surface on coated CC. Ti and Cr indicate the areas where the K_a lines of these elements would be observed. (b) EDX analysis of accumulated globular oxides on coated CC at 800°C. (c) EDX analysis of big oxide formed in the globular oxide region on CC at 800°C. (d) EDX analysis of big oxide formed in the globular oxide region on M2 at 900°C.

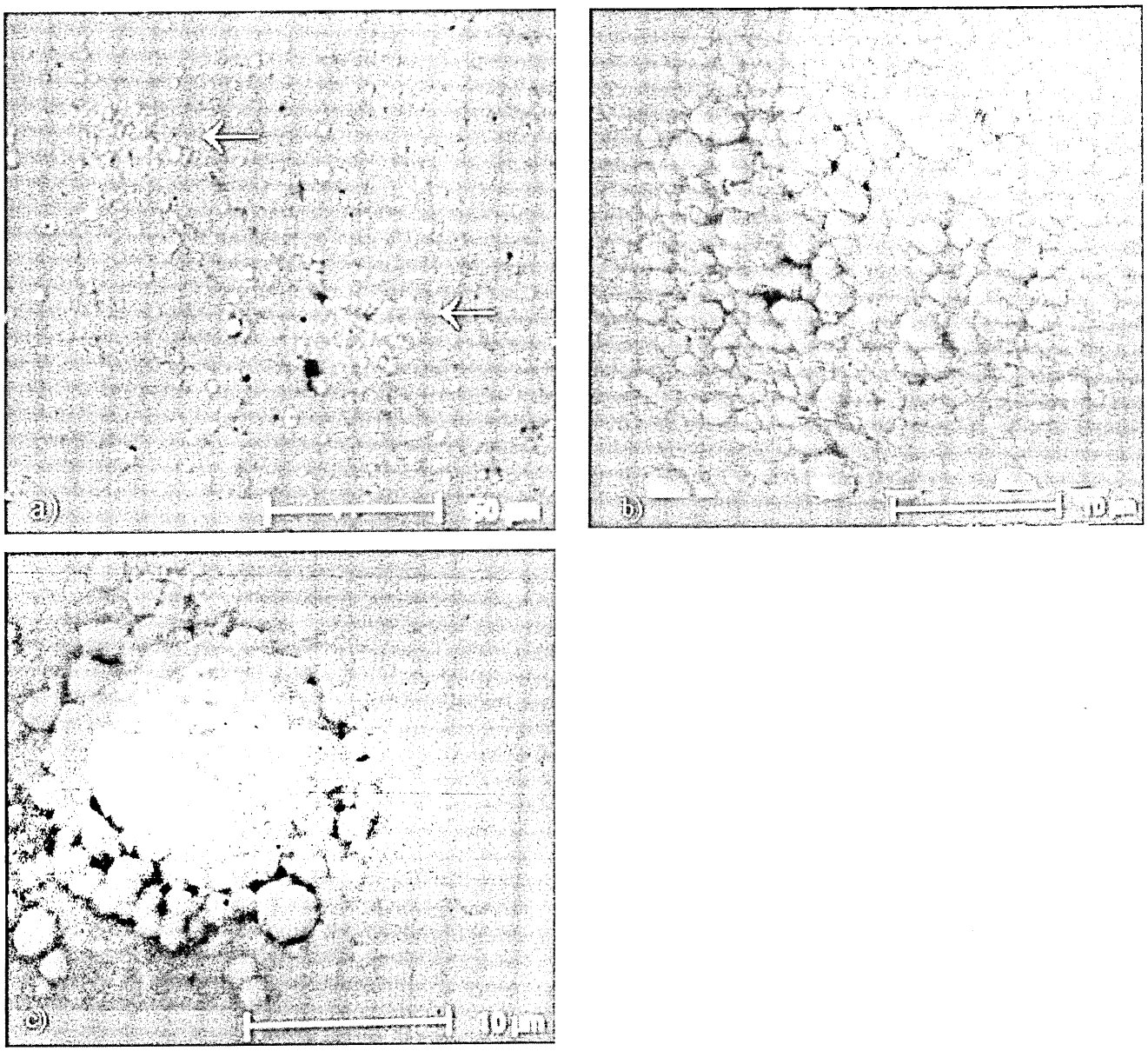

Fig. 5. (a) Low magnification survey on an oxidised coated CC at 700 °C. (b) Accumulated globular oxides in detail on CC at 800 °C. (c) Big oxide formed in globular oxides on CC at 800°C

results are again reflected in the relative oxidation resistance of the M2 high speed steel in comparison to CC as can be seen in Fig. 1a.

4. Conclusion

(1) The oxidation behaviour of the substrate material influences directly the generation of growth defects through craters caused by droplet formation.

(2) Particularly in the case of WC substrates, severe oxide defect growth is observed already at 700°C.

(3) These defects should be of significant influence in dry high speed cutting operations when cutting temperatures up to 1000°C are expected.

(4) Conversely, in the case of M2 high speed steel substrates the oxide defect formation should be of less importance as tools fabricated from M2 are usually operated at temperatures below 600°C.

References

[1] W.-D. Münz, J. Vac. Sci. Technol. A4 (6) (1986) 2701.
[2] I.J. Smith, D. Gillibrand, J.S. Brooks, W.-D. Münz, S. Harvey, R. Goodwin, Surf. Coat. Technol. 90 (1997) 164–171.
[3] I. Wadsworth, I.J. Smith, L.A. Donohue, W.-D. Münz, Surf. Coat. Technol. 94–95 (1997) 315–321.
[4] W.-D. Münz, D. Schulze, F.J.M. Hauzer, Surf. Coat. Technol. 50 (1992) 169–178.

[5] W.-D. Münz, D.B. Lewis, S. Creasey, T. Hurkmans, T. Trinh, W. van Ijezendorn, Vacuum 46 (4) (1995) 323–330.
[6] W.-D. Münz, I.J. Smith, D.B. Lewis, S. Creasey, Vacuum 48 (5) (1997) 473–481.
[7] S. Creasey, D.B. Lewis, I.J. Smith, W.-D. Münz, Surf. Coat. Technol. 97 (1997) 163–175.
[8] I. Petrov, P. Losbichler, D. Bergstrom, J.E. Greene, W.-D. Münz, T. Hurkmans, T. Trinh, Thin Solid Films 302 (1997) 179–192.
[9] JCPDS-ICDD Diffraction Data Database, International Centre for Diffraction Data, 1993.
[10] E.M. Trent, Metal Cutting, Butterworths, London, 1977. p. 106.

Instructions for Authors

Submission of Papers

Manuscripts (original and two clear copies) should be submitted to one of the Editors:

for authors in the Americas
Dr. B. D. Sartwell, Surface Chemistry Branch, Naval Research Laboratory, Code 6170, Washington, DC 20375, USA;

and for authors elsewhere
Professor A. Matthews, Director, The Research Centre in Surface Engineering, The University of Hull, Cottingham Road, North Humberside, HU6 7RX, UK.

Contributions are accepted on the understanding that the authors have obtained the necessary authority for publication. Submission of a manuscript implies that it is not under consideration for publication elsewhere.

Types of contributions

— original papers
— invited or contributed reviews on specific topics
— brief communications on topics of immediate interest
— notices of meetings, symposia and short courses
— technical notes for "Current Industrial Practices" section

Languages

Papers will be published in English. Both English and US spelling are permitted, provided that spelling is consistent within an article.

Authors in Japan please note that information about how to have the English of your paper checked, corrected and improved (*before submission*) is available from: Elsevier Science K.K., Editorial Service, 1-9-15 Higashi Azabu, Minato-ku, Tokyo 106-0044, Japan; Tel.: +81 3 5561 5032; Fax: +81 3 5561 5045.

Manuscript preparation

Three copies of the manuscript should be submitted, in double-spaced typing on pages of uniform size with a wide margin on the left. The title page should be a separate sheet, bearing title, author(s)' name(s) and their full addresses, and a footnote with the corresponding author's Telephone, Fax numbers and E-mail Address.

Some flexibility of presentation will be allowed but authors are urged to arrange the subject matter clearly under such headings as Introduction, Experimental details, Results, Discussion etc. Each paper should have an abstract of 100–200 words.

References should be numbered consecutively (numerals in square brackets) throughout the text and collected together in a reference list at the end of the paper. Journal titles should be abbreviated according to the Chemical Abstracts Service Source Index, 1970 edition, and supplements. The abbreviated title should be followed by volume number, year (in parentheses) and page number.

Submission of electronic text

The final text should be submitted on a 3.5 in or 5.25 in diskette (in addition to a hard copy with original figures). Double density (DD) or high density (HD) diskettes formatted for MS-DOS or Apple Macintosh compatibility are acceptable, but must be formatted to their capacity before the files are copied on to them. The files should be saved in the native format of the wordprocessing program used. Most popular wordprocessor file formats are acceptable. It is essential that the name and version of the wordprocessing program, type of computer on which the text was prepared, and format of the text files are clearly indicated.

Illustrations

Line drawings and cyclic or aromatic formulae should be in a form suitable for reproduction. They may be drawn in black ink on drawing paper (letter height, 3–5 mm), but the use of good quality computer-generated figures is encouraged. They should preferably all require the same degree of reduction, and should be submitted on paper of the same size as, or smaller than, the main text to prevent damage in transit. Photographs should be submitted as clear black-and-white prints on glossy paper. Each illustration must be clearly numbered.

Illustrations can be printed in colour when they are judged by the Editor to be essential to the presentation. The publisher and the author will each bear part of the extra costs involved. Further information concerning colour illustrations and the costs to the author can be obtained from the publisher.

Legends to the illustrations must be submitted in a separate list.

All tables and illustrations should be numbered consecutively and separately throughout the paper.

Proofs

Authors will receive proofs, which they are requested to correct and return as soon as possible. No new material may be inserted in the text at the time of proofreading. All joint communications must indicate the name and full postal address of the author to whom proofs should be sent.

Further information

All questions arising after the acceptance of manuscripts, especially those relating to proofs, should be directed to: Elsevier Science Ireland Ltd. Elsevier House, Brookvale Plaza, East Park, Shannon, Co. Clare, Ireland. Tel.: +353 61 709609; fax: +353 61 709107.

The full and complete instructions to authors can be found on the World Wide Web: please visit our website which is accessible via the Elsevier Surfaces and Interfaces HomePage at http://www.elsevier.nl/locate/surfaces

Offprints

Twenty-five offprints will be supplied free of charge to the author(s). Additional offprints can be ordered at prices shown on the offprint order form which accompanies the proofs.

Structural Changes after Heat Treatment of Physical Vapour Deposited TiAlCrYN Coatings

M.I. LEMBKE, D.B. LEWIS, J.M. TITCHMARSH AND W.-D. MÜNZ

Materials Research Institute, Sheffield Hallam University, City Campus, Sheffield S1 1WB, UK

ABSTRACT

TiAlCrYN coatings with an oxynitride top layer have been grown in a multiple target physical vapour deposition (PVD) coating unit using the combined cathodic steered arc/unbalanced magnetron sputter deposition technique. The deposition of the oxynitride layer resulted in a reduction in the coefficient of friction from 0.9 for the basic TiAlCrYN coating to 0.65 for the similar coating with an oxynitride top layer. The coating thickness was 2.3μm.

After heat treatment at temperatures up to 900 °C, cross sections examined using the transmission electron microscope (TEM) revealed that the microstructure of the coating changed from one of interrupted columnar growth in the as-deposited condition to one of competitive growth in the annealed condition. This is reflected by an increase in the measured average column diameter from 60nm in the as-deposited condition to 120nm after annealing at 900 °C. X-ray diffraction showed that the change in the microstructure was also accompanied by a reduction in the residual compressive stress from −4GPa in the as-deposited condition to −2GPa after annealing at 900 °C for one hour. Furthermore, preferential segregation of Y to the column boundaries was observed where the nominal concentration of Y was enhanced from 0.9at.% to 2.1at.%.

Examination of the surface of the as-deposited coating by cross sectional TEM revealed an oxynitride multilayer of 270nm in thickness with an average Cr content of ~20at.%. After annealing at 900 °C in air cross sectional TEM revealed an oxide-scale growth of 250nm formed on top of the 1h sample and of 950nm of the 5h sample. X-ray distribution maps of the surface oxide layer showed that the Cr-rich layer of the deposited oxynitride layer is still apparent after 5h but Cr ions out-diffused. After 5h Al and Ti form a bi-layer, as it is known from TiAlN oxidation, of which the top layer is Al-rich and the under layer is Ti-rich. Y-rich areas approximately 10nm in size were found below the Ti-rich zone.

INTRODUCTION

Dry high speed cutting operations has made it necessary to develop new high temperature resistant PVD coatings to protect the cutting tools, manufactured mainly out of cemented carbides. $Ti_{0.5}Al_{0.5}N$ PVD coating is widely

used and its oxidation resistance starts above 750 °C.[1] The improved oxidation resistance and thermal stability of TiAlN stems from its ability to form a stable passive double oxide layer, where the upper layer is Al-rich and the lower layer is Ti-rich. After 1.5h exposure at 900 °C elements from the type 304 stainless steel (SS) substrate can be found in the oxide layer.[2] The oxidation resistance and thermal stability of TiAlN based coatings can be improved still further (up to 950 °C) by the incorporation of Cr and the reactive element Y.[3] In dry high speed cutting operations TiAlCrYN has been compared with, and has outperformed TiCN and TiAlN by 1.6 or 3 times respectively.[4] A previous investigation of oxidation of TiAlCrYN showed the formation of an Al-rich surface oxide, a Ti-rich underlayer and the segregation of Y to the column boundaries near the oxide layer. To further improve the mechanical properties an oxynitride top layer has been introduced. This topcoat lowers the friction coefficient from 0.9 to 0.65 in a pin on disc test.[5] Transmission electron microscopy (TEM) and energy dispersive X-ray analysis (EDX) was used to investigate the changes, which occur during the oxidation of the $Ti_{0.30}Al_{0.65}Cr_{0.04}Y_{0.01}N$ with oxynitride top-layer (TCY+Ox). An explanation of the protection by the oxide film has been given based on the structural appearance and elemental distribution maps. A protective oxide layer should be thermodynamically stable, compact in the sense of not having interconnecting pores, should be slow growing and mechanically adherent.[6]

EXPERIMENTAL DETAILS

The TCY+Ox coatings were deposited by the ABS™ technology using an industrially sized (Hauzer HTC 1000/5 MK II ABS) physical vapour deposition machine. This machine uses up to 5 targets and can be run in either the steered cathodic-arc (CA) or unbalanced magnetron sputter mode (UBM). In this investigation it was operated with 4 targets (2 opposing pairs, each separated by 1m) simultaneously in a reactive atmosphere (Fig. 1). The TiAlCrYN was deposited with an additional oxynitride top layer. The process is described in detail elsewhere.[3, 4] A Cr cathodic-arc (CA) metal ion-etch was chosen, because it provides excellent adhesion with a small concentration of growth defects at the coating surface.[7] The coating was deposited using unbalanced magnetron sputtering (UBM) with two 50:50at.% TiAl targets (vacuum cast), one 48 at.% Ti:48 at.% Al and 4 at.% Y target (powder metallurgically prepared) and one 99.8at.% Cr target (powder metallurgically prepared). Condensation took place in a reactive $Ar+N_2$ atmosphere with an estimated ion to neutral ratio at the substrate of 3.5, an average substrate temperature of 450 °C and the substrates under going a 3-fold rotation (Fig.1). The substrate materials used were M2 high-speed steel (M2) and cold rolled stainless steel 304 (SS) polished to a roughness of $R_a \equiv 0.01$ μm finish.[4]

The samples were heat treated in air in a furnace at 900 °C for one and five hours, respectively. The temperature during the heat treatment was controlled with an accuracy of ±3 °C. A sample code A, B and C will subsequently be used to describe the as-deposited, the as-deposited and heat-treated for 1h at 900 °C and the as-deposited and heat-treated for 5h at 900 °C samples, respectively.

A conventional Philips CM 20 TEM operated with a LaB_6 filament at 200kV was used for the TEM imaging and a Vacuum Generators HB501 dedicated FEG scanning transmission electron microscope operated at 100kV was used for the high resolution EDX analyses and elemental mapping. A windowless detector was employed for such analyses. Cross sectional samples for the TEM were prepared by a mechanical grinding process to about 50 μm in thickness and then ion milled with a shallow incidence angle of 8° from the top surface and 5° from the bottom surface until electron transparency was reached. The SEM-EDX analysis was performed using an ultra thin window in front of the detector at a lower accelerating voltage of 10 kV. The quantitative analysis on sample A was performed on a polished cross section using a JEOL 840A SEM. Cross sectioning was necessary to avoid the influence of the oxynitride layer in the analysis.

X-ray diffraction (XRD) was performed using monochromatic Cu-K_α radiation using Bragg–Brentano geometry. The phases present were identified by comparing the peak positions with powder diffraction data.[8] The inherent stress in the coatings was determine using the Ω method

$$\sigma_{stress} = \frac{E \cdot slope}{a_o \cdot (1 + \upsilon)}$$

where E is the elastic-modulus of the material, the slope is the gradient measured from a lattice parameter a_ψ versus $\sin^2\psi$ plot, a_o is the unstressed lattice parameter and υ is Poisson's ratio.[9,10] For the investigation of the oxides present the XRD was used with a fixed incident angle of 0.5°. In glancing angle geometry the penetration depth is defined as the distance, x_e from the surface that the diffracting planes in the specimen contribute to the whole diffracted intensity by the ratio $1/e$.[10]

$$x_e = \frac{\sin\gamma \sin(2\theta - \gamma)}{\mu\,(\sin\gamma + \sin(2\theta - \gamma)}$$

where μ is the linear absorption coefficient and γ is the angle of incidence. This, gives in the oxidised sample a penetration depth in the film of 200 nm, assuming a linear absorption coefficient of 650 cm^{-1}.

RESULTS AND DISCUSSION

The structure of the as-deposited coating has been investigated using cross sectional TEM. Figure 1(a) shows a transmission electron micrograph of the

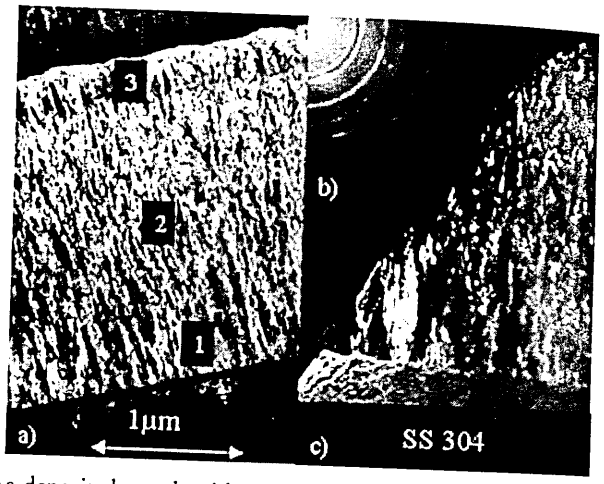

Fig. 1 (a) As-deposited sample with region 1 coarser structural base layer, region 2 fine structural coating and region 3 oxynitride top coat. (b) Selected area diffraction pattern out of the middle of the coating. (c) The dark field image shows the difference in structure between base layer and coating.

as-deposited TCY+Ox film. In this micrograph three distinct regions are clearly visible, namely the base layer (region 1), the middle TiAlCrYN layer (region 2) and the oxynitride layer (region 3). The base layer (region 1) exhibits a pronounced coarse columnar structure. In the middle TiAlCrYN layer (region 2) there is a distinct change from the coarse columnar structure of the base layer to a fine columnar structure showing interrupted growth. A selected area diffraction pattern (SADP) taken in this region (Fig. 1(b)) clearly shows a ring pattern, which is consistent with the fine grain structure observed. The presence of the small bright regions highlighted in the dark field image (Fig. 1(c)) further confirms a fine-grained structure. The change from a columnar structure in the base layer to the fine-grained structure in the middle layer results from the incorporation of 1 at % yttrium into the TiAlCrN film.[3] In contrast, the yttrium content of the base layer is low because the TiAlY target was run at 0.5 kW during deposition of the base layer, compared with 10.7 kW during the deposition of the 'bulk' TiAlCrYN coating. The oxynitride layer appears as a darker band on top of the coating (Fig. 1(a)). The intensity of this layer is different due to different compositions in base- and oxynitride layer, which changes the mass scattering contrast.

Sample B shows a different structure (Fig. 2). In contrast to sample A, in the bright field image (Fig. 2(a)) the microstructure of the coating in region 2 now shows a distinctly coarse columnar morphology. This change in the

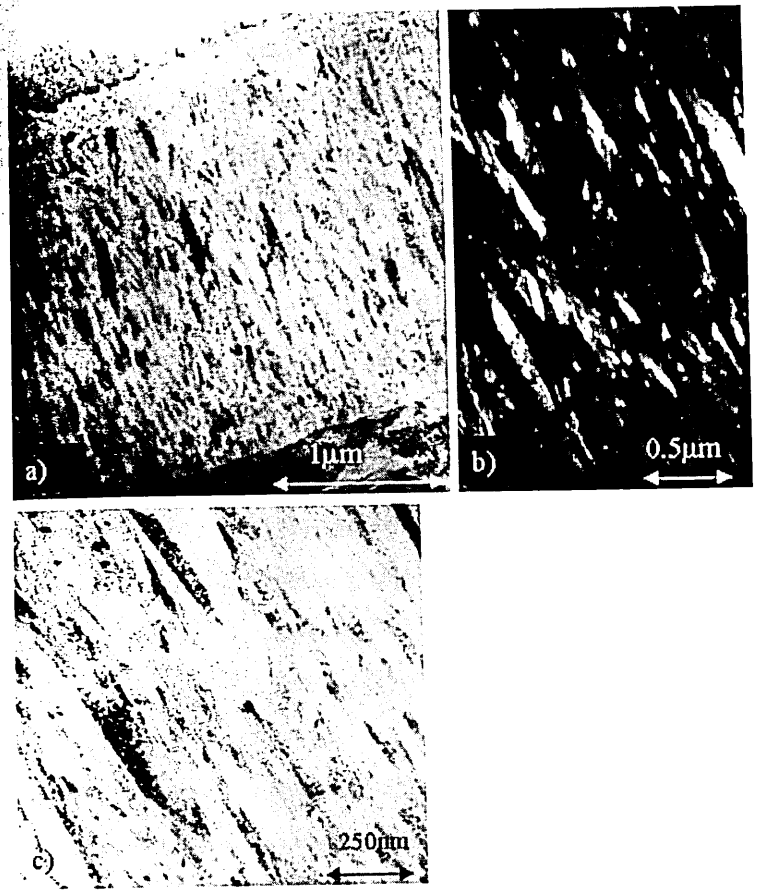

Fig. 2 (a) Bright field image of sample B. The white circle indicates the region of column measurement and Y measurement. (b) Dark field image showing the columnar structure of the coating. (c) Higher magnification bright field image of (a) showing voids along column boundaries.

microstructure is clearly more visible in the DF image (Fig. 2(b)) where the highlighted bright regions are broader and of similar dimensions to those of the base layer in sample A. This is further reflected by an increase in column size as measured by mean linear intercept method from 60 nm in sample A to 120 nm in sample B, with an error of 20%. Furthermore, after annealing at 900 °C, there was clear evidence of void formation at the column boundaries (Fig. 2(c)). The changes in structure during annealing have been investigated

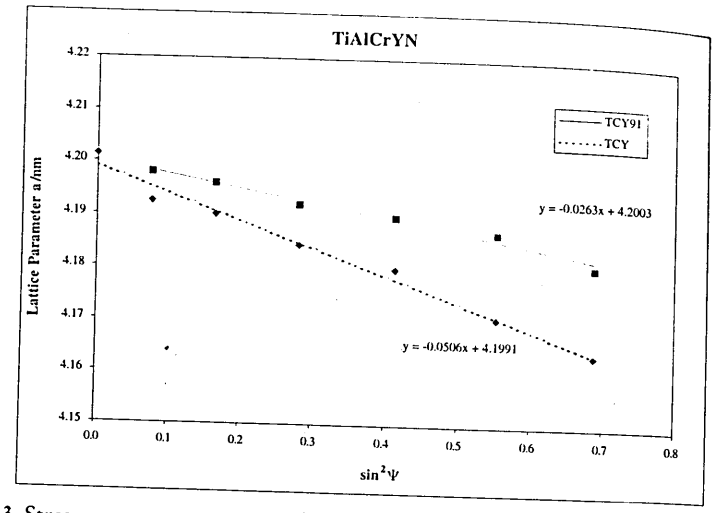

Fig. 3 Stress measurement on sample A (TCY + Ox) and sample B (TCY + Ox 900 °C 1h) based on the Omega method.

using XRD (Fig. 3). The residual stress decreased from −4GPa in the as deposited condition to −2GPa after annealing at 900 °C for 1h. Residual stresses in PVD coatings are generated by defects formed during the deposition process. Thus, stress relaxation at elevated temperatures is associated with either thermally activated plastic deformation[11] or with recovery due to annihilation of the stress active defects produced during coating [11,12].

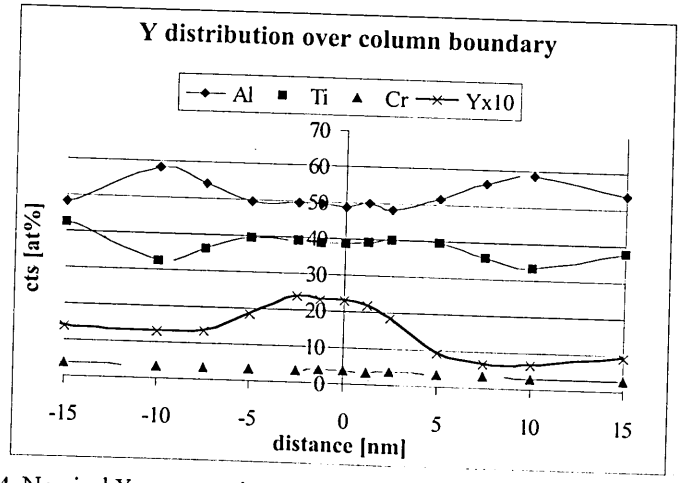

Fig. 4 Nominal Y concentration measured over a grain boundary at the 900 °C 1h sample.

The examination of the grain boundaries in sample B showed an increase of Y in the grain boundary region (Fig. 4). The nominal concentration of Y increased from 0.9 at % (bulk) to 2.1 at. % (boundary) in sample B. The size of the electron probe is large compared with the grain boundary and therefore the actual concentration of Y at the grain boundary is considerably higher than the nominal 2.1 at % value measured.[13] This preferential diffusion of Y to the grain boundary is understandable. The Y atom is large in comparison to Al, Ti and Cr. It distorts the lattice in as-deposited condition. In the heat-treated sample, the Y diffuses to the lower energy grain boundary sites, which decreases the distortion in the bulk TiAlCrN lattice. This diffusion is made even more attractive for a reactive element such as Y with a high affinity for oxygen, due to the easy ingress of oxygen at the column and grain boundaries.

A point analysis profile through the coating in sample A, perpendicular to coating/substrate interface, is shown in Fig. 5. An oxygen/nitrogen transition zone in the oxynitride layer region can be clearly seen. Additionally, elemental maps have been recorded to show the oxynitride layer (Fig. 6). Note that in all corresponding elemental maps the signal is less intense along the rim on top of each map due to a reduced thickness in this region. The change from bulk coating to oxynitride layer is again clearly visible. In corresponding areas

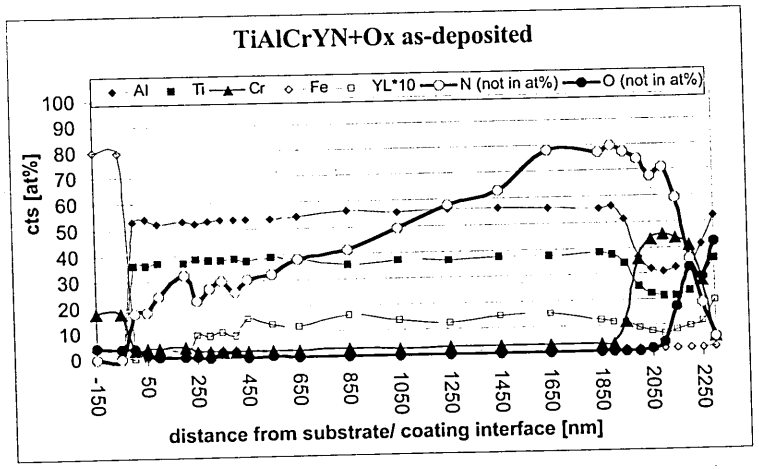

Fig. 5 Point analysis through sample A. N and O are peak integral values and hence dependent on the overall count rate.

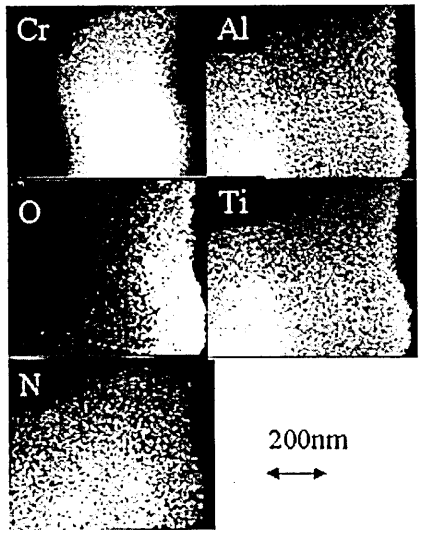

Fig. 6 Elemental distribution map of sample A. Note that the top of the sample appears less intense because of the difference in thickness.

the Ti map appears less intense than in in the Cr-rich area. Figure 14(a) shows a schematic of a proposed structure of sample A based on these EDX results.

The equivalent point analysis through the samples B and C revealed a sharp change in elemental composition ($Fe_{K\alpha}$ line) at the substrate coating interface indicating that the interface was unaffected by the heat treatment (Figs 7 and 8). In previous work on a $Ti_{0.44}Al_{0.53}Cr_{0.03}N$ coating, Fe started to diffuse into the coating after 1h at 900 °C.[3] At the oxynitride layer the point analysis showed that in sample B the step in the oxygen profile shifted further into the Cr-rich region towards the coating compared with sample A. At the same time, the Cr-rich region shrank by approximately 30nm. In sample C, rises in the O and Cr profiles occur at the same location. The Cr peak itself is approx. 70nm (FWHM) broad. This implies Cr out-diffusion to the scale/air interface. At the same time, minimal diffusion of O had occurred.

Elemental maps recorded from samples B and C show that the structure is rather complicated and disruption of a layered growth starts to occur in sample B (Fig. 9). The region adjacent to the nitride coating (region 1) consists of a mixture of Ti-rich, Al-rich and Cr-rich crystals of 10 ± 5nm dia. The structure of the outermost layer (region 2) is coarser and voided with a crystal size of 50 ± 15nm. A simplified schematic structure is shown in Fig. 14(b). In sample C, layers rich in one element are visible (Fig. 10). Closest to

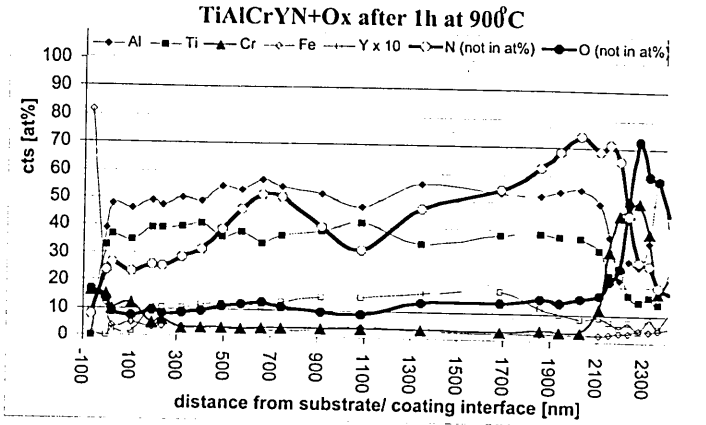

Fig. 7 Point analysis through sample B. N and O are peak integral values and hence dependent from the overall count rate.

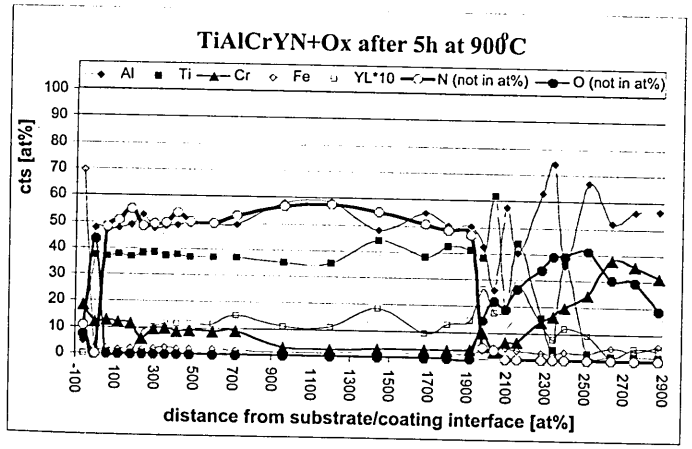

Fig. 8 Point analysis through sample C. N and O are peak integral values and hence dependent from the overall count rate.

the coating is a Ti-rich layer then a Al+Cr-rich layer and, finally, a Cr-rich layer. The outermost oxides are big large crystals containing Ti, Al and Cr with typical diameters of 200 nm ± 50 nm. Elemental maps indicate that the large crystals consist of a mixed Cr/Al oxide and Ti oxide (Fig. 11). Y par-

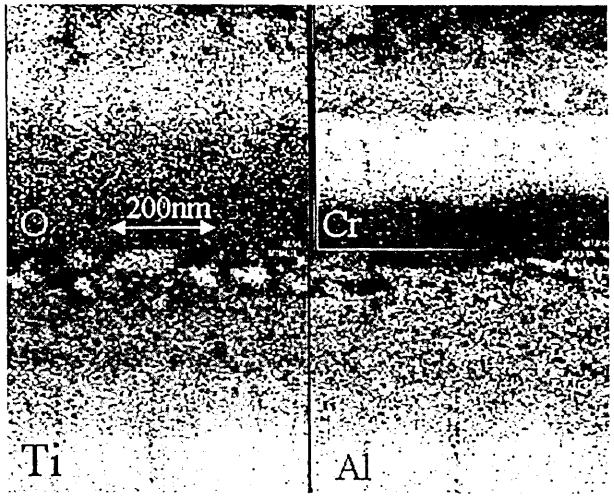

Fig. 9 Elemental distribution map of sample B.

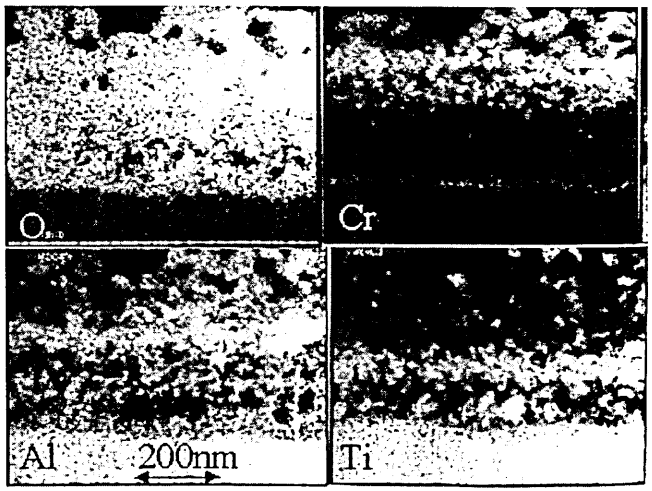

Fig. 10 Elemental distribution map of sample C.

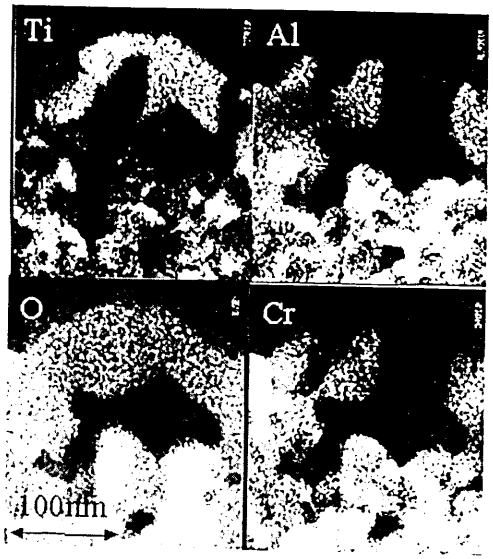

Fig. 11 Elemental distribution map of outermost oxide layer of sample C.

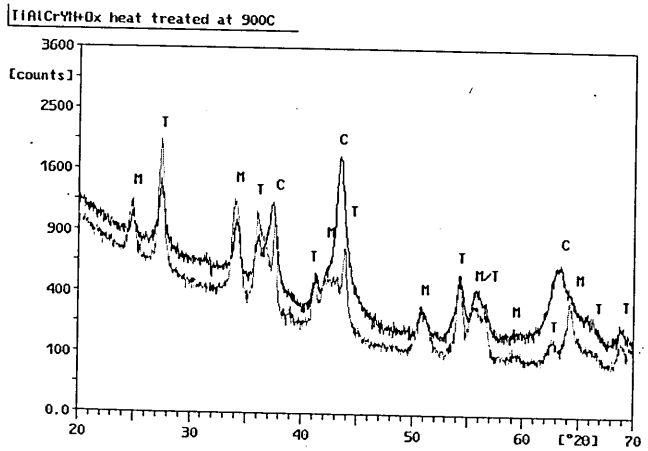

Fig. 12 Glancing angle XRD on TCY + Ox after 1h (black) and 5h (grey) at 900 °C with fixed incident angle 0.5°. M = mixed oxide of Al_2O_3/Cr_2O_3, T = TiO_2, C = coating.

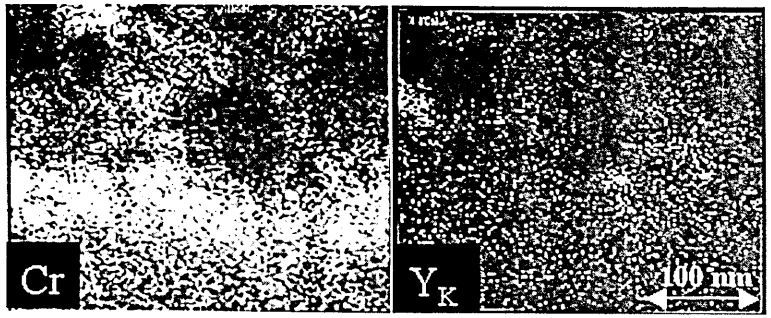

Fig. 13 Elemental distribution map of sample C showing Y particles.

ticles of approximately 10nm in size are detectable behind the 70nm Cr-band (Fig. 13). A simplified schematic version is shown in Fig. 14(c). Glancing angle X-ray diffraction has been used to further support the EDX results (Fig. 12). On samples B and C, an isostructural solid solution of Al_2O_3/Cr_2O_3 (rhombohedral) and TiO_2 (rutile) has been identified which is consistent with the observations in the elemental maps. The composition of the solid solution, assuming Vegard's law is obeyed, was calculated from the {012} and {104} reflections to be 66 mol % Al_2O_3 34 mol % Cr_2O_3. The miscibility of Al_2O_3 and Cr_2O_3 was reported in Ref. 14 for oxidation at a CrAlN PVD coating. It is noticeable that the (110) rutile peak is sharper in its appearance in sample C, which is consistent with the increase in crystal size of the rutile phase observed in the TEM. Pores and Y-rich particles of about 10nm in diameter are also observed in the Ti-rich layer. The pores increase in size towards the scale/air interface. Disruption in the outermost oxide layer is clearly visible in elemental maps in Fig. 11. This disruption in the oxide layer is caused by the difference in unit cell volumes of different oxides. The coefficients of volume expansion of the various oxides present are listed in Table 1, along with thermodynamic data. From thermodynamic considerations alumina is the most likely to form and, with Al being the smallest ion, Al is most likely to diffuse. Indeed, in the outermost layer, Al-rich crystals are detected. Using the same argument (ionic radius and free energy of formation) it is also understandable why Ti is found enriched in the inner layer. In Ref. 14 it is stated that Al oxidises initially because of the higher free energy state. However the diffusion rate of Cr was found to be higher and led to an increase of the Cr content in the oxide layer. This in turn hampered the outward diffusion of Al. Al was found to reduce the growth rate of the outer Cr-rich layer. This explains partially the oxide layer structure observed in the TiAlCrYN with the oxynitride topcoat. It is certainly an indication why the

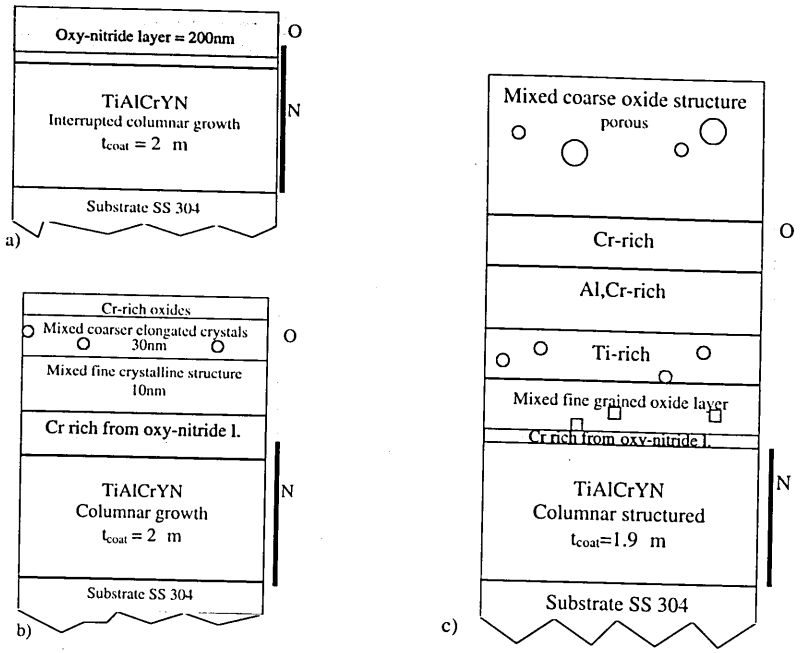

Fig. 14 Schematics based upon the elemental distribution maps from sample A (a); sample B (b); sample C (c) (900 °C 5h).

Table 1 Recorded values concerning the formation of oxides. ΔG nitrides have been calculated from the ΔG of metal nitrides and ΔG of metal oxides to get to the ΔG for oxides directly out of the nitrides, the nitride used is given in brackets. φ is the ratio between the molecular volume of compound Me_xO_y and the compound TiAlN, with regard of the amount of metal atoms, e.g. Al_2O_3 has 2 Al atoms hence TiAlN value has been doubled.

	Volume/ cm^3	Thermal expansion coef. $10^{-6}K^{-1}$	Ionic radius Me nm · Most common valence	φ	Activation Energy Ea eV	$\Delta G_{900\,°C}$, Kjmol^{-1} O_2	$\Delta G_{fromnitrides900\,°C}$, Kjmol^{-1} O_2
$Ti_{0.5}Al_{0.5}N$	11[2]			1	2.32[2]		
TiO_2	18.8[2]	9[15]	Ti 0.068[16]	1.71	2.0[2]	−170[19]	−500 (TiN)
αAl_2O_3	25.6[2]	8.4[15]	Al 0.053[16]	1.16	2.2–2.4[2]	−205[19]	−620 (AlN)
Cr_2O_3	29[17]	7.3[18]	Cr 0.063[16]	1.32	1.6[14]	−130[19]	−585 (CrN)

oxide layer growth is in the same order as for the TiAlCrYN without topcoat. The pores in the oxide layer will be detrimental for the adhesion of the oxide layer in real cutting applications; the formation of a dense layer is hindered. However, the adhesion of the oxide particles to the surface must still be good otherwise blistering would occur.[15] The inhomogenity of the oxide layer probably occurs when volume strain generally exceeds the cohesive energy between individual crystals.

CONCLUSIONS

- The oxide layer grown on top of the oxynitride layer is 250 nm for the 1h 900 °C sample and 950 nm for the 5h 900 °C sample. The layer thickness is similar to previously reported values for the TiAlCrYN without an oxynitride layer (310 nm after 1h at 950 °C).[3] In dry high speed cutting of HRC 58 steel the 6 mm end mills were able to cut 240 m in comparison to TiAlN with 170 m.[4]
- Yttrium enrichment was found at the grain boundaries in the coating annealed for 1 and 5 h at 900 °C. In an area of 8700 nm^2 an area of 415 nm^2 Y-rich particles were found in the oxide layer of the 5h 900 °C sample just after the 70nm band of Cr adjacent to the coating. No bulk diffusion of Fe was observed in point analysis profiles. Y is probably hindering the outward diffusion of Fe. Segregated Y at the grain boundaries will act as an oxygen catcher..
- The structure of the coating changed from fine-grained, interrupted columnar growth to a columnar growth structure.
- In the sample annealed for 5 h at 900 °C an interrupted, mixed oxide structure containing a Cr_2O_3/Al_2O_3 solid solution and TiO_2 (rutile) was observed in the outermost layer.

REFERENCES

1. W.-D. Münz: 'Titanium Aluminium Nitride Films: A New Alternative to TiN Coatings', *J. Vac. Sci. Technol.*, 1986, **A4** (6), 2701.
2. McIntyre, J.E. Greene, G. Håkansson and J.E. Sundgren: 'Oxidation of Metastable Single-Phase Polycrystalline TiAlN Films: Kinetics and Mechanism', *Journal of Applied Physics*, 1990, **67** (1542), 225–261.
3. L.A. Donohue, I.J. Smith, W-.D Münz , I. Petrov and J.E. Greene: 'Microstructure and Oxidation Resistance of TiAlCrYN Layers Grown by Combined Cathodic Arc/ Unbalanced Magnetron Sputter Deposition', *Surface and Coating Technology*, 1997, **94/95**, 226–231.
4. W.-D.Münz and I.J. Smith: 'Wear Resistant PVD Coatings for High Temperature (950 °C) Applications', *Conference Proceedings of the Society of Vacuum Coaters in Chicago* 17–22.4.1999, 350–356.
5. U. Scharf: Diploma Thesis, 'Vergleich tribologischer Eigenschaften von Monolytish und Mehrfach Abgeschiedenen PVD Hartsoffschichten', Westsächsische Hochschule Zwickau, 1998.
6. T.A. Ramanarayanan, R. Ayer, R. Petkovic-Luton, D.P. Leta: 'The Influence of Yttrium on Oxide Scale Growth and Adherence', *Oxidation of Metals*, 1988, **29**, 5–6, 445–472.
7. W.-D. Münz, I.J. Smith, D.B. Lewis, S. Creasey: 'Droplet Formation on Steel Substrates During Cathodic Steered Arc Metal Ion Etching, *Vacuum*, 1997, **48** (5), 473–481.
8. *JCPDS-ICDD Diffraction Data Database*, International Centre for Diffraction Data, 1993.
9. D. S. Rickerby, A.M. Jones, B.A. Bellamy: 'X-Ray Diffraction Studies of PVD Coatings', *Surface and Coating Technoogy*, 1989, **27**, 111–137.
10. A.J. Perry, J.A. Sue and P.J. Martin: 'Practical Measurement of the Residual Stress in Coatings', *Surface and Coating Technoogy*, 1996, **81**, 17–28.
11. S.J. Bull, D.S. Rickerby, J.C. Knight and T.F. Page: *Surface Engineering*, 1992, **8**, 193.
12. G. Kleer, R. Kassner, E.-M. Meyer, M.G. Schinker and W. Doell: Effect of Process Parameters on the Residual Stresses and Wear Behaviour of Aluminium Nitride PVD Coatings', *Surface and Coating Technology*, 1992, **54–55**, 172–176.
13. I.A. Vatter and J.M. Titchmarsh: 'Comparison of FEG-STEM Measurements of Equilibrium Segregation of Phosphorus in 9% Cr Ferritic Steel', *Surface and Interface Analysis,* 1997, **25**, 760–776.
14. S. Hofmann and H.A. Jehn: 'Oxidation Behaviour of CrN and (Cr,Al) N Hard Coatings', *Werkstoffe und Korrosion*, 1990, **41**, 756–760.
15. H. Holleck: 'Material Selection for Hard Coatings', *J. Vac. Sci. Technol.* A, 1986, **4**, 6, 2661–2669.
16. W. D. Callister: '*Materials Science and Engineering an Introduction*, 4th ed.', Wiley, 1997.
17. O. Kubaschewski and B.E. Hopkins: *Oxidation of Metals,* Butterworth, London, 1962.
18. N. Birks and G.H. Meier: *Introduction to High Temperature Oxidation of Metals*, Edward Arnold, London, 1983.
19. R.W. Gurry and L.S. Darken: *Physical Chemistry of Metals,* Fig.14–4 Ellingham Plot, McGraw-Hill, 1953.

ELSEVIER

Surface and Coatings Technology 114 (1999) 187–199

SURFACE & COATINGS TECHNOLOGY

The influence of the yttrium content on the structure and properties of $Ti_{1-x-y-z}Al_xCr_yY_zN$ PVD hard coatings ☆

D.B. Lewis [a,*], L.A. Donohue [a], M. Lembke [a], W.-D. Münz [a], R. Kuzel Jr. [b], V. Valvoda [b], C.J. Blomfield [c]

[a] *Sheffield Hallam University, Materials Research Institute, Pond Street, Sheffield S1 1WB, UK*
[b] *Department of Semiconductor Physics, Faculty of Mathematics and Physics, Charles University, Ke Karlovu 5, 121 16 Prague, Czech Republic*
[c] *Kratos Analytical, Wharfside, Trafford Wharf Road, Manchester, UK*

Received 2 May 1998; received in revised form 27 January 1999; accepted 2 February 1999

Abstract

$Ti_{1-x-y-z}Al_xCr_yY_zN$ and $Ti_{1-x-y}Al_xCr_yN$ coatings have been grown in a multiple target PVD coating unit using the combined steered arc evaporation/unbalanced magnetron deposition technique. $Ti_{1-x-y-z}Al_xCr_yY_zN$ film properties and yttrium distributions have been found to change significantly when three targets with equal yttrium content ($Ti_{0.495}Al_{0.495}Y_{0.01}$) or one yttrium-containing target ($Ti_{0.48}Al_{0.48}Y_{0.04}$) with two neighbouring pure $Ti_{0.5}Al_{0.5}$ targets to produce a non-homogeneous distribution were used.

The structural characteristics and residual stresses present in the coatings were determined by X-ray diffraction using both Bragg–Brentano and glancing angle parallel beam ($\sin^2\psi$ method) geometries. In all cases the state of stress was found to be compressive, with values at 1° incidence angles of −6.5 GPa using a single 4 at.% yttrium containing target and −3.2 GPa using three TiAlY targets each containing 1 at.% Y. The residual stress value at 1° angle of incidence for the $Ti_{1-x-y}Al_xCr_yN$ film was similar to that of the homogeneously grown yttrium containing film, i.e. −3.8 GPa.

The surface chemistry of the as-deposited and thermally treated films has been further analysed using high-resolution monochromatic X-ray photoelectron spectroscopy (XPS). Large area (700 μm × 300 μm) and small spot (55 μm) XPS analysis was used to examine the role of low concentrations of the elements Y and Cr during the oxidation process. XPS imaging using O 1s, Ti 2p, Cr 2p and Fe 2p photoelectron peaks has been used to study the distribution of oxides formed on the surface after heat treatment. High resolution analysis of the Y 3d core level identified two chemical species for the as-deposited TiAlCrYN films at positions Y 3d 156.0 and 158.1 eV respectively, whilst only single species were identified in the oxidised film at Y 3d 158 eV.

Keywords: Arc bond sputter (ABS); Crystallographic structure; Hard coatings; PVD; Residual stress; Texture

1. Introduction

The high oxidation and abrasive wear resistance of TiAlN coatings has been well known for more than one decade [1]. TiN oxidises at a temperature of 600°C owing to the formation of an oxide comprising mainly TiO_2 (rutile) which is susceptible to discontinuous spallation. Thus, the improved oxidation resistance and thermal stability of TiAlN (up to 900°C) stems from its ability to form a stable passive double oxide layer, where the upper layer is Al rich and the lower layer is Ti rich [2]. Recent work has shown that the oxidation resistance and thermal stability of TiAlN based coatings can be improved still further (up to 950°C) by the addition of up to 2 at.% Y [3] in films deposited by the combined cathodic arc/unbalanced magnetron (ABS: arc bond sputter [4]) deposition process. However, the hardness of these coatings was found to depend on the target configuration used during the deposition process. A hardness value of $HK_{0.025}$ 2700 was obtained in films grown in a multi-target PVD coater using one yttrium containing target ($Ti_{0.48}Al_{0.48}Y_{0.04}$) and two pure ($Ti_{0.5}Al_{0.5}$) targets, whilst the hardness obtained in similarly grown films using three targets with equal yttrium

☆ Paper presented at 25th International Conference on Metallurgical Coatings and Thin Films, 25 April–1 May 1998, San Diego, CA, USA

* Corresponding author. Tel.: +44 114 225 4074; fax: +44 114 225 3501.
E-mail address: B.D.LEWIS@SHU.AC.UK (D.B. Lewis)

0257-8972/99/$ – see front matter
PII: S0257-8972(99)00047-X

contents ($Ti_{0.495}Al_{0.495}Y_{0.01}$) was similar to that of $Ti_{1-x-y}Al_xCr_yN$ films, i.e. $HK_{0.025}$ 2400. Cross-sectional transmission electron microscopy (X-TEM) also revealed that the microstructure of such coatings differed substantially, exhibiting the well-known columnar growth for uniform Y distributions and a surprisingly equi-axed microstructure for the coating with the non-uniform Y distribution. This investigation compares the crystallographic structure and related properties of $Ti_{1-x-y}Al_xCr_yN$ and $Ti_{1-x-y-z}Al_xCr_yY_zN$ films with non-homogeneous and homogeneous Y distribution, grown by the cathodic arc/unbalanced magnetron process in detail.

2. Experimental details

2.1. Deposition conditions

The films were deposited in a multi-target PVD equipment HTC1000-ABS manufactured by Hauzer Techno Coating Europe BV Venlo, The Netherlands, comprising the combined steered arc/unbalanced magnetron ABS process [3,4]. This coating equipment is furnished with four cathodes, which can be used either as steered cathodic arc or as unbalanced magnetron sources. The unbalancing effect of the magnetron cathodes is achieved by externally arranged concentric electromagnetic coils which are also responsible for establishing closed magnetic field conditions [4] allowing sufficiently high ionisation of the discharge atmosphere in the vacuum chamber. One of the four cathodes is preserved for metal ion etching purposes. It is furnished with a Cr target, which is used to generate a Cr plasma by operating the cathode in the steered cathodic arc mode. It has been found, elsewhere [5,6], that in a chromium arc discharge droplets of minimum size and concentration are formed resulting in low roughness values of the subsequently deposited coatings. The same cathode was operated during the deposition process with low power dissipation (0.5 kW) in the magnetron mode thus, keeping the target surface free from contamination of randomly scattered TiAl. This preventive measure causes a certain Cr content in the TiAl-based coatings. Y-free coatings were deposited from three $Ti_{0.5}Al_{0.5}$ targets. The incorporation of Y into the coating was achieved as mentioned previously by two different approaches. In the first case 4 at.% Y was graded to 48 at.% Ti and 48 at.% Al. This target was then used in conjunction with two targets each consisting of 50 at.% Ti–50 at.% Al. Alternatively 1 at.% Y was alloyed into equally concentrated Ti and Al to form a $Ti_{0.495}Al_{0.495}Y_{0.01}$ target composition and then three cathodes were furnished with three targets of this kind. In the latter case a rather uniform distribution of Y in the growing coating may be expected whereas in the first case a layered incorporation of Y has to be assumed. Fig. 1 illustrates the target and cathode arrangement schematically. The test substrates were mounted on a threefold rotating turntable thus simulating the coating geometry of three-dimensional substrate bodies as closely as possible.

Effectively the substrates are turning during the etching phase with a base frequency of approximately 10 rpm through the vacuum chamber passing the ignited Cr cathode, which fills the space with Cr plasma and

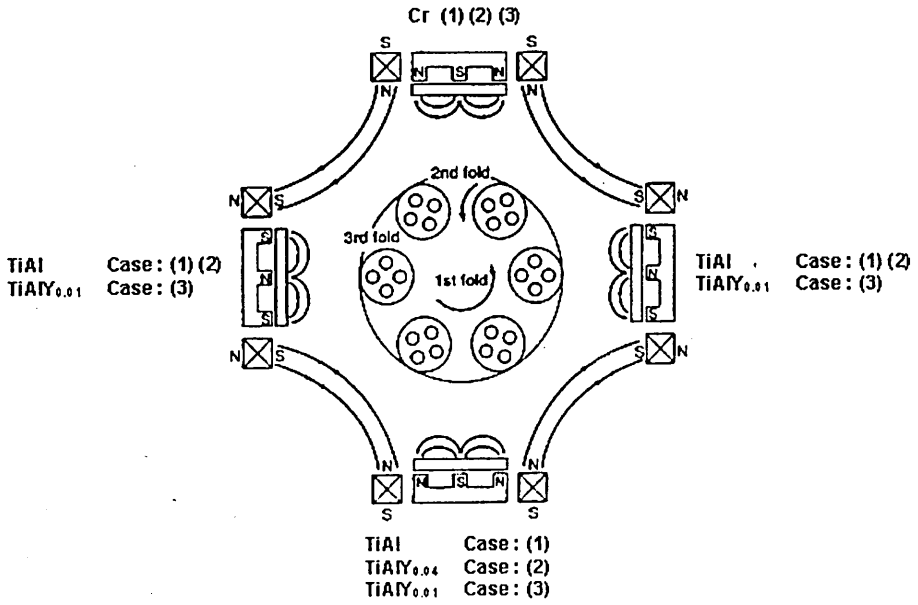

Fig. 1. Schematic diagram of the target arrangement used in the Hauzer HTC 1000-4 ABS® PVD coater.

vapour. The cathode is then operated in the steered arc mode. During the coating cycle all four cathodes are ignited simultaneously operating in the UBM mode. The following three procedures have been utilised.

Case (1): The substrates pass repeatedly and subsequently three fully powered $Ti_{0.5}Al_{0.5}$ targets and one low powered Cr target.

Case (2): The substrates pass repeatedly and subsequently a fully powered $Ti_{0.5}Al_{0.5}$ target then a $Ti_{0.48}Al_{0.48}Y_{0.04}$ target and afterwards a second $Ti_{0.05}Al_{0.5}$ target followed by the low powered Cr target.

Case (3): The substrates pass repeatedly and subsequently three fully powered $Ti_{0.0495}Al_{0.495}Y_{0.01}$ targets and one low-powered Cr target.

The exact process parameters are listed in Table 1. Under the sputter conditions described there, it may be estimated that approximately 1.7 nm of TiAlN is deposited during one turn. The contribution of the Cr target may be neglected.

2.2. Analytical methods used

Elemental analysis of the coatings was determined using Rutherford backscattering spectroscopy (RBS) and energy dispersive X-ray analysis (EDX) X-ray diffraction was carried out on all three coatings using Cu Kα radiation. Bragg–Brentano geometry diffractograms were collected using a scan step of 0.04° between 2θ values of 20–140°. Lattice parameters, a_o were plotted versus the Cohen–Wagner function [7,8] ($\cos\theta\cot\theta$) in order to eliminate systematic errors. An extrapolation to $\cos\theta\cot\theta=0$ gives the lattice parameter a_o. Texture, T^* was determined in accordance with the Harris inverse pole figure technique [9,10] and was calculated from the following equation:

$$T^* = \frac{I_{(hkl)}/R_{(hkl)}}{(1/n)\sum_0^n I_{(hkl)}/R_{(hkl)}} \quad (1)$$

where $I_{(hkl)}$ and $R_{(hkl)}$ are the intensities from the (hkl) reflections in the specimen and a random powder respectively and n is the number of reflections considered, i.e. 7. Thus, a T^* value of unity signifies a random orientation, whilst for T^* values greater than unity the plane is considered to have a preferred orientation.

The crystallite/domain size was determined using Eq. (2) [5]:

$$\frac{\beta\cos\theta}{\lambda} = \frac{1}{D} + \frac{4e\sin\theta}{\lambda} \quad (2)$$

where β is the peak width at full width half maximum (FWHM) after correcting for instrumental broadening, D is the domain size (crystallite), e is the lattice strain, θ is the Bragg angle and λ is the X-ray wavelength. The crystallite/domain size, D, determined for each film was separated from that of the strain, e, by measuring the corrected FWHM for pairs of parallel planes, i.e. {111} and {222}.

Low angle X-ray diffraction analysis was performed on each of the three films under investigation and the superlattice period, Δ, in the low angle region was measured directly from the standard Bragg equation:

$$\Delta = \frac{n\lambda}{2\sin\theta} \quad (3)$$

where θ is the Bragg angle, and λ is the X-ray wavelength and n is the order of wavelength.

Glancing angle parallel beam geometry was used to determine the state of residual stress present in the coatings [11]. For cubic structures the lattice parameters, $a_{hkl}(\psi)$ can be calculated for each diffraction peak where ψ is the angle between the diffraction vector of plane $\{hkl\}$ and the normal to the film surface, such that $\psi=\theta-\gamma$ where θ is the Bragg angle and γ is the angle of incidence of the X-ray beam relative to the specimen surface. For a thin film in a state of equi-biaxial stress the equation describing the stress dependence of the lattice parameter, a_ψ is related by the equation [12]:

$$a_\psi = \sigma a_0\left(\frac{1+\nu}{E}\sin^2\psi - \frac{2\nu}{E}\right) + a_0 \quad (4)$$

where a_0 is the unstressed lattice parameter, E is the elastic modulus and ν is the Poisson's ratio. For the Poisson's ratio, a value of 0.3 corresponding to that of

Table 1
Specific deposition parameters[a]

Process Stage 1. Glow discharge target cleaning
Targets shuttered, 5 kW per target, 200 sccm Ar, 0 V substrate bias voltage, 10 min, 400°C

Process Stage 2. Metal ion etching
Steered arc mode, Cr target only, 100 A, 6×10^{-4} mbar, 45 sccm Ar, −1200 V substrate bias voltage, 450°C, 20 min

Process Stage 3. Unbalanced magnetron sputter coating
−75 V Substrate bias voltage, 6 A unbalancing coil current, 3.45×10^{-4} mbar, 450°C, 240 min, Ar flow 200 sccm, N_2 flow ≈ 170 sccm, thickness ≈ 3 μm

Target power utilised
TiAlCrN: $3\times Ti_{0.5}Al_{0.5}$ = 8 kW, 1 Cr = 0.5 kW

Near equiaxed TiAlCrYN: 0.3 μm TiAlCrN base layer then $2\times Ti_{0.5}Al_{0.5}$ = 8 kW, $1\times Ti_{0.48}Al_{0.48}Y_{0.04}$ = 8 kW, 1 Cr 0.5 kW

Homogeneous TiAlCrYN: $3\times Ti_{0.495}Al_{0.495}Y_{0.01}$ = 8 kW, 1 Cr = 0.5 kW

[a] Targets: Case (1) TiAlCrN – 3 $Ti_{0.5}Al_{0.5}$ and 1 Cr; Case (2) Near equiaxed TiAlCrYN – 2 $Ti_{0.5}Al_{0.5}$, 1 $Ti_{0.48}Al_{0.48}Y_{0.04}$ and 1 Cr; Case (3) Homogeneous TiAlCrYN – 3 $Ti_{0.495}Al_{0.495}Y_{0.01}$ and 1 Cr. Working gas: argon (99.999% pure). Reactive gas: nitrogen (99.999% pure).

TiN was used. The elastic modulus of each film was determined using a nano-indentation method and the values are given in Table 2. The stress-free lattice parameter, a_0 was calculated from the Poisson's ratio using Eq. (5). The stress can be determined from the slope of the least-squares fit of the plot of a_ψ versus $\sin^2\psi$ [12,13]:

$$\sigma = \frac{\text{Slope } E}{a_0(1+\nu)}. \quad (5)$$

In addition the value for which $a_\psi = a_0$ is defined by the ratio [11]:

$$\sin^2\psi = \frac{2\nu}{1+\nu}. \quad (6)$$

In glancing angle geometry the penetration depth is defined as the distance, x_e from the surface that the diffracting planes in the specimen contribute to the whole diffracted intensity by the ratio 1/e [14]:

$$x_e \frac{\sin\gamma \sin(2\theta-\gamma)}{\mu[\sin\gamma+\sin(2\theta-\gamma)]} \quad (7)$$

where μ is the linear absorption coefficient for TiAlN, which was calculated to be 620 cm^{-1}. In the present work the measurements were performed at incidence angles of 1 and 5°. Thus, from Eq. (6), the depth of penetration averaged between 2θ values of 30–140° was 0.28 and 1.04 μm for angles of incidence of 1 and 5°, respectively.

XPS images and spectra were acquired using the Kratos Axis Ultra Electron Spectrometer to study the surface chemistry of the coatings in both as-deposited and oxidised condition. The Kratos Axis Ultra Electron Spectrometer is based upon a patented magnetic lens technology and a unique spherical mirror electron analyser. It has both a 165 mm mean radius hemispherical analyser with eight-channeltron detection system for spectroscopy and a concentric spherical mirror analyser with micro channel plate (MCP) for photoelectron imaging. It is possible to obtain images with both high spatial resolution (<3 μm) and high-energy resolution (<0.5 eV) in real time and in fixed analyser transmission (FAT) mode.All spectra were acquired utilising a monochromatic Al Kα X-ray source at 450 W (15 kV and 30 mA). Wide scan spectra were acquired at 160 eV pass energy and high-resolution spectra at 20 eV pass energy. XPS images were initially acquired at 160 eV pass energy for elemental images. The analyser pass energy was reduced to 40 eV for the chemical state images of the O 1s. Small spot analysis (27 μm spot size) was referenced directly from the photoelectron images for precise determination of the analysis area.

3. Results and discussion

3.1. As-deposited films

3.1.1. Compositional analysis

Elemental analysis showed that all $Ti_{1-x-y}Al_xCr_yN$ and $Ti_{1-x-y-z}Al_xCr_yY_zN$ films were stoichiometric and of composition shown in Table 3. Further analysis on the role of yttrium was carried out using high-resolution monochromatic X-ray photoelectron spectroscopy. High resolution analysis of the Y 3d core level (Fig. 2(a)) identified the presence of two chemical species at positions Y 3d of 156 and 158.1 eV, respectively.

3.1.2. Structural analysis

The structural characteristics of the three films were investigated by X-ray diffraction using θ–2θ scans (Bragg–Brentano geometry) and glancing angle parallel beam geometry. Initially the structure of the films was investigated using θ–2θ scans and X-ray diffraction patterns for $Ti_{0.44}Al_{0.53}Cr_{0.03}N$, $Ti_{0.43}Al_{0.52}Cr_{0.03}Y_{0.02}N$ and $Ti_{0.435}Al_{0.52}Cr_{0.03}Y_{0.015}N$ films as shown in Fig. 2(b–d). The structures were all single phase (NaCl). However, considerable differences existed in the integrated diffraction peak intensities of the three films. Texture measurements using the Harris inverse pole figure method [7,8] showed significant differences in the preferred orientations of the three films under investigation (Table 3). The $Ti_{0.44}Al_{0.53}Cr_{0.03}N$ film showed a strong {111} preferred orientation whilst the

Table 2
Results of domain size, lattice parameter, residual stress, elastic modulus and Poisson's ratio in TiAlCrN and TiAlCrYN coatings

Sample	Domain size (nm)	Calculated lattice parameters a_{cal} (nm)[a]	Lattice parameter Cohen– Wagner a_0 (nm)	Calculated lattice parameters from the individual diffraction peaks a_{hkl} (nm)			Residual stress values (GPa)		Elastic modulus (GPa)[b]	Poisson's ratio[c]
				{111}	{200}	{220}	1°	5°		
$Ti_{0.44}Al_{0.53}Cr_{0.3}N$	166	0.4174	0.4183	0.4183	0.4213	0.4186	−3.8	−4.5	410	0.3
$Ti_{0.43}Al_{0.52}Cr_{0.3}Y_{0.2}N$	18	0.4188	0.4221	0.4223	0.4245	0.4232	−6.5	−6.8	370	0.3
$Ti_{0.435}Al_{0.52}Cr_{0.3}Y_{0.15}N$	250	0.4185	0.4188	0.4194	0.4209	0.4188	−3.2	−4.1	370	0.3

[a] Calculated using Vegard's law.
[b] Determined by a nano-indentation.
[c] The value for TiN.

Table 3
Results of composition and texture in TiAlCrN and TiAlCrYN coatings

Sample	At.% of metallic elements				At.% of metalloid element	Texture parameter T^* (%)						
	Ti	Al	Cr		N	{111}	{100}	{110}	{311}	{331}	{210}	{211}
$Ti_{0.44}Al_{0.53}Cr_{0.3}N$	22	26.5	1.5	–	50	44	24	11	1	6	8	6
$Ti_{0.43}Al_{0.52}Cr_{0.3}Y_{0.2}N$	21	25.5	1.5	2	50	18	51	16	12	1	1	1
$Ti_{0.435}Al_{0.52}Cr_{0.3}Y_{0.15}N$	21.5	25.5	1.5	1.5	50	36	34	12	4	4	7	3

film containing 2 at.% Y had a strong {100} preferred orientation. The film containing 1.5 at.% Y however, had mixed {111} and {100} preferred orientations. Further more, X-ray line broadening measurements from {111} and {222} diffraction peaks (Table 2) showed that crystallite (domain) size of the $Ti_{0.43}Al_{0.52}Cr_{0.03}Y_{0.02}N$ film was approximately a factor of 10 smaller than either the $Ti_{0.44}Al_{0.53}Cr_{0.03}N$ or $Ti_{0.435}Al_{0.52}Cr_{0.03}Y_{0.015}N$ films. This is supported by previous evidence from TEM analysis [3,15], where $Ti_{0.44}Al_{0.53}Cr_{0.03}N$ and $Ti_{0.435}Al_{0.52}Cr_{0.03}Y_{0.015}N$ films, deposited under similar process conditions, exhibited a distinctly columnar morphology which evolved by a competitive columnar growth process, whereas the grain size of the $Ti_{0.43}Al_{0.52}Cr_{0.03}Y_{0.02}N$ film was much finer with an almost equi-axed grain morphology. The finer grain size in the $Ti_{0.43}Al_{0.52}Cr_{0.03}Y_{0.02}N$ film was attributed to continuous re-nucleation during deposition [3]. One has to assume that Y is incorporated rather uniformly into the coating when a target configuration, which leads to case (3) as outlined in Section 2.1. However, following case (2) a layered incorporation of Y is to be expected as outlined schematically in Fig. 3(a). It is assumed that Cr goes into solid solution because of its high mobility and low concentration, whereas Y, because of its low mobility, is segregated rather uniformly in Y-enriched $Ti_{0.43}Al_{0.52}Cr_{0.03}Y_{0.04}N$ layer segments. In the $Ti_{0.43}Al_{0.52}Cr_{0.03}Y_{0.02}N$ coating therefore, a film consisting of alternate yttrium enriched layers and practically yttrium free layers (Fig. 3(a)) is thought to deposit when the substrates pass in front of the $Ti_{0.48}Al_{0.48}Y_{0.04}$ and $Ti_{0.5}Al_{0.5}$ targets, respectively, forming a pseudo-multilayer or pseudo-superlattice architecture. A low angle X-ray diffraction pattern of the $Ti_{0.43}Al_{0.52}Cr_{0.03}Y_{0.02}N$ film (Fig. 3(b)), indeed, indicates the presence of a multilayer with a period of 1.55 nm which is in reasonable agreement with the calculated 1.7 nm thickness determined from the deposition parameters. In the $Ti_{0.435}Al_{0.52}Cr_{0.03}Y_{0.015}N$ film deposited using three $Ti_{0.495}Al_{0.495}Y_{0.01}$ targets, however, the distribution of yttrium is more uniform and the structure was similar to that observed in the $Ti_{0.44}Al_{0.53}Cr_{0.03}N$ coating [3,15]. Furthermore, the absence of peaks in the low angle X-ray diffraction patterns from the $Ti_{0.44}Al_{0.53}Cr_{0.03}N$ and $Ti_{0.435}Al_{0.52}Cr_{0.03}Y_{0.015}N$ films would further support the assumption that Cr, because of its high mobility and low concentration, goes into solid solution.

In order to explain the different textures present in these coatings, different theoretical predictions for the growing mechanism must be considered. Firstly, according to Knuyt et al. [16] the lowest surface energy must be considered as the driving force for the texture evolution and according to Pelleg et al. [17] texture evolution can be discussed on the basis of both surface and strain energies. Thus, for TiN and other f.c.c. nitrides, because the {100} plane has the highest packing density (4.0 at a^{-2} compared with {220} 2.83 at a^{-2} and {111} 2.3 at a^{-2} where a is the lattice parameter) and hence the lowest surface free energy [18,19], the {100} texture would develop when the surface energy is the dominant parameter [17]. Conversely, when the strain energy is the dominant the texture tends towards the {111} plane, which has the lowest strain energy. In very thin films the surface energy controls the growth so a {100} texture would be expected, whereas in thicker films the strain energy predominates and hence a {111} texture would be expected. In the $Ti_{0.44}Al_{0.53}Cr_{0.03}N$ and $Ti_{0.435}Al_{0.52}Cr_{0.03}Y_{0.015}N$ films the coatings evolved by a competitive columnar growth process, which after sufficient growth favours the development of a {111} texture [19]. In the competitive growth process as the layer thickness increases the {111} texture develops because the {111} oriented grains with the lowest strain energy grow and increase in diameter at the expense of other less favourable orientations with a higher strain energy, e.g. {100}. In contrast, the $Ti_{0.43}Al_{0.52}Cr_{0.03}Y_{0.02}N$ films evolved by a continuous re-nucleation of new grains rather than by competitive growth of existing grains. The immobile Y atoms cause repeated formation of new nuclei and therefore the texture develops as for very thin films where the surface energy is dominant and therefore favours the development of a {100} texture.

The structure of the coatings was further investigated by lattice parameter measurements from the θ–2θ scans. Plots of lattice parameter versus the Cohen–Wagner function ($\cos\theta\cot\theta$) for the $Ti_{0.44}Al_{0.53}Cr_{0.03}N$, $Ti_{0.43}Al_{0.52}Cr_{0.03}Y_{0.02}N$ and $Ti_{0.435}Al_{0.52}Cr_{0.03}Y_{0.015}N$ films are shown in Fig. 4(a–c), respectively. In all cases the lattice parameters measured were larger than those of the calculated lattice constants (Table 2, Vegard's law), indicating that a residual compressive stress was

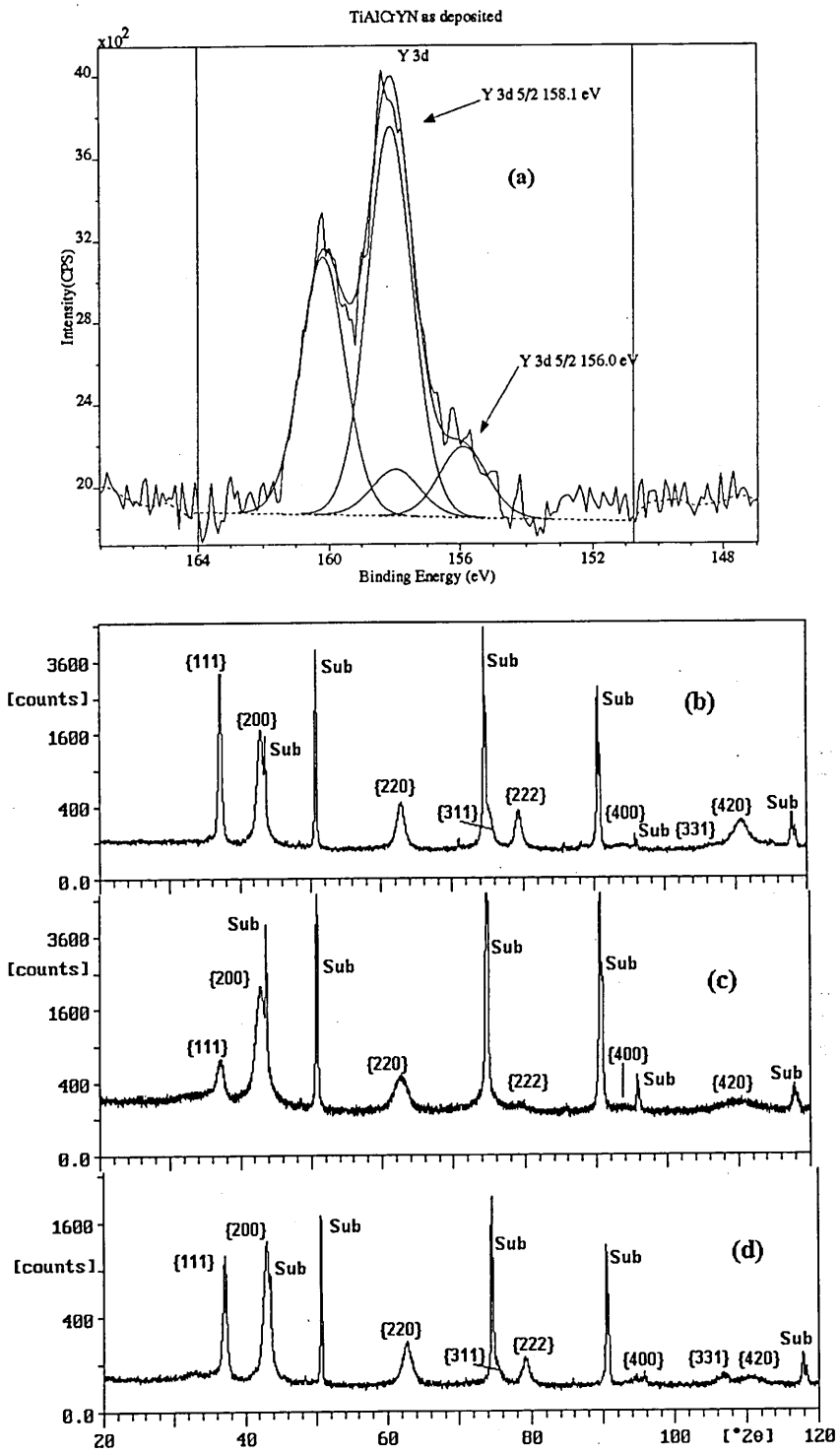

Fig. 2. (a) X-ray photoelectron spectrum in the region of the Y 3d peak for as-deposited specimen. (b–d) X-ray diffraction patterns *0–2θ* scans: (b) $Ti_{0.44}Al_{0.53}Cr_{0.03}N$ film, (c) $Ti_{0.43}Al_{0.52}Cr_{0.03}Y_{0.02}N$ film and (d) $Ti_{0.435}Al_{0.52}Cr_{0.03}Y_{0.015}N$ film.

present in all the films under investigation. For the $Ti_{0.44}Al_{0.53}Cr_{0.03}N$ film and homogeneously grown $Ti_{0.435}Al_{0.52}Cr_{0.03}Y_{0.015}N$ film, only relatively small increases in lattice parameter were measured compared with the calculated values. The differences between the measured values of the two films may be attributed to solid solution effects resulting from the incorporation of yttrium into the TiAlN lattice at the metal atom sites.

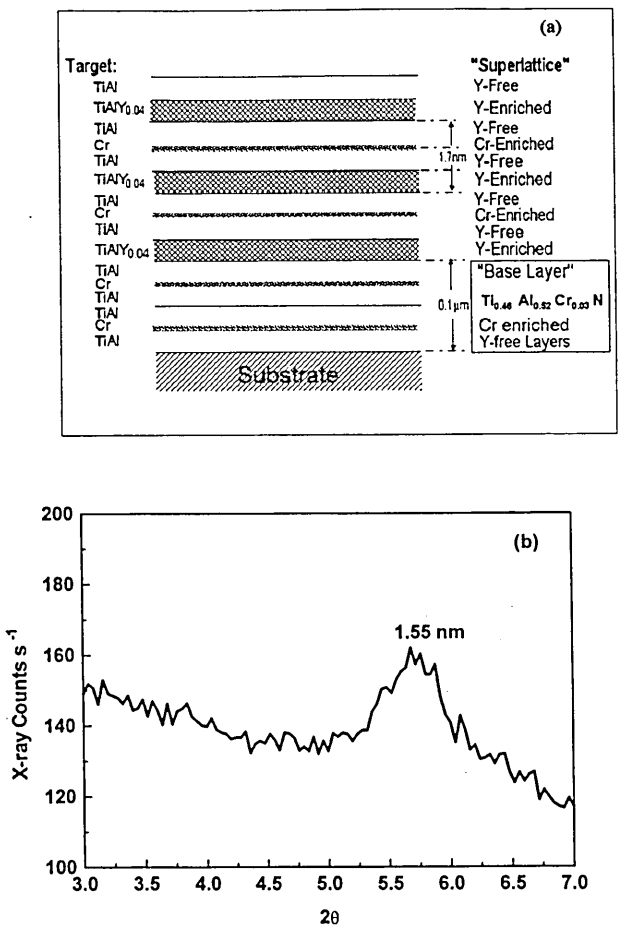

Fig. 3. (a) A schematic diagram of the layered incorporation of yttrium in the $Ti_{0.43}Al_{0.52}Cr_{0.03}Y_{0.02}N$ film. (b) A low angle X-ray diffraction pattern of the $Ti_{0.43}Al_{0.52}Cr_{0.03}Y_{0.02}N$ film.

However, for the equiaxed grained $Ti_{0.43}Al_{0.52}Cr_{0.03}Y_{0.02}N$ film a large increase in the lattice parameter was measured. The large increases in lattice parameter measured for the $Ti_{0.43}Al_{0.52}Cr_{0.03}Y_{0.02}N$ film indicates that residual compressive stress in this film was significantly higher than the other two films under investigation.

Residual stress determinations, using the $\sin^2\psi$ method, were used to investigate further the findings of the lattice parameter measurements. Lattice parameter a_ψ versus $\sin^2\psi$ determined at constant angles of incidence, $\gamma=1°$ and $\gamma=5°$, for the three coatings under investigation are shown in Fig. 5(a) and (b), respectively. The results show that in all three coatings the state residual stress was compressive. The stress levels measured in the $Ti_{0.44}Al_{0.53}Cr_{0.03}N$ and homogeneous $Ti_{0.435}Al_{0.52}Cr_{0.03}Y_{0.015}N$ films were similar. In fact for the coating containing yttrium a slightly lower residual stress value was obtained (Table 2) and values obtained were similar to previously reported results for UBM-deposited TiAlN films [20,21]. However, residual stress values calculated for the equiaxed grained

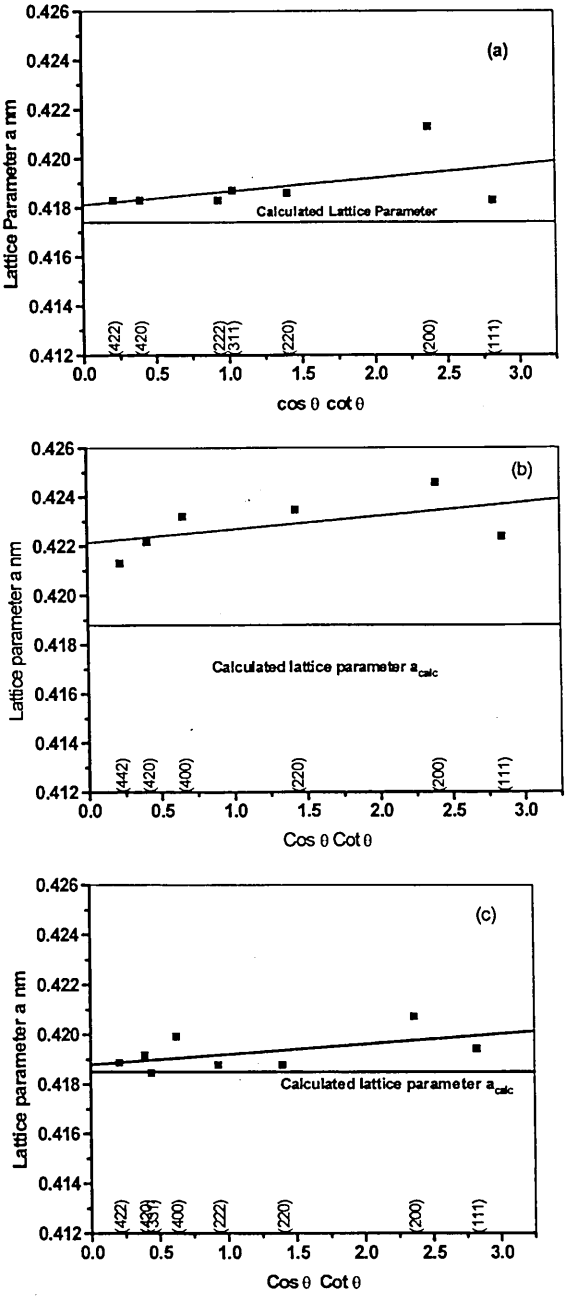

Fig. 4. Plots of lattice parameter a versus the Cohen–Wagner function ($\cos\theta\cot\theta$): (a) $Ti_{0.44}Al_{0.53}Cr_{0.03}N$ film , (b) $Ti_{0.43}Al_{0.52}Cr_{0.03}Y_{0.02}N$ film and (c) $Ti_{0.435}Al_{0.52}Cr_{0.03}Y_{0.015}N$ film.

$Ti_{0.43}Al_{0.52}Cr_{0.03}Y_{0.02}N$ film were significantly higher than those for the other two coatings under investigation by almost a factor of 2 (Table 2). In all three films there was a systematic increase in the calculated values of residual stress as the angle of incidence of the X-ray beam γ was increased from 1 to 5° (Table 2), indicating a residual stress gradient from surface to substrate–coating interface [22,23]. However, the residual stress gradient was far more pronounced in the

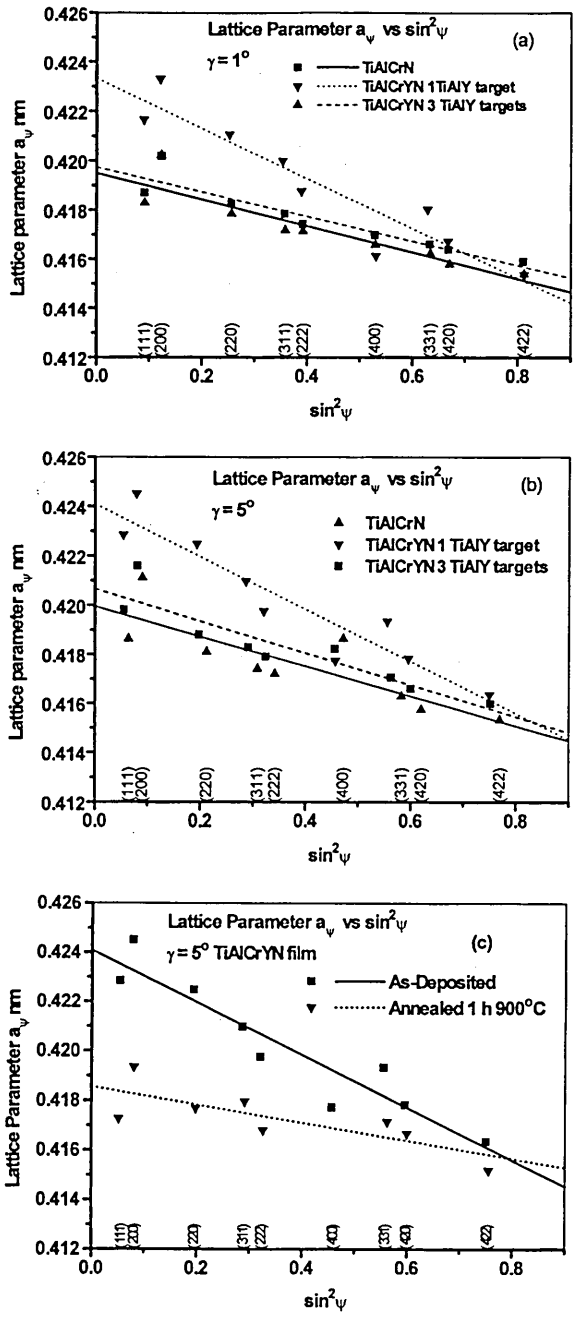

Fig. 5. Plots of lattice parameter a_ψ versus $\sin^2\psi$ for $Ti_{0.44}Al_{0.53}Cr_{0.03}N$, $Ti_{0.43}Al_{0.52}Cr_{0.03}Y_{0.02}N$ and $Ti_{0.435}Al_{0.52}Cr_{0.03}Y_{0.015}N$ films: (a) 1° incidence and (b) 5° incidence. (c) Plots of lattice parameter a_ψ versus $\sin^2\psi$ $Ti_{0.43}Al_{0.52}Cr_{0.03}Y_{0.02}N$.

$Ti_{0.44}Al_{0.53}Cr_{0.03}N$ and $Ti_{0.435}Al_{0.52}Cr_{0.03}Y_{0.015}N$ films (i.e. 18 and 28% increases, respectively) than in the $Ti_{0.43}Al_{0.52}Cr_{0.03}Y_{0.02}N$ film (5% increase). The major differences between the two yttrium-containing coatings are a finer grain size and a non-homogeneous yttrium distribution in the $Ti_{0.43}Al_{0.52}Cr_{0.03}Y_{0.02}N$ film. It is well known that the level of residual stress in hard coatings depends on deposition temperature, higher deposition temperatures favour the development of lower residual stresses [24–26], indicating that the temperature-dependent flow stress in hard coatings restricts the level of residual stresses during deposition [27], i.e. that either plastic deformation or some dynamic stress relaxation process (e.g. annihilation of point defects) is occurring during deposition. Furthermore, at a constant deposition temperature, according to the Hall–Petch relationship [28], a decrease in the grain size in the coating will increase the flow stress and hence favour the development of higher residual stresses. The observed stress gradient within the coatings under investigation, i.e. particularly in the $Ti_{0.44}Al_{0.53}Cr_{0.03}N$ and $Ti_{0.435}Al_{0.52}Cr_{0.03}Y_{0.015}N$ films which evolved by a competitive growth mechanism, further supports the assumption that the flow stress of the material limits the level of residual stress. During the deposition process, because of the competitive growth process, the grain size at the coating surface was coarser than that near the coating–substrate interface [3,15], resulting in the lower residual compressive stresses measured near the surface than near the coating–substrate interface. Therefore the significantly higher residual stress in the $Ti_{0.43}Al_{0.52}Cr_{0.03}Y_{0.02}N$ film may be attributed to the much finer grain size (a factor of 10 smaller) in this material than that in the other two materials under investigation. Furthermore, the systematically lower residual stresses measured in the $Ti_{0.435}Al_{0.52}Cr_{0.03}Y_{0.015}N$ film than in $Ti_{0.44}Al_{0.53}Cr_{0.03}N$ film (Table 2) may also reflect the larger crystallite/domain size of the $Ti_{0.435}Al_{0.52}Cr_{0.03}Y_{0.015}N$ film (i.e. 250 nm for the $Ti_{0.435}Al_{0.52}Cr_{0.03}Y_{0.015}N$ film compared with 160 nm for $Ti_{0.44}Al_{0.53}Cr_{0.03}N$ film).

3.2. Annealing and oxidation studies

3.2.1. Structural analysis

The residual stress was also determined in the $Ti_{0.43}Al_{0.52}Cr_{0.03}Y_{0.02}N$ film after heating in air for 1h at 900°C and plots of lattice parameter a_ψ versus $\sin^2\psi$ comparing the as-deposited with the annealed coating are shown in Fig. 5(c). The $\sin^2\psi$ plot shows that the state of stress in the coating after heating in air for 1 h at 900°C was still compressive. However, the measured stress level was significantly lower than that in the as-deposited coating, i.e. 2.3 GPa for the annealed coating compared with 6.8 GPa for the as-deposited coating. Thus, stress relaxation at elevated temperatures is associated with either thermally activated plastic deformation [25] or with recovery due to annihilation of the stress active defects produced during coating [24,25].

3.2.2. Compositional analysis

In a previous investigation the oxidation of these coatings was studied using TEM, EDX and SNMS [3].

In this investigation the surface chemistry of similar coatings annealed in air has been further studied using high resolution monochromatic XPS to complement the previous work. Large-area XPS analyses of the surface, in the region of the O 1s peak, of $Ti_{0.44}Al_{0.53}Cr_{0.03}N$ film and the equiaxed grained $Ti_{0.43}Al_{0.52}Cr_{0.03}Y_{0.02}N$ film oxidised at a temperature of 950°C for 1 h are shown in Fig. 6(a) and (b). Peak deconvolution indicates that oxygen was present at three different binding energies of 528.9, 531.8 and 533.3 eV respectively, associated with three different chemical species namely Ti–O, Al–O and C–O. The C–O present is due to hydrocarbon contaminants on the oxidised surface. The binding energies of the Ti–O and Al–O correspond to the positions of oxides TiO_2 and Al_2O_3. Integrated intensities of deconvoluted spectra from the O 1s for peak positions corresponding to TiO_2 and Al_2O_3 are plotted versus temperature for $Ti_{0.44}Al_{0.53}Cr_{0.03}N$ and equiaxed grained $Ti_{0.44}Al_{0.53}Cr_{0.03}Y_{0.02}N$ films oxidised for 1 h at 800, 850, 900, 950°C and 1000 °C (Fig. 7(a) and (b)). Previous work has shown that the rapid oxidation

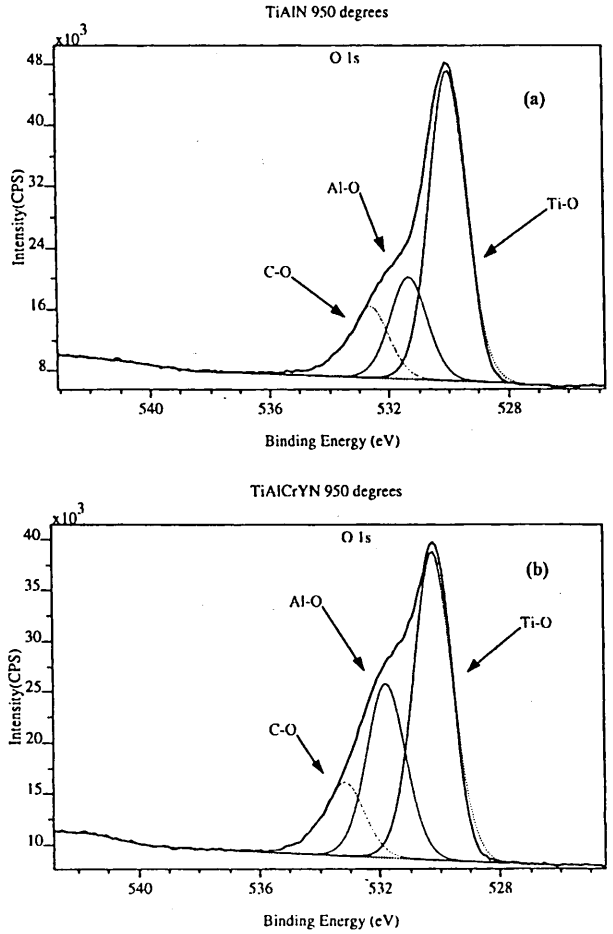

Fig. 6. X-ray photoelectron spectra in the region of the O 1s peak for coating oxidised at 950°C: (a) $Ti_{0.44}Al_{0.53}Cr_{0.03}N$ film, (b) $Ti_{0.43}Al_{0.52}Cr_{0.03}Y_{0.02}N$ film.

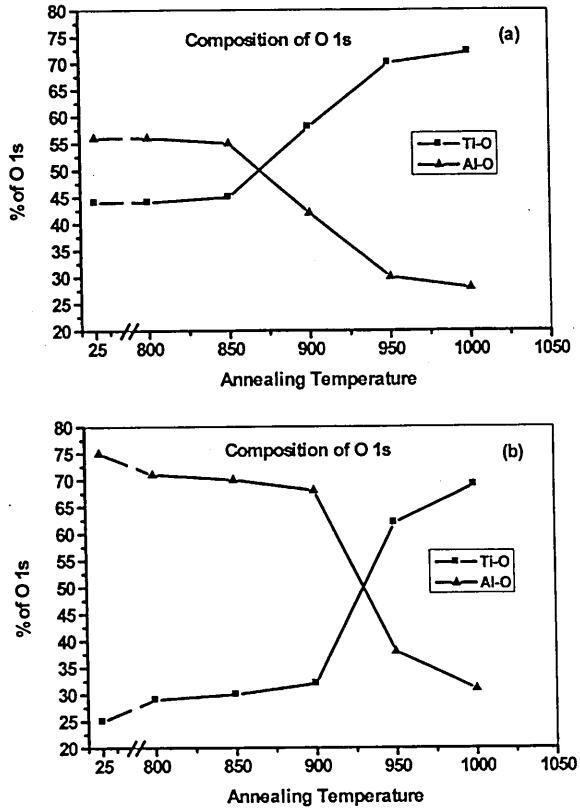

Fig. 7. Integrated intensities of deconvoluted spectra from the O 1s for peak positions corresponding to TiO_2 and Al_2O_3 versus annealing temperature in air: (a) $Ti_{0.44}Al_{0.53}Cr_{0.03}N$ film, (b) $Ti_{0.43}Al_{0.52}Cr_{0.03}Y_{0.02}N$ film.

of $Ti_{0.44}Al_{0.53}Cr_{0.03}N$, $Ti_{0.43}Al_{0.52}Cr_{0.03}Y_{0.02}N$ films occurs at 920 and 950°C, respectively [3] and it can be seen in Fig. 6(c) and (d)) that this approximates to the temperature at which percentage of TiO_2 increases, i.e. 900 and 950°C, respectively. The equiaxed structure of the non-homogeneously grown $Ti_{0.43}Al_{0.52}Cr_{0.03}Y_{0.02}N$ film is clearly more oxidation resistant than the $Ti_{0.44}Al_{0.53}Cr_{0.03}N$ film with a columnar structure. In previous work [3] using STEM–EDX profiles across grain boundaries in the annealed $Ti_{0.43}Al_{0.52}Cr_{0.03}Y_{0.02}N$ film, preferential segregation of Y to grain boundaries was observed where the concentration of Y at grain boundaries was enhanced by at least a factor of 2. The presence of Y or possibly YO_x at the grain boundaries of the $Ti_{0.43}Al_{0.52}Cr_{0.03}Y_{0.02}N$ alloy film may inhibit both cation out diffusion to the free surface and oxygen diffusion into the film.

XPS imaging, using the O 1s (531.8 and 529.7 eV), Fe 2p, Ti 2p and Cr 2p photoelectron peaks, has been used to investigate the spatial distribution of oxides formed on the surface of a $Ti_{0.44}Al_{0.53}Cr_{0.03}N$ coating when annealed in air at 950°C (Fig. 8(a)–(e)). The images of the surface using the Fe 2p, Ti 2p, Cr 2p and O 1s show that the surface is composed of discrete

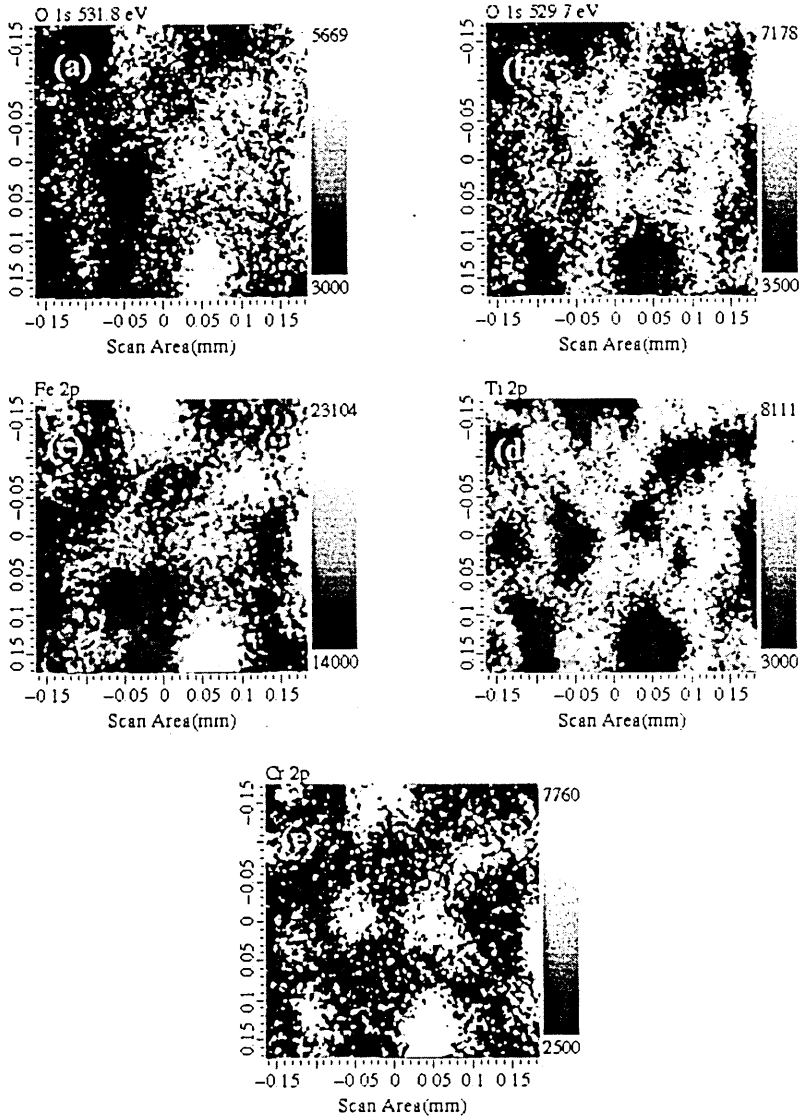

Fig. 8. X-ray photoelectron spectroscopy images for a $Ti_{0.44}Al_{0.53}Cr_{0.03}N$ film annealed for 1 h at 950°C: (a) O 1s (531.8 eV); (b) O 1s (529.7 eV); (c) Fe 2p; (d) Ti 2p; (e) Cr 2p.

regions containing iron, chromium and oxygen (O 1s, 531.8 eV) and discrete regions containing Ti and O (O 1s, 529.7 eV) thus indicating the presence of separate regions of iron–chromium oxides and titanium oxide (TiO_2). The iron–chromium oxides are formed by localised cation out-diffusion of the substrate elements Fe and Cr through the coating leading to the formation of their respective oxidation products on the surface, resulting in cavities at the coating/substrate interface [3]. Small spot analysis (55 μm) of the Ti regions showed no measurable concentrations of Fe or Cr indicating rejection of the elements Fe and Cr by the TiO_2 regions (Fig. 9).

XPS imaging, using the O 1s (531.8 and 529.7 eV), Al 2p and Ti 2p photoelectron peaks, has been used to investigate the spatial distribution of oxides formed on the surface of a $Ti_{0.43}Al_{0.52}Cr_{0.03}Y_{0.02}N$ coating when annealed in air at 950°C (Fig. 10(a–d)). These images show that the surface of the oxidised $Ti_{0.43}Al_{0.52}Cr_{0.03}Y_{0.02}N$ coating consisted only of regions of Al_2O_3 (corundum) and TiO_2 (rutile). There was no evidence of large regions of iron–chromium oxides that were present on the surface of the oxidised $Ti_{0.44}Al_{0.53}Cr_{0.03}N$ coating. Thus, the incorporation of Y into TiAlN coatings prevents both cation out diffusion of the substrate elements to the surface and ingression oxygen into the surface until a temperature of 950°C is reached. Small spot analysis Fig. 11 (55 μm) of the Ti and Al regions showed that the yttrium segregates to the Ti sites with a binding energy for the Y 3d of 158 eV. In the oxidised specimen, however, unlike the as-deposited specimen, only one chemical specie could

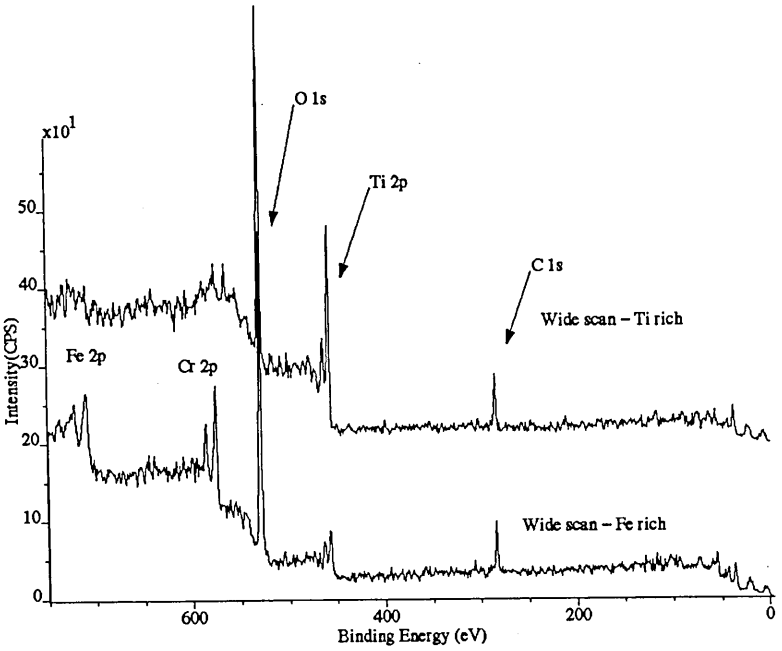

Fig. 9. X-ray photoelectron spectra from iron and titanium regions.

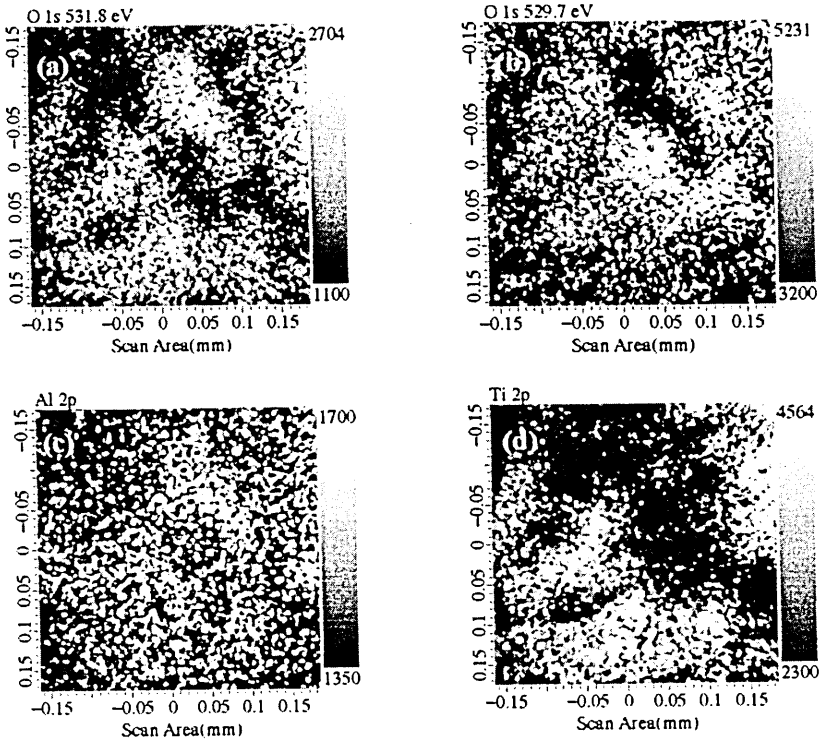

Fig. 10. X-photoelectron spectroscopy images for a $Ti_{0.43}Al_{0.52}Cr_{0.03}Y_{0.02}N$ film annealed for 1 h at 950°C: (a) O 1s (531.8 eV); (b) O 1s (529.7 eV); (c) Al 2p; (d) Ti 2p.

be identified at the Y 3d core level (Fig. 12). In the Al_2O_3 regions a small photoelectron peak corresponding to Cr $2p_{3/2}$ could be identified which resulted from the oxidation of the Cr present in the coating.

4. Conclusions

(1) Significant changes in texture evolution were observed when small concentrations of Y were incorpo-

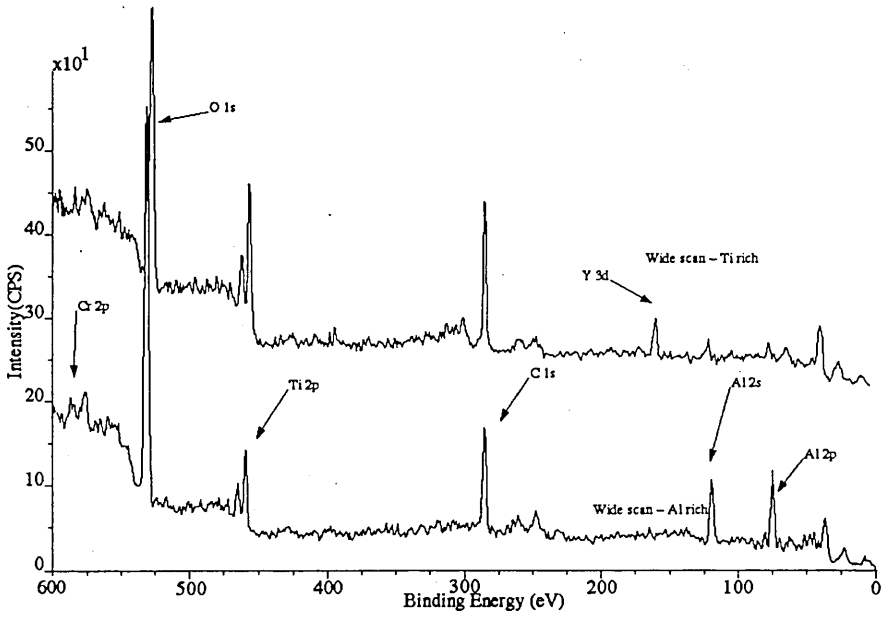

Fig. 11. X-ray photoelectron spectra from aluminium and titanium regions.

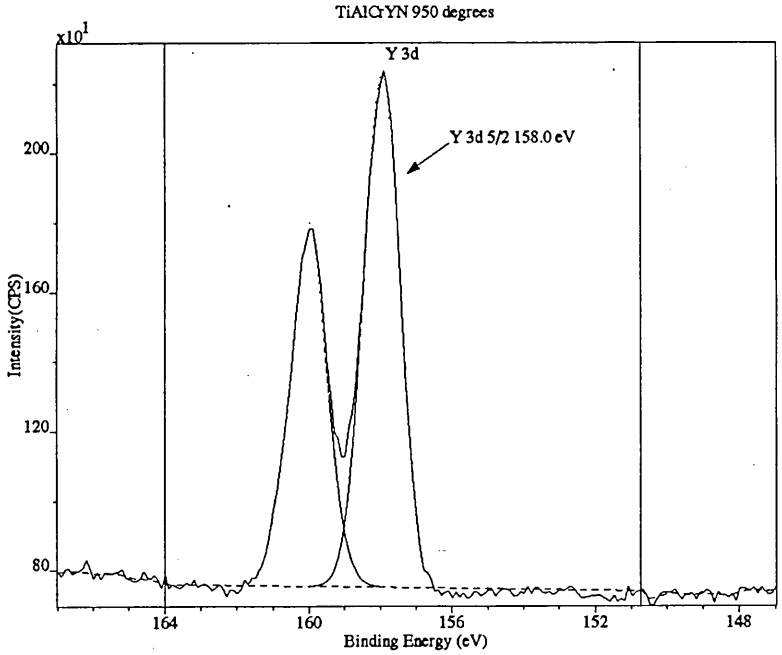

Fig. 12. X-ray photoelectron spectrum in the region of the Y 3d peak annealed specimen.

rated inhomogeneously into $Ti_{1-x-y}Al_xCr_yN$ films. When the distribution of Y in the films was non-uniform ($Ti_{0.43}Al_{0.52}Cr_{0.03}Y_{0.02}N$) then the texture changed from a strong {111} ($T^*=44\%$) in the $Ti_{0.44}Al_{0.53}Cr_{0.03}N$ to a strong {100} ($T^*=51\%$) in the $Ti_{0.43}Al_{0.52}Cr_{0.03}Y_{0.02}N$ film. If the Y was distributed uniformly the film evolved with mixed {111} and {100} textures.

(2) The residual stress state in all the coatings under investigation was found to be compressive. However, the level of stress, up to a factor of 2, was higher in $Ti_{0.43}Al_{0.52}Cr_{0.03}Y_{0.02}N$ film than in the $Ti_{0.435}Al_{0.52}Cr_{0.03}Y_{0.015}N$ film. The level of stress in the $Ti_{0.435}Al_{0.52}Cr_{0.03}Y_{0.015}N$ film was similar to that in the basic yttrium-free $Ti_{0.44}Al_{0.53}Cr_{0.03}N$ film and was similar to previously reported values.

(3) Annealing the $Ti_{0.43}Al_{0.52}Cr_{0.03}Y_{0.02}N$ for 1 h at 900°C in air film led to a reduction in residual stress from 6.8 to 2.3 GPa.

(4) During oxidation of the $Ti_{0.435}Al_{0.52}Cr_{0.03}Y_{0.015}N$ film the Y and Cr segregate to the TiO_2 and Al_2O_3 regions, respectively.

Acknowledgements

This research was supported by DTI-Link Surface Engineering under award number GK/K76351, MULTICOAT. Also the research work presented here was partially carried out at Charles University in Prague. Dr. Lewis wishes to acknowledge the Royal Academy of Engineering for their financial support during his stay in Prague.

References

[1] W.-D. Münz, J. Vac. Sci. Technol. A 4 (1986) 2717.
[2] D. McIntyre, J.E. Greene, G. Håkansson, J.-E. Sundgren, W.-D. Münz, J. Appl. Phys. 67 (1990) 1542.
[3] L.A. Donohue, I.J. Smith, W.-D. Münz, I. Petrov, J.E. Greene, Surf. Coat. Technol. 94/95 (1997) 226.
[4] W.-D. Münz, D. Schulze, F.J. Hauzer, Surf. Coat. Technol. 50 (1992) 169.
[5] W.-D. Münz, I.J. Smith, D.B. Lewis, S. Creasey, Vacuum 48 (5) (1997) 473.
[6] S. Creasey, D.B. Lewis, I.J. Smith, W.-D. Münz, Surf. Coat. Technol. 97 (1997) 163.
[7] R. Kuzel Jr., R. Cerny, V. Valvoda, M. Blomberg, M. Merisalo, Thin Solid Films 247 (1994) 64.
[8] C.N.J. Wagner, in: J.B. Cohen, J.E. Hilliard (Eds.), Local Atomic Arrangements Studied by X-ray Diffraction, Gordon and Breach, New York, 1966.
[9] G.B. Harris, Phil. Mag. 43 (1952) 113.
[10] D.S. Rickerby, A.M. Jones, B.A. Bellamy, Surf. Coat. Technol. 37 (1989) 111.
[11] D.E. Geist, A.J. Perry, J.R. Treglio, V. Valvoda, D. Rafaja, Adv. X-ray Anal. 38 (1995) 471.
[12] V. Valvoda, A.J. Perry, L. Hultman, J. Musil, S. Kadlec, Surf. Coat. Technol. 49 (1991) 181.
[13] A.J. Perry, Thin Solid Films 193/194 (1990) 463.
[14] A.J. Perry, D.E. Geist, K. Narasimhan, J.R. Treglio, Surf. Coat. Technol. 86/87 (1996) 364.
[15] I. Petrov, unpublished work
[16] G. Knuyt, C. Quaeyhaegens, J. D'Haen, L. Stals, Thin Solid Films 258 (1995) 159.
[17] J. Pelleg, L.Z. Zevin, S. Lungo, Thin Solid Films 197 (1991) 117.
[18] L. Hultman, J.-E. Sungren, J.E. Greene, J. Appl. Phys. 66 (1989) 536.
[19] J.E. Greene, J.-E. Sundgren, L. Hultman, I. Petrov, D.B. Bergstrom, Appl. Phys. Lett. 67 (1995) 2928.
[20] I. Petrov, P. Losbichler, D.B. Bergstrom, J.E. Greene, W.-.D Münz, T. Hurkmans, T. Trinh, Thin Solid Films 302 (1997) 179.
[21] W.D. Sproul, P.J. Rudnik, K.O. Legg, W.-.D Münz, I. Petrov, J.E. Greene, Surf. Coat. Technol. 56 (1993) 179.
[22] J.A. Thornton, Annu. Rev. Mater. Sci. 7 (1977) 239.
[23] J.A. Thornton, D.W. Hoffmann, Thin Solid Films 171 (1989) 5.
[24] S.J. Bull, D.S. Rickerby, J.C. Knight, T.F. Page, Surf. Eng. 8 (1992) 193.
[25] G. Kleer, R. Kassner, E.-M. Meyer, M.G. Schinker, W. Doell, Surf. Coat. Technol. 54/55 (1992) 173.
[26] H. Oettel, R. Wiedemann, S. Preißler, Surf. Coat. Technol. 74/75 (1995) 273.
[27] H. Oettel, R. Wiedemann, Surf. Coat. Technol. 76/77 (1995) 265.
[28] E.O. Hall, Yield Point Phenomena in Metals and Alloys, MacMillan, New York, 1970.

ELSEVIER

Surface and Coatings Technology 116–119 (1999) 1145–1151

SURFACE & COATINGS TECHNOLOGY

www.elsevier.nl/locate/surfcoat

Characterisation of co-sputtered Nb:Cr coatings grown by the combined cathodic arc/unbalanced magnetron sputtering technique

H. Paritong *, M. Lembke, D.B. Lewis, W.-D. Münz

Materials Research Institute, Sheffield Hallam University, City Campus, Pond Street, Sheffield S1 1WB, UK

Abstract

Niobium and chromium are both well known for their corrosion resistance due to the formation of protective oxide films. Sputtering is the preferred physical vapour deposition technique to deposit refractory metals such as Nb, but owing to its high melting point high ion bombardment and/or high deposition temperatures are necessary to grow dense Nb films. Further disadvantages of Nb are its relatively low hardness values and the low oxidation resistance of Nb. The present paper discusses experiments of co-sputtering Cr and Nb using the combined cathodic arc/unbalanced magnetron technique. The corrosion resistance of the 1 μm thick coatings deposited on 304 stainless steel substrates at 250 and 420°C is investigated by potentiodynamic polarisation measurements in a 3% NaCl solution. The formation of solid solutions of Cr in Nb and of the intermetallic phase of Cr_2Nb were found to increase the microhardness, as well as the oxidation resistance, of the sputtered coatings substantially in comparison with pure Nb films.

Keywords: Cr; Co-sputtering; Magnetron sputtering; Nb; Thin films

1. Introduction

The corrosion resistance of Nb and Cr is based on the formation of stable oxide films of Nb_2O_5 and Cr_2O_3 respectively in aqueous media. However, the corrosion resistance of chromium in solutions containing chloride ions is restricted by the transpassive dissolution of the protective oxide layer. Niobium, on the other hand, exhibits excellent corrosion behaviour and the stable oxide film remains intact in most highly corrosive environments [1,2]. Sputtering is the preferred physical vapour deposition (PVD) technology to deposit refractory metals like niobium, as the sputter yield is virtually independent of the melting point of the material [3]. However, owing to its high melting point (T_M= 2468°C) intensive ion bombardment [4,5] and/or deposition temperatures as high as 400°C are necessary to produce protective, non-porous Nb films [6,7]. Another way to improve and densify the niobium coating structure can be by co-deposition of alloying elements such as Cr [8–10] or Zr [7]. Turley [8] suggested that depositing Nb and Cr at a composition of mutual insolubility (50:50) would lead to a disruption of the open columnar-type growth structure and hence densification of the coating morphology. Hsieh et al. [10] report about dense and column-free Nb–30%Cr alloy coatings with improved corrosion resistance deposited by IBAD. Other aspects of alloying additions of Cr to Nb considered in this study are the influence on the oxidation resistance and the microhardness by solid solution hardening and by the formation of intermetallic phases respectively. In the present study approximately 1 μm thick Nb–Cr coatings of different composition were deposited by co-sputtering in an industrial-sized arc bond sputtering (ABS) coating chamber. The ABS technology combines the two PVD techniques of steered cathodic arc evaporation and unbalanced magnetron sputtering and allows deposition in highly ionised gas atmospheres as well as co-sputtering of various target materials [11]. The influence of the deposition parameters — i.e. substrate temperature, substrate bias voltage and the unbalancing effect of the magnetrons — as well as of the Cr content of the films was investigated with regard to their crystallographic structure and microstructure, hardness, corrosion- and oxidation-resistance.

* Corresponding author. Tel.: +44-114-225-3500; fax: +44-114-225-3501.
E-mail address: h.paritong@shu.ac.uk (H. Paritong)

0257-8972/99/$ – see front matter
PII: S0257-8972(99)00192-9

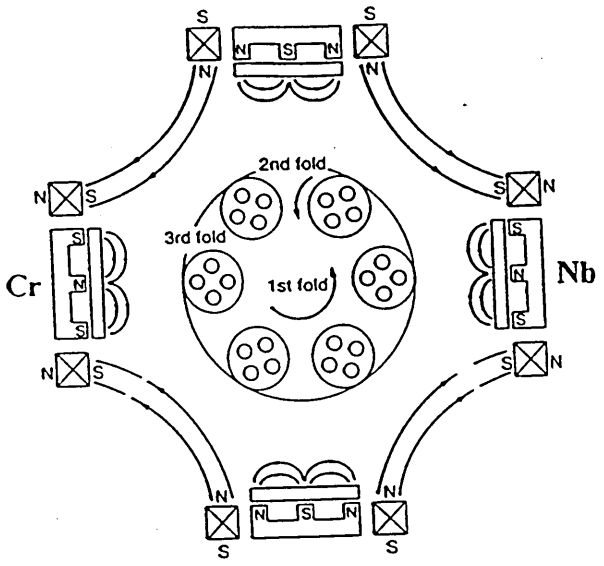

Fig. 1. Schematic cross-section of the Hauzer HTC 1000-4 coating chamber.

2. Experimental

2.1. Coating deposition

Fig. 1 shows a schematic cross-section of the HTC 1000-4 ABS coating chamber. The chamber is equipped with four dual purpose cathodes, which can be used in either the cathodic arc or the unbalanced magnetron mode. The magnetic pole arrangement of the cathodes leads to a closed magnetic field configuration in the coating chamber. Unbalancing of the magnetrons is accomplished by electromagnetic coils that are concentrically mounted to the cathodes [11]. During deposition only one Cr and one Nb target were used; these were opposite each other, as shown in Fig. 1. In situ substrate cleaning prior to coating deposition was performed in the steered cathodic arc mode using Cr ions as the etching species. Cr was chosen as the etching material owing to its characteristic of forming the smallest-sized droplets, in relatively low concentration, of refractory metals [12]. The etching time was 10 min and the substrate bias voltage was set to −1200 V. The substrates were coated in the unbalanced magnetron mode, undergoing three-axis planetary motion, at process temperatures of 420 and 250°C. The deposition parameters are given in Table 1. Coatings 1 and 7 are pure Nb coatings. Coatings 2–5 were deposited with an applied power of 0.5 kW to the Cr target. During deposition of coatings 2–5 the power on the Cr target was kept constant while the degree of ion bombardment of the growing film was increased for each process by increasing either the coil current or the substrate bias voltage. Higher Cr concentrations were achieved for coatings 6 and 8 by applying 1.0 kW and 1.5 kW respectively to the Cr target. The films were deposited on 304 stainless steel and on M2 high speed steel substrates, polished to a 1 μm finish.

2.2. Characterisation of the coatings

The chemical composition of the coatings was determined by glow discharge optical emission spectroscopy (Leco 750 GDS). A Philips powder diffractometer in Bragg–Brentano geometry was used to determine the phases present, the crystallographic texture and the lattice parameter. The texture was calculated using the inverse pole figure technique [13]; determination of the lattice parameter was performed by Cohen–Wagner plots. The hardness of the thin films was assessed with a Mitutoyo Knoop indentor using a load of 3 gf. Thermogravimetric measurements in a linear ramp mode (1 °C/min in air) were used to investigate the oxidation behaviour of the coated stainless steel coupons with an effective surface area of 16 cm^2 (Cahn TG131). Additionally, two selected samples were treated isothermally at 700°C for 8 h in air. The microstructure of two selected coatings was investigated with cross-sectional transmission electron microscopy (TEM) (Philips CM20). The corrosion resistance of the coated specimen

Table 1
Deposition parameters; Cr-content, lattice parameter, hardness and texture values of the deposited coatings

Coating number	Coating deposition						Cr-content (at.%)	Lattice parameter (Å)	Hardness ($HK_{0.003}$)	Texture	
	Temperature (°C)	Nb-target power (kW)	Cr-target power (kW)	Bias voltage (V)	Coil current (A)	Deposition rate (μm h^{-1})				{110}	{111}
1	420	8	0	−75	4×8	0.72	0	3.3529	820	0.62	3.90
2	420	8	0.5	−75	4×6	0.76	14	3.3526	1270	0.62	3.90
3	420	8	0.5	−75	4×8	0.74	12	3.3531	1250	1.40	3.00
4	420	8	0.5	−100	4×8	0.69	8	3.3608	1270	5.38	0.33
5	420	8	0.5	−125	4×8	0.63	5	3.3632	1200	5.00	0.76
6	420	7	0	−75	4×8	0.82	53	–	1320	–	–
7	250	8	0	−75	4×3	0.77	0	3.3341	560	5.447	0
8	250	8	1	−75	4×3	0.85	36	–	1230	–	–

was investigated by means of potentiodynamic polarisation scans from −800 to +900 mV in a 3% NaCl solution open to air. All potential are recorded versus a saturated calomel electrode. The equipment used was an EG&G Potentiostat/Galvanostat 263A.

3. Results and discussion

The Cr-contents and deposition rates are given in Table 1. A decrease in deposition rate and Cr content can be observed for coatings 2–5 with increasing unbalancing coil current (i.e. ion density) as well with increasing substrate bias voltage (i.e. ion energy). Increasing either parameter leads to enhanced ion bombardment of the growing film and hence causing an increase in the overall re-sputter rate of the condensed atoms. The observed change in relative Cr concentration is due to the differences in sputter yield between Nb and Cr (0.6 for Nb and 1.18 for Cr for 500 eV Ar^+ ions [14]), which leads to enhanced preferential re-sputtering of the condensed Cr atoms with increasing ion bombardment. X-ray diffraction (XRD) patterns of the coatings show the formation of solid solutions of Cr in Nb for coatings 2–5 (Fig. 2). The presence of the intermetallic phase of Cr_2Nb is evident for coating 6 with a Cr content of 53% (Fig. 3). The intermetallic phase is also present in coating 8 (36% Cr), but to a lesser extent than in coating 6. The calculated lattice parameters, as well as the values of the {110} and {111} major textural components, are given in Table 1. The lattice parameter increases with decreasing Cr content and increasing ion bombardment during deposition, as can be seen from coatings 2–5. The influence of the Cr content on the lattice parameter can be attributed to contraction of the Nb lattice by dissolving the smaller Cr atoms (atomic radii: Nb, 1.45 Å; Cr, 1.27 Å). Higher ion bombardment causes increased intrinsic compressive stresses induced during film growth. These stresses act in the planes perpendicular to the coating–substrate interface, hence increasing the lattice spacing in the planes parallel to the interface. A third parameter causing the lattice expansion described above is the thermal stress component, as indicated by the considerable difference in lattice parameters between the low and high temperature pure Nb coatings (coatings 1 and 7 respectively). Most films exhibit a pronounced {110} texture, except coatings 1 and 3 where a shift towards a {111} preferred orientation can be observed. The {110} texture is thermodynamically favoured for bcc metals such as Nb and Cr, as the texture development is driven by the reduction of surface and interface energies and, therefore, favours the closest packed {110} planes [15,16]. The shift in preferred orientation for coatings 1 and 3 cannot be explained at present.

A substantial increase in hardness was achieved by

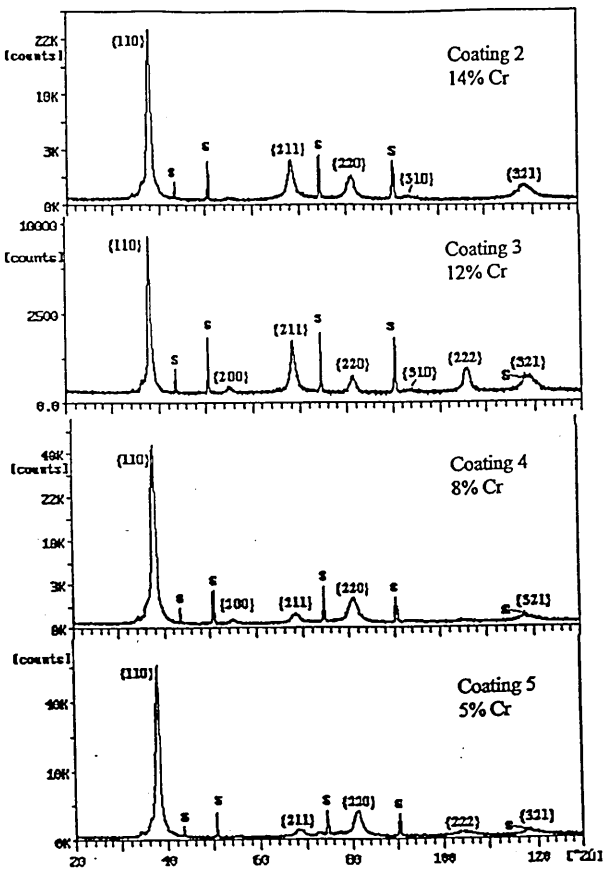

Fig. 2. XRD pattern of as-deposited coatings 2–5.

alloying additions of Cr, as shown in Table 1. Whereas the pure Nb films exhibit hardness values of $HK_{0.003} = 580$ for the low temperature coating and $HK_{0.003} = 820$ for the high temperature coating, hardness values of up to $HK_{0.003} = 1320$ were observed for the co-sputtered Nb–Cr coatings. Coating 6, with a Cr concentration of 53%, exhibits the highest hardness value, but Cr contents as low as 5–14% (coatings 2–5) already increase the hardness considerably to values between 1200 and 1270 $HK_{0.003}$. The hardness appears to be determined by two effects: i.e. solid solution hardening (Cr concentration) on the one hand and residual stresses, intrinsic or thermal, on the other hand. The effects become clear when comparing the microhardness values of the following coating pairs: (a) coating 1, coating 3 (increase in hardness by solid solution hardening); (b) coating 1, coating 7 (increase in hardness by increased residual stresses); (c) coating 2, coating 4 (same hardness by superimposing both effects). Despite overall higher hardness values due to residual stresses in the thin films, the results obtained are in good agreement with literature microhardness values of bulk Nb–Cr alloys [17]. The highest value is reported for

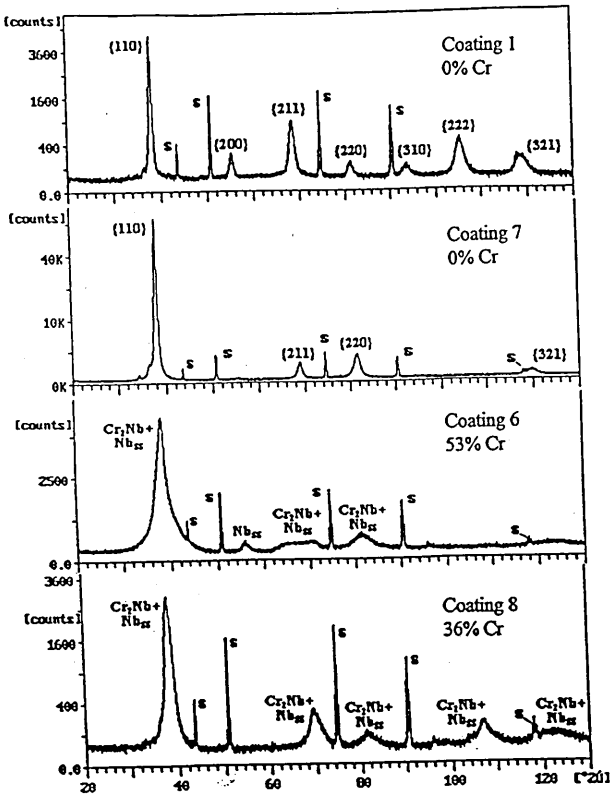

Fig. 3. XRD pattern of as-deposited coatings 1 and 7 and of coatings 6 and 8.

alloys containing 55–57% Cr, measured on a mixture of the phases $Nb + Cr_2Nb$.

TEM cross-sectional micrographs of the two films with the highest Cr contents (coatings 6 and 8) are shown in Fig. 4. Both films exhibit a clear columnar structure. The low temperature coating with a Cr content of 36% (coating 8) is characterised by a region of pronounced competitive growth followed by a broad columnar morphology and rounded column tops. Coating 6, with 52% Cr, grown under higher ion bombardment at a higher deposition temperature, shows a considerable refined film morphology with smaller column diameters and a smoother top surface. Smoothening of the surface is due to increased preferential re-sputtering of the column tops with increased ion bombardment. Selected-area diffraction patterns taken over the whole coating area showed weak reflection spots with a lattice spacing of 4.01 Å in both films, associated with the {111} reflection of the phase Cr_2Nb, thus confirming the XRD findings. However, the observed columnar morphology is not in agreement with the work by Turley [8] and Hsieh et al. [10], who suggested a disruption of the columnar structure by alloying additions of Cr of 30% and 50% respectively. It should be noted that the microstructural observations made by the authors, as well as in Refs. [9,18], were based on scanning electron microscopy and XRD analyses.

Polarisation curves of the coated specimens and of the uncoated 304 stainless steel substrate are given in Fig. 5. A substantial increase in corrosion resistance

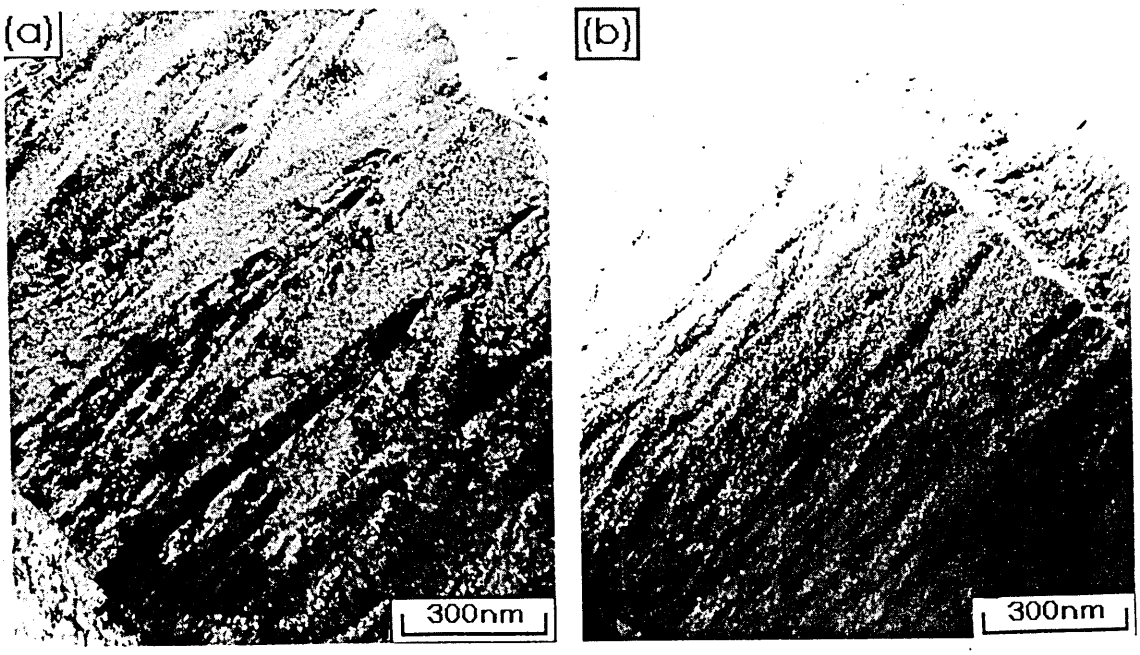

Fig. 4. TEM cross-sections of coating 8 (a) and coating 6 (b).

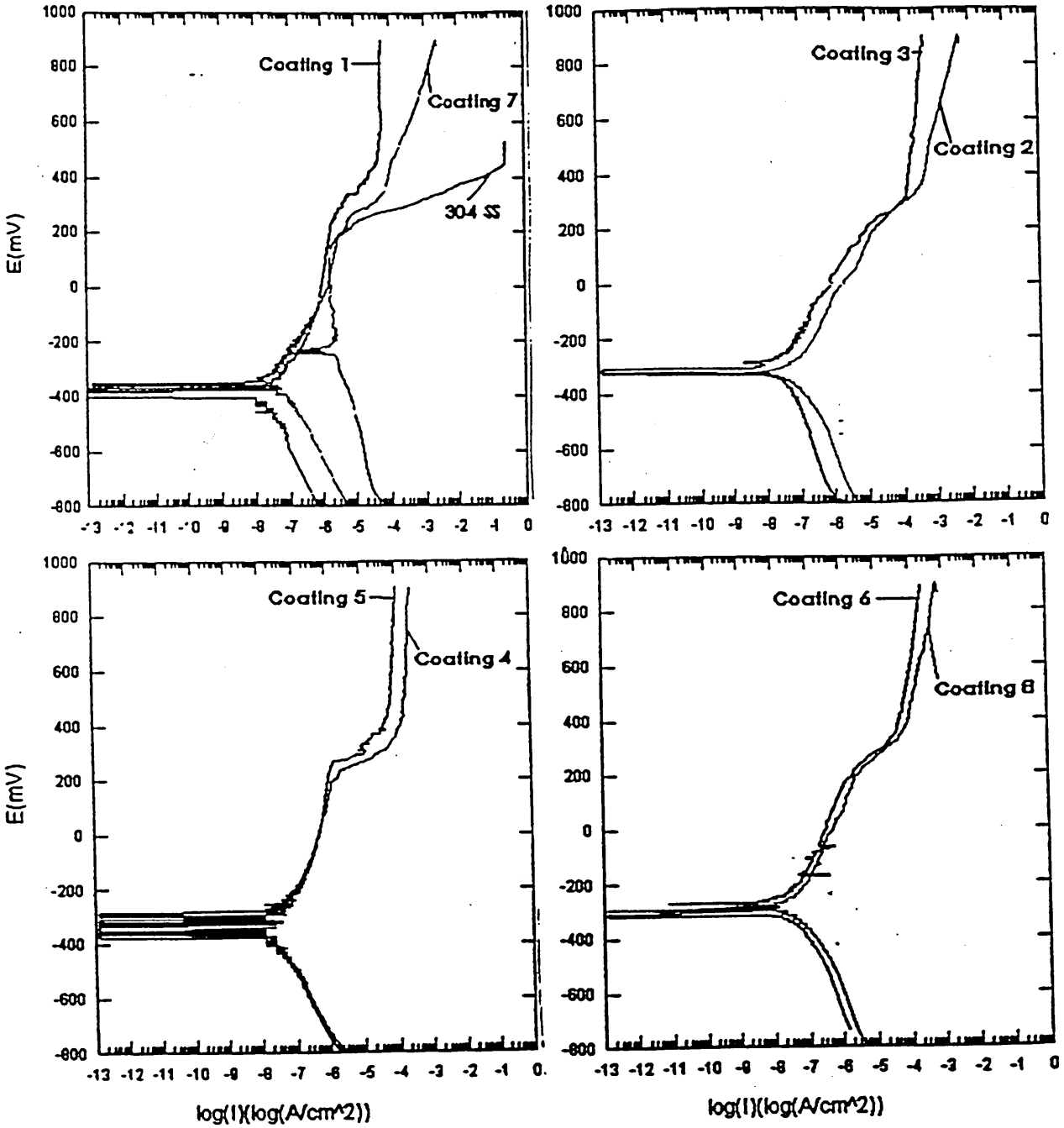

Fig. 5. Polarisation curves of uncoated 304 stainless steel and of coatings 1–8 on 304 stainless steel substrates in a 3% NaCl solution open to air.

compared with the uncoated steel substrate was observed for all coated specimens, as indicated by extended passive regions and lower current densities in the anodic region. However, none of the coatings shows a fully protective, i.e. passive behaviour; between +250 and +400 mV the onset of localised pitting can be observed for all coated samples. Comparison of the two pure Nb films (coatings 1 and 7) shows an improved corrosion resistance for coating 1, which most likely can be attributed to densification of the microstructure due to increased deposition temperature and ion bombardment during film growth. The influence of the ion bombardment on the corrosion behaviour is also evident when comparing coatings 2–5. Both increased coil current and substrate bias voltage clearly improved the corrosion performance of the coatings, as indicated by the decrease

in current densities in the passive as well as in the transpassive regions. Again, this can be attributed to densification of coating morphology with increasing ion bombardment. The difference in the corrosion resistance between the two coatings with the high Cr contents (coatings 6 and 8) is not as significant as might be expected from the microstructural observations made by TEM (Fig. 4). Further investigations are necessary to clarify the results. However, alloying additions of Cr do not seem to influence significantly the corrosion performance of the deposited films, which appears to be determined predominantly by the degree of ion bombardment, i.e. unbalancing coil current and substrate bias voltage. This is evident from the fact that coating 5 exhibits the best corrosion protection, i.e. the lowest current density, of all the co-sputtered Nb–Cr films. Furthermore, it is important to notice that the range of passivity, or the pitting potential, is highest for the pure Nb coatings, which indicates an electrochemical rather than a microstructural influence of the Cr concentration on the corrosion behaviour.

Fig. 6 shows the results of the thermogravimetric measurements of the coated specimens, as well as of the uncoated stainless steel substrate. No significant improvement in the oxidation behaviour was achieved with low alloying additions of Cr (coatings 2–5) compared with pure Nb; for reasons of simplification, only the curves of the pure Nb film (coating 1) and of coatings 6 and 8 are therefore shown in Fig. 6. Below 400°C the first stages of oxidation of the coated specimen are determined by the solution of oxygen in either the Nb lattice or the Nb–Cr lattice [19]. The formation of suboxides during this pre-transition period has also been reported for Nb [19,20]. The onset of accelerated oxidation (breakaway oxidation [19]) of the pure Nb film occurs between 450 and 500°C, which is associated with the formation of a cracked and porous scale of Nb_2O_5 that offers little or no protection against further oxidation. Calculations have shown that the increase in weight

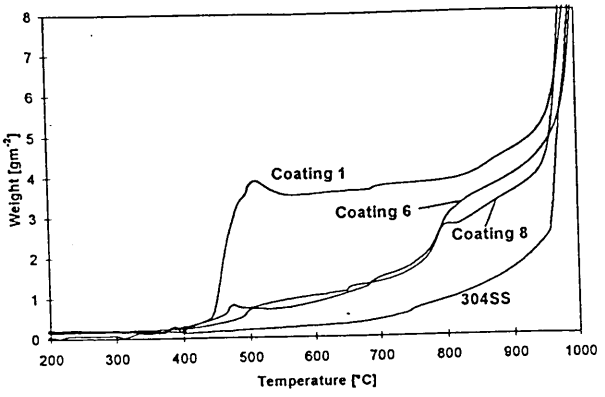

Fig. 6. Thermogravimetric oxidation rates in air of coatings 1, 6 and 8 on stainless steel substrates as well as of uncoated 304 stainless steel.

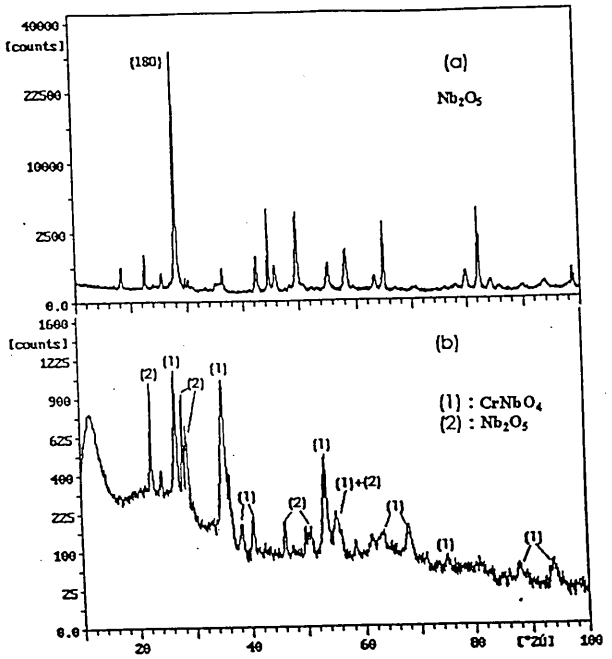

Fig. 7. XRD pattern of coating 1 (pure Nb coating) (a) and coating 6 (53% Cr) (b) after oxidation in air at 700°C for 8 h. Pattern (a) was obtained from the oxidation product on the coated substrate; pattern (b) was obtained from the oxidation product as a powder mounted on a glass slide.

in that temperature range reflects oxidation of the entire coating to stochiometric Nb_2O_5. The XRD pattern of coating 1 after oxidation at 700°C for 8 h [Fig. 7(a)] confirms the formation of Nb_2O_5. The rate and formation of the porous, non-protective scale of Nb_2O_5 is often regarded as a result of cracking of an initially adherent and protective scale. This is associated with the high oxide-to-metal volume ratio for Nb ($Nb_2O_5/Nb=2.69$ [21]), inducing high compressive biaxial stresses leading to breakdown of the protective scale [21–23]. A considerable improvement in the oxidation resistance was achieved with the high alloying additions of Cr in coatings 6 and 8. Between 450 and 800°C the weight gain is significantly reduced compared with the pure Nb film. The weight increases slowly and nearly linear in that temperature range, and only at temperatures above 800°C can a more rapid increase in oxidation be observed, which most probably can be attributed to cracking of a protective Cr-rich oxide scale. XRD analysis of coating 6 after oxidation at 700°C [Fig. 7(b)] identified the scale as $NbCrO_4$, which is in agreement with the Nb_2O_5–Cr_2O_3 phase diagram investigated by Goldschmidt [24]. The XRD pattern also showed the presence of Nb_2O_5. The improvement in oxidation resistance can hence most likely be attributed to the formation of a scale of greater stability that is less prone to cracking than Nb_2O_5. This can be explained by a decrease in oxide-to-metal volume ratio

($Cr_2O_3/Cr = 2.07$ [21]) increasing the stability of the adherent, protective oxide scale and hence offering greater protection against oxidation [21,22]. Other factors influencing the oxidation behaviour of Nb, not considered here, are a strong dependency of the onset and rate of the breakaway oxidation on the crystallographic orientation of the metal [19] and the valency effects of the alloying metal [19,21].

4. Conclusions

A considerable increase in hardness of sputtered Nb coatings can be observed with low alloying additions of Cr; hardness values of HK = 1320 can be achieved with a Cr content of 53%, leading to the formation of the intermetallic phase of Cr_2Nb.

All coatings deposited in the experiments described here show significantly improved corrosion behaviour in a 3% NaCl solution compared with 304 stainless steel, independent of their Cr content.

Ion bombardment during deposition clearly improves the corrosion performance of the coatings. However, fully protective behaviour was not achieved. This may be related to the Cr ion etching step chosen in the present experiments. Prior investigation [7] has shown that corrosion-resistant Nb coatings with passivation characteristics approaching bulk Nb can be achieved using Nb ion etching as the in vacuo pre-treatment.

High alloying additions of Cr considerably improve the oxidation resistance of PVD Nb coatings. Cr concentrations beyond 30% protect the films against severe oxidation up to 750°C.

Acknowledgement

The authors would like to thank Dr I. Wadsworth for his support in regard to the TEM analyses.

References

[1] G.L. Miller, Tantalum and Niobium, Butterworths Scientific, London, 1958.
[2] R.W. Balliet, M. Coscia, F.J. Hunkeler, J. Met. 38 (9) (1986) 25.
[3] R.W. Berry, P.M. Hall, F.M. Harris, Thin Film Technology, Van Nostrand, 1968.
[4] J.A. Thornton, Annu. Rev. Mater. Sci. 7 (1977) 239.
[5] R. Messier, A.P. Giri, R.A. Roy, J. Vac. Sci. Technol. A: 2 (2) (1984) 500.
[6] E.E. Salagean, D.B. Lewis, J.S. Brooks, W.-D. Münz, I. Petrov, J.E. Greene, Surf. Coat. Technol. 82 (1996) 57.
[7] H. Paritong, I. Wadsworth, W.-D. Münz, Trans. IMF 76 (4) (1998) 144.
[8] M. Turley, Surf. Coat. Technol. 39–40 (1989) 135.
[9] K.J.A. Mawella, J.A. Sheward, Thin Solid Films 193 (1990) 27.
[10] J.H. Hsieh, W. Wu, R.A. Erck, G.R. Fenske, Y.Y. Su, M. Marek, Surf. Coat. Technol. 51 (1992) 212.
[11] W.-D. Münz, F.J.M. Hauzer, D. Schulze, Surf. Coat. Technol. 50 (1992) 169.
[12] W.-D. Münz, I.J. Smith, D.B. Lewis, S. Creasey, Vacuum 48 (5) (1997) 473.
[13] D. Rickerby, A.M. Jones, B.A. Bellamy, Surf. Coat. Technol. 37 (1989) 111.
[14] J.L. Vossen, J.J. Cuomo, Glow discharge sputter deposition, in: J.L. Vossen, W. Kern (Eds.), Thin Film Processes, Academic Press, 1978, p. 12.
[15] H. Ji, J. Appl. Phys. 81 (10) (1997) 6754.
[16] C.V. Thompson, R. Carel, Mater. Sci. Forum 204–206 (1996) 83.
[17] D.A. Prokoshkin, E.V. Vasileva, Alloys of Niobium, S. Monson, Israel, 1965.
[18] L. Fedrizzi, Y. Massiani, J.P. Crousier, M. Dapor, P.L. Bonora, Corrosion 46 (1990) 499.
[19] P. Kofstad, High Temperature Oxidation of Metals, Wiley, New York, 1966.
[20] N. Norman, P. Kofstad, O.J. Krudtaa, J. Less-Common Met. 4 (1962) 124.
[21] W.D. Klopp, C.T. Sims, R.I. Jaffee, in: Proceedings of the 2nd U.N. International Conference on the Peacful Uses of Atomic Energy, Geneva (1958) 502.
[22] O. Kubaschewski, B.E. Hopkins, Oxidation of Metals and Alloys, Butterworths, London, 1962.
[23] D.W. Aylmore, S.J. Gregg, W.B. Jepsen, J. Electrochem. Soc. 107 (1960) 495.
[24] H.J. Goldschmidt, Metallurgica 373 (1960) 211.

ELSEVIER

Surface and Coatings Technology 111 (1999) 148–157

SURFACE & COATINGS TECHNOLOGY

Influence of sample geometry on the effect of pulse plasma nitriding of M2 steel[1]

G. Nayal [a,2], D.B. Lewis [a,*], M. Lembke [a], W.-D. Münz [a], J.E. Cockrem [b]

[a] *Sheffield Hallam University, Materials Research Institute, Pond Street, Sheffield, S1 1WB, UK*
[b] *ELTRO (GB) Limited, Unit 11, Fleet Business Park, Sandy Lane, Fleet, GU13 OBF, UK*

Received 2 July 1998; accepted 25 September 1998

Abstract

A comparison of pulse-plasma-nitrided flat coupons and complex shaped substrates such as twist drill test bits shows that the incorporation of nitrogen depends strongly on the substrate geometry. Glow discharge optical emission spectroscopy (GDOES), depth profiling and cross-sectional WDX analysis showed that the amount of nitrogen incorporated at the cutting edge of a drill was systematically higher than in flat coupons nitrided under identical plasma conditions. In fact, the observed increase in hardness reaches a value of $HV_{0.01}=1232$ (base hardness $HV_{0.01}=840$), whereas in the corresponding flat coupon, $HV_{0.01}=980$ at a depth typically 10 μm. Bragg–Brentano and glancing angle parallel beam XRD and SEM analysis confirmed that under the optimized process conditions used, the formation of the adhesion reducing compound layer, ϵ, can be completely suppressed. These findings clearly imply that caution must be exercised when extrapolating observations on flat coupons to those of geometrically more complex cutting tools, e.g. on twist drills.

Keywords: Nitriding; Pulse plasma; Substrate geometry

1. Introduction

Plasma nitriding of M2 high-speed steel (HSS) increases the adhesion of PVD-coated tools and improves their corrosion resistance. In nitrided steels, the case structure contains a diffusion zone with or without a compound layer. However, when the brittle highly stressed compound layer is present, the coating adhesion is reduced [1–3]. Currently, there are no real data published on the performance of plasma-nitrided cutting tools. Preliminary tests show, however, that plasma-nitrided and coated drills performed less well than non-nitrided and coated drills, despite the fact that the formation of the compound layer was avoided, or at least it was not present on microstructural examination of the coupons nitrided under identical conditions to those of the drills.

However, considerable caution must be exercised when applying the observations made on flat test coupons to tools with a complex geometry. The prediction of the presence of a compound on a drill from a microstructural examination of coupons is uncertain. The only certain method to characterize the microstructure on the cutting edge is by taking a metallographic cross-section through the drill. Thus, this work compares the nitriding behaviour of nitrided tools with test coupons that were nitrided together in the same chamber as the drills. Furthermore, a duplex treatment comprising pulse plasma nitriding and PVD coating was included in the current study using test coupons in order to investigate the re-distribution of interstitial elements during coating.

2. Experimental

Plasma nitriding was performed in an Eltropuls pulse plasma nitriding chamber and the process variables are given in Table 1. The specimens nitrided were 6 mm diameter double point twist drills and 32 mm diameter × 4 mm thick coupons both manufactured from M2 HSS in the hardened and tempered condition. The standard nitriding treatments were of 20 min duration,

* Corresponding author. Tel: +44 114 2254074; Fax: +44 0114 2253501.
[1] Presented at the ICMCTF '98 Conference in San Diego, CA, USA, April 1998.
[2] Permanent address: Aleppo University, Aleppo, Syria.

0257-8972/99/$ – see front matter
PII S0257-8972(98)00721-X

Table 1
Process parameters

Sample number	Nitriding time (min)	Pressure (Pa)	Temperature (°C)	Voltage (V)	Pulse duration (μs)	Pulse repetition (μs)	N_2 flow rate ($l\,h^{-1}$)	H_2 flow rate ($l\,h^{-1}$)
1	20	200	460	−470	50	200	20	40
2	20	350	460	−470	50	200	20	40
3	20	350	460	−470	50	250	40	40
4	90	350	460	−470	50	250	40	40

the 90 min treatment was used to induce the formation of a compound layer though this is not the only means of producing such a layer. Bulk temperature measurement was performed by connecting thermocouples into dummy drills and coupons located at similar positions within the nitriding chamber to those of the nitrided samples. In both cases, relative thermal equilibrium was reached prior to the nitriding step. However, local increases in temperature at the cutting edge of the drill may occur due to the relatively thinner cross-section where higher current densities are expected.

A 3 μm thick TiAlCrYN coating was subsequently deposited by the Arc Bond Sputter process [4] on coupons, using the four different nitriding conditions, at a temperature of 450 °C. The total coating duration at 450 °C was 240 min. A more detailed description of the process conditions used for deposition is given elsewhere [5].

Hardness (10 g Vickers) depth profiles of both coupons and drills were determined from cross-sections, metallographically prepared to a 1 μm diamond finish, through the nitrided layer.

Cross-sections through the nitrided layers of the coupons and drills were examined in the polished and etched condition (etched in 2% nital) using scanning electron microscopy. Composition depth profiles for the coupons in both nitrided and nitrided and coated conditions were determined using glow discharge optical emission

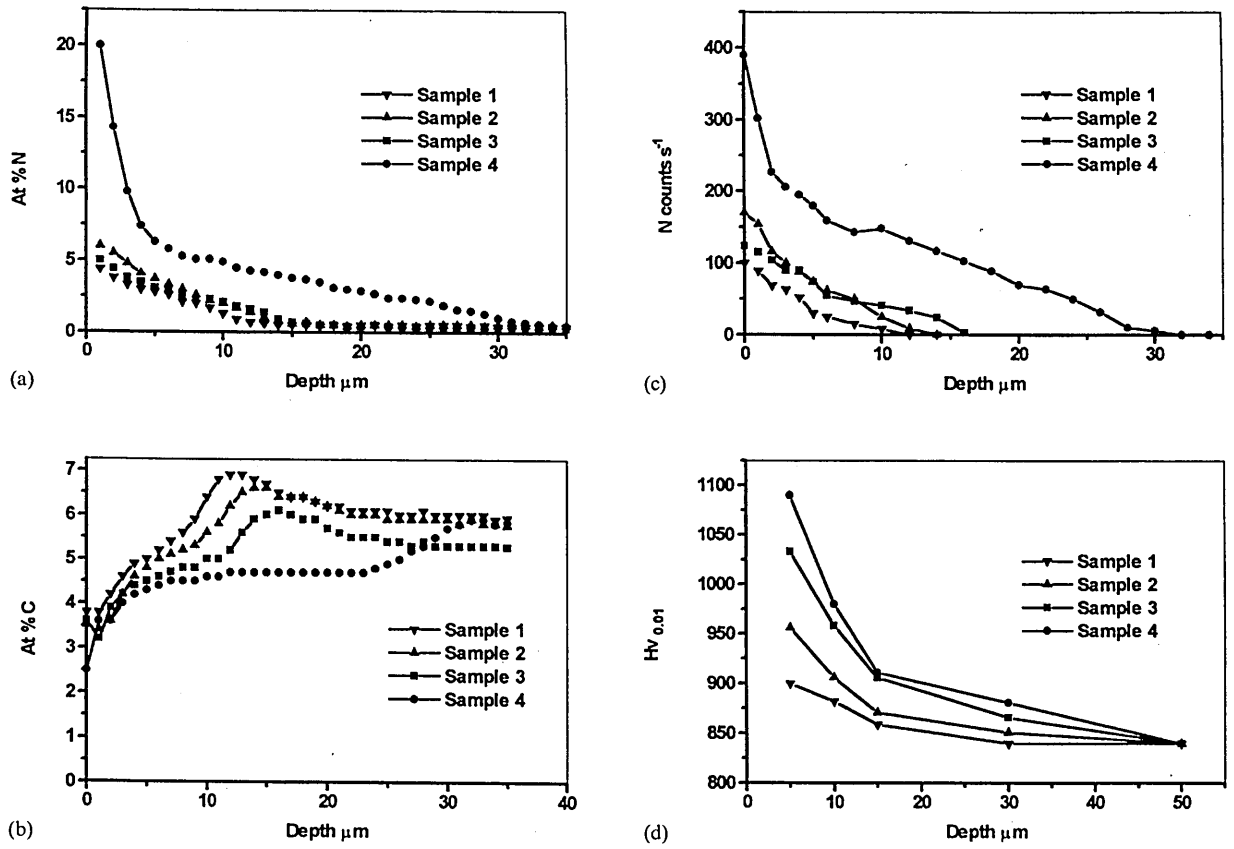

Fig. 1. (a) Glow discharge optical emission spectroscopy (GDOES) nitrogen depth profile on coupons 1, 2, 3 and 4. (b) Glow discharge optical emission spectroscopy (GDOES) carbon depth profile on coupons 1, 2, 3 and 4. (c) Wavelength dispersive X-ray analysis (WDX) nitrogen depth profile on coupons 1, 2, 3 and 4. 1d. Hardness ($HV_{0.01}$) depth profile on coupons 1, 2, 3 and 4.

Table 2
Hardness and analysis measurements (GDOES, WDX) on nitrided M2 HSS drills and coupons and nitrided and coated M2 HSS coupons

Sample number	Analysis of coupons (GDOES)		Analysis of coupons (WDX)		Hardness at 10 μm	Coated coupons GDOES Case depth (μm)	GDOES nitrogen analysis of nitrided coupons Interpolated analysis of surface composition at.% (least squares)	GDOES nitrogen analysis nitrided and coated coupons Interpolated analysis of surface composition at.% (least squares)	Analysis of drills (WDX)			Hardness at 10 μm
	At.% N Surface	Case depth (μm)	N counts s^{-1} surface	Case depth (μm)					N counts s^{-1} drill		Case depth (μm)	Drills
1	4.1	11	100	11	882	27	4.1	3.5	Point	144	21	997
									Flank	96	10	
									Face	60	7	
2	5.8	13	170	13	900	28	5.5	4	Point	174	29	1049
									Flank	111	18	
									Face	101	11	
3	5.0	16	124	16	959	35	4.9	3.7	Point	206	50	1082
									Flank	156	28	
									Face	127	22	
4	20	32	390	32	980	52	6.4	6.3	Point	494	90	1232
									Flank	388	49	
									Face	195	44	

spectroscopy (GDOES). Wavelength dispersive X-ray analysis (WDX) was performed on cross-sections of drills and coupons by point analysis from the nitrided surface through the nitrided zone to the un-nitrided core. For the drills, WDX depth profiles were carried out along the same axes as the hardness profiles, and an analysis was carried out using a JEOL JXA 840 electron probe microanalyser at an accelerating voltage of 10 kV with a probe current of 100 nA.

X-ray diffraction was carried out using monochromatic CuKα radiation in both Bragg–Brentano and glancing angle geometries.

3. Results and discussion

The influence of the process variables on the nitrogen depth profile (GDOES) for the coupons is shown in [Fig. 1(a)], and the results of nitrogen content at the surface and case depth are given in Table 2. For the coupons plasma-nitrided for 20 min duration, the change in nitrogen concentration profile was very smooth with an almost linear decay, thus indicating a case structure with a diffusion zone only, without the presence of a compound layer. When the nitriding time was increased from 20 to 90 min, two distinct slopes could be observed in the nitrogen concentration profile, a steep nitrogen concentration gradient at the surface indicating the presence of a compound layer [6], followed by a smooth decay in the nitrogen profile.

The influence of the various nitriding conditions on the carbon distribution profiles is shown in [Fig. 1(b)]. There is clear evidence of carbon migration leading to a carbon-enriched layer ahead of the nitrided case, resulting in considerable decarburization in the nitrided case [1,7,8]. It is suggested [1] that because of a stress build-up in the nitrided zone, the carbon diffuses to the stress-free regions, i.e. to the surface and ahead of the nitrided case leading to decarburization of the nitrided zone.

The complex geometry of the drills relative to the coupons rendered any GDOES analysis impossible, so the cross-sections through the cutting edge drills were analysed by point analysis using WDX. The results of the qualitative WDX nitrogen profiles for the coupons almost mirror those of the GDOES depth profiles of the same specimens [Fig. 1(c)], thus validating the use of WDX for nitrogen depth profiles for the drills.

The results of the hardness depth profile for the coupons [Fig. 1(d)] tend to mirror those of the nitrogen distributions, i.e. the coupon with the highest nitrogen concentration had the highest hardness. However, in all cases, the depth of the hardened case (hardness depth profile) was greater than the nitrogen penetration (nitro-

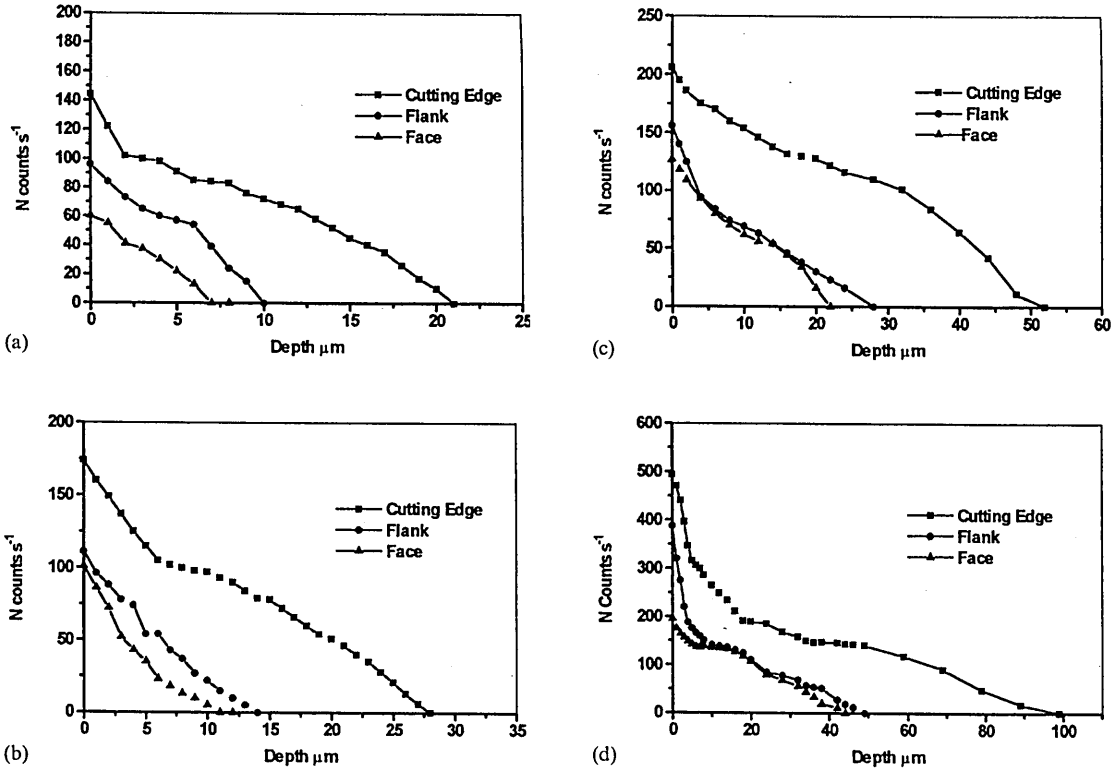

Fig. 2. Wavelength dispersive X-ray analysis (WDX) nitrogen depth profile from cutting edge, flank and face: (a) nitrided drill 1, (b) nitrided drill 2, (c) nitrided drill 3 and (d) nitrided drill 4.

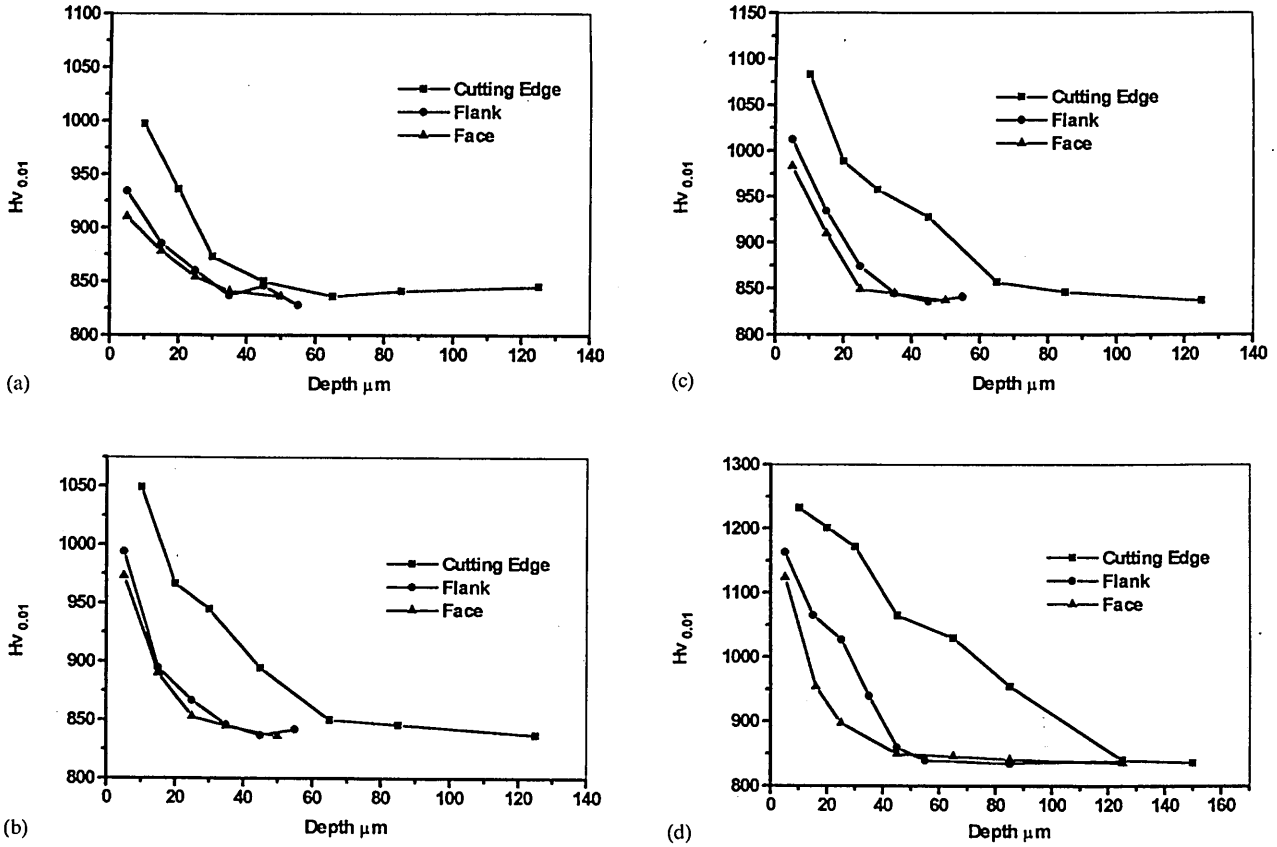

Fig. 3. Hardness ($HV_{0.01}$) depth profile from cutting edge, flank and face: (a) nitrided drill 1, (b) nitrided drill 2, (c) nitrided drill 3 and (d) nitrided drill 4.

gen depth profiles), thus suggesting that carbon enrichment ahead of the nitrided case contributes to the overall case depth in the form of secondary hardening.

Fig. 2(a)–(d) outlines the influence of process variables on nitrogen depth profiles obtained from qualitative WDX point analysis from cross-sections through the cutting edge, flank and face of 6-mm-diameter twist drills, and the results of apparent nitrogen concentration (counts s^{-1}) and case depth from the cutting edge flank and face are listed in Table 2. The increased surface area and current density at the cutting edge of the drills compared with the coupons resulted in an increase in both the nitrogen content at the cutting edge and the case depth (two to four times) when compared with coupons nitrided under identical conditions. The latter, i.e. current, density may also result in locally higher temperatures at the cutting edge of the drill due to the increased number of bombarding ions at such a location. This may result in a higher local nitrogen incorporation as well as a deeper local nitrided case in comparison with relatively flatter geometries where the current densities are lower. The nitrogen profiles for the drills nitrided for 20 min [Fig. 2(a)–(c)] showed a similar smooth decay in the nitrogen concentration profiles to those observed in the coupons, indicating a case structure with a diffusion zone only. At the higher nitriding pressure of 350 Pa, almost the same nitrogen contents were measured for flank and face regions, respectively. This is a well-known effect [9] and results from a more uniform plasma at the higher nitriding pressure. Increasing the nitriding time for the drill from 20 to 90 min [Fig. 2(d)], produced a nitrogen profile which indicates the presence of a compound layer at the surface of both the cutting edge and the flank region.

The hardness depth profiles [Fig. 3(a)–(d)] on the drills reflect the results of the corresponding nitrogen depth profile, and again, there was evidence to suggest that carbon enrichment ahead of the nitriding front contributed to the overall depth of the hardened case. However, the observed increase in hardness at the same depth (10 μm) was significantly higher on the drill than the flat coupon because of their higher nitrogen contents (Table 2).

The findings of the GDOES and WDX nitrogen depth profiles measurements on the coupons were confirmed by metallographic examination [Fig. 4(a)–(d)]. The coupons nitrided for 20 min duration, i.e. Fig. 4(a)–(c), did not show any evidence of a compound layer at the

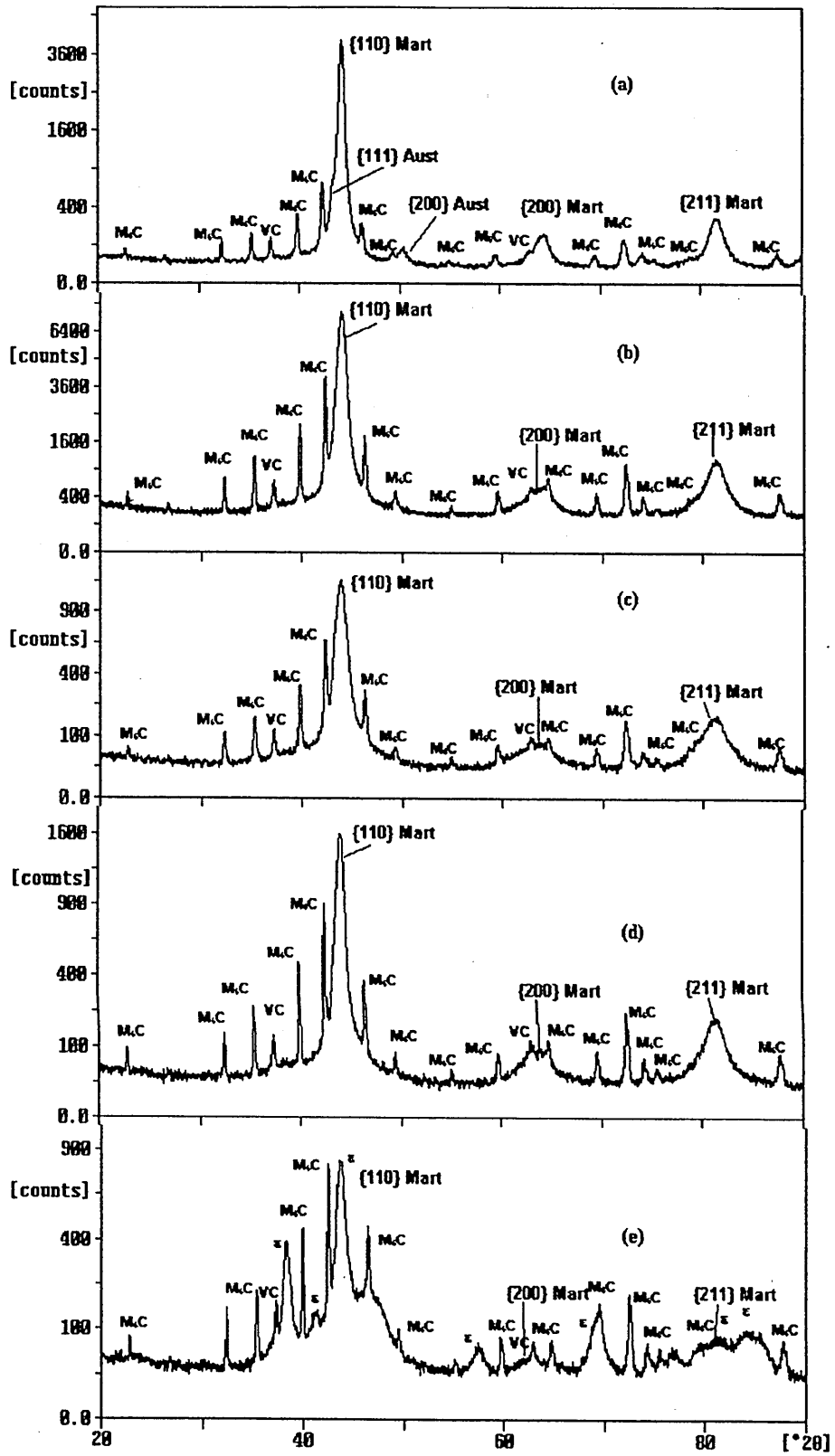

Fig. 6. X-ray diffraction patterns Bragg–Brentano geometry: (a) non-nitrided coupon, (b) nitrided coupon 1, (c) nitrided coupon 2, (d) nitrided coupon 3 and (e) nitrided coupon 4.

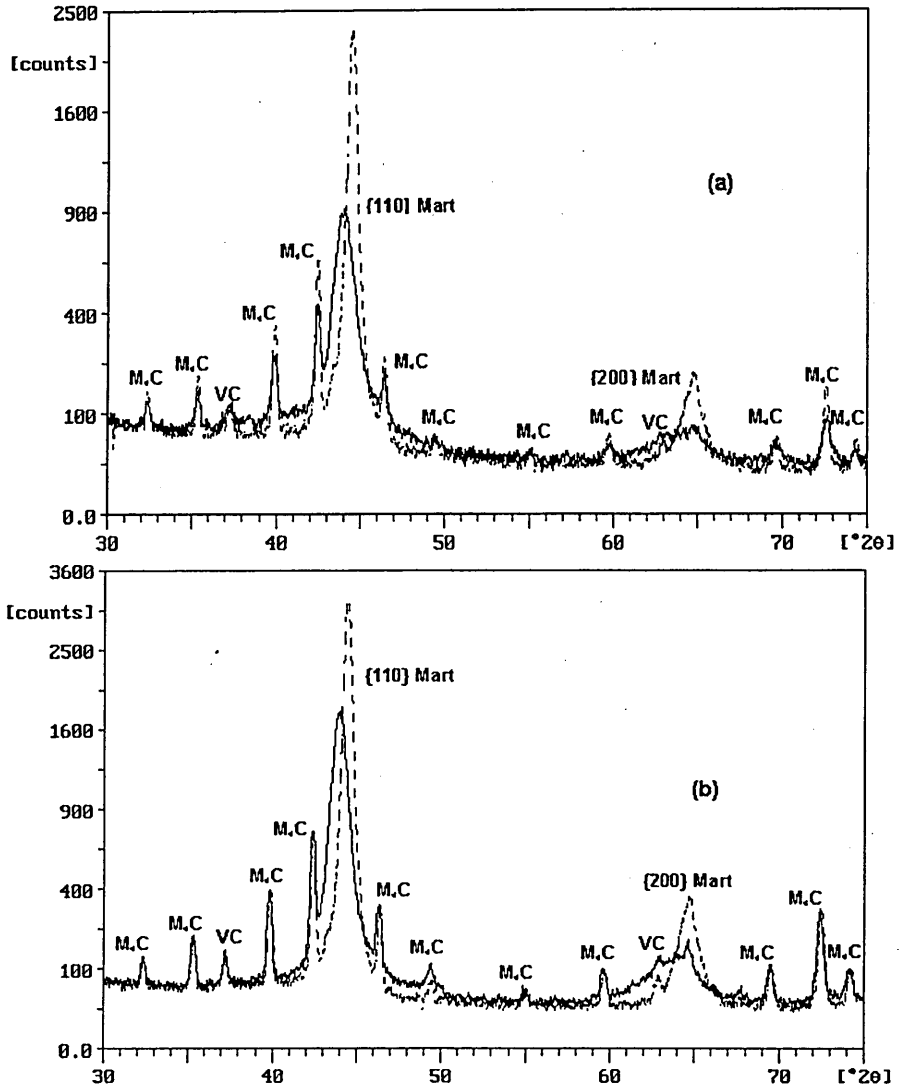

Fig. 7. X-ray diffraction patterns of nitrided coupon 1 (lines) and non-nitrided coupon (dashes) glancing angle parallel beam geometry: (a) 1° incidence and (b) 15° incidence.

the carbon, and eventually the nitrided case becomes more like an Fe–N alloy. Consequently, these similar phases in the nitrided case become more superheated, i.e. in comparison with the similar phases originally present before nitriding, although the nitriding temperature is normally selected to be lower than the tempering temperature of the Fe–C-based steel. Depending on the processing time and the nitrogen content, this may lead to phase coarsening with an associated reduction in hardness. However, this effect is overwhelmed by the level of hardness achieved due to the incorporation of nitrogen.

The XRD diffractograms on the nitrided coupons further substantiate the findings of the nitrogen depth profiles and metallographic examination. No evidence of a compound layer (i.e. either Fe_4N or $Fe_{2-3}N$ phases) was found on the coupons nitrided for 20 min [Fig. 6(a)–(d)]. However, after plasma nitriding, there was considerable broadening and shift of the {110} diffraction peak for α-Fe as the nitrogen content of the diffusion zone increased [Fig. 6(b) and (c)], hence indicating an increase in the residual compressive stress (peak shift) [10–12] and both the dissolution of nitrogen in the iron lattice [9] and the formation of fine precipitates [7,11] (peak broadening). The X-ray diffractogram [Fig. 6(e)] of sample 4 shows the presence of a hexagonal epsilon phase but not an Fe_4N phase, thus further confirming the presence of a compound layer at the surface of sample 4. The formation of epsilon rather than Fe_4N phase is favoured by the presence of carbon in the steel [1,13]. Glancing angle parallel beam X-ray diffractograms at incidence angles of 1 and 15° (penetra-

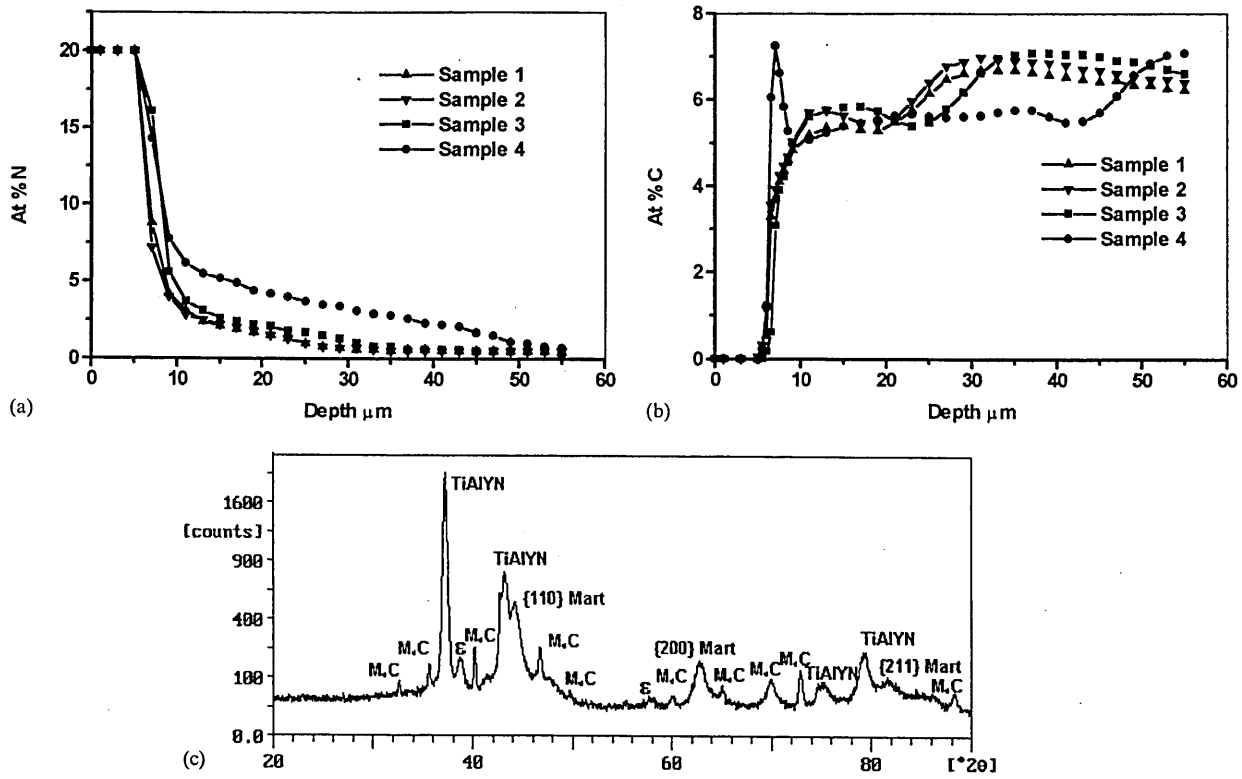

Fig. 8. (a) Glow discharge optical emission spectroscopy (GDOES) nitrogen depth profile on coated coupons 1, 2, 3 and 4. (b) Glow discharge optical emission spectroscopy (GDOES) carbon depth profile on coated coupons 1, 2, 3 and 4. (c) X-ray diffraction pattern of nitrided and coated coupon 4 Bragg–Brentano geometry.

tion depths of 0.3 and 2 μm) are shown in Fig. 7(a) and (b), respectively. At an incidence angle of 1°, the intensity of the reflections from the $(FeWMo)_6C$ phase is significantly lower in the nitrided (dashes) than in the corresponding non-nitrided specimen, whereas at an incidence angle of 15°, the intensity of the reflections from the $(FeWMo)_6C$ phase is similar for nitrided and non-nitrided specimens, respectively, thus indicating a decrease in volume fraction of $(FeWMo)_6C$ due to decarburization. Similar changes in volume fraction of $(FeWMo)_6C$ have been observed after plasma nitriding [13–15].

The previously presented explanation [1] of carbon re-distribution occurring during nitriding only takes into account the physical argument, i.e. carbon migration to stress-free regions. However, this does not take into consideration any possible chemical mechanisms and does not explain the existence of nitrogen under these stresses, though both have similar characteristics. Chemically speaking, the solubility of carbon in both α and γ iron is significantly less than that of nitrogen, and this may explain the interstitial effect of carbon migration during nitriding. From the ternary (Fe–N–C) system [16], nitrogen in ϵ-nitride occupies the octahedral sites in the hexagonal lattice. However, carbon in ϵ-carbide occupies the triangular prismatic sites in the hexagonal ϵ-carbide lattice. In other words, the nitrogen and carbon environments in both ϵ-type nitride and ϵ-type carbide are different. This may explain why nitrogen cannot replace carbon in such carbides. Indeed, the results of glancing-angle X-ray diffraction show that the volume fraction of carbide is decreased near the surface following nitriding, which implies carbide dissolution.

The effect of deposition of a TiAlCrYN hard coating deposited at 450 °C on the nitrogen depth profile on the test coupons has been investigated using GDOES depth profiling [Fig. 8(a)]. In all cases, the depth of nitrogen penetration increased by up to a factor 3. Interpolation of the data from the approximately linear portion of the composition depth profile was performed using a least-squares fit to predict surface concentrations (Table 2). The thermal treatment during coating at 450 °C resulted in further diffusion into the steel core and a decrease in predicted nitrogen content at the surface, for the coupons without a compound layer in the as-nitrided condition. For sample 4, however, the extrapolated values at the surface for coated and un-coated are almost the same. This would indicate that further decomposition of the compound layer occurred during the coating process which released nitrogen for further diffusion into the steel core. After coating the nitrided coupon with a TiAlCrYN film, there is clear

evidence of a further re-distribution of carbon in the nitrided case and a build-up of a carbon-enriched layer at the newly formed nitrided case/core interface [Fig. 8(b)]. This shows further evidence of migration of carbon ahead of the nitriding front. In coupon sample 4, there was also evidence of carbon enrichment at the coating/substrate interface. An XRD diffractogram for the nitrided and coated sample 4 is shown in Fig. 8(c). Although the extrapolated nitrogen profiles indicate some decomposition of the compound layer, the XRD diffraction pattern clearly shows the presence of the epsilon compound layer phase that existed prior to the deposition of a 3 μm thick TiAlCrYN coating.

4. Conclusions

- The nitrogen concentration at the cutting edge of a drill was always systematically higher than in the coupon nitrided under the same conditions due to an increased surface area and current density at the cutting edge.
- Under the standard nitriding conditions (20 min nitriding), there was no evidence of the formation of a compound layer on both drills and coupons. Increasing the nitriding time from 20 to 90 min increased the nitrogen content and produced a compound layer on both drills and coupons.
- The hardness of the drills 10 μm from the cutting edge was significantly higher than the corresponding depth on the flat coupon nitrided under identical conditions, which reflects the higher nitrogen contents present at this depth in the drills.
- Considerable re-distribution of carbon was observed in the nitrided case where the depth profile of carbon was dominated by both the amount of nitrogen and the rate of nitrogen incorporation into the substrate. This causes a secondary hardening effect beneath the primary one that is associated with the introduction of nitrogen.
- Further carbon re-distribution of the nitrided case occurs following the deposition of a 3 μm TiAlCrYN film at 450 °C. This results in an intense enrichment in carbon at the film/substrate interface only when the compound layer was present, which may detrimentally affect the film/substrate adhesion.
- The deposition of a 3 μm TiAlCrYN film on the nitrided coupons at 450 °C resulted in considerable further inward diffusion of nitrogen into the previously un-nitrided core. This reduced the nitrogen gradient but considerably increased the depth of the diffusion zone.

References

[1] Y. Sun, T. Bell, Mater. Sci. Eng. 140 (1991) 419.
[2] M. Van Stappen, B. Malliet, L. Stals, L. De Schepper, J. Roos, J.P. Celis, Mater. Sci. Eng. 140 (1991) 554.
[3] H.-J. Spies, K. Hoeck, E. Broszeit, B. Matthes, W. Herr, Surf. Coat. Technol. 60 (1993) 441.
[4] W.-D. Münz, D. Schulze, F.J. Hauzer, Surf. Coat. Technol. 50 (1992) 169.
[5] L.A. Donohue, I.J. Smith, W.-D. Münz, I. Petrov, J.E. Greene, Surf. Coat. Technol. 9495 (1997) 226.
[6] K. Ozbayal, O.T. Inal, A.D. Romig Jr., Mater. Sci. Eng. 78 (1986) 179.
[7] B.J. Lightfoot, D.H. Jack, Heat Treatment 73, The Metals Society, London, 1975, p. 60.
[8] A. Leyland, D.B. Lewis, P.R. Stevenson, A. Matthews, Surf. Coat. Technol. 62 (1993) 608.
[9] R. Grün, H.-J. Günther, Mater. Sci. Eng. A 140 (1991) 435.
[10] T. Gredic, M. Zlatanovic, N. Popovic, Z. Bogdanov, Surf. Coat. Technol. 5455 (1992) 502.
[11] H.H. Huang, J.L. He, M.H. Hon, Surf. Coat. Technol. 64 (1994) 41.
[12] T. Spalvins, Thin Solid Films 108 (1983) 157.
[13] O.T. Inal, C.V. Robino, Thin Solid Films 95 (1982) 195.
[14] B. Jordanovic, Prakt. Metallogr. 29 (1992) 143.
[15] C.V. Robino, O.T. Inal, Mater. Sci. Eng. 59 (1982) 79.
[16] D.H. Jack, K.H. Jack, Mater. Sci. Eng. 11 (1973) 1.